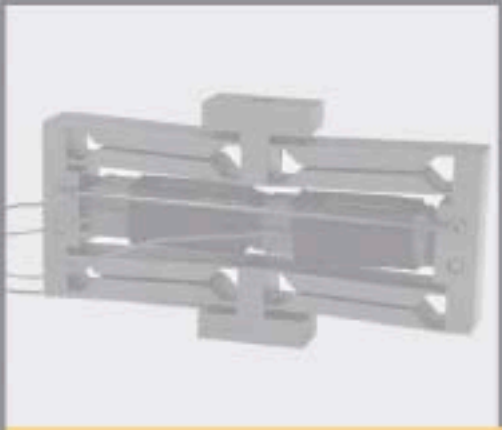

Nicolae Lobontiu

COMPLIANT MECHANISMS
Design of Flexure Hinges

CRC PRESS

COMPLIANT MECHANISMS
Design of Flexure Hinges

COMPLIANT MECHANISMS
Design of Flexure Hinges

Nicolae Lobontiu

CRC PRESS

Boca Raton London New York Washington, D.C.

Library of Congress Cataloging-in-Publication Data

Lobontiu, Nicolae.
Compliant mechanisms : design of flexure hinges / Nicolae Lobontiu.
p. cm.
Includes bibliographical references and index.
ISBN 0-8493-1367-8 (alk. paper)
1. Mechanical movements—Design and construction.
2. Hinges—Design and construction. I. Title
TJ181 .L63 2002
621.8′2—dc21 2002073795

International Standard Book Number 0-8493-1367-8
Library of Congress Card Number 2002073795
Printed in the United States of America 1 2 3 4 5 6 7 8 9 0
Printed on acid-free paper

Dedication

To Simona, Diana, and Ioana
for our loving togetherness

To my parents, Nicolae and Ana

To Dr. Ephrahim Garcia

Preface

This book is dedicated to flexure hinges, which are the main constituents of compliant mechanisms. The flexure hinge, alternatively called flexural pivot, consists of a flexible, slender region between two rigid parts that must undergo limited relative rotation in a mechanism (which will be called *compliant*) due to the presence of at least one flexure hinge. Under the combined action of external loading and actuation, the flexure hinge bends and thus produces the relative rotation between the adjacent members. Being monolithic with the rest of the mechanism for the vast majority of applications, a flexure hinge offers several advantages over classical rotation joints, such as no friction losses, no need for lubrication, no hysteresis, compactness, capacity to be utilized in small-scale applications, ease of fabrication, virtually no assembly, and no required maintenance.

The flexure hinges are incorporated in a large number of applications, both civil and military, including translation micropositioning stages, piezoelectric actuators and motors, high-accuracy alignment devices for optical fibers, missile-control devices, displacement and force amplifiers/deamplifiers, orthotic prostheses, antennas, valves, scanning tunneling microscopes, accelerometers, gyroscopes, high-precision cameras, nanolithography, robotic microdisplacement mechanisms, nanoscale bioengineering, small-scale insect-like walking robots, actuation devices for unmanned micro aerial vehicles, or nano-imprint technology. One of the rapidly growing areas where flexure hinges are massively applied is the microelectromechanical system (MEMS) sector, where the very nature of the microscale structure of such mechanisms, together with their fabrication technology, demands almost exclusive utilization of flexure hinges as connecting joints between quasi-rigid members.

The book is primarily intended for industrial practitioners, researchers, and academics involved in designing and developing flexure-based compliant mechanisms in such areas as mechanical engineering, aerospace engineering, robotics, MEMS, and biomedical engineering. It can also serve as a supplemental text for graduate students in universities where compliant mechanisms are a curriculum subject.

The book originated from the perceived need for an information source dedicated to current problems in the design of flexure hinges and flexure-based compliant mechanisms in both macroscale and MEMS applications in a manner that would resonate with the reality of a multitude of practical engineering cases. Two main directions have been taken in this book. The first targets the design pool of flexure hinges through a systematic approach and the introduction of several new flexure configurations in the hope that the interested designer might opt for a specific flexure solution if presented

with an ample variety of choices. This aspect is all but trivial, as minor changes in the geometry of a flexure hinge might result in substantial modifications at the output port of a compliant mechanism. The second direction of the book addresses the modeling tier by recognizing that in most cases the flexure hinges will operate under small displacements. The reader acquainted with flexure modeling and design would probably agree that, except for the finite-element analysis available through commercially available software (which is predominantly the variant of choice in a large number of applications), the accepted modeling paradigm currently in operation is based on two main hypotheses: (1) the flexure hinges are flexible *constant* cross-section members, and (2) they are subject to *large deformations*. Consequently, the modeling procedure substitutes a flexure hinge with a purely rotational joint equipped with a torsional-spring stiffness. The resulting model of the flexure hinge is subsequently incorporated into a classical rigid-link mechanism model of the specific device being studied, and further static and dynamic calculations are performed according to standard procedures.

The reality is that only in a few occasions are the two fundamental premises mentioned above (constant cross-section and large deformations) concomitantly met. In the vast majority of practical situations, the flexure hinges are actually and deliberately designed to function within a small-displacement environment. The supporting rationale is twofold, as either the application itself requires this type of condition (for instance, in precision mechanisms where the output displacements are inherently small) or the physical dimensions of the flexure hinge do not permit large deformations that would automatically generate stresses over the allowable limits. Moreover, the flexure hinge geometry is seldom of constant cross-section because the fabrication technology currently in use might not allow this particular geometry to be produced in either macroscale or MEMS monolithic applications. The radius of the wire tool in electrodischarge machining, for instance, has a finite, nonzero value and, as a result, the corner of a flexure hinge fabricated by this procedure will always be filleted. Similarly, the design process itself attempts to avoid the type of geometry that would induce undesirable stress concentration in the corner areas.

Previous work supports the approach followed in this book. A very solid paper written by Paros and Weisbord in the 1960s convincingly demonstrated that a circular flexure hinge is a complex spring that not only produces the desired relative rotation between two adjacent rigid links but is also deforming axially and out of plane. The vision expressed by the authors in this fundamental paper is compelling, and present-day flexure-based applications reveal that all deformational facets of a flexure hinge have to be accounted for if an accurate assessment of the performance of a compliant mechanism is to be achieved. The path followed by Paros and Weisbord has been revisited only recently, and the present work is a modest addition to this work.

This book attempts to provide practical answers to the problems of efficiently modeling, analyzing, deciding on, and designing devices that include flexure hinges. It contains many ready-to-use plots and simple equations describing

several flexure types for professionals who need speedy solutions to their current applications. For the researcher who would prefer to find specific answers to a particular design configuration (which is probably not covered here), the book contains self-contained, easy-to-apply mathematical tools that provide guidance for real-time problem solving of further applications.

Several original features are included in this book:

- The book introduces new types of single-axis flexure hinge configurations (e.g., parabolic, hyperbolic, inverse-parabolic, secant) that supplement such classic geometries as circular, corner-filleted, and elliptical and are designed for planar compliant mechanism applications.
- The same configurations are addressed for multiple-axis (revolute) flexure hinges for spatial compliant mechanism applications.
- Newly introduced are the two-axis flexure hinges that are capable of displaying a selective response over two different compliance ranges in spatial applications.
- For all the single-axis flexure hinges, both longitudinally symmetric and nonsymmetric configurations are analyzed, and their corresponding spring rates are explicitly given.
- Short flexures and the associated shearing effects are also modeled for all flexure configurations in terms of their compliance.
- Flexure hinges are studied from a performance-oriented viewpoint in a unitary manner: flexibility, precision of rotation, stress limitations, and energy consumption are factors defined and analyzed by means of closed-form compliance equations.
- Inertia and damping properties are also derived, consistent with the compliance formulation, so that a flexure hinge can be fully characterized and included in the dynamic model of a flexure-based compliant mechanism that can be solved to evaluate its free or forced response. The inertia and damping properties of a flexure hinge are modeled by following either the long (Euler–Bernoulli) or short (Timoshenko) member hypotheses.
- An original finite-element approach is developed whereby the flexure hinges are assimilated to line elements; this approach reduces the problem dimensionality and allows us to perform static and modal/time-history analyses in a simple fashion.
- Also treated are more advanced topics related to flexure hinges, such as shape optimization, buckling, torsion of noncircular variable cross-section members, nonhomogeneous flexures, thermal effects, and large deformations.
- The book includes a list of novel industrial applications, both macro- and microscale (MEMS), for which flexure hinges are instrumental.

The book is formally organized into seven chapters. The first chapter presents the basic characteristics, scope and applications, and advantages and limitations of using flexure hinges and flexure-based compliant mechanisms instead of mechanisms based on classical rotation joints. An argument is developed regarding the importance of flexure hinges in the overall design of compliant mechanisms. Also discussed is the approach taken here of modeling and analyzing the flexure hinges by considering their variable cross-sections and small-displacement conditions.

Chapter 2 develops the generic mathematical model resulting in the compliance closed-form equations for all the flexure types that are presented in this work. The nature of the presentation in this chapter is primarily mathematical and equation based. This chapter gives an alternative to the time-consuming classical finite-element analysis (by using commercially available software) through utilizing an approach of closed-form compliance equations to evaluate the performance of flexure hinges. Specifically, a flexure hinge is characterized by quantifying its rotation capacity, sensitivity to parasitic motions, precision of rotation, level of stress (fatigue failure considerations), and energy consumption. The generic mathematical model previously formulated is applied to be specific to several flexure configurations (the majority are new types). Included are flexure hinges for such two-dimensional applications as constant rectangular cross-section and conic sections (circular, elliptical, parabolic, hyperbolic), as well as inverse parabolic and secant profiles. The validity of the closed-form compliance equations for the various flexure types is checked out by finite-element simulation, experimental measurements, and verifying that the limit case of a constant rectangular cross-section flexure can be retrieved from each individual variable cross-section flexure. The configurations mentioned previously are also considered in deriving closed-form compliance equations for multiple-axis flexure hinges in three-dimensional applications (with rotational symmetry), as well as for two-axis configurations. Conclusions and design recommendations are thus derived regarding the adequacy of employing a specific flexure in a particular application where certain performance functions are required. Graphs, plots, and tables are given for handy selection of flexures in terms of design performance criteria.

Chapter 3 is dedicated to the static modeling and analysis of flexure-based compliant mechanisms (mechanisms that incorporate only rigid links, connected by flexure hinges). A methodology is presented that enables designing serial, parallel, and hybrid (serial/parallel) flexure-based compliant mechanisms for two- and three-dimensional applications. The procedure integrates the various compliance factors into a force–displacement model for the entire mechanism. Output performance qualifiers, such as mechanical advantage, bloc load, stiffness, energy efficiency, and precision of motion, are defined and discussed here.

Chapter 4 studies the dynamic aspects of flexure-based compliant mechanisms. Based on an approach that utilizes Lagrange's equations, inertia and damping properties are derived for the different types of flexure hinges

presented so far to allow formulation of the corresponding lumped-parameter dynamic equations of flexure-based compliant mechanisms. Both the inertia and damping properties are formulated in a manner that is consistent with the modality of deriving the compliance (stiffness) characteristics in such a way that a particular flexure hinge is unitarily represented as having finite degrees of freedom. Modal and time-history analyses are thus possible by integrating the flexure properties into the ensemble of rigid components.

Chapter 5 presents an original finite-element approach to flexure hinges and flexure-based compliant mechanisms, as an alternative modeling and analysis instrument. Instead of treating the flexure hinge with its full two- or three-dimensional geometry details (by using two- or three-dimensional finite elements), which is how the commercially available finite-element software solves these cases, this approach reduces the problem of dimensionality by defining the flexure hinge as a three-node line element. Elemental stiffness and mass matrices are formulated for the various flexure types that were previously introduced. It is thus possible to study the finite-element static and modal response of two- and three-dimensional flexure hinges.

Chapter 6 presents several miscellaneous topics that are important in accurately characterizing the flexure hinges. Addressed are topics that apply to both macroscale and MEMS applications, such as shape optimization, buckling, torsion of noncircular variable cross-section members, flexures fabricated of several materials, thermal effects, and large deformations. Presented also are aspects of actuation, materials, and fabrication procedures for both macro- and MEMS-scale applications.

Chapter 7 presents several classical and up-to-date examples of flexure-based applications and illustrates both macro- and microscale (MEMS) engineering designs.

As previously mentioned, the book is dedicated to flexure hinges that are indispensable construction bricks for miniature compliant mechanisms that are highly energy efficient and are capable of providing very finely tuned output in high-end industrial applications such as those in the photonics, laser optics, or telecommunications industries. Nano-engineering and nano-biomechanical engineering, as parts of the aggressively growing MEMS domain, are areas that benefit from incorporating specifically designed flexure hinges into their miniature compliant devices and mechanisms.

The major reason for writing this book is to offer a core of modeling tools that would enable the designer to play around a bit with different flexure hinge configurations in terms of their spring, inertia, and (possibly) damping characteristics and to make a more informed choice before (inevitably, perhaps) resorting to the classical finite-element software in order to fully solve a flexure-based compliant mechanism problem. Despite all efforts, the book probably is not error free, and I would welcome feedback from the interested reader.

Acknowledgments

My special gratitude goes to Dr. Ephrahim Garcia of Cornell University who, a few years ago in the cafeteria at Vanderbilt University, sketched a flexure hinge on a piece of paper and thus opened a door for me into this world. I would like to thank Dr. Jeffrey S.N. Paine of Dynamic Structures and Materials (Franklin, TN) who offered me the opportunity of analyzing the subject of flexure hinges from so many perspectives. I would also like to thank Dr. Michael Goldfarb of Vanderbilt University and Dr. Stephen Canfield of Tennessee Technological University for their fruitful interaction over the years. My thoughts and thanks go also to my fellow colleagues in the Strength of Materials Department of the Technical University of Cluj-Napoca, Romania.

I would like to express my gratitude to Mr. Murray Johns of Dynamic Structures and Materials; Dr. Peter Warren of Foster-Miller; Mr. Rick Donegan of TRW Aeronautical Systems; Dr. Jay Hammer of MEMS Optical; and Mr. John Biondi of Piezomax Technologies, who graciously allowed me to show their work in this book.

It is a real pleasure to address my special thanks to Ms. Cindy R. Carelli, the Acquisition Editor, who believed in this project from the beginning and who professionally assisted and guided me all along the long way. I was fortunate to be able to work with her. I was also lucky to meet Mr. Jamie B. Sigal, the Project Coordinator, whose prompt feedback, informative answers, and kind interaction helped me to sail smoothly through the more rocky technicalities of writing a book. I would also like to express my gratitude to Mrs. Gerry Jaffe, the Project Editor, who, intelligently and tactfully, added the final touch to the manuscript.

Last, but not least, I would like to thank my wife, Simona, and my daughters, Diana and Ioana, who stood by me in this enterprise despite the precious time that I was spending away from them.

About the Author

Nicolae Lobontiu received his B.Sc. and Ph.D. degrees in mechanical engineering from the Technical University of Cluj-Napoca, Romania, in 1985 and 1996, respectively. From 1985 to 1990, he worked as a mechanical engineer at two engineering companies in Romania and then, until 1997, as an assistant professor and junior associate professor in the Strength of Materials Department within the aforementioned university. He then worked as a postdoctoral associate at Vanderbilt University (Nashville, TN) until 1999, when he joined Dynamic Structures and Materials (Franklin, TN), where he worked as a Research Engineer until 2002. He currently holds a research position at Cornell University (Ithaca, NY) within the Sibley School of Mechanical and Aerospace Engineering. His research interests include modeling and designing flexure hinges and compliant mechanisms, finite/boundary element analysis, and rotordynamics.

Contents

1 Introduction 1

2 Compliance-Based Design of Flexure Hinges 17
2.1 Introduction 17
2.2 Generic Mathematical Formulation 24
2.2.1 Introduction 24
2.2.2 The Reciprocity Principle 25
2.2.3 Castigliano's Displacement Theorem 29
2.2.4 Theories and Criteria of Material Failure 34
2.3 Single-Axis Flexure Hinges for Two-Dimensional Applications 43
2.3.1 Introduction 43
2.3.2 Generic Formulation and Performance Criteria 45
2.3.3 Constant Rectangular Cross-Section Flexure Hinge 61
2.3.4 Circular Flexure Hinge 63
2.3.5 Corner-Filleted Flexure Hinge 67
2.3.6 Parabolic Flexure Hinge 72
2.3.7 Hyperbolic Flexure Hinge 76
2.3.8 Elliptical Flexure Hinge 79
2.3.9 Inverse Parabolic Flexure Hinge 82
2.3.10 Secant Flexure Hinge 85
2.3.11 Verification of the Closed-Form Compliance Equations 88
2.3.12 Numerical Simulations 91
2.4 Multiple-Axis Flexure Hinges for Three-Dimensional Applications 110
2.4.1 Introduction 110
2.4.2 Generic Formulation and Performance Criteria 111
2.4.3 Cylindrical Flexure Hinge 118
2.4.4 Circular Flexure Hinge 119
2.4.5 Corner-Filleted Flexure Hinge 120
2.4.6 Parabolic Flexure Hinge 121
2.4.7 Hyperbolic Flexure Hinge 122
2.4.8 Elliptical Flexure Hinge 123
2.4.9 Inverse Parabolic Flexure Hinge 124
2.4.10 Secant Flexure Hinge 125
2.4.11 Limit Verification of Closed-Form Compliance Equations 126
2.4.12 Numerical Simulations 126

2.5 Two-Axis Flexure Hinges for Three-Dimensional Applications 133
2.5.1 Introduction 133
2.5.2 Generic Formulation and Performance Criteria 134
2.5.3 Inverse Parabolic Flexure Hinge 138
2.6 Conclusions 141

3 Statics of Flexure-Based Compliant Mechanisms 145
3.1 Introduction 145
3.2 Planar Compliant Mechanisms 150
3.2.1 Planar Serial Compliant Mechanisms 150
3.2.2 Planar Parallel Compliant Mechanisms 181
3.2.3 Planar Hybrid Compliant Mechanisms 189
3.3 Spatial Compliant Mechanisms 195
3.3.1 Spatial Serial Compliant Mechanisms 195
3.3.2 Spatial Parallel and Hybrid Compliant Mechanisms 198

4 Dynamics of Flexure-Based Compliant Mechanisms 207
4.1 Introduction 207
4.2 Elastic Potential Energy for Individual Flexure Hinges 211
4.2.1 Single-Axis Flexure Hinges 211
4.2.2 Multiple-Axis Flexure Hinges 213
4.2.3 Two-Axis Flexure Hinges 213
4.3 Kinetic Energy for Individual Flexure Hinges 214
4.3.1 Introduction and the Rayleigh Principle 214
4.3.2 Inertia Properties of Flexure Hinges as Long (Euler–Bernoulli) Members 216
4.3.3 Inertia Properties of Flexure Hinges as Short (Timoshenko) Members 229
4.4 Free and Forced Response of Flexure-Based Compliant Mechanisms 231
4.4.1 Introduction 231
4.4.2 Planar Flexure-Based Compliant Mechanisms 236
4.4.3 Spatial Compliant Mechanisms 246
4.5 Damping Effects 251
4.5.1 Introduction 251
4.5.2 Damping Properties of Flexure Hinges as Long (Euler–Bernoulli) Members 257
4.5.3 Damping Properties of Flexure Hinges as Short (Timoshenko) Members 261

5 Finite-Element Formulation for Flexure Hinges and Flexure-Based Compliant Mechanisms 265
5.1 Introduction 265

5.2 Generic Formulation 269
5.2.1 Elemental Matrix Equation 271
5.2.2 Global Matrix Equation (Assembly Process) 272
5.3 Elemental Matrices for Flexure Hinges 276
5.3.1 Single-Axis Flexure Hinge Finite Element for Two-Dimensional Applications 277
5.3.2 Multiple-Axis Flexure Hinge Finite Element for Three-Dimensional Applications 285
5.3.3 Two-Axis Flexure Hinge Finite Element for Three-Dimensional Applications 293
5.4 Elemental Matrices for Rigid Links 299
5.4.1 Two-Dimensional Rigid Link Modeled as a Two-Node Line Element 299
5.4.2 Three-Dimensional Rigid Link Modeled as a Two-Node Line Element 305
5.5 Application Example 310
Appendix: Stiffness and Mass Matrices for Single-Axis, Corner-Filleted Flexure Hinge Finite Elements 317

6 Topics Beyond the Minimal Modeling Approach to Flexure Hinges 345
6.1 Large Deformations 345
6.2 Buckling 354
6.3 Torsion of Noncircular Cross-Section Flexure Hinges 365
6.3.1 Symmetric Single-Axis Flexure Hinges 367
6.3.2 Nonsymmetric Single-Axis Flexure Hinges 369
6.3.3 Parabolic-Profile Two-Axis Flexure Hinges 370
6.4 Composite Flexure Hinges 371
6.4.1 Compliance Properties 373
6.4.2 Inertia Properties 374
6.4.3 Damping Properties 375
6.5 Thermal Effects 376
6.5.1 Errors in Compliance Factors Induced through Thermal Effects 376
6.5.2 Compliance Aspects for Nonuniform Temperature Change: Castigliano's Displacement Theorem for Thermal Effects 380
6.6 Shape Optimization 382
6.7 Means of Actuation 390
6.7.1 Macro-Actuation 390
6.7.2 MEMS Actuation 396
6.8 Fabrication 400
6.8.1 Macroscale Fabrication 401
6.8.2 MEMS-Scale Fabrication 404

7 Applications of Flexure-Based Compliant Mechanisms 413
7.1 Macroscale Applications 413
7.2 Microscale (MEMS) Applications 421
7.2.1 Single-Flexure Microcompliant Mechanisms 422
7.2.2 Multi-Flexure Compliant Micromechanisms 431
7.2.3 Some Novel Microapplications 433

Index 437

1

Introduction

This introductory chapter gives a brief presentation of flexure hinges and flexure-based compliant mechanisms for macro- and microscale applications by highlighting the main traits defining these mechanical members/devices. An outline of the treated subjects and of the associated approach in this book is also sketched here in order to identify and possibly locate the work in the context of similar dedicated information that has already been published.

A flexure hinge is a thin member that provides the relative rotation between two adjacent rigid members through flexing (bending), as shown in Figure 1.1, where a conventional rotational joint is compared to a flexure hinge. In terms of this rotary function, a flexure hinge can be considered the structural correspondent of a bearing with limited rotation capability, as illustrated in Figure 1.2.

In a classical rotary bearing, the relative rotation takes place between a shaft and its housing, these mating parts being concentrically located, and the rotation can be limited to a specific angular sector, as indicated in Figure 1.2a. A flexure hinge can provide a similar rotary output, the only difference consisting in the fact that the "centers" of the two adjacent members undergoing the relative rotation are no longer collocated, as shown in Figure 1.2b.

Physically, a flexure hinge can be realized in two different ways:

- Use an independently fabricated member (such as a strip or shim in two-dimensional applications or a cylinder-like part in three-dimensional applications) to connect two rigid members that are designed to undergo relative rotation.
- Machine a blank piece of material so that a relatively slender portion is obtained that will be the flexure hinge. In this case, the flexure is integral (or monolithic) with the parts it joins together.

As already mentioned, the flexure hinge consists of an elastically flexible, slender region between two rigid parts that must undergo relative limited rotation in a mechanism (which we will call *compliant* due to the presence of at least one flexure hinge) that is supposed to achieve a specific task. The flexure hinge is monolithic with the rest of the mechanism for the vast

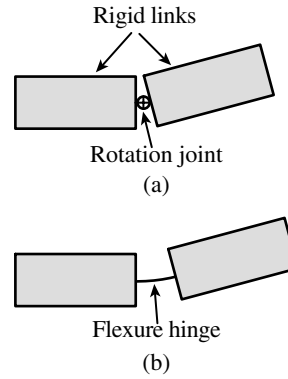

FIGURE 1.1
Joints enabling relative rotation in mechanisms: (a) classical rotation joint; (b) flexure hinge.

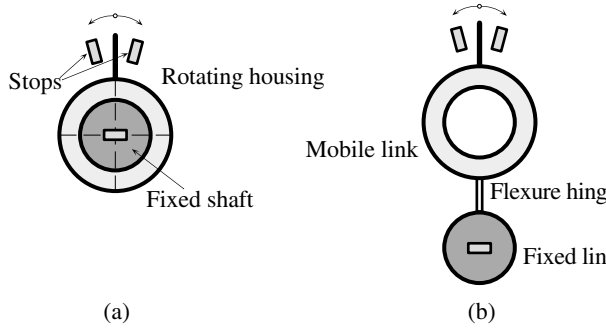

FIGURE 1.2
Functional similarity between rotary bearings and flexure hinges: (a) collocated (concentric) rotation produced by a classical rotary bearing; (b) noncollocated rotation produced by a flexure hinge.

majority of applications, and this is the source of its advantages over classical rotation joints. Among the benefits provided by flexure hinges, the most notable are:

- No friction losses
- No need for lubrication
- No hysteresis
- Compactness
- Capacity to be utilized in small-scale applications
- Ease of fabrication
- Virtually no maintenance needed

Flexure hinges that are monolithic with the mechanisms they are part of do not require repair, as the mechanisms will operate until something fails (usually the flexures) due to fatigue or overloading. They definitely require

inspection, which is particularly true immediately after fabrication, when it is necessary to check the errors induced in the ideal geometry by machining.

Flexure hinges do have limitations, however, and a few examples of such drawbacks are:

- The flexure hinges are capable of providing relatively low levels of rotations.
- The rotation is not pure because the deformation of a flexure is complex, as it is produced by axial shearing and possibly torsion loading, in addition to bending.
- The *rotation center* (for short flexure hinges, this role is assumed by the symmetry center of the flexure) is not fixed during the relative rotation produced by a flexure hinge as it displaces under the action of the combined load.
- The flexure hinge is usually sensitive to temperature variations; therefore, its dimensions change as a result of thermal expansion and contraction, which leads to modifications in the original compliance values.

For two-dimensional applications in which the flexure hinge is fabricated by removing material from a blank piece, the manufacturing processes that are being utilized for this purpose include end-milling, electrodischarge machining (EDM), laser cutting, metal stamping, or photolithographic techniques for microelectromechanical systems (MEMS). In two-dimensional applications, the flexure is supposed to be compliant only about one axis (the *input*, *compliant*, or *sensitive axis*), along which the relative rotation between the adjacent rigid parts is taking place, and stiff (as much as possible) about all other axes and motions. The two-dimensional flexure hinges are usually symmetric about both the longitudinal and middle transverse axes. There are cases in which the longitudinal-axis symmetry is violated (only one side of the flexure is machined whereas the other side is flat, for instance), but these cases are less frequent.

In three-dimensional applications, the flexure hinge can be machined by lathe-turning or precision casting. Two-axis flexure hinges, for instance, enable bending and the resulting relative rotation about two mutually perpendicular compliant axes generally at different spring rates. For other flexure hinge configurations that have rotational symmetry (they are revolute), bending is nonspecifically possible about any axis that is perpendicular to the axial direction; therefore, the compliant axis can instantaneously be set by the loading/boundary conditions of the three-dimensional compliant mechanism application. In order to be consistent with the terminology that has already been utilized so far, such flexure hinges are called *multi-axis*. Figure 1.3 illustrates single-, multi-, and two-axis flexure hinges. It is obvious that a reciprocal dependence exists between the geometry of a specific flexure hinge and the type of application in which it is incorporated, as illustrated in Figure 1.4.

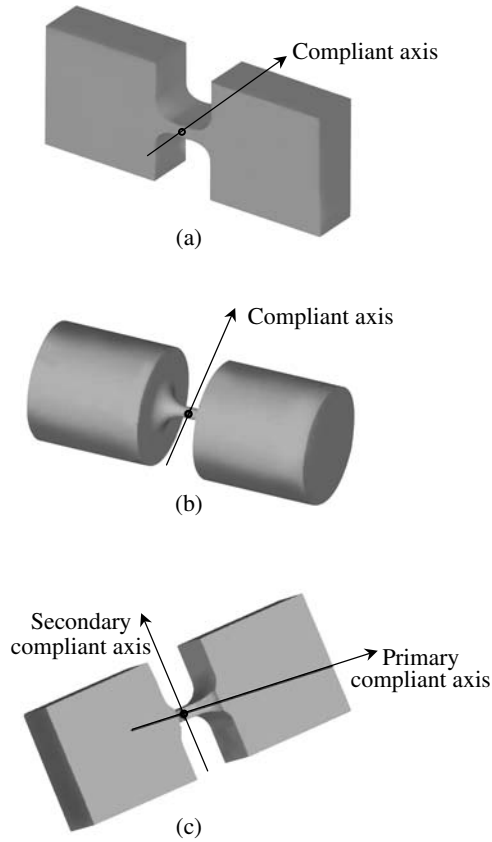

FIGURE 1.3
Three main categories of flexure hinge configurations: (a) single-axis; (b) multiple-axis (revolute); (c) two-axis.

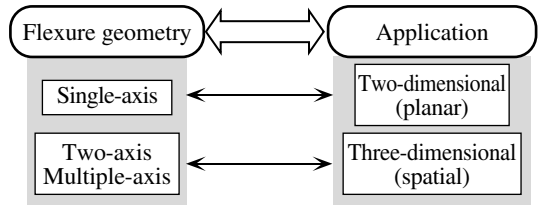

FIGURE 1.4
Relationship between the flexure hinge configuration and the type of application.

Single-axis flexure hinges are designed for two-dimensional compliant mechanisms that have a planar motion, whereas two- and multi-axis flexures are implemented in three-dimensional applications in order to take advantage of the capacity to producing relative rotation about two or more compliant axes.

Flexure hinges are largely utilized in the automobile and aviation industries in such applications as acceleration/speed/position sensors, adaptable seats, air bags, fault-tolerant connectors, single-surface independent aircraft control devices, actuators for configurable-geometry foils, steering columns, antifriction bearings, suspension systems, satellite small-angle tilting mechanisms, laser-beam communication systems between spacecraft, or flexible couplings. The biomedical industry is also a beneficiary of mechanisms that are based on flexure hinges, and applications in this category include devices for vascular catheters, urethral compression devices, intravascular endoprostheses, cardiac massage apparatuses, orthotic devices, and biopsy devices. Other areas such as the computers and fiberoptics industries also have applications that incorporate flexure hinges; examples here include disc drive suspensions, laser systems, optical mirrors, optical discs, microscopes, cameras, print heads, optical scanning equipment, vibrating beam accelerometers, keyboard assemblies, kinematic lens mountings, and rotary actuators for disc drives. Designs found in various other fields are based on flexure hinges; a few application examples are coin packaging systems, systems for remotely playing percussion musical instruments, collapsible fishing net mechanisms, table-tennis ball retrieving systems, snow blade attachments, foot propulsion devices for float tube users, bicycle seats, steerable wheels for roller and ice skates, respiratory masks, grinding/polishing machines, fluid jet cutting machines, and flywheels. The compliant MEMS are almost entirely based on microdevices that generate their motions by means of flexure-like members; examples in this industry include optical switches, miniature load cells, flexible mounts for imaging masks, load-sensitive resonators, gyroscopes, gravity gradiometers, disc memory head positioners, wire bonding heads, microfluidic devices, accelerometers, scan modules for bar code readers, and cantilevers for microscopy.

A compliant (or flexible) mechanism is a mechanism that is composed of at least one component (member) that is sensibly deformable (flexible or compliant) compared to the other rigid links. The compliant mechanisms, therefore, gain their mobility by transforming an input form of energy (mechanical, electric, thermal, magnetic, etc.) into output motion, as illustrated in Figure 1.5.

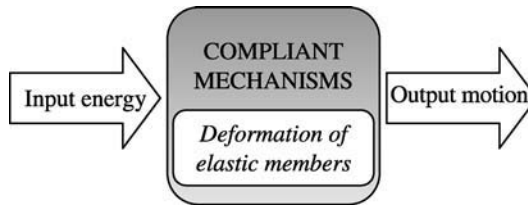

FIGURE 1.5
Schematic representation of a compliant mechanism in terms of its energy trade.

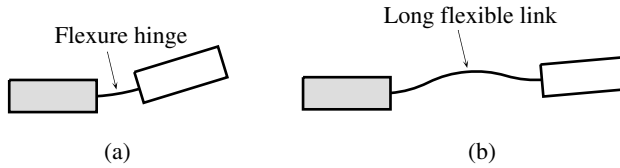

FIGURE 1.6
Compliant mechanisms base their motion on two types of flexible connectors: (a) flexure hinge; (b) long flexible link.

Large numbers of compliant mechanisms are constructed of rigid links that are interconnected by flexure hinges designed to undergo relatively low levels of rotation. Because of the advantages that were previously enumerated, the flexure hinges and the rigid links are most preferably built in a monolithic configuration (this is particularly valid for two-dimensional applications). The present work intends to cover this predominant category of compliant mechanisms that incorporate flexure hinges. A relatively reduced number of compliant mechanisms have compliant links, in addition to, or other than, the flexure hinges which are specifically designed to undergo large deformations; applications include snap-trough devices with compliant members that can substantially bend or buckle. Figure 1.6 illustrates the two different categories of flexible connectors mentioned earlier.

A brief discussion on terminology would be useful at this stage in order to clarify the two main denominations used in this book: *flexure hinges* and *compliant mechanisms*. In a paper published in 1965, Paros and Weisbord[1] gave a thorough analytical presentation of single-axis and two-axis circular flexure hinges. The authors of this paper interchangeably utilized the terms *flexure hinge* and *flexure* to denote a mechanical member that is "compliant in bending about one axis but rigid about the cross axes" and mentioned that flexure hinges are incorporated in applications where angular motion is required about an axis—the compliant axis. The key merit of this seminal work consisted in the clear mathematical definition of a flexure hinge as a spring element that displays two distinct behaviors: It is compliant about one axis, in order to produce the desired rotation, and stiff (as much as possible) in all other motions about the other axes, in order to prevent or minimize the respective motions. Paros and Weisbord[1] provided analytical equations, both exact and approximate, for the spring rates (reciprocal to compliances) of single-axis and two-axis circular symmetric flexures in terms of the motions generated through consideration of bending and axial effects. The alternative terminology of *flexural pivot* has also been utilized over the years in referring to the same mechanical member, but the term has also been applied to designate a special application design that will be presented in Chapter 7. The *notch hinge* terminology is also being employed by several authors (for instance, see Smith[2]), especially for single-axis flexure hinges, in order to emphasize the prevalent fabrication procedure of such flexures,

which mainly removes material from a blank piece in order to obtain the final flexure configuration. The intention of preserving the original terminology introduced by Paros and Weisbord[1] will be evident within this book, however. The terms *flexure hinge* or simply *flexure* will be used to denote the flexible member that produces relative and limited rotation between two rigid links through its bending. Also employed will be the notions of *single-axis*, *two-axis*, and *multi-axis* flexures to address the capability of producing rotation about one axis or about two or many different axes, respectively, as well as the term of *compliant* (*sensitive*) *axis* to denote the rotation axis. The term *compliance* will also be employed in the original definition given by Paros and Weisbord[1] such that the term will refer to the quantity that is the reciprocal of one flexure's spring rate (or stiffness).

Whereas there is relatively little dispute over the accepted terminology of flexure hinges, the other term, *compliant*, which is key to this book, deserves a bit of discussion. In a book written in 1993, Midha[3] employs the qualifiers *elastic* or *flexible* for all the mechanisms that are subject to elastic deformations, whereas *compliant* mechanisms are considered to be the subclass of flexible mechanisms that undergo *large* deformations. A closer consideration of this separation between elastic, as a larger group, and compliant, as a component subgroup, would suggest that the distinction is primarily situational/functional and not structural. It can easily lead to the interpretation or inference that a mechanism undergoing large deformations is compliant, whereas the same mechanism, subject to small deformations, is elastic. On the other hand, the literature dedicated to this topic currently utilizes the term *compliant* (see, for instance, Howell[4]) to denote mechanisms that gain mobility through deformations of their elastic components without any specific mention of the distinction between small and large displacements. Historically speaking, the term *compliance* is rather new, compared to *elastic* or *flexible*, but appears to be a convenient and therefore preferred qualifier in the vast majority of titles that cover research dedicated to large- and/or small-scale mechanisms. Based on these considerations, the term *compliant* will consistently be utilized throughout this book to denote and encompass those mechanisms that produce their output motion through the elastic deformation of their flexible connectors (the flexure hinges in the present case). Such usage is by no means a departure from the distinction promoted by Midha,[3] and *compliant*, in the sense utilized here, implies no specific and therefore substantial differences compared to the semantically equivalent terms of *elastic* and *flexible*. It is also consistent with the early denominations introduced by Paros and Weisbord,[1] who utilized the term *compliant* to denote the capacity of deformation in bending about an axis of a flexure hinge.

Another disputable topic is whether these devices that are based on flexure hinges are mechanisms or just plain structures. The problem is not trivial, at least from a formal standpoint, because, on one hand, the compliant devices are monolithic (and can therefore be considered as being structures), but, on the other hand, they are mobile and transform a form of energy into output motion (and as a consequence can be considered mechanisms). As also

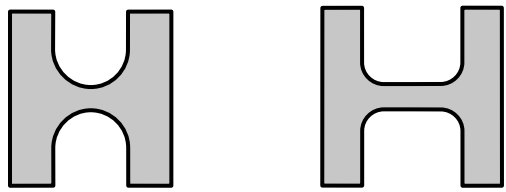

FIGURE 1.7
Two commonly utilized flexure hinge configurations for two-dimensional applications: (a) circular; (b) corner-filleted.

pointed out by Howell,[4] the functional role of these devices of producing output motion should outweigh the structural reality of their construction, and *mechanism* appears to be a term that is suitable for these applications. The similarity between flexure hinges and rotary bearings, as previously discussed, can also be invoked in favor of using the term *mechanism* in conjunction with *compliant*.

This book comes at a time when two excellent monographs dedicated to flexures and compliant mechanisms have already made their impact in this field. Specifically, the books of Smith[2] and Howell[4] bring a wealth of information that is particularly useful to the designer/researcher involved with flexure mechanisms. The two above-mentioned monographs are also instrumental to introducing the main notions, as well as the more subtle aspects of these topics, into the domain of graduate study. This book attempts to treat a few novel aspects, however, and a few explanations will be given next in this respect.

It is a matter of evidence that an overwhelming number of compliant mechanisms utilize a reduced pool of flexure hinge configurations. Apart from the constant (either rectangular or cylindrical, wire-like) cross-section designs that present the inconvenience of high stress concentration at the areas joining the rigid links, two other geometries—the circular and corner-filleted ones (the configurations are shown in Figure 1.7)—almost exclusively occupy the space of choices for flexure hinges. The simplicity of their geometry and the relative ease of fabrication are the main reasons for the widespread use of these two types of flexures, especially in two-dimensional, compliant mechanism applications. In addition, both configurations come with the advantage of being able to reduce the stress levels through the filleted regions at their corners (ends). Closed-form compliance equations giving the spring rates for circular flexure hinges were produced by Paros and Weisbord,[1] while the corner-filleted flexure hinges were defined more recently in terms of closed-form compliances by Lobontiu et al.[5]

In chronological sequence, some other new flexure configurations have made their debut lately, including the elliptic flexures, introduced by Smith et al.[6] and further modeled and characterized by Lobontiu et al.,[7] or the parabolic

and hyperbolic flexures, introduced by Lobontiu et al.[8] All these flexure hinges are single axis and therefore are designed to cover two-dimensional compliant mechanism applications. The book of Smith[2] includes presentation of and gives the simplified spring rates (based on an extrapolation of the results derived by Paros and Weisbord[1]) for a few revolute flexure configurations. Lobontiu and Paine[9] derived closed-form equations that fully define the compliant behavior of revolute corner-filleted flexure hinges. This book introduces several new configurations for both two- and three-dimensional applications by giving closed-form compliance equations in a unitary manner. In addition to the flexure types mentioned above, the inverse-parabolic and secant profiles are treated here as both single-axis constant-thickness members and multiple-axis revolute configurations. The inverse parabolic profile is also utilized to define the two-axis flexure hinge in terms of its compliances.

Newly introduced two-dimensional applications include flexure hinges that have a mixed and nonsymmetric longitudinal profile made up of a straight segment line and one of the curves that were already mentioned for the longitudinally symmetric flexure hinges. The matter of having an extended domain with several options for flexure configurations is not the result of a mere mathematical exercise and is not at all unnecessary, as it might first appear. The compliant behavior of flexure hinges and, therefore, the overall response of a flexure-based compliant mechanism largely depend on the specific geometry of the flexure for a given material. Slight alterations or variations in geometry can produce results that are sensible at the response level. This aspect is particularly important in mechanisms where precision is a key performance parameter or where a finely tuned output is expected in terms of displacement, force, or frequency (resonant) response. The book not only gives full compliance equations for a large variety of flexure hinge configurations but also qualifies and compares the flexures in terms of performance criteria such as:

- Capacity of rotation
- Precision of rotation (sensitivity to parasitic effects)
- Stress levels
- Energy consumption/storage

This complete (full) compliance approach is utilized to naturally model the quasi-static response of flexure-based compliant mechanisms in terms of performance criteria such as:

- Output displacement/force (mechanical advantage)
- Stiffness
- Energy consumption
- Precision of output motion

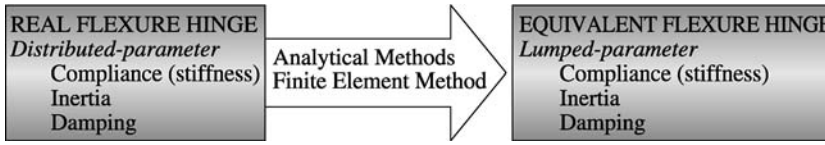

FIGURE 1.8
Discretization process for flexure hinges.

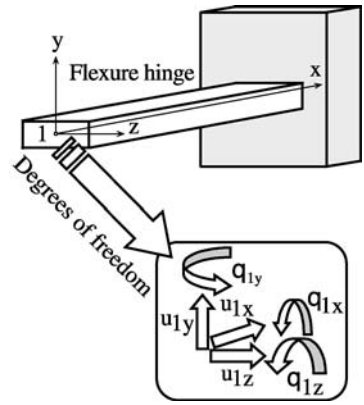

FIGURE 1.9
Three-dimensional flexure hinge with six degrees of freedom when the motion of one end is related to the opposite end.

All compliances for every flexure hinge discussed in this book, as well as the subsequent quasi-static analysis of flexure-based compliant mechanisms, are developed by utilizing Castigliano's displacement theorem, which is formulated based on the strain energy stored through elastic deformations. This book essentially develops a process of discretization through which the compliance (stiffness), inertia, and damping characteristics are derived for a large variety of flexure hinges, both analytically and by means of the finite element technique, as suggested in Figure 1.8.

By this modeling process, a flexure hinge is transformed into a complex mass-dashpot system defined individually and independently about its defining degrees of freedom (DOFs). For a three-dimensional flexure hinge, one of its ends can move with respect to the other one (presumed fixed) by three translations and three rotations as sketched in Figure 1.9. Consequently, a three-dimensional flexure hinge can be modeled as a six-DOF member when only the position of one end relative to the opposite one is of interest. As mentioned previously, this book will model and analyze an entire class of three-dimensional flexures (all flexure configurations possessing revolute symmetry), the so-called multiple-axis category.

Another class of three-dimensional flexure hinges comprises two-axis configurations that can accommodate bending about two perpendicular axes,

axial and shearing loads, but are not designed to handle torsion (in general) and therefore possess five DOFs (all displacements/rotations indicated in Figure 1.9, except the torsional rotation angle θ_{1x}). The three-DOF category is composed of flexure hinges that have a two-dimensional motion and are single axis. Bending, axial, and shearing effects can be modeled for this type of flexure so that only u_{1x}, u_{1y}, and θ_{1z} are valid displacements at point 1 in Figure 1.9. By defining the lumped-parameter compliance, inertia, and damping properties of a specific flexure hinge, modal and dynamic modeling and analysis of flexure-based compliant mechanisms become possible in a standard way.

In modeling and analyzing compliant mechanisms, the pseudo-rigid-body model approach is the almost-exclusive tool that is currently utilized. This concept has been introduced and then developed and extensively described in terms of applications by Midha et al.[10] and Howell and Midha[11–13] for macroscale compliant mechanisms, while Jensen et al.,[14] for instance, presented its implementation at the microscale level of MEMS applications. Essentially, the pseudo-rigid-body model treats a flexible link (a flexure hinge) as a torsional spring, in terms of its compliant behavior. The large-deformation assumption is utilized to derive an approximate expression for the flexure's torsional spring rate, and classical methods of rigid-body mechanisms are further used to study the compliant mechanism motion. Complete details of this modeling approach can be found in the recently published monograph of Howell.[4] Remarkable results from applying this concept to compliant mechanisms have been obtained and reported by Anathasuresh and Kota,[15] Murphy et al.,[16] Brockett and Stokes,[17] Saggere and Kota,[18] and Kota et al.,[19] to name just a few examples.

A few remarks will be made in the following regarding the application of the pseudo-rigid-body model to compliant mechanisms that incorporate flexure hinges of the types discussed in this book. A first question that arises is whether a flexure hinge can be comprehensively represented as a purely rotational joint equipped with a torsional spring. Figure 1.10 illustrates a single-axis flexure hinge with a bending moment, shearing force, and axial load acting at one end, as well as the corresponding torsional spring model that results from the pseudo-rigid-body approach. It is evident that the effect of the axial loading (which is almost always present in a flexure-based compliant mechanism) cannot be modeled through a torsional spring. Similarly, the effect of the force F_{1y} in Figure 1.10 produces shearing in addition to creating bending with respect to the opposite fixed end, but a torsional spring cannot model/capture the effect of compliance in the vertical translation, as generated by this force. The capacity of incorporating shearing effects in a spring-like model is particularly important for short beam-like members (and many flexure hinges in compliant mechanism applications are short). As a consequence, at least two other springs would have to accompany the regular (and single) torsional spring that defines the compliant behavior of a flexible connector according to the pseudo-rigid-body model approach.

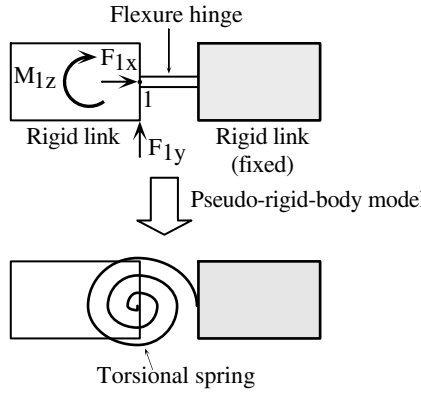

FIGURE 1.10
Two-dimensional flexure hinge modeled as a torsionally compliant spring by means of the pseudo-rigid-body model approach.

Another aspect that requires clarification is the large-displacement assumption that stands at the core of deriving the torsional spring stiffness according to the pseudo-rigid-body model approach. Several cases exist where the flexible connectors in compliant mechanisms are specifically designed to undergo large deformations and, generally, such components are built as long and slender members capable of being subjected to large deformations without exceeding the allowable stress limits. Applications of compliant mechanisms with flexible links that are operating under buckling conditions as snap-through components or return springs are in operation at both the macro- and MEMS-scale. A considerable number of flexure-based compliant mechanisms, however, are intended to produce small levels of output motion; therefore, the flexure hinges (often short) are experiencing only small deformations that confine them within acceptable levels of stress and the large-displacement theory does not have to apply. The main theoretical difference between the small- and large-displacement theories consists in the fact that for large-displacement problems the curvature produced through bending is taken in its exact form, namely:

$$\frac{1}{\rho} = \frac{\dfrac{d^2y}{dx^2}}{\left[1+\left(\dfrac{dy}{dx}\right)^2\right]^{3/2}} \tag{1.1}$$

whereas the small-displacement theory assumes that the slope is small and, as a consequence, the second power of the slope is negligible. Therefore, the curvature can be approximated to:

$$\frac{1}{\rho} \cong \frac{d^2y}{dx^2} \tag{1.2}$$

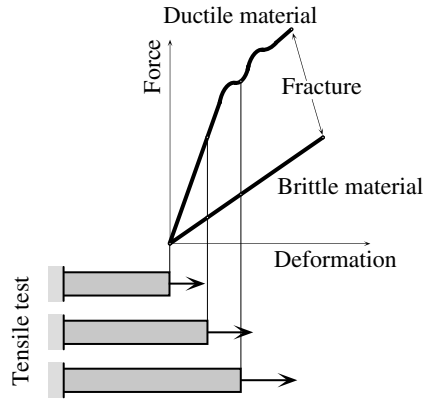

FIGURE 1.11
Force-deflection characteristics in the linear and nonlinear ranges for a ductile and a brittle material, respectively.

It should be noted that the flexure hinges are approached in this book primarily as members that are subjected to small-displacements. This assumption stems from the reality that in so many engineering applications the flexure hinges really behave according to this model, which enables utilization of the linear (or first-order) bending theory and derivation of the spring rates for various flexure configurations. A special subsection in Chapter 6 is, however, dedicated to flexure hinges that undergo large deformations.

Figure 1.11 shows the force-displacement characteristics for a ductile (metallic) material and for a brittle one. The characteristics are just qualitative, but they highlight two plausible material scenarios. Ductile materials are extensively utilized in macro compliant mechanisms, whereas silicon or other silicon-based materials that are quasi-exclusively applied in MEMS are recognized to be brittle.

For ductile materials, the deformations generally must be low in order to keep the operation point shown in Figure 1.11 on the linear portion of the characteristic, which automatically ensures small strains and stresses. In the case of the brittle material in the same figure, it fails at levels of deformations that can be considerably larger than the ones of a ductile material; therefore, components built of such materials can endure large deformations more easily and without the danger of fracture.

It should be mentioned that the large-displacement provision has been applied so far in all published research by following the pseudo-rigid-body model approach only for constant cross-section flexible members. The usual flexure hinges, however, are found in many cases of variable geometry, and the existing body of theory that treats the problem of large displacements of flexible connectors can hardly be applied to real-life flexures. Chapter 2 provides specific comments and a large amount of plots to indicate the

dispersion in compliance that can be expected when a variable-geometry flexure hinge is simplified to a constant cross-section counterpart.

The book also contains a chapter that is entirely dedicated to modeling the flexure hinges by means of the finite-element technique. A flexure hinge is modeled as a three-node beam element with three DOFs per node in the case of single-axis configurations, five DOFs per node for two-axis flexures, and six DOFs per node for multiple-axis (revolute) flexure hinges. A generic finite-element formulation is given for the three categories of flexure hinges mentioned above in terms of defining the elemental stiffness, mass, and damping matrices. Explicit forms of these elemental matrices are derived for single-axis corner-filleted and constant cross-section flexure hinges. These equations can simply be implemented in commercially available finite-element software and further utilized to perform static/dynamic analyses.

Another chapter is dedicated to more advanced problems involving the behavior of flexure hinges. Included are topics such as the torsion of prismatic flexures (single and multiple axis), thermal effects, flexures composed of several materials, actuation of flexure-based compliant mechanisms, buckling of flexure hinges, large deformations of flexure hinges, and fabrication procedures and materials for macro- and microsystem applications. Applications of flexure hinges and flexure-based compliant mechanisms that are taken from both the macroscale and microscale (MEMS) worlds are presented and discussed in yet another chapter.

References

1. Paros, J.M. and Weisbord, L., How to design flexure hinges, *Machine Design*, November, 1965, p. 151.
2. Smith, S.T., *Flexures—Elements of Elastic Mechanisms*, Gordon & Breach, Amsterdam, 2000.
3. Midha, A., Elastic mechanisms, in *Modern Kinematics: Developments in the Last Forty Years*, A.G. Erdman, Ed., John Wiley & Sons, New York, 1993.
4. Howell, L.L., *Compliant Mechanisms*, John Wiley & Sons, New York, 2001.
5. Lobontiu, N. et al., Corner-filleted flexure hinges, *ASME Journal of Mechanical Design*, 123, 346, 2001.
6. Smith, S.T. et al., Elliptical flexure hinges, *Revue of Scientific Instruments*, 68(3), 1474, 1997.
7. Lobontiu, N. et al., Design of symmetric conic-section flexure hinges based on closed-form compliance equations, *Mechanism and Machine Theory*, 37(5), 477, 2002.
8. Lobontiu, N. et al., Parabolic and hyperbolic flexure hinges: flexibility, motion precision and stress characterization based on compliance closed-form equations, *Precision Engineering: Journal of the International Societies for Precision Engineering and Nanotechnology*, 26(2), 185, 2002.
9. Lobontiu, N. and Paine, J.S.N., Design of circular cross-section corner-filleted flexure hinges for three-dimensional compliant mechanisms, *ASME Journal of Mechanical Design*, 124, 479, 2002.

10. Midha, A., Her, I., and Salamon, B.A., A methodology for compliant mechanisms design. Part I. Introduction and large-deflection analysis, in *Advances in Design Automation*, D.A. Hoeltzel, Ed., DE-Vol. 44–2, 18th ASME Design Automation Conference, 1992, p. 29.
11. Howell, L.L. and Midha, A., A method for the design of compliant mechanisms with small-length flexural pivots, *ASME Journal of Mechanical Design*, 116(1), 280, 1994.
12. Howell, L.L. and Midha, A., Parametric deflection approximations for end-loaded, large-deflection beams in compliant mechanisms, *ASME Journal of Mechanical Design*, 117(1), 156, 1995.
13. Howell, L.L. and Midha, A., Determination of the degrees of freedom of compliant mechanisms using the pseudo-rigid-body model concept, in *Proc. of the Ninth World Congress on the Theory of Machines and Mechanisms*, Milano, Italy, 2, 1995, p. 1537.
14. Jensen, B.D., Howell, L.L., Gunyan, D.B., and Salmon, L.G., The design and analysis of compliant MEMS using the pseudo-rigid-body model, *Microelectromechanical Systems (MEMS) 1997*, DSC-Vol. 62, ASME International Mechanical Engineering Congress and Exposition, Dallas, TX, 1997, p. 119.
15. Anathasuresh, G.K. and Kota, S., Designing compliant mechanisms, *Mechanical Engineering*, November, 1995, p. 93.
16. Murphy, M.D., Midha, A., and Howell, L.L., The topological synthesis of compliant mechanisms, *Mechanism and Machine Theory*, 31(2), 185, 1996.
17. Brockett, R.W. and Stokes, A., On the synthesis of compliant mechanisms, *Proc. of the IEEE International Conference on Robotics and Automation*, Sacramento, CA, 3, 1991, p. 2168.
18. Saggere, L. and Kota, S., Synthesis of distributed compliant mechanisms for adaptive structures application: an elasto-kinematic approach, *Proc. of DETC'97, ASME Design Engineering Technical Conferences*, Sacramento, CA, 1997, p. 3861.
19. Kota, S., Joo, J., Li, Z., Rodgers, S.M., and Sniegowski, J., Design of compliant mechanisms: applications to MEMS, *Analog Integrated Circuits and Signal Processing*, 29(1–2), 7, 2001.

2

Compliance-Based Design of Flexure Hinges

2.1 Introduction

This chapter is dedicated to defining a range of flexure hinge configurations based on their compliant characteristics. Several new flexure geometries are introduced here alongside the presentation of other known types; all of them are characterized by closed-form compliance equations that are derived analytically in a generic form and then specific expressions are given for all individual flexures.

A flexure hinge is actually a complex spring element that can respond to and transmit both rotation and translation, each individual flexure hinge being accompanied by a complete set of compliances (or, conversely, spring rates) that define its mechanical response to quasi-static loading. The rigorously derived closed-form compliance equations are instrumental in characterizing a flexure hinge in terms of its capacity of rotation, precision of rotation, sensitivity to parasitic input, and maximum stress levels. Functionally, a flexure hinge can be modeled as a member that is capable of flexible reaction to bending, axial loading, and, in the case of configurations for three-dimensional applications, torsion. The shearing forces and their effects must also be taken into consideration, especially for short flexure hinges. All these different loading effects will be separately analyzed and the respective compliances will be derived for each degree of freedom (DOF) describing a possible motion (either translation or rotation) by the flexures.

Paros and Weisbord[1] introduced the compliance-based approach to flexure hinges in 1965 by giving the exact compliance equations, as well as the approximate engineering formulas for symmetric circular and right circular flexure hinges with one and two sensitive axes. Only decades later were other flexure configurations presented using the analytical approach. Smith et al.,[2] for instance, introduced the elliptical flexure hinges by extrapolating the results of Paros and Weisbord[1] from circular to elliptical geometry. The same procedure of applying and conditioning the approach and equations given in Paros and Weisbord[1] was applied by Smith[3] to present the circular toroidal flexure hinge. Lobontiu et al.[4] gave the exact compliance equations for symmetric corner-filleted flexure hinges and introduced a more

complete form of the compliance-based approach to flexure hinges by quantifying and characterizing the capacity of rotation, precision of rotation, and stress levels. A similar approach was followed by Lobontiu et al.,[5] where the symmetric parabolic and hyperbolic flexure configurations were introduced, and by Lobontiu et al.,[6] who developed a unitary approach to circular, elliptical, parabolic, and hyperbolic flexure hinges as members of the conic-section family. The compliance-based approach was also utilized by Lobontiu and Paine[7] in order to characterize the revolute corner-filleted flexure hinge for three-dimensional applications. A three-dimensional application was also presented by Canfield et al.,[8] who formulated the compliances that characterize a cylindrical (wire-like) flexure hinge that is constructed of a superelastic shape memory alloy (Nitinol).

The vast majority of the specific research reported to date focuses on applications that utilize circular and/or corner-filleted flexure hinges for which the analysis is performed by means of commercial finite element software. All of these finite-element results, together with the few exceptions that pursued direct finite-element formulation without resorting to commercially available software, will be presented in the chapter dedicated to approaching the flexure hinges by means of the finite element technique.

A brief discussion will explore the taxonomy of flexure hinges, based on their functional principles and associated geometric configuration. At a general level, the flexure hinges can be separated into three main categories: *single-axis* (generally of constant width), *multiple-axis* (of revolute geometry), and *two-axis*, as indicated in Figure 2.1.

The sensitive axis, as discussed in Chapter 1, defines the operational motion and the main function of a flexure hinge, which is designed to produce limited relative rotation between two adjacent rigid members. The flexure hinges that pertain to the single-axis category must be sensitive only in rotation about one axis and, therefore, to bending that generates this type of motion. Figure 2.2 illustrates the geometry of a flexure hinge that possesses one sensitive axis.

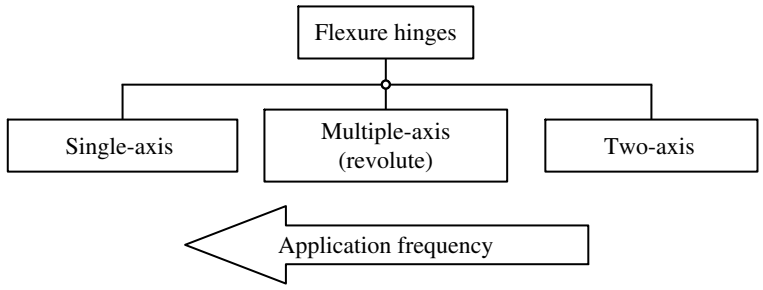

FIGURE 2.1
Main classes of flexure hinges.

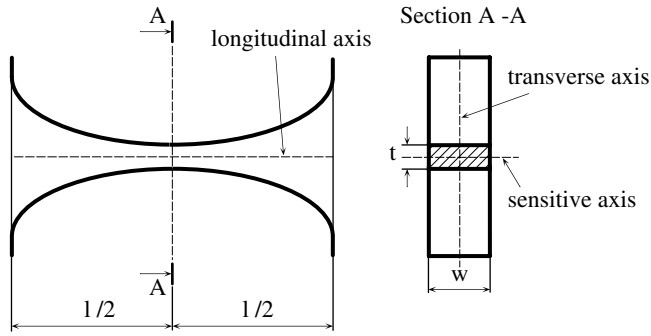

FIGURE 2.2
Single-axis flexure hinge of constant-width and rectangular cross-section.

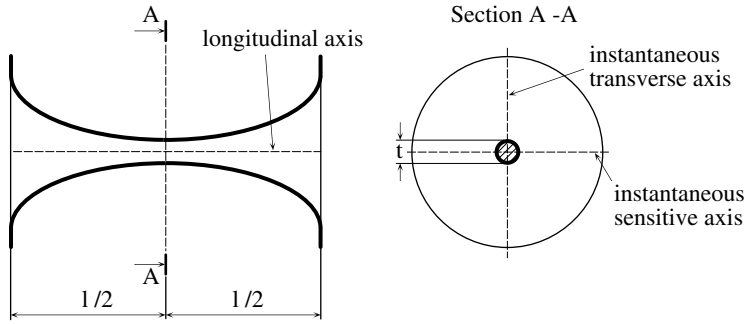

FIGURE 2.3
Multiple-axis flexure hinge of circular cross-section.

Generally, such a flexure hinge has a rectangular cross-section with constant width and variable thickness. The sensitive or compliant axis, as indicated in Figure 2.2, lies in the cross-section of minimum thickness where maximum bending compliance is present and is perpendicular to the plane formed by the longitudinal and transverse axes. This flexure configuration is designed for planar applications where the two adjacent rigid members are expected to experience relative rotation about the sensitive axis. Although not desired, translations along the flexure's longitudinal and transverse axes and/or out-of-plane motions accompany the bending about the sensitivity axis.

The flexure hinges with multiple sensitive axes have a revolute geometry, as illustrated in Figure 2.3. The sensitive axis still lies in the cross-section of minimum thickness but has no preferential orientation as permitted by the circular symmetry of the cross-section. This type of flexure hinge can thus be employed in three-dimensional applications where the direction of the rotation (sensitive) axis is not *a priori* specified, such as in cases where the two adjacent rigid members undergo nonpreferential relative rotation.

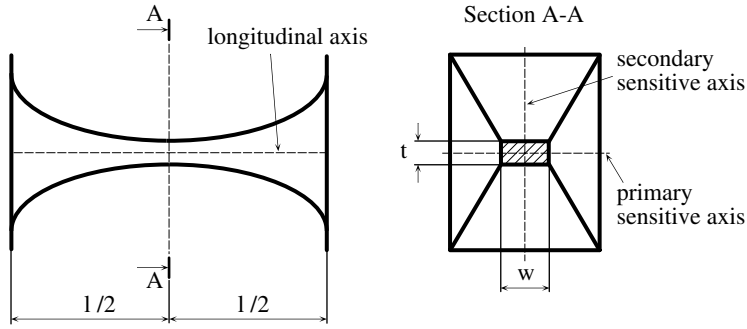

FIGURE 2.4
Two-axis flexure hinge of rectangular cross-section.

A flexure hinge that belongs to the two-axis category is sketched in Figure 2.4. Similar to a single-axis configuration, this flexure hinge will preferentially bend about an axis of minimum bending compliance, called the primary sensitive axis, that lies in the cross-section of minimum thickness t. Also positioned in the same cross-section, and most often perpendicular on the primary sensitive axis, is a secondary sensitive axis. Compared to the primary sensitive axis, the compliance of the secondary axis is slightly smaller, in order to capture and be able to react to higher bending loading that might act about this direction. Although not absolutely necessary, the cross-section of this flexure hinge is rectangular. Applications include cases where two adjacent rigid members must perform the relative rotation about the primary sensitive axis on a regular basis, while preserving the capacity of relative rotation about the secondary axis in exceptional situations such as when they have to react to higher loading. While the two-axis design that is presented in this book arranges the two flexures in a collocated manner, another possibility is also possible. Two-axis flexure hinges designed in a serial configuration and presented by Paros and Weisbord[1] for circular configurations preserve the convenience of having each flexure hinge produced according to the standard design (that gives the closed-form spring rates) but require the extra length necessary to locate the two flexures in a serial manner.

Another criterion of classifying the flexure hinges refers to their geometric symmetry. The flexure hinges can be identified by their symmetry about the longitudinal and/or transverse axis, as indicated in Figure 2.5, where several configurations are mentioned as the result of various possible symmetry combinations. For the sake of simplifying both explanation and understanding, the flexure hinges of Figures 2.2 to 2.4 are fully symmetric, although this is not a necessary requirement.

For single-axis flexures, four different cases are possible with respect to symmetry, ranging from a full-symmetry configuration (case 1 in Figure 2.5a) to a nonsymmetric one (case 4 in Figure 2.5a). The multiple-axis flexures are always symmetric about the longitudinal axis. As a direct result, only the two situations presented in Figure 2.5b are possible.

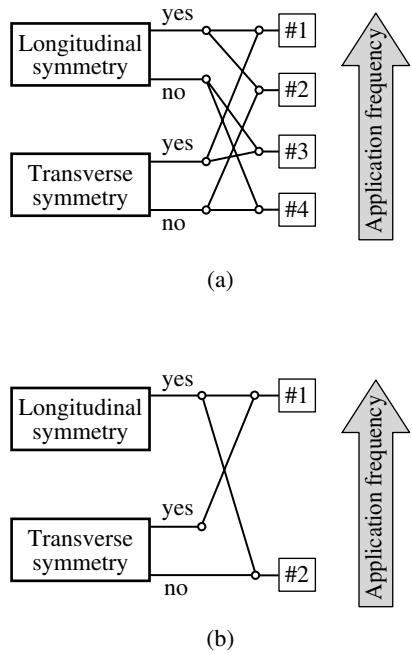

FIGURE 2.5
Flexure hinge typology defined in terms of symmetry: (a) constant-width, rectangular cross-section, single-axis flexure hinge; (b) multiple-axis revolute flexure hinge with circular cross-section.

The two-axis flexure hinge configurations can be derived from the single-sensitive-axis cases by combining the four possible situations defined in terms of the primary axis with four more independent and similar situations that occur from symmetry about the secondary axis. The overall palette will therefore consist of 16 individual configurations ranging within the domain bounded by the case of full-symmetry about both compliant axes to the design of no symmetry about both sensitive axes. Figure 2.6 illustrates flexure configurations that present longitudinal, transverse, and full or complete symmetry.

An important assumption that is basic to all further compliance derivation regards the boundary conditions of the flexure hinges. It is with tacit and common acceptance that a flexure hinge is assumed to be fixed–free, and this has been the case with all analytical approaches to flexure hinges ever since the work of Paros and Weisbord.[1] Figure 2.7 indicates this boundary condition for a generic flexure hinge. The boundary condition of Figure 2.7 is obviously valid when one rigid link is actually fixed, but it also stands when both adjoining rigid links are mobile, as the relative motion between the members can be replicated by considering that one link is fixed.

Another aspect related to the discussed boundary condition addresses the degrees of freedom provided by a flexure hinge, a subject that was briefly

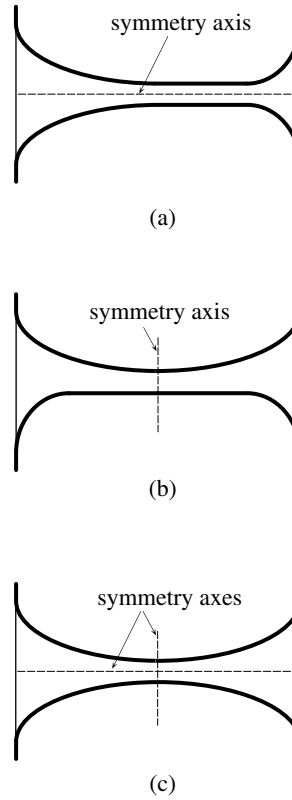

FIGURE 2.6
Symmetry in flexure hinges: (a) longitudinal; (b) transverse; (c) longitudinal and transverse (complete).

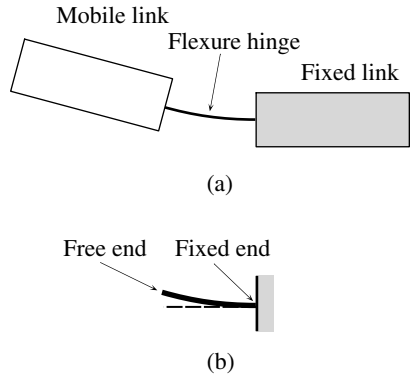

FIGURE 2.7
Boundary conditions for a generic flexure hinge: (a) link-flexure hinge-link sequence; (b) fixed–free boundary conditions.

introduced in Chapter 1. Figure 2.8 illustrates a fixed–free generic flexure hinge member subjected to three-dimensional loading at its free end. In this generic configuration, the free end has six DOFs: three translations, u_{1x}, u_{1y}, u_{1z}, and three rotations, θ_{1x}, θ_{1y}, θ_{1z}, with respect to the reference frame that

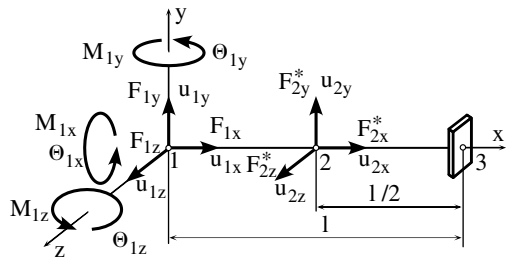

FIGURE 2.8
Main free-end and midpoint degrees of freedom in a generic flexure hinge.

is positioned at this point. These degrees of freedom can be transferred to the rigid link that is physically attached at this point in a real application. Characterizing the motion of the free end of the flexure with respect to the six DOFs will provide important information with respect to the capacity of rotation and sensitivity to parasitic motion, as well. Also important are the translations at midpoint 2 of the flexure hinge shown in Figure 2.8. This point will be referred to in the following discussion as the *center of rotation*, and its motion (the three translations, u_{2x}, u_{2y}, and u_{2z}) is very important in defining the precision of rotation.

As mentioned earlier in this chapter, a flexure hinge can functionally be considered as a compound spring that is capable of linear elastic reaction about the degrees of freedom that are subjected to external input motion. By considering that the bending-produced rotation is paramount to the flexural functionality, a flexure hinge can be modeled and represented as a pseudo-rigid body, according to the research of Howell and Midha,[9] Murphy et al.,[10] and Howell,[11] by attaching torsional stiffness to a classical rotation joint. It should be mentioned, however, that a single-axis flexure hinge, for instance, enables two-dimensional (plane) relative motion of one rigid link with respect to another about three DOFs. As indicated in Figure 2.9a, two translations about the x and y axes and one rotation about the sensitive axis of the hinge are generally possible. Each of these motions possesses the characteristics of a spring, and each corresponding stiffness plays a role in the overall deformation of the flexure in a realistic compliant mechanism where the loading is general and comprises forces that are directed along the x and y axes, in addition to a pure bending moment (that would produce the desired rotation about the sensitive axis and will activate the torsional stiffness of the flexure).

A model of the single-axis flexure hinge that captures the spring response corresponding to the three DOFs is represented in Figure 2.9b. The situation becomes even more complicated when additional degrees of freedom must be taken into consideration in cases where other motions become important and their effect cannot be overlooked. This aspect will be covered thoroughly in this chapter, as closed-form compliance equations will be derived to describe the spring behavior about every degree of freedom for all flexure hinges that will be presented.

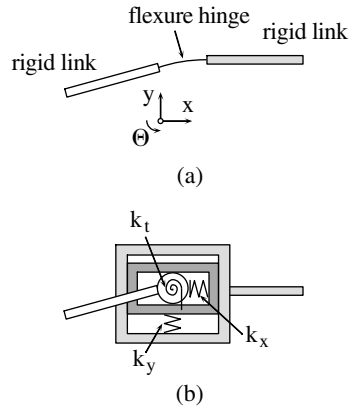

FIGURE 2.9
Model of the rectangular cross-section flexure hinge with a single axis: (a) degrees of freedom of one flexure end with respect to the other end (x,y, translation; θ, rotation); (b) spring-based model highlighting the three DOFs.

The generic mathematical formulation will be developed by first presenting the tools that are used in deriving the various compliance closed-form equations of a flexure hinge. These compliances are subsequently used to fully study a flexure hinge by defining and analyzing its capacity of rotation, sensitivity to parasitic motion, precision of rotation, and stress levels.

The single-axis class will include several flexure hinges for two-dimensional applications such as circular, corner-filleted, elliptical, parabolic, hyperbolic, inverse parabolic, and secant. The multiple-axis category will present revolute flexures for three-dimensional applications such as the ones named for the previous class. Closed-form compliance equations will be derived for the inverse parabolic flexure hinge with two sensitive axes. A comprehensive set of numerical simulations concluding this chapter will concentrate extensively on each flexure and will highlight the main individual features by comparisons that are based on several performance criteria.

2.2 Generic Mathematical Formulation

2.2.1 Introduction

This part of the work will briefly review some fundamental topics that are utilized in the subsequent closed-form compliance equation derivation and characterization of the flexure hinges presented here. The reciprocity principle will be presented first. The principle permits rigorous treatment of the compliance and stiffness notions and is particularly useful in situations where load-deformation aspects of elastic bodies are of interest. Castigliano's

displacement theorem will be reviewed next. This theorem represents the key tool for deriving all closed-form compliance equations that will follow. An example will accompany the theoretic presentation to better reinforce the main points of the theorem.

In flexure-based compliant mechanisms, the flexure hinges are the first components to be failure prone, as they have the foremost exposure to loading, given their smaller dimensions. A presentation of the theories and associated criteria of material failure will follow; the discussion is specifically dedicated to ductile materials and includes coverage of related topics such as fatigue and stress concentration.

2.2.2 The Reciprocity Principle

With a few exceptions, the majority of the topics in this book will focus on linear elastic materials and systems whose main properties are:

- The deformations (deflections or angular rotations) are small (infinitesimal).
- The bodies are elastic and therefore the deformations are proportional to the applied loads, according to Hooke's law.
- The bodies are homogeneous (their properties are the same at all locations within) and isotropic (their properties are identical irrespective of direction).

Although it can independently be utilized for direct calculation purposes, the reciprocity principle is better known to be useful in developing and demonstrating various energy principles and theorems in the area of elastic bodies, such as the virtual work theorem or Castigliano's theorems, as indicated by Den Hartog[12] or Barber,[13] for instance. In its most basic form, the reciprocity principle was first described and demonstrated by Maxwell in 1864, as mentioned by Den Hartog,[12] Volterra and Gaines,[14] and Timoshenko.[15] The principle states that for a linearly elastic system, the deformation produced at a location i by a unit load that is being applied at a different location j is equal to the deformation produced at location j by a unit load that acts at i. In 1872, Maxwell's reciprocity principle was given a broader scope through the variant proposed by Betti, who introduced the notion of "indirect" or "mutual" work to represent the work done by a load at a specific location through the action of a newly applied load at a different location. The definition of the reciprocity principle in Betti's interpretation was that the indirect or mutual work done by a loading system i during the application of a new loading system j is equal to the work done by the loading system j during the application of the loading system i. The proof of either Maxwell's or Betti's reciprocity principle formulations can be found in Den Hartog,[12] Timoshenko,[15] or Ugural and Fenster,[16] for instance.

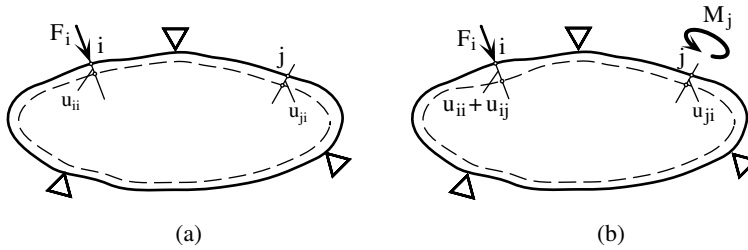

FIGURE 2.10
Illustration of the reciprocity principle as applied to a spatially constrained elastic body: (a) first loading system and its deformations; (b) first and second loading systems and their deformations.

A simple example is only discussed here to help in better visualizing the fundamental features of the principle. Figure 2.10 shows an elastic body that is kinematically restrained. A force, F_i, is first applied, as indicated in Figure 2.10a. The force stands for a more generic load consisting of forces and/or moments that can act on the elastic body at several locations. The force will generate an elastic deflection at point i, directed along F_i, that will be symbolized by u_{ii} (the first subscript denotes the application point and direction while the second one points out the load that generates it). Assume now that, while the force F_i continues to load the body, another load, the moment M_j, is applied at location j, as illustrated in Figure 2.10b. The action of this newly applied load will generate an additional deflection at i that can be denoted by u_{ij} according to the subscript notation that has previously been introduced. Over this two-phase process, denoted by a superscript $i–j$ to indicate the time sequence of applying the loads, the force F_i will perform a total work that is equal to:

$$W_{F_i}^{i-j} = \frac{1}{2} F_i u_{ii} + F_i u_{ij} \tag{2.1}$$

The first term in Eq. (2.1) shows that the work was done quasi-statically, as the force F_i is applied gradually from zero to its nominal value F_i. The second term of Eq. (2.1) indicates that this work was performed statically by a fully applied force F_i. During the same process, the moment M_j also produces a work that is equal to:

$$W_{M_j}^{i-j} = \frac{1}{2} M_j \theta_{jj} \tag{2.2}$$

The total work done during this loading sequence will sum up the contributions from F_i and M_j, namely:

$$W^{i-j} = \frac{1}{2} F_i u_{ii} + F_i u_{ij} + \frac{1}{2} M_j \theta_{jj} \tag{2.3}$$

Assume now that the order of applying the two loads is reversed, namely that M_j will first load the elastic body, followed by the force F_i. Applying a reasoning that is similar to the one previously developed will show that the total work performed during this reversed loading sequence is equal to:

$$W^{j-i} = \frac{1}{2} M_j \theta_{jj} + M_j \theta_{ji} + \frac{1}{2} F_i u_{ii} \tag{2.4}$$

Because the work done on an elastic structure by a load vector composed of at least two components should not depend on the order of applying the individual load components, the works expressed in Eqs. (2.3) and (2.4) should be equal:

$$W^{i-j} = W^{j-i} \tag{2.5}$$

Combining Eqs. (2.3), (2.4), and (2.5) results in:

$$F_i u_{ij} = M_j \theta_{ji} \tag{2.6}$$

Equation (2.6) is actually the mathematical expression of Betti's reciprocity principle for a particular case where the load vector consists of only two components. It is worth mentioning that Eq. (2.6) relates two distinct types of work: one component that is done by a force (a translatory work) and another component that is produced by a moment (a rotary work). The principle is obviously valid for connecting the same types of works (translatory to translatory or rotary to rotary), as well.

There were other developments of the reciprocity principle over the years. The Land–Colonnetti principle (1887 and 1912), for instance, proposed a model reflecting the reciprocity between the elastic deformations produced by constraints and those generated by external loading. Volterra (1905) stated the reciprocity of two elastic dislocations in multiconnected elastic bodies. In 1928, Volterra presented a generalized theorem of reciprocity that included all of the above-mentioned formulations as particular cases. More details on the reciprocity principles can be found in Volterra and Gaines.[14] The reciprocity principle is extremely useful in proving some properties of the load-deformation relationships for linearly elastic systems. A direct consequence of the characteristics that govern the behavior of linearly elastic bodies (as mentioned earlier) is the so-called principle of linear superposition. According to this principle, the deformation at any point in an elastic body under the action of a load system is equal to the sum of deformations produced by each load when acting separately. Assuming that n loads act on an elastic body, the deformation at a specific location i can be found as:

$$u_i = \sum_{j=1}^{n} C_{ij} L_j \tag{2.7}$$

where C_{ij} are termed influence or weight coefficients that together make up the compliance or flexibility matrix [C] when the deformations at several locations of the elastic body are under investigation. The compliance matrix will connect the deformation vector {u} to the load vector {L} according to the matrix equation:

$$\{u\} = [C]\{L\} \tag{2.8}$$

Generally, the number of components of the deformation vector {u} is not equal to the number of loads in the load vector {L}, which means that the compliance matrix [C] is not square. It is, however, relatively easy to transform [C] into a square matrix, as it is always advantageous for subsequent matrix manipulation and calculation. It is always possible to relate a deformation at a specific point with the corresponding load applied at the same point, as shown later in this chapter and, in doing so, the compliance matrix will become square.

Equation (2.7) clearly indicates that the individual influence coefficient C_{ij} represents the deformation produced at i by a unit load applied at j. Similarly, a coefficient C_{ji} will denote the deformation measured at j as produced by a unit load applied at i. However, according to Maxwell's reciprocity principle, these two deformations are always equal; therefore,

$$C_{ij} = C_{ji} \tag{2.9}$$

which indicates that the square compliance matrix [C] is symmetric. On the other hand, the superposition principle that was mathematically expressed in Eq. (2.7) can be formulated in a reverse manner for a linearly elastic system. Specifically, the load that is applied at a given location of the body is expressed as the sum of the loads that correspond to each individual displacement, according to the equation:

$$L_i = \sum_{j=1}^{n} K_{ij} u_j \tag{2.10}$$

where the influence coefficients K_{ij} are stiffness coefficients. Equations similar to Eq. (2.10) can be written for any of the other locations of interest on the elastic body. They can be collected in a generic equation of the form:

$$\{L\} = [K]\{u\} \tag{2.11}$$

where [K] is the stiffness matrix.

Comparison of Eqs. (2.8) and (2.11) indicates that the stiffness matrix [K] is the inverse of the compliance matrix [C]:

$$[K] = [C]^{-1} \tag{2.12}$$

which is indeed possible because, as previously shown, the compliance matrix [C] is square and symmetric. In addition, it can be shown that the

compliance matrix [*C*] is nonsingular. Therefore, the compliance matrix [*C*] always has an inverse, which is the stiffness matrix [*K*], as also demonstrated by the reasoning of Eqs. (2.8), (2.11), and (2.12).

2.2.3 Castigliano's Displacement Theorem

Several mathematical tools allow us to determine the deformations of elastic bodies. While some of them, such as the direct integration method, the superposition principle (Myosotis method), or the area–moment method, are specifically tailored for beam-like structures, other techniques based on energy or variational formulations are more generic and cover a larger area of mechanical part configuration. Well-known methods in the latter category include the principle of minimum potential energy (Rayleigh–Ritz), the principle of virtual work, Catigliano's second theorem, the Kantorovitch method, the Galerkin method, the Trefftz method, the Euler finite-difference method, and the finite-element method. The interested reader can find more details and additional data on energy- or variational-based methods in the excellent monographs of Timoshenko,[15] Richards,[17] Harker,[18] and Langhaar.[19]

Castigliano's second theorem (also known as Castigliano's displacement theorem) is a very useful technique that allows calculation of the deformations of elastic bodies under the action of external loading and support reactions. The theorem is restricted to materials that are linearly elastic and therefore obey Hooke's law for stress and strain or, equivalently, load and deformation. Essentially, the theorem gives a simple and yet elegant mathematical tool to calculate a local deformation (either linear or angular) that is produced by a corresponding external load/support reaction (either force or moment) acting at that specific location. Specifically, the local deformation of an elastic body is expressed as the partial derivative of the total strain energy stored in that body in terms of the force or moment acting at that location and along the direction of the specified deformation. A prerequisite of the theorem is that the elastic body under study is sufficiently supported, meaning that any rigid-body motions (motions allowed by the lax supports and not produced by elastic deformation) are prohibited. This precondition is, however, applicable to any other similar method. A second requirement, specific to Castigliano's second theorem, is that the strain energy must be expressed in terms of loads and, consequently, should contain no displacements. As shown in the following, this requirement is easy to comply with, by the very nature of formulating the strain energy.

The elastic body represented in Figure 2.11 undergoes both linear and angular deformations under the action of external loading and support reactions. According to Castigliano's second theorem, the linear displacement at point i is expressed in terms of the force F_i acting at that location as:

$$u_i = \frac{\partial U}{\partial F_i} \tag{2.13}$$

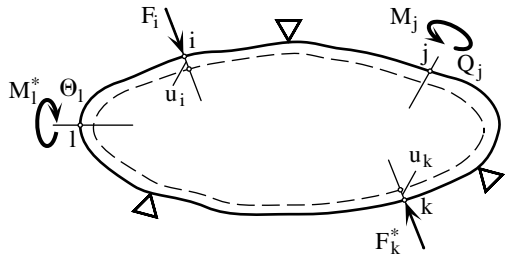

FIGURE 2.11
Schematic representation of Castigliano's second theorem as applied to a spatially constrained elastic body.

Similarly, the angular deformation is expressed in terms of the moment M_j acting at point j as:

$$\theta_j = \frac{\partial U}{\partial M_j} \tag{2.14}$$

When the deformation must be evaluated at a point where there is no external load/reaction, a fictitious load, corresponding to the type of deformation being sought, is artificially applied and the linear or angular deformation is determined by using equations similar to Eqs. (2.13) and (2.14). The deflection at point k in Figure 2.11 can be found by introducing the fictitious load F_k^* in the form:

$$u_k = \frac{\partial U}{\partial F_k^*} \tag{2.15}$$

Similarly, the rotation at another point l on the elastic body when there is no actual moment at that location (see Figure 2.11) is given by:

$$\theta_l = \frac{\partial U}{\partial M_l^*} \tag{2.16}$$

where M_l^* is a fictitious moment.

As an undergraduate, Castigliano formulated his versatile theorem in 1879 in his engineering degree's thesis. Another formulation, known as Castgliano's first theorem, reverses the causality of the second theorem by expressing the load that is necessary to produce a specific deformation of an elastic body based on the strain energy. It is worth noting that Catigliano's theorems are also valid for nonlinear elastic materials if the strain energy is substituted by the complementary energy, as demonstrated by Engesser in 1889. Figure 2.12 indicates the stress–strain curves and the related strain and

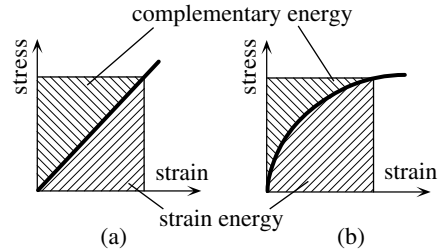

FIGURE 2.12
Strain energy and complementary energy in strain–stress curves: (a) linearly elastic material; (b) generally elastic material.

complementary energies for linear and nonlinear elastic materials. More insight into Castigliano's work, his second theorem, and related energy methods can be found in dedicated references such as Den Hartog,[12] Volterra and Gaines,[14] and Timoshenko.[15]

For a long, slender member that is generally subjected to bending, shearing, axial load, and torsion, the strain energy is expressed as:

$$U = U_{\text{bending}} + U_{\text{shearing}} + U_{\text{axial}} + U_{\text{torsion}} \tag{2.17}$$

with:

$$U_{\text{bending}} = U_{\text{bending},y} + U_{\text{bending},z} = \int_L \frac{M_y^2}{2EI_y} ds + \int_L \frac{M_z^2}{2EI_z} ds \tag{2.18}$$

$$U_{\text{shearing}} = U_{\text{shearing},y} + U_{\text{shearing},z} = \int_L \frac{\alpha V_y^2}{2GA} ds + \int_L \frac{\alpha V_z^2}{2GA} ds \tag{2.19}$$

where α is a coefficient that depends on the shape of the cross-section.

$$U_{\text{axial}} = U_{\text{axial},x} = \int_L \frac{N_x^2}{2EA} ds \tag{2.20}$$

$$U_{\text{torsion}} = U_{\text{torsion},x} = \int_L \frac{M_x^2}{2GJ} ds \tag{2.21}$$

All of the above formulations can be concentrated in the following generic equation that expresses the deformations at a generic point *i*:

$$\{u_i\} = [C_i]\{L_i\} \tag{2.22}$$

where $\{u_i\}$ is the deformation vector at point i made up of linear and angular terms, namely:

$$\{u_i\} = \{u_i, \theta_i\}^T \tag{2.23}$$

$\{L_i\}$ is the load vector comprised of all forces and moments (couples) acting on the mechanical component as summed up on the interval defined by one end of the component and the point of interest; $[C_i]$ is the compliance (flexibility) matrix that connects the two vectors defined above.

An example is presented in the following that attempts to clarify the details of applying Castigliano's second theorem.

Example

Consider the circular cross-section member that is subjected to a load vector, as illustrated in Figure 2.13. Assuming that all geometry parameters (cross-sectional diameter d and length l) and material properties (Young's modulus E and shear modulus G) are known, find the following deformations in algebraic form:

(a) u_{1y}, θ_{1x}
(b) u_{2x}, θ_{2y}

Solution

Figure 2.13 indicates that the deformations required by (a) can directly be expressed by using Castigliano's second theorem as given in Eqs. (2.13) and (2.14), as each can be related to a corresponding load, namely:

$$u_{1y} = \frac{\partial U}{\partial F_{1y}} \tag{2.24}$$

$$\theta_{1x} = \frac{\partial U}{\partial M_{1x}} \tag{2.25}$$

Because no external loads or reactions are acting at point 2, two fictitious loads, F^*_{2x} and M^*_{2y}, must be applied at that point in order to calculate the deformations required by (b) by means of Eqs. (2.15) and (2.16):

$$u_{2x} = \frac{\partial U}{\partial F^*_{2x}} \tag{2.26}$$

$$\theta_{2y} = \frac{\partial U}{\partial M^*_{2y}} \tag{2.27}$$

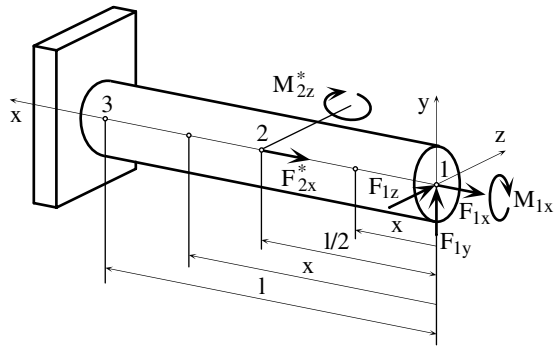

FIGURE 2.13
Fixed–free member of constant circular cross-section with free-end loading.

By taking the partial derivatives of Eqs. (2.17) through (2.21), the deflection at point 1 becomes:

$$u_{1y} = \frac{1}{EI}\left(\int_L \frac{\partial M_y}{\partial F_{1y}}dx + \int_L \frac{\partial M_z}{\partial F_{1y}}dx\right) + \frac{\alpha}{GA}\left(\int_L \frac{\partial V_y}{\partial F_{1y}}dx + \int_L \frac{\partial V_z}{\partial F_{1y}}dx\right)$$
$$+ \frac{1}{EA}\int_L \frac{\partial N_x}{\partial F_{1y}}dx + \frac{1}{GJ}\int_L \frac{\partial M_x}{\partial F_{1y}}dx \tag{2.28}$$

The other deformations, θ_{1x}, u_{2x}, and θ_{2y}, are expressed similarly by simply substituting F_{1y} with M_{1x}, F^*_{2x}, and M^*_{2y}, respectively, in Eq. (2.28).

The equations for bending moment, shearing force, axial force, and torque are taken with respect to a generic position on the two distinct intervals, 1–2 and 2–3, positioned at a distance x from the reference system origin. The equations are:

$$\begin{cases} M_y = F_{1z}x \\ M_z = F_{1y}x \\ V_y = -F_{1y} \\ V_z = -F_{1z} \\ N_x = F_{1x} \\ M_x = M_{1x} \end{cases} \tag{2.29}$$

for the 1–2 interval. The equations for the 2–3 interval are identical to those of the 1–2 interval, except for:

$$\begin{cases} M_y = F_{1z}x + M_{2y}^* \\ N_x = F_{1x} + F_{2x}^* \end{cases} \tag{2.30}$$

Equations (2.17) and (2.18) are used to determine the partial derivatives of Eq. (2.16), and the only nonzero partial derivatives are:

$$\begin{cases} \dfrac{\partial M_z}{\partial F_{1y}} = x \\ \dfrac{\partial V_y}{\partial F_{1y}} = -1 \end{cases} \tag{2.31}$$

Equations (2.29) through (2.31) are substituted into Eq. (2.28), which yields:

$$u_{1y} = \frac{1}{EI}\int_0^l F_{1y}x^2 dx + \frac{\alpha}{GA}\int_0^l F_{1y}dx \tag{2.32}$$

Carrying out the integrations in Eq. (2.32) produces:

$$u_{1y} = l\left(\frac{l^2}{3EI} + \frac{\alpha}{GA}\right)F_{1y} \tag{2.33}$$

The other required displacement can be expressed in a similar manner as:

$$\theta_{1x} = \frac{l}{GJ}M_{1x} \tag{2.34}$$

$$u_{2x} = \frac{l}{2EA}F_{1x} \tag{2.35}$$

$$\theta_{2y} = \frac{3l^2}{8EI}F_{1z} \tag{2.36}$$

2.2.4 Theories and Criteria of Material Failure

It is recognized that mechanical components usually do fail due to one of the following principal mechanisms: yield failure, fracture failure, or fatigue failure. The failure phenomenon is currently seen as an irreversible process that develops locally and through which the macrostructure and operational performance of the component are negatively altered. Ductile materials (especially metals) fail by yielding, whereby the deformations exceed the

proportionality limit and go into the nonrecoverable plastic region. Ductile materials (e.g., typical metals such as mild steel, aluminum, titanium, copper, and magnesium and some of their alloys, as well as non-metals such as Teflon®) are capable of undergoing large plastic deformations before fracture. Brittle materials fail by fracture as they incur only small deformations before breaking apart, compared to ductile materials. Example of brittle materials include cast iron, concrete, glass or ceramic compounds, silicon, and silicon-based compounds. Fatigue failure applies to both ductile and brittle materials and is caused by stresses less than the ultimate strength. Such stresses might occur statically on a less frequent basis, when the loads are not applied repeatedly, but failure manifests itself in time, because cracks, for instance, develop to critical sizes. More frequently though, the fatigue failure is generated by cyclic loading, whereby loads and deformations are applied to the mechanical component more than once in a repetitive manner, as mentioned by Sandor.[20]

Other mechanisms of failure, in addition to the ones already mentioned, are excessive elastic (recoverable) deformation, low stiffness and operation at resonant frequencies, time deformation under unchanged loading conditions (creep), and unstable response at critical loads (buckling). Because the vast majority of flexure hinges and flexure-based compliant mechanisms are fabricated out of metallic or ductile materials, the brief discussion that follows will focus on yielding and fatigue failure theories only.

2.2.4.1 Yielding Failure Theories and Criteria

As previously mentioned, ductile materials are capable of undergoing large deformations and entering the plastic domain before fracture occurs. The large plastic deformations are, in most occasions, unacceptable compared to the operational and precision requirements; as a consequence, in such circumstances it is considered that the respective component has failed. Figure 2.14 shows the stress–strain curve in a uniaxial (tension/compression) test for a typical metallic (ductile) material. It can be seen that, up to a limit (called the *proportionality limit*, σ_p), the stress–strain relationship is linear (complying with Hook's law), and the body is in the elastic domain where all of the deformation is recoverable. After that point, the loading enters into the partially plastic region, where the body will suffer unrecoverable deformation. The failure condition, therefore, is considered to take place when the proportionality limit is exceeded in the uniaxial state of stress.

For a more complex state of stress, as is often encountered in real-life applications, the failure can be predicted by means of theories of failures.

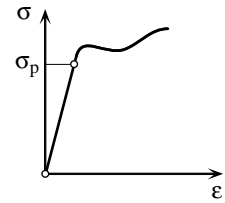

FIGURE 2.14
Stress–strain curve in uniaxial loading of a metallic member.

Fundamentally, any theory of failure attempts to establish an equivalence between the real complex state of stress and a simple, uniaxial state of stress condition by applying a specific prediction criterion, as shown by Barber,[13] Ugural and Fenster,[16] or Muvdi and McNabb.[21]

For ductile and isotropic materials, three failure theories can be utilized to predict the critical condition in a member under a complex state of stress: the maximum energy of deformation theory (von Mises), the maximum shear stress theory (Tresca), and the maximum total strain energy theory (Beltrami–Haigh). Other theories and criteria that better apply to brittle materials include the maximum principal stress theory (Rankine), the maximum principal strain theory (Saint Venant), and the maximum internal friction theory (Coulomb–Mohr), as indicated by Volterra and Gaines,[14] Ugural and Fenster,[16] or Muvdi and McNabb.[21] Also not discussed here are the failure theories for orthotropic materials, such as the Norris criterion (see Cook and Young[22] for more details) or the criteria dedicated to composite materials, such as those of Halpin–Tsai or Greszczuk (as shown by Kobayashi[23]).

According to Ugural[16] and Muvdi and McNabb,[21] for instance, experimental results have indicated that the maximum energy of deformation theory (von Mises) and the maximum shear stress theory (Tresca) provide the best predictions for ductile material members under a complex state of stress. They will be addressed in the following text with more emphasis being placed upon the von Mises failure criterion because this theory, in addition to being slightly more accurate than the Tresca theory, has an elegant mathematical formulation that is extensively employed in tools of engineering calculation, such as the finite-element technique.

Figure 2.15 illustrates the normal and shear stresses on the positive faces of an infinitesimal cube that has been removed from an elastic body which is subjected to a complex state of stress. As known from basic mechanics of materials (see, for example, Muvdi and McNabb[21] or Cook and Young[22]), given the particular orientation of the reference frame O_{xyz}, where the reference axes are aligned with the principal directions 1, 2, and 3 (as indicated in Figure 2.15), one can find the principal stresses (that have extreme values) as roots of the three-degree equation in σ:

$$\sigma^3 - I_1\sigma^2 + I_2\sigma - I_3 = 0 \tag{2.37}$$

where I_1, I_2, and I_3 are the stress invariants (they do not depend on the way the reference frame is directed) defined in terms of the normal and shear stresses acting on the faces of the elemental cube (Figure 2.15) as:

$$\begin{cases} I_1 = \sigma_x + \sigma_y + \sigma_z \\ I_2 = \sigma_x\sigma_y + \sigma_y\sigma_z + \sigma_z\sigma_x - \tau_{xy}^2 - \tau_{yz}^2 - \tau_{zx}^2 \\ I_3 = \sigma_x\sigma_y\sigma_z + 2\tau_{xy}\tau_{yz}\tau_{zx} - \sigma_x\tau_{yz}^2 - \sigma_y\tau_{zx}^2 - \sigma_z\tau_{xy}^2 \end{cases} \tag{2.38}$$

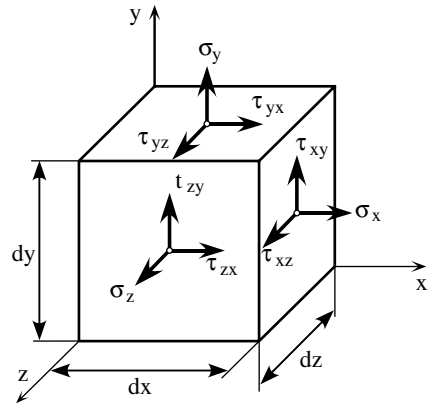

FIGURE 2.15
Stresses on an infinitesimal cube.

The Tresca theory (first mentioned by Coulomb) specifies that a ductile material will yield when the maximum shear stress in the body reaches the critical shear stress in the simple tension/compression test. According to this theory, the equivalent yield stress is given by:

$$\sigma_e = \max(|\sigma_1 - \sigma_2|, |\sigma_2 - \sigma_3|, |\sigma_3 - \sigma_1|) \tag{2.39}$$

where the principal stresses σ_1, σ_2, and σ_3, are given in Eq. (2.37). Equation (2.39) indicates that three expressions must be utilized and compared in order to determine the equivalent stress by the Tresca criterion.

The von Mises criterion (also known as the Huber–von Mises–Hencki criterion, after the researchers that have formulated it) states that the failure of a member under a complex state of stress occurs when its energy of distortion equals the critical energy of distortion in the uniaxial tension/compression test. Generally, the strain energy of an elastic body can be conceptually decomposed into two parts: one part produces the volume deformation without modifying the shape of the loaded body and is generated by a so-called hydrostatic load (actually an average stress). The other energy component does not affect the volume but alters the shape. This latter component is known as distortion or deviatoric energy and is generated by deviatoric stresses that represent the difference between the normal stresses and the average stress. Several experiments have been carried out (see Barber,[13] Ugural and Fenster,[16] Muvdi and McNabb,[21] or Cook and Young[22]) that have proven that elastic bodies usually do not fail under a hydrostatic state of stress alone. Therefore, a criterion that would predict failure based on the total strain energy (volumetric strain energy included), such as the Beltrami–Haigh theory, would be too loose.

The equivalent von Mises yield stress is given by the equation:

$$\sigma_e = \sqrt{\frac{(\sigma_1 - \sigma_2)^2 + (\sigma_2 - \sigma_3)^2 + (\sigma_3 - \sigma_1)^2}{2}} = \sqrt{I_1^2 - 3I_2^2} \tag{2.40}$$

Substituting I_1 and I_2 of Eq. (2.38) into Eq. (2.40) results in:

$$\sigma_e = \sqrt{\sigma_x^2 + \sigma_y^2 + \sigma_z^2 - (\sigma_x\sigma_y + \sigma_y\sigma_z + \sigma_z\sigma_x) + 3\left(\tau_{xy}^2 + \tau_{yz}^2 + \tau_{zx}^2\right)} \tag{2.41}$$

A condition encountered in many engineering applications is that of plane stress where:

$$\sigma_z = \tau_{yz} = \tau_{zx} = 0 \tag{2.42}$$

In a plane stress condition, the generic von Mises criterion of Eq. (2.41) becomes:

$$\sigma_e = \sqrt{\sigma_x^2 + \sigma_y^2 - \sigma_x\sigma_y + 3\tau_{xy}^2} \tag{2.43}$$

Moreover, for a state of plane stress where σ_y is zero, Eq. (2.43) simplifies to:

$$\sigma_e = \sqrt{\sigma_x^2 + 3\tau_{xy}^2} \tag{2.44}$$

which is a well-known equation that applies in a variety of cases, including the bending–torsion of shafts.

2.2.4.2 Fatigue Failure

In cases of fatigue failure, a mechanical part that is subjected to cyclic loading becomes unoperational for service either by yielding or due to fracture under loads that are smaller than the critical static values. In other words, fatigue failure occurs when a load is applied and removed a very large number of times (cycles) in a repetitive manner. The scientific investigation of the fatigue phenomenon began around 1850 with rigorous experimental research conducted by a German scientist, A. Wohler, who investigated the fracture of axles in railway equipment and stress raisers in machine components and designed a series of fatigue tests. An excellent account of the fatigue phenomenon can be found in Timoshenko.[15]

Classic examples of fatigue testing are the cyclic tension and compression and the rotating bending. The results of usually laborious and extensive fatigue tests are the so-called *S–N* curves that are plots of the fracture stress (*S*), the amplitude of purely alternating stress, actually, in terms of the number of cycles (*N*) necessary to produce the fracture for a given stress level. An *S–N* curve provides the values of two main parameters that characterize fatigue. The first amount is the fatigue life, which gives the number of cycles necessary to result in fracture for a given stress value. The second amount is the fatigue strength, which quantifies the stress required to produce fracture in a specified number of load cycles. Figure 2.16 illustrates the simplified *S–N* curve for a typical steel alloy. For a small number of cycles (less than N_s in Figure 2.16), the loading is considered to be static. A reasonable value for N_s that is often employed in practical calculations (see Barber[13] for more details) is 10^3. As the load that generates fracture is reduced (the stress decreases), the fatigue life *N* increases, as illustrated in Figure 2.16. For some materials (mild steel included), the fracture stress reaches a limit value after a certain number of cycles and remains constant thereafter. This stress limit is called the *endurance limit* and is denoted by σ_l while N_l stands for the corresponding number of cycles. Other materials, such as several aluminum alloys, do not display a firm value of this strength as the fracture continues to decrease when increasing the number of cycles. Practically, the fatigue testing is stopped after 10^8 cycles if fracture does not occur.

As is the case for static failure, it is impossible to perform exhaustive experiments in order to determine the *S–N* curves for each specific practical situation; therefore, fatigue criteria, expressed in equation form, are necessary to assess the fatigue parameters in various instances. Several criteria cover both the ductile and brittle materials for uniaxial loading. Figure 2.17 indicates the stress parameters that define a cyclic loading.

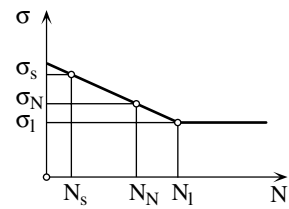

FIGURE 2.16
Generic representation of an *S–N* curve for a typical steel.

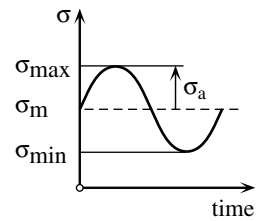

FIGURE 2.17
Normal stresses under cyclic loading.

Mention should be made that the notation σ is generic, as it stands for either normal or shear stresses. Assuming that the maximum and minimum values of the loading stress are known, the amplitude (or range) stress σ_a and the mean stress σ_m can be calculated as:

$$\begin{cases} \sigma_a = \dfrac{\sigma_{max} - \sigma_{min}}{2} \\ \sigma_m = \dfrac{\sigma_{max} + \sigma_{min}}{2} \end{cases} \tag{2.45}$$

The Goodman criterion is proven to be efficient for ductile materials, as mentioned by Ugural and Fenster,[16] for instance. Its corresponding equation is:

$$\frac{\sigma_a}{\sigma_N} + \frac{\sigma_m}{\sigma_u} = \frac{1}{SF} \tag{2.46}$$

The unknown of Eq. (2.46) is the fatigue stress, σ_N, that can be determined in terms of the loading history (σ_a and σ_m), the ultimate strength of the material σ_u, and a safety factor ($SF \geq 1$). Another theory regarding ductile materials is the Soderberg criterion, which is more conservative than Goodman's criterion as it uses the yield strength σ_Y instead of the ultimate strength σ_u, as given by the equation:

$$\frac{\sigma_a}{\sigma_N} + \frac{\sigma_m}{\sigma_Y} = \frac{1}{SF} \tag{2.47}$$

The vast majority of fatigue applications for ductile materials, however, involve combined (multi-axial) loading. In such cases, either the Goodman or Soderberg fatigue criterion is used in conjunction with a failure theory, such as von Mises or Tresca. The Goodman criterion will have to incorporate the equivalent range σ_{ea} and equivalent mean σ_{em} stresses in the case of a mechanical part that is subjected to fatigue through combined loading:

$$\frac{\sigma_{ea}}{\sigma_N} + \frac{\sigma_{em}}{\sigma_u} = \frac{1}{SF} \tag{2.48}$$

The equivalent stresses of Eq. 2.48 can be found by utilizing the von Mises failure criterion, for instance, in the form:

$$\begin{cases} \sigma_{ea} = \sqrt{\dfrac{(\sigma_{1a} - \sigma_{2a})^2 + (\sigma_{2a} - \sigma_{3a})^2 + (\sigma_{3a} - \sigma_{1a})^2}{2}} \\ \sigma_{em} = \sqrt{\dfrac{(\sigma_{1m} - \sigma_{2m})^2 + (\sigma_{2m} - \sigma_{3m})^2 + (\sigma_{3m} - \sigma_{1m})^2}{2}} \end{cases} \tag{2.49}$$

Another related aspect pertains to the fatigue life corresponding to a given fatigue strength under specific loading conditions. The *S–N* curve of Figure 2.16 is simplified to better convey the main trends, and the portion comprised between N_s and N_1 is nonlinear, unfortunately. A better approximation to that region is provided by the following equation given initially by Sullivan:[24]

$$N_N = N_s \left(\frac{\sigma_N}{\sigma_s} \right)^{\frac{1}{c}} \tag{2.50}$$

where the exponent c is defined as:

$$c = \frac{\ln\left(\frac{\sigma_s}{\sigma_1} \right)}{\ln\left(\frac{N_s}{N_1} \right)} \tag{2.51}$$

Directly connected to the fatigue phenomenon is the problem of stress raisers or concentrators, which are geometric discontinuities or irregularities in a mechanical part. Their presence alters the elementary stress formulas that are valid for members having a constant section or a section with only a gradual change in its defining contour. As a consequence, high localized stresses are set at points where stress raisers are present. The stress concentrators can act at microscopic scale in the form of cracks, inclusions, or voids, but they are also macroscopic in configurations such as holes, notches, grooves, threads, fillets, stepped sections, or sharp reentrant corners. The net effect of stress raisers is shortened lifetimes of both ductile and brittle materials. The stress concentrators are particularly important in flexure hinges that are in actuality discontinuities in the originally blank material. The sharp corners of a machined flexure hinge with either constant or variable cross-section are generally avoided by applying fillets at the respective areas. The stress raisers are mathematically characterized by a stress concentration factor, K_t, which is defined as the ratio of the maximum or peak stress to the nominal stress. For normal stresses that are produced through bending or axial loading, the stress concentration factor is:

$$K_{t,n} = \frac{\sigma_{max}}{\sigma_{nom}} \tag{2.52}$$

while, for shear stresses that are generated through shearing or torsion, the stress concentration factor is:

$$K_{t,s} = \frac{\tau_{max}}{\tau_{nom}} \tag{2.53}$$

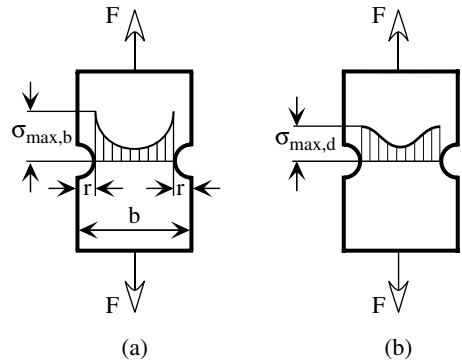

FIGURE 2.18
Symmetrically notched specimen made of ductile material under axial loading: (a) initial stresses; (b) redistributed stresses.

The first subscript of the stress concentration factor indicates that its value is theoretical, while the second one, oftentimes ignored, denotes the type of stress that is referred.

The stress concentration factor (also termed form factor, in order to emphasize that it is mainly determined by the geometry of a particular raiser) can be evaluated analytically by means of the theory of elasticity. Finite-element techniques permit direct evaluation of the peak stresses at regions with stress concentrators and therefore enable indirect calculation of the stress concentration factor. Experimental laboratory methods for stress analysis such as photoelasticity, other optomechanical techniques, or strain gauges can be employed in fatigue or impact tests as alternative means of assessing the stress concentration factor. Figure 2.18 illustrates the stress profile of a symmetrically notched specimen under axial load.

The nominal stress is calculated by taking the net cross-sectional area as:

$$\sigma_{nom} = \frac{F}{w(b-2r)} \tag{2.54}$$

where w is the constant cross-sectional width.

For a ductile material, as shown in Figure 2.18b, the plastic flow and stress redistribution at areas of stress concentration reduce the maximum stresses, compared to brittle materials, such that:

$$\sigma_{max,d} < \sigma_{max,b} \tag{2.55}$$

Under fatigue or dynamic conditions, the maximum stress that would normally be present under static loading conditions at a stress raiser is reduced through a similar process of stress redistribution in the presence of partially plastic deformations. Therefore, the actual strength of that member

is different from the value obtained by using the stress concentration factor procedure. A notch sensitivity factor q, as indicated by Peterson[25] and Pilkey,[26] is usually introduced that can range from 0 to 1 in order to define an effective stress concentration factor, K_e:

$$K_e = 1 + q(K_t - 1) \tag{2.56}$$

Equations (2.52) and (2.53) can be reformulated by using K_e instead of K_t as:

$$\sigma_{max} = [q(K_t - 1) + 1]\sigma_{nom} \tag{2.57}$$

$$\tau_{max} = [q(K_t - 1) + 1]\tau_{nom} \tag{2.58}$$

The notch sensitivity factor (introduced by Boresi et al.[27]) is usually determined experimentally. When $q = 0$, the stress concentration is considered to have no effect on the strength of a member; however, if $q = 1$, then $K_e = K_t$, and, as a consequence, the theoretical stress concentration factor acts at its maximum weight. A value of 1 can be used for the notch sensitivity factor q in conservative designs that require higher safety factors.

2.3 Single-Axis Flexure Hinges for Two-Dimensional Applications

2.3.1 Introduction

This section presents the flexure hinges categorized earlier as single-axis flexures and shown to have a constant width. These flexure configurations are largely utilized in two-dimensional applications where the flexure-based compliant mechanism performs a plane motion. Several closed-form compliance equations (or spring rates) will first be derived by using Castigliano's displacement theorem (as previously discussed) in a generic manner, in order to qualify the performance of a flexure hinge. Both long- and short-beam theory will be investigated, and the differences in the corresponding compliances will be expressed for each individual flexure. Various flexure geometric configurations will subsequently be analyzed and specific compliance equations given in explicit form for circular, corner-filleted, parabolic, hyperbolic, elliptical, inverse parabolic, and secant designs. In the vast majority of practical applications, the flexure hinges have transverse symmetry and, as a consequence, all configurations presented here will be transversely symmetric (this topic was previously discussed in the introduction to this chapter). For each individual flexure type, two related configurations will be presented: one that has longitudinal symmetry and a second one that does not present this symmetry feature. Figure 2.19 illustrates a longitudinally

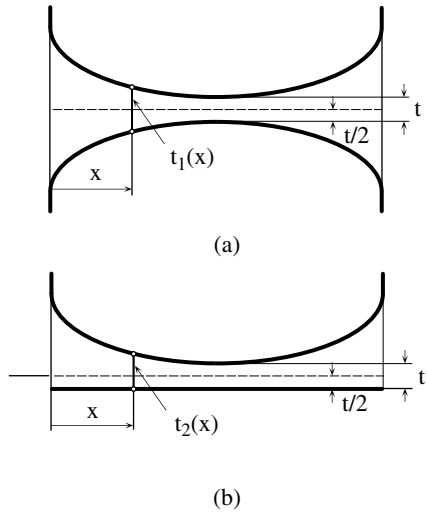

FIGURE 2.19
Variable thickness for two equal-length, constant-width flexure hinges: (a) flexure hinge of full symmetry (symmetric flexure); (b) flexure hinge presenting only transverse symmetry (nonsymmetric flexure).

symmetric configuration and its corresponding nonsymmetric counterpart. Both flexure geometric configurations have identical lengths l and minimum thickness t.

The reason for covering longitudinally nonsymmetric flexure configurations formed by two different profiles, each of which is a line segment parallel to the longitudinal axis of the flexure (as shown in Figure 2.19), is the large number of applications that must position the flexures on the outer boundary of the compliant mechanism. In such cases, the center of the flexure and the longitudinal axis cannot be moved toward the interior of the mechanism and longitudinal symmetry cannot be provided.

As shown in Figure 2.19, the relationship between the variable thicknesses of the two flexures can be written in terms of the common minimum thickness t as:

$$t_2(x) = \frac{t_1(x) + t}{2} \tag{2.59}$$

Equation (2.59) is valuable, as it allows us to simply relate the compliance derivation of longitudinally nonsymmetric flexure hinges (simply called nonsymmetric in the following text) to derivation of the longitudinally symmetric flexures.

A comprehensive numerical simulation phase will take the closed-form compliance equations and use several criteria to compare the performance of the flexure hinges that were introduced here. A large number of plots will

enable deriving conclusions with respect to specific features of each individual flexure.

2.3.2 Generic Formulation and Performance Criteria

The flexure hinges can be designed and analyzed based on their effectiveness during operation according to the following criteria:

- Capacity of producing the desired limited rotation
- Sensitivity to parasitic loading
- Precision of rotation
- Stress levels under fatigue conditions

The above-mentioned criteria will be discussed in the following in more detail for several flexure configurations that are designed to operate in two- and three-dimensional applications. It will be shown that the analysis can be carried out and quantified in a unitary manner, by utilizing several compliances (spring rates) to assess the behavior of one flexure.

2.3.2.1 Capacity of Rotation

For a single-axis, constant-width flexure hinge, as illustrated in Figure 2.2, for which the generic loading and deformations can be visualized in Figure 2.8, the loading at end 1 has six components: two bending moments, M_{1y}, M_{1z}; two shearing forces, F_{1y}, F_{1z}; one axial load, F_{1x}; and one torsional moment, M_{1x}. For two-dimensional applications, where all active and resistive loads are planar, only the in-plane components M_{1z}, F_{1y}, and F_{1x} have substantive effects on the flexure operation. The other components specified (M_{1y}, F_{1z}, and M_{1x}) are out-of-plane agents that usually have a lesser magnitude, and therefore impact, on the flexure. They mainly produce parasitic effects and occur as a result of errors caused by defective actuation or positioning of external loads or manufacturing and assembly. Because torsion is quite rare in a two-dimensional, flexure-based compliant mechanism, the effect of M_{1x} will be neglected in all following derivations within this chapter but will be approached later. The shear and bending action of F_{1z} and M_{1y} might occasionally amount to sensible effects that cannot be overlooked.

Equation (2.8) can be reformulated as:

$$\begin{Bmatrix} \{u_1^{ip}\} \\ \{u_1^{op}\} \end{Bmatrix} = \begin{bmatrix} [C_1^{ip}] & 0 \\ 0 & [C_1^{op}] \end{bmatrix} \begin{Bmatrix} \{L_1^{ip}\} \\ \{L_1^{op}\} \end{Bmatrix} \tag{2.60}$$

where the displacement vectors $\{u\}$ and load vectors $\{L\}$ have been formally divided into one in-plane (superscript *ip*) and one out-of-plane (superscript *op*) subvectors. Accordingly, the symmetric compliance matrix will comprise the

corresponding in-plane and out-of-plane submatrices. The subvectors introduced in Eq. (2.60) are:

$$\left\{u_1^{ip}\right\} = \{u_{1x}, u_{1y}, \theta_{1z}\}^T \tag{2.61}$$

$$\left\{u_1^{op}\right\} = \{u_{1z}, \theta_{1y}\}^T \tag{2.62}$$

$$\left\{L_1^{ip}\right\} = \{F_{1x}, F_{1y}, M_{1z}\}^T \tag{2.63}$$

$$\left\{L_1^{op}\right\} = \{F_{1z}, M_{1y}\}^T \tag{2.64}$$

The in- and out-of-plane submatrices of Eq. (2.60) are:

$$[C_1^{ip}] = \begin{bmatrix} C_{1,x-F_x} & 0 & 0 \\ 0 & C_{1,y-F_y} & C_{1,y-M_z} \\ 0 & C_{1,\theta_z-F_y} & C_{1,\theta_z-M_z} \end{bmatrix} \tag{2.65}$$

$$[C_1^{op}] = \begin{bmatrix} C_{1,z-F_z} & C_{1,z-M_y} \\ C_{1,\theta_y-F_z} & C_{1,\theta_y-M_y} \end{bmatrix} \tag{2.66}$$

In Eqs. (2.65) and (2.66):

$$C_{1,y-M_z} = C_{1,\theta_z-F_y} \tag{2.67}$$

and:

$$C_{1,z-M_y} = C_{1,\theta_y-F_z} \tag{2.68}$$

according to the principle of reciprocity presented in the introductory part of this chapter. The in-plane generic compliance equations are:

$$C_{1,x-F_x} = \frac{1}{Ew} I_1 \tag{2.69}$$

$$C_{1,y-F_y} = \frac{12}{Ew} I_2 \tag{2.70}$$

$$C_{1,y-M_z} = \frac{12}{Ew} I_3 \tag{2.71}$$

$$C_{1,\theta_z-M_z} = \frac{12}{Ew} I_4 \tag{2.72}$$

The out-of-plane compliance equations are:

$$C_{1,z-F_z} = \frac{12}{Ew^3} I_5 \tag{2.73}$$

$$C_{1,z-M_y} = \frac{12}{Ew^3} I_6 \tag{2.74}$$

$$C_{1,\theta_y-M_y} = \frac{12}{Ew^3} I_1 = \frac{12}{w^2} C_{1,x-F_x} \tag{2.75}$$

The I_1 through I_6 integrals that appear in the compliance equations presented above are:

$$I_1 = \int_0^l \frac{dx}{t(x)} \tag{2.76}$$

$$I_2 = \int_0^l \frac{x^2 dx}{t(x)^3} \tag{2.77}$$

$$I_3 = \int_0^l \frac{x dx}{t(x)^3} \tag{2.78}$$

$$I_4 = \int_0^l \frac{dx}{t(x)^3} \tag{2.79}$$

$$I_5 = \int_0^l \frac{x^2 dx}{t(x)} \tag{2.80}$$

$$I_6 = \int_0^l \frac{x dx}{t(x)} \tag{2.81}$$

The compliance formulation so far was concerned with flexure hinges that are relatively long, compared to their cross-sectional dimensions, and are usually treated as Euler–Bernoulli-beam-type members. For such a model, the planar cross-section remains perpendicular to the neutral axis after the external bending has been applied. This model also ignores the shearing stresses and associated deformations. However, for relatively short beams, the shearing effects need to be taken into account together with their corresponding additional deformation. A model that accounts for such additional shearing effects is the Timoshenko short-beam model, which also incorporates rotary inertia effects to better describe the dynamic response of such

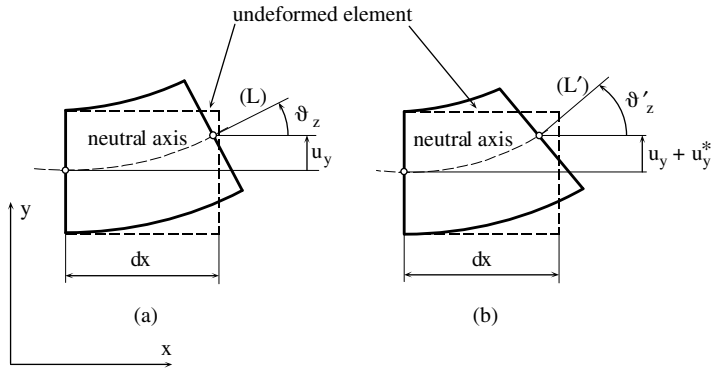

FIGURE 2.20
Deflection and slope for bent elements that are isolated from: (a) Euler–Bernoulli beams; (b) Timoshenko beams.

members, as will be shown later in Chapter 3. Figure 2.20 illustrates two elementary portions that have been isolated from deformed Euler–Bernoulli and Timoshenko beams, respectively.

The line (L') for a Euler–Bernoulli beam element is both tangent to the neutral axis and perpendicular on the right face, whereas the line (L) for a Timoshenko beam element, while perpendicular to the right face of the element, is no longer tangent to the deformed neutral axis, as indicated in Figure 2.20. It is clear that for a Timoshenko model the extra deflection and slope generated through shearing add up to the respective deformations that are normally produced through bending effects such that the total deformations become:

$$u_{1y}^{s} = u_{1y} + u_{1y}^{*} \tag{2.82}$$

and:

$$\theta_{1z}^{s} = \theta_{1z} + \theta_{1z}^{*} \tag{2.83}$$

where the * superscript denotes addition due to consideration of the shearing effects.

The extra shearing-produced strain energy into an elastic beam-like component along the y-axis, as shown by Young,[28] for instance, is expressed as:

$$U^{*} = \int_{l} \frac{\alpha F_{y}^{2}}{2GA(x)} dx \tag{2.84}$$

where F_y is the shearing force and α is a correction factor that depends on the shape of the cross-section. By applying Castigliano's displacement

theorem, the shearing-generated extra deformations are calculated as:

$$u_{1y}^{*} = \frac{\partial U^{*}}{\partial F_{1y}} \tag{2.85}$$

and:

$$\theta_{1z}^{*} = \frac{\partial U^{*}}{\partial M_{1z}} = 0 \tag{2.86}$$

Eq. (2.86) actually reflects the fact that the angle between the tangent to the deformed neutral axis and horizontal direction is not affected by shearing effects.

After performing the required calculations indicated in Eqs. (2.84) and (2.85), the additional deformations of Eq. (2.85) can be put in the form:

$$u_{1y}^{*} = C_{1,y-F_y}^{*} F_{1y} \tag{2.87}$$

A brief inspection of Eqs. (2.86) and (2.87) shows that only the shearing force F_{1y} influences the extra deflection produced through considering the shearing effects of relatively short flexure hinges. As a consequence, the compliances $C_{1,y-Mz}$ and $C_{1,z-Mz}$ should be zero. It can easily be demonstrated that the compliance of Eq. (2.87) is:

$$C_{1,y-F_y}^{*} = \frac{\alpha E}{G} C_{1,x-F_x} \tag{2.88}$$

As a consequence, the total compliances (that sum up bending and shearing effects) will be:

$$C_{1,y-F_y}^{s} = C_{1,y-F_y} + \frac{\alpha E}{G} C_{1,x-F_x} \tag{2.89}$$

and:

$$C_{1,y-M_z}^{s} = C_{1,y-M_z} \tag{2.90}$$

By applying a similar reasoning, it can be shown that the out-of-plane compliances that are considering by shearing effects are:

$$C_{1,z-F_z}^{s} = C_{1,z-F_z} + \frac{\alpha E}{G} C_{1,x-F_x} \tag{2.91}$$

and:

$$C^{s}_{1,Z-MY} = C_{1,Z-MY} \tag{2.92}$$

In regard to shearing deflections with respect to long (Euler–Bernoulli) vs. short (Timoshenko) beam theory, it has become somewhat of an undisputed truism that a long beam is one whose length is "sufficiently long" compared to its cross-sectional dimensions. The threshold length-to-thickness ratio that separates long from short beams is assigned values ranging from 3 to 5 in most of the dedicated literature (a value of 3 is given in Young,[28] while Den Hartog[29] assumes a limit value of 5). It is also recognized that the deflection produced by shearing in a short beam becomes comparable to the regular deflection produced by bending. The criterion, therefore, that discriminates between short and long beams evaluates the shearing-to-bending deflection ratio and compares it to a limit value (called "error"). The situation where this ratio exceeds the error limit for a particular geometry will place that particular beam into the "short" category; otherwise, it will be placed in the "long" class. As shown in the following discussion, deciding the short or long character of a beam directly from the error limit set by a specific length-to-thickness ratio is a bit more involved, and aspects regarding the cross-section type and material properties must be taken into account.

A constant cross-section (rectangular and circular) cantilevered beam constructed of homogeneous metallic material (steel or aluminum) will be analyzed first. A more generalized approach is presented afterwards that applies to variable cross-section members such as flexure hinges.

The shear deflection and bending deflection for a cantilever beam under the action of a tip force are:

$$u^{*}_{1y} = \frac{\alpha l}{GA} F_{1y} \tag{2.93}$$

and:

$$u_{1y} = \frac{l^3}{3EI_z} F_{1y} \tag{2.94}$$

By considering the relationship between the shear modulus G and the Young's modulus E:

$$G = \frac{E}{2(1+\mu)} \tag{2.95}$$

where μ is the Poisson's ratio, the ratio of shear deflection to bending deflection can be expressed by combining Eqs. (2.93) and (2.94) as:

$$\frac{u_{1y}^{*}}{u_{1y}} = 6\alpha(1+\mu)\frac{I_z}{Al^2} \tag{2.96}$$

Equation (2.96) gives the relationship between the shearing-to-bending deflection ratio and the beam geometry (cross-section and length) as well as the material properties. Equation (2.96) has been used to run some simple calculations for two different cross-sections (rectangular and circular) and two different materials (mild steel and an aluminum alloy). The cross-sectional parameters of Eq. (2.96) for a rectangular cross-section of dimensions w and t are:

$$\begin{cases} I_z = \dfrac{wt^3}{12} \\ A = wt \end{cases} \tag{2.97}$$

Substitution of Eq. (2.97) into Eq. (2.96) produces the deflection ratio for a constant rectangular cross-section cantilever beam:

$$\frac{u_{1y}^{*}}{u_{1y}} = \frac{\alpha(1+\mu)}{2}\left(\frac{t}{l}\right)^2 \tag{2.98}$$

For a circular cross-section, the geometric parameters of Eq. (2.96) are:

$$\begin{cases} I_z = \dfrac{\pi t^4}{64} \\ A = \dfrac{\pi t^2}{4} \end{cases} \tag{2.99}$$

The deflection ratio for a circular cross-section can be obtained by substituting Eq. (2.99) into Eq. (2.96):

$$\frac{u_{1y}^{*}}{u_{1y}} = \frac{3\alpha(1+\mu)}{8}\left(\frac{t}{l}\right)^2 \tag{2.100}$$

TABLE 2.1

Length-to-Thickness Ratios and Error Limits for Rectangular and Circular Constant Cross-Section Cantilevers

	Error (%)							
Cantilever	**1**	**2**	**3**	**4**	**5**	**6**	**7**	**8**
Mild steel								
r	9.87	6.98	5.70	4.94	4.42	4.03	3.73	3.49
c	8.06	5.70	4.65	4.03	3.60	3.29	3.05	2.85
Aluminum alloy								
r	9.68	6.85	5.59	4.84	4.33	3.95	3.66	3.43
c	7.91	5.59	4.56	3.95	3.53	3.23	2.99	2.79

Note: *r* = rectangular, *c* = circular.

Equations (2.99) and (2.100) were utilized to calculate length-to-thickness ratios in terms of an error threshold defined as:

$$\frac{u_{1y}^{*}}{u_{1y}} = error \tag{2.101}$$

For values smaller than a specified value of the error, the shearing deflection is small compared to the bending deflection and, therefore, the shearing effects can be neglected.

Table 2.1 provides several values of the length-to-thickness ratio as a function of the threshold error for rectangular or circular cross-section cantilevers that are built of mild steel ($\mu = 0.3$) or aluminum alloy ($\mu = 0.25$). As indicated by Table 2.1, circular cross-section cantilevers can be considered long beams for length-to-thickness ratios that are slightly smaller than those corresponding to rectangular cross-section beams at the same error limit. Also, aluminum alloy beams pass into the long-beam domain for lower length-to-thickness ratios than steel beams.

For variable cross-section beams (such as the flexure hinge configurations that will be analyzed in the following text), Eqs. (2.93) and (2.94) are no longer valid and one must use the more generic Eq. (2.87) as well as the equation:

$$u_{1y} = C_{1,y-F_y} F_{1y} + C_{1,y-M_z} M_{1z} \tag{2.102}$$

The compliances of Eqs. (2.87) and (2.102) were previously given. By using them and by only considering the loading produced by the tip force F_{1y}, the generic length-to-thickness ratio becomes:

$$\frac{u_{1y}^{*}}{u_{1y}} = \frac{C_{1,y-F_y}^{*}}{C_{1,y-F_y}} = \frac{\alpha(1+\mu)}{6}\frac{I_1}{I_2} \tag{2.103}$$

where integrals I_1 and I_2 are defined as in Eqs. (2.76) and (2.77). Similarly, when only the bending produced by tip moment M_{1z} is taken into consideration, the ratio of Eq. (2.103) becomes:

$$\frac{u_{1y}^*}{u_{1y}} = \frac{C_{1,y-M_z}^*}{C_{1,y-M_z}} = \frac{\alpha(1+\mu)}{6l}\frac{I_1}{I_3} \tag{2.104}$$

where integral I_3 is defined as in Eq. (2.78).

It is therefore obvious that deciding whether a flexure hinge responds like a long or short beam with respect to bending depends on the specific geometry of the analyzed configuration as well as on the material of the flexure. A brief discussion will be carried out with respect to long vs. short behavior when each flexure type is presented in more detail, supported by the corresponding numerical simulation results.

2.3.2.2 Precision of Rotation

The relative rotation of two mechanical members connected by a conventional rotation joint is produced along an axis that passes through the geometric center of the joint, which is fixed provided one member is also fixed. In the case of a symmetric flexure hinge, the center of rotation (the geometric symmetry center of the flexure) is no longer fixed because the forces and moments acting on the flexure produce elastic deformations that alter its position.

The displacement of the rotation center of a flexure hinge (point 2 in Figure 2.8) can be assessed by applying three fictitious loads, F_{2x}^*, F_{2y}^*, and F_{2z}^*, in addition to the load vector applied at point 1. Castigliano's second theorem is again utilized to find the displacements of the rotation center in the form:

$$u_{2x} = \frac{\partial U'}{\partial F_{2x}^*} \tag{2.105}$$

$$u_{2y} = \frac{\partial U'}{\partial F_{2y}^*} \tag{2.106}$$

$$u_{2z} = \frac{\partial U'}{\partial F_{2z}^*} \tag{2.107}$$

where the strain energy U' is:

$$U' = U_{bending} + U_{shearing} + U_{axial} \tag{2.108}$$

where $U_{bending}$, $U_{shearing}$, and U_{axial} are as given in Eqs. (2.18), (2.19), and (2.20), respectively. The bending moments, shearing, and axial forces need only to

be taken on the 2–3 interval, as F_{2x}^{*}, F_{2y}^{*}, and F_{2z}^{*}, (the "variables" of the partial derivatives in Eqs. (2.105) through (2.107)) only intervene over that load segment. They are:

$$\begin{cases} M_y = F_{1z}x + F_{2z}^{*}\left(x - \dfrac{l}{2}\right) \\ M_z = F_{1y}x + F_{2y}^{*}\left(x - \dfrac{l}{2}\right) \\ V_y = F_{1y} + F_{2y}^{*} \\ V_z = F_{1z} + F_{2z}^{*} \\ N_x = F_{1x} + F_{2x}^{*} \end{cases} \tag{2.109}$$

Application of Castigliano's second theorem results in the following equation:

$$\{u_2\} = [C_2]\{L_1\} \tag{2.110}$$

which can be reformulated by separating its components into in-plane and out-of-plane subcomponents, as:

$$\begin{Bmatrix} \{u_2^{ip}\} \\ \{u_2^{op}\} \end{Bmatrix} = \begin{bmatrix} [C_2^{ip}] & 0 \\ 0 & [C_2^{op}] \end{bmatrix} \begin{Bmatrix} \{L_2^{ip}\} \\ \{L_2^{op}\} \end{Bmatrix} \tag{2.111}$$

The displacement subvectors at the center of the flexure are:

$$\{u_2^{ip}\} = \{u_{2x}, u_{2y}\}^T \tag{2.112}$$

and:

$$\{u_2^{op}\} = u_{2z} \tag{2.113}$$

As indicated by Eq. (2.110), the load vector is the one also utilized in Eqs. (2.63) and (2.64), as there is no additional loading.

The compliance submatrices of Eq. (2.110) are:

$$C_2^{ip} = \begin{bmatrix} C_{2,x-F_x} & 0 & 0 \\ 0 & C_{2,y-F_y} & C_{2,y-M_z} \end{bmatrix} \tag{2.114}$$

and:

$$C_2^{op} = [C_{2,z-F_z} \quad C_{2,z-M_y}] \tag{2.115}$$

The in-plane compliances of Eq. (2.115) are calculated as follows:

$$C_{2,x-F_x} = \frac{1}{Ew} I_1' \tag{2.116}$$

$$C_{2,y-F_y} = \frac{12}{Ew}\left(I_2' - \frac{l}{2} I_3'\right) \tag{2.117}$$

$$C_{2,y-F_y}^s = \frac{1}{w}\left[\frac{12}{E}\left(I_2' - \frac{l}{2} I_3'\right) + \frac{\alpha}{G} I_1'\right] \tag{2.118}$$

Equation (2.118) is valid for relatively short beams when shearing is taken into account. Again, this equation can be reformulated in compliance form by combining it with Eqs. (2.116) and (2.117) as:

$$C_{2,y-F_y}^s = C_{2,y-F_y} + \frac{\alpha E}{G} C_{2,x-F_x} \tag{2.119}$$

The other in-plane compliance is:

$$C_{2,y-M_z} = \frac{12}{Ew}\left(I_3' - \frac{l}{2} I_4'\right) \tag{2.120}$$

The out-of-plane compliances of Eq. (2.115) are:

$$C_{2,z-F_z} = \frac{12}{Ew^3}\left(I_5' - \frac{l}{2} I_6'\right) \tag{2.121}$$

and:

$$C_{2,z-F_z}^s = \frac{1}{w}\left[\frac{12}{Ew^2}\left(I_5' - \frac{l}{2} I_6'\right) + \frac{\alpha}{G} I_1'\right] \tag{2.122}$$

for relatively short beams where shearing is taken into account. In a manner similar to the procedure previously applied, Eq. (2.122) can be written in

compliance form by combining it with Eqs. (2.116) and (2.121) as:

$$C^s_{2,z-F_z} = C_{2,z-F_z} + \frac{\alpha E}{G} C_{2,x-F_x} \tag{2.123}$$

The other out-of-plane compliance is:

$$C_{2,z-M_y} = \frac{12}{Ew^3}\left(I'_6 - \frac{l}{2} I'_1\right) \tag{2.124}$$

The I'_1 through I'_6 integrals that enter the compliance equations previously introduced are:

$$I'_1 = \int_{l/2}^{l} \frac{dx}{t(x)} \tag{2.125}$$

$$I'_2 = \int_{l/2}^{l} \frac{x^2 dx}{t(x)^3} \tag{2.126}$$

$$I'_3 = \int_{l/2}^{l} \frac{x dx}{t(x)^3} \tag{2.127}$$

$$I'_4 = \int_{l/2}^{l} \frac{dx}{t(x)^3} \tag{2.128}$$

$$I'_5 = \int_{l/2}^{l} \frac{x^2 dx}{t(x)} \tag{2.129}$$

$$I'_6 = \int_{l/2}^{l} \frac{x dx}{t(x)} \tag{2.130}$$

In regard to compliances describing the capacity of rotation vs. the precision of rotation, it was seen that the compliances defining the capacity of rotation, as well as those quantifying the precision of rotation, are given in terms of several integrals. In a few cases, for similar compliances in the two distinct problem groups, the only difference consisted in taking the corresponding integrals over the full length of the flexure (in the case of studying the capacity of rotation) vs. integrating over half the length—the second half, actually—when analyzing the precision of rotation. The temptation would be to look to the possibility that the value of an integral calculated

over the full-length interval is twice the value of the same integral when taken over only half the interval. Unfortunately, this is only true when the integrand is an even function, and this will briefly be demonstrated in the following.

Consider the generic integrals defined as:

$$I = \int_{-l/2}^{l/2} f(x)dx \tag{2.131}$$

and:

$$I' = \int_{0}^{l/2} f(x)dx \tag{2.132}$$

It can easily be seen that Eq. (2.131) defines a compliance that is related to the capacity of rotation, while Eq. (2.132) defines a compliance that describes the precision of rotation in the case where the y reference axis is translated with a positive quantity equal to $l/2$. Equation (2.131) can be rewritten as:

$$\begin{aligned} I &= \int_{-l/2}^{0} f(x)dx + \int_{0}^{l/2} f(x)dx = -\int_{0}^{-l/2} f(x)dx + \int_{0}^{l/2} f(x)dx \\ &= \int_{0}^{l/2} f(-x)dx + \int_{0}^{l/2} f(x)dx \end{aligned} \tag{2.133}$$

By inspecting Eq. (2.133), it becomes clear that the only case where:

$$I = 2I' \tag{2.134}$$

occurs when:

$$f(-x) = f(x) \tag{2.135}$$

which indicates that the function must be even (or symmetric with respect to the y axis). As illustrated by the many compliances that will be formulated next for several particular flexure hinges, only in a few occasions is the integrand symmetric, thus permitting us to directly express a compliance defining the precision of rotation as half its corresponding compliance related to the capacity of rotation.

2.3.2.3 Stress Considerations

The cutout areas of a two-dimensional flexure hinge are actually stress concentrators that augment the cross-sectional nominal stresses. When the out-of-plane and shearing load effects are ignored, the stresses are only normal, as they are produced solely through axial and bending loading. The maximum stress will occur at one of the outer fibers, according to the equation:

$$\sigma_{max} = \sigma_a + \sigma_{b,max} \tag{2.136}$$

where the subscripts a and b denote axial and bending, respectively.

The stresses generated through axial loading are constant over the cross-section and are expressed as:

$$\sigma_a = K_{ta} \frac{F_{1x}}{wt} \tag{2.137}$$

where K_{ta} is the theoretical stress concentration factor in axial loading (either tension or compression). The normal bending stresses are maximum on either of the outer fibers as given by:

$$\sigma_{b,max} = K_{tb} \frac{6(F_{1y}l + M_{1z})}{wt^2} \tag{2.138}$$

where K_{tb} is the theoretical stress concentration factor in bending. Both K_{ta} and K_{tb} can be found in the works of Peterson[25] or Young,[28] for instance, for a series of different stress concentration geometries. Substituting Eqs. (2.137) and (2.138) into Eq. (2.136) gives:

$$\sigma_{max} = \frac{1}{wt}\left[K_{ta}F_{1x} + \frac{6K_{tb}}{t}(F_{1y}l + M_{1z})\right] \tag{2.139}$$

Equation (2.139) is useful when the loading on a flexure can be estimated.

Other cases exist where evaluating the loading is difficult but assessing the linear or angular displacements (deformations) at the end of a flexure can be achieved with relative ease. Therefore, Eq. (2.139) must be altered accordingly to include deformations instead of loads. The compliance-based deformation-load equation can be expressed in the reverse manner as a stiffness-based load-deformation equation:

$$\{L_1\} = [K_1]\{u_1\} \tag{2.140}$$

where the stiffness matrix $[K_1]$ is simply the inverse of the compliance matrix $[C_1]$:

$$[K_1] = [C_1]^{-1} \tag{2.141}$$

Because only in-plane compliances have been retained for the purpose of discussing stress issues, the explicit form of the compliance matrix is:

$$[C_1]=\begin{bmatrix} C_{1,x-F_x} & 0 & 0 \\ 0 & C_{1,y-F_y} & C_{1,y-M_z} \\ 0 & C_{1,y-M_z} & C_{1,\theta_z-M_z} \end{bmatrix} \tag{2.142}$$

Therefore the stiffness matrix will be:

$$[K_1]=\begin{bmatrix} K_{1,x-F_x} & 0 & 0 \\ 0 & K_{1,y-F_y} & K_{1,y-M_z} \\ 0 & K_{1,y-M_z} & K_{1,\theta_z-M_z} \end{bmatrix} \tag{2.143}$$

where the stiffness terms are expressed in terms of compliance terms by the inversion indicated in Eq. (2.141) as:

$$\begin{cases} K_{1,x-F_x}=\dfrac{1}{C_{1,x-F_x}} \\ K_{1,y-F_y}=\dfrac{C_{1,\theta_z-M_z}}{C_{1,\theta_z-M_z}C_{1,y-F_y}-C_{1,y-M_z}^2} \\ K_{1,y-M_z}=-\dfrac{C_{1,y-M_z}}{C_{1,\theta_z-M_z}C_{1,y-F_y}-C_{1,y-M_z}^2} \\ K_{1,\theta_z-M_z}=\dfrac{C_{1,y-F_y}}{C_{1,\theta_z-M_z}C_{1,y-F_y}-C_{1,y-M_z}^2} \end{cases} \tag{2.144}$$

Equation (2.140) is written explicitly as:

$$\begin{Bmatrix} F_{1x} \\ F_{1y} \\ M_{1z} \end{Bmatrix}=\begin{bmatrix} K_{1,x-F_x} & 0 & 0 \\ 0 & K_{1,y-F_y} & K_{1,y-M_z} \\ 0 & K_{1,y-M_z} & K_{1,\theta_z-M_z} \end{bmatrix}\begin{Bmatrix} u_{1x} \\ u_{1y} \\ \theta_{1z} \end{Bmatrix} \tag{2.145}$$

The load components of Eq. (2.145) are substituted into Eq. (2.139), which transforms into:

$$\sigma_{max}=\frac{1}{wt}\left\{K_{ta}K_{1,x-F_x}u_{1x}+\frac{6K_{tb}}{t}[(lK_{1,y-F_y}+K_{1,\theta_z-M_z})u_{1y} + (lK_{1,y-M_z}+K_{1,\theta_z-M_z})\theta_{1z}]\right\} \tag{2.146}$$

Equation (2.146) enables evaluation of the maximum stress levels in a single-axis flexure hinge when the relative displacements (deformations) are known (or can be predicted/measured) at one end.

2.3.2.4 Strain-Energy-Based Efficiency

The criteria utilized so far to compare the performance of various flexure hinges were the capacity of rotation, the precision of rotation (including the sensitivity to parasitic loading), and stress levels. Another criterion of analyzing the performance of different flexure hinges introduced here is based on an energy approach. For a single-axis flexure hinge that is part of a two-dimensional compliant mechanism, for instance, the loading at the free end is composed of F_{1y}, F_{1x}, and M_{1z}, as previously shown. When this load vector is applied, the free end is displaced by the in-plane quantities u_{1x} and u_{1y}, while the corresponding tip slope is θ_{1z}. The equations connecting displacements and load are:

$$\begin{cases} u_{1x} = C_{1,x-F_x} F_{1x} \\ u_{1y} = C_{1,y-F_y} F_{1y} + C_{1,y-M_z} \theta_{1z} \\ u_{1y} = C_{1,y-M_z} F_{1y} + C_{1,\theta_z-M_z} \theta_{1z} \end{cases} \tag{2.147}$$

Assuming that the loads are applied quasi-statically, the total work performed can be expressed as:

$$W_{in} = \frac{1}{2}(F_{1x}u_{1x} + F_{1y}u_{1y} + M_{1z}\theta_{1z}) \tag{2.148}$$

The useful work is the one that directly produces the rotation of the flexure, and for an ideal flexural joint without length (point-like) that possesses only torsional stiffness, the output work is:

$$W_{out} = \frac{1}{2} M_{1z}\theta_{1z} \tag{2.149}$$

The energy-related efficiency of a flexure hinge can therefore be defined as:

$$\eta = \frac{W_{out}}{W_{in}} \tag{2.150}$$

Utilizing Eq. (2.147) in conjunction with Eqs. (2.148) and (2.149) and then substituting them into Eq. (2.150) results in:

$$\eta = \frac{C_{1,\theta_z-M_z} M_{1z}^2}{C_{1,x-F_x} F_{1x}^2 + C_{1,y-F_y} F_{1y}^2 + C_{1,\theta_z-M_z} M_{1z}^2 + 2C_{1,y-M_z} F_{1y} M_{1z}} \tag{2.151}$$

In order to make Eq. (2.151) non-dependent on the loading, unit values can be taken for the three loads, which simplifies Eq. (2.151) to:

$$\eta = \frac{C_{1,\theta_z - M_z}}{C_{1,x-F_x} + C_{1,y-F_y} + C_{1,\theta_z - M_z} + 2C_{1,y-M_z}} \tag{2.152}$$

For short flexure hinges, where shearing effects must be taken into account, the compliance factor $C_{1,y-Fy}$ is substituted by the corresponding factor $C^s_{1,y-Fy}$, according to the previous discussion related to this subject.

2.3.3 Constant Rectangular Cross-Section Flexure Hinge

The constant rectangular cross-section flexure hinge analyzed first presents the simplest geometry because, in addition to its width being constant (provision which applies to all single-axis flexure configurations), the thickness is also constant and equal to the minimum thickness of all other flexures, namely:

$$t(x) = t \tag{2.153}$$

The compliances given for a constant rectangular cross-section flexure hinge will be utilized at a later stage to compare various other flexures to this simple configuration.

2.3.3.1 Capacity of Rotation

The in-plane compliances are obtained by solving the generic integrals given in Eqs. (2.76) through (2.79) and substituting the results into the corresponding Eqs. (2.69) through (2.72) and (2.91). The final equations are:

$$C_{1,x-F_x} = \frac{l}{Ewt} \tag{2.154}$$

$$C_{1,y-F_y} = \frac{4l^3}{Ewt^3} \tag{2.155}$$

and:

$$C^s_{1,y-F_y} = \frac{l}{wt}\left(\frac{4l^2}{Et^2} + \frac{\alpha}{G}\right) \tag{2.156}$$

for relatively short beam theory, where shearing is accounted for. The other compliances are:

$$C_{1,y-M_z} = \frac{6l^2}{Ewt^3} \tag{2.157}$$

$$C_{1,\theta_z - M_z} = \frac{12l}{Ewt^3} \tag{2.158}$$

The out-of-plane compliances are obtained by solving first the generic integrals of Eqs. (2.80) and (2.81) and then substituting the results into the corresponding Eqs. (2.73) through (2.75) and (2.93). The final equations are:

$$C_{1,z-F_z} = \frac{4l^3}{Ew^3t} \tag{2.159}$$

$$C^s_{1,z-F_z} = \frac{l}{wt}\left(\frac{4l^2}{Ew^2} + \frac{\alpha}{G}\right) \tag{2.160}$$

(for relatively short beam theory, where shearing is taken into account)

$$C_{1,z-M_y} = \frac{6l^2}{Ew^3t} \tag{2.161}$$

$$C_{1,\theta_y-M_y} = \frac{12l}{Ew^3t} \tag{2.162}$$

2.3.3.2 Precision of Rotation

The in-plane compliances that describe the precision of rotation are expressed by first solving the generic integrals of Eqs. (2.125) through (2.128) and then substituting the results into the corresponding compliance Eqs. (2.116) through (2.120). The final equations are:

$$C_{2,x-F_x} = \frac{C_{1,x-F_x}}{2} \tag{2.163}$$

$$C_{2,y-F_y} = \frac{5l^3}{4Ewt^3} \tag{2.164}$$

$$C^s_{2,y-F_y} = \frac{l}{2wt}\left(\frac{5l^2}{2Et^2} + \frac{\alpha}{G}\right) \tag{2.165}$$

(for relatively short beam theory, where shearing is taken into account)

$$C_{2,y-M_z} = \frac{3l^2}{2Ewt^3} \tag{2.166}$$

Similarly, the out-of-plane compliances are obtained by first solving the generic integrals of Eqs. (2.129) and (2.130) and then substituting the results into the corresponding Eqs. (2.115), (2.117), and (2.118). The final equations are:

$$C_{2,z-F_z} = \frac{5l^3}{4Ew^3t} \tag{2.167}$$

$$C^s_{2,z-F_z} = \frac{l}{2wt}\left(\frac{5l^2}{2Ew^2} + \frac{\alpha}{G}\right) \tag{2.168}$$

(for relatively short beam theory, where shearing is taken into account)

$$C_{2,z-M_y} = \frac{3l^2}{2Ew^3t} \tag{2.169}$$

2.3.4 Circular Flexure Hinge

A circular flexure hinge will be now analyzed, following the path presented for the constant rectangular flexure hinge. The generic equations indicated as being the ones to be utilized to obtain the specific compliance equations for the constant cross-section beam are the same and will not be indicated again; this will also apply for all subsequent flexure configurations that will be treated. Because the compliance equations that apply when shearing is taken into consideration can be obtained as a linear combination of two basic compliances, as shown in Eqs. (2.89) and (2.91), these equations also will not be rewritten. A longitudinally symmetric circular flexure hinge will be first analyzed and then similar results will be given for a nonsymmetric one (details about the longitudinal nonsymmetry were provided at the beginning of this section).

2.3.4.1 Symmetric Circular Flexure Hinge

The longitudinal section of a symmetric circular flexure hinge is illustrated in Figure 2.21. The variable thickness, $t(x)$, can be expressed in terms of the flexure geometry as:

$$t(x) = t + 2[r - \sqrt{x(2r-x)}] \tag{2.170}$$

The closed-form compliance equations describing the capacity of rotation and the precision of rotation are given next.

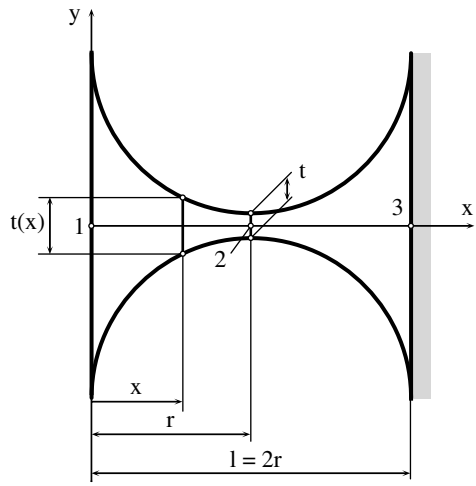

FIGURE 2.21
Cross-sectional profile of a symmetric right-circular flexure hinge.

2.3.4.1.1 Capacity of Rotation

The in-plane compliances are:

$$C_{1,x-F_x} = \frac{1}{Ew}\left[\frac{2(2r+t)}{\sqrt{t(4r+t)}}\arctan\sqrt{1+\frac{4r}{t}} - \frac{\pi}{2}\right] \tag{2.171}$$

$$\begin{aligned} C_{1,y-F_y} = \frac{3}{4Ew(2r+t)}\Bigg\{ & 2(2+\pi)r + \pi t + \frac{8r^3(44r^2+28rt+5t^2)}{t^2(4r+t)^2} \\ & + \frac{(2r+t)\sqrt{t(4r+t)}[-80r^4+24r^3t+8(3+2\pi)r^2t^2+4(1+2\pi)rt^3+\pi t^4]}{\sqrt{t^5(4r+t)^5}} \\ & - \frac{8(2r+t)^4(-6r^2+4rt+t^2)}{\sqrt{t^5(4r+t)^5}}\arctan\sqrt{1+\frac{4r}{t}}\Bigg\} \end{aligned} \tag{2.172}$$

$$\begin{aligned} C_{1,y-M_z} = & \frac{24r^2}{Ewt^3(2r+t)(4r+t)^3}[t(4r+t)(6r^2+4rt+t^2) \\ & + 6r(2r+t)^2\sqrt{t(4r+t)}\arctan\sqrt{1+\frac{4r}{t}} \end{aligned} \tag{2.173}$$

$$C_{1,\theta_z-M_z} = \frac{C_{1,y-M_z}}{r} \tag{2.174}$$

The out-of-plane compliances are:

$$C_{1,z-F_z} = \frac{24r^2}{Ew^3}\log\frac{t}{2r+t} \tag{2.175}$$

$$C_{1,z-M_y} = \frac{C_{1,z-F_z}}{2r} \tag{2.176}$$

$$C_{1,\theta_y-M_y} = \frac{6}{Ew^3t}\left[4(2r+t)\sqrt{\frac{t}{4r+t}}\arctan\sqrt{\frac{t}{4r+t}} - \pi t\right] \tag{2.177}$$

It is simple to check that the particular form of Eq. (2.177) satisfies the condition expressed by Eq. (2.75).

2.3.4.1.2 Precision of Rotation

The axial compliance is:

$$C_{2,x-F_x} = \frac{C_{1,x-F_x}}{2} \tag{2.178}$$

This situation where the axial compliance corresponding to the symmetry center of a flexure is half the value of the full axial compliance was previously discussed in the context of the general formulation of compliances in terms of their defining integrals, and it was shown that this particular situation occurs only in a few cases. The axial compliance is one such occurrence, and this situation will apply for many of the flexure configurations that will be presented later in this chapter. Equation (2.178) will be repeated at times when it applies or will be expressed per se when another relationship applies.

The in-plane compliances are:

$$\begin{aligned} C_{2,y-F_y} = \frac{3}{4Ewt^2(2r+t)}\Bigg\{&16r^3 + 2(2+\pi)rt^2 + \pi t^3 - \frac{32r^4}{4r+t} \\ &- \frac{4\sqrt{t}(2r+t)^2(-2r^2+4rt+t^2)}{\sqrt{(4r+t)^3}}\arctan\sqrt{1+\frac{4r}{t}}\Bigg\} \end{aligned} \tag{2.179}$$

$$C_{2,y-M_z} = \frac{6r^2}{Ewt^2(2r+t)} \tag{2.180}$$

The out-of-plane compliances are:

$$C_{2,z-F_z} = \frac{3r}{Ew^3}\left\{2(2+\pi)r + \frac{\pi t}{2} - (2r-t)\left[2\sqrt{1+\frac{4r}{t}}\arctan\sqrt{1+\frac{4r}{t}} + \log\frac{t}{2r+t}\right]\right\} \tag{2.181}$$

$$C_{2,z-M_y} = \frac{3}{Ew^3}\left[2r + (2r+t)\log\frac{t}{2r+t}\right] \tag{2.182}$$

2.3.4.2 Nonsymmetric Circular Flexure Hinge

2.3.4.2.1 Capacity of Rotation

The in-plane compliances are:

$$C_{1,x-F_x} = \frac{1}{Ew}\left\{\frac{2(r+t)}{\sqrt{t(2r+t)}}\arctan\left[\frac{r}{\sqrt{t(2r+t)}}\right] + \pi\left[\frac{r+t}{\sqrt{t(2r+t)}} - 1\right]\right\} \tag{2.183}$$

$$C_{1,y-F_y} = \frac{12}{Ew}\left\{\frac{3r^3(r+t)}{t^2(2r+t)^2} + \frac{2r}{r+t} + \pi - \frac{(r+t)^3(-3r^2+4rt+2t^2)}{\sqrt{t^5(2r+t)^5}}\left[\arctan\left[\frac{r}{\sqrt{t(2r+t)}}\right] + \frac{\pi}{2}\right]\right\} \tag{2.184}$$

$$C_{1,y-M_z} = \frac{12r^2}{Ew(r+t)\sqrt{t^5(2r+t)^5}}\left\{(3r^2+4rt+2t^2)\sqrt{t(2r+t)} + 3r(r+t)^2\left[\arctan\left[\frac{r}{\sqrt{t(2r+t)}}\right] + \frac{\pi}{2}\right]\right\} \tag{2.185}$$

$$C_{1,\theta_z-M_z} = \frac{C_{1,y-M_z}}{r} \tag{2.186}$$

The out-of-plane compliances are:

$$C_{1,z-F_z} = \frac{6}{Ew^3}\left\{(4-\pi)r^2 + 4(1+\pi)rt + 2\pi t^2 + \frac{4(r+t)(r^2-2rt-t^2)}{\sqrt{t(2r+t)}}\left[\arctan\left[\frac{r}{\sqrt{t(2r+t)}}\right] + \frac{\pi}{2}\right]\right\} \tag{2.187}$$

$$C_{1,z-M_y} = \frac{12r}{Ew^3}\left\{\pi\left[\frac{r+t}{\sqrt{t(2r+t)}} - 1\right] + \frac{2(r+t)}{\sqrt{t(2r+t)}}\arctan\left[\frac{r}{\sqrt{t(2r+t)}}\right]\right\} \tag{2.188}$$

2.3.4.2.2 Precision of Rotation

The in-plane compliances are:

$$C_{2,x-F_x} = \frac{1}{Ew}\left\{\pi\left[\frac{r+t}{\sqrt{t(2r+t)}} - \frac{1}{2}\right] - \frac{2(r+t)}{\sqrt{t(2r+t)}}\arctan\sqrt{\frac{t}{2r+t}}\right\} \tag{2.189}$$

$$C_{2,y-F_y} = \frac{6}{Ewt^2(r+t)(2r+t)}\left[2r^4 + 2r^3t + 2(2+\pi)r^2t^2 + (2+3\pi)rt^3 + \pi t^4 + 2(r+t)^2(-r^2+4rt+2t^2)\sqrt{\frac{t}{2r+t}}\left(\arctan\sqrt{\frac{t}{2r+t}} - \frac{\pi}{2}\right)\right] \tag{2.190}$$

$$C_{2,y-M_z} = \frac{6r^2}{Ewt^2(r+t)} \tag{2.191}$$

The out-of-plane compliances are:

$$C_{2,z-F_z} = \frac{3}{Ew^3}\left[\pi r^2 + 4(1+\pi)rt + 2\pi t^2 - 4\pi(r+t)\sqrt{t(2r+t)} + 8(2r^2+3rt+t^2)\sqrt{\frac{t}{2r+t}}\arctan\sqrt{\frac{t}{2r+t}} + 4r(r+t)\log\left(1+\frac{r}{t}\right)\right] \tag{2.192}$$

$$C_{2,z-M_y} = \frac{12}{Ew^3}\left[(r+t)\log\left(1+\frac{r}{t}\right) - r\right] \tag{2.193}$$

2.3.5 Corner-Filleted Flexure Hinge

Closed-form compliance equations are presented here for longitudinally symmetric and nonsymmetric corner-filleted flexure hinges in order to characterize their capacity of rotation and precision of rotation.

2.3.5.1 Symmetric Corner-Filleted Flexure Hinge

A longitudinally symmetric flexure hinge and its defining geometric parameters are shown in Figure 2.22. The variable thickness, $t(x)$, is expressed in terms of the fillet radius, r, and flexure length, l, as:

$$t(x) = \begin{cases} t + 2\left[r - \sqrt{x(2r-x)}\right], x \in [0, r] \\ t, x \in [r, l-r] \\ t + 2\left\{r - \sqrt{(l-x)[2r-(l-x)]}\right., x \in [l-r, r] \end{cases} \tag{2.194}$$

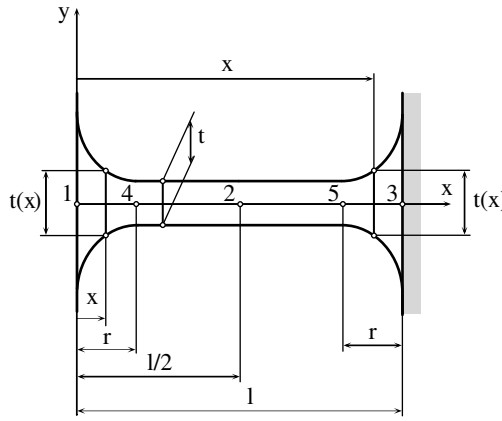

FIGURE 2.22
Cross-sectional profile of a symmetric corner-filleted flexure hinge.

2.3.5.1.1 Capacity of Rotation

The in-plane compliances are:

$$C_{1,x-F_x} = \frac{1}{Ew}\left[\frac{l-2r}{t} + \frac{2(2r+t)}{\sqrt{t(4r+t)}}\arctan\sqrt{1+\frac{4r}{t}} - \frac{\pi}{2}\right] \tag{2.195}$$

$$\begin{aligned} C_{1,y-F_y} = \frac{3}{Ew}\Bigg\{ & \frac{4(l-2r)(l^2-lr+r^2)}{3t^3} \\ & + \frac{\sqrt{t(4r+t)}[-80r^4+24r^3t+8(3+2\pi)r^2t^2+4(1+2\pi)rt^3+\pi_t^4]}{4\sqrt{t^5(4r+t)^5}} \\ & + \frac{(2r+t)^3(6r^2-4rt-t^2)\arctan\sqrt{1+\dfrac{4r}{t}}}{\sqrt{t^5(4r+t)^5}} \\ & + \frac{-40r^4+8lr^2(2r-t)+12r^3t+4(3+2\pi)r^2t^2+2(1+2\pi)rt^3+\dfrac{\pi t^4}{2}}{2t^2(4r+t)^2} \\ & + \frac{4l^2r(6r^2+4rt+t^2)}{t^2(2r+t)(4r+t)^2} - \frac{(2r+t)[-24(l-r)^2r^2-8r^3t+14r^2t^2+8rt^3+t^4]}{\sqrt{t^5(4r+t)^5}} \\ & \arctan\sqrt{1+\frac{4r}{t}}\Bigg\} \end{aligned} \tag{2.196}$$

$$C_{1,y-M_z} = -\frac{6l}{Ewt^3(2r+t)(4r+t)^2}\left\{(4r+t)[l(2r+t)(4r+t)^2 - 4r^2(16r^2+13rt+3t^2)] + 12r^2(2r+t)^2\sqrt{t(4r+t)}\arctan\sqrt{1+\frac{4r}{t}}\right\} \tag{2.197}$$

$$C_{1,\theta_z-M_z} = \frac{12}{Ewt^3}\left\{l-2r+\frac{2r}{(2r+t)(4r+t)^3}\left[t(4r+t)(6r^2+4rt+t^2) + 6r(2r+t)^2\sqrt{t(4r+t)}\arctan\sqrt{1+\frac{4r}{t}}\right]\right\} \tag{2.198}$$

The out-of-plane compliances are:

$$C_{1,z-F_z} = \frac{12}{Ew^3}\left\{\frac{(l-2r)(l^2-lr+r^2)}{3t}+lr\left[\log\frac{t}{2r+t}-\frac{2(l-2r)}{\sqrt{t(4r+t)}}\arctan\sqrt{1+\frac{4r}{t}}\right]\right\} \tag{2.199}$$

$$C_{1,z-M_y} = \frac{6}{Ew^3t}\left\{l(l-2r)+2r\left[t\log\frac{t}{2r+t}-2(l-2r)\sqrt{\frac{t}{4r+t}}\arctan\sqrt{1+\frac{4r}{t}}\right]\right\} \tag{2.200}$$

$$C_{1,\theta_y-M_y} = \frac{6}{Ew^3t}\left[2l-4r-\pi t+4(2r+t)\sqrt{\frac{t}{4r+t}}\arctan\sqrt{\frac{t}{4r+t}}\right] \tag{2.201}$$

Equation (2.201) confirms again the more generic Eq. (2.75) and therefore, the corresponding compliance will no longer be given in explicit form for the other flexure hinge configurations.

2.3.5.1.2 Precision of Rotation

The in-plane compliance equations that describe the precision of rotation are:

$$C_{2,x-F_x} = \frac{1}{2}C_{1,x-F_x} \tag{2.202}$$

$$C_{2,y-F_y} = \frac{1}{4Ewt^3(2r+t)\sqrt{(4r+t)^5}}\left\{\sqrt{4r+t}\{-5l^3(2r+t)(4r+t)^2-72lr^3 \times(2r+t)(8r+5t)+48l^2r^2(16r^2+13rt+3t^2)+(2r+t)[256r^5+368r^4t - 56r^3t^2-24(3+2\pi)r^2t^3-12(1+2\pi)rt^4-3\pi t^5]\}+12\sqrt{t}(2r+t)^2[-12l^2r^2 + 36lr^3-(2r+t)^2(6r^2-4rt-t^2)]\arctan\sqrt{1+\frac{4r}{t}}\right\} \tag{2.203}$$

$$C_{2,y-M_z} = \frac{3}{2Ewt^3(2r+t)\sqrt{(4r+t)^5}}\left\{\sqrt{4r+t}[l^2(2r+t)(4r+t)^2 + 8r^3(2r+t)\right.$$
$$\left.\times(8r+5t) - 8lr^2(16r^2+13rt+3t^2)] + 24\sqrt{t}(l-2r)r^2(2r+t)^2\arctan\sqrt{1+\frac{4r}{t}}\right\} \tag{2.204}$$

The out-of-plane compliance equations that describe the precision of rotation are:

$$C_{2,z-F_z} = \frac{12}{Ew^3}\left\{\frac{(5l-4r)(l-2r)^2}{48t} + \frac{\pi l^2 + (\pi-2)lr + [2(\pi+2)r+\pi t]r}{8}\right.$$
$$-\frac{(l-r)(6lr+lt-4r^2) - rt(4r+t)}{2\sqrt{t(4r+t)}}\arctan\sqrt{1+\frac{4r}{t}} \tag{2.205}$$
$$\left.+\frac{8r^2-6lr+lt}{8}\log\frac{t}{2r+t}\right\}$$

$$C_{2,z-M_y} = \frac{12}{Ew^3}\left[\frac{(l-2r)^2}{8t} + \frac{2(\pi-2)r-\pi l}{8} + \frac{(l-2r)(2r+t)}{2\sqrt{t(4r+t)}}\arctan\sqrt{1+\frac{4r}{t}}\right. \tag{2.206}$$
$$\left.-\frac{2r+t}{4}\log\frac{t}{2r+t}\right]$$

2.3.5.2 Nonsymmetric Corner-Filleted Flexure Hinge

2.3.5.2.1 Capacity of Rotation

The in-plane compliances are:

$$C_{1,x-F_x} = \frac{1}{Ewt}\left\{l - 2r - \pi t + 2(r+t)\left[\arctan\frac{r}{\sqrt{t(2r+t)}} + \frac{\pi}{2}\right]\right\} \tag{2.207}$$

$$C_{1,y-F_y} = \frac{12}{Ew}\left\{\frac{2l^3(r+t)(2r+t)^2 + 6lr^3(r+t)(4r+5t) - 3l^2r^2(8r^2+13rt+6t^2)}{6t^3(r+t)(2r+t)^2}\right.$$
$$-\frac{2(r+t)[8r^5+23r^4t-7r^3t^2-6(3+2\pi)r^2t^3-6(1+2\pi)rt^4-3\pi t^5]}{6t^3(r+t)(2r+t)^2}$$
$$\left.+\frac{3l^2r^2-6lr^3+2(r+t)^2(3r^2-4rt-2t^2)}{\sqrt{t^5(2r+t)^5}}\arctan\sqrt{1+\frac{2r}{t}}\right\} \tag{2.208}$$

$$C_{1,y-M_z}=\frac{12}{Ew}\left\{\frac{l(l-2r)}{2t^3}+\frac{3r^4+4r^3t+6r^2t^2+4rt^3+t^4-(r+t)^2(t-r)(3r+t)}{2t^2(r+t)(2r+t)^2}\right.$$
$$\left.-\frac{3r^3(r+t)}{\sqrt{t^5(2r+t)^5}}\left[\arctan\frac{r}{\sqrt{t(2r+t)}}-\frac{\pi}{2}\right]\right\} \tag{2.209}$$

$$C_{1,\theta_z,M_z}=\frac{12}{Ew}\left[\frac{l-2r}{t^3}+\frac{r(3r^2+4rt+2t^2)}{t^2(r+t)(2r+t)^2}+\frac{6r^2(r+t)}{\sqrt{t^5(2r+t)^5}}\arctan\sqrt{1+\frac{2r}{t}}\right] \tag{2.210}$$

The out-of-plane compliances are:

$$C_{1,z-F_z}=\frac{12}{Ew^3}\left\{-\frac{\pi l^2}{2}+(\pi-2)lr+\left(6-\frac{\pi}{2}\right)r^2+\frac{(l-r)^3-r^3}{3t}+2(\pi+1)rt+\pi t^2\right.$$
$$+\frac{2(r+t)[(l-r)^2+r^2-4rt-2t^2]}{\sqrt{t(2r+t)}}\arctan\sqrt{1+\frac{2r}{t}}$$
$$\left.+2(r+t)(l-2r)\log\left(1+\frac{r}{t}\right)\right\} \tag{2.211}$$

$$C_{1,z-M_y}=\frac{6l}{Ew^3}\left[\frac{4(r+t)}{\sqrt{t(2r+t)}}\arctan\sqrt{1+\frac{2r}{t}}+\frac{(l-2r)}{t}-\pi\right] \tag{2.212}$$

2.3.5.2.2 Precision of Rotation

The in-plane compliances are:

$$C_{2,x-F_x}=\frac{1}{2Ewt}\left[l-2r-\pi t+4(r+t)\sqrt{\frac{t}{2r+t}}\arctan\sqrt{1+\frac{2r}{t}}\right] \tag{2.213}$$

$$C_{2,y-F_y}=\frac{1}{4Ewt^3}\left\{-3l\left[(l-2r)(3l-2r)+\frac{4r^2t(7r^2+8rt+3t^2)}{(r+t)(2r+t)^2}+12\pi r^3(r+t)\right.\right.$$
$$\left.\times\sqrt{\frac{t}{(2r+t)^5}}\right]+2\left\{-l^3+8(l-r)^3+12t\left[-2r^2+2rt+\pi t^2+\frac{l^2r}{r+t}\right.\right.$$
$$\left.\left.-\frac{3r^2(l-r)^2}{(2r+t)^2}+\frac{r(l^2-2lr+3r^2)}{2r+t}\right]\right\}+24\sqrt{\frac{t}{(2r+t)^5}}\left\{3lr^3(2r+t)\arctan\right.$$
$$\left.\left.\sqrt{\frac{t}{2r+t}}+2(r+t)\left[3l^2r^2-6lr^3+(r+t)^2(3r^2-4rt-2t^2)\arctan\sqrt{1+\frac{2r}{t}}\right]\right\}\right\} \tag{2.214}$$

$$C_{2,y-M_z} = \frac{3}{2Ewt^3}\left\{(l-2r)(3l-2r) + \frac{4r^2t(7r^2+8rt+3t^2)}{(r+t)(2r+t)^2}\right.$$
$$+12\pi r^3(r+t)\sqrt{\frac{t}{(2r+t)^5}} - 2l\left[l-2r+\frac{rt(3r^2+4rt+2t^2)}{(r+t)(2r+t)^2}\right] \quad (2.215)$$
$$\left.-12r(r+t)\sqrt{\frac{t}{(2r+t)^5}}\left(2r^2\arctan\sqrt{\frac{t}{2r+t}} + l^2\arctan\sqrt{1+\frac{2r}{t}}\right)\right\}$$

The out-of-plane compliances are:

$$C_{2,z-F_z} = \frac{1}{4Ew^3t}\left\{(5l-4r)(l-2r)^2 - 12t[\pi l^2 - 3(\pi-2)lr - (12-\pi)r^2]\right.$$
$$+48(\pi+1)rt^2 + 24\pi t^3 - \frac{48\sqrt{t}(r+t)(-l^2+3lr-2r^2+4rt+2t^2)}{\sqrt{2r+t}} \quad (2.216)$$
$$\left.\arctan\sqrt{1+\frac{2r}{t}} + 24t(t+r)(3l-4r)\log\left(1+\frac{r}{t}\right)\right\}$$

$$C_{2,z-M_y} = \frac{12}{Ew^3}\left[\frac{(l-2r)^2 - 2t[\pi l - 2(\pi-2)r]}{8t} + \frac{(t+r)(l-2r)}{\sqrt{t(2r+t)}}\right.$$
$$\left.\arctan\sqrt{1+\frac{2r}{t}} + (r+t)\log\left(1+\frac{r}{t}\right)\right] \quad (2.217)$$

Several flexures are presented in the following text that share a common trait, namely that the longitudinal sections for all of them can be expressed in terms of a new parameter, denoted by c, in addition to the ones already defined: flexure length l and minimum thickness t. Figure 2.23 shows the longitudinal section of a symmetric elliptical flexure hinge, but the figure is also representative for other profiles, such as: the parabola, hyperbola, inverse parabola, and secant. Parameter c enables us to alter the value of the variable thickness. By increasing c, the thickness, $t(x)$, also increases, as indicated in Figure 2.24, where several plots are presented for the profiles that were previously mentioned and for three different values of c ($c_1 < c_2 < c_3$).

2.3.6 Parabolic Flexure Hinge

Closed-form compliance equations will be presented here for longitudinally symmetric and nonsymmetric parabolic flexure hinges. The geometric profiles of three different parabolas are shown in Figure 2.24a. Similar to other

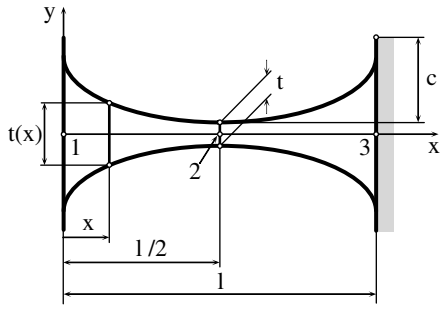

FIGURE 2.23
Cross-sectional profile of a symmetric elliptical flexure hinge.

flexure configurations that have been presented, the compliances will serve to characterize the capacity of rotation and precision of rotation of these flexure hinges.

2.3.6.1 Symmetric Parabolic Flexure Hinge

The variable thickness, $t(x)$, is:

$$t(x) = t + 2c\left(1 - 2\frac{x}{l}\right)^2 \tag{2.218}$$

2.3.6.1.1 Capacity of Rotation

The in-plane compliances are:

$$C_{1,x-F_x} = \frac{l}{\sqrt{2}Ew\sqrt{ct}}\operatorname{arccot}\sqrt{\frac{t}{2c}} \tag{2.219}$$

$$C_{1,y-F_y} = \frac{3l^3}{16Ewt^2c}\left[\frac{12c^2 + 12ct - t^2}{(2c+t)^2} + \frac{6c+t}{\sqrt{2ct}}\operatorname{arccot}\sqrt{\frac{t}{2c}}\right. \tag{2.220}$$

$$C_{1,y-M_z} = \frac{3l^2}{8Ewt^3(2c+t)^2}\left[2t(6c+5t) + 3\sqrt{\frac{2t}{c}}(4c^2+t^2)\operatorname{arccot}\sqrt{\frac{t}{2c}}\right. \tag{2.221}$$

$$C_{1,\theta_z-M_z} = \frac{2}{l}C_{1,y-M_z} \tag{2.222}$$

Equation (2.222) is valid for all following flexure configurations, except for the secant. As a consequence, this equation will not be repeated for the cases where it is valid.

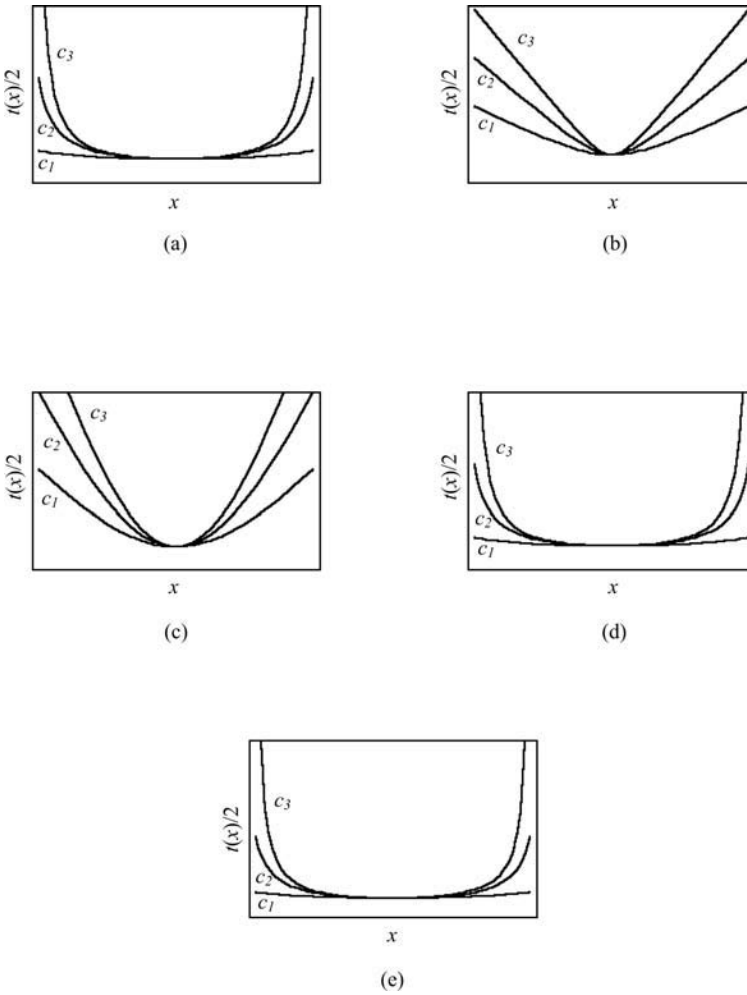

FIGURE 2.24
Profiles of other flexure hinges: (a) parabolic; (b) hyperbolic; (c) elliptical; (d) inverse parabolic; (e) secant.

The out-of-plane compliances are:

$$C_{1,z-F_z} = \frac{3l^3}{4Ew^3tc}\left[2t + (2c-t)\sqrt{\frac{2t}{c}}a\cot an\sqrt{\frac{t}{2c}}\right] \tag{2.223}$$

$$C_{1,z-M_y} = \frac{3\sqrt{2}l^2}{Ew^3\sqrt{ct}}a\cot an\sqrt{\frac{t}{2c}} \tag{2.224}$$

$$C_{1,\theta_y-M_y} = \frac{12}{w^2}C_{1,x-F_x} \tag{2.225}$$

Equation (2.225) is also valid for all following flexure configurations, except for the secant. This equation, therefore, will not be repeated for the cases where it is valid.

2.3.6.1.2 Precision of Rotation

The in-plane compliance equations that describe the precision of rotation are:

$$C_{2,x-F_x} = \frac{l}{2\sqrt{2}Ew\sqrt{ct}}\operatorname{arccot}\sqrt{\frac{t}{2c}} \tag{2.226}$$

$$C_{2,y-F_y} = \frac{3l^3}{64Ewt^2c(2c+t)}\left[2(4c+t) - \sqrt{\frac{2t}{c}}(2c+t)\operatorname{arccot}\sqrt{\frac{t}{2c}}\right. \tag{2.227}$$

$$C_{2,y-M_z} = \frac{3c(c+t)l^2}{2Ewt^3(2c+t)^2} \tag{2.228}$$

The out-of-plane compliance equations that describe the precision of rotation are:

$$C_{2,z-F_z} = \frac{3l^3}{8Ew^3c}\left[2 - \sqrt{\frac{2t}{c}}\arctan\sqrt{\frac{2c}{t}} + \log\left(\frac{2c+t}{t}\right)\right] \tag{2.229}$$

$$C_{2,z-M_y} = \frac{3l^2}{4Ew^3c}\log\frac{2c+t}{t} \tag{2.230}$$

2.3.6.2 Nonsymmetric Parabolic Flexure Hinge

2.3.6.2.1 Capacity of Rotation

The in-plane compliances are:

$$C_{1,x-F_x} = \frac{l}{Ew\sqrt{tc}}\arctan\sqrt{\frac{c}{t}} \tag{2.231}$$

$$C_{1,y-F_y} = \frac{3l^3}{8Ew\sqrt{t^5c^3}}\left[\frac{(3c^2+6ct-t^2)\sqrt{ct}}{(c+t)^2} + (3c+t)\arctan\sqrt{\frac{c}{t}}\right] \tag{2.232}$$

$$C_{1,y-M_z} = \frac{3l^2}{4Ew\sqrt{t^5}}\left[\frac{(3c+5t)\sqrt{t}}{(c+t)^2} + \frac{3}{\sqrt{c}}\arctan\sqrt{\frac{c}{t}}\right] \tag{2.233}$$

The out-of-plane compliances are:

$$C_{1,z-F_z} = \frac{3l^3}{Ew^3\sqrt{c^3}}\left[\sqrt{c} + \frac{c-t}{\sqrt{t}}\arctan\sqrt{\frac{c}{t}}\right. \tag{2.234}$$

$$C_{1,z-M_y} = \frac{6l^2}{Ew^3\sqrt{ct}}\arctan\sqrt{\frac{c}{t}} \tag{2.235}$$

2.3.6.2.2 Precision of Rotation

The in-plane compliances are:

$$C_{2,x-F_x} = \frac{1}{2}C_{1,x-F_x} \tag{2.236}$$

$$C_{2,y-F_y} = \frac{3l^3}{16Ewt^2(c+t)^2}\left[2c + 5t - \frac{t^2}{c} + (c+t)^2\sqrt{\frac{t}{c^3}}\arctan\sqrt{\frac{c}{t}}\right] \tag{2.237}$$

$$C_{2,y-M_z} = \frac{3l^2(c+2t)}{4Ewt^2(c+t)^2} \tag{2.238}$$

The out-of-plane compliances are:

$$C_{2,z-F_z} = \frac{3l^3}{4Ew^3\sqrt{c^3}}\left[2\left(\sqrt{c} - \sqrt{t}\arctan\sqrt{\frac{c}{t}}\right) + \sqrt{c}\log\left(1+\frac{c}{t}\right)\right] \tag{2.239}$$

$$C_{2,z-M_y} = \frac{3l^2}{2Ew^3c}\log\left(1+\frac{c}{t}\right) \tag{2.240}$$

2.3.7 Hyperbolic Flexure Hinge

Longitudinally symmetric and then nonsymmetric flexure hinges of hyperbolic profile, as plotted in Figure 2.24b, are analyzed in this section by formulating closed-form compliance equations that allow us to qualify them in terms of their capacity of rotation and precision of rotation, as well.

2.3.7.1 Symmetric Hyperbolic Flexure Hinge

The variable thickness, $t(x)$, is:

$$t(x) = \sqrt{t^2 + 4c(c+t)\left(1-2\frac{x}{l}\right)^2} \tag{2.241}$$

2.3.7.1.1 Capacity of Rotation

The in-plane compliances are:

$$C_{1,x-F_x} = \frac{l}{2Ew\sqrt{c(c+t)}} \log \frac{t+2c\left(1+\sqrt{1+\frac{t}{c}}\right)}{t+2c\left(1-\sqrt{1+\frac{t}{c}}\right)} \tag{2.242}$$

$$C_{1,y-F_y} = \frac{l^3}{32Ewt^2c(c+t)(2c+t)}\left[2(4c^2+4ct-t^2) - \frac{t^2(2c+t)}{\sqrt{c(c+t)}}\right.$$
$$\left.\log \frac{t+2c\left(1-\sqrt{1+\frac{t}{c}}\right)}{t+2c\left(1+\sqrt{1+\frac{t}{c}}\right)}\right] \tag{2.243}$$

$$C_{1,y-M_z} = \frac{6l^2}{Ewt^2(2c+t)} \tag{2.244}$$

The out-of-plane compliances are:

$$C_{1,z-F_z} = \frac{3l^3}{32Ew^3c(c+t)}\left[4(2c+t) + \frac{8c^2+8ct-t^2}{\sqrt{c(c+t)}} \log \frac{t+2c\left(1+\sqrt{1+\frac{t}{c}}\right)}{t+2c\left(1-\sqrt{1+\frac{t}{c}}\right)}\right. \tag{2.245}$$

$$C_{1,z-M_y} = \frac{3l}{w^2} C_{1,x-F_x} \tag{2.246}$$

2.3.7.1.2 Precision of Rotation

The in-plane compliance equations that describe the precision of rotation are:

$$C_{2,x-F_x} = \frac{l}{4Ew\sqrt{c(c+t)}} \log \frac{t}{t+2c\left(1-\sqrt{1+\frac{t}{c}}\right)} \tag{2.247}$$

$$C_{2,y-F_y} = \frac{3l^3}{16Ewtc(c+t)}\left[2 - \frac{t}{\sqrt{c(c+t)}} \log \frac{t}{t+2c\left(1-\sqrt{1+\frac{t}{c}}\right)}\right] \tag{2.248}$$

$$C_{2,y-M_z} = \frac{3l^2}{2Ewtc(2c+t)} \tag{2.249}$$

The out-of-plane compliance equations that describe the precision of rotation are:

$$C_{2,z-F_z} = \frac{3l^3}{16Ew^3c(c+t)^2}\left[(c+t)(6c+t)+t\sqrt{c(c+t)}\log\frac{t}{t+2c\left(1+\sqrt{1+\frac{t}{c}}\right)}\right] \tag{2.250}$$

$$C_{2,z-M_y} = \frac{3l^2}{2Ew^3(c+t)} \tag{2.251}$$

2.3.7.2 Nonsymmetric Hyperbolic Flexure Hinge

2.3.7.2.1 Capacity of Rotation

The in-plane compliances are:

$$C_{1,x-F_x} = \frac{l}{2Ew\sqrt{c(c+2t)}}\log\left[\frac{c+t+\sqrt{c(c+2t)}}{c+t-\sqrt{c(c+2t)}}\right] \tag{2.252}$$

$$C_{1,y-F_y} = \frac{3l^3}{2Ewt^2}\left\{\frac{2(c^2+2ct-t^2)}{c(c+t)(c+2t)} + \frac{t^2}{\sqrt{c^3(c+2t)^3}}\log\left[\frac{c+t+\sqrt{c(c+2t)}}{c+t-\sqrt{c(c+2t)}}\right]\right\} \tag{2.253}$$

$$C_{1,y-M_z} = \frac{6l^2}{Ewt^2(c+t)} \tag{2.254}$$

The out-of-plane compliances are:

$$C_{1,z-F_z} = \frac{3l^3}{4Ew^3}\left\{\frac{2(c+t)}{c(c+2t)} + \frac{2c^2+4ct-t^2}{\sqrt{c^3(c+2t)^3}}\log\left[\frac{c+t+\sqrt{c(c+2t)}}{c+t-\sqrt{c(c+2t)}}\right]\right\} \tag{2.255}$$

$$C_{1,z-M_y} = \frac{3l^2}{Ew^3\sqrt{c(c+2t)}}\log\left[\frac{c+t+\sqrt{c(c+2t)}}{c+t-\sqrt{c(c+2t)}}\right] \tag{2.256}$$

2.3.7.2.2 Precision of Rotation

The in-plane compliances are:

$$C_{2,x-F_x} = \frac{l}{2Ew\sqrt{c(c+2t)}} \log\left[\frac{c+t+\sqrt{c(c+2t)}}{t}\right] \tag{2.257}$$

$$C_{2,y-F_y} = \frac{3l^3}{2Ewt(c+2t)\sqrt{c^3}} \left\{\frac{\sqrt{c}(c-t)}{c+t} - \frac{t}{\sqrt{c+2t}} \log\left[\frac{t}{c+t+\sqrt{c(c+2t)}}\right]\right\} \tag{2.258}$$

$$C_{2,y-M_z} = \frac{3l^2}{Ewt(c+t)(c+2t)} \tag{2.259}$$

The out-of-plane compliances are:

$$C_{2,z-F_z} = \frac{3l^3}{4Ew^3\sqrt{c^3}(c+2t)} \left\{\sqrt{c}(3c+t) - \frac{t^2}{\sqrt{c+2t}} \log\left[\frac{c+t+\sqrt{c(c+2t)}}{t}\right]\right\} \tag{2.260}$$

$$C_{2,z-M_y} = \frac{3l^2}{Ew^3(c+2t)} \tag{2.261}$$

2.3.8 Elliptical Flexure Hinge

The flexure hinges of elliptic profile, as shown in Figure 2.24c, are analyzed here. Closed-form compliance equations will be formulated for longitudinally symmetric and nonsymmetric elliptical flexure hinges in order to qualify their capacity of rotation and precision of rotation.

2.3.8.1 Symmetric Elliptical Flexure Hinge

The variable thickness of a longitudinally symmetric flexure hinge is:

$$t(x) = t + 2c\left[1 - \sqrt{1 - \left(1 - \frac{2x}{c}\right)^2}\right] \tag{2.262}$$

2.3.8.1.1 Capacity of Rotation

The in-plane compliances are:

$$C_{1,x-F_x} = \frac{l}{4Ewc}\left[\frac{4(2c+t)}{\sqrt{t(4c+t)}} \arctan\sqrt{1+\frac{4c}{t}} - \pi\right] \tag{2.263}$$

$$C_{1,y-F_y} = \frac{3l^3}{16Ewt^3c^3(2c+t)(4c+t)^2}\left\{t[96c^5 + 96c^4t + 8(11+4\pi)c^3t^2 + 32(1+\pi)c^2t^3 + 2(2+5\pi)ct^4 + \pi t^5] - 4\sqrt{\frac{t}{4c+t}}(2c+t)^4 (-6c^2 + 4ct + t^2)\arctan\sqrt{1+\frac{4c}{t}}\right\} \quad (2.264)$$

$$C_{1,y-M_z} = \frac{6l^2}{Ewt^2(2c+t)(8c^2+t^2)}\left[6c^2 + 4ct + t^2 + \frac{6c(2c+t)^2}{\sqrt{t(4c+t)}}\arctan\sqrt{1+\frac{4c}{t}}\right] \quad (2.265)$$

The out-of-plane compliances are:

$$C_{1,z-F_z} = \frac{3l^3}{16Ew^3c^3}\left\{2(4-\pi)c^2 + 4(1+\pi)ct + \frac{(2c+t)(-4c^2+4ct+t^2)}{\sqrt{t(4c+t)}} \times\left[2\arctan\frac{2c}{\sqrt{t(4c+t)}} - \pi\right]\right\} \quad (2.266)$$

$$C_{1,z-M_y} = \frac{3l^2}{2Ew^3c}\left\{\frac{2c+t}{\sqrt{t(4c+t)}}\left[2\arctan\frac{2c}{\sqrt{t(4c+t)}} + \pi\right] - \pi\right\} \quad (2.267)$$

2.3.8.1.2 Precision of Rotation

The in-plane compliances are:

$$C_{2,y-F_y} = \frac{3l^3}{32Ewt^2c^3(4c+t)^3}\left\{(4c+t)^2[16c^3 - 8c^2t - 4(1+\pi)ct^2 - \pi t^3] + 4(2c+t)\left[24\sqrt{1+\frac{4c}{t}}c^4 - (2c+t)^2(6c^2 - 4ct - t^2)\right]\arctan\sqrt{1+\frac{4c}{t}}\right\} \quad (2.268)$$

$$C_{2,y-M_z} = \frac{3l^2}{2Ewt^2(2c+t)} \quad (2.269)$$

The out-of-plane compliances are:

$$C_{2,z-F_z} = \frac{3l^3}{32Ew^3c^3}\left\{2\pi c^2 + 4(1+\pi)ct + \pi t^2 + 4(2c+t)\left[c\log\left(1+\frac{2c}{t}\right)\right.\right.$$
$$\left.\left. - \sqrt{t(4c+t)}\arctan\sqrt{1+\frac{2c}{t}}\right]\right\} \tag{2.270}$$

$$C_{2,z-M_y} = \frac{3l^2}{4Ew^3c^3}\left[(2c+t)\log\left(1+\frac{2c}{t}\right) - 2c\right] \tag{2.271}$$

2.3.8.2 Nonsymmetric Elliptical Flexure Hinge

2.3.8.2.1 Capacity of Rotation

The in-plane compliances are:

$$C_{1,x-F_x} = \frac{l}{2Ewc}\left\{\pi\left[\frac{c+t}{\sqrt{t(2c+t)}} - 1\right] + \frac{2(c+t)}{\sqrt{t(2c+t)}}\arctan\left[\frac{c}{\sqrt{t(2c+t)}}\right]\right\} \tag{2.272}$$

$$C_{1,y-F_y} = \frac{3l^3}{4Ew\sqrt{t^5}c^3}\left\{-\frac{\sqrt{t}}{(2c+t)^2}\left[-3c^4 - 3c^3t + 8\pi c^2t^2 + 8\pi ct^3 + 2\pi t^4\right.\right.$$
$$\left. + \frac{\pi(c+t)^3(-3c^2+4ct+2t^2)}{\sqrt{t(2c+t)}}\right] + \frac{\sqrt{t}}{(c+t)(c+2t)^2}[3c^5 + 6c^4t$$
$$+ (19+16\pi)c^3t^2 + 16(1+2\pi)c^2t^3 + 4(1+5\pi)ct^4 + 4\pi t^5]$$
$$\left. + \frac{2(c+t)^3(3c^2-4ct-2t^2)}{\sqrt{(2c+t)^5}}\arctan\left[\frac{c}{\sqrt{t(2c+t)}}\right]\right\} \tag{2.273}$$

$$C_{1,y-M_z} = \frac{3l^2}{2Ew(c+t)\sqrt{t^5(2c+t)^5}}\left\{\sqrt{t(2c+t)}\left[4t^2 + 8tc + 6c^2 + \frac{3\pi c(c+t)^2}{\sqrt{t(2c+t)}}\right]\right.$$
$$\left. + 6c(c+t)^2\arctan\left[\frac{c}{\sqrt{t(2c+t)}}\right]\right\} \tag{2.274}$$

The out-of-plane compliances are:

$$C_{1,z-F_z} = \frac{3l^3}{4Ew^3c^3}\left\{2\pi t^2 + 4(1+\pi)ct + (4-\pi)c^2 + \frac{4(c+t)(c^2-2ct-t^2)}{\sqrt{t(2c+t)}}\left(\arctan\left[\frac{c}{\sqrt{t(2c+t)}}\right]+\frac{\pi}{2}\right)\right\} \quad (2.275)$$

$$C_{1,z-M_y} = \frac{3l^2}{Ew^3c}\left\{\pi\left[\frac{c+t}{\sqrt{t(2c+t)}}-1\right]+\frac{2(c+t)}{\sqrt{t(2c+t)}}\arctan\left[\frac{c}{\sqrt{t(2c+t)}}\right]\right\} \quad (2.276)$$

2.3.8.2.2 Precision of Rotation

The in-plane compliances are:

$$C_{2,x-F_x} = \frac{l}{4Ewc}\left[\frac{4(c+t)}{\sqrt{t(2c+t)}}\arctan\sqrt{1+\frac{2c}{t}}-\pi\right] \quad (2.277)$$

$$C_{2,y-F_y} = \frac{3l^3}{4Ewt^2c^3(c+t)}\left[2c^3+(2+\pi)ct^2+\pi t^3-\frac{2c^4}{2c+t} + 2\sqrt{\frac{t}{(2c+t)^3}}(c+t)^2(c^2-4ct-2t^2)\arctan\sqrt{1+\frac{2c}{t}}\right] \quad (2.278)$$

$$C_{2,y-M_z} = \frac{3l^2}{2Ewt^2(c+t)} \quad (2.279)$$

The out-of-plane compliances are:

$$C_{2,z-F_z} = \frac{3l^3}{8Ew^3c^3}\left\{\pi c^2+4(1+\pi)ct+2\pi t^2+4(c+t)\left[c\log\left(1+\frac{c}{t}\right) - 2\sqrt{t(2c+t)}\arctan\sqrt{1+\frac{2c}{t}}\right]\right\} \quad (2.280)$$

$$C_{2,z-M_y} = \frac{3l^2}{Ew^3c^2}\left[(c+t)\log\left(1+\frac{c}{t}\right)-c\right] \quad (2.281)$$

2.3.9 Inverse Parabolic Flexure Hinge

The flexure hinges of inverse parabolic profile (see three plots provided in Figure 2.24d) are analyzed here by their closed-form compliance equations. The capacity of rotation and precision of rotation will be discussed for longitudinally symmetric and nonsymmetric flexure hinges.

2.3.9.1 Symmetric Inverse Parabolic Flexure Hinge

The variable thickness of a symmetric inverse parabolic flexure hinge can be expressed as:

$$t(x) = \frac{2a}{b^2 - \left(x - \frac{l}{2}\right)^2} \tag{2.282}$$

where geometric parameters a_1 and b_1 are:

$$\begin{cases} a_1 = \dfrac{tl^2}{8}\left(1 + \dfrac{t}{2c}\right) \\ b_1 = \dfrac{l}{2}\sqrt{1 + \dfrac{t}{2c}} \end{cases} \tag{2.283}$$

2.3.9.1.1 Capacity of Rotation

The in-plane compliances are:

$$C_{1,x-F_x} = \frac{l(4c + 3t)}{3Ewt(2c + t)} \tag{2.284}$$

$$C_{1,y-F_y} = \frac{4l^3(320c^3 + 576c^2t + 378ct^2 + 105t^3)}{105Ewt^3(2c + t)^3} \tag{2.285}$$

$$C_{1,y-M_z} = \frac{6l^2(128c^3 + 224c^2t + 140ct^2 + 35t^3)}{35Ewt^3(2c + t)^3} \tag{2.286}$$

The out-of-plane compliances are:

$$C_{1,z-F_z} = \frac{4l^3(6c + 5t)}{5Ew^3t(2c + t)} \tag{2.287}$$

$$C_{1,z-M_y} = \frac{2l^2(4c + 3t)}{Ew^3t(2c + t)} \tag{2.288}$$

2.3.9.1.2 Precision of Rotation

The in-plane compliances are:

$$C_{2,y-F_y} = \frac{l^3(886c^3 + 1836c^2t + 1449ct^2 + 525t^3)}{420Ewt^3(2c + t)^3} \tag{2.289}$$

$$C_{2,y-M_z} = \frac{3l^2(c + t)(2c^2 + 2ct + t^2)}{2Ewt^3(2c + t)^3} \tag{2.290}$$

The out-of-plane compliances are:

$$C_{2,z-F_z} = \frac{l^3(23c+25t)}{20Ew^3t(2c+t)} \tag{2.291}$$

$$C_{2,z-M_y} = \frac{3l^2(c+t)}{2Ew^3t(2c+t)} \tag{2.292}$$

2.3.9.2 Nonsymmetric Inverse Parabolic Flexure Hinge

2.3.9.2.1 Capacity of Rotation

The in-plane compliances are:

$$C_{1,x-F_x} = \frac{l}{Ewt}\left(2-\sqrt{2+\frac{t}{c}}\arctan h\sqrt{\frac{c}{2c+t}}\right) \tag{2.293}$$

$$C_{1,y-F_y} = \frac{l^3}{8Ewt^3(c+t)^2\sqrt{c^3}}\left[\sqrt{c}(1186c^3+2645c^2t+1804ct^2+357t^3)\right.$$
$$\left.-3(c+t)^2(313c+119t)\sqrt{2c+t}\arctan h\sqrt{\frac{c}{2c+t}}\right] \tag{2.294}$$

$$C_{1,y-M_z} = \frac{3l^2}{4Ewt^3(c+t)^2}\left[98c^2+183ct+83t^2-75(c+t)^2\sqrt{2+\frac{t}{c}}\arctan\sqrt{\frac{c}{2c+t}}\right] \tag{2.295}$$

The out-of-plane compliances are:

$$C_{1,z-F_z} = \frac{l^3}{Ew^3tc}\left[14c+3t-3(3c+t)\sqrt{2+\frac{t}{c}}\arctan h\sqrt{\frac{c}{2c+t}}\right] \tag{2.296}$$

$$C_{1,z-M_y} = \frac{6l^2}{Ew^3t}\left(2-\sqrt{2+\frac{t}{c}}\arctan h\sqrt{\frac{c}{2c+t}}\right) \tag{2.297}$$

2.3.9.2.2 Precision of Rotation

The in-plane compliances are:

$$C_{2,y-F_y} = \frac{l^3}{16Ewt^3(c+t)^2\sqrt{c^3}}\left\{\sqrt{c}\left[1096c^3+2462c^2t+1711ct^2+357t^3\right.\right.$$
$$\left.\left.+144(c+t)^2(2c+t)\log\frac{c+t}{2c+t}\right]-357(c+t)^2\sqrt{(2c+t)^3}\arctan h\sqrt{\frac{c}{2c+t}}\right\} \tag{2.298}$$

$$C_{2,y-M_z} = \frac{3l^2}{4Ewt^3c(c+t)^2}\left[24(c+t)^2(2c+t) - c(34c^2+61ct+26t^2)\log\frac{2c+t}{c+t}\right] \tag{2.299}$$

The out-of-plane compliances are:

$$C_{2,z-F_z} = \frac{l^3}{4Ew^3t\sqrt{c^3}}\left\{-6\sqrt{(2c+t)^3}\arctan h\sqrt{\frac{c}{2c+t}} + \sqrt{c}\left[22c+6t+3(2c+t)\log\frac{c+t}{2c+t}\right]\right\} \tag{2.300}$$

$$C_{2,z-M_y} = \frac{3l^2}{2Ew^3tc}\left[2c+(2c+t)\log\frac{c+t}{2c+t}\right] \tag{2.301}$$

2.3.10 Secant Flexure Hinge

Longitudinally symmetric and nonsymmetric flexure hinges of secant profile (as plotted in Figure 2.24e) are discussed in this section. The capacity of rotation and precision of rotation will be expressed by the closed-form compliance equations pertaining to this type of flexure hinge.

2.3.10.1 Symmetric Secant Flexure Hinge

The variable thickness, $t(x)$, of a longitudinally symmetric flexure hinge is expressed as:

$$t(x) = \frac{t}{\cos\left(\frac{2x-l}{l}\arccos\frac{t}{2c+t}\right)} \tag{2.302}$$

2.3.10.1.1 Capacity of Rotation

The in-plane compliances are:

$$C_{1,x-F_x} = \frac{2l\sqrt{c(c+t)}}{Ewt(2c+t)y} \tag{2.303}$$

$$C_{1,y-F_y} = \frac{l^3}{36Ewt^3(2c+t)^3y^3}\left[24t(24c^2+24ct+7t^2)y + 144\frac{\sqrt{c(c+t)}}{2c+t}(16c^3+24c^2t+14ct^2+3t^3)y^2 - 2\sqrt{c(c+t)}(644c^2+644ct+165t^2) - (2c+t)^3\sin(3y)\right] \tag{2.304}$$

$$C_{1,y-M_z} = \frac{l^2}{12Ewt^3(2c+t)^3}\left\{-4t(24c^2+24ct+7t^2)+(2c+t)^2\right.$$
$$\left.\times\left\{27t+(2c+t)\left[\cos(3y)+6y\left(\frac{18\sqrt{c(c+t)}}{2c+t}+\sin(3y)\right)\right]\right\}\right\} \quad (2.305)$$

$$C_{1,\theta_z,M_z} = \frac{l}{Ewt^3 y}\left[\frac{18\sqrt{c(c+t)}}{2c+t}+\sin(3y)\right] \quad (2.306)$$

where:

$$y = \arccos\frac{t}{2c+t} \quad (2.307)$$

The out-of-plane compliances are:

$$C_{1,z-F_z} = \frac{6l^3}{Ew^3t(2c+t)y^3}[ty+\sqrt{c(c+t)}(y^2-1)] \quad (2.308)$$

$$C_{1,z-M_y} = \frac{12l^2}{Ew^3t(2c+t)y} \quad (2.309)$$

2.3.10.1.2 Precision of Rotation

The in-plane compliances are:

$$C_{2,y-F_y} = \frac{l^3}{72Ewt^3(2c+t)y^3}\left\{3y[-56c+53t+3(2c+t)\cos(3y)]\right.$$
$$+18(2c+t)y^2\left[\frac{18\sqrt{c(c+t)}}{2c+t}+\sin(3y)\right]$$
$$\left.-2(2c+t)\left[\frac{162\sqrt{c(2c+t)}}{2c+t}+\sin(3y)\right]\right\} \quad (2.310)$$

$$C_{2,y-M_z} = \frac{l^2}{12Ewt^3(2c+t)y^2}\left\{-56c-t+(2c+t)\cos(3y)\right.$$
$$\left.+3(2c+t)y\left[\frac{18\sqrt{c(c+t)}}{2c+t}+\sin(3y)\right]\right\} \quad (2.311)$$

The out-of-plane compliances are:

$$C_{2,z-F_z} = \frac{3l^3}{Ew^3t(2c+t)y^3}[(t-c)y + 2\sqrt{c(c+t)}(y^2-1] \tag{2.312}$$

$$C_{2,z-M_y} = \frac{6l^2}{Ew^3t(2c+t)y^2}[\sqrt{c(c+t)}y - c] \tag{2.313}$$

2.3.10.2 Nonsymmetric Secant Flexure Hinge

2.3.10.2.1 Capacity of Rotation

The in-plane compliances are:

$$C_{1,x-F_x} = \frac{l\sqrt{c(c+2t)}}{Ewt(c+t)z} \tag{2.314}$$

$$C_{1,z-F_z} = \frac{l^3}{36Ewt^3z^3}\left\{-\frac{81\sqrt{c(c+2t)}}{c+t} - \frac{4\sqrt{c(c+2t)}}{(c+t)^3}(20c^2+40ct+21t^2)\right.$$
$$\left. + \frac{24t}{(c+t)^3}(6c^2+12ct+7t^2)z + \frac{72\sqrt{c(c+2t)}}{(c+t)^3}(2c^2+4ct+3t^2)z^2 - \sin(3z)\right\} \tag{2.315}$$

$$C_{1,z-M_z} = \frac{l^2}{12Ewt^3(c+t)^3z^2}\left\{-4t(6c^2+12ct+7t^2)\right.$$
$$\left. + (c+t)^2\left\{27t + (c+t)\left[\cos(3z) + 6z\left[\frac{9\sqrt{c(c+2t)}}{c+t} + \sin(3z)\right]\right]\right\}\right\} \tag{2.316}$$

$$C_{1,\theta_z,M_z} = \frac{l}{Ewt^3z}\left[\frac{9\sqrt{c(c+2t)}}{c+t} + \sin(3z)\right] \tag{2.317}$$

where:

$$z = \arccos\frac{t}{c+t} \tag{2.318}$$

The out-of-plane compliances are:

$$C_{1,z-F_z} = \frac{6l^3}{Ew^3t(c+t)z^3}[tz + \sqrt{c(c+2t)}(z^2-1)] \tag{2.319}$$

$$C_{1,z-M_y} = \frac{6l^2\sqrt{c(c+2t)}}{Ew^3t(c+t)z} \tag{2.320}$$

2.3.10.2.2 Precision of Rotation

The in-plane compliances are:

$$C_{2,x-F_x} = \frac{l\sqrt{c(c+4t)}}{4Ewt(c+2t)u} \tag{2.321}$$

where:

$$u = \arccos\frac{2t}{c+2t} \tag{2.322}$$

$$C_{2,z-F_z} = \frac{l^3}{72Ewt^3(c+t)z^3}\left\{3z[-28c+53t+3(c+t)\cos(3z)]\right.$$
$$\left.+18(c+t)z^2\left[\frac{9\sqrt{c(c+2t)}}{c+t}+\sin(3z)\right]-2(c+t)\left[\frac{81\sqrt{c(c+2t)}}{c+t}+\sin(3z)\right]\right\} \tag{2.323}$$

$$C_{2,z-M_z} = \frac{l^2}{12Ewt^3(c+t)z^2}\left\{-28c-t+(c+t)\cos(3z)\right.$$
$$\left.+3(c+t)z\left[\frac{9\sqrt{c(c+2t)}}{c+2t}+\sin(3z)\right]\right\} \tag{2.324}$$

The out-of-plane compliances are:

$$C_{2,z-F_z} = \frac{3l^2}{2Ew^3t(c+t)z^3}[(c-2t)z+2\sqrt{c(c+2t)}(z^2-1)] \tag{2.325}$$

$$C_{2,z-M_z} = \frac{3l^2}{Ew^3t(c+t)z^2}[\sqrt{c(c+2t)}z-c] \tag{2.326}$$

2.3.11 Verification of the Closed-Form Compliance Equations

Several checks have been performed in order to ensure that the closed-form compliance equations derived for the different flexure types are accurate. The results will be presented briefly in the following discussion.

2.3.11.1 Limit Verification

An overall limit check was performed for all the closed-form compliance equations of all the flexure hinges presented in this chapter. Specifically, the purpose was to verify whether or not, by forcing the geometry of a given

flexure configuration to be identical to that of a constant rectangular cross-section flexure, the corresponding closed-form compliance equations will also be identical to the those of the constant rectangular cross-section flexure configuration. Other limit checks were also carried out, as well. It should be mentioned that the limit calculations were performed for both longitudinally symmetric and nonsymmetric flexure hinges, and they proved the correctness of the closed-form compliance equations of the various flexure configurations.

2.3.11.1.1 Circular Flexure Hinges

A circle becomes a straight line when the radius of the circle goes to infinity. As a consequence, it was considered that $r \to \infty$ in all the compliance equations defining the symmetric circular flexure hinges and the nonsymmetric circular flexure hinges. For both sets of equations, the limit results retrieved the corresponding equations of the constant cross-section flexure hinge.

2.3.11.1.2 Corner-Filleted Flexure Hinges

Two types of limit checks were performed for both symmetric and nonsymmetric flexure hinges. As Figure 2.22 shows, a corner-filleted flexure hinge spans a domain bounded by the straight, constant cross-section flexure when the fillet radius is minimum and therefore goes to zero ($r \to 0$), and the right circular flexure hinge when the fillet radius is maximum and therefore is equal to half the length of the flexure ($r \to l/2$). The first set of checks revealed that, indeed, when $r \to 0$, the compliance equations that describe the symmetric corner-filleted flexure hinges, as well as the compliance equations that define the nonsymmetric corner-filleted flexure hinges, are identical to the corresponding equations of a constant cross-section flexure hinge. The second set of checks indicated that when $r \to l/2$, the compliance equations for both symmetric and nonsymmetric flexure hinges transform into the corresponding compliance equations of symmetric/nonsymmetric circular flexure hinges.

2.3.11.1.3 All Other Flexure Hinges

The geometries of all the other flexure configurations (namely, the parabolic, hyperbolic, elliptic, inverse parabolic, and secant) were unitarily defined by means of the parameter c. Figure 2.23 indicates that when $c \to 0$ each of these flexure hinges becomes a constant cross-section straight flexure. Indeed, by taking $c \to 0$ in all the compliance equations defining the above-mentioned flexures (both symmetric and nonsymmetric), it was found that they are identical to the corresponding compliance equations that define a straight constant cross-section flexure. Because an ellipse becomes a circle when its two semi-axes are equal, another check was performed to check the elliptical flexure hinges. It was found that when $c \to l/2$ (when, geometrically, an ellipse changes into a circle; see Figure 2.22), the compliance equations of symmetric/nonsymmetric flexure hinges are identical to the corresponding compliance equations of right circular flexure hinges.

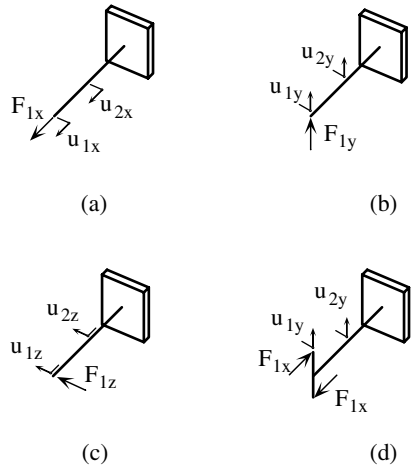

FIGURE 2.25
Schematic representation of experimental settings for evaluation of the following flexure hinge compliances: (a) $C_{1,x-Fx}$ and $C_{2,x-Fx}$; (b) $C_{1,y-Fy}$ and $C_{2,y-Fy}$; (c) $C_{1,z-Fz}$ and $C_{2,z-Fz}$; (d) $C_{1,y-Mz}$ and $C_{2,y-Mz}$.

2.3.11.2 Experimental and Finite Element Verification

In addition to the limit checks that have been performed for all the flexure hinges, as previously detailed, several additional experimental and finite-element verifications were carried out for a few flexure configurations. The experiments were performed according to the schematic illustrated in Figure 2.25. By applying an axial load to a flexure hinge and by measuring the axial displacements at the free end and at the midpoint it was possible to determine the compliances $C_{1,x-Fx}$ and $C_{2,x-Fx}$ according to the load-measuring scheme indicated in Figure 2.25a. When the force was applied along the transverse axis (y) of the flexure, the compliances $C_{1,y-Fy}$ and $C_{2,y-Fy}$ were determined by means of measured displacements u_{1y} and u_{2y}, as suggested in Figure 2.25b. A similar procedure was utilized to evaluate the out-of-plane compliances $C_{1,z-Fz}$ and $C_{2,z-Fz}$, as shown in Figure 2.25c. When a couple formed by two equal and opposite forces, F_{1x}, was applied at the free end of the flexures, the compliances $C_{1,y-Mz}$ and $C_{2,y-Mz}$ were determined by means of measured displacements u_{1y} and u_{2y}, as indicated in Figure 2.25d.

Finite-element simulations were also performed following the load-measuring experimental schemes of Figure 2.25. The ANSYS finite-element software was employed to run the simulations with two-dimensional elements. In both the experimental measurements and finite-element simulations, the flexure samples were made or considered being made of aluminum alloy. For corner-filleted flexure hinges, the experimental measurements were within 6% error margins of the theoretical predictions while the finite element results were within 10% of model results. More details of the experimental setup, finite-element simulation, and results can be found in Lobontiu et al.[4] Similar tests were performed for parabolic and hyperbolic flexure hinges,

as detailed in Lobontiu et al.[5] Compared to experimental data and finite-element results, the closed-form compliance equation predictions produced relative errors that were less than 8%. Smith et al.[2] reported experimental measurements presenting errors of less than 10% when compared to the theoretical results given by approximate compliance equations for elliptical flexure hinges. The error differences between experimental measurements and finite-element simulations were less than 12% error margins for the same elliptical flexure hinges.

2.3.12 Numerical Simulations

The closed-form compliance equations are utilized in this section to evaluate the performance of each flexure type that has previously been presented in terms of the geometry defining it. The task is performed by conducting a thorough numerical simulation that follows several criteria in order to capture either the individual response of flexures or the relative behavior of two different flexure types. Specifically, four different categories of numerical simulation are performed by focusing on the following objectives:

- Individual trends in flexure compliances
- "Internal" comparison of the compliances of one flexure
- Compliance comparison to a constant cross-section flexure hinge
- Compliance comparison between longitudinally nonsymmetric and symmetric flexure hinges

Details of each class of numerical testing will be presented next, together with results in the form of plots and tables.

2.3.12.1 Individual Trends

This group of numerical simulations is intended to evaluate the way in which the defining geometric parameters influence the absolute values of compliances. Combining all the geometric parameters with individual compliances and flexure types results in a large number of functions that must be studied, and presenting all the results in a graphical form would be unfeasible. Fortunately, the trends in compliances as a function of geometry were quite consistent for all flexure hinges, thus it is possible to present just a few sample results.

2.3.12.1.1 Symmetric Circular Flexure Hinges

Figure 2.26, for instance, displays the three-dimensional plot of $C_{1,\theta z,Mz}$ for a symmetric circular flexure hinge in terms of its radius r and minimum thickness t. Not shown here are similar plots for all the other compliances that have been defined for a symmetric circular flexure hinge, but they displayed remarkably consistent trend similarities with those pictured in

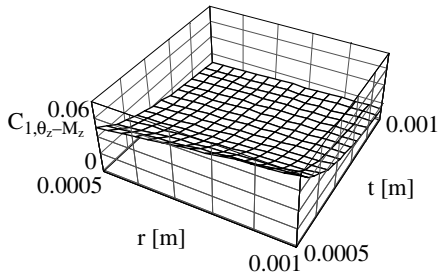

FIGURE 2.26
Variation trends of $C_{1,\theta z-Mz}$ for a symmetric circular flexure hinge in terms of notch radius r and minimum thickness t.

Figure 2.26. By also inspecting the compliance equations, it became clear how the width, w, enters into play. Therefore, either compliance of a symmetric circular flexure hinge will increase when:

- r increases quasi-linearly.
- t decreases highly nonlinearly.
- w varies inversely proportional for in-plane compliances and inversely proportional with the third power for out-of-plane compliances.

The parameters t and w presented the same features as highlighted above for all other flexures and compliances and therefore they will not be mentioned again.

2.3.12.1.2 Symmetric Corner-Filleted Flexure Hinges

A procedure similar to the one previously described has been applied for symmetric corner-filleted flexure hinges. The defining parameters are the fillet radius, r; flexure length, l; minimum thickness, t; and width, w. Figure 2.27 illustrates the same compliance, $C_{1,\theta z,Mz}$, that is plotted as a function of the geometric parameters defining its longitudinal profile.

The following conclusions, which are valid for any other compliance, are derived. Either compliance of a symmetric corner-filleted flexure hinge increases when:

- Fillet radius r decreases quasi-linearly.
- Flexure length l increases quasi-linearly.

2.3.12.1.3 All Other Flexure Types

As previously discussed, all other flexure configurations (parabolic, hyperbolic, elliptic, inverse parabolic, and secant) are longitudinally defined in terms of a geometric parameter c, in addition to l and t. Figure 2.28 displays plots of the compliance factor $C_{1,\theta z,Mz}$ for a symmetric elliptical flexure hinge

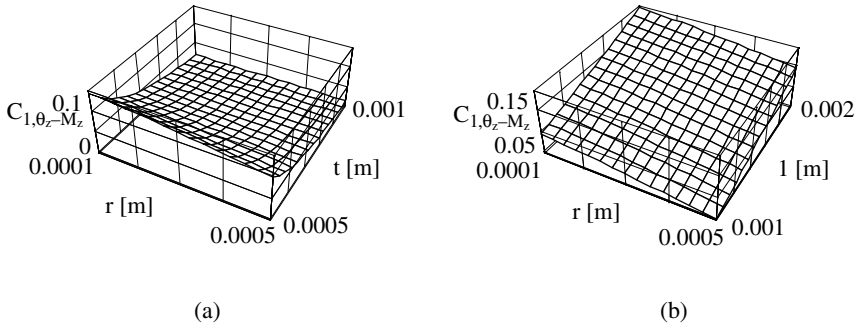

FIGURE 2.27
Variation trends of $C_{1,\theta z-Mz}$ for a symmetric corner-filleted flexure hinge in terms of: (a) fillet radius r and minimum thickness t; (b) fillet radius r and length l.

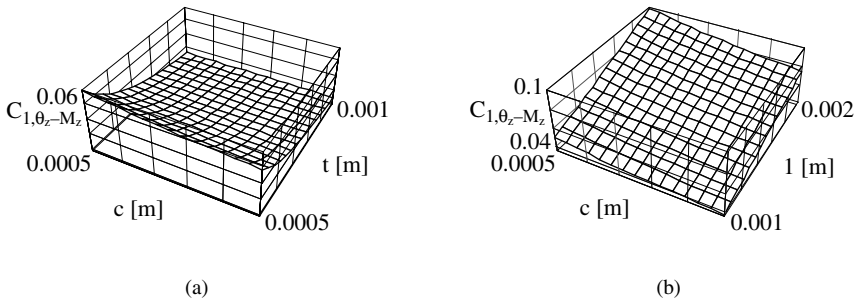

FIGURE 2.28
Variation trends of $C_{1,\theta z-Mz}$ for a symmetric elliptical flexure hinge in terms of: (a) the parameter c and minimum thickness t; (b) the c parameter and length l.

in terms of the parameter c, minimum thickness t, and length l. Similar trends were obtained for all other compliances and flexures. The conclusions derived here were almost identical with those related to corner-filleted flexure hinges, with the amendment that the new parameter c substituted for the fillet radius r.

All the conclusions presented within this section are also valid for longitudinally nonsymmetric flexure hinges; however, a more complete picture of the actual compliance values for each flexure type is given in Table 2.2 (for symmetric flexure hinges) and Table 2.3 (for nonsymmetric flexure hinges). The data in these tables capitalize on the monothonic trend in every compliance in terms of all defining geometric parameters. This way, by knowing, for instance, that $C_{1,\theta z,Mz}$ increases with r increasing, t decreasing, and w decreasing for a symmetric circular flexure hinge, it was possible to calculate the extreme boundaries of that compliance when the geometric parameters were allowed to vary within a given (and feasible) interval.

The data in Tables 2.2 and 2.3 were obtained when the geometric parameters ranged within the intervals:

TABLE 2.2

Extreme Values of Compliances for Single-Axis Symmetric Flexure Hinges

		Flexure Type						
		C	**CF**	**E**	**H**	**P**	**IP**	**S**
$C_{1,x-Fx}$ (m/N)	Min	8.5×10^{-10}	1.4×10^{-9}	1.3×10^{-9}	1.4×10^{-9}	1.2×10^{-9}	1.3×10^{-9}	1.2×10^{-9}
	Max	6.5×10^{-9}	9.9×10^{-9}	9.3×10^{-9}	8.6×10^{-9}	8.9×10^{-9}	9.0×10^{-9}	9.0×10^{-9}
$C_{1,y-Fy}$ (m/N)	Min	2.4×10^{-9}	9.6×10^{-9}	8.0×10^{-9}	5.9×10^{-9}	6.5×10^{-9}	7.7×10^{-9}	7.5×10^{-9}
	Max	2.1×10^{-7}	6.2×10^{-7}	5.0×10^{-7}	4.3×10^{-7}	4.4×10^{-7}	4.6×10^{-7}	4.5×10^{-7}
$C_{1,y-Mz}$ (1/N)	Min	3.9×10^{-6}	1.0×10^{-5}	1.9×10^{-5}	6.7×10^{-6}	5.4×10^{-6}	8.5×10^{-6}	8.4×10^{-6}
	Max	1.9×10^{-4}	4.7×10^{-4}	8.4×10^{-4}	3.4×10^{-4}	2.8×10^{-4}	3.6×10^{-4}	3.6×10^{-4}
$C_{1,\theta y-My}$ (1/Nm)	Min	1.7×10^{-4}	6.6×10^{-4}	6.1×10^{-4}	5.5×10^{-4}	5.6×10^{-4}	6.0×10^{-4}	6.0×10^{-4}
	Max	3.7×10^{-3}	2.5×10^{-2}	2.8×10^{-2}	2.6×10^{-2}	2.7×10^{-2}	2.7×10^{-2}	2.7×10^{-2}
$C_{1,z-Fz}$ (m/N)	Min	1.7×10^{-10}	3.3×10^{-10}	4.4×10^{-10}	3.9×10^{-10}	4.0×10^{-10}	4.3×10^{-10}	4.3×10^{-10}
	Max	2.4×10^{-8}	2.6×10^{-8}	3.6×10^{-8}	3.5×10^{-8}	3.5×10^{-8}	3.5×10^{-8}	$3.5\text{x}\times10^{-8}$
$C_{1,z-My}$ (1/N)	Min	1.7×10^{-7}	1.3×10^{-7}	4.6×10^{-7}	4.1×10^{-7}	4.2×10^{-7}	4.5×10^{-7}	4.5×10^{-7}
	Max	1.2×10^{-5}	2.3×10^{-5}	2.8×10^{-5}	2.6×10^{-5}	2.7×10^{-5}	2.7×10^{-5}	2.7×10^{-5}
$C_{1,\theta z-Mz}$ (1/Nm)	Min	7.8×10^{-3}	1.4×10^{-2}	1.2×10^{-2}	9.0×10^{-3}	7.1×10^{-3}	1.2×10^{-2}	1.1×10^{-2}
	Max	1.9×10^{-1}	4.7×10^{-1}	3.9×10^{-1}	3.4×10^{-1}	2.8×10^{-1}	3.6×10^{-1}	3.6×10^{-1}
$C_{2,x-Fx}$ (m/N)	Min	4.2×10^{-10}	6.7×10^{-10}	6.3×10^{-10}	5.7×10^{-10}	5.9×10^{-10}	6.3×10^{-10}	6.2×10^{-10}
	Max	3.2×10^{-9}	5.0×10^{-9}	4.6×10^{-9}	4.4×10^{-9}	4.5×10^{-9}	4.5×10^{-9}	4.5×10^{-9}
$C_{2,y-Fy}$ (m/N)	Min	5.8×10^{-10}	2.5×10^{-9}	2.9×10^{-9}	4.0×10^{-10}	4.5×10^{-10}	1.8×10^{-9}	1.8×10^{-9}
	Max	3.4×10^{-8}	1.9×10^{-7}	1.7×10^{-7}	2.9×10^{-8}	3.0×10^{-8}	1.2×10^{-7}	1.2×10^{-7}
$C_{2,y-Mz}$ (1/N)	Min	7.5×10^{-7}	2.7×10^{-6}	1.7×10^{-6}	3.4×10^{-6}	1.3×10^{-6}	1.6×10^{-6}	1.5×10^{-6}
	Max	2.4×10^{-5}	8.3×10^{-5}	8.6×10^{-5}	4.3×10^{-5}	7.3×10^{-5}	7.8×10^{-5}	7.7×10^{-5}
$C_{2,z-Fz}$ (m/N)	Min	3.8×10^{-11}	1.3×10^{-10}	1.3×10^{-10}	1.1×10^{-10}	1.1×10^{-10}	1.2×10^{-10}	1.2×10^{-10}
	Max	6.0×10^{-9}	9.9×10^{-9}	1.1×10^{-8}	1.4×10^{-8}	1.0×10^{-8}	1.1×10^{-8}	1.0×10^{-8}
$C_{2,z-My}$ (1/N)	Min	4.6×10^{-8}	9.7×10^{-8}	1.0×10^{-7}	9.0×10^{-8}	9.4×10^{-8}	1.0×10^{-7}	1.0×10^{-7}
	Max	3.8×10^{-6}	5.3×10^{-6}	6.7×10^{-6}	6.3×10^{-6}	6.3×10^{-6}	6.4×10^{-6}	6.4×10^{-6}

Note: C = circular; CF = corner-filleted; E = elliptical; H = hyperbolic; P = parabolic; IP = inverse parabolic; and S = secant.

TABLE 2.3

Extreme Values of Compliances for Single-Axis Nonsymmetric Flexure Hinges

		Flexure Type						
		C	**CF**	**E**	**H**	**P**	**IP**	**S**
$C_{1,x\text{–}Fx}$ (m/N)	Min	9.1×10^{-10}	1.4×10^{-9}	1.4×10^{-9}	1.3×10^{-9}	1.3×10^{-9}	1.4×10^{-9}	1.3×10^{-9}
	Max	7.6×10^{-9}	1.0×10^{-8}	9.6×10^{-9}	9.4×10^{-9}	9.4×10^{-9}	9.5×10^{-9}	9.4×10^{-9}
$C_{1,y\text{–}Fy}$ (m/N)	Min	2.9×10^{-9}	1.1×10^{-8}	9.9×10^{-9}	8.3×10^{-9}	8.6×10^{-9}	9.6×10^{-9}	9.1×10^{-9}
	Max	2.9×10^{-7}	6.3×10^{-7}	5.6×10^{-7}	5.1×10^{-7}	5.2×10^{-7}	5.3×10^{-7}	5.2×10^{-7}
$C_{1,y\text{–}Mz}$ (1/N)	Min	4.6×10^{-6}	9.1×10^{-6}	1.0×10^{-5}	9.0×10^{-6}	9.3×10^{-6}	1.6×10^{-5}	9.7×10^{-6}
	Max	2.5×10^{-4}	4.4×10^{-4}	4.3×10^{-4}	4.0×10^{-4}	4.0×10^{-4}	4.2×10^{-4}	4.0×10^{-4}
$C_{1,\theta y\text{–}My}$ (1/Nm)	Min	4.4×10^{-4}	6.8×10^{-4}	6.6×10^{-4}	6.2×10^{-4}	6.3×10^{-4}	6.5×10^{-4}	6.4×10^{-4}
	Max	2.3×10^{-2}	3.0×10^{-2}	2.9×10^{-2}	2.8×10^{-2}	2.8×10^{-2}	2.8×10^{-2}	2.8×10^{-2}
$C_{1,z\text{–}Fz}$ (m/N)	Min	1.4×10^{-10}	5.0×10^{-10}	4.8×10^{-10}	4.5×10^{-10}	4.6×10^{-10}	4.8×10^{-10}	4.7×10^{-10}
	Max	2.9×10^{-8}	4.0×10^{-8}	3.8×10^{-8}	3.7×10^{-8}	3.7×10^{-8}	3.8×10^{-8}	3.7×10^{-8}
$C_{1,z\text{–}My}$ (1/N)	Min	2.2×10^{-7}	5.1×10^{-7}	4.9×10^{-7}	4.6×10^{-7}	4.7×10^{-7}	4.9×10^{-7}	4.8×10^{-7}
	Max	2.3×10^{-5}	3.0×10^{-5}	2.9×10^{-5}	2.8×10^{-5}	2.8×10^{-5}	2.8×10^{-5}	2.8×10^{-5}
$C_{1,\theta z\text{–}Mz}$ (1/Nm)	Min	9.3×10^{-3}	1.5×10^{-2}	1.4×10^{-2}	1.2×10^{-2}	1.2×10^{-2}	1.4×10^{-2}	1.3×10^{-2}
	Max	2.5×10^{-1}	4.7×10^{-1}	4.3×10^{-1}	4.0×10^{-1}	4.0×10^{-1}	4.1×10^{-1}	4.1×10^{-1}
$C_{2,x\text{–}Fx}$ (m/N)	Min	4.6×10^{-10}	7.1×10^{-10}	6.8×10^{-10}	6.5×10^{-10}	6.5×10^{-10}	6.8×10^{-10}	7.0×10^{-10}
	Max	3.8×10^{-9}	5.0×10^{-9}	4.8×10^{-9}	4.7×10^{-9}	4.7×10^{-9}	4.7×10^{-9}	4.8×10^{-9}
$C_{2,y\text{–}Fy}$ (m/N)	Min	8.0×10^{-10}	4.8×10^{-9}	2.7×10^{-9}	2.1×10^{-9}	2.2×10^{-9}	2.6×10^{-9}	2.4×10^{-9}
	Max	6.0×10^{-8}	2.3×10^{-7}	1.6×10^{-7}	1.5×10^{-7}	1.5×10^{-7}	1.5×10^{-7}	1.5×10^{-7}
$C_{2,y\text{–}Mz}$ (1/N)	Min	1.0×10^{-6}	2.1×10^{-6}	2.2×10^{-6}	1.8×10^{-6}	1.9×10^{-6}	2.1×10^{-6}	2.0×10^{-6}
	Max	4.0×10^{-5}	8.0×10^{-5}	1.0×10^{-4}	9.0×10^{-5}	9.2×10^{-5}	9.5×10^{-5}	9.3×10^{-5}
$C_{2,z\text{–}Fz}$ (m/N)	Min	4.3×10^{-11}	1.5×10^{-10}	1.4×10^{-10}	1.3×10^{-10}	1.4×10^{-10}	1.4×10^{-10}	1.4×10^{-10}
	Max	7.8×10^{-9}	1.8×10^{-8}	1.7×10^{-8}	1.1×10^{-8}	1.1×10^{-8}	1.1×10^{-8}	1.1×10^{-8}
$C_{2,z\text{–}My}$ (1/N)	Min	5.2×10^{-8}	1.2×10^{-7}	1.2×10^{-7}	1.1×10^{-7}	1.1×10^{-7}	1.1×10^{-7}	1.1×10^{-7}
	Max	4.9×10^{-6}	7.4×10^{-6}	7.0×10^{-6}	6.8×10^{-6}	6.8×10^{-6}	6.9×10^{-6}	6.9×10^{-6}

Note: C = circular; CF = corner-filleted; E = elliptical; H = hyperbolic; P = parabolic; IP = inverse parabolic; and S = secant.

- $r \rightarrow$ [0.0005 m, 0.001 m] (for circular flexure hinges)
- $r \rightarrow$ [0.0001 m, 0.0005 m] (for corner-filleted flexure hinges)
- $c \rightarrow$ [0.0001 m, 0.0005 m] (for parabolic, hyperbolic, elliptic, inverse parabolic, and secant flexure hinges)
- $t \rightarrow$ [0.0005 m, 0.001 m]
- $l \rightarrow$ [0.0015 m, 0.002 m]
- $r \rightarrow$ [0.002 m, 0.005 m]

2.3.12.2 Internal Comparison

This numerical simulation attempted to detect the compliant response of each flexure hinge type internally. In other words, the objective here was to compare the different compliances for one flexure hinge at a time. The analysis is important, as it can reveal the relative strengths or weaknesses of a flexure in terms of its performance relative to the capacity of rotation, sensitivity to parasitic effects, and precision of rotation. Again, just a few plots are included here that are representative for all other covered situations.

From a formal viewpoint, the compliances that define any flexure hinge can be grouped into the following categories:

- Direct compliances that relate similar loads and deformations, namely:
  - Deflection–force, connecting the deflection to the corresponding force (called *deflection compliances* here and consisting of $C_{1,x-Fx}$, $C_{1,y-Fy}$, and $C_{1,z-Fz}$ when the capacity of rotation is analyzed)
  - Rotation–moment, connecting the rotation to the corresponding moment (called *rotation compliances* here and consisting of $C_{1,\theta z-Mz}$ and $C_{1,\theta y-My}$ for this class of flexure hinges)
- Cross-compliances that relate unsimilar loads and deformations, namely a linear deflection to a moment and a rotation (angle) to a force; they are $C_{1,y-Mz}$ and $C_{1,z-My}$.

The following compliance ratios are formulated:

- Deflection compliance ratios:

$$rC_{1d,yx} = \frac{C_{1,y-F_y}}{C_{1,x-F_x}} \tag{2.327}$$

$$rC_{1d,yz} = \frac{C_{1,y-F_y}}{C_{1,z-F_z}} \tag{2.328}$$

- Rotation compliance ratio:

$$rC_{1r,\theta_z\theta_y} = \frac{C_{1,\theta_z - M_z}}{C_{1,\theta_y - M_y}} \tag{2.329}$$

- Cross compliance ratio:

$$rC_{1c,yz} = \frac{C_{1,y-M_z}}{C_{1,z-M_y}} \tag{2.330}$$

The above-defined compliance ratios were formulated in a convenient manner by placing in the numerator compliances that are proportional to the capacity of rotation of a flexure hinge and should have large values, while selecting compliances in the denominator that must be small, as they describe unwanted effects, such as axial or out-of-plane. In this way, the compliance ratios are directly indicative of the rotation capacity of one flexure because the ratio will increase, for instance, when either the numerator increases (which is desired) or the denominator decreases (which is also desired).

The plots presented in the following were drawn for symmetric flexure hinges but they are also representative for nonsymmetric configurations.

2.3.12.2.1 Circular Flexure Hinges

Figure 2.29 displays several plots illustrating the way in which the compliance ratios that were defined in Eqs. (2.327) through (2.330) vary when the geometric parameters range within feasible intervals. As shown in Figure 2.29, all compliance ratios present similar trends with respect to the geometric parameters r, t, and w; therefore, the following conclusions have an overall validity. An internal compliance ratio increases and, therefore, the rotation performance of a flexure hinge is enhanced when:

- Radius r increases.
- Minimum thickness t decreases.
- Cross-section width w decreases.

2.3.12.2.2 Corner-Filleted Flexure Hinges

Symmetric corner-filleted flexure hinges were analyzed in a similar way by inspecting the plots of the corresponding compliance ratios as a function of the geometric parameters r, t, l, and w, as shown in Figure 2.30. The following conclusions that can be derived are also valid for nonsymmetric flexure hinges:

- The compliance ratios increase when the radius r is larger; an exception is the compliance ratio $C_{1d,yx}$, which slightly decreases, indicating a relative axial stiffening for larger values of r.
- All compliance ratios decrease when the minimum thickness t increases.

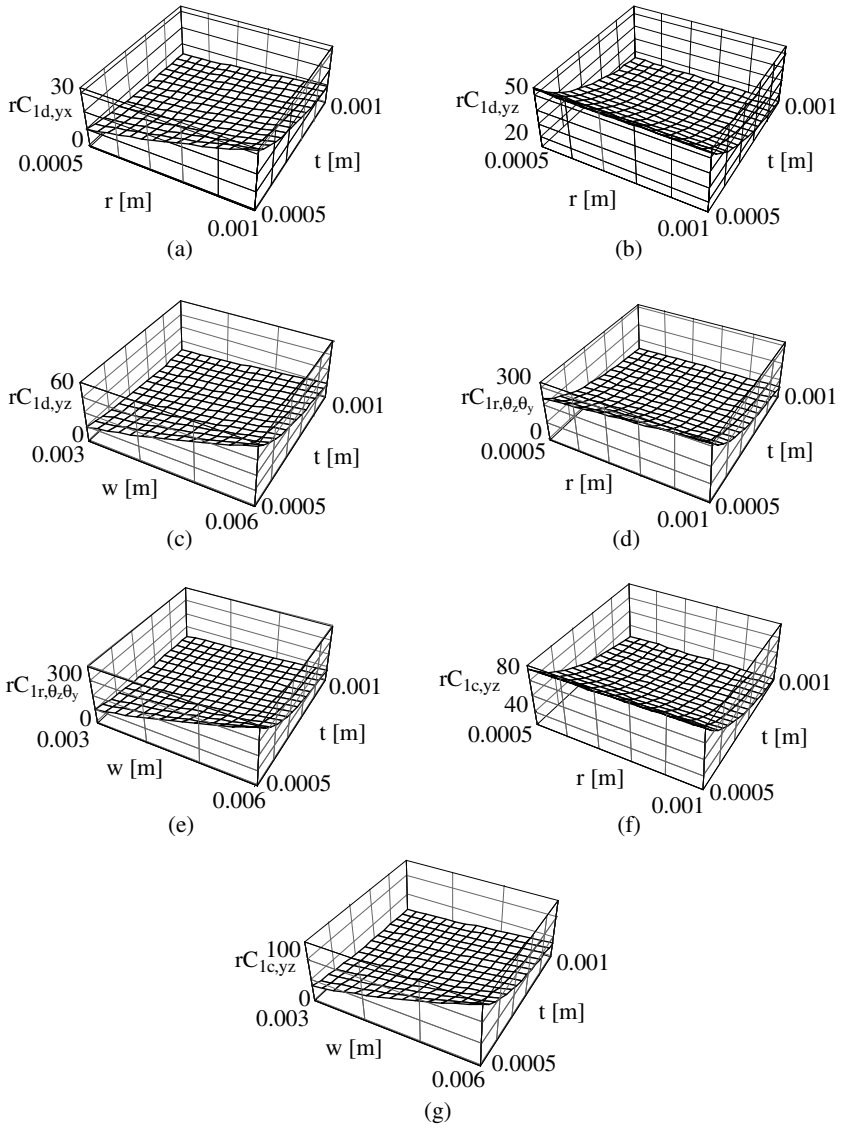

FIGURE 2.29
Characterization of a symmetric circular flexure hinge by internal compliance ratios: (a–g) deflection, rotation, and cross compliance ratios in terms of notch radius *r*, minimum thickness *t*, and width *w*.

- The deflection compliances increase when the flexure length, *l*, increases, while the rotation and cross compliance ratios decrease with *l* increasing.
- All the compliance ratios increase when the cross-section width, *w*, increases.

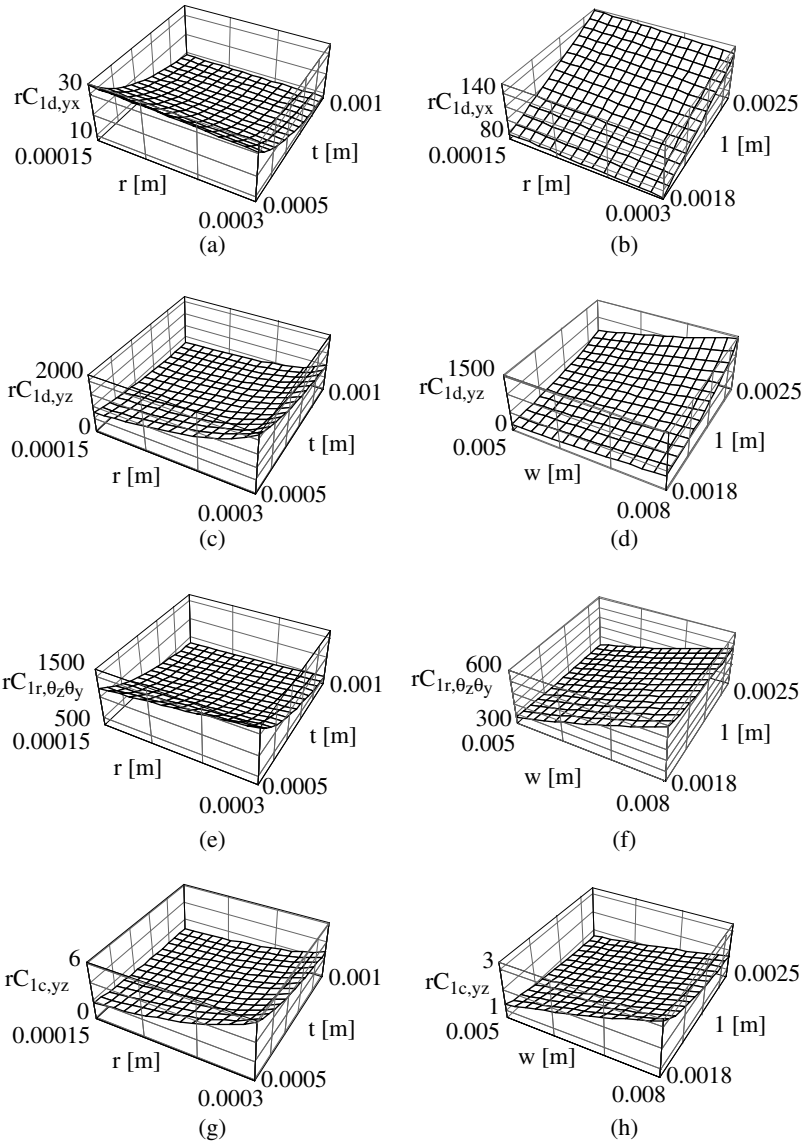

FIGURE 2.30
Characterization of a symmetric corner-filleted flexure hinge by internal compliance ratios: (a–g) Deflection, rotation, and cross compliance ratios in terms of fillet radius r, minimum thickness t, and width w.

2.3.12.2.3 All Other Flexure Hinges

Although plots are only presented here for a symmetric elliptical flexure hinge, all other flexure types (parabolic, hyperbolic, inverse parabolic, and secant) displayed similar trends. Figure 2.31 illustrates the plots of the internal compliance ratios as functions of c, t, and w. It must be noted that the length of the flexure, l, does not enter into any of the compliance ratios.

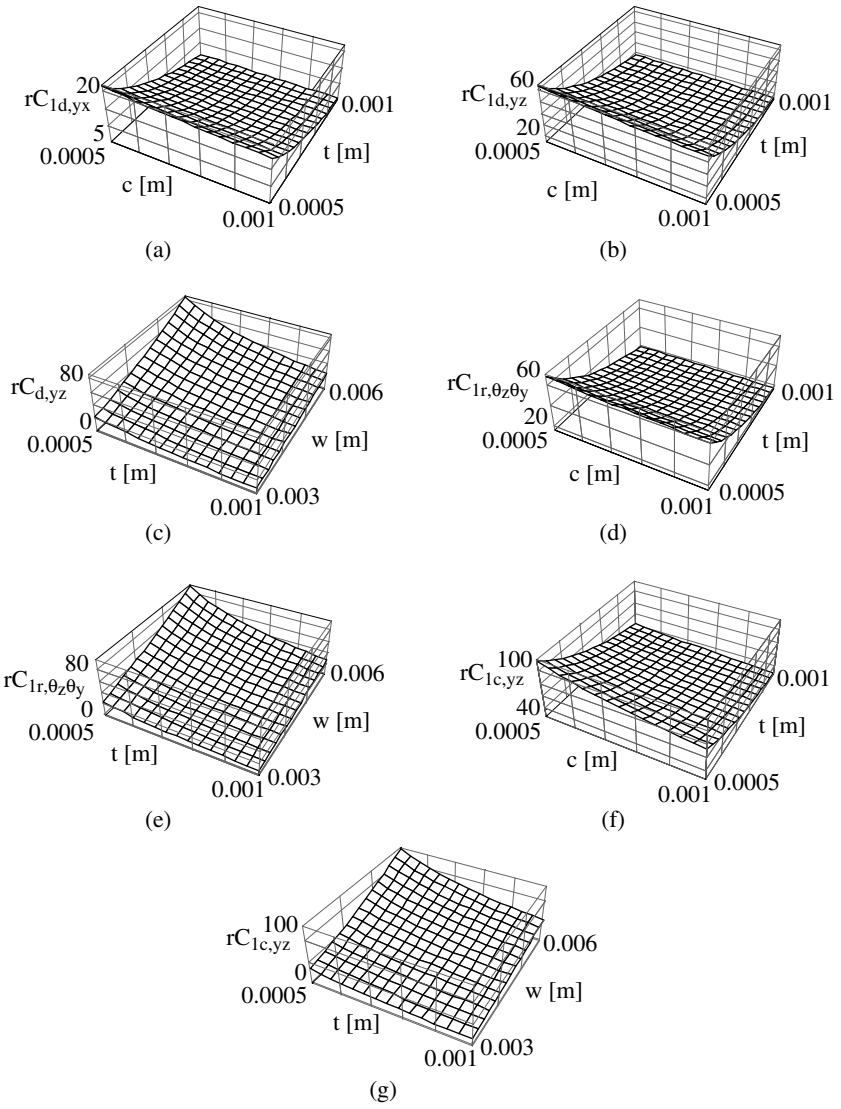

FIGURE 2.31
Characterization of a symmetric elliptical flexure hinge by internal compliance ratios: (a–g) deflection, rotation, and cross compliance ratios in terms of the parameter c, minimum thickness t, and width w.

The following conclusions correspond to symmetric flexure hinges but are also valid for nonsymmetric flexure hinges:

- All the internal compliance ratios decrease when the parameter c increases; the most affected is the cross compliance ratio $C_{1c,yz}$ which, for several of the flexure types, drops around a value of approximately 50; out of all the flexures, the elliptic ones appear to be most sensitive to the variation of c.
- Similarly, all the internal compliance ratios decrease when the minimum thickness t increases; the elliptic, inverse parabolic, and secant appear to be most sensitive to the change in this parameter.
- All the internal compliance ratios increase with increasing w but only slightly and quasi-linearly.

2.3.12.3 Constant Cross-Section Flexure Hinge Comparison and Shearing Effects

The seven different flexure hinge configurations are also compared to the constant cross-section flexure hinge by means of their similar compliances. In doing so, several compliance ratios are formulated that do not depend on the cross-section width. Formally, these compliance ratios are defined as:

$$rC_{1,x-F_x} = \frac{(C_{1,x-F_x})_{ccsfh}}{(C_{1,x-F_x})_{fh}} \tag{2.331}$$

where the subscript *ccsfh* means "constant cross-section flexure hinge" and *fh* denotes a generic flexure hinge standing for either of the seven different types. Similar compliance ratios are formulated for the other compliances that describe either the capacity of rotation (1 is in the subscript notation) or the precision of rotation (2 is in the subscript notation). In formulating the compliance ratios described above, it is considered that the thickness of the constant cross-section flexure hinge is equal to the minimum thickness of the compared flexure hinge. As a consequence, the compliance ratios will always be greater than 1.

The influence of taking into account the shearing effects is also discussed within this group of numerical simulations by means of the ratios:

$$rC^{sh,n}_{1,y-F_y} = \frac{C^{sh}_{1,y-F_y}}{C_{1,y-F_y}} \tag{2.332}$$

where the superscript *sh* indicates that shearing is included in the compliance. This compliance ratio, too, will be greater than 1 because the compliance including shearing effects is always larger than the one not including those effects. Again, plots and corresponding conclusions will be presented in

direct mode only for symmetric flexure hinges, but their validity extends to nonsymmetric flexures, as well.

2.3.12.3.1 Circular Flexure Hinges

Figure 2.32 presents several plots that describe the comparative response of a circular flexure hinge with respect to a constant cross-section flexure hinge, as well as the effects of considering shearing in the compliance of a circular flexure hinge. The following conclusions can be derived when comparing the circular flexure hinge to the constant cross-section flexure hinge:

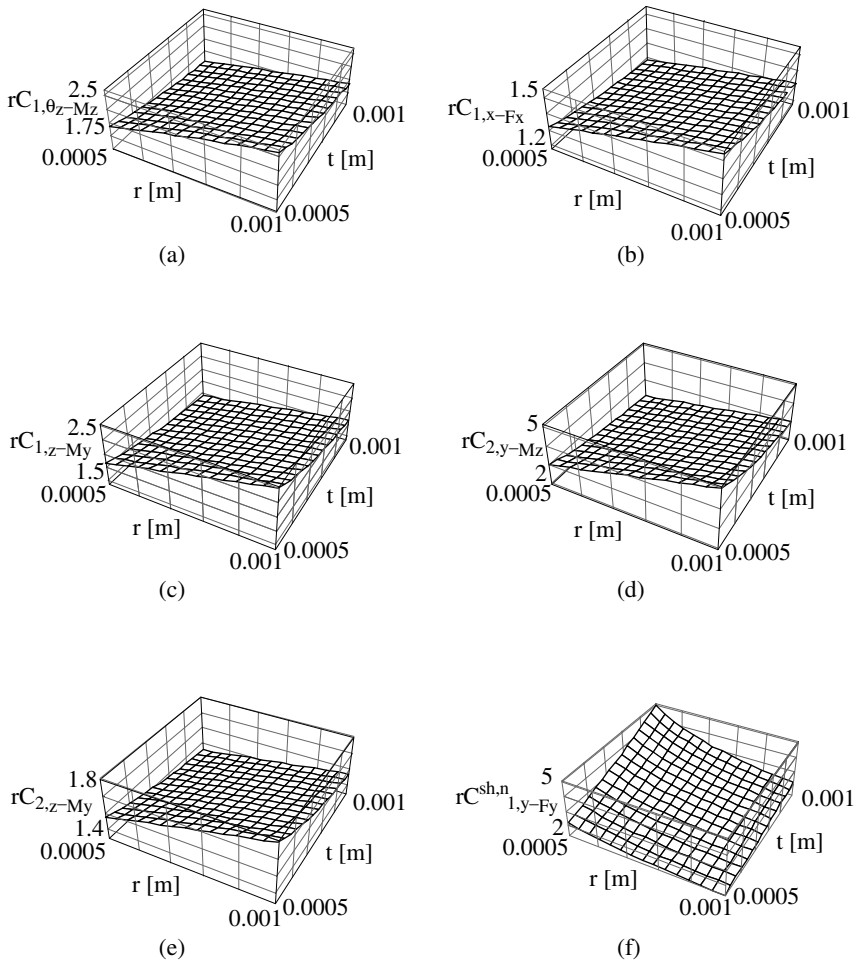

FIGURE 2.32
Characterization of a symmetric circular flexure hinge in terms of notch radius r and minimum thickness t: (a–e) beam-referenced compliance ratios; (f) shear-referenced compliance ratio.

- All compliance ratios increase with increasing r and decreasing t.
- A circular flexure hinge can be up to 2.5 times less compliant in rotation than its corresponding constant cross-section counterpart (Figure 2.32a).
- A circular flexure hinge is up to 1.5 times less axially compliant compared to its corresponding constant cross-section flexure hinge (Figure 2.32b).
- The circular flexure can be up to 2.5 times less sensitive to out-of-plane effects (Figure 2.32c) than a constant cross-section flexure hinge in terms of the rotation capacity.
- The circular flexure hinge can be 5 times better than a corresponding constant cross-section flexure hinge, in terms of its precision of rotation (Figure 2.32d).
- When the shearing effects are taken into consideration, the short flexure hinge can be up to 5 times more compliant than a corresponding flexure when shearing is not accounted for (Figure 2.32f). It is therefore extremely important that shearing be included in compliance evaluations for short flexure members.

2.3.12.3.2 Corner-Filleted Flexure Hinges

Figure 2.33 shows the plots that define the relative response of a corner-filleted flexure hinge in comparison to its constant cross-section counterpart, as well as the effects of shearing. The following remarks can be formulated from inspection of the compliance ratios:

- All the compliance ratios increase with increasing r, decreasing t, and decreasing l.
- The rotation capacity of a corner-filleted flexure hinge can be up to 1.4 times larger than the corresponding constant flexure hinge (Figure 2.33b).
- A corner-filleted flexure can be 30% less sensitive to axial effects (Figure 2.33d) and up to 50% less sensitive to out-of-plane effects with respect to its precision of rotation (Figure 2.33f).
- Shearing effects are, again, important factors in correctly assessing the compliance of a corner-filleted flexure for shorter lengths, as illustrated in Figure 2.33g and h.

2.3.13.3.3 All Other Flexure Hinges

Figure 2.34 shows the plots that correspond to an elliptical flexure hinge. They are similar in trends with plots for parabolic, hyperbolic, inverse parabolic, and secant flexure hinges—plots that are not included here. In the ratios that compare the different flexure hinges to a constant cross-section flexure hinge, the length, l, does not enter explicitly, so no plots in terms of l are shown in Figure 2.34. The following conclusions can be extracted:

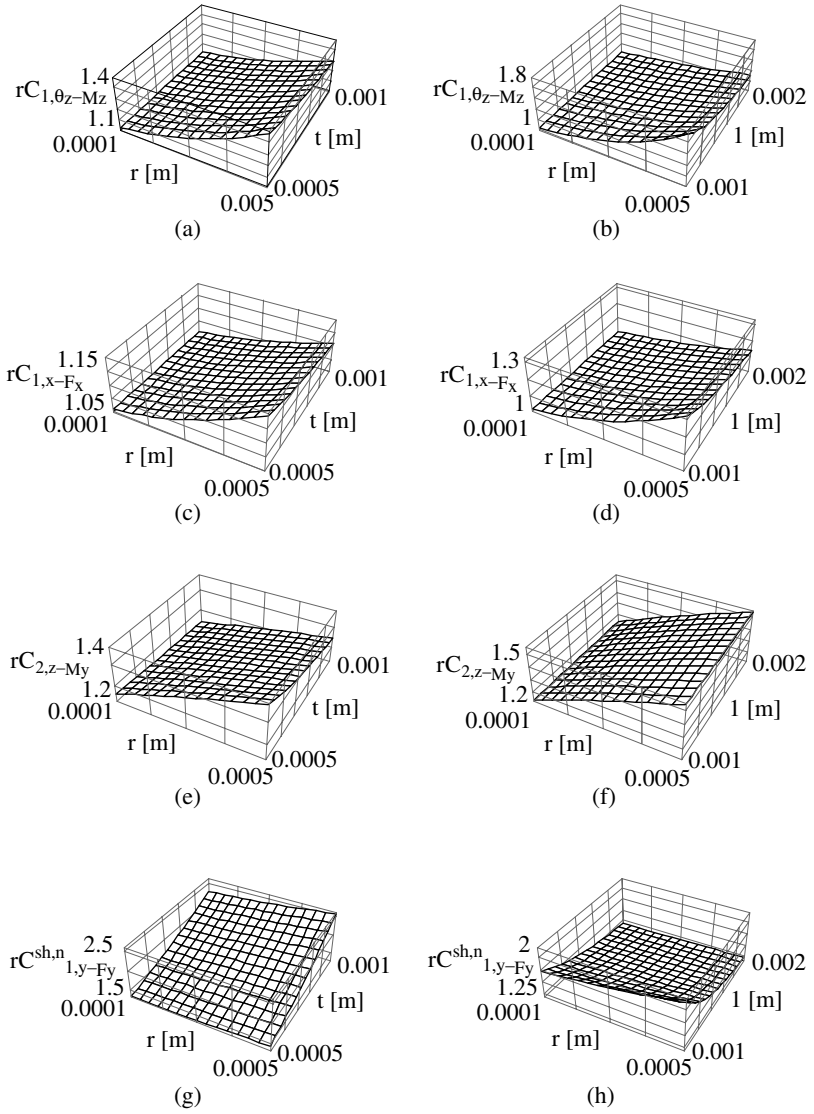

FIGURE 2.33
Characterization of a symmetric corner-filleted flexure hinge in terms of fillet radius *r*, minimum thickness *t*, and length *l*: (a–f) beam-referenced compliance ratios; (g–h) shear-referenced compliance ratio.

- All the compliance ratios, for all the mentioned flexure hinges, increase when *c* increases and when *t* decreases.
- In terms of the rotation capacity, the best performer is the inverse parabolic flexure (1.4 compliance ratio), followed by the secant, elliptic (2.5 ratio, as shown in Figure 2.33a), parabolic, and hyperbolic (5 ratio).

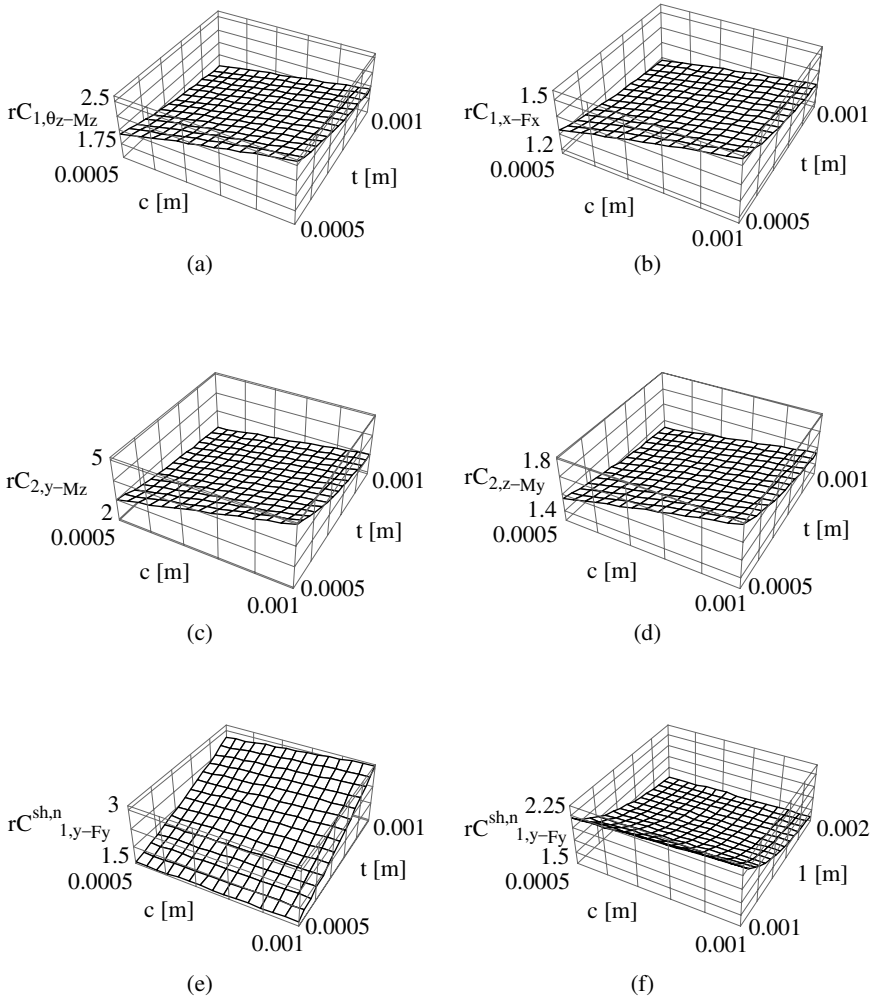

FIGURE 2.34
Characterization of a symmetric elliptical flexure hinge in terms of the parameter *c*, minimum thickness *t*, and length *l*: (a–d) beam-referenced compliance ratios; (e–f) shear-referenced compliance ratio.

- The least axially sensitive is the hyperbolic flexure hinge (2 ratio), followed in order by the parabolic, elliptic (1.5 ratio, as shown in Figure 2.33b), secant, and inverse parabolic (1.35 ratio).
- The best performance in terms of rotation precision is recorded by the parabolic flexure hinge (3 ratio), followed by the secant, elliptic (5 ratio, as indicated in Figure 2.33c), hyperbolic (7.5 ratio), and parabolic (8 ratio).

- In terms of the shearing effects, all the flexures in this category behave remarkably similarly as all present a shearing-to-nonshearing compliance ratio with a maximum value of approximately 3 for short flexure hinges.

2.3.12.4 Nonsymmetric/Symmetric Flexure Hinges Comparison

The last set of numerical simulations aims at quantitatively relating the longitudinally nonsymmetric flexure hinges to their symmetric counterparts that have been directly analyzed so far. Compliance ratios are formulated by taking any compliance of a nonsymmetric flexure hinge into the numerator and the same compliance of the corresponding (equal minimum thickness) symmetric flexure hinge into the denominator. Evidently, these ratios are greater than 1 as a nonsymmetric flexure hinge is always more compliant than its symmetric counterpart.

2.3.12.4.1 Circular Flexure Hinges

Figure 3.35 presents several plots illustrating the nonsymmetric-to-symmetric compliance ratios as a function of r and t. The following conclusions can be formulated:

- All compliance ratios increase with increasing r and decreasing t.
- A nonsymmetric flexure hinge can be up to 30% more compliant compared to the symmetric one in terms of the rotation capacity (Figure 2.35a).
- The nonsymmetric flexure hinge is also up to only 16% more axially sensitive than its symmetric counterpart (Figure 2.35b).
- The nonsymmetric flexure, at the same time, may be up to 80% more exposed to out-of-plane effects (Figure 2.35c) and up to 60% less precise in keeping the position of the rotation center (Figure 2.35d).
- The shearing effects show an increase in the corresponding compliance of up to 25% for the nonsymmetric flexure hinge, compared to the symmetric hinge, for short lengths.

2.3.12.4.2 Corner-Filleted Flexure Hinges

Similar numerical simulations were performed for corner-filleted flexure hinges, and several results are presented in the plots of Figure 2.36. The following conclusions are noted:

- All compliance ratios increase when r increases, t decreases, and l decreases.

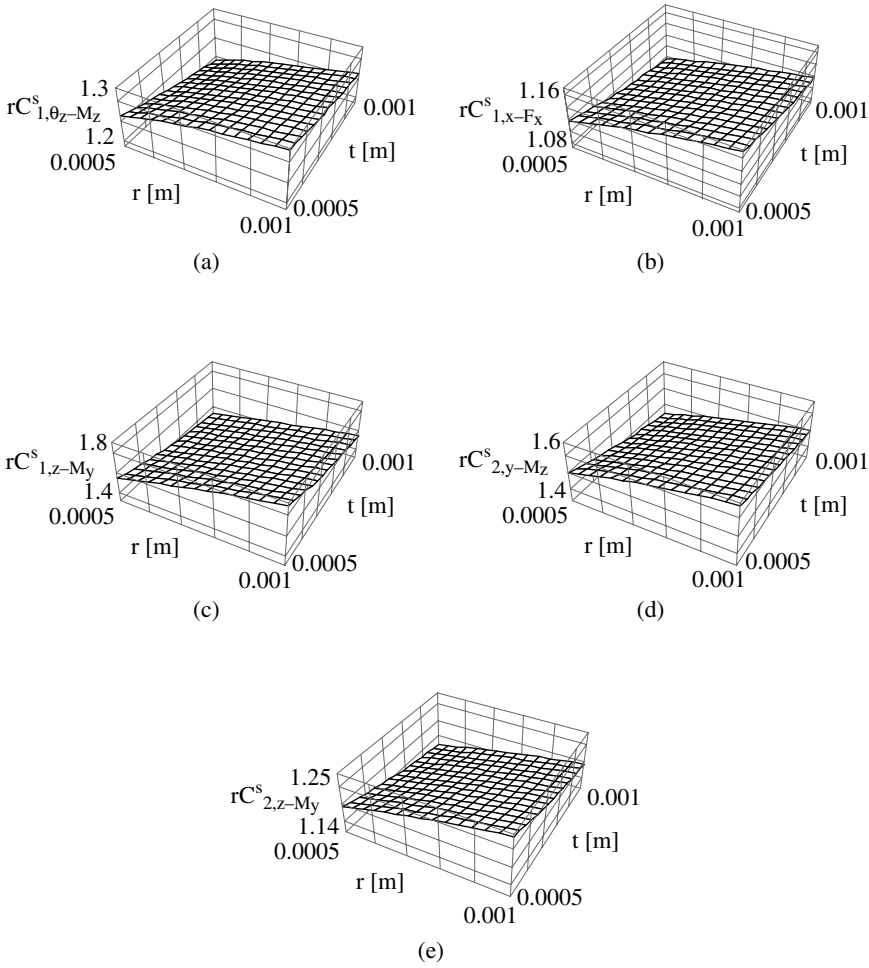

FIGURE 2.35
Nonsymmetric vs. symmetric circular flexure hinges in terms of notch radius *r* and minimum thickness *t*: (a–e) compliance ratios.

- The differences between nonsymmetric corner-filleted flexure hinges and their symmetric variants are not so marked in terms of capacity of rotation (20% maximum, as shown in Figure 2.36b) and axial sensitivity (10%, as shown in Figure 2.36d); however, the differences become sensible when analyzing the capacity of rotation (the nonsymmetric flexure can be up to 3.5 times larger than the symmetric one; see Figure 2.36f).
- A nonsymmetric flexure hinge is up to 75% more compliant than a symmetric one (see Figure 2.36g) when the shearing effects are taken into consideration for relatively short lengths.

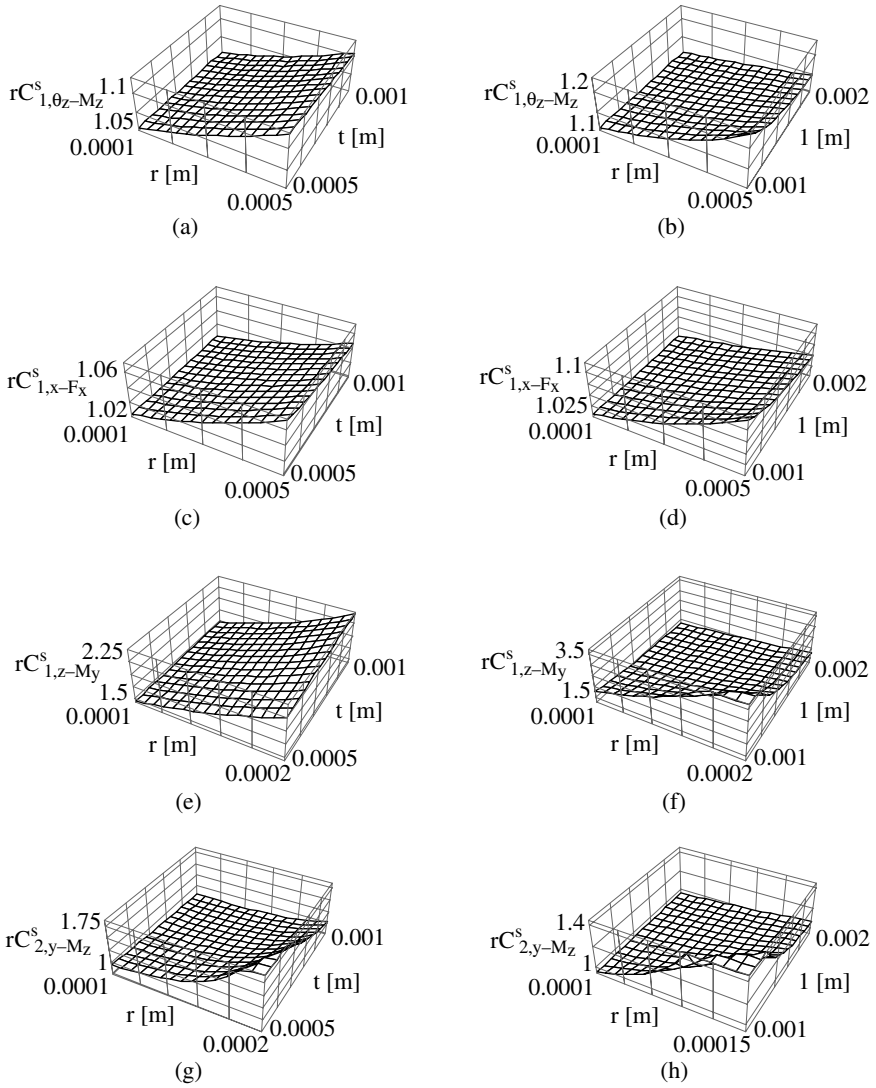

FIGURE 2.36
Nonsymmetric vs. symmetric corner-filleted flexure hinges in terms of fillet radius *r*, minimum thickness *t*, and length *l*: (a–h) compliance ratios.

2.3.12.4.3 All Other Flexure Hinges

Based on plots that were drawn for elliptical flexure hinges (see Figure 2.37), the results and discussion that follow are also valid for parabolic, hyperbolic, inverse parabolic, and secant flexure hinges. In all compliance ratios, the flexure length, *l*, and width, *w*, do not enter into the formulations; as a consequence, these two geometric variables are not accounted for in any of the plots. The following conclusions are noted:

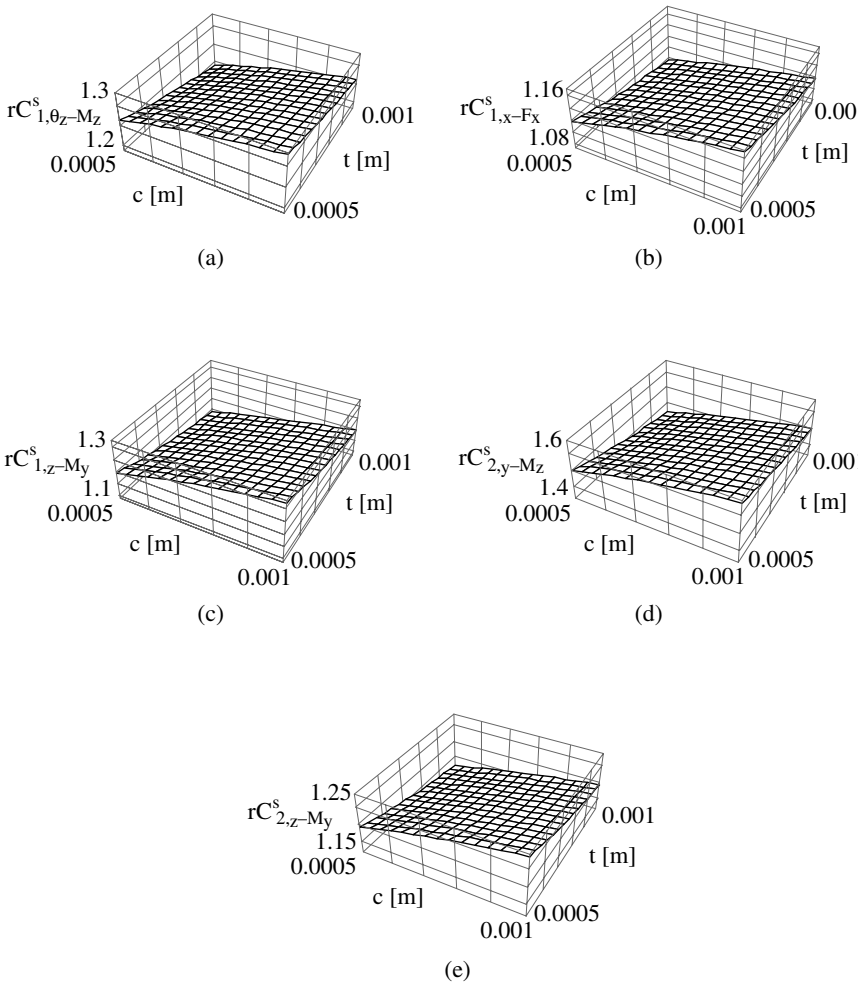

FIGURE 2.37
Nonsymmetric vs. symmetric elliptical flexure hinges in terms of the parameter *c* and minimum thickness *t*: (a–e) compliance ratios.

- All the compliance ratios increase when *c* increases and *t* decreases, for all mentioned flexure configurations.
- The nonsymmetric parabolic flexure hinge can be up to 85% more efficient in terms of rotation capacity when compared to the corresponding symmetric configuration; next in this classification is the hyperbolic flexure hinge (60% more efficiency), followed by the elliptic one (30% more efficiency, see Figure 3.37a), inverse parabolic (about 20% more efficiency), and secant (with approximately 15% efficiency increase).

- In terms of sensitivity to axial effects, the above-mentioned hierarchy remains unaltered, in the sense that nonsymmetric flexures are more sensitive to axial loading than their symmetric counterparts with margins ranging from 30% (hyperbolic), to 16% (elliptic, as illustrated in Figure 3.37b), and down to 8% (secant).
- The flexure hinge types analyzed here perform similarly in terms of reaction to out-of-plane input; the nonsymmetric configuration is again more sensitive to these effects; leading the standings are the elliptic (see Figure 3.37c), hyperbolic, and secant with 30% more compliance, followed by parabolic (20% more compliance) and secant (only 12% additional compliance).
- When ranking the precision of rotation of nonsymmetric vs. symmetric flexure hinges, the worst performance is recorded by the parabolic flexure configuration (80% more sensitivity in motion about the transverse axis at the center of the flexure), followed by the elliptic hinge (60% more compliance, as seen in Figure 3.37d), hyperbolic (50% more compliance), inverse parabolic (45% additional compliance), and secant (35% more compliance).

2.4 Multiple-Axis Flexure Hinges for Three-Dimensional Applications

2.4.1 Introduction

The multiple-axis flexure hinges will be studied in this section of the work in terms of their compliant behavior. As mentioned in Section 2.1, these flexures have rotary symmetry because all configurations are revolute; therefore, their cross-section is circular, as illustrated in Figure 2.3. Due to their innate circular symmetry, the revolute flexure hinges will also possess longitudinal symmetry. In addition, as previously mentioned, only configurations with transverse symmetry are analyzed in this work, thus the revolute flexure hinges will have full (complete) symmetry. These flexure hinges are implemented in three-dimensional applications where the flexure-based compliant mechanism performs a space motion and the flexure hinges are not required to have specific sensitivity about any particular cross-sectional direction.

Closed-form compliance equations (or spring rates) will again be formulated by applying Castigliano's displacement theorem. As in the previous section, the formulation will first be generic. Both long- and short-beam theory will be investigated, and the differences arising by including/excepting shearing effects will be expressed and discussed for each individual flexure. The configurations that were analyzed for one-sensitivity-axis flexure hinges will also be approached here. Specific compliance equations will explicitly be derived for circular, corner-filleted, elliptic, parabolic, hyperbolic, inverse parabolic, and secant designs.

A numerical simulation section will thoroughly analyze trends and compare flexures in terms of their rotation performance and sensitivity to parasitic effects, in a manner similar to the one already applied. Several three-dimensional plots will be utilized again to enable formulating conclusions with respect to specific features of each flexure.

2.4.2 Generic Formulation and Performance Criteria

2.4.2.1 Capacity of Rotation

For a three-dimensional revolute-geometry flexure hinge, as illustrated in Figure 2.3, the loading at the free end, point 1, consists of a maximum of six components: two bending moments, M_{1y} and M_{1z}; two shearing forces, F_{1y}, F_{1z}; one axial load, F_{1x}; and one torsional moment, M_{1x} (as indicated in Figure 2.8). Unlike the single-axis flexure hinges for two-dimensional applications, where the loads and corresponding displacements are planar, in the case of three-dimensional flexures all loads must be considered, as there is no geometrically preferential direction. The notion of parasitic loads and effects becomes therefore unusable from a geometry viewpoint. It no longer makes sense to distinguish between in-plane and out-of-plane compliant behavior; therefore, Eq. (2.22) is valid in its original form without any discrimination between in- and out-of-plane components. The vectors of Eq. (2.22) are comprised of the following members when the free end (point 1 in Figure 2.8) is referred:

$$\{u_1\} = \{u_{1x}, u_{1y}, u_{1y}, \theta_{1x}, \theta_{1y}, \theta_{1z}\}^T \tag{2.333}$$

$$\{L_1 = \{F_{1x}, F_{1y}, F_{1z}, M_{1x}, M_{1y}, M_{1z}\}^T \tag{2.334}$$

The expanded form of the compliance matrix of Eq. (2.22) is:

$$[C_1] = \begin{bmatrix} C_{1,x-F_x} & 0 & 0 & 0 & 0 & 0 \\ 0 & C_{1,y-F_y} & 0 & 0 & 0 & C_{1,y-M_z} \\ 0 & 0 & C_{1,z-F_z} & 0 & C_{1,z-M_y} & 0 \\ 0 & 0 & 0 & C_{1,\theta_x-M_x} & 0 & 0 \\ 0 & 0 & C_{1,\theta_y-F_z} & 0 & C_{1,\theta_y-M_y} & 0 \\ 0 & C_{1,\theta_z-F_y} & 0 & 0 & 0 & C_{1,\theta_z-M_z} \end{bmatrix} \tag{2.335}$$

According to the principle of reciprocity the following identities apply:

$$\begin{cases} C_{1,y-M_z} = C_{1,\theta_z-F_y} \\ C_{1,z-M_y} = C_{1,\theta_y-F_z} \end{cases} \tag{2.336}$$

The following compliances are also identical because of the circular symmetry of the cross-section:

$$\begin{cases} C_{1,y-F_y} = C_{1,z-F_z} \\ C_{1,y-M_z} = C_{1,z-M_y} \\ C_{1,\theta_y-M_y} = C_{1,\theta_z-M_z} \end{cases} \tag{2.337}$$

The compliance equations are:

$$C_{1,x-F_x} = \frac{4}{\pi E} I_1 \tag{2.338}$$

$$C_{1,y-F_y} = \frac{64}{\pi E} I_2 \tag{2.339}$$

$$C^s_{1,y-F_y} = C_{1,y-F_y} + \frac{4\alpha}{\pi G} I_1 \tag{2.340}$$

(for relatively short beam-theory, where shearing is taken into account).

Combining Eqs. (2.338) and (2.340) gives:

$$C^s_{1,y-F_y} = C_{1,y-F_y} + \frac{\alpha E}{G} C_{1,x-F_x} \tag{2.341}$$

The other compliances are:

$$C_{1,y-M_z} = \frac{64}{\pi E} I_3 \tag{2.342}$$

$$C_{1,\theta_x-M_x} = \frac{32}{\pi G} I_4 \tag{2.343}$$

$$C_{1,\theta_y-M_y} = \frac{64}{\pi E} I_4 \tag{2.344}$$

Equation (2.344) can be rewritten by considering Eq. (2.343) as:

$$C_{1,\theta_y-M_y} = \frac{2G}{E} C_{1,\theta_x-M_x} \tag{2.345}$$

The I_1 through I_4 integrals are:

$$I_1 = \int_0^l \frac{dx}{t(x)^2} \tag{2.346}$$

$$I_2 = \int_0^l \frac{x^2 dx}{t(x)^4} \tag{2.347}$$

$$I_3 = \int_0^l \frac{x dx}{t(x)^4} \tag{2.348}$$

$$I_4 = \int_0^l \frac{dx}{t(x)^4} \tag{2.349}$$

2.4.2.2 Precision of Rotation

The precision of rotation for a revolute flexure hinge is again quantified by means of the translations of the geometric center (point 2 in Figure 2.8) along the x, y, and z directions. The translatory offset of the rotation center of a flexure hinge is assessed in a similar manner by applying three fictitious loads F_{2x}^*, F_{2y}^*, and F_{2z}^*, in addition to the load vector applied at point 1. Castigliano's second theorem is again utilized to find the displacements of the rotation center by means of the equations, which were previously formulated for single-axis flexure hinge. The strain energy U′ will also include torsion; therefore, Eq. (2.17) is valid in this situation, as well.

The bending and torsion moments, shearing, and axial forces are again evaluated only on the 2–3 interval, as F_{2x}, F_{2y}, and F_{2z} only intervene in that load segment. They were formulated in Eq. (2.109). The torsion moment that enters the compliance formulation for revolute joints is:

$$M_x = M_{1x} \tag{2.350}$$

Castigliano's second theorem is applied again and produces the generic Eqs. (2.105) through (2.107).

The displacement vector at the center of the flexure is:

$$\{u_2\} = \{u_{2x}, u_{2y}, u_{2z}\}^T \tag{2.351}$$

The load vector is the one applied at extremity point 1 and is comprised of all the components shown in Eq. (2.334) less torsion (which produces no

translation of the flexure center). The expanded form of the compliance matrix in this case is:

$$[C_2]=\begin{bmatrix} C_{2,x-F_x} & 0 & 0 & 0 & 0 \\ 0 & C_{2,y-F_y} & 0 & 0 & C_{2,y-M_z} \\ 0 & 0 & C_{2,y-F_y} & C_{2,y-M_z} & 0 \end{bmatrix} \tag{2.352}$$

The in-plane compliances of Eq. (2.352) are:

$$C_{2,x-F_x}=\frac{4}{\pi E}I_1' \tag{2.353}$$

$$C_{2,y-F_y}=\frac{64}{\pi E}\left(I_2'-\frac{l}{2}I_3'\right) \tag{2.354}$$

$$C^s_{2,y-F_y}=C_{2,y-F_y}+\frac{4\alpha}{\pi G}I_1' \tag{2.355}$$

(for relatively short beams, where shearing is taken into account).

Combining Eqs. (2.353) and (2.355) gives:

$$C^s_{2,y-F_y}=C_{2,y-F_y}+\frac{\alpha E}{G}C_{2,x-F_x} \tag{2.356}$$

The last compliance of Eq.(2.352) is:

$$C_{2,y-M_z}=\frac{64}{\pi E}\left(I_3'-\frac{l}{2}I_4'\right) \tag{2.357}$$

The I_1' through I_4' integrals are:

$$I_1'=\int_{l/2}^{l}\frac{dx}{t(x)^2} \tag{2.358}$$

$$I_2'=\int_{l/2}^{l}\frac{x^2dx}{t(x)^4} \tag{2.359}$$

$$I_3'=\int_{l/2}^{l}\frac{xdx}{t(x)^4} \tag{2.360}$$

$$I_4'=\int_{l/2}^{l}\frac{dx}{t(x)^4} \tag{2.361}$$

2.4.2.3 Stress Considerations

Similar to the single-axis flexure hinges, the revolute cutouts that form the multiple-sensitive-axis flexure configurations constitute stress concentrators that increase the nominal stresses over the cross-section. A three-dimensional state of stress is set up in this case consisting of normal and shearing components. The normal stresses are produced through axial and double (two-axis) bending, while the shear stresses are generated through torsion and shearing (for relatively short flexures). The maximum normal stress will occur at an outer fiber, according to Eq. (2.136). The stresses generated through axial loading are constant over the cross-section and are expressed as:

$$\sigma_a = K_{ta} \frac{4F_{1x}}{\pi t^2} \tag{2.362}$$

where K_{ta} is the theoretical stress concentration factor in axial loading (either tension or compression). The normal bending stresses are maximum on an outer fiber and are the result of combining the effects of the two bending moments, M_y and M_z, as given by:

$$\sigma_{b,max} = K_{tb} \frac{64\sqrt{M_y^2 + M_z^2}}{\pi t^4} \tag{2.363}$$

where K_{tb} is the theoretical stress concentration factor in bending and M_y and M_z are bending moments about the y and z axes, respectively. In the worst-case scenario, the maximum bending (which occurs at the root of the flexure) gathers similar contributions from the tip moment and force that act at the flexure's free end; therefore, Eq. (2.363) can be reformulated as:

$$\sigma_{b,max} = K_{tb} \frac{64\sqrt{(M_{1y} + lF_{1z})^2 + (M_{1z} + lF_{1y})^2}}{\pi t^4} \tag{2.364}$$

Substituting Eqs. (2.362) and (2.364) into Eq. (2.136) gives:

$$\sigma_{max} = \frac{4}{\pi t^2}\left[K_{ta}F_{1x} + \frac{16K_{tb}}{t^2}\sqrt{(M_{1y} + lF_{1z})^2 + (M_{1z} + lF_{1y})^2}\right] \tag{2.365}$$

The effects of shearing are usually neglected (for long flexures) such that the shearing stresses are only produced through torsion. The maximum shear

stress, in this case, is:

$$\tau_{max} = \frac{32M_{1x}}{\pi t^4} \tag{2.366}$$

The von Mises criterion is applied for this plane state of stress in order to find the maximum equivalent stress:

$$\sigma_{e,max} = \sqrt{\sigma_{max}^2 + 3\tau_{max}^2} \tag{2.367}$$

Substituting σ_{max} and τ_{max} of Eqs. (2.365) and (2.366) into Eq. (2.367) produces:

$$\sigma_{e,max} = \frac{4}{\pi t^2} \sqrt{[K_{ta}F_{1x} + \frac{16K_{tb}}{t^2}\sqrt{(M_{1y} + lF_{1z})^2 + (M_{1z} + lF_{1y})^2}]^2 + \frac{192K_{tt}^2 M_{1x}^2}{t^4}} \tag{2.368}$$

Equation (2.368) can be utilized in cases where the loading on a flexure can be estimated. In situations where deformations are more readily available, Eq. (2.368) can be modified by expressing it in terms of deformations instead of loads. Similar to the procedure that has been detailed for single-axis flexure hinges, stiffness-based, load-deflection Eq. (2.368) will be transformed into a compliance-based, deflection-load equation. The stiffness matrix, which is the inverse of the compliance matrix, is of the form:

$$[K_1] = \begin{bmatrix} K_{1,x-F_x} & 0 & 0 & 0 & 0 & 0 \\ 0 & K_{1,y-F_y} & 0 & 0 & 0 & K_{1,y-M_z} \\ 0 & 0 & K_{1,z-F_z} & 0 & K_{1,z-M_y} & 0 \\ 0 & 0 & 0 & K_{1,\theta_x-M_x} & 0 & 0 \\ 0 & 0 & K_{1,\theta_y-F_z} & 0 & K_{1,\theta_y-M_y} & 0 \\ 0 & K_{1,\theta_z-F_y} & 0 & 0 & 0 & K_{1,\theta_z-M_z} \end{bmatrix} \tag{2.369}$$

where the stiffness factors can be expressed in terms of compliance terms by the inversion indicated in Eq. (2.141). They are precisely the stiffness factors given in Eq. (2.144) plus the new torsional stiffness, which is:

$$K_{1,\theta_x-M_x} = \frac{1}{C_{1,\theta_x-M_x}} \tag{2.370}$$

The explicit form of the stiffness in Eq. (2.140) is:

$$\begin{Bmatrix} F_{1x} \\ F_{1y} \\ F_{1z} \\ M_{1x} \\ M_{1y} \\ M_{1z} \end{Bmatrix} = \begin{bmatrix} K_{1,x-F_x} & 0 & 0 & 0 & 0 & 0 \\ 0 & K_{1,y-F_y} & 0 & 0 & 0 & K_{1,y-M_z} \\ 0 & 0 & K_{1,y-F_y} & 0 & K_{1,y-M_z} & 0 \\ 0 & 0 & 0 & K_{1,\theta_x-M_x} & 0 & 0 \\ 0 & 0 & K_{1,y-M_z} & 0 & K_{1,\theta_y-M_y} & 0 \\ 0 & K_{1,y-M_z} & 0 & 0 & 0 & K_{1,\theta_y-M_y} \end{bmatrix} \begin{Bmatrix} u_{1x} \\ u_{1y} \\ u_{1z} \\ \theta_{1x} \\ \theta_{1y} \\ \theta_{1z} \end{Bmatrix} \tag{2.371}$$

The stiffness factors are first expressed in terms of compliances according to Eqs. (2.144) and (2.370) and then are utilized in Eq. (2.371) to evaluate the loading components. These load components are eventually substituted back into Eq. (2.368), which gives the maximum equivalent von Mises stress in terms of deformations.

2.4.2.4 Strain Energy-Based Efficiency

In the case of a multiple-axis flexure hinge, an evaluation of its efficiency can be made based on the strain energy stored during deformation by the overall load vector. The development here is similar to the one performed previously for single-axis flexure hinges; therefore, more details can be found in that section. In the present case, the loading at the free end of the flexure consists of bending on two perpendicular planes (planes of axial symmetry), axial tension/compression, and torsion. The deformation-loading equations are:

$$\begin{cases} u_{1x} = C_{1,x-F_x} F_{1x} \\ u_{1y} = C_{1,y-F_y} F_{1y} + C_{1,y-M_z} M_{1z} \\ u_{1z} = C_{1,y-F_y} F_{1z} + C_{1,y-M_z} M_{1z} \\ \theta_{1y} = C_{1,y-M_z} F_{1z} + C_{1,\theta_z-M_z} M_{1y} \\ \theta_{1z} = C_{1,y-M_z} F_{1y} + C_{1,\theta_z-M_z} M_{1z} \\ \theta_{1x} = C_{1,\theta_x-M_x} M_{1x} \end{cases} \tag{2.372}$$

The work done by the loads is:

$$W_{in} = \frac{1}{2}(F_{1x}u_{1x} + F_{1y}u_{1y} + F_{1z}u_{1z} + M_{1y}\theta_{1y} + M_{1z}\theta_{1z} + M_{1x}\theta_{1x}) \tag{2.373}$$

By successive substitution of Eq. (2.372) into Eq. (2.373), the energy efficiency can be expressed as:

$$\eta = \frac{C_{1,\theta_z-M_z} M_{1z}^2}{C_{1,x-F_x} F_{1x}^2 + C_{1,y-F_y}(F_{1y}^2 + F_{1z}^2) + C_{1,\theta_z-M_z}(M_{1y}^2 + M_{1z}^2) + 2C_{1,y-M_z}(F_{1y}M_{1z} + F_{1z}M_{1y})} \tag{2.374}$$

In case of overall unit loading, Eq. (3.374) transforms into:

$$\eta = \frac{C_{1,\theta_z-M_z}}{C_{1,x-F_x} + 2C_{1,y-F_y} + 2C_{1,\theta_z-M_z} + 4C_{1,y-M_z}} \tag{2.375}$$

In the case of short flexure hinges that take into consideration the shearing effects, the compliance factor $C_{1,y-Fy}$ is substituted by the corresponding factor $C^s_{1,y-F_y}$.

Based on the generic formulation that was presented here, the following discussion will detail the compliances that describe the capacity of rotation and precision of rotation for multiple-axis flexures (cylindrical, circular, corner-filleted, parabolic, hyperbolic, elliptic, inverse parabolic, and secant).

2.4.3 Cylindrical Flexure Hinge

The cylindrical flexure hinge is included here because further numerical simulation will utilize its simpler compliance equations as a reference for several comparisons to be performed. The cylindrical flexure has a constant diameter, so that:

$$t(x) = t \tag{2.376}$$

2.4.3.1 Capacity of Rotation

The compliances that describe the capacity of rotation are:

$$C_{1,x-F_x} = \frac{4l}{\pi E t^2} \tag{2.377}$$

$$C_{1,y-F_y} = \frac{64l^3}{3\pi E t^4} \tag{2.378}$$

$$C_{1,y-M_z} = \frac{32l^2}{\pi E t^4} \tag{2.379}$$

$$C_{1,\theta_x-M_x} = \frac{32l}{\pi G t^4} \tag{2.380}$$

2.4.3.2 Precision of Rotation

The compliances that describe the precision of rotation are:

$$C_{2,x-F_x} = \frac{4l}{\pi E t^2} \tag{2.381}$$

$$C_{2,y-F_y} = \frac{20l^3}{3\pi E t^4} \tag{2.382}$$

$$C_{2,y-M_z} = \frac{8l^2}{\pi E t^4} \tag{2.383}$$

2.4.4 Circular Flexure Hinge

The variable thickness/diameter $t(x)$ is given in Eq. (2.170). Actually, for all the other flexure configurations, the diameter will be equal to the thickness $t(x)$ that was given for the corresponding single-axis profile.

2.4.4.1 Capacity of Rotation

The compliances that describe the capacity of rotation are:

$$C_{1,x-F_x} = \frac{16r}{\pi E t^2}\left[\frac{2r+t}{4r+t} + 2r\sqrt{\frac{t}{(4r+t)^3}}\arctan\sqrt{1+\frac{4r}{t}}\right] \tag{2.384}$$

$$C_{1,y-F_y} = \frac{256r^3}{3\pi E t^4(2r+t)^2\sqrt{(4r+t)^7}}\left[\sqrt{4r+t}(1664r^5 + 3340r^4 t + 2620r^3 t^2 + \right.$$

$$\left. 987r^2 t^3 + 188rt^4 + 16t^5) + 3r(2r+t)^2\sqrt{t}(100r^2 + 84rt + 21t^2)\arctan\sqrt{1+\frac{4r}{t}}\right] \tag{2.385}$$

$$C_{1,y-M_z} = \frac{256r^2}{3\pi E t^4}\left[3 + \frac{t(120r^4 + 176r^3 t + 92r^2 t^2 + 24rt^3 + 3t^4)}{(2r+t)^2(4r+t)^3}\right.$$

$$\left. + 24r(5r^2 + 4rt + t^2)\sqrt{\frac{t}{(4r+t)^7}}\arctan\sqrt{1+\frac{4r}{t}}\right] \tag{2.386}$$

$$C_{1,\theta_x-M_x} = \frac{E}{4rG}C_{1,y-M_z} \tag{2.387}$$

2.4.4.2 Precision of Rotation

The equations that describe the precision of rotation are:

$$C_{2,y-F_y} = \frac{128r^3}{3\pi Et^4(2r+t)^2\sqrt{(4r+t)^7}}\left[\sqrt{4r+t}(512r^5+1332r^4t+1268r^3t^2\right.$$
$$+541r^2t^3+112rt^4+10t^5)+3r(2r+t)^2(60r^2+52rt+13t^2)$$
$$\left.\sqrt{t}\arctan\sqrt{1+\frac{4r}{t}}\right] \tag{2.388}$$

$$C_{2,y-M_z} = \frac{128r^2}{3\pi Et^4(2r+t)^2\sqrt{(4r+t)^7}}\left[\sqrt{4r+t}(192r^5+460r^4t+412r^3t^2\right.$$
$$\left.+169r^2t^3+34rt^4+3t^5)+12r(2r+t)^2(5r^2+4rt+t^2)\sqrt{t}\arctan\sqrt{1+\frac{4r}{t}}\right] \tag{2.389}$$

2.4.5 Corner-Filleted Flexure Hinge

2.4.5.1 Capacity of Rotation

The compliances describing the capacity of rotation are:

$$C_{1,x-F_x} = \frac{4}{\pi Et^2}\left[l+\frac{2rt}{4r+t}+8r^2\sqrt{\frac{t}{(4r+t)^3}}\arctan\sqrt{1+\frac{4r}{t}}\right] \tag{2.390}$$

$$C_{1,y-F_y} = \frac{64}{\pi E}\left\{\frac{(l-r)^3-r^3}{3t^4}+\frac{r}{3t^3(2r+t)^2(4r+t)^3}[8r^4(15l^2+62lr+30r^2)\right.$$
$$+16r^3t(11l^2+46lr+25r^2)+4r^2t^2(23l^2+94lr+57r^2)+8rt^3(l+r)(3l+8r)$$
$$+t^4(3l^2+9lr+8r^2)]+\frac{4r^2}{\sqrt{t^7(4r+t)^7}}[5r^2(2r+t)^2+2l(l+2r)(5r^2+4rt+t^2)]$$
$$\left.\arctan\sqrt{1+\frac{4r}{t}}\right\} \tag{2.391}$$

$$C_{1,y-M_z} = \frac{64}{\pi E}\left\{\frac{(l+r)^2-r^2}{2t^4}+r(l+2r)\left[\frac{120r^4+176r^3t+92r^2t^2+24rt^3+3t^4}{3t^3(2r+t)^2(4r+t)^3}\right.\right.$$
$$\left.\left.+\frac{8r(5r^2+4rt+t^2)}{\sqrt{t^7(4r+t)^7}}\arctan\sqrt{1+\frac{4r}{t}}\right]\right\} \tag{2.392}$$

$$C_{1,\theta_x-M_x}=\frac{32}{\pi G}\left\{\frac{l}{t^4}+2r\left[\frac{120r^4+176r^3t+92r^2t^2+24rt^3+3t^4}{3t^3(2r+t)^2(4r+t)^3}\right.\right.$$
$$\left.\left.+\frac{8r(5r^2+4rt+t^2)}{\sqrt{t^7(4r+t)^7}}\arctan\sqrt{1+\frac{4r}{t}}\right]\right\} \tag{2.393}$$

2.4.5.2 Precision of Rotation

The compliances describing the precision of rotation are:

$$C_{2,y-F_y}=\frac{4}{3\pi E}\left\{\frac{l^2(5l+6r)}{t^4}+\frac{4rt^3}{(4r+t)^3}\left[\frac{2r^2(256r^4+432r^3t+236r^2t^2}{t^6(2r+t)^2}\right.\right.$$
$$+\frac{2r^2(56rt^3+5t^4)+l^2(240r^4+352r^3t+184r^2t^2+48rt^3+6t^4)}{t^6(2r+t)^2}$$
$$+\frac{lr(1008r^4+1504r^3t+760r^2t^2+168rt^3+15t^4)}{t^6(2r+t)^2}$$
$$\left.\left.+24r\frac{r^2t(4r+t)+2l(l+r)(5r^2+4rt+t^2)}{\sqrt{t^{13}(4r+t)}}\arctan\sqrt{1+\frac{4r}{t}}\right]\right\} \tag{2.394}$$

$$C_{2,y-M_z}=\frac{64}{\pi E}\left\{\frac{l^2}{8t^4}+\frac{rt^2}{6(2r+t)^2}\left\{\frac{r(4r+3t)}{t^5}+\frac{l}{t\sqrt{(4r+t)^7}}\left[\sqrt{4r+t}\left[3\right.\right.\right.\right.$$
$$\left.+\frac{4r(30r^3+44r^2t+23rt^2+6t^3)}{t^4}\right]$$
$$\left.\left.\left.+\frac{24r(2r+t)^2(5r^2+4rt+t^2)}{\sqrt{t^9}}\arctan\sqrt{1+\frac{4r}{t}}\right]\right\}\right\} \tag{2.395}$$

2.4.6 Parabolic Flexure Hinge

2.4.6.1 Capacity of Rotation

The compliances describing the capacity of rotation are:

$$C_{1,x-F_x}=\frac{l}{\pi E\sqrt{t^3c}(2c+t)}\left[2\sqrt{ct}+\sqrt{2}(c+t)\arctan\sqrt{\frac{2c}{t}}\right] \tag{2.396}$$

$$C_{1,y-F_y} = \frac{l^3}{12\pi E\sqrt{t^7c^3}(2c+t)^3}\left[2\sqrt{ct}(120c^3+172c^2t+82ct^2-3t^3)\right. \\ \left. +3\sqrt{2}(2c+t)^3(10c+t)\arctan\sqrt{\frac{2c}{t}}\right] \tag{2.397}$$

$$C_{1,y-M_z} = \frac{l^2}{3\pi E\sqrt{t^7c}(2c+t)^3}\left[2\sqrt{ct}(60c^2+80ct+33t^2)\right. \\ \left. +15\sqrt{2}(2c+t)^3\arctan\sqrt{\frac{2c}{t}}\right] \tag{2.398}$$

$$C_{1,\theta_x-M_x} = \frac{E}{lG}C_{1,y-M_z} \tag{2.399}$$

Note that all similar torsional compliances for the next flexure configurations are given by Eq. (2.399); therefore, this equation will not be mentioned again.

2.4.6.2 Precision of Rotation

The compliances describing the precision of rotation are:

$$C_{2,y-F_y} = \frac{l^3}{24\pi Et^3(2c+t)^3}\left[128c^2+216ct+128t^2-\frac{6t^3}{c}\right. \\ \left. +3\sqrt{2}(2c+t)^3\sqrt{\frac{t}{c^3}}\arctan\sqrt{\frac{2c}{t}}\right] \tag{2.400}$$

$$C_{2,y-M_z} = \frac{8l^2(4c^2+6ct+3t^2)}{3\pi Et^3(2c+t)^3} \tag{2.401}$$

2.4.7 Hyperbolic Flexure Hinge

2.4.7.1 Capacity of Rotation

The compliances describing the capacity of rotation are:

$$C_{1,x-F_x} = \frac{2l}{\pi Et\sqrt{c(c+t)}}\arctan\left[\frac{2\sqrt{c(c+t)}}{t}\right] \tag{2.402}$$

$$C_{1,y-F_y} = \frac{l^3}{\pi E t^3 (2c+t)^2 \sqrt{c^3(c+t)^3}} \left[2t\sqrt{c(c+t)}(4c^2+4ct-t^2) + (2c+t)^4 \arctan\left[\frac{2\sqrt{c(c+t)}}{t}\right]\right] \tag{2.403}$$

$$C_{1,y-M_z} = \frac{8l^2}{\pi E t^3} \left[\frac{2t}{(2c+t)^2} + \frac{\arctan\left[\frac{2\sqrt{c(c+t)}}{t}\right]}{\sqrt{c(c+t)}} \right] \tag{2.404}$$

2.4.7.2 Precision of Rotation

The compliances describing the precision of rotation are:

$$C_{2,y-F_y} = \frac{l^3}{2\pi E t^2 (2c+t)^2 (c+t)\sqrt{c^3}} \left[2\sqrt{c}(4c^2+4ct-t^2) + \frac{t(2c+t)^2}{\sqrt{c+t}} \arctan\left[\frac{2\sqrt{c(c+t)}}{t}\right]\right] \tag{2.405}$$

$$C_{2,y-M_z} = \frac{8l^2}{\pi E t^2 (2c+t)^2} \tag{2.406}$$

2.4.8 Elliptical Flexure Hinge

2.4.8.1 Capacity of Rotation

The compliances defining the capacity of rotation are:

$$C_{1,x-F_x} = \frac{4}{\pi E t (2c+t)(4c+t)} \left[l(t+2c) + \frac{2cl(2c+t)}{\sqrt{t(4c+t)}} \left(\arctan\left[\frac{2c}{\sqrt{t(4c+t)}}\right] - \frac{\pi}{2}\right)\right] \tag{2.407}$$

$$C_{1,y-F_y} = \frac{16l^3}{\pi E t^3 (4c+t)^3} \left[\frac{2(60c^4+100c^3t+57c^2t^2+16ct^3+2t^4)}{3(2c+t)^2} + \frac{5c(2c+t)^2}{\sqrt{t(4c+t)}} \left(\arctan\left[\frac{2c}{\sqrt{t(4c+t)}}\right] - \frac{\pi}{2}\right)\right] \tag{2.408}$$

$$C_{1,y-M_z} = \frac{64l^2}{\pi E t^3 (4c+t)^3}\left[\frac{120c^4 + 176c^3 t + 92c^2 t^2 + 24ct^3 + 3t^4}{6(2c+t)^2}\right.$$
$$\left. + \frac{2c(5c^2 + 4ct + t^2)}{\sqrt{t(4c+t)}}\left(\arctan\left[\frac{2c}{\sqrt{t(4c+t)}}\right] - \frac{\pi}{2}\right)\right] \tag{2.409}$$

2.4.8.2 Precision of Rotation

The compliances describing the precision of rotation are:

$$C_{2,x-F_x} = \frac{4l}{\pi E t}\left[\frac{1}{4(2c+t)} - \frac{2c}{\sqrt{t^3(4c+t)}}\arctan\sqrt{\frac{t}{4c+t}}\right] \tag{2.410}$$

$$C_{2,y-F_y} = \frac{4l^3}{3\pi E\sqrt{t^5(4c+t)^5}}\left[\sqrt{\frac{t}{4c+t}}\,\frac{48c^3 + 44c^2 t + 24ct^2 + 5t^3}{(2c+t)^2}\right.$$
$$\left. - 12c\arctan\sqrt{\frac{t}{4c+t}}\right] \tag{2.411}$$

$$C_{2,y-M_z} = \frac{8l^2(8c+3t)}{3\pi E(2c+t)^2(4c+t)^3} \tag{2.412}$$

2.4.9 Inverse Parabolic Flexure Hinge

2.4.9.1 Capacity of Rotation

The compliances describing the capacity of rotation are:

$$C_{1,x-F_x} = \frac{4l(32c^2 + 40ct + 15t^2)}{15\pi E t^2 (2c+t)^2} \tag{2.413}$$

$$C_{1,y-F_y} = \frac{64l^3(6144c^4 + 14080c^3 t + 12672c^2 t^2 + 5544ct^3 + 1155t^4)}{3465\pi E t^4 (2c+t)^4} \tag{2.414}$$

$$C_{1,y-M_z} = \frac{32l^2(2048c^4 + 4608c^3 t + 4032c^2 t^2 + 1680ct^3 + 315t^4)}{315\pi E t^4 (2c+t)^4} \tag{2.415}$$

2.4.9.2 Precision of Rotation

The compliances describing the precision of rotation are:

$$C_{2,y-F_y} = \frac{4l^3(15184c^4 + 38984c^3t + 40392c^2t^2 + 21252ct^3 + 5775t^4)}{3465\pi Et^4(2c+t)^4} \tag{2.416}$$

$$C_{2,y-M_z} = \frac{8l^2(16c^4 + 40c^3t + 40c^2t^2 + 20ct^3 + 5t^4)}{5\pi Et^4(2c+t)^4} \tag{2.417}$$

2.4.10 Secant Flexure Hinge

2.4.10.1 Capacity of Rotation

The compliances describing the capacity of rotation are:

$$C_{1,x-F_x} = \frac{l}{\pi Et^2}\left[2 + \frac{\sin(2y)}{y}\right] \tag{2.418}$$

$$C_{1,y-F_y} = \frac{l^3}{16\pi Et^4y^3}\{128y^3 + 4y[16\cos(2y) + \cos(4y)] - 32\sin(2y) - \sin(4y) + 16y^2[8\sin(2y) + \sin(4y)]\} \tag{2.419}$$

$$C_{1,y-M_z} = \frac{l^2}{\pi Et^4y}[12y + 8\sin(2y) + \sin(4y)] \tag{2.420}$$

with:

$$y = \arccos\left(\frac{t}{2c+t}\right) \tag{2.421}$$

2.4.10.2 Precision of Rotation

The compliances describing the precision of rotation are:

$$C_{2,y-F_y} = \frac{l^3}{32\pi Et^4y^3}\{80y^3 + 2y[-17 + 48\cos(2y) + 3\cos(4y)] - 32\sin(2y) - \sin(4y) + 16y^2[8\sin(2y) + \sin(4y)]\} \tag{2.422}$$

$$C_{2,y-M_z} = \frac{l^2}{8\pi Et^4y^2}\{-17 + 24y^2 + 16\cos(2y) + \cos(4y) + 4y[8\sin(2y) + \sin(4y)]\} \tag{2.423}$$

2.4.11 Limit Verification of Closed-Form Compliance Equations

The correctness of the closed-form compliance equations for multiple-sensitive-axis flexure hinges has been verified by using the limit procedure, in a manner similar to the one employed in limit-checking the single-axis symmetric flexure hinge. Because two corresponding flexure configurations from the one- and multiple-sensitive-axis flexures, respectively, have identical longitudinal sections, a planar constant cross-section flexure hinge can easily be mapped onto a cylindrical hinge, a planar circular flexure hinge onto a revolute circular hinge, and so on. As a consequence, all the checks that have been performed for single-axis flexure hinges and have been presented in detail in previous sections have also been applied here. All the confirmation necessary was obtained with respect to limit calculations.

2.4.12 Numerical Simulations

The performance of multiple-sensitive-axis flexure hinges is assessed through numerical simulation, similar to the procedure that has been utilized for single-axis flexure hinges. The closed-form compliance equations are analyzed in terms of the geometric parameters that define the various revolute flexure configurations. Compared to the single-axis flexure hinges, where four criteria were taken into consideration, only two different groups of numerical simulation are carried out here that target the following objectives:

- Internal compliance comparison
- Compliance comparison to constant cross-section flexure hinge

Analyzing the trend in the absolute values of compliances in terms of the geometric parameters that define a revolute flexure reveals the same patterns noted for single-axis flexure hinges, so these results have not been replicated here. At the same time, the nonsymmetric vs. symmetric comparison is not applicable because the revolute flexure hinges are always longitudinally symmetric. Table 2.4 illustrates the minimum and maximum limits reached by the compliances of revolute flexure hinges when the geometric parameters that define them range within the feasible domains that were specified for the corresponding simulation of single-axis flexure hinges (see parameter values for Tables 2.2 and 2.3).

2.4.12.1 Internal Comparison

Similar to the procedure utilized for single-axis flexure hinges, the focus here falls on analyzing the performance of each flexure type internally, by comparing different compliances that are similar in nature. As previously shown, three compliance ratios can be defined: direct deflection, direct rotation, and crossed, as defined in the equations that defined similar amounts for single-axis

TABLE 2.4

Extreme Values of Compliances for Multiple-Sensitive-Axis (Revolute) Flexure Hinges

		Flexure Type						
		C	**CF**	**E**	**H**	**P**	**IP**	**S**
$C_{1,x-Fx}$ (m/N)	Min	4.7×10^{-9}	7.9×10^{-9}	7.0×10^{-9}	5.8×10^{-9}	6.1×10^{-9}	6.8×10^{-9}	6.7×10^{-9}
	Max	2.4×10^{-8}	5.0×10^{-8}	4.4×10^{-8}	4.0×10^{-8}	4.1×10^{-8}	4.2×10^{-8}	4.2×10^{-8}
$C_{1,y-Fy}$ (m/N)	Min	3.6×10^{-9}	3.3×10^{-8}	6.0×10^{-8}	4.2×10^{-8}	4.7×10^{-8}	5.7×10^{-8}	5.6×10^{-8}
	Max	3.5×10^{-7}	3.7×10^{-6}	3.1×10^{-6}	2.6×10^{-6}	2.7×10^{-6}	2.8×10^{-6}	2.8×10^{-6}
$C_{1,y-Mz}$ (1/N)	Min	9.7×10^{-6}	4.8×10^{-5}	6.7×10^{-5}	5.0×10^{-5}	5.4×10^{-5}	6.5×10^{-5}	6.4×10^{-5}
	Max	4.2×10^{-4}	3.0×10^{-3}	2.5×10^{-3}	2.1×10^{-3}	2.2×10^{-3}	2.3×10^{-3}	2.2×10^{-3}
$C_{1,\theta y-My}$ (1/Nm)	Min	6.0×10^{-2}	1.1×10^{-1}	9.0×10^{-2}	6.6×10^{-2}	7.2×10^{-2}	8.7×10^{-2}	8.8×10^{-2}
	Max	1.1	3.1	2.5	2.1	2.2	2.3	2.3
$C_{1,\theta x-Mx}$ (1/Nm)	Min	1.4×10^{-1}	2.6×10^{-1}	2.1×10^{-1}	1.5×10^{-1}	1.7×10^{-1}	2.0×10^{-1}	1.9×10^{-1}
	Max	2.5	7.3	5.7	4.9	5.0	5.3	5.2
$C_{2,x-Fx}$ (m/N)	Min	2.3×10^{-9}	3.9×10^{-9}	3.5×10^{-10}	2.9×10^{-9}	3.1×10^{-9}	3.4×10^{-9}	$3.4x \times 10^{-9}$
	Max	1.2×10^{-8}	2.5×10^{-8}	2.2×10^{-8}	2.0×10^{-8}	2.1×10^{-8}	2.1×10^{-8}	2.1×10^{-8}
$C_{2,y-Fy}$ (m/N)	Min	5.1×10^{-10}	2.9×10^{-8}	1.4×10^{-8}	8.0×10^{-9}	9.3×10^{-9}	1.3×10^{-8}	1.2×10^{-8}
	Max	6.6×10^{-7}	1.1×10^{-6}	8.4×10^{-7}	$6.5v \times 10^{-7}$	6.8×10^{-7}	7.3×10^{-7}	7.2×10^{-7}
$C_{2,y-Mz}$ (1/N)	Min	1.5×10^{-5}	2.0×10^{-5}	1.2×10^{-5}	7.2×10^{-6}	8.4×10^{-6}	1.1×10^{-5}	1.0×10^{-5}
	Max	5.2×10^{-4}	5.4×10^{-4}	5.3×10^{-4}	4.2×10^{-4}	4.3×10^{-4}	4.6×10^{-4}	4.6×10^{-4}

Note: C = circular; CF = corner-filleted; E = elliptical; H = hyperbolic; P = parabolic; IP = inverse parabolic; and S = secant.

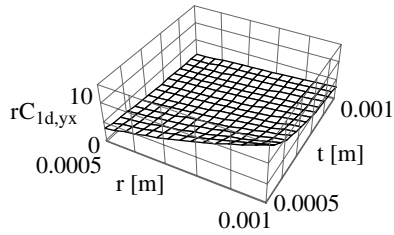

FIGURE 2.38
Characterization of a revolute circular flexure hinge by the internal direct compliance ratio defined in terms of notch radius *r* and minimum thickness *t*.

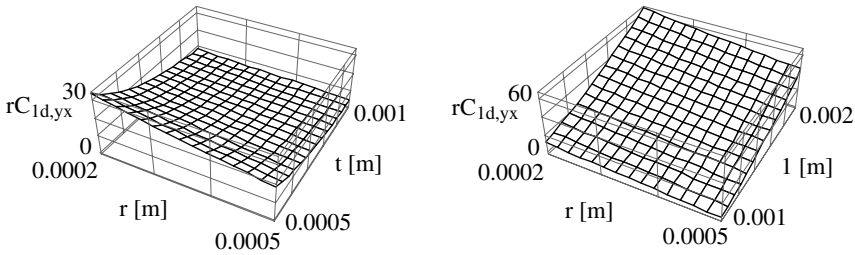

FIGURE 2.39
Characterization of a revolute corner-filleted flexure hinge by the internal direct compliance ratio defined in terms of fillet radius *r*, minimum thickness *t*, and length *l*.

flexure hinges. Details will be given for the results corresponding to different types of flexure hinges.

2.4.12.1.1 Circular Flexure Hinges

Figure 2.38 shows the three-dimensional plot of the single direct compliance ratio as a function of the geometric parameters *r* and *t*. The deflection compliance ratio, as shown in Figure 2.38, increases when *r* increases and *t* decreases.

2.4.12.1.2 Corner-Filleted Flexure Hinges

Two plots of the same deflection compliance ratio are illustrated in Figure 2.39 for revolute corner-filleted flexure hinges in terms of the fillet radius, *r*, and flexure length, *l*. The width cancels out and therefore is not accounted for in the compliance ratio plots. The deflection compliance ratio increases with decreasing *r* and increasing *l*, as indicated in Figure 2.39.

2.4.12.1.3 All Other Flexure Hinges

Plots are shown only for elliptical flexure hinges, but they are representative for all other flexure types (parabolic, hyperbolic, inverse parabolic, and secant). Figure 2.40 illustrates the plots of the same deflection compliance

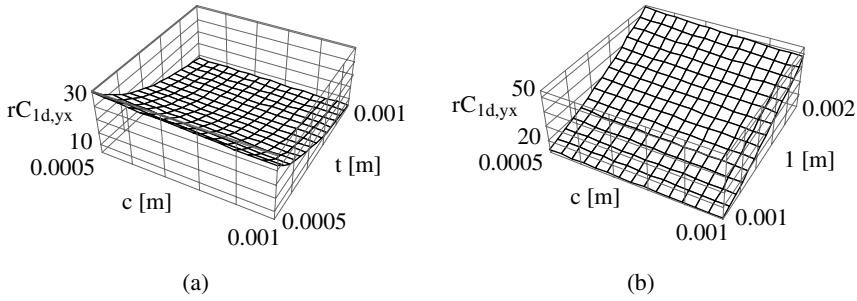

FIGURE 2.40
Characterization of a revolute elliptical flexure hinge by the internal direct compliance ratio defined in terms of the parameter c, minimum thickness t, and length l.

ratio that was analyzed for previously considered flexure configurations. The width of the flexure, w, does not enter into the compliance ratio equation; therefore, the variables in the plots of Figure 2.40 are c, t, and l only. The deflection compliance ratio decreases when the parameter c increases, the minimum thickness t decreases, and the length l decreases. The parabolic and hyperbolic flexure hinges reveal higher maximum values of this ratio (up to 50), while the elliptical (see Figure 2.40), inverse parabolic, and secant flexure hinges display a lower maximum value (up to 40).

2.4.12.2 Constant Cross-Section Flexure Hinge Comparison and Shearing Effects

The seven different flexure hinge configurations are also compared to the constant cross-section (cylindrical) flexure hinge by means of the corresponding compliances. The compliance ratios that were previously defined are also used here. The shearing effects, which are extremely important for smaller flexure lengths, are also analyzed by means of the previously formulated compliance ratios.

2.4.12.2.1 Circular Flexure Hinges

Figure 2.41 shows several plots that illustrate the comparative response of circular flexure hinges with respect to cylindrical flexure hinges. Also presented is the plot of the compliance ratio, which reflects the influence of the shearing effects for circular flexure configurations. The following conclusions can be derived when comparing the circular flexure hinge to the corresponding cylindrical flexure hinge:

- All compliance ratios increase when r increases and t decreases.
- A circular flexure hinge can be up to 7 times less compliant in rotation than its corresponding cylindrical counterpart (Figure 2.41b).

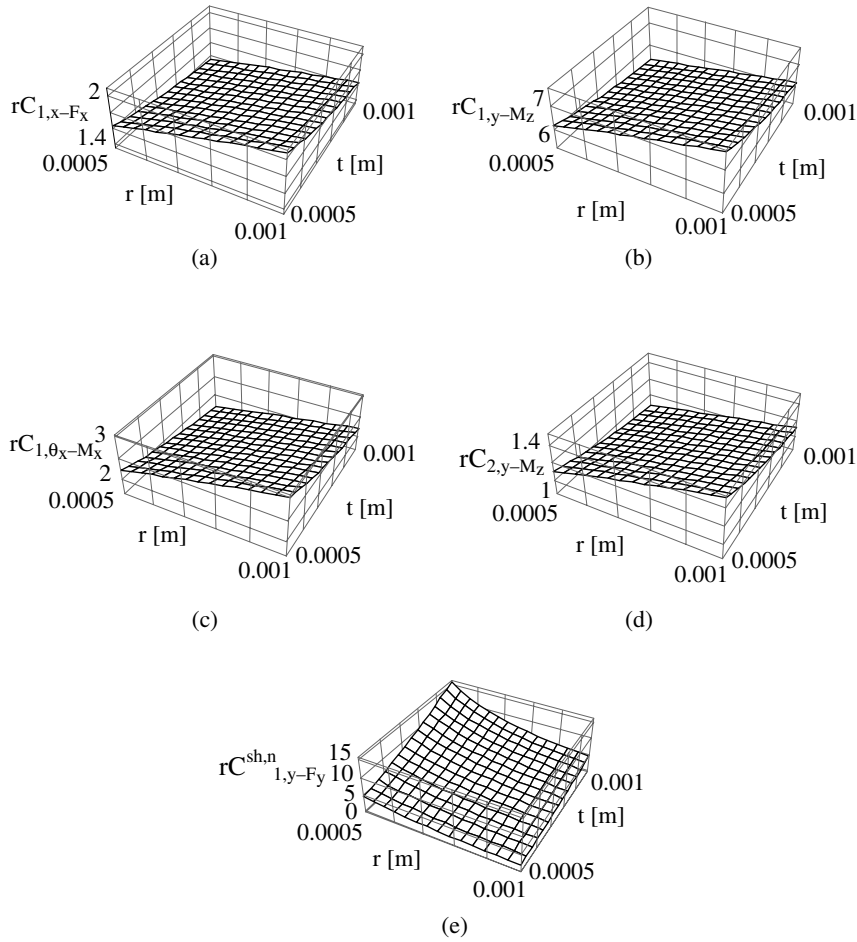

FIGURE 2.41
Characterization of a revolute circular flexure hinge in terms of notch radius *r* and minimum thickness *t*: (a–d) cylindrical beam-referenced compliance ratios; (e) shear-referenced compliance ratio.

- A circular flexure hinge is up to 2 times less axially compliant, compared to its corresponding cylindrical flexure hinge (Figure 2.41a).
- The circular flexure hinge can be up to 3 times less compliant in torsion than a cylindrical flexure (Figure 2.41a).
- The circular flexure hinge can be 40% more efficient than a corresponding cylindrical flexure hinge, in terms of its precision of rotation (Figure 2.41d).
- With respect to shearing effects, the circular flexure hinge can be up to 15 times more compliant than a corresponding circular flexure where shearing is not taken into account (Figure 2.41e).

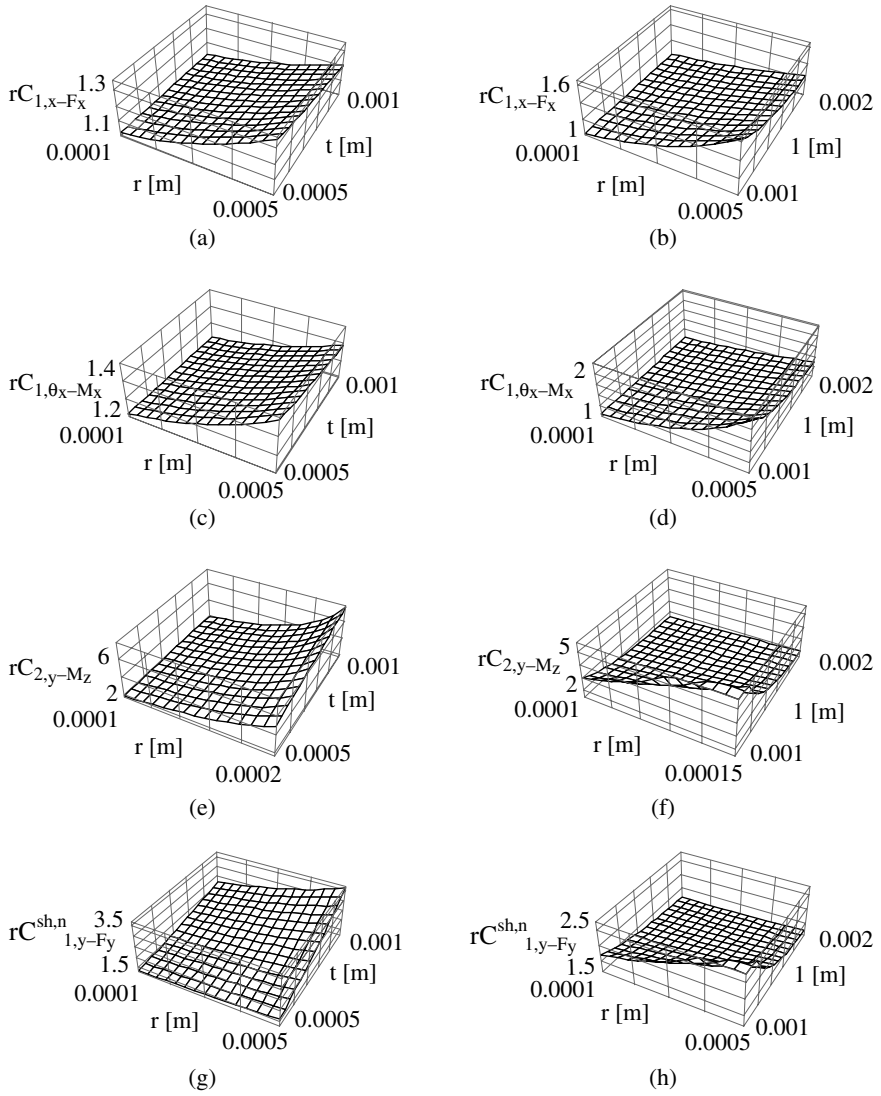

FIGURE 2.42
Characterization of a revolute corner-filleted flexure hinge in terms of fillet radius *r*, minimum thickness *t*, and length *l*: (a–f) cylindrical beam-referenced compliance ratios; (g–h) shear-referenced compliance ratio.

2.4.12.2.2 Corner-Filleted Flexure Hinges

Figure 2.42 displays the plots describing the relative response of a corner-filleted flexure hinge in comparison to its cylindrical counterpart, as well as the effects of shearing when the defining geometric parameters are

ranging within feasible intervals. The following observations can be formulated:

- All the compliance ratios increase with increasing r, decreasing t, and decreasing l.
- The rotation capacity of a corner-filleted flexure hinge can be up to 3 times larger than the corresponding constant flexure hinge (plot not shown here, but similar in trend to Figure 2.42a and b).
- A corner-filleted flexure can be 60% less sensitive to axial effects (Figure 2.42b).
- The corner-filleted flexure configuration can also be up to 6 times less sensitive to effects perturbing its precision of rotation (Figure 2.42e).
- Shearing effects are, again, important factors in correctly assessing a corner-filleted flexure's compliance for shorter lengths, as illustrated in Figure 2.42g and h, and a flexure that incorporates the shearing effects can be 3.5 times more compliant than a flexure not including these effects.

2.4.12.2.3 All Other Flexures

Figure 2.43 illustrates the compliance ratio plots for an elliptical flexure hinge. They are again similar in trends with the plots for parabolic, hyperbolic, inverse parabolic, and secant flexure hinges, plots that are not presented here. In the ratios that compare the different flexure hinges to a cylindrical flexure hinge, the length, l, and width, w, do not appear explicitly; therefore, the plots are drawn only in terms of the geometric parameters c and t. The following trends can be outlined:

- All compliance ratios for all the mentioned flexure hinges increase with c increasing and t decreasing.
- The least axially sensitive are the inverse parabolic and secant flexure hinges (2.2 ratio), followed, in order, by the elliptical (3 ratio, as shown in Figure 2.43b), parabolic (4 ratio), and hyperbolic (6 ratio).
- The best performing in terms of rotation precision are the inverse parabolic and secant flexure hinges (4 ratio), followed by the elliptic (6 ratio, as indicated in Figure 2.43c), parabolic (12 ratio), and hyperbolic (20 ratio).
- The shearing effects condition all the flexures in this category very similarly (both in trends and amount) as indicated by shearing-to-nonshearing compliance ratio maximum values of around 2.5 for short flexure hinges.

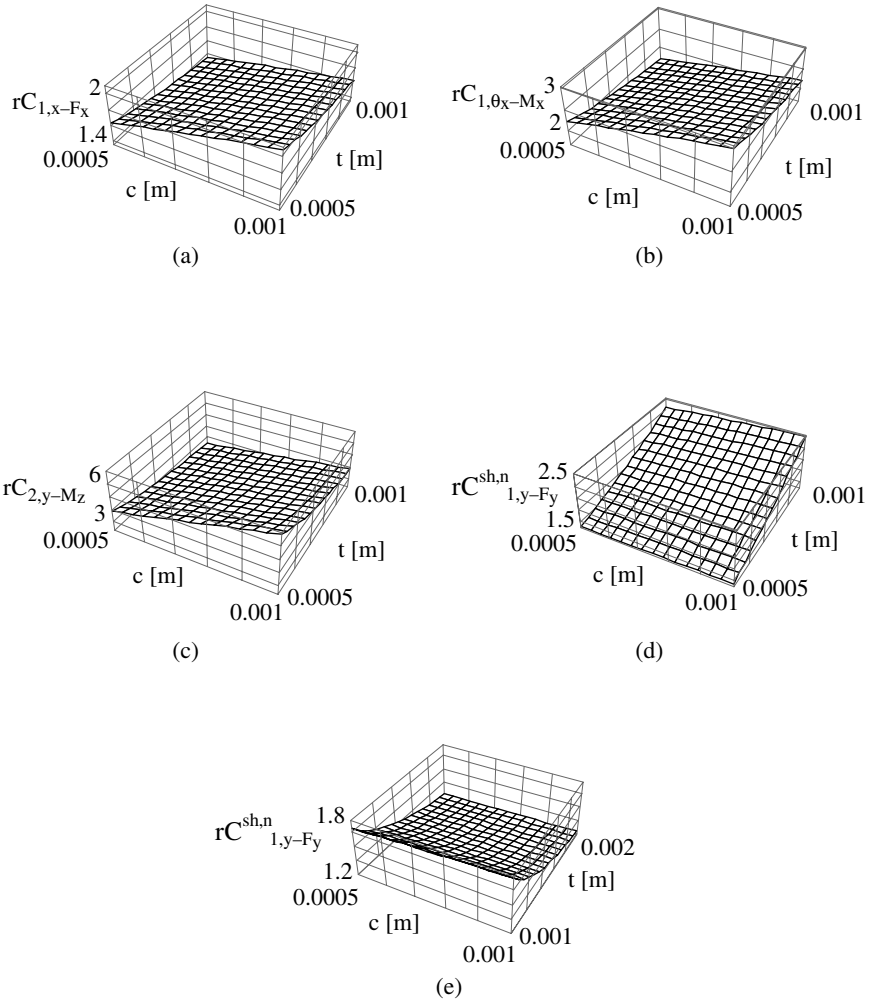

FIGURE 2.43
Characterization of a revolute elliptical flexure hinge in terms of the parameter c and minimum thickness t: (a–c) cylindrical beam-referenced compliance ratios; (d,e) shear-referenced compliance ratio.

2.5 Two-Axis Flexure Hinges for Three-Dimensional Applications

2.5.1 Introduction

Several practical applications require a compliant mechanism to produce rotation locally about specified axes—for instance, about two perpendicular directions. Such cases were pointed out by Paros and Weisbord,[1] who also

provided the solution of disposing two mutually perpendicular flexural cutouts in series. The solution works satisfactorily as long as the two rotation centers do not have to be collocated. An alternative solution is proposed here for designs where collocation of the two perpendicular flexures is necessary. Such a configuration acts as a two-DOF flexure that provides relative rotation between two rigid links around either of two perpendicular directions passing trough the flexure center of rotation. This flexure type has a rectangular cross-section with both defining dimensions varying continuously as a function of the in-plane profile of each. A generic illustration of this design is presented in Figure 2.4.

2.5.2 Generic Formulation and Performance Criteria

A generic formulation is derived here using a procedure similar to that utilized to present the one- and multiple-sensitive-axis flexure hinges, whereby compliances are introduced to describe the performance of this flexure type by analyzing them from the viewpoints of capacity of rotation and precision of rotation. Stress considerations are also discussed.

2.5.2.1 Capacity of Rotation

The loading at the free end point 1 (see Figure 2.8) consists of five components in this case: two bending moments, M_{1y}, M_{1z}; two shearing forces, F_{1y}, F_{1z}; and one axial load, F_{1x}. The torsional effects are generally small compared to the bending and axial ones, and will be neglected in the following.

Similar to the single-axis flexure hinges for two-dimensional applications, where the loads and corresponding displacements are planar and formally disposed in two perpendicular planes by separating them into in-plane and out-of-plane components, two perpendicular planes will also be utilized here to locate the loading agents mentioned above. Therefore, the formulation developed for single-axis, constant-width flexure hinges is formally valid for this case as well and can be maintained with only minor modifications, as indicated next.

The in-plane generic compliance equations are:

$$C_{1,x-F_x} = \frac{1}{E} I_1 \tag{2.424}$$

$$C_{1,y-F_y} = \frac{12}{E} I_2 \tag{2.425}$$

$$C^s_{1,y-F_y} = \frac{12}{E} I_2 + \frac{\alpha}{G} I_1 \tag{2.426}$$

(for relatively short beam-theory, where shearing is taken into account)

$$C_{1,y-M_z} = \frac{12}{E} I_3 \tag{2.427}$$

$$C_{1,\theta_z-M_z} = \frac{12}{E} I_4 \tag{2.428}$$

The out-of-plane compliance equations are:

$$C_{1,z-F_z} = \frac{12}{E} I_5 \tag{2.429}$$

$$C^s_{1,z-F_z} = \frac{12}{E} I_5 + \frac{\alpha}{G} I_1 \tag{2.430}$$

(for relatively short beam theory, where shearing is taken into account)

$$C_{1,z-M_y} = \frac{12}{E} I_6 \tag{2.431}$$

$$C_{1,\theta_y-M_y} = \frac{12}{E} I_7 \tag{2.432}$$

The I_1 through I_7 integrals that define the compliances previously formulated are:

$$I_1 = \int_0^l \frac{dx}{t(x)w(x)} \tag{2.433}$$

$$I_2 = \int_0^l \frac{x^2 dx}{t(x)^3 w(x)} \tag{2.434}$$

$$I_3 = \int_0^l \frac{x dx}{t(x)^3 w(x)} \tag{2.435}$$

$$I_4 = \int_0^l \frac{dx}{t(x)^3 w(x)} \tag{2.436}$$

$$I_5 = \int_0^l \frac{x^2 dx}{t(x) w(x)^3} \tag{2.437}$$

$$I_6 = \int_0^l \frac{x dx}{t(x) w(x)^3} \tag{2.438}$$

$$I_7 = \int_0^l \frac{dx}{t(x) w(x)^3} \tag{2.439}$$

2.5.2.2 Precision of Rotation

The precision of rotation for a three-dimensional, two-axis flexure hinge is characterized in a manner similar to that for the other main flexure types that have been presented—by translations of the geometric centers along the x, y, and z directions. The formulation here is formally identical to the one presented for single-axis, constant-width flexure hinges.

The compliances in the xy plane are:

$$C_{2,x-F_x} = \frac{1}{E} I_1' \tag{2.440}$$

$$C_{2,y-F_y} = \frac{12}{E}\left(I_2' - \frac{l}{2} I_3'\right) \tag{2.441}$$

$$C^s_{2,y-F_y} = \frac{12}{E}\left(I_2' - \frac{l}{2} I_3' + \frac{\alpha}{G} I_1'\right) \tag{2.442}$$

(for relatively short beams, where shearing is taken into account)

$$C_{2,y-M_z} = \frac{12}{E}\left(I_3' - \frac{l}{2} I_4'\right) \tag{2.443}$$

The compliances in the zx plane are:

$$C_{2,z-F_z} = \frac{12}{E}\left(I_5' - \frac{l}{2} I_6'\right) \tag{2.444}$$

$$C^s_{2,z-F_z} = \frac{12}{E}\left(I_5' - \frac{l}{2} I_6'\right) + \frac{\alpha}{G} I_1' \tag{2.445}$$

(for relatively short beams, where shearing is taken into account)

$$C_{2,z-M_y} = \frac{12}{E}\left(I_6' - \frac{l}{2} I_7'\right) \tag{2.446}$$

The I_1' through I_7' integrals that appear in the compliance equations are:

$$I_1' = \int_{l/2}^{l} \frac{dx}{t(x)w(x)} \tag{2.447}$$

$$I_2' = \int_{l/2}^{l} \frac{x^2 dx}{t(x)^3 w(x)} \tag{2.448}$$

$$I_3' = \int_{l/2}^{l} \frac{xdx}{t(x)^3 w(x)} \tag{2.449}$$

$$I_4' = \int_{l/2}^{l} \frac{dx}{t(x)^3 w(x)} \tag{2.450}$$

$$I_5' = \int_{l/2}^{l} \frac{x^2 dx}{t(x) w(x)^3} \tag{2.451}$$

$$I_6' = \int_{l/2}^{l} \frac{xdx}{t(x) w(x)^3} \tag{2.452}$$

$$I_7' = \int_{l/2}^{l} \frac{dx}{t(x) w(x)^3} \tag{2.453}$$

2.5.2.3 Stress Considerations

When neglecting the effects produced through direct shearing forces and torsion, the stresses will only be normal to the cross-section because they are produced through bending and axial effects. The stresses produced by axial loading are constant over the cross-section while the stresses generated through bending on each of the two perpendicular planes vary linearly over the cross-section. As a consequence, the maximum stress will occur at one vertex of the rectangular cross-section where both stresses coming from the double bending are maximum. Reasoning similar to that used for the single-axis, constant-width flexure hinges gives the maximum stress as:

$$\sigma_{max} = \frac{1}{wt}\left\{K_{ta}F_{1x} + 6\left[\frac{K_{tb,z}}{t}(F_{1y}l + M_{1z}) + \frac{K_{tb,y}}{w}(F_{1z}l + M_{1y})\right]\right\} \tag{2.454}$$

where $K_{tb,z}$ and $K_{tb,y}$ denote stress concentration factors for bending about the z and y axes, respectively. Equation (2.454) is useful when the loading on a flexure hinge is known. For cases where the displacement is rather available, a formulation similar to the one developed for single-axis, constant-width flexures produces the following equation:

$$\begin{aligned}\sigma_{max} = \frac{1}{wt}\Bigg\{ & K_{ta}K_{1,x-F_x}u_{1x} + \frac{6K_{tb,z}}{t}[(lK_{1,y-F_y} + K_{1,\theta_z-M_z})u_{1y} \\ & + (lK_{1,y-M_z} + K_{1,\theta_z-M_z})\theta_{1z}] + \frac{6K_{tb,z}}{w}[(lK_{1,z-F_z} + K_{1,\theta_{yz}-M_y})u_{1z} \\ & + (lK_{1,z-M_y} + K_{1,\theta_{yz}-M_y})\theta_{1y}]\Bigg\}\end{aligned} \tag{2.455}$$

2.5.3 Inverse Parabolic Flexure Hinge

A design is analyzed consisting of two pairs of symmetrical inverse parabolic cutouts placed in two perpendicular planes with their rotation centers collocated. The variable thickness and width are:

$$t(x) = \frac{2a_t}{b_t^2 - \left(x - \frac{l}{2}\right)^2} \tag{2.456}$$

with:

$$\begin{cases} a_t = \dfrac{tl^2}{8}\left(1 + \dfrac{t}{2c_t}\right) \\ b_t = \dfrac{l}{2}\sqrt{1 + \dfrac{t}{2c_t}} \end{cases} \tag{2.457}$$

and:

$$w(x) = \frac{2a_w}{b_w^2 - \left(x - \frac{l}{2}\right)^2} \tag{2.458}$$

with:

$$\begin{cases} a_w = \dfrac{wl^2}{8}\left(1 + \dfrac{t}{2c_w}\right) \\ b_w = \dfrac{l}{2}\sqrt{1 + \dfrac{t}{2c_w}} \end{cases} \tag{2.459}$$

The parameters c_t and c_w are similar to the parameter c that defines the maximum thickness of parabolic, hyperbolic, elliptical, inverse parabolic, and secant flexure hinges, as shown in Figure 2.23. These two parameters are located in the planes of the minimum dimensions t and w and their subscripts indicate this relationship.

2.5.3.1 Capacity of Rotation

The in-plane compliances that characterize the capacity of rotation are:

$$C_{1,x-F_x} = \frac{l[32c_tc_w + 20(c_wt + c_tw) + 15wt]}{15Ewt(2c_t + t)(2c_w + w)} \tag{2.460}$$

$$C_{1,y-F_y} = \frac{4l^3[2112c_t^2t(5c_w+3w)+231t^3(6c_w+5w)+198c_tt^2(32c_w+21w)]}{1155Ewt^3(2c_t+t)^3(2c_w+w)} + \frac{256l^3c_t^3(96c_w+55w)}{1155Ewt^3(2c_t+t)^3(2c_w+w)} \tag{2.461}$$

$$C_{1,y-M_z} = \frac{2l^2[105t^3(4c_w+3w)+252c_tt^2(8c_w+5w)+288c_t^2t(12c_w+7w)]}{105Ewt^3(2c_t+t)^3(2c_w+w)} + \frac{256l^2c_t^3(16c_w+9w)}{105Ewt^3(2c_t+t)^3(2c_w+w)} \tag{2.462}$$

$$C_{1,\theta_z-M_z} = \frac{2}{l}C_{1,y-M_z} \tag{2.463}$$

The out-of-plane compliances are:

$$C_{1,z-F_z} = \frac{4l^3[2112c_w^2w(5c_t+3t)+231t^3(6c_t+5t)+198c_ww^2(32c_t+21t)]}{1155Ew^3t(2c_w+w)^3(2c_t+t)} + \frac{256l^3c_w^3(96c_t+55t)}{1155Ew^3t(2c_w+w)^3(2c_t+t)} \tag{2.464}$$

$$C_{1,z-M_y} = \frac{2l^2[105w^3(4c_t+3t)+252c_ww^2(8c_t+5t)+288c_w^2w(12c_t+7t)]}{105Ew^3t(2c_w+w)^3(2c_t+t)} + \frac{256l^2c_w^3(16c_t+9t)}{105Ew^3t(2c_w+w)^3(2c_t+t)} \tag{2.465}$$

$$C_{1,\theta_y-M_y} = \frac{2}{l}C_{1,z-M_y} \tag{2.466}$$

2.5.3.2 Precision of Rotation

The in-plane compliances are:

$$C_{2,y-F_y} = \frac{l^3[66c_t^2t(443c_w+306w)+231t^3(23c_w+25w)]}{4620Ewt^3(2c_t+t)^3(2c_w+w)} + \frac{l^3[c_t^3(15184c_w+9746w)+99c_tt^2(204c_w+161w)]}{4620Ewt^3(2c_t+t)^3(2c_w+w)} \tag{2.467}$$

$$C_{2,y-M_z} = \frac{3l^2[c_w(16c_t^3+30c_t^2t+20c_tt^2+5t^3)+5(c_t+t)(2c_t^2+2c_tt+t^2)]}{10Ewt^3(2c_t+t)^3(2c_w+w)} \tag{2.468}$$

The out-of-plane compliances are:

$$C_{2,z-F_z} = \frac{l^3[66c_w^2 w(443c_t + 306t) + 231w^3(23c_t + 25t)]}{4620Ew^3t(2c_w + w)^3(2c_t + t)} + \frac{l^3[c_w^3(15184c_t + 9746t) + 99c_w w^2(204c_t + 161t)]}{4620Ew^3t(2c_w + w)^3(2c_t + t)} \quad (2.469)$$

$$C_{2,z-M_y} = \frac{3l^2[c_t(16c_w^3 + 30c_w^2 w + 20c_w w^2 + 5w^3)]}{10Ew^3t(2c_w + w)^3(2c_t + t)} + \frac{15l^2(c_w + w)(2c_w^2 + 2c_w w + w^2)}{10Ew^3t(2c_w + w)^3(2c_t + t)} \quad (2.470)$$

A limit check was applied to all the compliances that have been derived for a two-axis inverse parabolic flexure hinge in order to verify their correctness. As Figure 2.4 indicates, a double inverse parabolic flexure hinge becomes a constant cross-section flexure when the symmetric profiles in the two mutually perpendicular sensitive planes are forced to lines. Mathematically, this condition requires that the two parameters c_1 and c_2 go to zero. These limits have been applied to all the compliances derived here, and the results are the corresponding compliance equations for a constant rectangular cross-section flexure hinge.

2.5.3.3 Numerical Simulation

The compliance equations previously developed for a two-axis inverse parabolic flexure hinge are utilized to perform numerical simulation, as illustrated in Figure 2.44. Specifically, the comparison to constant cross-section flexure hinges was one objective (Figure 2.44a–c). Also studied were the shearing effects (Figure 2.44g). The following conclusions can be derived:

- A two-axis flexure hinge can be up to 2.1 times less compliant in terms of its capacity of rotation, compared to its constant cross-section counterpart (Figure 2.44b).
- The two-axis flexure hinge is up to 60% less sensitive to axial effects than a constant cross-section configuration (Figure 2.44a) and can be up to 2 times less sensitive to out-of-plane effects (Figure 2.44c).
- Its precision of rotation can be up to 3 times better compared to a constant cross-section flexure hinge (Figure 2.44d).
- The shearing effects are important factors in correctly assessing the compliant behavior of this flexure type, as they can amount to ratios of 2.5, as shown in Figure 2.44e.

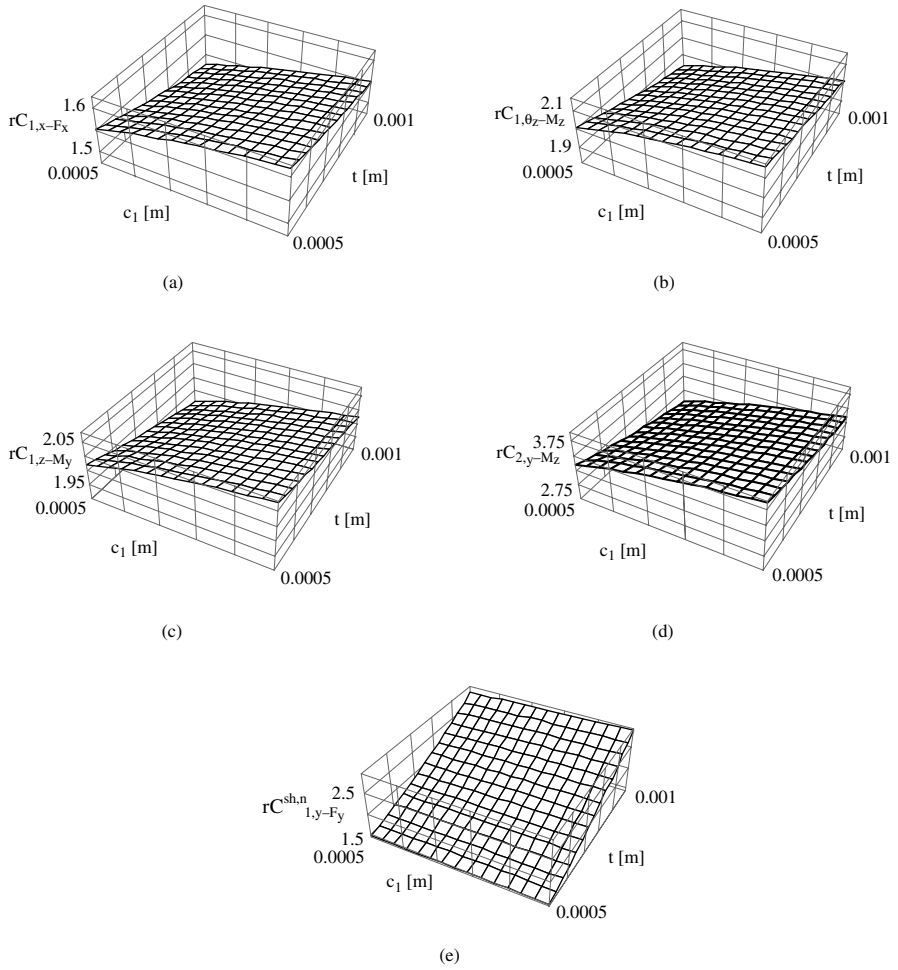

FIGURE 2.44
Characterization of an inverse parabolic flexure hinge with two axes in terms of the parameter c_1, which denotes either c_t or c_w and minimum thickness t: (a–d) beam-referenced compliance ratios; (e) shear-referenced compliance ratio.

2.6 Conclusions

This chapter has presented a large set of flexure hinge configurations for both two- and three-dimensional applications. Three different classes of flexure hinges are analyzed: constant-width, single-axis flexure designs; revolute multiple-sensitive-axis flexure hinges; and variable-width, two-axis flexures. Several configurations are new and add to the ones that have

already been introduced in the dedicated literature. The flexure hinge can be compared to a complex spring element that is sensitive to both rotation and translation. As a direct result of this interpretation, each individual flexure hinge is presented with its complete set of compliances (or spring rates) that define its behavior. A flexure hinge responds in a compliant fashion to bending, axial loading, and, in the case of revolute configurations for three-dimensional applications, torsion. The shearing effects are also taken into considerations for short flexures. Closed-form compliance equations are derived in a rigorous manner in order to characterize the performance of the various flexure hinges in terms of their capacity of rotation, precision of rotation, and maximum stress levels.

References

1. Paros, J.M. and Weisbord, L., How to design flexure hinges, *Machine Design*, November, 151, 1965.
2. Smith, S.T. et al., Elliptical flexure hinges, *Revue of Scientific Instruments*, 68(3), 1474, 1997.
3. Smith, S.T., *Flexures. Elements of Elastic Mechanisms*, Gordon & Breach, Amsterdam, 2000.
4. Lobontiu, N. et al., Corner-filleted flexure hinges, *ASME Journal of Mechanical Design*, 123, 346, 2001.
5. Lobontiu, N. et al., Parabolic and hyperbolic flexure hinges: flexibility, motion precision and stress characterization based on compliance closed-form equations, *Precision Engineering: Journal of the International Societies for Precision Engineering and Nanotechnology*, 26(2), 185, 2002.
6. Lobontiu, N. et al., Design of symmetric conic-section flexure hinges based on closed-form compliance equations, *Mechanism and Machine Theory*, 37(5), 477, 2002.
7. Lobontiu, N. and Paine, J.S.N., Design of circular cross-section corner-filleted flexure hinges for three-dimensional compliant mechanisms, *ASME Journal of Mechanical Design*, 124, 479, 2002.
8. Canfield, S. et al., Development of spatial miniature compliant manipulator, *International Journal of Robotics and Automation*, Special Issue on Compliance and Compliant Mechanisms (in press).
9. Howell, L.L. and Midha, A., A method for the design of compliant mechanisms with small-length flexural pivots, *ASME Journal of Mechanical Design*, 116, 280, 1994.
10. Murphy, M.D., Midha, A., and Howell, L.L., The topological synthesis of compliant mechanisms, *Mechanism and Machine Theory*, 31, 185, 1996.
11. Howell, L.L., *Compliant Mechanisms*, John Wiley & Sons, New York, 2001.
12. Den Hartog, J.P., *Advanced Strength of Materials*, Dover, New York, 1987.
13. Barber, J.R., *Mechanics of Materials*, McGraw-Hill, New York, 2001, chaps. 2 and 3.
14. Volterra, E. and Gaines, J.H., *Advanced Strength of Materials*, Prentice-Hall, Englewood Cliffs, NJ, 1971.
15. Timoshenko, S.P., *History of Strength of Materials*, Dover, New York, 1982.

16. Ugural, A.C. and Fenster, S.K., *Advanced Strength and Applied Elasticity*, Prentice-Hall, Englewood Cliffs, NJ, 1995.
17. Richards, T.H., *Energy Methods in Stress Analysis with an Introduction to Finite Element Techniques*, Ellis Horwood, Chichester, 1977.
18. Harker, R.J., *Elastic Energy Methods of Design Analysis*, Chapman & Hall, 1986.
19. Langhaar, H.L., *Energy Methods in Applied Mechanics*, Krieger, Melbourne, FL, 1989.
20. Sandor, B.I., *Strength of Materials*, Prentice-Hall, Englewood Cliffs, NJ, 1978.
21. Muvdi, B.B. and McNabb, J.W., *Engineering Mechanics of Materials*, 2nd ed., Macmillan, New York, 1984.
22. Cook, R.D. and Young, W.C., *Advanced Mechanics of Materials*, Macmillan, New York, 1985.
23. Kobayashi, A.S., Ed., *Handbook on Experimental Mechanics*, 2nd rev. ed., VCH Publishers, Weinheim/New York, 1993.
24. Sullivan, J.L., Fatigue life under combined stress, *Machine Design*, January 25, 1979.
25. Peterson, R.E., *Stress Concentration Factors*, Wiley, New York, 1974.
26. Pilkey, W.D., *Peterson's Stress Concentration Factors*, John Wiley & Sons, New York, 1997.
27. Boresi, A.P., Schmidt, R.J., and Sidebottom, O.M., *Advanced Mechanics of Materials*, 5th ed., John Wiley & Sons, 1993.
28. Young, W.C., *Roark's Formulas for Stress and Strain*, McGraw-Hill, New York, 1989.
29. Den Hartog, J.P., *Strength of Materials*, Dover, New York, 1977

3

Statics of Flexure-Based Compliant Mechanisms

3.1 Introduction

The aim of this chapter is to incorporate the flexure hinges that were introduced and modeled by means of their compliances within the previous chapter into various mechanisms, either planar or spatial, in order to derive static (quasi-static) models that can naturally include, develop, and take advantage of the compliance-defined flexures. Such mechanisms that are formed by connecting rigid links and flexure hinges will be called flexure-based compliant mechanisms. Each individual component of these compliant mechanisms, either flexible or rigid, will be considered as a separate *link*, and generically it can be considered that any compliant mechanism is composed of flexure hinges solely because a rigid link is virtually a flexure hinge with zero compliance. Formally, the links will be connected at *nodes* that are only graphical representations of the junctions between adjacent links (or between links and supports).

The flexure-based compliant mechanisms can formally be divided into two main categories: planar (or two-dimensional) and spatial (or three-dimensional), depending on the design and the overall motion of the mechanism. Single-axis flexure hinges, which were shown to mainly perform a two-dimensional motion, are included in planar mechanisms, whereas two- and multiple-axis flexures are practical solutions to spatial compliant mechanisms, because, by their geometry, these flexure configurations are designed to perform three-dimensional motion. Each category can further be subdivided into serial, parallel, and hybrid (serial/parallel) mechanisms. In a serial mechanism, all links (at least one being a flexure hinge) are connected serially in such a manner that the resulting configuration is an open chain consisting of at least one input port (where the incoming energy is fed into the system) and one output port (where the resulting motion is delivered outside the system). The input and output ports (or platforms) are generally rigid links that can be located anywhere within the serial mechanism. A parallel mechanism is formed of two or more flexure hinges that are connected

in parallel to a rigid link, which plays the role of output port/platform. In a hybrid mechanism, several legs in the form of serial open chains (actually serial mechanisms, according to their recently introduced definition) are placed in a parallel fashion, and they all connect to a rigid link (the output platform).

As the title of this chapter indicates, the response of flexure-based compliant mechanisms will be studied when the external loads are applied statically (or quasi-statically). The serial mechanisms are treated first, and it is subsequently demonstrated that either a parallel or a hybrid flexure-based compliant mechanism can be regarded as being statically equivalent to a specific "source" serial mechanism composed of a rigid link (the output platform) that is interposed between either two serial open chains (in the case of hybrid mechanisms) or two flexure hinges (in the case of parallel mechanisms).

Also discussed in this chapter are several specific aspects of the static modeling of flexure-based compliant mechanisms, which allows us to analyze their performance in terms of a few criteria that are of practical importance. All of these specific subproblems are treated by formulating mathematical models that, in essence, reflect the load-deformation behavior of a compliant mechanism based on the various compliances that define the flexure hinges composing the studied compliant mechanism. One subgroup in the static modeling focuses on expressing the output displacement of a compliant mechanism in terms of the external load, boundary conditions, and topology (structure) and geometry of the mechanism. Two methods are discussed here together with their corresponding mathematical models: the loop-closure method and Castigliano's displacement theorem. Both methods give the equations that relate the displacement vector at a given port to the input load vector, in the form:

$$\overline{u} = f(\overline{L}) \tag{3.1}$$

Another topic in the static modeling/analysis of flexure-based compliant mechanisms is assessing the stiffness of the mechanism by analyzing different ports and loads about various directions. Basically, the following generic equation is solved within this subproblem and gives a composed (overall) stiffness k_{ij}:

$$k_{ij} = \frac{\left|\overline{L}_{i,d_i}\right|}{\left|\overline{u}_{j,d_j}\right|} \tag{3.2}$$

where the load L (either force or moment) is being applied at a location i along a direction d_i, whereas the displacement u (either linear or angular) is determined at a location j about a direction d_j. This generic approach allows for necessary flexibility by not requiring the load and displacement to be

either collocated or parallel, such as in cases where the force is applied at the input port and the displacement is determined at the output port. An important problem in many flexure-based compliant mechanisms is to evaluate the output-to-input amplification (or deamplification) ratio, also called *mechanical advantage*, which is mathematically defined as:

$$m.a. = \frac{\left|\overline{u}_{out}\right|}{\left|\overline{u}_{in}\right|} \tag{3.3}$$

In amplification mechanisms, the mechanical advantage is greater than one, whereas in deamplification mechanisms the mechanical advantage is less than one. The performance of a specific flexure-based compliant mechanism can also be assessed by calculating the block load, which is the force and/or moment that, being generally applied at the output port, completely annihilates the (output) motion of the mechanism. The block load will be expressed in terms of the external load acting on the mechanism as:

$$\overline{L}_b = f(\overline{L})\Big|_{\overline{u}_{out}=0} \tag{3.4}$$

Another topic of interest in studying the static response of flexure-based compliant mechanisms is evaluating their energy efficiency. This aspect is approached in this chapter by utilizing the equations giving the energy efficiency of individual flexure hinges, as derived within the previous chapter. In flexure-based compliant mechanisms that are designed to deliver high-precision output motion, predicting the precision of motion with a high degree of accuracy is paramount. A model is developed in this chapter that compares the output displacement of a given mechanism when considering that the flexure hinges are either purely rotational or rotational with torsional springs (stiffnesses) with the model that considers the flexures as fully compliant members, according to the compliance equations derived within the previous chapter.

Tremendous work has been performed and reported in the field of compliant mechanisms. The accomplishments in theoretical modeling and analysis/synthesis, as well as in engineering applications, of A. Midha, A.G. Erdman, L.L. Howell, S.T. Smith, S. Kota, N. Kikuchi, G.K. Ananthasuresh, and M. Frecker, to name just a few of the researchers that have a sustained interest in this field, are well known and highly appreciated. The contributions that have been published over the years cover a large spectrum of the contemporary fundamental and application research of compliant mechanisms ranging from small-scale microelectromechanical systems (MEMS)-type devices to macroscale ones.

Modeling the static response of compliant mechanisms involves establishing the mobility of such mechanisms as studied in direct relation with the

degrees of freedom (DOFs) brought in by the flexible members in a compliant system. Smith,[1] for instance, considers that a flexure hinge is a one-DOF member described by the rotation it produces or enables and then discusses the mobility of a flexure-based mechanism in terms of the total number of links, constraints, and the so-called "freedoms" at joints. A similar approach is followed by Howell,[2] who treats a flexure as a pseudo-joint equipped with a single DOF, the rotational one. This approach of considering that a flexure is a one-DOF member is actually embraced by almost all the researchers who analyzed this subject. It should be mentioned that in doing so, the modeling scope is limited to those flexures that are incorporated in two-dimensional (planar) compliant mechanisms, where the main function (and the only one being recognized, according to this modeling approach) is the relative rotation between adjacent links. Flexure hinges that have a different geometry and functionality, such as the two- or multiple-axis flexure configurations that have been described in the previous chapter or even single-axis flexures that are subject to out-of-plane (parasitic) loading/motion, can simply not be modeled as single DOF members because they do transfer different types of motions in addition to rotation.

As mentioned in Chapter 2, a single-axis flexure hinge will be modeled here as a three-DOF component, a two-axis flexure will be considered as a five-DOF link, and a multiple-axis (revolute) flexure hinge will be modeled as a (full) six-DOF link. As a consequence, the total number of degrees of freedom of a specific compliant mechanism will be imposed entirely by the flexure hinges that are incorporated in it and the constraints imposed by boundary conditions. The rigid links will only act as simple followers, and they will have no effect on the total number of degrees of freedom because their position/orientation is determined completely by the degrees of freedom introduced by the flexures. A similar approach to considering the degrees of freedom of a flexure hinge was proposed by Murphy et al.,[3] who characterized a link by the so-called *compliance content*, a qualifier that attaches a number to a specific link according to its capacity of creating different relative and distinct motions between adjacent joints. By this concept, a rigid link has zero compliance content, whereas a planar elastica (a relatively long member that can be subject to large deformations) possesses a compliance content of three, very similar to the single-axis flexure hinges presented in this book.

The degrees of freedom of compliant mechanisms are also approached by Howell and Midha,[4,5] who discuss the classical Grubler formula (which is valid with rigid-link mechanisms) as applied to compliant mechanisms. An interesting concept is presented by Howell[2] whereby a flexure can be divided in several segments delimited by points where the external loads are applied. Unlike the present approach, where each member (either rigid or elastic) in a compliant mechanism is considered as being an individual link, Howell[2] treats a serial chain composed, for instance, of two flexures bordering a rigid part as a one-link mechanism. It should be mentioned that, in the same field

of denominations, the nomenclature introduced by Saggere and Kota[6] discriminates between relatively short flexures (modeled or treated as lumped-compliance members) and long flexures (distributed-compliance members).

A large amount of the specialized literature is dedicated to studying compliant mechanisms that include flexures, according to the pseudo-rigid-body model that was presented in more detail in the introductory chapter of this book. Essentially, the pseudo-rigid-body model transforms a real flexure into a one-DOF rotation joint equipped with torsional stiffness, under the assumption of large deformations. In doing so, this flexure model can be utilized in subsequent modeling of compliant mechanisms according to the classical principles of rigid-body mechanics/mechanisms. The concept of the pseudo-rigid-body model is presented in detail by Howell[2] and a few examples of the papers treating this subject in conjunction with the topic of large displacement, as applied to macroscale compliant mechanisms, include those reported by Midha et al.,[7] Howell and Midha,[8–10] Saxena and Kramer,[11] Midha et al.,[12] and Dado.[13] More recently, the area of MEMS has also been approached by means of the same model and concept. The papers by Ananthasuresh et al.,[14] Ananthasuresh and Kota,[15] Jensen et al.,[16] Salmon et al.,[17] and Kota et al.[18] are just a few examples illustrating the application of the pseudo-rigid-body model to small or microscale systems.

A few topics approached in this chapter have also received attention from similar research reported in the dedicated literature. Howell and Midha,[19] for instance, utilized the pseudo-rigid-body approach to develop a generalized loop-closure theory for the analysis and synthesis of compliant mechanisms. Kota et al.[20] proposed a generalized method for designing compliant mechanisms that includes topology generation and shape/size optimization for various types of conventional and unconventional means of actuation. More recently, Hsiao and Lin[21] studied a planar serial chain composed of two rigid links and five flexure hinges (of which two are fully circular, two are nonsymmetric circular, and one is a curved flexure in the form of a quarter circle). By fixing one end, Hsiao and Lin[21] formulated implicit integral load-displacement equations that express the motions about the three DOFs of the opposite free end. Carricato et al.[22] studied the inverse kinematics of a planar compliant mechanism with flexural pivots by expressing the input displacements that are needed to create a given output position. Kim et al.[23] analyzed the position of the so-called remote center of compliance for a three-DOF compliant mechanism.

In terms of dedicated software that is currently being utilized for the static (quasi-static) analysis of compliant mechanisms, the finite-element technique, through various commercially available packages, appears to be the favored tool, for both macro- and microscale applications. More recently, specialized software for MEMS applications has been designed, and the results of a research group at the University of California–Berkeley in this area were incorporated into a software code that performs nodal analysis for microsystems (see, for example, the paper by Clark et al.[24]).

3.2 Planar Compliant Mechanisms

A static analysis will be first performed for planar flexure-based compliant mechanisms that are subject to different boundary conditions. The basic boundary configuration is fixed–free, but other boundary conditions will be discussed as well. The static analysis will focus on aspects such as force and displacement relationships, amplification and deamplification of displacement or force (mechanical advantage), block load, stiffness, energy efficiency, and precision.

3.2.1 Planar Serial Compliant Mechanisms

A fixed–free planar open chain that is composed of flexure hinges connecting rigid links is studied in the following text. Figure 3.1a gives a schematic representation of the planar mechanism that is referenced to a global frame, *xy*. A generic link is sketched in Figure 3.1b, together with its local frame $x_j y_j$, its position in the global frame, the assumed boundary conditions,

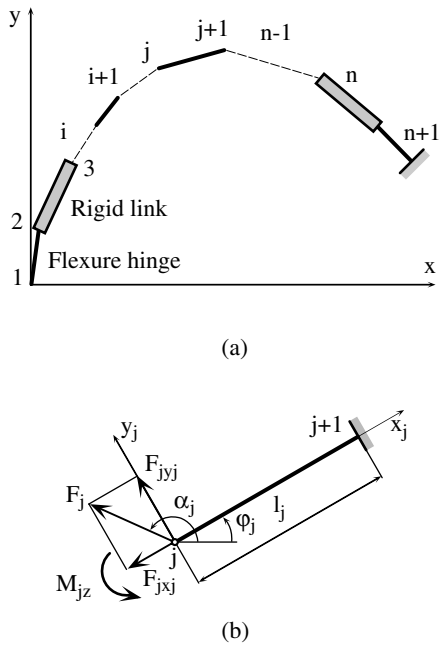

FIGURE 3.1
Planar serial mechanism: (a) fixed–free open-chain compliant mechanism shown in the global reference frame; (b) generic flexure hinge with geometry, position, loading, and its local reference frame.

and the loading at the free end j. The links represented in Fig. 3.1a can be either compliant (specifically, flexure hinges) or rigid.

The rigid links are assumed to be perfect in the sense that they have zero compliance. All the compliances that have been discussed in Chapter 2 were of the form:

$$C_j = \frac{1}{E} f_j(geometry) \tag{3.5}$$

where E is the Young's modulus of elasticity and f_j is a function formulated in terms of the geometric configuration of one flexure. Equation (3.5) is also valid for a rigid link; enforcing $E \to \infty$ results in the respective compliance tending toward zero, $C_j \to 0$. This aspect is particularly convenient in allowing a unitary formulation for both compliant and rigid links.

As detailed in Chapter 2, the three deformations at the free end of the single-axis flexure hinge illustrated in Figure 3.1b are related to the corresponding loading by means of the following equations:

$$\begin{cases} u_{jx_j} = C_{j,x-F_x} F_{jx} \\ u_{jy_j} = C_{j,y-F_y} F_{jy} + C_{j,y-M_z} M_{jz} \\ \theta_{jz_j} = C_{j,y-M_z} F_{jy} + C_{j,\theta_z-M_z} M_{jz} \end{cases} \tag{3.6}$$

As previously discussed, Eq. (3.6) is valid for both compliant members (flexure hinges, actually) that are long (under the conditions that were detailed in Chapter 2 with respect to the long/short separation) and rigid links. For flexure hinges that are relatively short, the only affected equation in Eq. (3.6) is the second one, where the compliance $C_{j,y-Fy}$ needs to be substituted with its counterpart $C^s_{j,y-Fy}$, which incorporates the short-beam theory effects. In order to simplify all further derivation and to make it more uniform, it is assumed that every node of the planar compliant mechanism is loaded with a point load and moment (that can be either external or reaction).

3.2.1.1 Displacement-Load Equations

The aim of this section is to calculate the displacement components in the global reference frame at a given node of the planar structure under the action of the static loading mentioned above. Two methods will be utilized to solve the problem. The loop-closure method will be developed first to determine the displacement components at a generic node of the planar fixed–free compliant mechanism and then Castigliano's second theorem will be utilized for the same purpose.

3.2.1.1.1 The Loop-Closure Method

The loading at the free end, j, of the generic flexure hinge of Figure 3.1b represents the sum of all external forces or moments applied on the planar fixed–free open-chain compliant mechanism between point 1 and the current node j. The corresponding load components on the axes of the local frame are:

$$\begin{cases} F_{jx_j} = \sum_{i=1}^{j} F_i \cos(\alpha_i - \varphi_j) \\ F_{jy_j} = \sum_{i=1}^{j} F_i \sin(\alpha_i - \varphi_j) \\ M_{jz} = \sum_{i=1}^{j-1} M_i + \sum_{i=1}^{j} \left[F_i \sin(\alpha_i - \varphi_j) \sum_{k=i}^{j} l_k \cos(\alpha_k - \varphi_j) \right] \end{cases} \tag{3.7}$$

The first two equations in Eq. (3.7) simply express the local frame force components as the sum of all forces (a total of j forces from point 1 through the current point j) projected on the x_j and y_j axes, respectively. The moment equation in Eq. (3.7) sums up all point moments that are perpendicular on the plane of the compliant mechanism (a total of j moments acting from point 1 through the current point j). In addition, it also includes the contributions to the bending moment produced by all the forces that act on the mechanism between point 1 and j having a component that is perpendicular on the direction of l_j.

Equations (3.6) and (3.7) give the deformations of a compliant member in local coordinates at its free end as they are produced through bending, axial loading, and shearing (if applicable). These deformations displace the free end from its initial position to a different one determined by the local coordinates u_{jx_j} and u_{jy_j} (expressed in Eq. (3.6)). At the same time, the free-end slope, also measured in the local reference frame, becomes θ_{jz_j} (given in the last equation of Eq. (3.6)).

Each subsequent flexure hinge, when covering the remaining links from the current jth member to the nth member (which has a physically fixed end, as illustrated in Figure 3.1), deforms locally according to the equations presented previously for the generic free end of the jth flexure hinge. As a result, the actual displacements of point j must take into account the displacements of point $j + 1$ and the slope of member $j + 1$ (which rotates the jth member and, therefore, adds complementary displacements to node j) measured in the $j + 1$ local reference frame, because the node $j + 1$ is considered free in its local frame. The sequence continues by connecting the node $j + 1$ to its neighbor $j + 2$ and, similarly, travels through all subsequent endpoints to the last one, the fixed point n. Figure 3.2 illustrates two adjacent flexure hinges, k and $k + 1$, which are part of the sequence previously described. The corresponding loop-closure diagram is superimposed on the drawing to highlight the deformations and displacements that occur in this case.

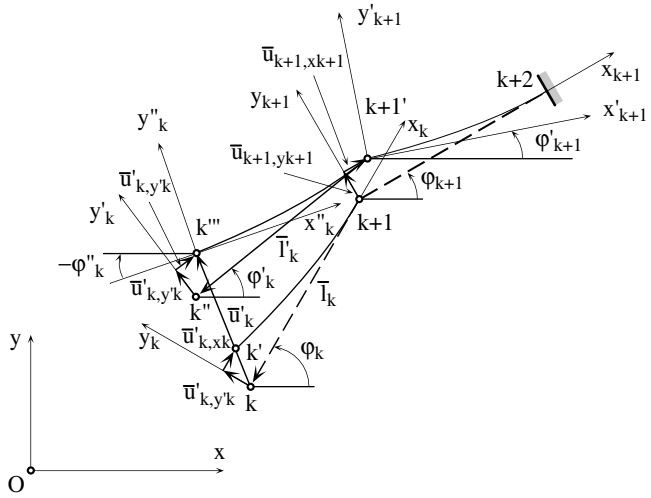

FIGURE 3.2
Loop-closure diagram indicating the deformations and displacements of two adjacent flexure hinges.

The following vector equation can be written, based on the loop-closure diagram:

$$\bar{u}_k = \bar{l}'_k - \bar{l}_k + \bar{u}_{k+1,y_{k+1}} + \bar{u}_{k+1,x_{k+1}} + \bar{u}'_{k,y_k} + \bar{u}'_{k,x_k} \tag{3.8}$$

where $\bar{u}_k$ is the total vector displacement of point k.

The primed symbols in Eq. (3.8) denote the amounts that have been rotated in the k reference frame due to a change in slope produced at node $k + 1$ in the $k + 1$ local frame, as also shown in Figure 3.2; therefore:

$$\begin{cases} \left|\bar{l}'_k\right| = \left|\bar{l}_k\right| \\ \left|\bar{u}'_{k,y_k}\right| = \left|\bar{u}_{k,y_k}\right| \\ \left|\bar{u}'_{k,x_k}\right| = \left|\bar{u}_{k,x_k}\right| \end{cases} \tag{3.9}$$

When all the links from j to n are considered, Eq. (3.8) can be extended to include all deformations/displacements from the other links in order to determine the real displacement of point j, namely:

$$\bar{u}_j = \sum_{k=j}^{n-1} (\bar{l}'_k - \bar{l}_k + \bar{u}'_k) \tag{3.10}$$

where $\overline{u}_k'$ represents the total rotated displacement of generic point k and is given by the vector equation:

$$\overline{u}_k' = \overline{u}_{k,x_k}' + \overline{u}_{k,y_k}' \tag{3.11}$$

while $\overline{u}_j$ is the total displacement of point 'j' which can be expressed vectorially in terms of its components in the global reference frame as:

$$\overline{u}_j = \overline{u}_{jx} + \overline{u}_{jy} \tag{3.12}$$

An important aspect in evaluating the displacements of various points of a planar compliant mechanism is expressing the scalar components that define the position of a given point in the global reference frame, after the mechanism has deformed. As previously indicated, three parameters completely define this point. In addition to the x and y coordinates, the slope θ at that specific point needs to also be known since the respective point belongs to a member that can bend and therefore present a slope at its tip. Expressing the x and y coordinates reduces, in essence, to projecting the vector Eq. (3.10) onto the axes of the global frame. It is well known from vector calculus that the projection of a vector along another direction is equal to the dot product of that vector and the unit vector of the other direction. Given the unit vectors that correspond to the global axes x and y (as shown in Figure 3.1a) of the generic point j, the components of the total displacement vector at that generic point j are:

$$\begin{cases} u_{jx} = \overline{u}_j \overline{e}_x \\ u_{jy} = \overline{u}_j \overline{e}_y \end{cases} \tag{3.13}$$

The explicit components of Eqs. (3.13) are obtained by projecting Eq. (3.10) on the x and y global axes, namely:

$$\begin{cases} u_{jx} = \sum_{k=j}^{n-1} \left[(l_k + u_{k,x_k}) \cos\left(\varphi_k - \sum_{i=k+1}^{n} \theta_i \right) - l_k \cos\varphi_k - u_{k,y_k} \sin\left(\varphi_k - \sum_{i=k+1}^{n} \theta_i \right) \right] \\ u_{jy} = \sum_{k=j}^{n-1} \left[-(l_k + u_{k,x_k}) \sin\left(\varphi_k - \sum_{i=k+1}^{n} \theta_i \right) + l_k \sin\varphi_k - u_{k,y_k} \cos s\left(\varphi_k - \sum_{i=k+1}^{n} \theta_i \right) \right] \end{cases} \tag{3.14}$$

The total rotation angle θ_j at the tip j of the generic link $j \rightarrow j + 1$ is the sum of all rotation angles (slopes) at the tip of all links covering the compliant mechanism from the current link to the last one (with its end actually fixed). The equation for θ_j is:

$$\theta_j = \sum_{k=j}^{n} \theta_k \tag{3.15}$$

3.2.1.1.2 Castigliano's Displacement Theorem Method

An alternative to evaluating the displacement components at a generic node of a planar serial fixed–free compliant mechanism is Castigliano's second theorem, which was utilized for all core derivation in Chapter 2. The three displacement components at a generic node l (located anywhere between the first and the last node and not shown in Figure 3.1) in the global reference frame can be found by means of Castigliano's second theorem equations:

$$\begin{cases} u_{lx} = \dfrac{\partial U}{\partial F_{lx}} \\ u_{ly} = \dfrac{\partial U}{\partial F_{ly}} \\ \theta_{lz} = \dfrac{\partial U}{\partial M_{lz}} \end{cases} \tag{3.16}$$

According to the assumption stated at the beginning of this paragraph, node l is loaded by the forces F_{lx} and F_{ly}, as well as the moment M_{lz}. As previously noted, the displacements at node l are the result of adding up all elastic deformations and rigid-body motions of all subsequent members (when covering the links of the mechanism from node l to node $n + 1$). When only bending (as produced by both the point forces and point moments) and axial effects are taken into account, Eq. (3.16) can be formulated as:

$$\begin{cases} u_{lx} = \displaystyle\sum_{i=l}^{n} \left(\int_0^{l_i} \frac{M_{bi}}{E_i I_{iz_i}} \frac{\partial M_{bi}}{\partial F_{lx}} dx_i + \int_0^{l_i} \frac{N_i}{E_i A_i} \frac{\partial N_i}{\partial F_{lx}} dx_i \right) \\ u_{ly} = \displaystyle\sum_{i=l}^{n} \left(\int_0^{l_i} \frac{M_{bi}}{E_i I_{iz_i}} \frac{\partial M_{bi}}{\partial F_{ly}} dx_i + \int_0^{l_i} \frac{N_i}{E_i A_i} \frac{\partial N_i}{\partial F_{ly}} dx_i \right) \\ \theta_{lz} = \displaystyle\sum_{i=l}^{n} \int_0^{l_i} \frac{M_{bi}}{E_i I_{iz_i}} \frac{\partial M_{bi}}{\partial M_{lz}} dx_i \end{cases} \tag{3.17}$$

Equation (3.17) indicates that regular Casigliano's second theorem calculations have to be performed over each individual link starting from the link of interest (link l) and ending with the last fixed-end link (link n). In other words, the displacement at a specific node of the planar serial mechanisms is the sum of all corresponding deformations and rigid-body motions calculated over each individual interval (link) from the link of interest (which comprises the node of interest) to the last one, which is bounded by the fixed node. The three load components are first expressed at a generic node i in the local coordinate frame $x_i y_i$ by statically adding up all corresponding loads

that act on the serial system and are located between the free node, 1, of the mechanism and the current node, *i*. They are:

$$M_{iz}^{t} = \sum_{j=1}^{i} M_{jz} - \sum_{j=1}^{i-1}\left[F_{jx}\sum_{k=j}^{i-1}(l_k \sin\varphi_k)\right] + \sum_{j=1}^{i-1}\left[F_{jy}\sum_{k=j}^{i-1}(l_k \cos\varphi_k)\right] \tag{3.18}$$

In the equation above, the point moment acting at node *l* is included in the moment sum, and also included in the respective terms are the nodal forces F_{lx} and F_{ly}, so that the partial differentiation required by Castigliano's second theorem is possible. The x_i load component that acts at node *i* is:

$$F_{i,x_i} = \sin\varphi_i \sum_{j=1}^{j}(-F_{jx}) + \cos\varphi_i \sum_{j=1}^{j}(F_{jy}) \tag{3.19}$$

and the y_i force component is:

$$F_{i,y_i} = \cos\varphi_i \sum_{j=1}^{j}(F_{jx}) + \sin\varphi_i \sum_{j=1}^{j}(F_{jy}) \tag{3.20}$$

The bending moment and axial force at a generic point located at a distance x_i from node *i* on the flexure that is bounded by the nodes *i* and *i* + 1 are:

$$\begin{cases} M_{bi} = F_{i,y_i} x_i + M_{iz}^{t} \\ N_i = F_{i,x_i} \end{cases} \tag{3.21}$$

The partial derivatives that are connected to bending moment M_{bi} can simply be calculated by combining Eqs. (3.18), (3.20), and (3.21):

$$\begin{cases} \dfrac{\partial M_{bi}}{\partial F_{lx}} = -\displaystyle\sum_{k=l}^{i-1}(l_k \sin\varphi_k) - \sin\varphi_i x_i \\ \dfrac{\partial M_{bi}}{\partial F_{ly}} = \displaystyle\sum_{k=l}^{i-1}(l_k \cos\varphi_k) + \cos\varphi_i x_i \\ \dfrac{\partial M_{bi}}{\partial M_{lz}} = 1 \end{cases} \tag{3.22}$$

Similarly, the nontrivial partial derivatives of N_i can be obtained from Eqs. (3.19) and (3.21) as:

$$\begin{cases} \dfrac{\partial N_i}{\partial F_{lx}} = \cos\varphi_i \\ \dfrac{\partial N_i}{\partial F_{ly}} = \sin\varphi_i \end{cases} \tag{3.23}$$

Equations (3.18) through (3.23) are now substituted back into Eq. (3.17) and, after performing calculations and conveniently rearranging terms, the three displacement components at node l can be formulated explicitly. The displacement component along the global axis x is:

$$u_{lx} = \sum_{i=l}^{n} (A_{ix} C_{i,x-F_x} + B_{ix} C_{i,y-F_y} + D_{ix} C_{i,y-M_z} + H_{ix} C_{i,\theta_z-M_z}) \tag{3.24}$$

where the coefficients that multiply the compliance factors are:

$$\begin{cases} A_{ix} = \cos\varphi_i \left[\cos\varphi_i \sum_{j=1}^{i} (F_{jx}) + \sin\varphi_i \sum_{j=1}^{i} (F_{jy}) \right] \\ B_{ix} = \sin\varphi_i \left[\sin\varphi_i \sum_{j=1}^{i} (F_{jx}) - \cos\varphi_i \sum_{j=1}^{i} (F_{jy}) \right] \\ D_{ix} = -\sin\varphi_i \left\{ \sum_{j=1}^{i} \left[M_{jz} - F_{jx} \sum_{k=j}^{i-1} (l_k \sin\varphi_k) + F_{jy} \sum_{k=j}^{i-1} (l_k \cos\varphi_k) \right] \right\} \\ -\sum_{k=l}^{i-1} (l_k \sin\varphi_k) \left[\cos\varphi_i \sum_{j=1}^{i} (F_{jy}) - \sin\varphi_i \sum_{j=1}^{i} (F_{jx}) \right] \\ H_{ix} = -\sum_{k=l}^{i-1} (l_k \sin\varphi_k) \left\{ \sum_{j=1}^{i} \left[M_{jz} - F_{jx} \sum_{k=j}^{i-1} (l_k \sin\varphi_k) + F_{jy} \sum_{k=j}^{i-1} (l_k \cos\varphi_k) \right] \right\} \end{cases} \tag{3.25}$$

The displacement component along the global axis y is:

$$u_{ly} = \sum_{i=l}^{n} (A_{iy} C_{i,x-F_x} + B_{iy} C_{i,y-F_y} + D_{iy} C_{i,y-M_z} + H_{iy} C_{i,\theta_z-M_z}) \tag{3.26}$$

where the new coefficients of Eq. (3.26) are:

$$\begin{cases} A_{iy} = \sin\varphi_i \left[\cos\varphi_i \sum_{j=1}^{i} (F_{jx}) + \sin\varphi_i \sum_{j=1}^{i} (F_{jy}) \right] \\ B_{iy} = \cos\varphi_i \left[-\sin\varphi_i \sum_{j=1}^{i} (F_{jx}) + \cos\varphi_i \sum_{j=1}^{i} (F_{jy}) \right] \\ D_{iy} = \cos\varphi_i \left\{ \sum_{j=1}^{i} \left[M_{jz} - F_{jx} \sum_{k=j}^{i-1} (l_k \sin\varphi_k) + F_{jy} \sum_{k=j}^{i-1} (l_k \cos\varphi_k) \right] \right\} \\ \qquad + \sum_{k=l}^{i-1} (l_k \cos\varphi_k) \left[\cos\varphi_i \sum_{j=1}^{i} (F_{jy}) - \sin\varphi_i \sum_{j=1}^{i} (F_{jx}) \right] \\ H_{iy} = \sum_{k=l}^{i-1} (l_k \cos\varphi_k) \left\{ \sum_{j=1}^{i} \left[M_{jz} - F_{jx} \sum_{k=j}^{i-1} (l_k \sin\varphi_k) + F_{jy} \sum_{k=j}^{i-1} (l_k \cos\varphi_k) \right] \right\} \end{cases} \tag{3.27}$$

The rotation angle of the link *l* is:

$$\theta_{l,z} = \sum_{i=l}^{n} (D_{i\theta_z} C_{i,y-M_z} + H_{i\theta_z} C_{i,\theta_z-M_z}) \tag{3.28}$$

where the new coefficients are:

$$\begin{cases} D_{i\theta_z} = -\sin\varphi_i \sum_{j=1}^{i} (F_{jx}) + \cos\varphi_i \sum_{j=1}^{i} (F_{jy}) \\ H_{i\theta_z} = \sum_{j=1}^{i} \left[M_{jz} - F_{jx} \sum_{k=j}^{i-1} (l_k \sin\varphi_k) + F_{jy} \sum_{k=j}^{i-1} (l_k \cos\varphi_k) \right] \end{cases} \tag{3.29}$$

Equations (3.24) through (3.29) have been checked by applying them to a simpler compliant mechanism that comprises only one (compliant) link, as shown in Figure 3.3. The input node, in this case, is node 1 (as there are no other links and node 2 is fixed). In this case, Eq. (3.25) becomes:

$$\begin{cases} A_{ix} = F\cos(\alpha-\varphi)\cos\varphi \\ B_{ix} = -F\sin\varphi\sin(\alpha-\varphi) \\ D_{ix} = M\sin\varphi \\ H_{ix} = 0 \end{cases} \tag{3.30}$$

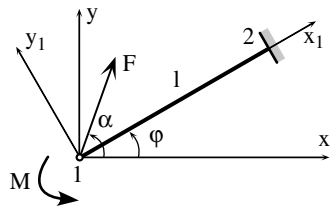

FIGURE 3.3
Single-axis flexure hinge with relevant loading, geometry, and local/global reference frames.

Substitution of Eq. (3.30) into Eq. (3.24) results in:

$$u_{1x} = F\cos\varphi\cos(\alpha-\varphi)C_{1,x-F_x} - F\sin\varphi\sin(\alpha-\varphi)C_{1,y-F_y} + M\sin\varphi\, C_{1,y-M_z} \quad (3.31)$$

Equation (3.27) simplifies for this particular case to:

$$\begin{cases} A_{iy} = F\sin\varphi\cos(\alpha-\varphi) \\ B_{iy} = F\cos\varphi\sin(\alpha-\varphi) \\ D_{iy} = -M\cos\varphi \\ H_{iy} = 0 \end{cases} \quad (3.32)$$

Substituting Eq. (3.32) into Eq. (3.26) gives:

$$u_{1y} = F\sin\varphi\cos(\alpha-\varphi)C_{1,x-F_x} + F\cos\varphi\sin(\alpha-\varphi)C_{1,y-F_y} - M\cos\varphi\, C_{1,y-M_z} \quad (3.33)$$

Equation (3.29) simplifies to:

$$\begin{cases} D_{i\theta_z} = F\sin(\alpha-\varphi) \\ H_{i\theta_z} = -M \end{cases} \quad (3.34)$$

therefore, the corresponding end rotation angle is:

$$\theta_{1z} = F\sin(\alpha-\varphi)C_{1,y-M_z} - MC_{1,\theta_z-M_z} \quad (3.35)$$

Equations (3.31), (3.33), and (3.35) can simply be obtained by expressing in standard form the displacements of the single flexure hinge of Figure 3.3 in the local reference frame (by using Eq. (3.6)) and then projecting them on the global reference axes.

3.2.1.2 Displacement Amplification/Deamplification (Mechanical Advantage)

A compliant mechanism needs to fulfill at least one of the following tasks, according to its main functional objective:

- It should provide a specified output displacement.
- It should provide a specified output force.

Either task has to be solved in terms of output level (a predesigned displacement or force has to be provided) or output orientation (a predesigned path or load pose history are the requisite performance criteria). Fundamentally, a compliant mechanism is designed to either amplify or deamplify (reduce) the output displacement or force. Figure 3.4 attempts to represent these two antagonistic functions. Because of work conservation reasons, a mechanism that amplifies the output displacement, for instance, will necessarily reduce the force that it can deliver at its output port. Conversely, a mechanism that is designed to amplify the output force will have to produce less output displacement.

The current terminology utilizes the notions of amplification and deamplification (reduction) quasi-unanimously with reference to displacement; therefore, an amplification mechanism is one that amplifies the output displacement. The objective in this section is to relate the output displacement to the input displacement by formulating the so-called *mechanical advantage* of the compliant mechanism in the form defined by Eq. (3.3)

Figure 3.5 illustrates in a schematic fashion a planar compliant mechanism highlighting the input and output links together with their defining nodes, denoted by in_1 and in_2 for the input link and out_1 and out_2 for the output link. Because the emphasis in this particular case falls on the displacement amplification capability of a generic planar compliant mechanism, the assumption will be used that there are no load components, except the input force, F_{in}, which is necessary to produce the input displacement u_{in} (see Figure 3.5).

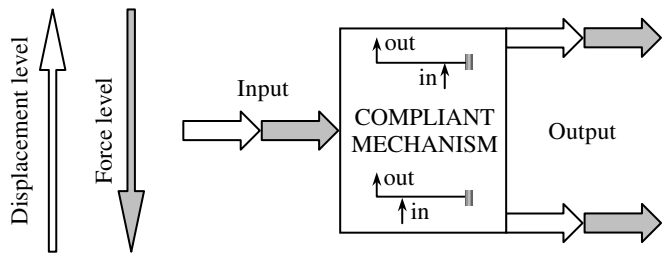

FIGURE 3.4
Amplification/deamplification in terms of displacement and force levels for compliant mechanisms.

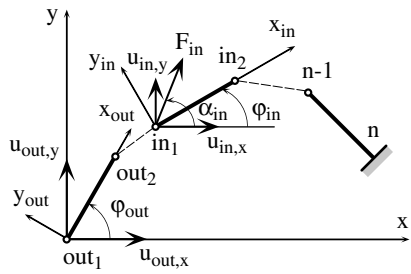

FIGURE 3.5
Schematic representation of the input and output links of a planar serial compliant mechanism for Castigliano's second theorem approach.

In order to express the generically defined mechanical advantage of Eq. (3.3), a two-phase sequence will be applied. The first phase will give the relationship between the input force F_{in} and the input displacement u_{in}, as well as the connection between the input force F_{in} and the output displacement u_{out}. The second phase will produce the transition between the two relationships previously mentioned and will establish a direct relationship between output and input displacement components in the form of Eq. (3.3). The results of the previous section, which gave the explicit connection between the overall load and a specific displacement for a given configuration of a planar compliant mechanism, will directly be applied here by means of Castigliano's displacement theorem approach.

The input force/input displacement equation is formulated by expressing first the coefficients of Eq. (3.25), which, in the case of the loading of Figure 3.5, becomes:

$$\begin{cases} A_{ix} = F_{in}\cos\varphi_i\cos(\varphi_i - \alpha_{in}) \\ B_{ix} = F_{in}\sin\varphi_i\sin(\varphi_i - \alpha_{in}) \\ D_{ix} = F_{in}\left\{2\sin\varphi_i\cos\alpha_{in}\sum_{k=in}^{i-1}(l_k\sin\varphi_k) - \sin\alpha_{in}\left[\sin\varphi_i\sum_{k=in}^{i-1}(l_k\cos\varphi_k)\right.\right. \\ \qquad \left.\left. + \cos\varphi_i\sum_{k=in}^{i-1}(l_k\sin\varphi_k)\right]\right\} \\ H_{ix} = -F_{in}\sum_{k=in}^{i-1}(l_k\sin\varphi_k)\left[-\cos\alpha_{in}\sum_{k=in}^{j-1}(l_k\sin\varphi_k) + \sin\alpha_{in}\sum_{k=in}^{j-1}(l_k\cos\varphi_k)\right] \end{cases} \tag{3.36}$$

Substituting the required equations of Eq. (3.36) into Eq. (3.24) gives the horizontal component (on the x global reference axis) at the input node:

$$u_{in,x} = C_{in,x} F_{in} \tag{3.37}$$

where:

$$C_{in,x} = \sum_{i=in}^{n} \Bigg\{ \cos\varphi_i \cos(\varphi_i - \alpha_{in}) C_{i,x-F_x} + \sin\varphi_i \sin(\varphi_i - \alpha_{in}) C_{i,y-F_y} + \Bigg\{ 2\sin\varphi_i \cos\alpha_{in} \sum_{k=in}^{i-1} (l_k \sin\varphi_k) - \sin\alpha_{in} \Bigg[\sin\varphi_i \sum_{k=in}^{i-1} (l_k \cos\varphi_k) + \cos\varphi_i \sum_{k=in}^{i-1} (l_k \sin\varphi_k) \Bigg] \Bigg\} C_{i,y-M_z} + \sum_{k=in}^{i-1} (l_k \sin\varphi_k) \Bigg[\cos\alpha_{in} \sum_{k=in}^{j-1} (l_k \sin\varphi_k) - \sin\alpha_{in} \sum_{k=in}^{j-1} (l_k \cos\varphi_k) \Bigg] C_{i,\theta_z-M_z} \Bigg\} \tag{3.38}$$

The vertical input displacement (the y global reference axis component) is determined in a similar manner by first simplifying the coefficient equations, Eq. (3.27), and then substituting them into Eq. (3.26); the result is:

$$u_{in,y} = C_{in,y} F_{in} \tag{3.39}$$

with:

$$C_{in,y} = \sum_{i=in}^{n} \Bigg\{ \sin\varphi_i \cos(\varphi_i - \alpha_{in}) C_{i,x-F_x} - \cos\varphi_i \sin(\varphi_i - \alpha_{in}) C_{i,y-F_y} + \Bigg\{ 2\cos\varphi_i \sin\alpha_{in} \sum_{k=in}^{i-1} (l_k \cos\varphi_k) - \cos\alpha_{in} \Bigg[\sin\varphi_i \sum_{k=in}^{i-1} (l_k \cos\varphi_k) + \cos\varphi_i \sum_{k=in}^{i-1} (l_k \sin\varphi_k) \Bigg] \Bigg\} C_{i,y-M_z} + \sum_{k=in}^{i-1} (l_k \cos\varphi_k) \Bigg[\sin\alpha_{in} \sum_{k=in}^{j-1} (l_k \cos\varphi_k) - \cos\alpha_{in} \sum_{k=in}^{j-1} (l_k \sin\varphi_k) \Bigg] C_{i,\theta_z-M_z} \Bigg\} \tag{3.40}$$

Similarly, the rotation at the input node can be determined by means of Eqs. (3.28) and (3.29) and is expressed as:

$$\theta_{in,z} = C_{in,\theta_z} F_{in} \tag{3.41}$$

with:

$$C_{in,\theta_z} = \sum_{i=in}^{n} \left\{ -\sin(\varphi_i - \alpha_{in}) C_{i,y-M_z} + \left[\sin\alpha_{in} \sum_{k=in}^{i-1} (l_k \cos\varphi_k) - \cos\alpha_{in} \sum_{k=in}^{i-1} (l_k \sin\varphi_k) \right] C_{i,\theta_z-M_z} \right\} \tag{3.42}$$

The total input displacement can be expressed in terms of its global components as:

$$u_{in} = \sqrt{u_{in,x}^2 + u_{in,y}^2} \tag{3.43}$$

which, by using Eqs. (3.37) and (3.39), can also be written as:

$$u_{in} = C_{in} F_{in} \tag{3.44}$$

The input compliance of Eq. (3.44) is:

$$C_{in} = \sqrt{C_{in,x}^2 + C_{in,y}^2} \tag{3.45}$$

and the x and y compliance terms are given in Eqs. (3.38) and (3.40).

Similar reasoning and calculations based on the equations that were used while solving the first phase will give the output displacement components at the node out_1 in Figure 3.5 when the planar compliant mechanism is loaded by the input force F_{in} at the node in_1. The output horizontal displacement is:

$$u_{out,x} = C_{out,x} F_{in} \tag{3.46}$$

with:

$$C_{out,x} = \sum_{i=out}^{n} \left\{ \cos\varphi_i \cos(\varphi_i - \alpha_{in}) C_{i,x-F_x} + \sin\varphi_i \sin(\varphi_i - \alpha_{in}) C_{i,y-F_y} + \left\{ \sin\varphi_i \left[\cos\alpha_{in} \sum_{k=in}^{i-1} (l_k \sin\varphi_k) - \sin\alpha_{in} \sum_{k=in}^{i-1} (l_k \cos\varphi_k) \right] + \sin(\varphi_i - \alpha_{in}) \sum_{k=out}^{i-1} (l_k \sin\varphi_k) \right] \right\} C_{i,y-M_z} + \sum_{k=out}^{i-1} (l_k \sin\varphi_k) \left[\cos\alpha_{in} \sum_{k=in}^{j-1} (l_k \sin\varphi_k) - \sin\alpha_{in} \sum_{k=in}^{j-1} (l_k \cos\varphi_k) \right] C_{i,\theta_z-M_z} \right\} \tag{3.47}$$

The output vertical displacement is:

$$u_{out,y} = C_{out,y} F_{in} \tag{3.48}$$

with:

$$C_{out,y} = \sum_{i=out}^{n} \Bigg\{ \sin\varphi_i \cos(\varphi_i - \alpha_{in}) C_{i,x-F_x} - \cos\varphi_i \sin(\varphi_i - \alpha_{in}) C_{i,y-F_y} + \Bigg\{ \cos\varphi_i \Bigg[-\cos\alpha_{in} \sum_{k=in}^{i-1} (l_k \sin\varphi_k) + \sin\alpha_{in} \sum_{k=in}^{i-1} (l_k \cos\varphi_k) \Bigg] - \sin(\varphi_i - \alpha_{in}) \sum_{k=\mathbf{out}}^{i-1} (l_k \cos\varphi_k) \Bigg] \Bigg\} C_{i,y-M_z} + \sum_{k=out}^{i-1} (l_k \cos\varphi_k) \Bigg[-\cos\alpha_{in} \sum_{k=in}^{j-1} (l_k \sin\varphi_k) + \sin\alpha_{in} \sum_{k=in}^{j-1} (l_k \cos\varphi_k) \Bigg] C_{i,\theta_z-M_z} \Bigg\} \tag{3.49}$$

The deformation angle at the output node, *o*, is of the form:

$$\theta_{out,z} = C_{out,\theta_z} F_{in} \tag{3.50}$$

with:

$$C_{out,\theta_z} = \sum_{i=out}^{n} \Bigg\{ -\sin(\varphi_i - \alpha_{in}) C_{i,y-M_z} + \Bigg[\sin\alpha_{in} \sum_{k=in}^{i-1} (l_k \cos\varphi_k) - \cos\alpha_{in} \sum_{k=in}^{i-1} (l_k \sin\varphi_k) \Bigg] C_{i,\theta_z-M_z} \Bigg\} \tag{3.51}$$

The total output displacement is:

$$u_{out} = \sqrt{u_{out,x}^2 + u_{out,y}^2} \tag{3.52}$$

which can be expressed in the alternate form by means of Eqs. (3.46) and (3.48):

$$u_{out} = C_{out} F_{in} \tag{3.53}$$

where the output compliance C_{out} is:

$$C_{out} = \sqrt{C_{out,x}^2 + C_{out,y}^2} \tag{3.54}$$

Combining Eqs. (3.44) and (3.53) and substituting them into Eq. (3.3) give the mechanical advantage of the planar serial mechanism as:

$$m.a. = \frac{C_{out}}{C_{in}} \tag{3.55}$$

where C_{out} and C_{in} are given in Eqs. (3.54) and (3.45), respectively. As Figure 3.5 shows it, the output node is located before the input node in the node sequence, when the serial mechanism is covered starting from the free node to the fixed one. It is also possible that the output and input nodes switch their positions in the serial mechanism topology but it is simple to check that the equations defining the input and output displacements for the particular disposition shown in Figure 3.5 are also valid for the reversed situation.

In many instances it is useful to express the equations that give the mechanical advantage of a planar serial fixed–free compliant mechanism in terms of stiffness instead of compliance. Equation (3.44), for instance, can be reformulated as:

$$F_{in} = k_{in} u_{in} \tag{3.56}$$

where k_{in} is the input stiffness of the entire mechanism and, by means of Eq. (3.44), is defined as:

$$k_{in} = \frac{1}{C_{in}} \tag{3.57}$$

Another global way of qualifying a compliant mechanism is by expressing the input force in terms of the displacement at the output port, which yields the output stiffness of the compliant mechanism as:

$$F_{in} = k_{out} u_{out} \tag{3.58}$$

The output stiffness, k_{out}, can be obtained from Eq. (3.53) as:

$$k_{out} = \frac{1}{C_{out}} \tag{3.59}$$

As a result of these reformulations, the mechanical advantage of Eqs. (3.3) and (3.55) can alternatively be expressed as:

$$m.a. = \frac{k_{in}}{k_{out}} \tag{3.60}$$

As mentioned, the output stiffness defined in Eq. (3.58) relates the input force to the output displacement; therefore, it is not the "true" stiffness, in

the original sense that would relate load to displacement in a collocated manner. The true output stiffness is therefore defined as:

$$k_{out}^{*} = \frac{F_{out}}{u_{out}} \tag{3.61}$$

and can easily be determined in a manner similar to that for expressing the input compliance (and corresponding stiffness), as previously done, but it will not be detailed here.

The mechanical advantage of a planar serial compliant mechanism was discussed exclusively in terms of displacement, but it can be defined equally well in terms of the input and output rotation angles, in case these amounts are of interest:

$$m.a._r = \frac{\theta_{out,z}}{\theta_{in,z}} \tag{3.62}$$

By utilizing Eqs. (3.41) and (3.50), the rotational mechanical advantage (the subscript r denotes rotation in Eq. (3.62)) can be put into the alternative form:

$$m.a._r = \frac{C_{out,\theta_z}}{C_{in,\theta_z}} \tag{3.63}$$

where $C_{out,\theta z}$ and $C_{in,\theta z}$ are given in Eqs. (3.51) and (3.42), respectively.

3.2.1.3 Bloc Output Load

Another qualifier of a compliant mechanism, especially of force-amplification ones, is the so-called bloc load, which represents the load (force and/or moment) that must be applied, generally at the output port, in order to completely deny the output displacement under a given input load. The problem is actually the inverse formulation of the mechanical advantage aspect because the aim is finding the relationship between the input force and the corresponding zero-displacement output force. The load on the planar serial fixed–free compliant mechanism of Figure 3.5 consists of the input force, F_{in}, which is considered known, both in magnitude and direction, and the output force, F_{out}, and moment, M_{out}, which are the amounts that must be determined in terms of the input load. The constraint equations that will be utilized in this case refer to the node out_1 in Figure 3.5 (where F_{in}, F_{out}, and M_{out} are not represented):

$$\begin{cases} u_{out,x} = 0 \\ u_{out,y} = 0 \\ \theta_{out,z} = 0 \end{cases} \tag{3.64}$$

Equation (3.64) must be solved for the unknown bloc load at the output port. In order to simplify calculation, the output force is projected on the global reference frame axes x and y such that its components are $F_{out,x}$ and $F_{out,y}$. The output displacement components of Eq. (3.64) are now expressed in terms of the load acting on the entire mechanism and which consists of the output and input forces. The specific loading conditions that have just been mentioned are applied accordingly to express the coefficients of Eq. (3.25) as:

$$A_{ix} = \begin{cases} \cos\varphi_i (F_{out,x}\cos\varphi_i + F_{out,y}\sin\varphi_i),\ i \in [out_1, in_1] \\ \cos\varphi_i [\cos\varphi_i (F_{out,x} + F_{in}\cos\alpha_{in}) + \sin\varphi_i (F_{out,y} + F_{in}\sin\alpha_{in})],\ i \in [in_1, n] \end{cases} \tag{3.65}$$

$$B_{ix} = \begin{cases} \sin\varphi_i (F_{out,x}\sin\varphi_i - F_{out,y}\cos\varphi_i),\ i \in [out_1, in_1] \\ \sin\varphi_i [\sin\varphi_i (F_{out,x} + F_{in}\cos\alpha_{in}) - \cos\varphi_i (F_{out,y} + F_{in}\sin\alpha_{in})],\ i \in [in_1, n] \end{cases} \tag{3.66}$$

$$D_{ix} = \begin{cases} -\sin\varphi_i \left[M_{out,z} - F_{out,x}\sum_{k=out}^{i-1}(l_k \sin\varphi_k) + F_{out,y}\sum_{k=out}^{i-1}(l_k \cos\varphi_k) \right] - \\ \sum_{k=out}^{i-1}(l_k \sin\varphi_k)[\cos\varphi_i F_{out,y} - \sin\varphi_i F_{out,x}],\ i \in [out_1, in_1] \\ -\sin\varphi_i \left[M_{out,z} - F_{out,x}\sum_{k=out}^{i-1}(l_k \sin\varphi_k) - F_{in}\cos\alpha_{in}\sum_{k=in}^{i-1}(l_k \sin\varphi_k) + F_{out,y} \right. \\ \left. \sum_{k=out}^{i-1}(l_k \cos\varphi_k) \right] + F_{in}\sin\alpha_{in}\sum_{k=in}^{i-1}(l_k \cos\varphi_k) - \sum_{k=out}^{i-1}(l_k \sin\varphi_k)[\cos\varphi_i (F_{out,y} + \\ F_{in}\sin\alpha_{in}) - \sin\varphi_i (F_{out,x} + F_{in}\cos\alpha_{in})],\ i \in [in_1, n] \end{cases} \tag{3.67}$$

$$H_{ix} = \begin{cases} -\sum_{k=out}^{i-1}(l_k \sin\varphi_k)\left[M_{out,z} - F_{out,x}\sum_{k=out}^{i-1}(l_k \sin\varphi_k) + F_{out,y}\sum_{k=out}^{i-1}(l_k \cos\varphi_k) \right],\ i \in [out_1, in_1] \\ -\sum_{k=out}^{i-1}(l_k \sin\varphi_k)\left[M_{out,z} - F_{out,x}\sum_{k=out}^{i-1}(l_k \sin\varphi_k) - F_{in}\cos\alpha_{in}\sum_{k=in}^{i-1}(l_k \sin\varphi_k) + F_{out,y} \right. \\ \left. \sum_{k=out}^{i-1}(l_k \cos\varphi_k) + F_{in}\sin\alpha_{in}\sum_{k=in}^{i-1}(l_k \cos\varphi_k) \right],\ i \in [in_1, n] \end{cases} \tag{3.68}$$

Similar calculations must be performed in order to determine the coefficients that define the y- and θ_z components of the output displacement by considering again that the load consists of force and moment components at the input and output nodes only, but the explicit derivation of those coefficients is not given here. Equation (3.64) can be rearranged in the matrix form:

$$[a]\{L_{out}\} = \{b\} \tag{3.69}$$

where $\{L_{out}\}$ is the unknown load output vector defined as:

$$\{L_{out}\} = \{F_{out,x}, F_{out,y}, M_{out,z}\}^T \tag{3.70}$$

The matrix $[a]$ of Eq. (3.69) is a 3×3 symmetric matrix of the form:

$$[a] = \begin{bmatrix} a_{11} & a_{12} & a_{13} \\ a_{12} & a_{22} & a_{23} \\ a_{13} & a_{23} & a_{33} \end{bmatrix} \tag{3.71}$$

The components of matrix $[a]$ of Eq. (3.71) are:

$$a_{11} = \sum_{i=out}^{n} \left\{ \cos^2 \varphi_i C_{i,x-F_x} + \sin^2 \varphi_i C_{i,y-F_y} + 2 \sin \varphi_j \sum_{k=out}^{i-1} (l_k \sin \varphi_k) C_{i,y-M_z} + \left[\sum_{k=out}^{i-1} (l_k \sin \varphi_k) \right]^2 C_{i,\theta_z-M_z} \right\} \tag{3.72}$$

$$a_{12} = \sum_{i=out}^{n} \left\{ \sin \varphi_i \cos \varphi_i (C_{i,x-F_x} - C_{i,y-F_y}) - \left[\cos \varphi_i \sum_{k=out}^{i-1} (l_k \sin \varphi_k) + \sin \varphi_i \sum_{k=out}^{i-1} (l_k \cos \varphi_k) \right] C_{i,y-M_z} - \sum_{k=out}^{i-1} (l_k \cos \varphi_k) \sum_{k=out}^{i-1} (l_k \sin \varphi_k) C_{i,\theta_z-M_z} \right\} \tag{3.73}$$

$$a_{13} = \sum_{i=out}^{n} \left[-\sin \varphi_i C_{i,y-M_z} - \sum_{k=out}^{i-1} (l_k \sin \varphi_k) C_{i,\theta_z-M_z} \right] \tag{3.74}$$

$$a_{22} = \sum_{i=out}^{n} \left\{ \sin^2 \varphi_i C_{i,x-F_x} + \cos^2 \varphi_i C_{i,y-F_y} + 2 \cos \varphi_i \sum_{k=out}^{i-1} (l_k \cos \varphi_k) C_{i,y-M_z} + \left[\sum_{k=out}^{i-1} (l_k \cos \varphi_k) \right]^2 C_{i,\theta_z-M_z} \right\} \tag{3.75}$$

$$a_{23} = \sum_{i=out}^{n} \left[\cos\varphi_i C_{i,y-M_z} + \sum_{k=out}^{i-1} (l_k \cos\varphi_k) C_{i,\theta_z-M_z} \right] \tag{3.76}$$

$$a_{33} = \sum_{i=out}^{n} (C_{i,\theta_z-M_z}) \tag{3.77}$$

The vector $\{b\}$ of Eq. (3.69) is defined as:

$$\{b\} = -F_{in}\{C_{in,x}, C_{in,y}, C_{in,\theta_z}\}^T \tag{3.78}$$

where its components are given in Eqs. (3.38), (3.40), and (3.42), respectively. The solution to Eq. (3.69) that gives the three components of output load is:

$$\{F_{out}\} = [a]^{-1}\{b\} \tag{3.79}$$

which shows that the bloc load components are functions of the input force F_{in}.

3.2.1.4 Energy Efficiency

The energy efficiency of an individual flexure hinge was discussed in Chapter 2 by defining the energy necessary to produce the desired rotation of the flexure vs. the total energy that has to be spent overall with all types of elastic deformation during loading of a flexure hinge. A similar approach can be applied to quantify the energy efficiency of a planar serial compliant mechanism comprised of several single-axis flexure hinges by simply summing up the energy terms that were defined for a single flexure hinge. It will be assumed that the generic flexure-based compliant mechanism is composed of n links, of which n_f are flexure hinges. In doing so Eqs. (2.156) and (2.157), which express the energy efficiency for a single flexure hinge, are now extended to the n_f flexure hinges of the planar compliant mechanism. In the case where the point bending moments and point forces that are normal to the longitudinal axis of one flexure produce opposite effects, the efficiency of the whole mechanism is minimum and is given by:

$$\eta_{min} = \frac{\sum_{j=1}^{n_f} (C_{j,\theta_z-M_z} M_{jz}^2)}{\sum_{j=1}^{n_f} (C_{j,x-F_x} F_{jx}^2 + C_{j,y-F_y} F_{jy}^2 + C_{j,\theta_z-M_z} M_{jz}^2 + 2C_{j,y-M_z} F_{jy} M_{jz})} \tag{3.80}$$

Conversely, when the point bending moment and point force that is normal to the longitudinal axis of one flexure generate the same effect (namely, they both help the flexure hinge rotation), the energy efficiency is maximum and is expressed as:

$$\eta_{max} = \frac{\sum_{j=1}^{n_f} (C_{j,\theta_z-M_z} M_{jz}^2 + C_{j,y-F_y} F_{jy}^2 + 2C_{j,y-M_z} F_{jy} M_{jz})}{\sum_{j=1}^{n_f} (C_{j,x-F_x} F_{jx}^2 + C_{j,y-F_y} F_{jy}^2 + C_{j,\theta_z-M_z} M_{jz}^2 + 2C_{j,y-M_z} F_{jy} M_{jz}} \quad (3.81)$$

To make the energy efficiency expressions independent of loading, unit values must be taken in both Eqs. (3.80) and (3.81), which leaves only the compliances of all flexure hinges in the equations:

$$\eta_{min} = \frac{\sum_{j=1}^{n_f} (C_{j,\theta_z-M_z})}{\sum_{j=1}^{n_f} (C_{j,x-F_x} + C_{j,y-F_y} + C_{j,\theta_z-M_z} + 2C_{j,y-M_z})} \quad (3.82)$$

$$\eta_{max} = \frac{\sum_{j=1}^{n_f} (C_{j,\theta_z-M_z} + C_{j,y-F_y} + 2C_{j,y-M_z})}{\sum_{j=1}^{n_f} (C_{j,x-F_x} + C_{j,y-F_y} + C_{j,\theta_z-M_z} + 2C_{j,y-M_z})} \quad (3.83)$$

For short flexure hinges, where shearing effects have to be taken into account, the compliance factors $C_{j,y-Fy}$ need to be replaced by the corresponding factors $C^s_{j,y-Fy}$ that incorporate the influence of shearing and that were formulated in Chapter 2.

3.2.1.5 Precision of Motion

It was previously shown that the output displacement can be calculated by multiplying the input displacement and the mechanical advantage, which was expressed in terms of the compliant mechanism geometric configuration and the various compliances of the flexure hinges that composed the mechanism. Because the output displacement is a function of the compliant properties of the flexure hinges, the way in which one choses to model a flexure hinge in terms of its compliances is crucial to the accuracy of evaluating the displacement response of the compliant mechanism; therefore, it has direct implications for the precision of motion.

The pseudo-rigid-body model, as previously mentioned, considers that a flexure hinge is a purely rotational, lengthless joint that has one DOF and

only torsional stiffness (compliance). It was also shown that a flexure hinge for planar applications has, in actuality, three DOFs (two translations and one rotation) and, as a direct consequence, must be defined as a complex spring by using four compliance factors, namely: $C_{1,x-Fx}$, $C_{1,y-Fy}$, $C_{1,y-Mz}$, and $C_{1,\theta z-Mz}$. It is interesting to compare the differences in output displacement of two identical compliant mechanisms that have flexure hinges being defined as either purely torsional (the pseudo-rigid-body approach) or fully compliant (conditioned by the four compliance factors mentioned above). Both mechanisms will be subject to the same input displacement, and the corresponding displacement will be calculated for each. For a planar mechanism that comprises fully compliant flexure hinges, the output displacement can be determined by means of generic Eqs. (3.46), (3.48), and (3.50). In the case of the same mechanism that has purely rotational flexure hinges and torsional compliance only, the output displacement components can be formulated by making zero all compliance factors, except for the torsional one that connects angular rotation to bending moment. They can be expressed as:

$$\begin{cases} u_{out,x}^{t} = \dfrac{C_{out,x}^{t}}{C_{in,x}^{t}} u_{in,x} \\ u_{out,y}^{t} = \dfrac{C_{out,y}^{t}}{C_{in,y}^{t}} u_{in,y} \\ \theta_{out,z}^{t} = \dfrac{C_{out,\theta_z}^{t}}{C_{in,\theta_z}^{t}} \theta_{in,z} \end{cases} \tag{3.84}$$

The input compliance factors of Eq. (3.84) are:

$$\begin{cases} C_{in,x}^{t} = \displaystyle\sum_{i=in}^{n} \left\{ \left[\sum_{k=in}^{i-1} (l_k \sin\varphi_k) \right] \left[-\sin\alpha_{in} \sum_{k=in}^{i-1} (l_k \cos\varphi_k) + \cos\alpha_{in} \right. \right. \\ \left. \left. \displaystyle\sum_{k=in}^{i-1} (l_k \sin\varphi_k) \right] C_{i,\theta_z - M_z} \right\} \\ C_{in,y}^{t} = \displaystyle\sum_{i=in}^{n} \left\{ \left[\sum_{k=in}^{i-1} (l_k \cos\varphi_k) \right] \left[\sin\alpha_{in} \sum_{k=in}^{i-1} (l_k \cos\varphi_k) - \cos\alpha_{in} \right. \right. \\ \left. \left. \displaystyle\sum_{k=in}^{i-1} (l_k \sin\varphi_k) \right] C_{i,\theta_z - M_z} \right\} \\ C_{in,\theta_z}^{t} = \displaystyle\sum_{i=in}^{n} \left\{ \left[\sin\alpha_{in} \sum_{k=in}^{i-1} (l_k \cos\varphi_k) - \cos\alpha_{in} \sum_{k=in}^{i-1} (l_k \sin\varphi_k) \right] C_{i,\theta_z - M_z} \right\} \end{cases} \tag{3.85}$$

Similarly, the output compliance factors of Eq. (3.84) are:

$$\begin{cases} C^t_{out,x} = \sum_{i=out}^{n} \left\{ \left[\sum_{k=out}^{i-1} (l_k \sin\varphi_k) \right] - \sin\alpha_{in} \sum_{k=in}^{i-1} (l_k \cos\varphi_k) + \cos\alpha_{in} \right. \\ \left. \sum_{k=in}^{i-1} (l_k \sin\varphi_k) \right] C_{i,\theta_z - M_z} \Bigg\} \\ C^t_{out,y} = \sum_{i=out}^{n} \left\{ \left[\sum_{k=out}^{i-1} (l_k \cos\varphi_k) \right] \sin\alpha_{in} \sum_{k=in}^{i-1} (l_k \cos\varphi_k) - \cos\alpha_{in} \right. \\ \left. \sum_{k=in}^{i-1} (l_k \sin\varphi_k) \right] C_{i,\theta_z - M_z} \Bigg\} \\ C^t_{out,\theta_z} = \sum_{i=out}^{n} \left\{ \left[\sin\alpha_{in} \sum_{k=in}^{i-1} (l_k \cos\varphi_k) - \cos\alpha_{in} \sum_{k=in}^{i-1} (l_k \sin\varphi_k) \right] C_{i,\theta_z - M_z} \right\} \end{cases} \tag{3.86}$$

The following relative error functions are introduced:

$$\begin{cases} e_{u_x} = \dfrac{\left| u_{out,x} - u^t_{out,x} \right|}{u_{out,x}} \\ e_{u_y} = \dfrac{\left| u_{out,y} - u^t_{out,y} \right|}{u_{out,y}} \\ e_{\theta_z} = \dfrac{\left| \theta_{out,z} - \theta^t_{out,z} \right|}{\theta_{out,z}} \end{cases} \tag{3.87}$$

Substituting Eq. (3.84) into Eq. (3.87) results in:

$$\begin{cases} e_{u_x} = 1 - \dfrac{C_{in,x} C^t_{out,x}}{C_{out,x} C^t_{in,x}} \\ e_{u_y} = 1 - \dfrac{C_{in,y} C^t_{out,y}}{C_{out,y} C^t_{in,y}} \\ e_{\theta_z} = 1 - \dfrac{C_{in,\theta_z} C^t_{out,\theta_z}}{C_{out,\theta_z} C^t_{in,\theta_z}} \end{cases} \tag{3.88}$$

The error functions of Eq. (3.88) can be calculated by utilizing Eqs. (3.85) and (3.86).

3.2.1.6 Planar Serial Compliant Mechanisms with Other Boundary Conditions

It was assumed so far in this section that the serial compliant mechanism has the following boundary conditions: The terminal node of the first link is free while the terminal node of the last link is fixed. Other boundary conditions are, of course, possible, and Figure 3.6 illustrates several boundary conditions and corresponding reactions that can apply to the first and last links of the serial mechanism.

Boundary conditions that are different from the fixed–free situation somewhat complicate the overall situation because additional reaction forces/moments are added and these are generally unknown amounts. In the fixed–free configuration the tacit procedure was to always start from the free end of the first link and proceed toward the last link, which was the fixed one.

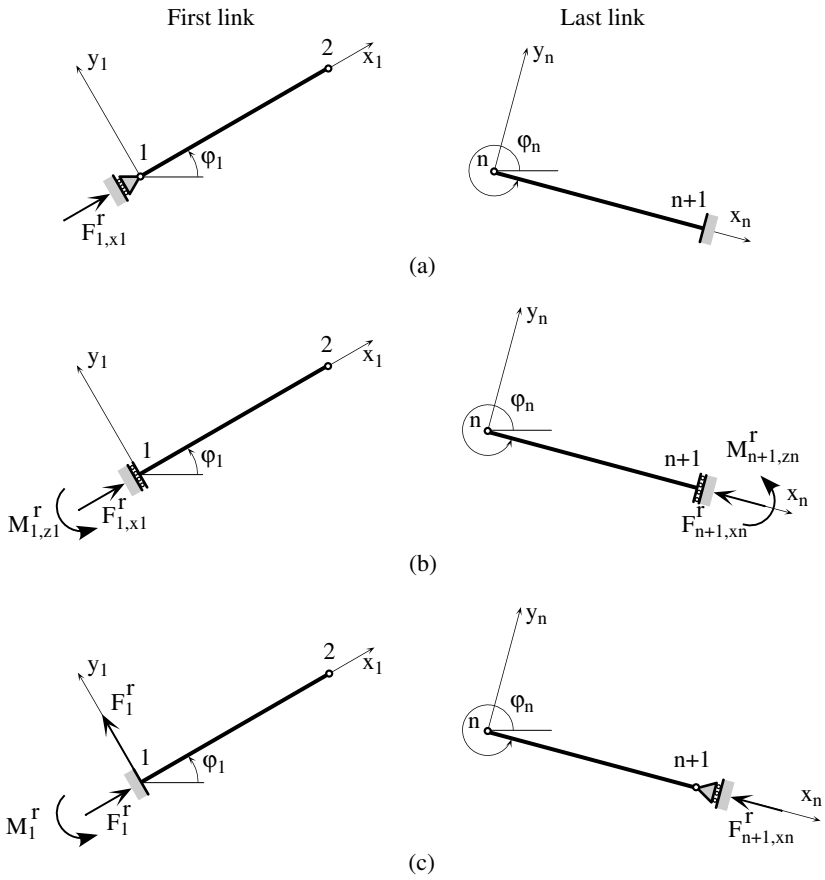

FIGURE 3.6
Various boundary conditions for the terminal nodes of the first and last link of a planar serial compliant mechanism: (a) pinned–fixed; (b) slide–slide; (c) fixed–pinned.

In doing so, it was possible to avoid the physically fixed node and its three reactions (two forces and one moment). When other boundary conditions are present, this approach is no longer possible because, irrespective of the order in which one covers the serial chain, at least one reaction load (that is unknown) will always exist at one terminal node. Fortunately, these reaction loads are accompanied by corresponding displacement constraints, which enable formulating additional equations to solve for the unknown reactions. Once the reaction loads are determined for one terminal node, that node can be considered as the free node of the basic configuration discussed so far, and the corresponding already-determined reaction loads can be treated as external loads.

It is important, however, to apply a procedure that would minimize calculations, and this depends on the specific combination of boundary conditions. Figure 3.7 shows a flowchart that explains the directions that are applicable for various boundary conditions in order to make a given situation equivalent to the fixed–free problem.

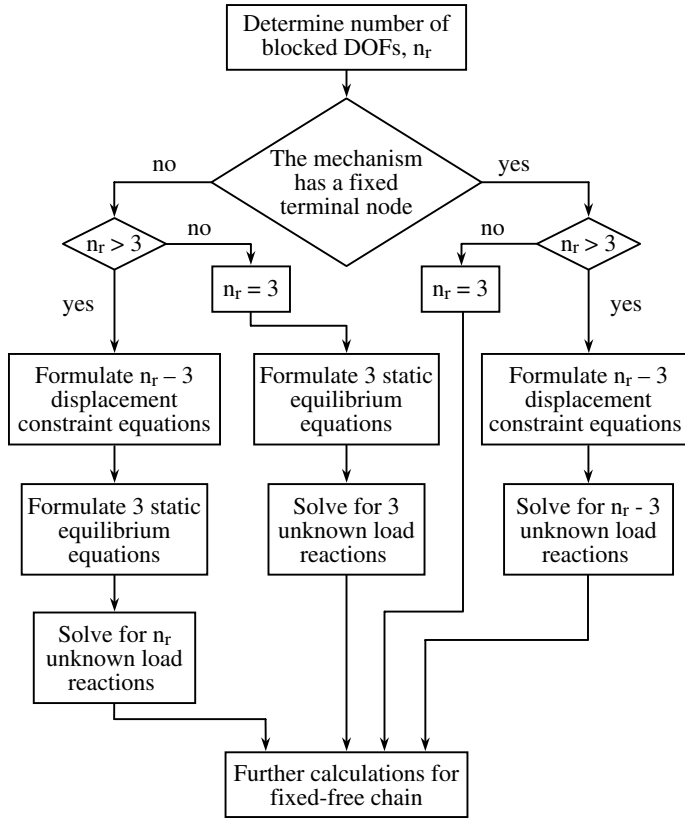

FIGURE 3.7
Flowchart with directions for calculating reaction loads under various boundary conditions.

The first step consists of counting the number of degrees of freedom that are blocked by the boundary constraints being applied to the planar serial mechanism. Let us assume that n_r denotes the number of blocked degrees of freedom, which is identical to the number of unknown reaction loads. Two distinct paths can be followed, depending on whether the mechanism has a physically fixed node (either the first one or the last one, according to the convention of considering that constraints are applied at the terminal nodes of the mechanism). In the cases where there is a fixed node, the problem branches out into two subproblems as well. The simplest one is when $n_r = 3$, which means that no other boundary constraints exist apart from the ones introduced by the fixed node; this case is the fixed–free one that has been discussed so far within this section. When n_r is greater than 3, we need to formulate $n_r - 3$ displacement constraint equations and solve for the $n_r - 3$ unknown reaction loads introduced at the other constrained node. When a simple support is located at this node (see Figure 3.6a), one unknown force needs to be determined, say $F^r_{1,x1}$. The related displacement constraint measured in the local frame is:

$$u_{1,x_1} = 0 \tag{3.89}$$

The displacement of Eq. (3.89) can be expressed in terms of the global displacements at the same node, namely:

$$u_{1,x_1} = u_{1,x}\cos\varphi_1 - u_{1,y}\sin\varphi_1 \tag{3.90}$$

The global components $u_{1,x}$ and $u_{1,y}$ are given in Eqs. (3.24) and (3.26); therefore, combining Eqs. (3.89) and (3.90) will result in one equation that can be solved for the unknown force $F^r_{1,x1}$.

When a support of the type shown in Figure 3.6b is located at node 1, two unknown forces must be determined; therefore, two displacement constraint equations have to be formulated. In this case, the boundary conditions at node 1 require that:

$$\begin{cases} u_{1,x_1} = 0 \\ \theta_{1,z} = 0 \end{cases} \tag{3.91}$$

As previously indicated, Eq. (3.91) must be expressed in terms of the global displacement components. In addition to Eq. (3.90), which remains valid, the second equation in Eq. (3.91) can be expressed by means of Eq. (3.28), which gives θ_{1z}. Eqs. (3.90), (3.91), and (3.28) must be combined again to solve for the unknown reaction loads $F^r_{1,x1}$ and $M^r_{1,z}$.

When node 1 is fixed (as shown in Figure 3.6c), three unknown reaction loads have to be determined by utilizing three displacement constraint equations. Equation (3.91) is still valid because the node is denied translation

about the local axis x_1 and rotation about the axis z. In addition, the translation about the axis y_1 at this node is also blocked; therefore:

$$u_{1,y_1} = 0 \tag{3.92}$$

The displacement of Eq. (3.92) can be expressed in terms of the global coordinates in the form:

$$u_{1,y_1} = u_{1,x} \sin\varphi_1 + u_{1,y} \cos\varphi_1 \tag{3.93}$$

Equation (3.93) is utilized in conjunction with Eqs. (3.91) and (3.92), resulting in three algebraic equations that can be solved for the three reaction loads shown in Figure 3.6c. A note should be mentioned here regarding the possibility that several other displacement constraints (and the corresponding reaction loads) might be present at intermediate nodes. The problem can simply be solved by formulating a number of displacement constraint equations that will solve for the reactions introduced by the additional blocked degree of freedom.

For the cases where there is no fixed terminal node, the number of reaction loads (or blocked degrees of freedom) must be compared again with 3. When $n_r = 3$ (as indicated in Figure 3.7), the three unknown loads can be determined by formulating three static equilibrium equations, and this is always possible because the mechanism is planar. When $n_r > 3$ (see Figure 3.7), one needs to formulate $n_r - 3$ equations based on displacement constraints, in addition to the 3 static equilibrium equations, and then solve for the n_r unknown reaction loads. The additional displacement constraint equations are similar to the ones presented previously.

It is thus possible to always convert a given boundary conditions situation into the equivalent fixed–free one by solving for the additional reaction loads and treating them, after being determined, as external loads that act on the fixed–free planar serial compliant mechanism. In order to better understand all the concepts discussed in this section an example will be analyzed next.

Example

Consider the five-link planar serial mechanism shown in Figure 3.8, where three links are rigid and two are flexure hinges, one corner-filleted and the other one elliptic. Figure 3.8a shows the physical model of the structure, while Figure 3.8b and c provide schematic (line) representations of the physical model. Assume that the mechanism is constructed of steel with a Young's modulus of E = 200 GPa and Poisson's ratio = 0.3. Also assume that the geometry of the structures is given as: l_1 = 0.01 m, l_3 = 0.01 m, l_5 = 0.005 m, l_2 = 0.002 m, t_2 = 0.0005 m, r_2 = 0.00025 m, l_4 = 0.00175 m, t_4 = 0.0005 m, c_4 = 0.0005 m, and $\beta = 10°$. Also given is the constant width of the whole structure,

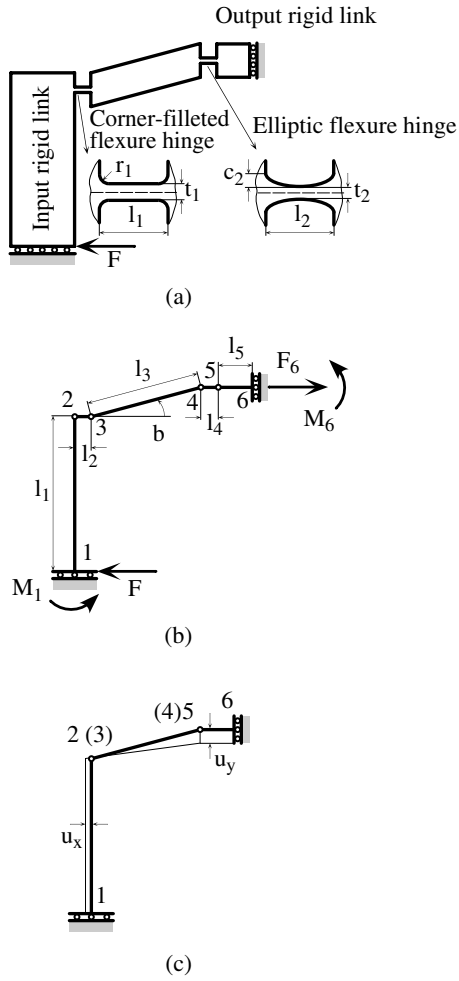

FIGURE 3.8
Five-link compliant mechanism in planar serial configuration: (a) physical model with flexure hinges representation; (b) schematic representation with main geometric parameters and external and reaction loads; (c) schematic representation with zero-length flexure hinges and displaced position.

namely $w = 0.004$ m. The load on the structure consists of a single force $F = 50$ N, as indicated in Figure 3.8. Find the following:

(a) Output displacement at point 6
(b) Mechanical advantage
(c) Input and output stiffness
(d) Bloc force

(e) Energy efficiency
(f) Precision of motion, by comparing the real flexure mechanism with a mechanism that has only rotary flexure hinges with torsional compliance and also by comparison with the same mechanism that possesses purely rotational joints

Solution for (a)

The structure of Figure 3.8 introduces four reactions at its end nodes 1 and 6; therefore, one additional displacement equation is needed to render the system determinate. Because the rotation angle at point 1 is zero, Eq. (3.28) can be utilized as the additional displacement condition in order to directly find the reaction moment at node 1. The two compliant members are the flexure hinges 2 and 4; therefore, the rotation angle at 1 is:

$$\theta_{1z} = D_{2,\theta_z} C_{2,y-M_z} + H_{2,\theta_z} C_{2,\theta_z-M_z} + D_{4,\theta_z} C_{4,y-M_z} + H_{4,\theta_z} C_{4,\theta_z-M_z} \tag{3.94}$$

where the coefficients of the sum in Eq. (3.94) are, in this case, according to Eqs (3.29):

$$\begin{cases} D_{2,\theta_z} = 0 \\ H_{2,\theta_z} = M_1 \end{cases} \tag{3.95}$$

and:

$$\begin{cases} D_{4,\theta_z} = 0 \\ H_{4,\theta_z} = M_1 + F(l_1 + l_3 \sin\beta) \end{cases} \tag{3.96}$$

Substituting Eqs. (3.95) and (3.96) into Eq. (3.94) gives the zero rotation angle at 1, resulting in the reaction moment M_1:

$$M_1 = -\frac{l_1 C_{2,\theta_z-M_z} + (l_1 + l_3 \sin\beta) C_{4,\theta_z-M_z}}{C_{2,\theta_z-M_z} + C_{4,\theta_z-M_z}} \tag{3.97}$$

The unknown reactions at node 6 can now be determined by writing two equilibrium equations at that node about the x and z axes, which results in:

$$\begin{cases} F_6 = F \\ M_6 = \dfrac{l_3 \sin\beta C_{2,\theta_z-M_z}}{C_{2,\theta_z-M_z} + C_{4,\theta_z-M_z}} \end{cases} \tag{3.98}$$

A change of the global reference frame is now applied so that the new reference frame is moved at point 6. In addition to this, both reference axes

are mirrored so that the positive x axis goes from point 6 to the left and the positive y axis goes from node 6 downward. It should be noted that the positive direction for angles is clockwise whereas for bending moments the positive direction is counterclockwise. These changes are necessary here, as the aim is to find the y displacement at node 6, which is a terminal node; therefore, one needs to start the calculations from this node. The coefficients that enable evaluating the y displacement at node 6 are given in Eq. (3.27), and by applying the specific geometry and loading conditions of this application the u_{6y} displacement (as expressed in Eq. (3.27)) becomes:

$$\begin{aligned} u_{6y} = &-M_6[C_{4,y-M_z} + C_{2,y-M_z} + l_5 C_{4,\theta_z-M_z} + (l_5 + l_4 + l_3\cos\beta)C_{2,\theta_z-M_z}] \\ &+ Fl_3\sin\beta[C_{2,y-M_z} + (l_5 + l_4 + l_3\cos\beta)C_{2,\theta_z-M_z}] \end{aligned} \tag{3.99}$$

By substituting all numerical values in Eq. (3.99) and by utilizing the corresponding equations that give the corresponding compliances for the corner-filleted flexure hinge and the elliptic one, the searched vertical displacement is 0.00007 m.

Solution for (b)

The input (horizontal) displacement at node 1 must be determined in order to find the mechanical amplification because the output displacement was already calculated. Because node 1 is also a terminal one, all evaluations have to be related to a global reference frame that is attached at this point. Correspondingly, a reference frame that is positioned at node 1 will be used with its positive x axis extending to the right and the positive y axis going upward. The direction of measuring angles is counterclockwise (the direction that superimposes x over y), while the positive direction for bending moments is clockwise. By applying the specific geometry and loading of this case to generic Eqs. (3.24) and (3.25), the x displacement at node 1 can be expressed as:

$$\begin{aligned} u_{1x} = &-F(C_{2,x-F_x} + C_{4,x-F_x}) - \{l_1(M_1 + Fl_1)C_{2,\theta_z-M_z} + (l_1 + l_3\sin\beta \\ &[M_1 + F(l_1 + l_3\sin\beta)]C_{4,\theta_z-M_z}\} \end{aligned} \tag{3.100}$$

The numerical value given by Eq. (3.100) by substituting all numerical values in it is 0.00001135 m. As a consequence, the mechanical advantage, which in the case of this application is expressed as:

$$m.a. = \frac{|u_{6y}|}{|u_{1x}|} \tag{3.101}$$

will have a value of 6.18.

Solution for (c)

The input stiffness in this case is:

$$k_{in} = \frac{F}{|u_{1x}|} \tag{3.102}$$

and has a value of 4404000 N/m. Similarly, the output stiffness with respect to input force F, as defined in Eq. (3.58), becomes:

$$k_{out} = \frac{F}{|u_{6y}|} \tag{3.103}$$

and has a value of 712300 N/m.

Solution for (d)

The output node 6 can only displace vertically so its motion is denied by blocking it with a vertical force F_{6y}, which is also the unknown bloc force. The three-unknowns equation system, Eq. (3.64), must be solved in order to find F_{6y}. The problem can be further simplified as the other two reactions at node 6 are known, which means that solving one single equation for the unknown F_{6y} is sufficient. For instance, the first equation of the generic matrix Eq. (3.69) will result in:

$$F_{6y} = -\frac{C_{in,x}F_{in} + a_{11}F_{6x} + a_{13}M_{6z}}{a_{12}} \tag{3.104}$$

The coefficients a_{11}, a_{12}, and a_{13} of the equation above are given by Eqs. (3.72), (3.73), and (3.74), respectively, and they must be calculated by positioning the global reference frame at the end node 6, as previously described. These coefficients are:

$$a_{11} = C_{2,x-F_x} + C_{4,x-F_x} + l_3^2 \sin^2\beta\, C_{2,\theta_z-M_z} \tag{3.105}$$

$$a_{12} = -l_3 \sin\beta[C_{2,y-M_z} + (l_5 + l_4 + l_3\cos\beta)C_{2,\theta_z-M_z}] \tag{3.106}$$

$$a_{13} = -l_3 \sin\beta\, C_{2,\theta_z-M_z} \tag{3.107}$$

The coefficient $C_{in,x}$ of Eq. (3.104) is given by the original Eq. (3.38), and the global reference frame has to be positioned at node 1. The coefficient's actual expression becomes in this case:

$$C_{in,x} = -C_{2,x-F_x} + l_1^2 C_{2,\theta_z-M_z} - C_{4,x-F_x} + (l_1 + l_3\sin\beta)^2 C_{4,\theta_z-M_z} \tag{3.108}$$

By utilizing the numerical values of all the amounts in Eqs (3.104) through (3.108), the calculated value of the bloc force F_{6y} is 8.33 N.

Solution for (e)

The energy efficiency quantifiers can simply be calculated by means of Eqs. (3.82) and (3.83) and by utilizing the given numerical values and considering that there are two flexure members that contribute with their stored energy. The maximum and minimum energy output ratios are:

$$\eta_{min} = 99.7\% \text{ and } \eta_{max} = 99.9\%$$

Solution for (f)

The precision of rotation is first discussed by comparing the mechanism with fully compliant flexure hinges (see Figure 3.8a) and the same mechanism equipped with flexure hinges that has only torsional compliance (see Figure 3.8b). By using Eqs. (3.85), (3.86), and (3.88), the numerical value of the error at the output port 6 is $e_{6,uy} = 12.1$.

Another comparison is performed with the mechanism that is comprised of point-like ideal joints instead of the real flexure hinges 2 and 4. In this case (see Figure 3.8c), the output displacement at node 6 can simply be calculated as:

$$u_{6y}^{i} = l_3 \sin\beta + \sqrt{l_3^2 \sin^2\beta - u_{1x}(u_{1x} + 2l_3 \cos\beta)} \tag{3.109}$$

where the superscript *i* denotes the "ideal" situation where the flexure hinges are point-like and purely rotational without any stiffness. By assuming that an input displacement of $u_{1x} = 0.00002$ m is utilized, the output displacement given by Eq. (3.109) is 0.00012366 m. By comparing it with the output displacement when the flexure hinges are assumed to be fully compliant, which is 0.000147 m, the relative error in output displacement is:

$$e = \frac{u_{6y} - u_{6y}^{i}}{u_{6y}} \tag{3.110}$$

and its numerical value is 19%.

3.2.2 Planar Parallel Compliant Mechanisms

A generic flexure-based planar parallel mechanism will be discussed next that is composed of *n* independent flexure hinges and a rigid link, which is the output platform, as shown in Figure 3.9a. Each flexure hinge is fixed at one end (for a generic configuration) and rigidly connected to the output platform at the other end, as illustrated in Figure 3.9b. The external load

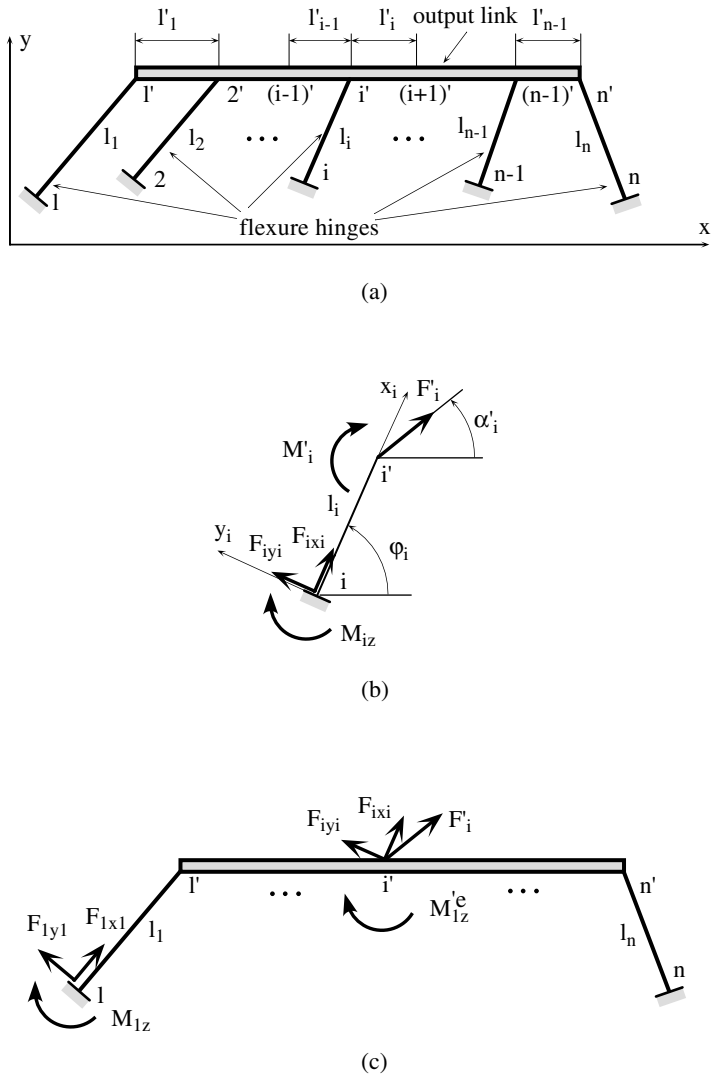

FIGURE 3.9
Schematic representation of a planar parallel compliant structure: (a) components; (b) defining geometry and external and reaction loading for a generic flexure hinge component; (c) statically equivalent planar serial structure.

acting on the structure consists of forces F_i' (inclined at an angle α_i') and moments M_{iz}' that are applied at the flexures-output platform connection points. Without reducing the generality of the problem, it is assumed that the output platform is horizontal and therefore parallel to the x axis of the global reference frame. The first task in such a case is to determine as many

reaction loads at the fixed ends of the flexures as possible, in order to render the model determinate. The n fixed ends of the flexure hinges introduce $3n$ unknowns: two forces and one moment. For the convenience of further solving the problem, it will be considered that the two force components are directed along the x and y axes of the local reference frames. This will simplify expressing the normal force and bending moment for each individual flexure hinge. Because the problem is analyzed from a quasi-static viewpoint, three equilibrium equations can be written involving both external and reaction loading. It is therefore necessary to formulate $3(n-1)$ additional equations to enable solving for the unknown reaction loads. The additional equations will result in imposing three zero-displacement conditions at each of the fixed ends for $n-1$ successive flexures. The determined reaction loads will be superimposed to the known external ones, so that the real mechanism will be equivalent to a fixed–free planar serial compliant mechanism made up of two flexure hinges (the first one and the last one of the real mechanism) and one rigid link (the output platform) that is interposed between the two flexures, as indicated in Figure 3.9c.

The zero-displacement conditions can be again formulated by means of Castigliano's displacement theorem as:

$$\begin{cases} u_{jx_j} = \dfrac{\partial U}{\partial F_{jx_j}} = 0 \\ u_{jy_j} = \dfrac{\partial U}{\partial F_{jy_j}} = 0 \\ \theta_{jz} = \dfrac{\partial U}{\partial M_{jz}} = 0 \end{cases} \tag{3.111}$$

The equations above are valid for $j = 1 \rightarrow (n-1)$. The strain energy, U, will include again the normal forces and bending moments on all corresponding flexure members, so Eq. (3.111) will be used in the form:

$$\begin{cases} u_{jx_j} = \displaystyle\sum_{i=1}^{n} \int_0^{l_i} \left(\frac{N_i}{E_i A_i} \frac{\partial N_i}{\partial F_{jx_j}} + \frac{M_{bi}}{E_i A_i} \frac{\partial M_{bi}}{\partial F_{jx_j}} \right) dx \\ u_{jy_j} = \displaystyle\sum_{i=1}^{n} \int_0^{l_i} \left(\frac{N_i}{E_i A_i} \frac{\partial N_i}{\partial F_{jy_j}} + \frac{M_{bi}}{E_i A_i} \frac{\partial M_{bi}}{\partial F_{jy_j}} \right) dx \\ \theta_{jz} = \displaystyle\sum_{i=1}^{n} \int_0^{l_i} \frac{M_{bi}}{E_i A_i} \frac{\partial M_{bi}}{\partial M_{jz}} dx \end{cases} \tag{3.112}$$

Both the axial force and bending moment of Eq. (3.112) can be expressed on either one of the 1 to $n-1$ flexure hinges as:

$$N_i = \begin{cases} F_{ix_i}, i < n \\ -\sum_{i=1}^{n-1}[F_{ix_i}\cos(\varphi_n - \varphi_i) + F_{iy_i}\sin(\varphi_n - \varphi_i)] - \sum_{i=1}^{n} F_i'\cos(\varphi_n - \alpha_i') \end{cases} \tag{3.113}$$

$$M_{bi} = \begin{cases} M_{iz} + F_{iy_i}x_i, i < n \\ \sum_{i=1}^{n-1}\left\{ M_{iz} + F_{ix_i}\sin\varphi_i \sum_{k=i}^{n-1} l_k' + F_{iy_i}\left[l_i + \cos\varphi_i \sum_{k=i}^{n-1} l_k' \right] + [F_{ix_i}\sin(\varphi_n - \varphi_i) \right. \\ \left. F_{iy_i}\cos(\varphi_n - \varphi_i)]x_n + \sum_{i=1}^{n}\left[M_{iz}' + F_i'\sin\varphi_i \sum_{k=i}^{n} l_k' + F_i'\sin(\varphi_n - \varphi_i)x_n \right] \right\} \end{cases} \tag{3.114}$$

The last equations in both Eqns. (3.113) and (3.114) are written for the last flexure hinge of the 1 to n parallel set. Equations (3.113) and (3.114) also allow determination of the partial derivatives of Eq. (3.112):

$$\frac{\partial N_i}{\partial F_{jx_j}} = \begin{cases} 0, i < n, j \neq i \\ 1, i < n, j = i \\ -\cos(\varphi_n - \varphi_j), i = n \end{cases} \tag{3.115}$$

$$\frac{\partial N_i}{\partial F_{jy_j}} = \begin{cases} 0, i < n, \\ -\sin(\varphi_n - \varphi_j), i = n \end{cases} \tag{3.116}$$

$$\frac{\partial M_{bi}}{\partial F_{jx_j}} = \begin{cases} 0, i < n, \\ \sin\varphi_j \sum_{k=j}^{n-1} l_k' + x_n \sin(\varphi_n - \varphi_j), i = n \end{cases} \tag{3.117}$$

$$\frac{\partial M_{bi}}{\partial F_{jy_j}} = \begin{cases} 0, i < n, j \neq i \\ x_j, i < n, j = i \\ l_j + \cos\varphi_j \sum_{k=j}^{n-1} l_k' - x_n \cos(\varphi_n - \varphi_j), i = n \end{cases} \tag{3.118}$$

$$\frac{\partial M_{bi}}{\partial M_{jz}} = \begin{cases} 0, i < n, j \neq i \\ 1, i < n, j = i \\ 1, i = n \end{cases} \tag{3.119}$$

Substituting Eqs. (3.112) through (3.119) into Eq. (3.111) results in 3(n – 1) equations with 3(n – 1) unknowns that can be written in matrix form as:

$$[C_R]\{R\} = [C_L]\{L\} \tag{3.120}$$

where $\{R\}$ is the unknown reaction load vector, $\{L\}$ is the known external load vector, and $[C_R]$ and $[C_L]$ are compliance-based matrices that will be formulated next. The $\{R\}$ vector is:

$$\{R\} = \{\{F_{1x_1}, F_{1y_1}, M_{1z}\}^T, \ldots \{F_{jx_j}, F_{jy_j}, M_{jz}\}^T, \ldots \{F_{n-1x_{n-1}}, F_{n-1y_{n-1}}, M_{n-1z}\}^T\}^T \tag{3.121}$$

The $\{L\}$ vector gathers all known external loads at the points where the flexure hinges connect to the rigid output platform in the form:

$$\{L\} = \{\{F_1', M_{1z}'\}^T, \ldots \{F_j', M_{1j}'\}^T, \ldots \{F_n', M_{nz}'\}^T\}^T \tag{3.122}$$

The $[C_R]$ matrix has a dimension of 3(n – 1) × 3(n – 1) and can be expressed in terms of the following generic 3 × 3 submatrix:

$$[C_{ji}] = \begin{bmatrix} C_{R,3j-2,3i-2} & C_{R,3j-2,3i-1} & C_{R,3j-2,3i} \\ C_{R,3j-1,3i-2} & C_{R,3j-1,3i-1} & C_{R,3j-1,3i} \\ C_{R,3j,3i-2} & C_{R,3j,3i-1} & C_{R,3j,3i} \end{bmatrix} \tag{3.123}$$

The terms composing the submatrix of Eq. (3.123) are:

$$C_{R,3j-2,3i-2} = C_{j,x-F_x} + \cos(\varphi_n - \varphi_i)\cos(\varphi_n - \varphi_j)C_{n,x-F_x} +$$

$$\sin(\varphi_n - \varphi_i)\sin(\varphi_n - \varphi_j)C_{n,y-F_y} + \left[\sin\varphi_i \sin(\varphi_n - \varphi_j)\sum_{k=i}^{n-1} l_k' + \sin\varphi_j \sin(\varphi_n - \varphi_i)\right.$$

$$\left.\sum_{k=i}^{n-1} l_k'\right] C_{n,y-M_z} + \sin\varphi_i \sin\varphi_j \sum_{k=i}^{n-1} l_k' \sum_{k=j}^{n-1} l_k' C_{n,\theta_z-M_z} \tag{3.124}$$

$$C_{R,3j-2,3i-1} = \sin(\varphi_n - \varphi_i)\cos(\varphi_n - \varphi_j)C_{n,x-F_x} -$$

$$\cos(\varphi_n - \varphi_i)\sin(\varphi_n - \varphi_j)C_{n,y-F_y} + \left\{\left[l_i + \cos\varphi_i \sum_{k=i}^{n-1} l'_k\right]\sin(\varphi_n - \varphi_j) - \right. \tag{3.125}$$

$$\left.\cos(\varphi_n - \varphi_i)\sin\varphi_j \sum_{k=j}^{n-1} l'_k\right\}C_{n,y-M_z} + \left[l_i + \cos\varphi_i \sum_{k=i}^{n-1} l'_k\right]\sin\varphi_j \sum_{k=j}^{n-1} l'_k C_{n,\theta_z-M_z}$$

$$C_{R,3j-2,3i} = \sin(\varphi_n - \varphi_j)C_{n,y-M_z} + \sin\varphi_j \sum_{k=j}^{n-1} l'_k C_{n,\theta_z-M_z} \tag{3.126}$$

$$C_{R,3j-1,3i-2} = \cos(\varphi_n - \varphi_i)\sin(\varphi_n - \varphi_j)C_{n,x-F_x} - \sin(\varphi_n - \varphi_i)$$

$$\cos(\varphi_n - \varphi_j)C_{n,y-F_y} + \left\{\left[l_j + \cos\varphi_j \sum_{k=j}^{n-1} l'_k\right]\sin(\varphi_n - \varphi_i) - \sin\varphi_i\cos(\varphi_n - \varphi_j)\right\}$$

$$C_{n,y-M_z} + \left[l_j + \cos\varphi_j \sum_{k=j}^{n-1} l'_k\right]\sin\varphi_i \sum_{k=i}^{n-1} l'_k C_{n,\theta_z-M_z} \tag{3.127}$$

$$C_{R,3j-1,3i-1} = C_{j,y-F_y} + \sin(\varphi_n - \varphi_i)\sin(\varphi_n - \varphi_j)C_{n,x-F_x} + \cos(\varphi_n - \varphi_i)$$

$$\cos(\varphi_n - \varphi_j)C_{n,y-F_y} - \left\{\left[l_i + \cos\varphi_i \sum_{k=i}^{n-1} l'_k\right]\cos(\varphi_n - \varphi_i) + \cos(\varphi_n - \varphi_i)\right. \tag{3.128}$$

$$\left.\left[l_j + \cos\varphi_i \sum_{k=j}^{n-1} l'_k\right]\right\}C_{n,y-M_z} + \left[l_i + \cos\varphi_i \sum_{k=i}^{n-1} l'_k\right]\left[l_j + \cos\varphi_j \sum_{k=j}^{n-1} l'_k\right]C_{n,\theta_z-M_z}$$

$$C_{R,3j-1,3i} = C_{j,y-M_z} - \cos(\varphi_n - \varphi_j)C_{n,y-M_z} + \left[l_j + \cos\varphi_j \sum_{k=j}^{n-1} l'_k\right]C_{n,\theta_z-M_z} \tag{3.129}$$

$$C_{R,3j,3i-2} = \sin\varphi_i \sum_{k=i}^{n-1} l'_k C_{n,\theta_z-M_z} + \sin(\varphi_n - \varphi_i)C_{n,y-M_z} \tag{3.130}$$

$$C_{R,3j,3i-1} = C_{j,y-M_z} + \left[l_i + \cos\varphi_i \sum_{k=i}^{n-1} l'_k \right] C_{n,\theta_z-M_z} - \cos(\varphi_n - \varphi_i) C_{n,y-M_z} \tag{3.131}$$

$$C_{R,3j,3i} = C_{j,\theta_z-M_z} + C_{n,\theta_z-M_z} \tag{3.132}$$

It can easily be checked by interchanging the subscripts i and j that the matrix $[C_{R,ji}]$ of Eq. (3.123) is symmetric. The $[C_L]$ matrix has a dimension of $3(n-1) \times 2n$ and can be expressed in terms of the following generic 3×2 submatrix:

$$[C_L] = \begin{bmatrix} C_{L,j,i} & C_{L,j,i+1} \\ C_{L,j+1,i} & C_{L,j+1,i+1} \\ C_{L,j+2,i} & C_{L,j+2,i+1} \end{bmatrix} \tag{3.133}$$

The terms entering the submatrix of Eq. (3.133) are:

$$\begin{aligned} C_{L,j,i} = {} & -\cos(\varphi_n - \alpha'_i)\cos(\varphi_n - \varphi_j) C_{n,x-F_x} - \sin(\varphi_n - \alpha'_i)\sin(\varphi_n - \varphi_j) C_{n,y-F_y} \\ & - \left[\sin\alpha'_i \sin(\varphi_n - \varphi_j) \sum_{k=i}^{n-1} l'_k + \sin(\varphi_n - \alpha'_i)\sin\varphi_j \sum_{k=j}^{n-1} l'_k \right] C_{n,y-M_z} \\ & - \sum_{k=i}^{n} l'_k \sum_{k=j}^{n-1} l'_k \sin\alpha'_i \sin\varphi_j C_{n,\theta_z-M_z} \end{aligned} \tag{3.134}$$

$$C_{L,j,i+1} = -\sin(\varphi_n - \varphi_i) C_{n,y-M_z} - \sin\varphi_j \sum_{k=j}^{n-1} l'_k C_{n,\theta_z-M_z} \tag{3.135}$$

$$\begin{aligned} C_{L,j+1,i} = {} & -\cos(\varphi_n - \alpha'_i)\sin(\varphi_n - \varphi_j) C_{n,x-F_x} + -\sin(\varphi_n - \alpha'_i)\cos(\varphi_n - \varphi_j) \\ & C_{n,y-F_y} + \left\{ \sin\alpha'_i \cos(\varphi_n - \varphi_j) \sum_{k=i}^{n} l'_k - \sin(\varphi_n - \alpha'_i) \left[l_j + \cos\varphi_j \sum_{k=j}^{n-1} l'_k \right] \right\} \\ & C_{n,y-M_z} - \sin\alpha'_i \sum_{k=i}^{n} l'_k \left[l_j + \cos\varphi_j \sum_{k=j}^{n-1} l'_k \right] C_{n,\theta_z-M_z} \end{aligned} \tag{3.136}$$

$$C_{L,j+1,i+1} = \cos(\varphi_n - \varphi_j) C_{n,y-M_z} - \left[l_j + \cos\varphi_j \sum_{k=j}^{n-1} l'_k \right] C_{n,\theta_z-M_z} \tag{3.137}$$

$$C_{L,j+2,i} = -\sin(\varphi_n - \alpha_i')C_{n,y-M_z} - \sin\alpha_i' \sum_{k=i}^{n} l_k' C_{n,\theta_z - M_z} \tag{3.138}$$

$$C_{L,j+2,i+1} = -C_{n,\theta_z - M_z} \tag{3.139}$$

The unknown load vector $\{R\}$ can be found by solving Eq. (3.120) as:

$$\{R\} = [C_R]^{-1}[C_L]\{L\} \tag{3.140}$$

where all the quantities entering the right-hand side were previously defined in Eqs. (3.121) through (3.139) and are assumed known.

It is possible that some boundary conditions, other than the assumed fixed condition, apply for the end of the flexure that opposes the end connected to the output platform. By recalling the original problem that was formulated here—namely, that $3(n-1)$ equations were utilized to express zero displacements for the fixed ends of the first $(n-1)$ flexure hinges—it is simple to just erase a line in the original matrix equation that corresponds to an actual nonzero displacement boundary condition and then take a zero instead of the external load component that is related to the respective boundary condition.

All the reactions that were determined by means of Eq. (3.140) can now be transferred to the corresponding flexure-output platform junction points 2′ through $(n-1)'$. In doing so, the original parallel mechanism that is composed of n flexure hinges and a rigid output platform can be transformed into an equivalent serial fixed–free mechanism composed of two terminal flexure hinges, 1 and n, and an intermediate rigid link (the output platform), as illustrated in Figure 3.9c.

The procedure described above is extremely useful, as it allows the static transformation of a generic purely parallel mechanism composed of n individual flexure hinges and an output rigid link into an equivalent fixed–free serial mechanism consisting of only two flexure hinges and the rigid platform. It is thus possible to qualify a planar parallel mechanism by revisiting all the problems that were dealt with in detail when discussing the planar serial mechanisms.

Due to the action of transferring the newly determined reaction loads of $\{R\}$ from their original location to corresponding ones on the output platform, the resulting load components can be expressed as:

$$\begin{cases} F_{ix}'^{e} = F_i' \cos\alpha_i' + F_{ix_i}\cos\varphi_i - F_{iy_i}\sin\varphi_i \\ F_{iy}'^{e} = F_i' \sin\alpha_i' + F_{ix_i}\sin\varphi_i + F_{iy_i}\cos\varphi_i \quad \textit{for } i = 2 \to n-1 \\ M_{iz}'^{e} = M_{iz}' + F_{iy_i} l_i \end{cases} \tag{3.141}$$

The prime superscript in Eq. (3.141) indicates that the respective forces and moments are applied to the nodes on the output platform. The load components on the last node, n', on the output platform are the original ones as no additional load is being transferred to that node.

3.2.3 Planar Hybrid Compliant Mechanisms

A hybrid mechanism has links that are connected serially and links that are connected in parallel. We will now analyze a generic planar hybrid mechanism that is composed of n independent serial chains, each connected to a rigid output platform. Each chain is built by n_i flexure hinges that are rigidly and serially interconnected so that one end of the chain (or leg) is fixed, while the other one attaches to the platform. A sketch of this structure is presented in Figure 3.10a.

Similar to the case of a parallel compliant structure, it is assumed here that the output platform is parallel to the x axis of the global reference frame. The load on the platform consists of the same point forces and moments located at the flexures-platform junctions (see Figure 3.10d). In addition, it is assumed that one point force, arbitrarily oriented in the plane of the structure, acts on each of the n serial legs, as shown in Figure 3.10c. All of these forces mimic the motive forces that would set the structure into motion while the forces and moments acting on the platform represent the external loads that must be counteracted. The main problem with this type of structure is again determining the unknown reaction loads that are set at the fixed ends of the serial chains (as illustrated in Figure 3.10b). From this point of view the problem is identical to the case of a planar parallel mechanism constrained by the same boundary conditions. In actuality, no fundamental difference exists between a parallel and a hybrid mechanism; the procedure of calculating the reaction loads is exactly the same and will not be repeated again in detail. The real planar hybrid mechanism can be transformed into a statically equivalent serial mechanism composed of the output platform and two serial chains, one chain having its external flexure fixed at one end and the other chain being free at its end opposing the junction to the platform. This transformation can be achieved by going through the following steps:

- Select the $n-1$ neighboring serial chains that have $3(n-1)$ unknown reactions to be determined by formulating the $3(n-1)$ equations for the corresponding zero displacements at the respective fixed ends.
- Use Castigliano's displacement theorem to formulate the $3(n-1)$ zero-displacement equations by defining the normal force and bending moments over the flexible links (the flexure hinges) in the following order:
  - Start from the fixed end of the first serial chain.

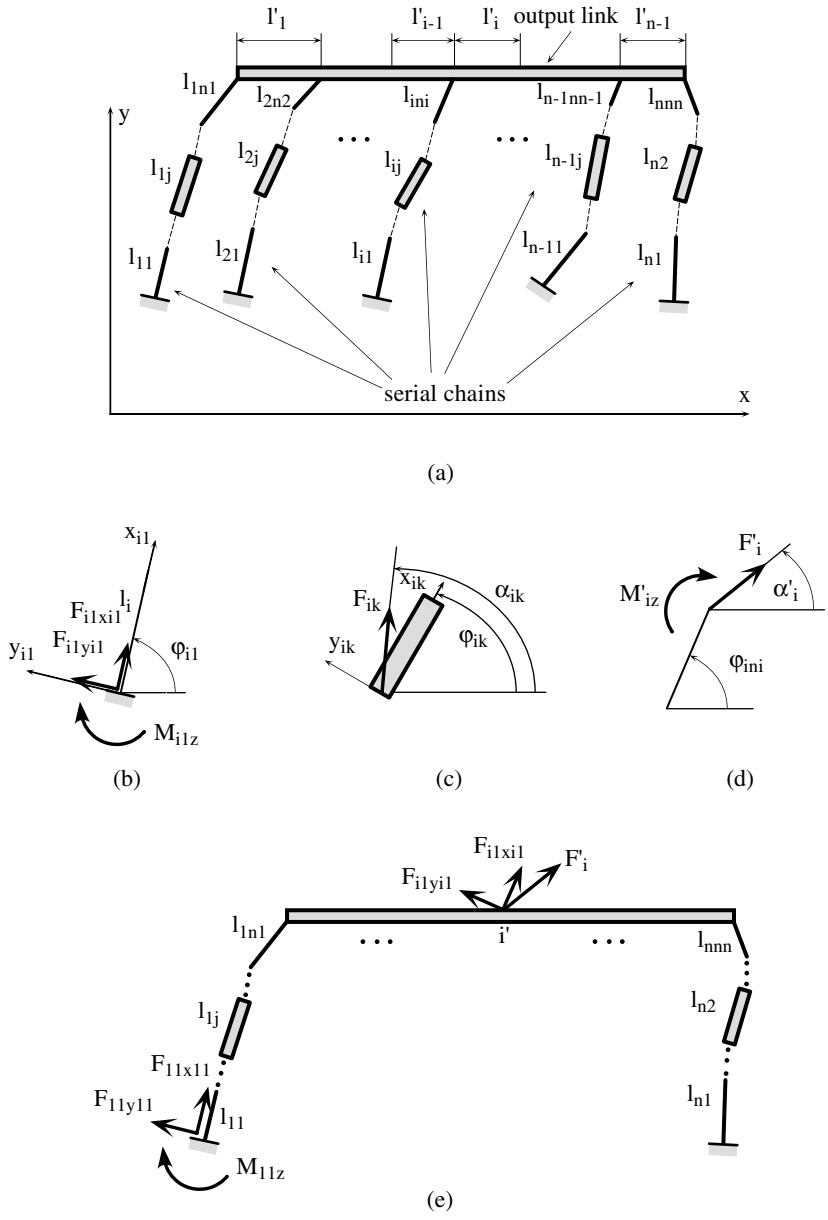

FIGURE 3.10
Schematic representation of a hybrid (serial-parallel) compliant structure: (a) components; (b) defining geometry and reaction loading for a generic fixed flexure hinge component; (c) defining geometry and external loading for a generic intermediate member in a serial chain; (d) defining geometry and external loading for a generic connecting member in a serial chain; (e) statically equivalent planar serial structure.

  - Continue over all subsequent flexure hinges and rigid links, including the last one that connects the serial chain to the output platform.
  - Repeat these two phases independently for all subsequent $n - 2$ serial chains.
  - Go to the nth (last) serial chain and start from the point that connects the chain to the output platform and again formulate the normal forces, bending moments, and necessary derivatives for all flexure hinges down to the last one. Make sure that the normal forces and bending moments on all separate intervals of this last serial chain include all other external and reaction loads.
- Formulate the $[C_R]$ and $[C_L]$ matrices and the load vector $\{L\}$ and solve for the unknown reaction load vector $\{R\}$, by utilizing Eq. (3.140).
- Transport all reaction loads and intermediate external forces from their original application points to the corresponding points that connect the respective serial chains to the rigid platform for chain number 2 through chain number $n - 1$. In doing so, calculate all necessary moments that must be taken into account when statically moving the forces to their new locations.

The end result of all the above-mentioned steps is a fixed–free serial mechanism that is statically equivalent to the original hybrid mechanism and is composed of the output rigid platform interposed between the first serial chain (that has a free end) and the last one (that has a fixed end). All aspects that were analyzed and solved for serial mechanisms can thus be dealt with for hybrid structures. Next, an example of a planar hybrid flexure-based compliant mechanism will be presented and solved algebraically.

Example

Find the equivalent serial mechanism of the tilt-type planar hybrid mechanism shown in Figure 3.11.

Solution

It can be seen that the mechanism pictured in Figure 3.11 consists of three different serial chains that are mutually parallel; therefore, the mechanism is a hybrid one. As indicated in the brief presentation of hybrid structures, it is necessary to cover the structure by starting from the external end of one serial chain and then continue over the output platform by adding up external and reaction loads from all subsequent serial chains. The trip ends after reaching the outer end of the last flexure hinge. If the mechanism is covered by starting from the two-link serial chain, five unknown reaction loads will

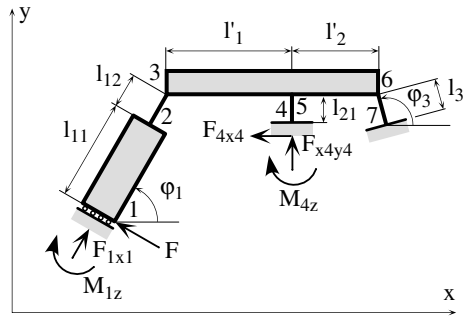

FIGURE 3.11
Example of a planar hybrid compliant structure.

have to be determined in order to transform the given structure into its equivalent serial one, so five displacement equations must be formulated:

$$u_{1x_1} = \int_0^{l_{12}} \frac{N_{23}}{EA_{23}} \frac{\partial N_{23}}{\partial F_{1x_1}} dx_{23} + \int_0^{l_{21}} \frac{N_{45}}{EA_{45}} \frac{\partial N_{45}}{\partial F_{1x_1}} dx_{45} + \int_0^{l_{31}} \frac{N_{67}}{EA_{67}} \frac{\partial N_{67}}{\partial F_{1x_1}} dx_{67} + \int_0^{l_{12}} \frac{M_{b23}}{EI_{23}} \frac{\partial M_{b23}}{\partial F_{1x_1}} dx_{23} + \int_0^{l_{21}} \frac{M_{b45}}{EI_{45}} \frac{\partial M_{b45}}{\partial F_{1x_1}} dx_{45} + \int_0^{l_{31}} \frac{M_{b67}}{EI_{67}} \frac{\partial M_{b67}}{\partial F_{1x_1}} dx_{67} = 0 \tag{3.142}$$

$$\theta_{1z} = \int_0^{l_{12}} \frac{M_{b23}}{EI_{23}} \frac{\partial M_{b23}}{\partial M_{1z}} dx_{23} + \int_0^{l_{21}} \frac{M_{b45}}{EI_{45}} \frac{\partial M_{b45}}{\partial M_{1z}} dx_{45} + \int_0^{l_{31}} \frac{M_{b67}}{EI_{67}} \frac{\partial M_{b67}}{\partial M_{1z}} dx_{67} = 0 \tag{3.143}$$

$$u_{4x_4} = \int_0^{l_{12}} \frac{N_{23}}{EA_{23}} \frac{\partial N_{23}}{\partial F_{4x_4}} dx_{23} + \int_0^{l_{21}} \frac{N_{45}}{EA_{45}} \frac{\partial N_{45}}{\partial F_{4x_4}} dx_{45} + \int_0^{l_{31}} \frac{N_{67}}{EA_{67}} \frac{\partial N_{67}}{\partial F_{4x_4}} dx_{67} + \int_0^{l_{12}} \frac{M_{b23}}{EI_{23}} \frac{\partial M_{b23}}{\partial F_{4x_4}} dx_{23} + \int_0^{l_{21}} \frac{M_{b45}}{EI_{45}} \frac{\partial M_{b45}}{\partial F_{4x_4}} dx_{45} + \int_0^{l_{31}} \frac{M_{b67}}{EI_{67}} \frac{\partial M_{b67}}{\partial F_{4x_4}} dx_{67} = 0 \tag{3.144}$$

$$u_{4y_4} = \int_0^{l_{12}} \frac{N_{23}}{EA_{23}} \frac{\partial N_{23}}{\partial F_{4y_4}} dx_{23} + \int_0^{l_{21}} \frac{N_{45}}{EA_{45}} \frac{\partial N_{45}}{\partial F_{4y_4}} dx_{45} + \int_0^{l_{31}} \frac{N_{67}}{EA_{67}} \frac{\partial N_{67}}{\partial F_{4y_4}} dx_{67} + \int_0^{l_{12}} \frac{M_{b23}}{EI_{23}} \frac{\partial M_{b23}}{\partial F_{4y_4}} dx_{23} + \int_0^{l_{21}} \frac{M_{b45}}{EI_{45}} \frac{\partial M_{b45}}{\partial F_{4y_4}} dx_{45} + \int_0^{l_{31}} \frac{M_{b67}}{EI_{67}} \frac{\partial M_{b67}}{\partial F_{4y_4}} dx_{67} = 0 \tag{3.145}$$

$$\theta_{4z} = \int_0^{l_{12}} \frac{M_{b23}}{EI_{23}} \frac{\partial M_{b23}}{\partial M_{4z}} dx_{23} + \int_0^{l_{21}} \frac{M_{b45}}{EI_{45}} \frac{\partial M_{b45}}{\partial M_{4z}} dx_{45} + \int_0^{l_{31}} \frac{M_{b67}}{EI_{67}} \frac{\partial M_{b67}}{\partial M_{4z}} dx_{67} = 0 \tag{3.146}$$

The axial force is:

$$\begin{cases} N_{23} = F_{1x_1} \\ N_{45} = F_{4x_4} \\ N_{67} = -F_{1x_1}\cos(\varphi_3 - \varphi_1) - F\sin(\varphi_3 - \varphi_1) - F_{4x_4}\sin\varphi_3 + F_{4y_4}\cos\varphi_3 \end{cases} \tag{3.147}$$

The bending moment is:

$$\begin{cases} M_{b23} = M_{1z} + Fl_{11} + Fx_{12} \\ M_{b45} = M_{4z} + F_{4y_4}x_{45} \\ M_{b67} = M_{1z} + F_{1x_1}(l_1' + l_2')\sin\varphi_1 + F[l_{11} + l_{12} + (l_1' + l_2')\cos\varphi_1 + M_{4z} + F_{4x_4}l_2' + \\ F_{4y_4}l_{21} + [F_{1x_1}\sin(\varphi_1 - \varphi_3) - F\cos(\varphi_1 - \varphi_3) - F_{4x_4}\cos\varphi_3 - F_{4y_4}\sin\varphi_3]x_{67} \end{cases} \tag{3.148}$$

It is simple now to calculate the partial derivatives of Eqs. (3.142) through (3.146) by using Eqs. (3.147) and (3.148).

Generic Eq. (3.140) is utilized to solve for the unknown reaction loads. The relevant terms of the 5×5 symmetric $[C_R]$ matrix are:

$$\begin{aligned} C_{R1,1} = {} & C_{12,x-F_x} + \cos^2(\varphi_3 - \varphi_1)C_{31,x-F_x} + \sin^2(\varphi_3 - \varphi_1)C_{31,y-F_y} \\ & + 2(l_1' + l_2')\sin\varphi_1\sin(\varphi_3 - \varphi_1)C_{31,y-M_z} + (l_1' + l_2')^2\sin^2\varphi_1 C_{31,\theta_z-M_z} \end{aligned} \tag{3.149}$$

$$C_{R1,2} = \sin(\varphi_3 - \varphi_1)C_{31,y-M_z} + (l_1' + l_2')C_{31,\theta_z-M_z} \tag{3.150}$$

$$\begin{aligned} C_{R1,3} = {} & \sin\varphi_3\cos(\varphi_3 - \varphi_1)C_{31,x-F_x} - \cos\varphi_3\sin(\varphi_3 - \varphi_1)C_{31,y-F_y} \\ & + [l_2'\sin(\varphi_3 - \varphi_1) - (l_1' + l_2')\sin\varphi_1\cos\varphi_3]C_{31,y-M_z} \\ & + l_2'(l_1' + l_2')\sin\varphi_1 C_{31,\theta_z-M_z} \end{aligned} \tag{3.151}$$

$$\begin{aligned} C_{R1,4} = {} & -\cos\varphi_3\cos(\varphi_3 - \varphi_1)C_{31,x-F_x} - \sin\varphi_3\sin(\varphi_3 - \varphi_1)C_{31,y-F_y} \\ & + [l_{21}\sin(\varphi_3 - \varphi_1) - (l_1' + l_2')\sin\varphi_1\sin\varphi_3]C_{31,y-M_z} + l_{21}(l_1' + l_2')\sin\varphi_1 C_{31,\theta_z-M_z} \end{aligned} \tag{3.152}$$

$$C_{R1,5} = \sin(\varphi_3 - \varphi_1)C_{31,y-M_z} + (l_1' + l_2')\sin\varphi_1 C_{31,\theta_z-M_z} \tag{3.153}$$

$$C_{R22} = C_{12,\theta_z-M_z} + C_{31,\theta_z-M_z} \tag{3.154}$$

$$C_{R2,3} = -\cos\varphi_3 C_{31,y-M_z} + l'_2 C_{31,\theta_z-M_z} \tag{3.155}$$

$$C_{R2,4} = -\sin\varphi_3 C_{31,y-M_z} + l_{21} C_{31,\theta_z-M_z} \tag{3.156}$$

$$C_{R2,5} = C_{31,\theta_z-M_z} \tag{3.157}$$

$$C_{R3,3} = C_{21,x-F_x} + \sin^2\varphi_3 C_{31,x-F_x} + \cos^2\varphi_3 C_{31,y-F_y} - 2l'_2\cos\varphi_3 C_{31,y-M_z} + l'^2_2 C_{31,\theta_z-M_z} \tag{3.158}$$

$$C_{R3,4} = \sin\varphi_3\cos\varphi_3(-C_{31,x-F_x} + C_{31,y-F_y}) - (l_{21}\cos\varphi_3 - l'_2\sin\varphi_3)C_{31,y-M_z} + l_{21}l'_2 C_{31,\theta_z-M_z} \tag{3.159}$$

$$C_{R3,5} = -\cos\varphi_3 C_{31,y-M_z} + l'_2 C_{31,\theta_z-M_z} \tag{3.160}$$

$$C_{R4,4} = \cos^2\varphi_3 C_{31,x-F_x} + \sin^2\varphi_3 C_{3,y-F_y} - 2l_{21}\sin\varphi_3 C_{31,y-M_z} + l^2_{21} C_{31,\theta_z-M_z} \tag{3.161}$$

$$C_{R4,5} = C_{21,y-M_z} - \sin\varphi_3 C_{31,y-M_z} + l_{21} C_{31,\theta_z-M_z} \tag{3.162}$$

$$C_{R5,5} = C_{21,\theta_z-M_z} + C_{31,\theta_z-M_z} \tag{3.163}$$

The $[C_L]$ matrix is actually a vector defined as:

$$[C_L] = \{C_{L1,1}, C_{L2,1}, C_{L3,1}, C_{L4,1}, C_{L5,1}\}^T \tag{3.164}$$

and its components are:

$$C_{L1,1} = \sin(\varphi_3 - \varphi_1)\cos(\varphi_3 - \varphi_1)(-C_{31,x-F_x} + C_{31,y-F_y}) + \{-[l_{11} + l_{12} + (l'_1 + l'_2)\cos\varphi_1]\sin(\varphi_1 - \varphi_3) + (l'_1 + l'_2)\sin\varphi_1\cos(\varphi_3 - \varphi_1)\}C_{31,y-M_z} - [l_{11} + l_{12} + (l'_1 + l'_2)\cos\varphi_1](l'_1 + l'_2)\sin\varphi_1 C_{31,\theta_z-M_z} \tag{3.165}$$

$$C_{L2,1} = -C_{12,y-M_z} - l_{11}C_{12,\theta_z-M_z} + \cos\varphi_3 C_{31,y-M_z} - [l_{11} + l_{12} + (l'_1 + l'_2)\cos\varphi_1] C_{31,\theta_z-M_z} \tag{3.166}$$

$$C_{L3,1} = -\sin\varphi_3\sin(\varphi_3 - \varphi_1)C_{31,x-F_x} - \cos\varphi_3\cos(\varphi_3 - \varphi_1)C_{3,y-F_y} + \{[l_{11} + l_{12} + (l'_1 + l'_2)\cos\varphi_1]\cos\varphi_3 + l'_2\cos(\varphi_3 - \varphi_1)\}C_{31,y-M_z} - [l_{11} + l_{12} + (l'_1 + l'_2)\cos\varphi_1]C_{31,\theta_z-M_z} \tag{3.167}$$

$$C_{L4,1} = \sin(\varphi_3 - \varphi_1)\cos\varphi_3 C_{31,x-F_x} - \cos(\varphi_3 - \varphi_1)\sin\varphi_3 C_{31,y-F_y} -$$
$$[l_{11} + l_{12} + (l_1' + l_2')\cos\varphi_1 \sin\varphi_3 - l_{21}\cos(\varphi_3 - \varphi_1)]C_{31,y-M_z} - \quad (3.168)$$
$$[l_{11} + l_{12} + (l_1' + l_2')\cos\varphi_1]l_{21}C_{31,\theta_z-M_z}$$

$$C_{L5,1} = \cos(\varphi_3 - \varphi_1)C_{31,y-M_z} - [l_{11} + l_{12} + (l_1' + l_2')\cos\varphi_1 C_{31,\theta_z-M_z} \quad (3.169)$$

The load vector consists of only one component in this case; therefore:

$$\{L\} = \{F\} \quad (3.170)$$

Equation (1.140) is now utilized to solve for the five unknown reaction loads: F_{1x1}, M_{1z}, F_{4x4}, F_{4y4}, and M_{z4}. As mentioned in the presentation of the generic algorithm pertaining to a planar hybrid mechanism, the next step in the solving sequence is to transfer the forces and/or moments of all inner serial chains to the corresponding endpoint that connects the respective chain to the output platform. In the specific case of this example, there is a single inner chain, namely the second one that is formed of one flexure hinge, so the reactions F_{4x4}, F_{4y4}, and M_{z4} must be relocated from node 4 to node 5, according to Figure 3.11. The corresponding equivalent load components in the global reference system, *xy*, at node 5 are, according to Eq. (3.141):

$$\begin{cases} F_{5x}'^{e} = -F_{4y_4} \\ F_{5y}'^{e} = F_{4x_4} \\ M_{5z}'^{e} = M_{4z} + F_{4y_4}l_{21} \end{cases} \quad (3.171)$$

The original planar hybrid mechanism shown in Figure 3.11 is therefore transformed into a statically equivalent serial mechanism that is composed of the first serial chain 1–2–3, the rigid platform 3–6, and the last flexure 6–7 subjected to the external plus reaction loading at node 1 and the equivalent load applied at node 5.

3.3 Spatial Compliant Mechanisms

3.3.1 Spatial Serial Compliant Mechanisms

A three-dimensional serial mechanism is composed of flexure hinges and rigid links that are disposed in the three-dimensional space and rigidly interconnected to form one serial chain, which is generically considered free at one end and fixed at the other, similar to the planar serial mechanisms that were analyzed at the beginning of this chapter. Because both the structure and loading are now three dimensional, revolute flexure hinges can be utilized

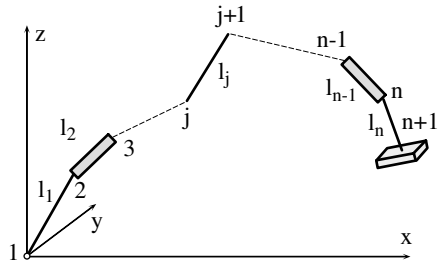

(a)

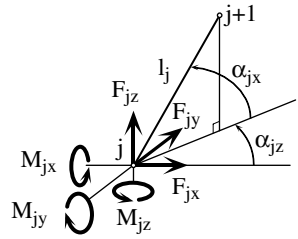

(b)

FIGURE 3.12
Schematic representation of a three-dimensional serial compliant structure: (a) components; (b) defining geometry and external loading for a generic flexure hinge component.

that, as shown in Chapter 2, have the capacity of accommodating bending about any instantaneous axis and torsion in addition to the bending and axial effects. All the detailed study that was performed for planar serial mechanisms is also valid in its principles for spatial mechanisms, too, and it will not be explicitly given for all the aspects that have been discussed there. Figure 3.12 shows the configuration of a spatial serial mechanism together with the defining geometry and the loading on a generic flexure hinge. It is again considered, in order to keep the problem tractable, that the loading to the mechanism is applied at one single node (the input node, denoted by *i*).

Castigliano's displacement theorem will again be the tool selected to solve the main problem in a fixed–free serial structure (i.e., the displacement-load equations). For the planar case, Eqs. (3.24), (3.26), and (3.28) reflected this relationship explicitly by highlighting the contributions brought about by the various compliances of the flexure hinges that had to be taken into consideration. As indicated in Figure 3.12b, the load at a node of a generic flexure hinge resulting from transferring the actual load onto the input node *i* consists of six components, three forces and three moments, directed about

the axes of the local reference frame $x_j y_y z_j$. In order to define the axes of a local reference frame, the projection of node $j + 1$ is taken onto a plane that passes through node j and is parallel to global plane xOy. The plane formed by the flexure, $j - j + 1$, and its projection on the above-mentioned plane will be the local $x_j y_j$ plane with the x_j axis directed along the longitudinal axis of the revolute flexure. The third local axis, z_j, will be perpendicular to the plane of the first two local axes and directed according to the right-hand rule, as shown in Figure 3.12. By applying Castigliano's displacement theorem, the displacement and rotations at node i can be calculated as:

$$u_{ix} = \sum_{j=i}^{n} \left(\int_0^{l_j} \frac{M_{bj,z_j}}{E_j I_j} \frac{\partial M_{bj,z_j}}{\partial F_{ix}} dx_j + \int_0^{l_j} \frac{M_{bj,y_j}}{E_j I_j} \frac{\partial M_{bj,y_j}}{\partial F_{ix}} dx_j + \int_0^{l_j} \frac{M_{tj}}{E_j I_{pj}} \frac{\partial M_{tj}}{\partial F_{ix}} dx_j + \int_0^{l_j} \frac{N_j}{E_j A_j} \frac{\partial N_j}{\partial F_{ix}} dx_j \right) \tag{3.172}$$

Similar equations can be written for the other displacement components u_{iy}, u_{iz}, θ_{ix}, θ_{iy}, and θ_{iz} by taking the partial derivatives of the previous equation with respect to F_{iy}, F_{iz}, M_{ix}, M_{iy}, and M_{iz}, respectively. The final equations that express the displacement-load relationships at the input node can simply be obtained by performing the calculations of Eq. (3.172) and by recognizing the following compliance terms:

$$\begin{cases} C_{j,x-F_x} = \int_{l_j}^{l_j} \dfrac{dx_j}{E_j A_j} \\ C_{j,y-F_y} = C_{j,z-F_z} = \int_0^{l_j} \dfrac{x_j^2 dx_j}{E_j I_j} \\ C_{j,y-M_z} = C_{j,z-M_y} = \int_0^{l_j} \dfrac{x_j dx_j}{E_j I_j} \\ C_{j,\theta_z-M_z} = C_{j,\theta_y-M_y} = \int_0^{l_j} \dfrac{dx_j}{E_j I_j} \\ C_{j,\theta_x-M_x} = \int_0^{l_j} \dfrac{dx_j}{E_j I_{pj}} \end{cases} \tag{3.173}$$

The aspects of mechanical advantage and bloc output load can be solved by utilizing the previous differences within the reasoning framework presented

at planar serial mechanisms. The same remarks are also valid when quantifying the energy efficiency of a three-dimensional serial mechanism. The differences arise again due to the three-dimensional nature of the loading and geometry of such a configuration. Similar to Eq. (3.80), the minimum energy efficiency can be calculated as:

$$\eta_{min} = \frac{i_{min}}{o} \tag{3.174}$$

while the maximum output, similar to the one expressed in Eq. (3.81) for planar serial mechanism, is given by:

$$\eta_{max} = \frac{i_{max}}{o} \tag{3.175}$$

with:

$$i_{min} = \sum_{j=1}^{n_f} (C_{j,\theta_z - M_z} M_{bj,z_j}^2) \tag{3.176}$$

$$i_{max} = \sum_{j=1}^{n_f} (C_{j,\theta_z - M_z} M_{bj,z_j}^2 + C_{j,y-F_y} F_{jy_j}^2 + 2C_{j,y-M_z} F_{jy_j} M_{bj,z_j} \tag{3.177}$$

$$\begin{aligned} o = \sum_{j=1}^{n_f} [&C_{j,x-F_x} N_j^2 + C_{j,y-F_y} (F_{jy_j}^2 + F_{jz_j}^2) + C_{j,\theta_z - M_z} (M_{bj,z_j}^2 + M_{bj,y_j}^2) \\ &+ 2C_{j,y-M_z} (F_{jy_j} M_{bj,z_j} + F_{jz_j} M_{bj,y_j}) + C_{j,\theta_x - M_x} M_{tj}^2] \end{aligned} \tag{3.178}$$

Equations similar to Eqs. (3.82) and (3.83) can be obtained from the equations above by taking unit loads and thus keeping only the influence of the flexures geometry.

3.3.2 Spatial Parallel and Hybrid Compliant Mechanisms

The three-dimensional parallel and hybrid mechanisms will be analyzed in this subchapter in a manner similar to the one developed when discussing their planar counterparts. The three-dimensional parallel mechanisms will be studied first, and it will be shown that the scenario followed in solving for a planar parallel mechanism can safely be replicated for the present case with only minor alterations. As for the situation with planar hybrid mechanisms, which were shown to have their solution in the static regime by a simple extension from a corresponding parallel mechanism, the pattern will repeat itself in the case of three-dimensional hybrid and parallel structures, and only a brief discussion of the few differences will be given for three-dimensional hybrid mechanisms.

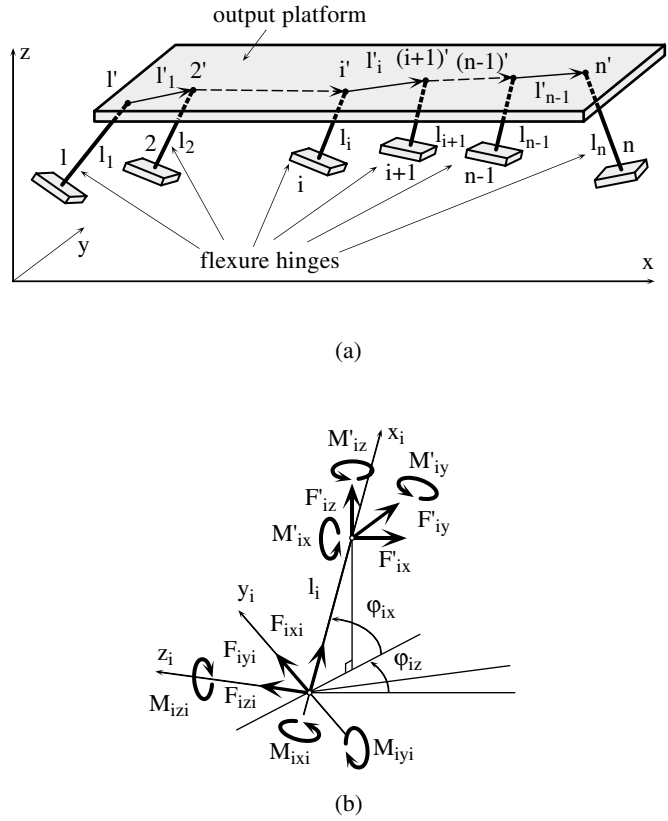

FIGURE 3.13
Schematic representation of a three-dimensional parallel compliant structure: (a) components; (b) defining geometry and external and reaction loading for a generic flexure hinge component.

3.3.2.1 Spatial Parallel Compliant Mechanisms

A three-dimensional parallel mechanism is now introduced and studied that is formed of a rigid plate and n revolute (three-dimensional) flexure hinges that have one end fixed and the other rigidly attached to the output platform. As illustrated in Figure 3.13, the flexure hinges are arbitrarily oriented in the three-dimensional space. A global reference frame is defined that has its xy plane parallel to the plane of the rigid platform. Point loads and moments, arbitrarily oriented and representing either active or load agents, act at the flexures–platform junction nodes. It will be shown next that this type of mechanism can be studied by following the same path that was defined when discussing a planar parallel mechanism. The primary concern here again is finding a sufficient number of unknown reaction loads at the fixed ends of the flexures so that the problem becomes statically determined. By inspecting

Figure 3.13, it is clear that the same procedure that was utilized for planar parallel mechanisms can be employed in this case, too. Moreover, by conveniently defining the local frames, it is possible to keep the dimension of the problem unchanged and therefore to solve the same $3(n-1)$ equations system as in the case for planar structures. The following steps must be performed in order to solve for $3(n-1)$ reaction loads:

- Select a sequence that will cover all the flexures–platform junction nodes in such a way that by starting from an arbitrary node (the first one) a broken line will connect all subsequent nodes in a continuous manner until a last node is reached (see the arrow sequence connecting points 1′, 2′, …, n′ on the platform of Figure 3.13a).
- Define the axial force, the bending moment, and their corresponding partial derivatives for use of Castigliano's displacement theorem over all flexure hinges by carrying out the following steps:
  - Define the plane formed by l_i and l_i' for a generic flexure hinge (Figure 3.13).
  - Define the local reference frame for this flexure so that the x_i axis coincide with the l_i direction, y_i is perpendicular on the plane of $l_i - l_i'$, and z_i is located in the $l_i - l_i'$ plane in a direction perpendicular to l_i (see Figure 3.13b).
  - Locate the reactions at node i so that F_{ixi} is directed along the x_i axis, F_{iyi} along the y_i axis, and M_{izi} along the local z_i axis.
  - Express the normal force and bending moment together with the corresponding partial derivatives for the current flexure hinge by starting from its fixed end and therefore by only taking into considerations the contributions from the local reaction forces and moment.
  - Repeat these three steps for all flexure hinges from the first one to the $(n-1)$th one.
  - Use the same definition to determine the local frame for the last flexure by positioning it on the end that is connected to the rigid output platform.
  - Express the normal force and bending moment together with the corresponding partial derivatives for the last flexure hinge by starting from its node connected to the output platform and by taking into account all contributions from the previous $n-1$ flexure hinges as well as the external loads on the $n-1$ points on the platform.
- Formulate the $3(n-1)$ equations that comprise the $3(n-1)$ unknown reactions and solve for them by using the $[C_R]$ and $[C_L]$ matrices and the external load vector $\{L\}$ as indicated in Eq. (3.140).

Transfer the reaction loads from their original location i to i' (see Figure 3.13a and b) for nodes 2 through $n-1$ and calculate the equivalent loads (expressed in the global reference frame) at the new locations as:

$$\begin{cases} F'^{e}_{ix} = F'_{ix} + F_{ix_i}\cos\varphi_{ix}\cos\varphi_{iz} - F_{iy_i}\sin\varphi_{iz} - F_{iz_i}\sin\varphi_{ix}\cos\varphi_{iz} \\ F'^{e}_{iy} = F'_{iy} + F_{ix_i}\cos\varphi_{ix}\sin\varphi_{iz} + F_{iy_i}\cos\varphi_{iz} - F_{iz_i}\sin\varphi_{ix}\sin\varphi_{iz} \\ F'^{e}_{iz} = F'_{iz} + F_{ix_i}\sin\varphi_{ix} + F_{iz_i}\cos\varphi_{ix} \\ M'^{e}_{ix} = M'_{ix} + M_{ix_i}\cos\varphi_{ix}\cos\varphi_{iz} - M_{iy_i}\sin\varphi_{iz} - M_{iz_i}\sin\varphi_{ix}\cos\varphi_{iz} + \\ F_{iy_i}l_i\cos\varphi_{ix}\cos\varphi_{iz} - F_{iz_i}l_i\sin\varphi_{iz} \\ M'^{e}_{iy} = M'_{iy} + M_{ix_i}\cos\varphi_{ix}\sin\varphi_{iz} + M_{iy_i}\cos\varphi_{iz} - M_{iz_i}\sin\varphi_{ix}\sin\varphi_{iz} + \\ F_{iy_i}l_i\cos\varphi_{ix}\sin\varphi_{iz} + F_{iz_i}l_i\cos\varphi_{iz} \\ M'^{e}_{iz} = M'_{iz} + M_{ix_i}\sin\varphi_{ix} + M_{iz_i}\cos\varphi_{ix} - F_{iy_i}l_i\sin\varphi_{ix} \end{cases} \tag{3.179}$$

The equations above are valid for $i = 2, \ldots, n-1$. As shown in Figure 3.13, the angle α'_i positions the line l'_i with respect to the global x axis, while l_i is positioned by the angles φ_{iz} with respect to the xy global plane and φ_{iz} with respect to the global x axis. The other loads consist of the reaction loads on fixed node 1, already calculated at this step, and are expressed in global coordinates as:

$$\begin{cases} F_{1x} = F_{1x_1}\cos\varphi_{1z}\cos\varphi_{1x} - F_{1y_1}\sin\varphi_{1z}\sin\varphi_{1x} \\ F_{1y} = F_{1x_1}\cos\varphi_{1z}\sin\varphi_{1x} - F_{1y_1}\sin\varphi_{1z}\cos\varphi_{1x} \\ F_{1z} = F_{1x_1}\sin\varphi_{1z} + F_{1y_1}\cos\varphi_{1z} \\ M_{1x} = M_{1z_1}\cos\varphi_{1x} \\ M_{1y} = M_{1z_1}\sin\varphi_{1x} \end{cases} \tag{3.180}$$

The loads at node 1′ are purely external. The moment components were directly given in the global reference frame while the global components of the point force are:

$$\begin{cases} F'_{ix} = F'_i\cos\alpha'_{iz}\cos\alpha'_{ix} \\ F'_{iy} = F'_i\cos\alpha'_{iz}\sin\alpha'_{ix} \\ F'_{iz} = F'_i\sin\alpha'_{iz} \end{cases} \tag{3.181}$$

The external loads at node n' can be expressed in a similar manner.

It is thus possible to transform a three-dimensional parallel structure into a statically equivalent serial one that is composed of the output platform, loaded at the nodes 1′ through n′, by the forces and moments mentioned in the equations above and connected by two flexure hinges. The procedure described above is formal and was developed following the lines indicated when solving the problem of a planar parallel mechanism, in order to emphasize the absolute similitude in solving for the unknown reaction loads. Although it might seem at least a bit odd that a plate-like component (as the output rigid platform) is supported out of its plane by two legs (flexure hinges) only, the solution is indeed correct, as the other displacement constraints, imposed by the other flexure hinges, are still in place. In addition, it should be remembered that the assumption has been used so far that all junctions (link–link or link–support/platform) are rigid.

It should also be noted, however, that the number of applications that are purely parallel in three dimensions is quite reduced, as supporting an output platform directly on several flexure hinges that are mounted in parallel would serve little purpose from the viewpoint of either displacement or force modification. Many practical applications are designed having serial compliant chains that are placed in parallel instead of the single flexures, as is the case for three-dimensional hybrid mechanisms, which will be discussed next.

3.3.2.2 Spatial Hybrid Compliant Mechanisms

As mentioned previously, a hybrid mechanism can be analyzed for the three-dimensional case by extending the conclusions derived from a corresponding spatial parallel mechanism in the same manner that was explained for planar mechanisms. Figure 3.14 represents the schematic of a three-dimensional hybrid mechanism that is composed of n serial chains, each fixed at one end and rigidly connected to a rigid output platform at the other end. Each chain is composed of several flexure hinges and rigid links that are rigidly and serially connected. Similar to the planar case, a point load, mimicking the motive agent, acts on each of the serial links, while the loads acting on the flexures–output platform junctions are the same as the one utilized for three-dimensional parallel mechanisms.

The first task, again, is to determine a number of unknown reaction loads at the fixed ends of the serial chains that would render the problem determinate. It is obvious that the solving procedure used for parallel structures is also valid here. The only difference is that the serial chains are multiple and not singular, as in the situation with a purely parallel structure, which brings about the additional task of expressing normal forces, bending moments, and the partial derivatives that are required by Castigliano's displacement theorem for several flexure hinges instead of a single hinge per chain. It would be untractable and probably of only questionable usefulness to develop a formal mathematical algorithm that would explicitly give the

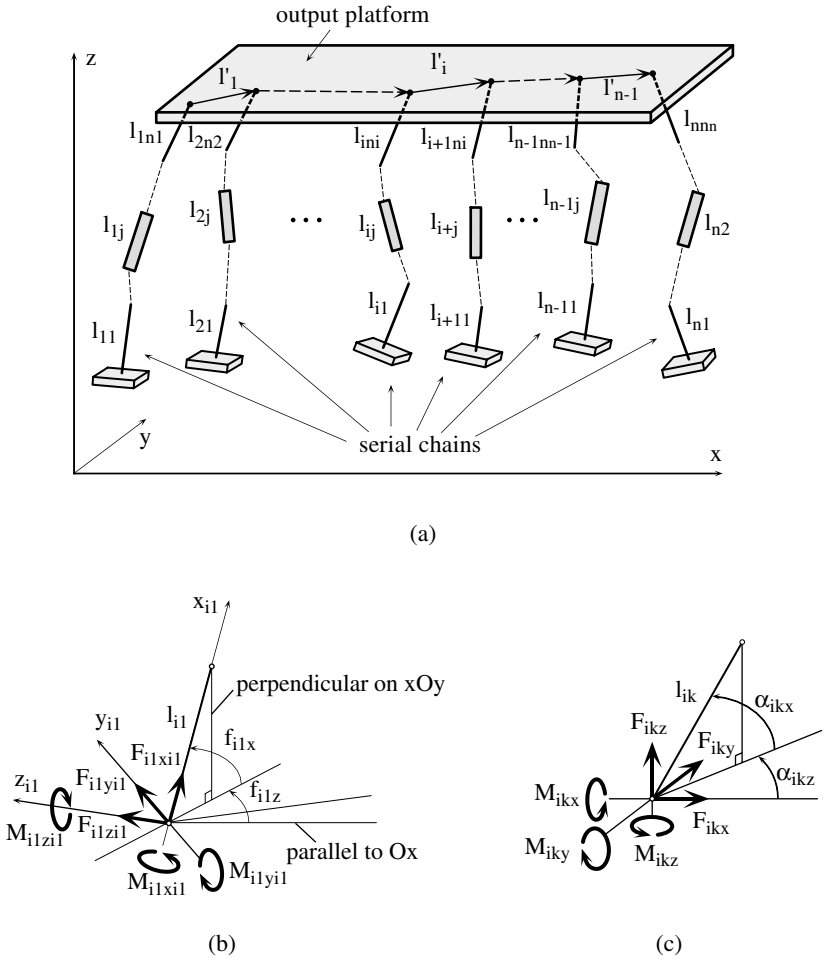

FIGURE 3.14
Schematic representation of three-dimensional hybrid compliant structure: (a) components; (b) defining geometry and reaction loading for a generic fixed flexure hinge component; (c) defining geometry and external loading for a generic intermediate member in a serial chain.

matrices and load vector necessary to solve for the $3(n - 1)$ component reaction load vector $\{R\}$ of Eq. (3.140).

Of real importance in many three-dimensional applications that are either parallel or hybrid is the position of the output platform as a function of the input. Determining the final position of the output plate is not at all difficult after solving for the reaction loads of the first $n - 1$ chains as previously detailed. The position of a plane (the output plate) is determined by three points that belong to that plane, as is well known, and finding the final positions of three points of the plane would solve the problem. The following algorithm can be applied:

- Take three points on the output plate (for instance, the points where three serial chains intersect the plate).
- Calculate their final position by applying Castigliano's displacement theorem and solving for a system made up of nine equations where the unknowns are the coordinates of the selected points: x_i, y_i, and z_i ($i = 1, 2, 3$).
- Make any other related calculations that would determine amounts of interest such as the displacement components of the center of the output plate (or of any other point that is relevant to the output) or angles determining the position of the output plate such as the roll, yaw, and pitch angles, which are generally used to specify the angular position of the output platform in three-dimensional applications.

References

1. Smith, S.T., *Flexures: Elements of Elastic Mechanisms*, Gordon & Breach, Amsterdam, 2000.
2. Howell, L.L., *Compliant Mechanisms*, John Wiley & Sons, New York, 2001.
3. Murphy, D.M., Midha, A., and Howell, L.L., The topological synthesis of compliant mechanisms, *Mechanism and Machine Theory*, 31(2), 185, 1996.
4. Howell, L.L. and Midha, A., Determination of the degrees of freedom of compliant mechanisms using the pseudo-rigid-body model concept, in *Proc. of the Ninth World Congress on the Theory of Machines and Mechanisms*, Milano, 1995, p. 1537.
5. Howell, L.L. and Midha, A., Compliant mechanisms, in *Modern Kinematics: Developments in the Last Forty Years*, A.G. Erdman, Ed., John Wiley & Sons, New York, 1993.
6. Saggere, L. and Kota, S., Synthesis of distributed compliant mechanisms for adaptive structures application: an elasto-kinematic approach, in *Proc. of DETC'97*, 1997 ASME Design Engineering Technical Conference, Sacramento, CA, 1997, p. 1.
7. Midha, A., Her, I., and Salamon, B.A., A methodology for compliant mechanism design. Part I. Introduction and large-deflection analysis, *Advances in Design Automation*, 44(2), 29, 1992.
8. Howell, L.L. and Midha, A., A method for the design of compliant mechanisms with small-length flexural pivots, *ASME Journal of Mechanical Design*, 116(1), 280, 1994.
9. Howell, L.L. and Midha, A., The development of force-deflection relationships for compliant mechanisms, *Machine Elements and Machine Dynamics*, 71, 501, 1994.
10. Howell, L.L. and Midha, A., Parametric deflection approximations for end-loaded, large-deflection beams in compliant mechanisms, *ASME Journal of Mechanical Design*, 117(1), 156, 1995.
11. Saxena, A. and Kramer, S.N., Simple and accurate method for determining large deflections in compliant mechanisms subjected to end forces and moments, *ASME Journal of Mechanical Design*, 120(3), 392, 1998.
12. Midha, A., Howell, L.L., and Norton, T.W., Limit positions of compliant mechanisms using the pseudo-rigid-body model concept, *Mechanism and Machine Theory*, 35, 99, 2000.

13. Dado, M.H., Variable parametric pseudo-rigid-body model for large-deflection beams with end loads, *International Journal of Non-Linear Mechanics*, 36, 1123, 2001.
14. Anathasuresh, G.K. et al., Systematic synthesis of microcompliant mechanisms: preliminary results, in *Proc. of the Third National Applied Mechanisms and Robotics Conference*, Cincinnati, OH, 1993, p. 82.1.
15. Ananthasuresh, G.K. and Kota, S., The role of compliance in the design of MEMS, in *Proc. of DETC/MECH'96,* 1996 ASME Design Engineering Technical Conference, 1996, p. 1309 (available on CD-ROM).
16. Jensen, B.D. et al., The design and analysis of compliant MEMS using the pseudo-rigid-body model, in *Proc. of the 1997 ASME International Mechanical Engineering Congress and Expo*, Dallas, TX, 1997, p. 119.
17. Salmon, L.G. et al., Use of the pseudo-rigid-body model to simplify the description of compliant micro-mechanisms, in *Proc. of the 1996 IEEE Solid-State and Actuator Workshop*, Hilton Head Island, SC, 1996, p. 136.
18. Kota, S. et al., Design of compliant mechanisms: applications to MEMS, *Analog Integrated Circuits and Signal Processing*, 29(1–2), 7, 2001.
19. Howell, L.L. and Midha, A., A loop-closure theory for the analysis and synthesis of compliant mechanisms, *ASME Journal of Mechanical Design*, 118(1), 121, 1996.
20. Kota, S. et al., Tailoring unconventional actuators using compliant transmissions: design methods and applications, *IEEE/ASME Transactions on Mechatronics*, 4, 396, 1999.
21. Hsiao, F.-Z. and Lin, T.-W., Analysis of a novel flexure hinge with three degrees of freedom, *Revue of Scientific Instruments*, 72(2), 1565, 2001.
22. Carricato, M., Parenti-Castelli, V., and Duffy, J., Inverse static analysis of a planar system with flexural pivots, *ASME Journal of Mechanical Design*, 123(2), 43, 2001.
23. Kim, W.-K., Yi, B.-J., and Cho, W., RCC characteristics of planar/spherical three degree-of-freedom parallel mechanisms with joint compliances, *ASME Journal of Mechanical Design*, 123, 10, 2000.
24. Clark, J.W. et al., Three-dimensional MEMS simulation modeling using modified nodal analysis, in *Proc. of the Microscale Systems: Mechanics and Measurements Symposium*, Orlando, FL, 2000, p. 68.

4

Dynamics of Flexure-Based Compliant Mechanisms

4.1 Introduction

The dynamics of mechanisms that include flexible links has received a lot of consideration in the last years, directly reflecting the increase in both the number and scope of applications for which the dynamic response must be accurately modeled in order to ensure that the mechanisms operate properly in the dynamic range. *Flexible multibody systems* is a general term that refers to and includes the formulation, solution, and analysis of rigid–flexible mechanical systems (the compliant mechanisms are part of this group) in terms of their dynamic response. Basic and more evolved topics of multibody flexible systems are detailed in specialty monographs, such as the one of Shabana.[1] The dynamics of multibody systems can be approached by means of two main categories of methods: distributed parameter and finite element. For distributed-parameter methods, the elastically deformable links are modeled as continuous members and the resulting mathematical formulation (that also includes the contributions of the rigid links) is a boundary-value problem described by a system of partial differential equations, as mentioned by Meirovitch.[2] Such a complex system of equations seldom yields easy-to-find closed-form solutions; therefore, approximate methods are further employed that generally use spatial discretization (the continuous spatial dependence of the unknowns of the problem are concentrated at several stations, according to assumed distribution laws) in order to simplify the problem. The procedure actually transforms a distributed-parameter system into an equivalent lumped-parameter one for which the equations can be solved with less effort and oftentimes produce closed-form solutions.

The works of Gao[3] and Bagci and Streit[4] provide a concise and valuable overview of the relevant literature that treats the research of the dynamic response of flexible mechanisms and manipulators. A key aspect in formulating the dynamic model of a compliant mechanism is selecting the modality in which the deformations of the elastic members are expressed. The majority of such formulations, as noted by Boutaghou and Erdman,[5] start the

modeling by formulating the elastic deformations in terms of local reference frames, which is rather straightforward initially but imposes further transformation of the mathematical model in terms of the global frame, which generally leads to highly nonlinear problems. The other option is to directly formulate the dynamic model with respect to the global frame, as performed by Simo and Vu-Quoc,[6] who analyzed mechanical systems that include flexible beams with large deformation capabilities. This approach is more difficult to tackle in its original phase but produces systems of differential equations that are simpler. Because of the importance of adequately selecting the reference frames, a great part of the research focus in this area is directed toward defining reference frames that would simplify the mathematical formulation and solution of the dynamic problem. McPhee,[7] for instance, utilized the concept of "branch coordinates" in order to develop an algorithm that automatically generates a minimum number of differential equations, whereas Liew et al.[8] developed a procedure that is aimed at reducing the number of elastic coordinates through the direct inclusion of the free- and fixed-interface boundary conditions into the main formulation.

Utilizing symbolic calculation appears to be another route for simplifying the mathematical complexity posed by the dynamic modeling of compliant mechanisms. Examples of this approach include the works of Engstler and Kaps,[9] who formulated a dynamic model in descriptor form by means of differential algebraic equations; Cui and Haque,[10] who gave a symbolic vector–matrix formulation resulting in improved simulation efficiency; and Boyer and Coiffet,[11] who reduced the number of dynamic equations by applying a symbolic variant of d'Alembert's principle. Other methods for formulating the dynamic model of compliant (flexible) mechanisms utilize Lagrange's equations, such as applied by Vibet[12] to multibody systems without loops or Surdilovic and Vukobratovic,[13] who developed a generalized method in order to model several types of flexible links.

Other methods of dynamic model formulation are Hamilton's variational principle, as mentioned by Yu[14] in studying a class of flexible robots with two rigid links and three flexible joints, and Lyapunov analysis, as exemplified by Indri and Tornambe.[15] Generally, the dynamic modeling of compliant mechanisms addresses the modal, steady-state, and transient responses of such mechanisms. In a recent paper, Lyon et al.[16] utilized the pseudo-rigid-body model to predict the natural frequency of four different compliant mechanisms, and the results differed by less than 9% from the finite-element simulation results.

Except for the recent monograph by Smith,[17] information regarding the dynamic modeling of flexure-based compliant mechanisms (the flexure hinges being of variable geometry, as discussed in this book) is rather scarce. Smith[17] discussed the dynamic modeling and corresponding modal responses of several planar flexible mechanisms, including a four-bar mechanism with two flexures and a similar mechanism having four flexure hinges. The flexure hinges were modeled in these examples as one-degree-of-freedom (DOF) members, so only their direct-bending stiffness was taken into consideration.

A first generalization was also formulated to enable modeling a single-axis flexure hinge as a three-DOF subsystem by applying Lagrange's equations. The kinetic energy was considered as being strictly produced by the motion of the rigid links, whereas the elastic potential energy was given by the elastic deformations of the flexures. The stiffness matrix of a single-axis flexure hinge was expressed as a diagonal matrix that is reformulated here by using the notations that were introduced in Chapter 2, namely:

$$[K] = \begin{bmatrix} K_{1,x-F_x} & 0 & 0 \\ 0 & K_{1,y-F_y} & 0 \\ 0 & 0 & K_{1,\theta_z-M_z} \end{bmatrix} \tag{4.1}$$

With regard to symbolism, it should be remembered that the subscript 1 indicates that the displacement (translatory or rotary) is determined at the end 1 of the flexure hinge with respect to the other fixed end (denoted by 2), whereas the *a–b* subscript that follows the number 1 represents the displacement–load relationship. The formulation mentioned above as given by Smith[17] differs slightly from the one developed in this book, which basically formulates the stiffness matrix of a single-axis flexure hinge as:

$$[K] = \begin{bmatrix} K_{1,x-F_x} & 0 & 0 \\ 0 & K_{1,y-F_y} & K_{1,y-M_z} \\ 0 & K_{1,y-M_z} & K_{1,\theta_z-M_z} \end{bmatrix} \tag{4.2}$$

As can be seen by comparing Eqs. (4.1) and (4.2), the formulation developed by Smith[17] neglects the cross-bending term $K_{1,y-Mz}$ (which is equal to $K_{1,\theta z-Fy}$, as shown in Chapter 2; this equality has been used in Eq. (4.2) for the corresponding stiffness term on the third row), which connects the tip deflection to a moment applied at the same point or, equivalently, the tip slope to the tip force that produces bending. Smith[17] also presents the matrix equations that enable transformation of the dynamic equations between different reference frames for both planar and spatial compliant mechanism applications. Also discussed in Smith[17] is the influence of the drive elements (piezoelectric or feed screws), which are treated as additional linear springs that add axial stiffness (and the corresponding potential elastic energy) into the compliant mechanism system.

The modeling procedure presented in this chapter aims to extend the formulation that so far has concentrated on thoroughly defining the single-, multiple-, and two-axis flexure hinges in terms of their compliances (or, conversely, stiffnesses, as detailed in Chapter 2) and in qualifying the static (quasi-static) response of flexure-based compliant mechanisms in either a planar or spatial configuration for serial, parallel, and hybrid structures, as discussed in Chapter 3. The extension here targets the response of flexure-based

compliant mechanisms in the dynamic range; namely, it focuses on formulating the dynamic equations that would enable studying the modal (free) response or the forced response (under steady-state or transitory excitation) by possibly considering the internal and external damping.

It was shown in Chapter 2 that single-axis flexure hinges can be modeled as three-DOF members, whereas multiple- and two-axis flexures can be represented as six- and five-DOF members, respectively, and this definition will be kept unaltered. Inertia and damping fractions will be derived corresponding to each individual degree of freedom for single-, multiple-, and two-axis flexure hinges so that these properties consistently add to the already-defined stiffness (compliance) characteristics and, together, thoroughly define a given flexure. The Rayleigh principle is utilized for deriving both inertia and damping lumped fractions, but the resulting solutions are generally not closed form because of the complexity induced by the generally variable cross-section of the flexures.

Providing a tool that is capable of formulating inertia and damping properties corresponding to each separate degree of freedom of a flexure hinge is particularly important in systems that must be precisely designed in order to provide a finely tuned dynamic response. In many MEMS applications, for instance, the influence of the inertia and/or damping owing to flexure hinges is key to their operation, especially when such flexures are not attached to other links that are substantially larger (heavier). The inertia and damping properties are derived for both long (Euler–Bernoulli) flexure hinges and short (Timoshenko) flexures, where rotary inertia and shearing effects have to be taken into consideration. By adding the contribution of the rigid links, primarily in terms of inertia, Lagrange's equations are utilized to derive and discuss in a generic manner the dynamic equations of motions for planar/spatial serial, parallel, and hybrid flexure-based compliant mechanisms, and corresponding numerical solution techniques are subsequently presented.

The dynamics of flexure-based compliant mechanisms will be approached by means of Lagrange's equations formulated based on the scalar quantities of kinetic energy, potential energy, and dissipation energy. In its general form and for an undamped dynamic system, the Lagrange's equations are:

$$\frac{d}{dt}\left(\frac{\partial T}{\partial \dot{q}_i}\right) - \frac{\partial T}{\partial q_i} + \frac{\partial U}{\partial q_i} = Q_i \tag{4.3}$$

where T is the kinetic energy, U is the potential energy, and Q_i is the generalized force (can be either a force or a moment derivable from the corresponding work done by the respective agent). In the case of the free response (modal analysis), the generalized force is zero. For a dynamic system where the damping is present, the corresponding Lagrange's equations are:

$$\frac{d}{dt}\left(\frac{\partial T}{\partial \dot{q}_i}\right) - \frac{\partial T}{\partial q_i} + \frac{\partial U}{\partial q_i} + \frac{\partial U_d}{\partial \dot{q}_i} = Q_i \tag{4.4}$$

where U_d is the dissipation energy lost by a system through internal viscous damping.

The quantities q_i are the generalized coordinates or degrees of freedom that uniquely define the position of the system under dynamic excitation. It should be noted that the generalized coordinates are not always identical to the physical coordinates that apparently represent the minimum number of parameters fully determining the state of a dynamic system. In order to qualify as generalized coordinates, the candidate coordinates must be independent. Most of the time, however, the motion of a system is such that the coordinates are related through constraint equations, which bring about several dependence relationships and therefore eliminate some of the coordinates that were considered as possible generalized coordinates. The general rule is (see Thomson,[18] for instance) that the number of generalized coordinates is equal to the total number of candidate-generalized coordinates minus the number of superfluous coordinates (coordinates that are not necessary to completely define the state of a dynamic system). When the number of superfluous coordinates is equal to the number of constraint equations that can be formulated, such a system is called *holonomic*, and the flexure-based compliant mechanisms that are analyzed here are all holonomic. Establishing the number of generalized coordinates or degrees of freedom for a given flexure-based compliant mechanism is of primary importance, as Lagrange's equations are formulated in terms of such coordinates. As a consequence, for each type of mechanism that will be studied, an initial analysis will be carried out first in order to establish the correct number of degrees of freedom for that specific mechanism.

The potential and kinetic energy will be first formulated for the three types of flexure hinges that have been discussed so far: single-, multiple-, and two-axis configurations. Subsequently, the potential and kinetic energy terms will be expressed for planar and spatial flexure-based compliant mechanisms, and Lagrange's equations will be formulated and then solved for several applications by studying the free and forced response of the respective systems. The damping in flexure hinges, both internal and external, will further be discussed, and the dynamic equations for flexure-based compliant mechanisms will be completed by adding the corresponding damping contributions.

4.2 Elastic Potential Energy for Individual Flexure Hinges

4.2.1 Single-Axis Flexure Hinges

For a planar serial compliant mechanism that is composed of only single-axis flexure hinges, each flexure hinge can be treated as a three-DOF component, where the said degrees of freedom are the axial displacement, deflection, and slope (rotation angle) of one end in terms of the other fixed end,

as previously mentioned. As a consequence, a system that is composed of n links (generally treated as flexure hinges, as a rigid link is a flexure hinge with zero compliance) will possess a maximum of $3n$ DOFs (in the absence of constraints), so the dimension of the differential equations system, Eq. (4.2), will be $3n$ as well.

By utilizing the assumption that the work done by the external load on a planar flexure hinge converts into internal strain energy:

$$W = U \tag{4.5}$$

one can start by expressing the work performed quasi-statically by the load vector formed by F_{1x}, F_{1y}, and M_{1z} as:

$$W = \frac{1}{2}(F_{1x}u_{1x} + F_{1y}u_{1y} + M_{1z}\theta_{1z}) \tag{4.6}$$

where the loads and displacements are noted according to their definitions introduced in Chapter 2. As also shown in Chapter 2, the force–deformation relationship for this type of three-DOF flexure hinge can be put in matrix form in terms of stiffness as:

$$\begin{Bmatrix} F_{1x} \\ F_{1y} \\ M_{1z} \end{Bmatrix} = \begin{bmatrix} K_{1,x-F_x} & 0 & 0 \\ 0 & K_{1,y-F_y} & K_{1,y-M_z} \\ 0 & K_{1,y-M_z} & K_{1,\theta_z-M_z} \end{bmatrix} \begin{Bmatrix} u_{1x} \\ u_{1y} \\ \theta_{1z} \end{Bmatrix} \tag{4.7}$$

By expressing the load components of Eq. (4.7), substituting them into Eq. (4.6), and by considering the equality of Eq. (4.5), the strain energy of one planar single-axis flexure hinge becomes:

$$U = U_a + U_{db,z} + U_{cb,z} \tag{4.8}$$

where U_a is the axial strain energy and is given by:

$$U_a = \frac{1}{2}K_{1,x-F_x}u_{1x}^2 \tag{4.9}$$

$U_{db,z}$ represents the z-axis direct-bending strain energy and is given by:

$$U_{db,z} = \frac{1}{2}(K_{1,y-F_y}u_{1y}^2 + K_{1,\theta_z-M_z}\theta_{1z}^2) \tag{4.10}$$

while $U_{cb,z}$ is the z-axis cross-bending strain energy, formulated as:

$$U_{cb,z} = K_{1,y-M_z}u_{1y}\theta_{1z} \tag{4.11}$$

4.2.2 Multiple-Axis Flexure Hinges

The multiple-axis (or revolute) flexure hinges were shown to possess six DOFs through discretization of their elastic (compliant) and inertia properties. As a consequence, a compliant mechanism that incorporates such members can be described by a maximum number of $6n$ DOFs. The force–displacement matrix equation for this type of flexure hinge is:

$$\begin{Bmatrix} F_{1x} \\ F_{1y} \\ F_{1z} \\ M_{1x} \\ M_{1y} \\ M_{1z} \end{Bmatrix} = \begin{bmatrix} K_{1,x-F_x} & 0 & 0 & 0 & 0 & 0 \\ 0 & K_{1,y-F_y} & 0 & 0 & 0 & K_{1,y-M_z} \\ 0 & 0 & K_{1,y-F_y} & 0 & K_{1,y-M_z} & 0 \\ 0 & 0 & 0 & K_{1,\theta_x-M_x} & 0 & 0 \\ 0 & 0 & K_{1,y-M_z} & 0 & K_{1,\theta_y-M_y} & 0 \\ 0 & K_{1,y-M_z} & 0 & 0 & 0 & K_{1,\theta_y-M_y} \end{bmatrix} \begin{Bmatrix} u_{1x} \\ u_{1y} \\ u_{1z} \\ \theta_{1x} \\ \theta_{1y} \\ \theta_{1z} \end{Bmatrix} \tag{4.12}$$

Following a reasoning that is similar to the one applied for single-axis flexure hinges, the potential energy of a generic revolute flexure hinge is of the form:

$$U = U_a + U_{db,z} + U_{cb,z} + U_{db,y} + U_{cb,y} + U_t \tag{4.13}$$

where it has been acknowledged that the bending takes place about two perpendicular directions z and y, and the torsion (indicated by the subscript t) is also present. The terms that are new in Eq. (4.13) are:

$$U_{db,y} = \frac{1}{2}(K_{1,y-F_y} u_{1z}^2 + K_{1,\theta_y-M_y} \theta_{1y}^2) \tag{4.14}$$

$$U_{cb,y} = K_{1,y-M_z} u_{1z} \theta_{1y} \tag{4.15}$$

$$U_t = \frac{1}{2}(K_{1,\theta_x-M_x} \theta_{1x}^2) \tag{4.16}$$

4.2.3 Two-Axis Flexure Hinges

It was demonstrated in Chapter 2 that a two-axis flexure hinge can be discretized by utilizing five DOFs to describe the free-end motion capabilities in terms of the fixed end. As a consequence, a system that is composed of n such

members will have a maximum number of 5*n* DOFs. The force–displacement stiffness-based matrix equation is, in this case:

$$\begin{Bmatrix} F_{1x} \\ F_{1y} \\ F_{1z} \\ M_{1y} \\ M_{1z} \end{Bmatrix} = \begin{bmatrix} K_{1,x-F_x} & 0 & 0 & 0 & 0 \\ 0 & K_{1,y-F_y} & 0 & 0 & K_{1,y-M_z} \\ 0 & 0 & K_{1,z-F_z} & 0 & K_{1,z-M_y} \\ 0 & 0 & K_{1,z-M_y} & K_{1,\theta_y-M_y} & 0 \\ 0 & K_{1,y-M_z} & 0 & 0 & K_{1,\theta_z-M_z} \end{bmatrix} \begin{Bmatrix} u_{1x} \\ u_{1y} \\ u_{1z} \\ \theta_{1y} \\ \theta_{1z} \end{Bmatrix} \tag{4.17}$$

The total strain energy stored in this type of flexure is:

$$U = U_a + U_{db,z} + U_{cb,z} + U_{db,y} + U_{cb,y} \tag{4.18}$$

and it shows the contributions brought by the axial and mixed bending effects. The terms that are different compared to the ones that were already introduced are:

$$U_{db,y} = \frac{1}{2}(K_{1,z-F_z} u_{1z}^2 + K_{1,\theta_y-M_y} \theta_{1y}^2) \tag{4.19}$$

$$U_{cb,y} = K_{1,z-M_y} u_{1z} \theta_{1y} \tag{4.20}$$

4.3 Kinetic Energy for Individual Flexure Hinges

4.3.1 Introduction and the Rayleigh Principle

The aim of Chapter 2 was to define various configurations of flexure hinges in terms of their compliances (or stiffnesses) by expressing the displacements or rotations of either one end (the one considered free) or the midpoint with respect to the other (fixed) end. In doing so it was possible to choose a finite number of degrees of freedom to fully describe the compliant behavior of a given flexure hinge. In a nutshell, this process is actually a discretization one, as it transforms the distributed elastic properties of a member into a finite number of degrees of freedom that are equivalent to the original properties. A similar discretization process is applied now in order to transform the distributed mass properties of a flexure hinge into lumped inertia fractions that are equivalent to the original system about the degrees of freedom that were already defined by the elastic properties discretization. The criterion of realizing this equivalence will be an energy one; specifically, it will define a discrete inertia system whose kinetic energy is equal to the

kinetic energy of the original distributed-inertia flexure hinge. The purpose of discretizing the inertia of a flexure hinge is to permit further development of the dynamic equations that all involve inertia properties in either the undamped free response (modal analysis) where the governing linearized matrix equation is:

$$[M]\left\{\frac{d^2u}{dt^2}\right\}+[K]\{u\}=\{0\} \tag{4.21}$$

or the undamped forced response for which the dynamic equation is of the form:

$$[M]\left\{\frac{d^2u}{dt^2}\right\}+[K]\{u\}=\{F\} \tag{4.22}$$

In both Eqs. (4.21) and (4.22), $[K]$ is the stiffness matrix that is the inverse of the compliance matrix $[C]$ whose components have been derived for various flexure hinge configurations in Chapter 2, while $[M]$ is the mass matrix that will be derived here. Discussion will include the process of inertia discretization for single-, multiple-, and two-axis flexure hinges. It should be pointed out that axial, bending, and torsional effects will be considered as acting independently and therefore will be decoupled, as this assumption is consistent with the customary first-order beam theory, where such effects are considered separately. It is beyond the scope of this work to attack the problem of deriving lumped-parameter inertia fractions based on the second-order beam theory where bending is coupled to axial and/or torsional effects.

It is well known that two models are most often utilized when analyzing the vibratory response of beam-type members. The Euler–Bernoulli model is applied with accurate results in the majority of engineering applications that contain beam-like elements, which can be considered long as discussed in Chapter 2. The free response of a Euler–Bernoulli beam in bending consists of a fourth-order partial differential equation, the unknown, and the deflection, depending on two variables, one spatial (the position on the beam of a current point) and the other time. Details on solving this partial differential equation are given, for example, in Thomson,[18] Inman,[19] and Weaver et al.[20] A more precise description of the vibratory response of a beam is given by the Timoshenko model (again, details can be found in the references cited above), which accounts for two additional effects: shearing effects (which are present in short components that are subjected to bending, as analyzed in Chapter 2) and rotary inertia. The vibratory model of a Timoshenko beam consists of two coupled fourth-order partial differential equations (again, details can be found in the references mentioned above). It was shown in Chapter 2 how the compliant nature of a flexure hinge modifies when the shearing effects are considered vs. the situations where such aspects

are neglected. The two models mentioned above will be utilized here to derive the inertia properties of flexure hinges that vibrate in bending.

The effective inertia or Rayleigh method, as indicated by Thomson,[18] provides the means for taking into account the contribution of a distributed-mass member, such as a bar or a beam, that is connected to other massive members whose masses are customarily the only ones considered in modal (natural frequency) calculation, for instance. The method basically transforms the distributed inertia of such a light, flexible member into an equivalent (effective) inertia property that is lumped at a given location by equating the kinetic energies of the actual and equivalent systems. In this equivalence process, the velocity distribution is assumed to be identical to that of the source displacement. In other words, a linear velocity will have a distribution that is identical to that of the corresponding linear displacement, while an angular velocity is assumed to be distributed in a fashion that is identical to that of the corresponding angular displacement.

4.3.2 Inertia Properties of Flexure Hinges as Long (Euler–Bernoulli) Members

The assumptions under which the Euler–Bernoulli beam model is operational were mentioned at the beginning of Chapter 2, but, in a nutshell, two assumptions are basic to this model:

1. Plane sections remain plane and perpendicular to the deformed neutral axis, after the bending/loading has been applied (Bernoulli hypothesis).
2. The beam-like members are considered long; therefore, no shearing effects are taken into consideration.

The distributed-inertia system of a flexure hinge will be transformed into equivalent discrete inertia properties that are located at the end of the flexure hinge, which is considered free. As shown next, the model is not a pure Euler-beam model as it will generate a rotary inertia fraction to account for a rotational degree of freedom that characterizes the compliant behavior of any flexure hinge. A simpler approach for a Euler–Bernoulli beam was followed by Lobontiu et al.,[21] where the rotary inertia was ignored in deriving the lumped-parameter mass corresponding to the bending vibrations of a piezoelectrically actuated cantilevered beam. Lee et al.[22,23] investigated the transverse vibrations of nonuniform beams that have either fixed (homogeneous) or elastic nonhomogeneous boundary conditions in terms of both material properties and cross-sectional area by solving the fourth-order partial differential equation that was formulated through using several nondimensional parameters and approximation polynomials. An approach that includes the rotary effects can be found in Weaver et al.,[20] where the importance

of including the rotary inertia in the dynamic model of a vibrating beam is highlighted, especially when attempting to accurately model the high-frequency response of such systems.

4.3.2.1 Single-Axis Flexure Hinges

As previously mentioned in this chapter, a single-axis flexure hinge can be described in terms of inertia by a diagonal 3 × 3 inertia matrix that corresponds to the three DOFs of such a flexure hinge according to the compliance/stiffness discretization. The three inertia fractions (namely, m_x, m_y, and J_z) denote three entities that are inertia decoupled and, therefore, can be considered as capable of independent motion. Because m_x and m_y are mass fractions that translate along the local axes x and y, respectively, of one flexure, they will possess kinetic energy of the form:

$$T_{tr} = \frac{1}{2} m_x v_x^2 + \frac{1}{2} m_y v_y^2 \tag{4.23}$$

where v_x and v_y are the velocities of the translation mass fractions m_x and m_y, respectively, recorded with respect to a fixed reference frame. More details will be given when analyzing the dynamics of specific flexure-based compliant mechanisms. Discretization of the inertia for a single-axis flexure hinge also includes a rotary inertia term, for which the kinetic energy is:

$$T_{rot} = \frac{1}{2} J_z \omega_z^2 \tag{4.24}$$

The angular velocity ω_z is again calculated with respect to a fixed frame; more details will be given when studying different examples of specific compliant mechanisms. The total kinetic energy is, of course, the sum of the translatory and rotary kinetic energy terms:

$$T = T_{tr} + T_{rot} \tag{4.25}$$

It was shown in Chapter 2 that a single-axis flexure hinge can basically be defined in terms of its in-plane compliant behavior by four compliance factors: $C_{1,x-Fx}$ (describing axial effects), $C_{1,y-Fy}$ and $C_{1,\theta z-Mz}$ (quantifying direct-bending effects), and $C_{1,y-Mz}$ (denoting cross-bending effects). These four distinct compliance parameters can be arranged into a 3 × 3 compliance matrix that is associated with a dimension-3 displacement vector $\{u\}$ that is formed of the free-end axial displacement u_{1x}, deflection u_{1y}, and rotation angle (slope) θ_{1z}. It is clear that this type of discretization is based on three DOFs, which are the above-mentioned nodal displacements. It is therefore necessary that the mass matrix also be a 3 × 3 matrix, as the dynamic

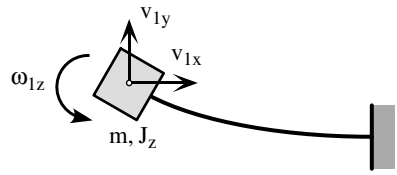

FIGURE 4.1
Mass attached to a flexible member and having a three-DOF plane motion.

equation (corresponding to the force response, for instance) must be compatible and of the general form:

$$\begin{bmatrix} m_{1x} & 0 & 0 \\ 0 & m_{1y} & 0 \\ 0 & 0 & J_{1z} \end{bmatrix} \begin{Bmatrix} \ddot{u}_{1x} \\ \ddot{u}_{1y} \\ \ddot{\theta}_{1z} \end{Bmatrix} + \begin{bmatrix} K_{1,x-F_x} & 0 & 0 \\ 0 & K_{1,y-F_y} & K_{1,y-M_z} \\ 0 & K_{1,y-M_z} & K_{1,\theta_z-M_z} \end{bmatrix} \begin{Bmatrix} u_{1x} \\ u_{1y} \\ \theta_{1z} \end{Bmatrix} = \begin{Bmatrix} F_{1x} \\ F_{1y} \\ M_{1z} \end{Bmatrix} \quad (4.26)$$

It has been assumed in Eq. (4.26) that the nodal load vector components are applied at node 1. The mass matrix in Eq. (4.26) is formulated in a diagonal form as it can be assumed that the three-DOFs are inertia decoupled. Such a hypothesis has a physical background, as we can imagine a solid that is fixed at the end of a massless flexible member which can deform both axially and in bending, as illustrated in Figure 4.1, and which is bound to have a plane motion.

The solid can translate along the x axis due to axial deformation of the flexible member and the y-axis due to deflection of the same member and can rotate around its central axis due to the end slope of the flexible link. A similar problem is posed when attempting to transform the distributed-inertia flexure hinge into a discretized (lumped) mass equivalent system. The only difference consists in the fact that different inertia fractions (m_{1x}, m_{1y}, and J_{1z}, as shown in Eq. (4.26)) have to result from the equivalence process corresponding to the three-DOF system.

The assumption that stands at the basis of Rayleigh's principle can be justified simply by analyzing the free response of a flexible member with distributed properties. The solution in such cases can be expressed as the product between a space-dependent solution and a time-dependent one, as shown in Inman,[19] for instance, in the form:

$$u(x,t) = u(x)u(t) \quad (4.27)$$

Because the velocity at a given point on the flexible member and at a given time is the time derivative of the displacement function, it follows from Eq. (4.27) that:

$$v(x,t) = u(x)\frac{du(t)}{dt} \quad (4.28)$$

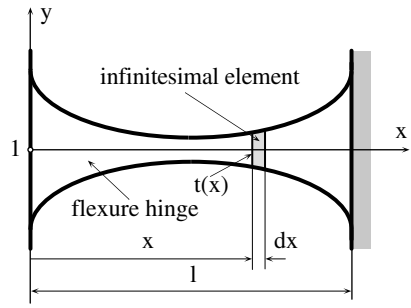

FIGURE 4.2
Vibrating flexure hinge and infinitesimal element for effective inertia derivation.

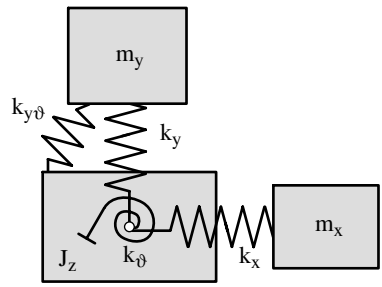

FIGURE 4.3
Alternative representation of a single-axis flexure hinge with discretized stiffness and inertia.

which demonstrates that the velocity field has the same space distribution as the source displacement field.

The axial loading and bending of a flexure hinge will be analyzed separately in terms of mass discretization based on Figure 4.2. The two-dimensional flexure hinge will be discretized into three distinct and mechanically decoupled inertia fractions, as previously mentioned: one mass fraction, denoted by m_x, which corresponds to the axial vibrations of the flexure hinge; one mass fraction, m_y, resulting from the distributed mass that vibrates in bending and has a translatory motion; and one body that rotates and therefore is defined by a mass moment of inertia J_z and which is also produced through bending. The last two inertia properties will be determined through a coupled process as they are produced by causes that are also connected (as is the case for the deflection and rotation angle of a flexing beam). An illustration of this situation is shown in Figure 4.3, where the equivalent mass–stiffness model of a flex–tensional member is indicated.

4.3.2.1.1 Axial Vibration

The kinetic energy of the element shown in Figure 4.2 about the x axis can be generically expressed as:

$$dT_a = \frac{1}{2}\rho A(x) v_x^2(x)\, dx \tag{4.29}$$

where ρ is the material density, $A(x)$ is the cross-sectional area, and $v_x(x)$ is the velocity at a distance x measured from the free end of the flexure. It has been shown in Chapter 2 that the axial displacement of free end 1 can be expressed in terms of an axial force acting at that point in terms of the axial compliance $C_{1,x-Fx}$ as:

$$u_{1x} = C_{1,x-F_x} F_{1x} \tag{4.30}$$

and the axial compliance has explicitly been given for several flexure hinge configurations. A similar relationship is valid when expressing the displacement of the generic point situated at a distance x from the free end as produced by the same force F_{1x}:

$$u_x(x) = C_{x,x-F_x}(x) F_{1x} \tag{4.31}$$

where the axial compliance is formulated by taking into consideration the elastic properties of the segment between the free end and the current point as:

$$C_{x,x-F_x}(x) = \frac{1}{E}\int_0^x \frac{1}{A(x)}\, dx \tag{4.32}$$

Combining Eqs. (4.30) and (4.31) gives:

$$u_x(x) = f_a(x) u_{1x} \tag{4.33}$$

with:

$$f_a(x) = \frac{C_{x,x-F_x}(x)}{C_{1,x-F_x}} \tag{4.34}$$

By applying the assumption that the velocity field distribution is identical to that of the displacement field, it follows that:

$$v_x(x) = f_a(x) v_{1x} \tag{4.35}$$

Substituting Eq. (4.35) into Eq. (4.29) and integrating over the entire length of the flexure hinge gives the total kinetic energy when the flexure vibrates axially:

$$T_a = \frac{\rho v_{1x}^2}{2} \int_0^l A(x) f_a^2(x)\, dx \tag{4.36}$$

The kinetic energy of an equivalent mass that vibrates axially with a velocity v_{1x} and is attached at the free end of the flexure is simply:

$$T = \frac{1}{2} m_x v_{1x}^2 \tag{4.37}$$

Because the actual and equivalent systems must have the same kinetic energy (which means that Eqs. (4.36) and (4.37) give the same quantity), the effective mass, m_x, is:

$$m_x = \rho \int_0^l A(x) f_a^2(x)\, dx \tag{4.38}$$

Obviously, the effective mass corresponding to the axial vibration is dependent on the geometry of the specific flexure under consideration, and, unfortunately, the integral of Eq. (4.38) cannot be solved analytically to yield a closed-form expression for m_x in the form of the compliances that were given in Chapter 2.

A check has been performed to verify that the generic formulation developed here, of the effective mass for variable cross-section bars (as the flexure hinges are) in axial vibration, reduces to the known corresponding expression of a similar constant cross-section fixed–free bar. Thomson[18] demonstrates that for such a bar the effective mass (the mass that must be placed at the free end) is one third of the total mass. Equations (4.34) and (4.38) have been solved for all the single-axis flexure hinges that were introduced in Chapter 2 by imposing the corresponding geometric conditions that would render a specific variable cross-section flexure into a constant cross-section one. For instance, as also mentioned in Chapter 2, for the corner-filleted flexure hinge, the condition that the fillet radius tends to zero has been applied, whereas for all the other flexure configurations (except the circular one) the condition that the parameter c tends to zero has been enforced. In all cases, the value of the effective mass mentioned above was retrieved.

4.3.2.1.2 Bending Vibration

A similar approach will be taken in order to find the equivalent (effective) inertia properties of a flexure hinge that vibrates in bending. As shown in Chapter 2, because coupling effects between forces and moments are present

when analyzing bending, a few details must be mentioned to develop a formulation that would go along the path taken for axial vibration effective mass determination. The free-end slope and deflection of a flexure hinge can be expressed, as shown in Chapter 2, as:

$$\begin{cases} \theta_{1z} = C_{1,y-M_z} F_{1y} + C_{1,\theta_z-M_z} M_{1z} \\ u_{1y} = C_{1,y-F_y} F_{1y} + C_{1,y-M_z} M_{1z} \end{cases} \tag{4.39}$$

Similar relationships are valid when expressing the slope and deflection at a generic point, as produced by the same endpoint load, namely:

$$\begin{cases} \theta_z(x) = C_{x,y-M_z}(x) F_{1y} + C_{x,\theta_z-M_z}(x) M_{1z} \\ u_y(x) = C_{x,y-F_y}(x) F_{1y} + C_{x,y-M_z}(x) M_{1z} \end{cases} \tag{4.40}$$

The variable compliance factors in Eq. (4.40) are:

$$\begin{cases} C_{x,y-F_y}(x) = \dfrac{1}{E}\displaystyle\int_0^x \frac{x^2}{I_z(x)}\,dx \\ C_{x,y-M_z}(x) = \dfrac{1}{E}\displaystyle\int_0^x \frac{x}{I_z(x)}\,dx \\ C_{x,\theta_z-M_z}(x) = \dfrac{1}{E}\displaystyle\int_0^x \frac{1}{I_z(x)}\,dx \end{cases} \tag{4.41}$$

It is known that the slope function is the derivative of the deflection function in terms of the space variable, according to the small-displacement beam theory, namely:

$$\theta_z(x) = \frac{du_y(x)}{dx} \tag{4.42}$$

and, as a consequence, the slope function can be formulated by taking the space derivative of $u_y(x)$ as shown in the second expression of Eq. (4.40):

$$\theta_z(x) = \frac{dC_{x,y-F_y}(x)}{dx} F_{1y} + \frac{dC_{x,y-M_z}(x)}{dx} M_{1z} \tag{4.43}$$

Combining the first expression in Eq. (4.40) with Eq. (4.43) gives M_{1z} in terms of F_{1y}:

$$M_{1z} = f_y(x)F_{1y} \tag{4.44}$$

with:

$$f_y(x) = \frac{\frac{dC_{x,y-F_y}(x)}{dx} - C_{x,y-M_z}(x)}{C_{x,\theta_z-M_z}(x) - \frac{dC_{x,y-M_z}(x)}{dx}} \tag{4.45}$$

Equations (4.44) and (4.45) permit expression of the slope and deflection at a generic position in terms of only one load component which renders the problem tractable for the axial vibration-related mass fraction.

The elemental kinetic energy pertaining to bending-related translation vibration about the y axis can be expressed as:

$$dT_{by} = \frac{1}{2}\rho A(x)v_y^2(x)\,dx \tag{4.46}$$

The Rayleigh hypothesis, according to which the space-dependent velocity distribution is identical to the space-dependent deflection distribution, is again utilized, which means that the velocity at a current position on the flexure hinge relates to the velocity of the free endpoint by the equation:

$$v_y(x) = f_{by}v_{1y} \tag{4.47}$$

where:

$$f_{by}(x) = \frac{C_{x,y-F_y}(x) + f_y(x)C_{x,y-M_z}(x)}{C_{1,y-F_y} + f_y(x)C_{1,y-M_z}} \tag{4.48}$$

The total kinetic energy related to the bending vibrations and corresponding to the y axis translation is found by integrating the elemental kinetic energy of Eq. (4.46) as:

$$T_{by} = \frac{\rho v_{1y}^2}{2}\int_0^l A(x)f_{by}^2(x)dx \tag{4.49}$$

The kinetic energy of an equivalent (effective) mass that vibrates along a direction perpendicular to the longitudinal axis of a flexure hinge with a velocity v_{1x} and is attached at the free end of the flexure is:

$$T_{by} = \frac{1}{2}m_y v_{1y}^2 \tag{4.50}$$

Because Eqs. (4.49) and (4.50) express the same amount, it follows that the equivalent mass in the *y*-axis direction is:

$$m_y = \rho \int_0^l A(x) f_{by}^2(x)\, dx \tag{4.51}$$

A limit check was again performed to verify that, by forcing the appropriate geometric parameters and thus transforming the variable cross-section flexures into constant cross-section flexures, the equations that were previously formulated with respect to the effective mass pertaining to bending vibrations will indeed reduce to the corresponding equation of the effective mass for the constant cross-section beam. As shown in Lobontiu,[24] the distribution function for a fixed–free constant cross-section cantilever is:

$$f_{by}^* = 1 - \frac{3}{2}\frac{x}{l} + \frac{1}{2}\frac{x^3}{l^3} \tag{4.52}$$

Combining Eqs. (4.52), (4.49), and (4.50) gives the effective mass of the constant cross-section cantilever as:

$$m_y^* = \frac{33}{140} m \tag{4.53}$$

where m is the total mass of the beam. By applying the same geometric limit conditions that were used when determining the effective mass in axial vibration—namely, zero fillet radius for corner-filleted flexure hinges and zero for parameter c in the case of all other single-axis flexures (except for the circular one)—Eqs. (4.48) and (4.51) give the value indicated in Eq. (4.53) for all flexure hinges.

Quite similarly, the rotary effects generated through bending produce a kinetic energy, which, for the element of Figure 2.20a in Chapter 2, is:

$$dT_{b\theta_z} = \frac{1}{2}\rho I_z(x)\omega_z^2(x)dx \tag{4.54}$$

where $\omega_z(x)$ is the angular velocity of the elemental portion under consideration. Again, the Rayleigh principle allows us to consider that the angular velocity due to bending has the same distribution as the source angular distribution; therefore:

$$\theta_z(x) = f_{b\theta_z}(x)\theta_{1z} \tag{4.55}$$

as well as:

$$\omega_z(x) = f_{b\theta_z}(x)\omega_{1z} \tag{4.56}$$

Similar considerations that were utilized for deriving the axial and *y*-translation bending mass fractions are applied here, and the equivalent polar mass moment of inertia is:

$$J_z = \rho \int_0^l I_z(x) f_{b\theta_z}^2(x)\, dx \tag{4.57}$$

where:

$$f_{b\theta_z}(x) = \frac{C_{x,y-M_z}(x) + f_y(x) C_{x,\theta_z-M_z}(x)}{C_{1,y-M_z} + f_y(x) C_{1,\theta_z-M_z}} \tag{4.58}$$

4.3.2.2 Multiple-Axis Flexure Hinges

For a multiple-axis flexure hinge, the discretization process pertaining to the elastic properties results in a six-DOF lumped-parameter equivalent member. In this case, the kinetic energy owing to translation is:

$$T_{tr} = \frac{1}{2} m_x v_x^2 + \frac{1}{2} m_y (v_y^2 + v_z^2) \tag{4.59}$$

while the rotary kinetic energy is:

$$T_{rot} = \frac{1}{2} J_x \omega_x^2 + \frac{1}{2} J_y (\omega_y^2 + \omega_z^2) \tag{4.60}$$

The multiple-axis (revolute and therefore three-dimensional) flexure hinges were defined in Chapter 2 in terms of their flexibility by five compliance factors: $C_{1,x-Fx}$ (connected to axial effects), $C_{1,y-Fy}$ and $C_{1,\theta z-Mz}$ (describing direct-bending effects, respectively), $C_{1,y-Mz}$ (denoting cross-bending effects), and $C_{1,\theta x-Mx}$. These five compliance parameters are the components of a 6×6 compliance matrix that corresponds to a displacement vector $\{u\}$ that is of the form:

$$\{u_1\}^T = \{u_{1x},\, u_{1y},\, u_{1z},\, \theta_{1x},\, \theta_{1y},\, \theta_{1z}\}^T \tag{4.61}$$

Similar to the process explained when deriving the mass–inertia matrix for single-axis flexure hinges, a 6×6 diagonal mass–inertia matrix can be formulated for multiple-axis flexures with the following nonzero components:

$$\begin{cases} m_{11} = m_x \\ m_{22} = m_{33} = m_y \\ m_{44} = J_x \\ m_{55} = m_{66} = J_y \end{cases} \tag{4.62}$$

The inertia fractions m_x, m_y, and J_y are the ones that were derived when dealing with the one-sensitivity flexure hinges. The polar moment of mass, J_x, is related to torsion and can be calculated in a way similar to the mass fraction related to axial effects. The torsional kinetic energy of an infinitesimal element of the flexure hinge can be expressed as:

$$dT_t = \frac{1}{2}\rho I_p(x)\omega_x^2(x)\,dx \tag{4.63}$$

where $\omega_x(x)$ is the angular velocity of the infinitesimal element produced by torsional vibration and $I_p(x)$ is the polar moment of area of the variable circular cross-section. The torsional rotation angle at the free end of the revolute flexure hinge is given by:

$$\theta_{1x} = C_{1,\theta_x - M_x} M_{1x} \tag{4.64}$$

as shown in Chapter 2. Similarly, the rotation angle of the infinitesimal element is:

$$\theta_x(x) = C_{x,\theta_x - M_x}(x) M_{1x} \tag{4.65}$$

where:

$$C_{x,\theta_x - M_x}(x) = \frac{1}{G}\int_0^x \frac{1}{I_p(x)}\,dx \tag{4.66}$$

Combining Eqs. (4.64) and (4.65) gives:

$$\theta_x(x) = f_t(x)\theta_{1x} \tag{4.67}$$

with:

$$f_t(x) = \frac{C_{x,\theta_x - M_x}(x)}{C_{1,\theta_x - M_x}} \tag{4.68}$$

According to Rayleigh's principle, the angular velocity about the longitudinal axis of the flexure hinge will have the same spatial distribution as the one of the axial angular deformation; therefore:

$$\omega_x(x) = f_t(x)\omega_{1x} \tag{4.69}$$

The total kinetic energy related to torsion will be:

$$T_t = \frac{\rho\omega_1^2}{2}\int_0^l I_p(x) f_t^2(x)\,dx \tag{4.70}$$

An equivalent disc that would be attached at the free end of the revolute flexure hinge would have a kinetic energy of:

$$T_t = \frac{1}{2} J_x \omega_1^2 \tag{4.71}$$

Because Eqs. (4.70) and (4.71) denote the same kinetic energy, it follows that the effective polar moment of mass is:

$$J_x = \rho \int_0^l I_p(x) f_t^2(x)\, dx \tag{4.72}$$

It can easily be shown that the distribution function for the angular (torsional) deformation of a fixed–free constant circular cross-section bar that is subjected to torsion is of the form:

$$f_t^*(x) = 1 - \frac{x}{l} \tag{4.73}$$

where, again, l is the total length of the bar and x is the variable distance measured from the free end. By utilizing Eq. (4.73) in combination with Eqs. (4.68) and (4.72), the effective polar moment of mass of the constant cross-section bar is found to be:

$$J_x^* = \frac{1}{3} J \tag{4.74}$$

where J is the polar moment of mass of the entire bar with respect to its longitudinal axis. Equation (4.74) was retrieved when Eqs. (4.68) and (4.72) were used by imposing the geometry limit conditions previously applied—that is, by considering that the fillet radius tends to zero for corner-filleted flexure hinges and that parameter c tends to zero for all other flexures (except, again, for the circular one), which gave a validation of the generic equations derived for the effective polar moment of mass for the multiple-axis flexure hinges.

4.3.2.3 Two-Axis Flexure Hinges

A two-axis flexure hinge was discretized with respect to both mass and stiffness as an equivalent five-DOF member. The translation kinetic energy will be provided by the three independent masses as:

$$T_{tr} = \frac{1}{2} m_x v_x^2 + \frac{1}{2} m_y v_y^2 + \frac{1}{2} m_z v_z^2 \tag{4.75}$$

whereas the rotary kinetic energy is:

$$T_{rot} = \frac{1}{2} J_y \omega_y^2 + \frac{1}{2} J_z \omega_z^2 \tag{4.76}$$

The three-dimensional two-axis flexure hinges were introduced and dealt with in Chapter 2. They were defined by the following compliances: $C_{1,x-Fx}$ (connected to axial effects); $C_{1,z-Fz}$, $C_{1,\theta y-My}$, $C_{1,y-Fy}$, and $C_{1,\theta z-Mz}$ (describing direct-bending effects); and $C_{1,y-Mz}$ and $C_{1,z-My}$ (denoting cross-bending effects). These compliance parameters form together a 5×5 compliance matrix because the displacement vector $\{u\}$ has a dimension of 5 and is defined as:

$$\{u_1\} = \{u_{1x}, u_{1y}, u_{1z}, \theta_{1y}, \theta_{1z}\}^T \tag{4.77}$$

The corresponding lumped mass matrix is a 5×5 diagonal matrix having the following nonzero components:

$$\begin{cases} m_{11} = m_x \\ m_{22} = m_y \\ m_{33} = m_z \\ m_{44} = J_y \\ m_{55} = J_z \end{cases} \tag{4.78}$$

The procedure of formulating the inertia fractions of Eq. (4.78) is exactly the same as the one developed for single-axis flexure hinges, and it will not be exposed in detail here. In actuality, the axial mass, m_x, the y-bending mass, m_y, and the z rotary inertia, J_z, are given in Eqs. (4.38), (4.51), and (4.57), respectively. The derivation of m_z and J_y follows along the lines presented when deriving m_y and J_z. It is straightforward to formulate them as:

$$m_z = \rho \int_0^l A(x) f_{bz}^2(x)\, dx \tag{4.79}$$

with:

$$f_{bz}(x) = \frac{C_{x,z-F_z}(x) + f_z(x) C_{x,z-M_y}(x)}{C_{1,z-F_z} + f_z(x) C_{1,z-M_y}} \tag{4.80}$$

and:

$$f_z(x) = \frac{\frac{dC_{x,z-F_z}(x)}{dx} - C_{x,z-M_y}(x)}{C_{x,\theta_y-M_y}(x) - \frac{dC_{x,z-M_y}(x)}{dx}} \tag{4.81}$$

A check was performed for an inverse-parabolic flexure hinge of the type presented in Chapter 2 for which the compliances were explicitly derived. By making c_1 and c_2 zero in all the compliances that are involved in Eqs. (4.79), (4.80), and (4.81)—which actually means forcing the double-profile inverse parabolic flexure to become a constant cross-section cantilever—Eq. (4.53) can again be retrieved to confirm the validity of the effective mass as expressed in Eq. (4.79).

In a similar fashion, the rotary inertia about the y axis is:

$$J_y = \rho \int_0^l I_y(x) f_{b\theta_y}^2(x)\, dx \tag{4.82}$$

where:

$$f_{b\theta_y}(x) = \frac{C_{x,z-M_y}(x) + f_z(x) C_{x,\theta_y-M_y}(x)}{C_{1,z-M_y} + f_z(x) C_{1,\theta_y-M_y}} \tag{4.83}$$

4.3.3 Inertia Properties of Flexure Hinges as Short (Timoshenko) Members

Earlier it was mentioned that the Timoshenko approach to the bending vibrations of beam-type elements constitutes a better description for short elements where the shearing effects must be taken into account. Intrinsically, the Timoshenko beam model also includes effects induced by rotary inertia, but it was shown previously that the Euler–Bernoulli model can also accommodate such effects in order to generate the inertia fraction that corresponds to a rotational degree of freedom. Based on the details given in Chapter 2, when treating the flexure hinges as short elements that incorporate shearing effects, the Timoshenko approach will be used here to determine the corresponding discretized inertia properties. The inertia properties that are generated through axial vibrations are obviously identical to those derived for Euler–Bernoulli flexure hinges, as there is no difference between the two models in terms of axial vibrations; therefore, the axial mass fraction subject will not be dealt with again.

The procedure and equations for inertia discretization in the case of single-axis flexure hinges are detailed next. It was discussed in Chapter 2 that short flexure hinges change their compliance in bending, as additional shearing

effects that generate corresponding strains must be taken into account. As a result, the equation that gives the deflection at the free end of such a flexure hinge is:

$$u_{1y}^{s} = (C_{1,y-F_y} + C_{1,y-F_y}^{*})F_{1y} + C_{1,y-M_z}M_{1z} \tag{4.84}$$

where the superscript s indicates the total deformation that results from both bending and shearing while the superscript * denotes the compliance that is changed through consideration of the shearing effects and was formulated in Chapter 2.

As already shown in the portion treating the mass discretization process Euler-Bernoulli flexure hinges, an equation similar to Eq. (4.84) can be formulated when analyzing the deflection of a point situated at a distance x from the free end of the flexure, in the form:

$$u_{y}^{s}(x) = [C_{x,y-F_y}(x) + C_{x,y-F_y}^{*}(x)]F_{1y} + C_{x,y-M_z}(x)M_{1z} \tag{4.85}$$

where the x-dependent compliances $C_{x,y-F_y}(x)$ and $C_{x,y-M_z}(x)$ are given in Eqs. (4.41) and the compliance bearing a * superscript is similar to the corresponding one of Eq. (4.84). Based on the development presented in Chapter 2, the shear-related compliances can be calculated as:

$$\begin{aligned} C_{1,y-F_y} &= \frac{\alpha E}{G} C_{1,x-F_x} \\ C_{x,y-F_y}^{*}(x) &= \frac{\alpha E}{G} C_{x,x-F_x}(x) \end{aligned} \tag{4.86}$$

with $C_{x,x-F_x}(x)$ defined as in Eq. (4.32). By combining Eq. (4.84) with the first Eq. (4.86) results in:

$$u_{1y}^{s} = \left(C_{1,y-F_y} + \frac{\alpha E}{G} C_{1,x-F_x} \right) F_{1y} + C_{1,y-M_z}M_{1z} \tag{4.87}$$

In a similar fashion, by combining Eq. (4.85) and the second Eq. (4.86) produces:

$$u_{y}^{s}(x) = \left[C_{x,y-F_y}(x) + \frac{\alpha E}{G} C_{x,y-F_y}(x) \right] F_{1y} + C_{x,y-M_z}(x)M_{1z} \tag{4.88}$$

By following a calculation similar to the one detailed when deriving the translatory inertia for single-axis flexure hinges, it can be shown that the

deflection is distributed following the law:

$$u_y^s(x) = f_{by}^s u_{1y}^s \tag{4.89}$$

where the corresponding distribution function is:

$$f_{by}^s(x) = \frac{C_{x,y-F_y}(x) + \frac{\alpha E}{G} C_{x,x-F_x}(x) + f_y(x) C_{x,y-M_z}(x)}{C_{1,y-F_y} + \frac{\alpha E}{G} C_{1,x-F_x} + f_y(x) C_{1,y-M_z}} \tag{4.90}$$

The Rayleigh's assumption is applied again, according to which the velocity field for the translatory bending-generated vibrations is distributed in a manner that is analogous to the distribution of the corresponding deflection. Following again the reasoning that was detailed in the case of Euler-Bernoulli beams, the equivalent discrete inertia fraction that corresponds to the translatory vibrations of a Timoshenko single-axis flexure hinge is:

$$m_y^s = \rho \int_0^l A(x)[f_{by}^s(x)]^2 dx \tag{4.91}$$

It requires only straightforward mathematics to derive the inertia fractions in the case of Timoshenko multi- and two-axis flexure hinges; therefore, the corresponding equations will not be developed here, as only mimimal changes are necessary to write them, following the indications given previously when analyzing similar Euler–Bernoulli flexure hinges. It is worth mentioning, however, that closed-form solutions to the inertia fractions whose equations were derived here in a generic format are not available for the configurations that were presented in Chapter 2, and, as a consequence, numerical solution procedures are necessary to solve this problem.

4.4 Free and Forced Response of Flexure-Based Compliant Mechanisms

4.4.1 Introduction

Through the mathematical modeling developed so far in this book it is possible to characterize the different types of flexure hinges that are analyzed in terms of their compliance (or stiffness) and inertia properties. This would be sufficient to further approach a specific flexure-based compliant mechanism

by formulation of its total elastic potential energy and kinetic energy, which are the main instruments for applying Lagrange's equations. The elastic potential energy in a flexure-based compliant mechanism represents the sum of all elastic contributions from the flexure hinges that were modeled as complex springs equipped with individual spring rates corresponding to different degrees of freedom. The overall kinetic energy, on the other hand, is produced by the motion of both the rigid links and the flexure hinges, and this chapter has given a detailed presentation of the effective inertia properties of flexures. Utilization of the Lagrange's equations procedure in the form of Eq. (4.3) generally produces a system of nonlinear partial differential equations that cannot easily be solved in their original form. It is therefore necessary to apply a linearization of the differential equations system consisting of measures such as neglecting powers higher than 1 for all the variables (generalized coordinates) and for all of their derivatives, as well as neglecting the products of variables and the products of derivatives of variables. After applying all the necessary steps that would remove the nonlinearities in the variables, the result of employing Lagarange's equations is generally of the form shown in Eq. (4.22).

Equation (4.22) represents the mathematical model that describes the forced undamped response of a mechanical system and is, of course, valid for a flexure-based compliant mechanism. The same equation serves as the basis for a different set of problems that analyze the situation where there is no external load acting on the compliant mechanism and therefore the governing matrix equation is of the form shown in Eq. (4.21).

Equation (4.21) describes the free undamped response of a dynamic system and is the source of determining the modal response of a given mechanism, which basically consists of the modal frequencies and eigenvectors/eigenforms that offer a description of the resonant behavior of a mechanical system. The aspect of correctly evaluating the modal frequencies and especially the natural frequency (the first one in an ascending series of values) is particularly important because a compliant mechanism might be designed in such a way that it operates by either matching a specific modal frequency (when the entire device resonates and achieves maximum performance) or by completely avoiding a given resonant frequency that would harm the overall performance of the system.

Figure 4.4 attempts to give a visualization of a few modes (the first ones) that are possible in a fixed–free beam with a mass attached at its free end that is restricted to a planar motion. A simple simulation by means of a commercially available finite-element code would reveal these modes plus a plethora of other higher order ones. Visualizing these first modes is important, as it shows how the inertia and stiffness interplay can reflect individual behavior about the different degrees of freedom that define a specific flexure hinge. In the case illustrated in Figure 4.4, it is perfectly possible to capture these three modes by the lumped-parameter (discretized) models that were developed so far for flexure hinges in terms of both stiffness (compliance) and inertia.

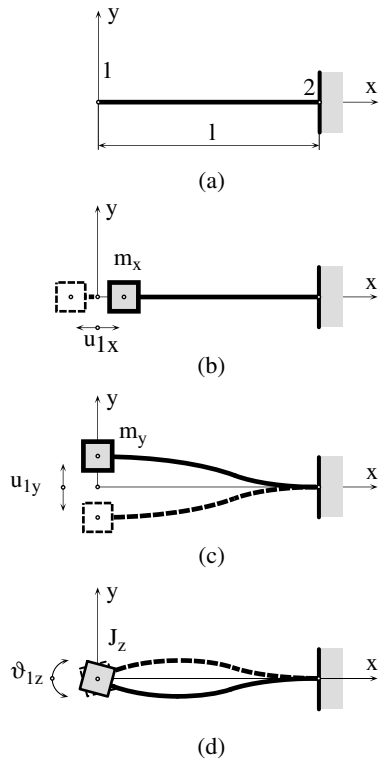

FIGURE 4.4
In-plane modes of a flexible cantilever with a tip mass: (a) original (undeformed) shape; (b) axial mode; (c) translatory mode produced through bending; (d) rotary mode produced through bending.

Equation (4.21) describes the free response of a dynamic system and is usually brought to the following form:

$$[A]\{\Phi\} = \lambda\{\Phi\} \tag{4.92}$$

where $[A]$ is called the dynamic (or system) matrix and is calculated as:

$$[A] = [K]^{-1}[M] \tag{4.93}$$

The eigenvalue, λ, is defined in terms of a specific circular frequency, ω, of the analyzed system as:

$$\lambda = \omega^2 \tag{4.94}$$

whereas $\{\Phi\}$ is the eigenvector that corresponds to a certain eigenvalue λ. The matrix in Eq. (4.92) is related to the so-called characteristic equation:

$$\left|[A] - \lambda[I]\right| = 0 \tag{4.95}$$

which is solved for the eigenvalues λ ($[I]$ is the unit matrix in Eq. (4.95)). After determining the eigenvalues from Eq. (4.95), the corresponding eigenvectors can be formed by substituting the newly found eigenvalues into Eq. (4.92). Several versions of mathematical software, such as Matlab, Mathematica, Mathcad, or Maple, offer routines that solve for the free response of a system and therefore give the modal solution in the form of eigenvalues and eigenvectors, in either numerical or symbolic (when possible) form.

As pointed out previously, Eq. (4.22) defines the forced undamped response of a dynamic system and can be used to determine the steady-state response of a system to long transients or the full time-history response of a system to short transients. The long transient situation implies that the excitation $\{F\}$ is applied over a relatively long time and in a manner that allows us to make a reduction in the problem, generally in the form of selecting just part of the total number of degrees of freedom to describe the response of the entire system. Representative of this approach is the method of modal synthesis that selects a vector subspace from the eigenvectors (already determined) of a dynamic system. A vector subspace $\{S\}$ can be formed as:

$$\{S\} = \sum_{i=1}^{m} v_i \{\Phi_i\} \tag{4.96}$$

where v_i are weight coefficients that accompany the known eigenvector $\{\Phi_i\}$. By substituting Eq. (4.96) into Eq. (4.22) and after making the necessary calculations and simplifications pertaining to the properties of eigenvectors (for more details on this topic, see the works of Meirovitch,[2] Thomson,[18] or Inman[19]), the resulting equation will be:

$$\frac{d^2 v_i}{dt^2} + \omega_i^2 v_i = F_i \tag{4.97}$$

where F_i is a reduced-form component that is calculated as:

$$F_i = \{\Phi_i\}^T \{F\} \tag{4.98}$$

whereas the reduced eigenvalue ω_i is defined as:

$$\omega_i^2 = \{\Phi_i\}^T [K] \{\Phi_i\} \tag{4.99}$$

Equation (4.97) represents a system of m similar differential equations that can be solved for the weight coefficients v_i ($i = 1 \rightarrow m$); therefore, after determining the weight coefficients, they are substituted back into Eq. (4.96), which defines the response of the reduced dynamic system.

For short transients where the external loading is applied over a short time and might often have an impulsive character, Eq. (4.22) must be directly integrated in the time domain, in order to find a reliable solution that would not skip important aspects in the dynamic response of a mechanical system. The mathematical software just mentioned offers, again, routines that perform direct time integration by means of various time-stepping schemes. Essentially, a time-stepping scheme applies a time discretization of the total time by defining time stations that are separated by means of time steps that connect the known and unknown amounts in a dynamic equation. Two consecutive time intervals are time related by means of the time step Δt (which can be constant or may vary), according to:

$$t_{j+1} = t_j + \Delta t \tag{4.100}$$

Several dedicated procedures allow time discretization and integration of Eq. (4.22) (for more details, see the monograph of Wood[25]), including situations where the matrices that define the equation are nonlinear. The Runge–Kutta algorithm is a well-known tool, and other algorithms such as predictor–corrector are also available to solve Eq. (4.22). The Newmark scheme will briefly be presented here as it offers a fast and reliable tool to solve for the unknown displacement vector $\{u\}$. The Newmark scheme is unconditionally stable and is based on the following two equations:

$$\begin{cases} \{u_{j+1}\} = \{u_j\} + \Delta t\left\{\dfrac{du_j}{dt}\right\} + \dfrac{\Delta t^2}{2}(1-\beta_2)\left\{\dfrac{d^2u_j}{dt^2}\right\} + \dfrac{\Delta t^2}{2}\beta_2\left\{\dfrac{d^2u_{j+1}}{dt^2}\right\} \\ \left\{\dfrac{du_{j+1}}{dt}\right\} = \left\{\dfrac{du_j}{dt}\right\} + \Delta t(1-\beta_1)\left\{\dfrac{d^2u_j}{dt^2}\right\} + \Delta t\beta_1\left\{\dfrac{d^2u_{j+1}}{dt^2}\right\} \end{cases} \tag{4.101}$$

Equation (4.101) must be utilized in conjunction with the dynamic equation describing the forced response, Eq. (4.22), and the initial conditions (generally, initial values of displacement and velocity) in order to solve for the displacement vector $\{u\}$.

Similar to the topics covered in Chapter 3 when discussing the static (quasi-static) response of flexure-based compliant mechanisms, this section analyzes the main features of formulating the potential elastic energy and kinetic energy for planar and spatial flexure-based compliant mechanisms of serial, parallel, or hybrid configuration in order to enable application of Lagrange's

equations and to solve for the generalized coordinates (DOFs) that describe a specific mechanism. The final form of the dynamic equations for either the free or forced response, in the generic form, is not approached here because this is a task that exceeds the scope of the present work and whose complex mathematical form would probably blur the physical significance of a problem at hand through unnecessary symbolism.

4.4.2 Planar Flexure-Based Compliant Mechanisms

The kinetic and potential energy terms, which are the main ingredients in formulating and solving Lagrange's equations, will be derived next, in generic form, for planar serial, parallel, and hybrid (serial–parallel) flexure-based compliant mechanisms. Also discussed will be the number of generalized coordinates that have to be accounted for in each specific case.

4.4.2.1 Serial Compliant Mechanisms

The potential and kinetic energy terms will be formulated now for a planar serial compliant mechanism that contains n single-axis flexure hinges (as shown in Figure 3.1) in order to enable formulation of Lagrange's equations as given in Eq. (4.3). Developing the dynamic equations in a generic fashion, as mentioned previously, would be cumbersome (although tractable) and therefore will not be developed to the last detail here. Because every flexure hinge can be described as a three-DOF subsystem and a fixed–free chain (as the one pictured in Figure 4.5) has no constraints, the number of generalized coordinates is:

$$DOF = 3n \tag{4.102}$$

The potential energy of such a system will sum up contributions from all single-axis flexure hinges in the form of two translation terms and one rotary, namely:

$$U = \frac{1}{2}\sum_{i=1}^{n}\left(K_{i,x-F_x}u_{ix_i}^2 + K_{i,y-F_y}u_{iy_i}^2 + K_{i,\theta_z-M_z}\theta_{iz}^2 + 2K_{i,y-M_z}u_{ix_i}\theta_{iz}\right) \tag{4.103}$$

where the stiffness terms of Eq. (4.103) can be determined by means of the formulation presented in Chapter 2. It should be noted that the axial, deflection, and rotary deformations of a flexure hinge are expressed in local coordinates.

The total kinetic energy of a planar serial compliant mechanism is formed of two translation terms and one rotary term for each single-axis flexure hinge. The translation kinetic energy is:

$$T_{tr} = \frac{1}{2}\sum_{i=1}^{n}\left(m_{ix}v_{ix_i}^2 + m_{iy}v_{iy_i}^2\right) \tag{4.104}$$

where the mass fractions are calculated according to the procedure developed within this chapter. The velocity components in Eq. (4.104) are absolute values that are afterwards projected on the local axes of each individual flexure. It is necessary to proceed that way because the mass discretization process resulted in two independent translation masses, m_x and m_y. Although kinematically independent, the two masses reflect the unique position of the free end of a flexure hinge that is capable of simultaneous axial and deflection deformation, which enables calculation of one single-velocity vector v_i in the form:

$$\overline{v}_i = \frac{d}{dt}\overline{R_i} \tag{4.105}$$

where R_i is the position vector of the tip i of the flexure hinge bounded by the nodes $i - 1$ and i (not represented in Figure 4.5) and is expressed as:

$$\overline{R_i} = \sum_{j=1}^{i}[(l_j + u_{jx_j})\overline{e}_{x_j} + u_{jy_j}\overline{e}_{y_j}] \tag{4.106}$$

As Eq. (4.106) indicates, the position vector of the node I is defined based on the deformed state of the compliant mechanism. The unit vectors e_{xj} and e_{y_j} that appear in Eq. (4.106) belong to the local reference frame that is attached to the analyzed generic flexure hinge. In taking the time derivative

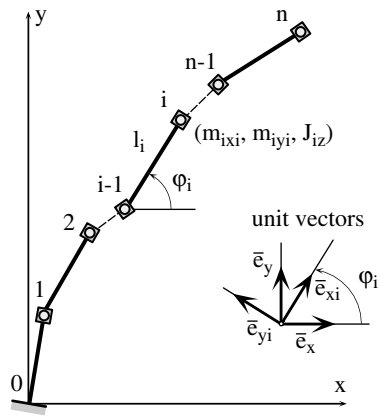

FIGURE 4.5
Geometry and symbolic representation of inertia discretization for a planar serial compliant mechanism with single-axis flexure hinges.

of the position vector given in Eq. (4.106), it should be remembered that the local reference frame of the flexure hinge $(i-1, i)$ is a rotating one. Its rotation is produced by the sum of rotations of all flexure hinges from 1 to $i-1$ as quantified by their tip slope angles θ_z. In such cases, the time derivative of a vector with respect to a fixed reference frame can be calculated (see Beer and Johnston,[26] for instance) in terms of the time derivative of the same vector taken with respect to a mobile reference frame that rotates with the absolute angular velocity ω as:

$$\frac{d}{dt}\overline{R_i}_{,fixed} = \frac{d}{dt}\overline{R_i}_{,mobile} + \overline{\omega_i} \times \overline{R_i} \tag{4.107}$$

The angular velocity in this case is:

$$\overline{\omega_i} = \left[\sum_{j=1}^{i-1} \frac{d}{dt}(\theta_{iz})\right]\overline{e_z} \tag{4.108}$$

where e_z is the unit vector of the fixed z axis. Eventually, the velocity vector v_i becomes:

$$\overline{v_i} = \sum_{j=1}^{i}\left\{\left[\frac{d}{dt}(u_{jx_j}) - u_{jy_j}\sum_{k=1}^{j-1}\left(\frac{d}{dt}(\theta_{kz})\right)\right]\overline{e_{x_j}} + \left[\frac{d}{dt}(u_{jy_j}) + \left(l_j + u_{jx_j}\sum_{k=1}^{j-1}\left(\frac{d}{dt}(\theta_{kz})\right)\right)\right]\overline{e_{y_j}}\right\} \tag{4.109}$$

The components of the velocity vector of Eq. (4.109) are found by projecting this vector onto the local axes x_i and y_i as:

$$\overline{v_{ix_i}} = \sum_{j=1}^{i}\left\{\left[\frac{d}{dt}(u_{jx_j}) - u_{jy_j}\sum_{k=1}^{j-1}\left(\frac{d}{dt}(\theta_{kz})\right)\right]\cos\beta_{ij} + \left[\frac{d}{dt}(u_{jy_j}) + \left(l_j + u_{jx_j}\sum_{k=1}^{j-1}\left(\frac{d}{dt}(\theta_{kz})\right)\right)\right]\sin\beta_{ij}\right\}\overline{e_{x_i}} \tag{4.110}$$

and:

$$\overline{v_{iy_i}} = \sum_{j=1}^{i} \left\{ -\left[\frac{d}{dt}(u_{jx_j}) - u_{jy_j} \sum_{k=1}^{j-1} \left(\frac{d}{dt}(\theta_{kz}) \right) \right] \sin \beta_{ij} + \left[\frac{d}{dt}(u_{jy_j}) + \left(l_j + u_{jx_j} \sum_{k=1}^{j-1} \left(\frac{d}{dt}(\theta_{kz}) \right) \right) \right] \cos \beta_{ij} \right\} \overline{e_{y_i}} \tag{4.111}$$

where:

$$\beta_{ij} = \varphi_i - \varphi_j + \sum_{k=j+1}^{i} (\theta_{kz}) \tag{4.112}$$

By inspecting the equations that give the translation kinetic energy, it can be noticed that they do not explicitly depend on the generalized coordinates u_{ix_i}, u_{iy_i}, and θ_{iz} and, as a consequence, the partial derivatives that involve them in Lagrange's equations, Eq. (4.3), are zero. The partial derivatives that are taken with respect to the rate of the above-mentioned generalized coordinates can formally be computed as:

$$\begin{cases} \dfrac{\partial T_{tr}}{\partial \dot{u}_{ix_i}} = \displaystyle\sum_{i=1}^{n} \left(m_{ix} v_{ix_i} \frac{\partial v_{ix_i}}{\partial \dot{u}_{ix_i}} + m_{iy} v_{iy_i} \frac{\partial v_{iy_i}}{\partial \dot{u}_{ix_i}} \right) \\ \dfrac{\partial T_{tr}}{\partial \dot{u}_{iy_i}} = \displaystyle\sum_{i=1}^{n} \left(m_{ix} v_{ix_i} \frac{\partial v_{ix_i}}{\partial \dot{u}_{iy_i}} + m_{iy} v_{iy_i} \frac{\partial v_{iy_i}}{\partial \dot{u}_{iy_i}} \right) \\ \dfrac{\partial T_{tr}}{\partial \dot{\theta}_{iz}} = \displaystyle\sum_{i=1}^{n} \left(m_{ix} v_{ix_i} \frac{\partial v_{ix_i}}{\partial \dot{\theta}_{iz}} + m_{iy} v_{iy_i} \frac{\partial v_{iy_i}}{\partial \dot{\theta}_{iz}} \right) \end{cases} \tag{4.113}$$

The rotary kinetic energy is:

$$T_{rot} = \frac{1}{2} \sum_{i=1}^{n} \left\{ J_{iz} \left[\sum_{j=1}^{i} (\dot{\theta}_{jz}) \right]^2 \right\} \tag{4.114}$$

and it can be seen that, as in the case with translation kinetic energy, none of the generalized coordinates explicitly enters this equation. As a consequence, the corresponding partial derivatives in terms of these generalized

coordinates are zero in Lagrange's equations, Eq. (4.3). The partial derivatives taken with respect to the rate of change of the generalized coordinates are:

$$\begin{cases} \dfrac{\partial T_{rot}}{\partial \dot{u}_{ix_i}} = \dfrac{\partial T_{tr}}{\partial \dot{u}_{iy_i}} = 0 \\ \dfrac{\partial T_{tr}}{\partial \dot{\theta}_{iz}} = \displaystyle\sum_{i=1}^{n} \left[J_{iz} \sum_{j=1}^{i} (\dot{\theta}_{jz}) \right] \end{cases} \tag{4.115}$$

The total potential energy of a planar serial compliant mechanism that is based on one-sensitivity axis flexure hinges is given in Eq. (4.103). The partial derivatives of Lagrange's equations are:

$$\begin{cases} \dfrac{\partial U}{\partial u_{ix_i}} = \displaystyle\sum_{i=1}^{n} (K_{i,x-F_x} u_{ix_i}) \\ \dfrac{\partial U}{\partial u_{iy_i}} = \displaystyle\sum_{i=1}^{n} (K_{i,y-F_y} u_{iy_i} + K_{i,y-M_z} \theta_{iz}) \\ \dfrac{\partial U}{\partial \theta_{iz}} = \displaystyle\sum_{i=1}^{n} (K_{i,\theta_z-M_z} \theta_{iz} + K_{i,y-M_z} u_{iy_i}) \end{cases} \tag{4.116}$$

Combining all the derivatives involved in Lagrange's equations, Eq. (4.3), results in a system of $3 \times n$ second-order nonlinear differential equations in u_{ix_i}, u_{iy_i}, and θ_{iz}. Because the assumption of small displacements/deformation applies here, the terms containing the unknowns (deformations) in their second powers and terms based on products of the unknowns can be neglected. In doing so, the differential equations system becomes linear and can be solved through the regular procedure.

One might encounter the case where a serial chain also includes one or several rigid links that will add kinetic energy to the system of flexure hinges. Unless the planar serial mechanism is operating in a horizontal plane, the rigid links will also bring in gravitational potential energy that will add up to the elastic potential energy stored in flexure hinges. However, this aspect will be neglected here, and it will be considered that the contribution of a rigid link will only consist of kinetic energy. Because the motion of a rigid link in the serial chain is essentially planar, its kinetic energy contains translatory and rotary terms in the form:

$$T_r = \frac{1}{2} m_r (\dot{x}_{Cr}^2 + \dot{y}_{Cr}^2) + \frac{1}{2} J_{Crz} \dot{\theta}_{Crz}^2 \tag{4.117}$$

where the subscript r denotes rigid, x_{Cr} and y_{Cr} represent the coordinates of the center of mass of the rigid link in the global reference plane, and J_{Crz} is the

mass moment of inertia of the same rigid body with respect to a z axis passing through its center of mass. Clearly, the coordinates defining the position of the rigid link can be expressed in terms of the generalized coordinates of the whole system to enable formulation of Lagrange's equations.

To facilitate a better understanding of the general algorithm presented above, a practical example of a simple planar serial compliant mechanism is analyzed next.

Example

Find the natural frequencies of the two-member planar serial compliant mechanism shown in Figure 4.6. Also find the corresponding eigenvectors. The single-axis flexure hinge is hyperbolic and the mechanism is constructed of a steel plate of constant width w = 0.004 m. The Young's modulus is E = 200 GPa. The other geometric parameters are l_1 = 0.006 m, t_1 = 0.001 m, c_1 = 0.001 m, l_2 = 0.015 m, and t_2 = 0.015 m.

Solution

The analytical model presented in this chapter has been applied as well as a finite-element simulation by means of the ANSYS software, in order to check the results. The analytical model simulation started by calculating the stiffness matrix of the single-axis hyperbolic flexure hinge, according to the procedure developed in Chapter 2. The overall mass matrix of the two-link planar serial compliant mechanism was numerically calculated and the modal frequencies were then determined by means of the algorithm presented in this chapter (the Mathematica code has been used for both inertia and modal frequencies calculations). The results of the two types of analysis are given next:

- First mode (bending of the flexure hinge with the rigid link following the flexure without any rotation):
  - 1100-Hz resonant frequency by means of the analytical/numerical procedure

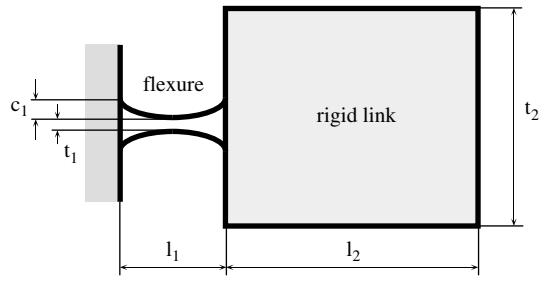

FIGURE 4.6
Two-member, constant-width planar serial compliant mechanism with a single-axis flexure hinge of hyperbolic configuration.

  - 1315 Hz by means of the ANSYS software

- Second mode (bending of the flexure hinge with the rigid link independently rotating):
  - 12,023-Hz resonant frequency by means of the dedicated finite-element procedure
  - 12,436 Hz by means of the ANSYS software

- Third mode (pure axial vibration of the entire system due to axial deformation of the flexure hinge element)
  - 25,030-Hz resonant frequency by means of the dedicated finite-element procedure
  - 26,368 Hz by means of the ANSYS software

The errors between the two procedures were less than 6%. The finite-element predictions are always higher than the results yielded by the analytical/numerical technique developed in this chapter because the finite-element code produces a mesh, which introduces more internal constraints at its nodes; therefore, the entire model is stiffer.

4.4.2.2 Parallel Compliant Mechanisms

As previously shown, a purely parallel planar flexure-based compliant mechanism is composed of one rigid output link (or platform) and, in the most general case, of n flexure hinges, each attached to the output platform at one end and fixed (or otherwise attached) to the ground at the other end. Deriving Lagrange's equations, based on the potential and kinetic energy of the system, is formally identical to the path followed and described in the case of planar serial flexure-based compliant mechanisms; therefore, it will not be analyzed here in its entirety. The major difference, however, consists in the constraints that the output platform planar motion imposes on the deformation and displacement of the attached flexure hinges. These constraints, which we discuss next, reduce the number of degrees of freedom of the entire mechanism. Figure 4.7 shows the output platform in two positions: one initial (which has an orientation that makes the longer dimension of the platform parallel to the x axis of the global reference frame O_{xy}), corresponding to a state where all the flexure hinges are undeformed, and another position, which is displaced, as produced by deformations in the flexure hinges. The center of mass of the output platform moves in the plane by the quantities u_{Cx} and u_{Cy}, whereas the entire platform rotates around the center of mass by an angle θ_{Cz}, as suggested in Figure 4.7.

The motion of the output platform is related to the deformations of the flexure hinges that are connected in parallel to it. Figure 4.8 shows the main geometric parameters defining the deformations and displacements of the end attached to the rigid output platform for a generic flexure hinge denoted by i.

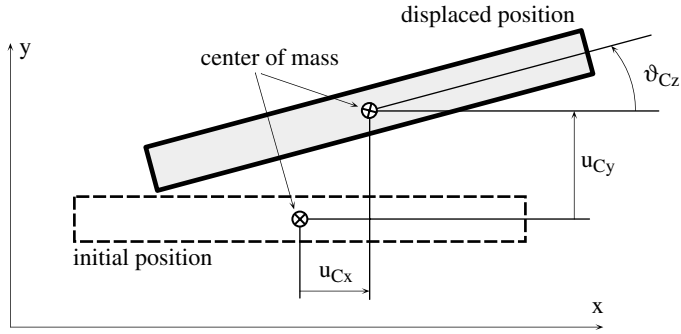

FIGURE 4.7
Initial and displaced position of the output platform for a planar parallel/hybrid flexure-based compliant mechanism.

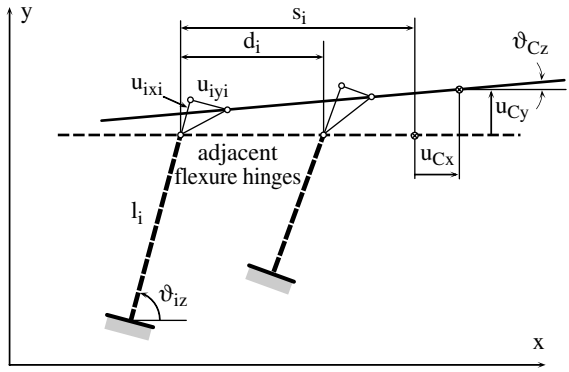

FIGURE 4.8
Deformations and displacements of two adjacent flexure hinges in relation to the displacements of the output platform from a planar parallel/hybrid compliant mechanism.

The generic flexure that has a length l_i and is inclined at an initial angle φ_i is situated at a distance d_i from its immediate neighboring flexure hinge and at a distance s_i from the center of mass of the output platform, as sketched in Figure 4.8. It is clear that the coordinates of any two points on the output platform where two flexure hinges are attached must be connected at any moment during the motion of the mechanism. It is straightforward to express the following relationships between the coordinates of two attachment points corresponding to two adjacent flexure hinges:

$$\begin{cases} x_{i+1} = x_i + d_i \cos\theta_{cz} \\ y_{i+1} = y_i + d_i \sin\theta_{cz} \\ \theta_{iz} = \theta_{Cz} \end{cases} \tag{4.118}$$

Equation (4.118) can be written, in a transitional manner, for a total of $n - 1$ times in order to cover the n flexure hinges. At the same time, the coordinates of Eq. (4.118) will be functions of the elastic deformations of the single-axis flexure hinges, as the following relationships can be written, based on Figure 4.8:

$$\begin{cases} x_i = x_i^0 + u_{ix_i} \cos\varphi_i + u_{iy_i} \sin\varphi_i \\ x_{i+1} = x_{i+1}^0 + u_{i+1x_{i+1}} \cos\varphi_{i+1} + u_{i+1y_{i+1}} \sin\varphi_{i+1} \end{cases} \tag{4.119}$$

$$\begin{cases} y_i = y_i^0 + u_{ix_i} \sin\varphi_i - u_{iy_i} \cos\varphi_i \\ y_{i+1} = y_{i+1}^0 + u_{i+1x_{i+1}} \sin\varphi_{i+1} - u_{i+1y_{i+1}} \cos\varphi_{i+1} \end{cases} \tag{4.120}$$

where the superscript 0 is formally employed to denote the initial value of a coordinate (either x or y) measured in the (fixed) global reference frame. It is obvious now that substituting Eqs. (4.119) and (4.120) into the first two expressions in Eq. (4.118) results in the above-mentioned relationships between the would-be degrees of freedom of the entire system. It has already been shown that the state of deformation of a given flexure hinge can be expressed in terms of its axial deformation, as well as bending-produced deflection and slope at its free end (in the present case, the point attached to the output platform). As a result, the $3(n - 1)$ constraints that can be formulated by means of Eqs. (4.118), (4.119), and (4.120) will reduce the total number of degrees of freedom from $3n$ (each flexure is a 3-DOF element, and there are n flexure hinges overall) to $3n - 3(n - 1) = 3$. Therefore, the number of generalized coordinates of a planar flexure-based parallel compliant mechanism is:

$$DOF = 3 \tag{4.121}$$

The conclusion is that three generalized coordinates will suffice to characterize a planar parallel compliant mechanism that is made up of n flexure hinges and a rigid output platform. By inspecting Figure 4.8 and by taking the projections of deformations and other distances on the x and y axes, it is simple to notice the following relationships exhibited among the geometric parameters:

$$\begin{cases} s_i + u_{Cx} = u_{ix_i} \sin\varphi_i + u_{iy_i} \cos\varphi_i + s_i \cos\theta_{Cz} \\ u_{Cy} = u_{ix_i} \cos\varphi_i - u_{iy_i} \sin\varphi_i + s_i \sin\theta_{Cz} \end{cases} \tag{4.122}$$

Rearranging Eq. (4.122) results in:

$$\begin{cases} u_{ix_i} = u_{Cx}\sin\varphi_i + u_{Cy}\cos\varphi_i + [(1-\cos\theta_{Cz})\sin\varphi_i - \sin\theta_{Cz}\cos\varphi_i]s_i \\ u_{iy_i} = u_{Cx}\cos\varphi_i - u_{Cy}\sin\varphi_i + [(1-\cos\theta_{Cz})\cos\varphi_i + \sin\theta_{Cz}\sin\varphi_i]s_i \\ \theta_{iz} = \theta_{Cz} \end{cases} \tag{4.123}$$

The last expression in Eq. (4.123) shows that the slope of each flexure hinge at its endpoint that is attached to the output platform is equal to the rotation angle of the output platform. Equation (4.123) is valid for all n flexure hinges that compose the planar parallel compliant mechanism, and, basically, Eq. (4.123) indicates that it is convenient to select the parameters u_{Cx}, u_{Cy}, and θ_{Cz} in order to define the position of the output platform as the three generalized coordinates that allow formulation of Lagrange's equations:

$$\begin{cases} \dfrac{d}{dt}\left(\dfrac{\partial T}{\partial \dot{u}_{Cx}}\right) - \dfrac{\partial T}{\partial u_{Cx}} + \dfrac{\partial U}{\partial u_{Cx}} = 0 \\ \dfrac{d}{dt}\left(\dfrac{\partial T}{\partial \dot{u}_{Cy}}\right) - \dfrac{\partial T}{\partial u_{Cy}} + \dfrac{\partial U}{\partial u_{Cy}} = 0 \\ \dfrac{d}{dt}\left(\dfrac{\partial T}{\partial \dot{\theta}_{Cz}}\right) - \dfrac{\partial T}{\partial \theta_{Cz}} + \dfrac{\partial U}{\partial \theta_{Cz}} = 0 \end{cases} \tag{4.124}$$

The potential and kinetic energy corresponding to all the flexure hinges must be formulated, as discussed in the segment dedicated to planar serial flexure-based compliant mechanisms, by utilizing connection Eq. (4.123) to express all energy terms in terms of the three generalized coordinates u_{Cx}, u_{Cy}, and θ_{Cz}. It should be noted that the total kinetic energy must include the contribution from the output platform, namely:

$$T_{op} = \frac{1}{2}m_{op}(\dot{u}_{Cx}^2 + \dot{u}_{Cy}^2) + \frac{1}{2}J_{op}\dot{\theta}_{Cz}^2 \tag{4.125}$$

4.4.2.3 Hybrid Compliant Mechanisms

A planar hybrid mechanism, as previously discussed and illustrated in Figure 3.10, is composed of n parallel chains, each comprising n_i single-axis flexure hinges. In each serial chain, the external end of a terminal flexure is fixed, whereas the external end of the opposite terminal flexure is fixed to a rigid output platform. Because a flexure hinge of this type has three DOFs, the total number of physical coordinates that would define the hybrid mechanism is $3n_in$. It has been demonstrated, however, that the n points where the flexure

hinges connect to the output platform pose $3(n-1)$ constraint equations in the case of a planar parallel mechanism. The same condition is valid for a hybrid mechanism; therefore, the number of generalized coordinates or real degrees of freedom will be reduced to:

$$DOF = 3[(n_i - 1)n + 1] \tag{4.126}$$

A quick check of Eq. (4.126) indicates that when $n_i = 1$, the number of degrees of freedom is three, which confirms the previous suggestion that a planar parallel mechanism (which is a particular case of a hybrid mechanism with one flexure hinge in each serial leg) has three DOFs. Eq. (4.126) can be formally rearranged to better outline the physical quantities that must be treated as generalized coordinates. It is clear that one can select three generalized coordinates as the displacement components of the output platform's center of mass u_{Cx}, u_{Cy}, and θ_{Cz}, as well as the three elastic deformations of the first $n_i - 1$ flexure hinges (starting from the fixed one) for each of the n serial chains. As a consequence, Eq. (4.126) can be written as:

$$DOF = 3 + 3(n_i - 1)n \tag{4.127}$$

Lagrange's equations must be formulated in a number equal to the above-mentioned number of generalized coordinates in order to eventually solve for the said coordinates. When formulating the kinetic and potential energy terms, as indicated in the discussion dealing with planar serial flexure-based compliant mechanisms, the $3(n-1)$ constraint equations given for planar parallel mechanisms have to be employed as well.

4.4.3 Spatial Compliant Mechanisms

4.4.3.1 Serial Compliant Mechanisms

A spatial serial compliant mechanism that is composed of n multi-axis (revolute) flexure hinges is analyzed next. Similar to the case of the planar serial flexure-based compliant mechanism, the three-dimensional chain has a fixed end while the opposite end is free. This type of boundary condition imposes no constraints on the physical coordinates that define the system, such that the number of generalized coordinates is:

$$DOF = 6n \tag{4.128}$$

because each of the n revolute flexure hinges possesses six DOFs, according to the manner in which the stiffness and inertia properties were lumped. The generic expression of the total potential and kinetic energy pertaining to the components of a spatial flexure-based chain are derived in the following to allow formulation of the $6n$ Lagrange's equations that are necessary to solve for the $6n$ unknown elastic deformations of the flexure hinges.

The total potential energy stored in the flexure hinges is:

$$U = \frac{1}{2}\sum_{i=1}^{n}[K_{i,x-F_x}u_{ix_i}^2 + K_{i,y-F_y}(u_{iy_i}^2 + u_{iz_i}^2) + K_{i,\theta_z-M_z}(\theta_{yz}^2 + \theta_{iz}^2) + 2K_{i,y-M_z}(u_{iy_i}\theta_{iz} + u_{iz_i}\theta_y) + K_{i,x_i-Mx}\theta_{iz}] \quad (4.129)$$

In Eq. (4.129) axial, double direct, and cross bending, as well as torsion effects, have been taken into account. The total kinetic energy has, again, a translatory and a rotary component. The total translatory kinetic energy produced by the motion of the n revolute flexure hinges is:

$$T_{tr} = \frac{1}{2}\sum_{i=1}^{n}[m_{ix}v_{ix_i}^2 + m_{iy}(v_{iy_i}^2 + v_{iz_i}^2)] \quad (4.130)$$

where m_{ix} and m_{iy} are the lumped masses placed at the end of one flexure which were calculated by means previously detailed within this chapter. It should be noted that three lumped masses are in fact located at the end of one flexure, but because of the rotation symmetry of the cross-section the mass fractions that are produced through bending vibrations along the local y and z reference axes are identical. The velocity vector at one flexure end will be first calculated and then projected on the local reference frame axes of the generic node i in order to enable utilization of Eq. (4.130). The position vector corresponding to the ith flexure hinge is:

$$\overline{R_i} = \sum_{j=1}^{i}[(l_j + u_{jx_j})\overline{e_{x_j}} + u_{jy_j}\overline{e_{y_j}} + u_{jz_j}\overline{e_{z_j}}] \quad (4.131)$$

where three unit vectors have been used for the local reference frames, in a manner similar to the one utilized when expressing the kinetic energy of planar serial flexure-based compliant mechanisms. The velocity at node i, recorded in terms of the global (fixed) reference frame, is defined according to Eq. (4.105) and can be calculated by following the rule of differentiation given in Eq. (4.107). Through simple vector calculations, the velocity at node i can be expressed as:

$$\overline{v_i} = \sum_{j=1}^{i}\left\{\left[\frac{d}{dt}(u_{jx_j}) - u_{jy_j}\sum_{k=1}^{j-1}\left(\frac{d}{dt}(\theta_{kz})\right)\right]\overline{e_{x_j}} + \left[\frac{d}{dt}(u_{jy_j}) + \left(l_j + u_{jx_j}\sum_{k=1}^{j-1}\left(\frac{d}{dt}(\theta_{kz})\right)\right)\right]\overline{e_{y_j}} + \frac{d}{dt}(u_{jx_j})\overline{e_{z_j}}\right\} \quad (4.132)$$

The components of this velocity vector in its local reference frame can be found simply by taking the dot product of the velocity vector and the respective unit vectors of the local axes, namely:

$$\begin{cases} v_{ix_i} = \overline{v}_i \overline{e}'_{x_i} \\ v_{iy_i} = \overline{v}_i \overline{e}'_{y_i} \\ v_{iz_i} = \overline{v}_i \overline{e}'_{z_i} \end{cases} \tag{4.133}$$

The unit vectors in Eqs. (4.133) are given a superscript prime in order to signal that they correspond to the rotated positions of their corresponding reference frames as produced through the rotations of all reference frames that are placed before the *i*th reference frame. Equation (4.133) suggests that the position of the rotated reference frame in terms of its initial position must be determined.

The total rotary kinetic energy for a three-dimensional serial flexure-based compliant chain is:

$$T_{rot} = \frac{1}{2} \sum_{i=1}^{n} \left\{ J_{iy} \left[\sum_{j=1}^{i} (\dot{\theta}_{yz} + \dot{\theta}_{jz}) \right]^2 + J_{iy} \dot{\theta}^2_{jx} \right\} \tag{4.134}$$

therefore, the total kinetic energy that enters Lagrange's equations can be expressed by summing up the translatory kinetic energy, as given in Eq. (4.130), and the rotational energy of Eq. (4.134). The kinetic energy of any rigid link that may be part of the spatial serial chain can be expressed as:

$$T_r = \frac{1}{2} m_r (\dot{x}^2_{Cr} + \dot{y}^2_{Cr} + \dot{z}^2_{Cr}) + \frac{1}{2} J_{Cry} (\dot{\theta}^2_{Cry} + \dot{\theta}^2_{Cry}) + \frac{1}{2} J_{Crx} \dot{\theta}^2_{Cx} \tag{4.135}$$

and should be added to the total kinetic energy produced by the flexure hinges.

4.4.3.2 Parallel Compliant Mechanisms

The planar parallel flexure-based compliant mechanism that was just studied had *n* flexural members that were disposed in parallel, with one end fixed and the other attached to a rigid output platform. Such a mechanism was demonstrated to possess three DOFs, which were conveniently chosen as the three coordinates defining the planar motion of the output plate. Similarly, the spatial variant of a flexure-based compliant mechanism will have the same composition, the only differences being the three-dimensional disposition of the flexure hinges and the revolute configuration of the flexures. The total number of physical coordinates that would describe the motion of the system is 6*n*, as each of the *n* parallel flexures was discretized as a 6-DOF subsystem. As for the case with the planar variant of the parallel mechanism, here, too, constraints between the physical coordinates will reduce the number of generalized coordinates. Figure 4.9 illustrates a projection onto the

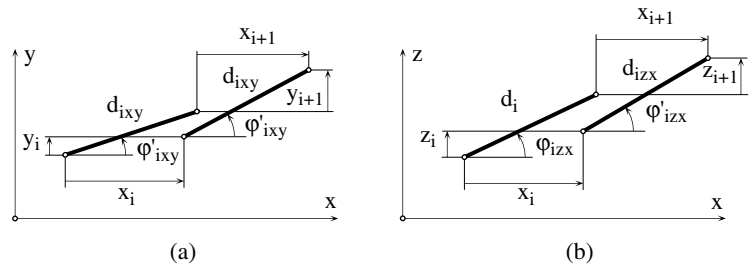

FIGURE 4.9
Projection of the output platform of a spatial parallel compliant mechanism (a) onto the *xy* plane; (b) onto the *xz* plane.

(horizontal) plane *xy* of the output platform of two adjacent connection points in undisplaced and displaced conditions.

A similar projection could be imagined in the *zx* plane with the corresponding index modifications (actually, *z* will replace *y*). The following connection equations can be formulated:

$$\begin{cases} d_i \cos\varphi_{ixy} + x_{i+1} = x_i + d_i \cos\varphi'_{ixy} \\ y_i + d_i \sin\varphi'_{ixy} = d_i \sin\varphi_{ixy} + y_{i+1} \\ z_i + d_i \sin\varphi'_{zix} = d_i \sin\varphi_{izx} + z_{i+1} \\ l'_i = l'_C \\ m'_i = m'_C \\ n'_i = n'_C \end{cases} \tag{4.136}$$

where l'_i, m'_i, and n'_i represent the cosines of the unit vectors defining the displaced position of the segment d_i, whereas the similar quantities with the subscript *C* denote a segment line that passes through the center of mass of the output platform and is parallel to the segment d_i. It is clear that the displacements *x*, *y*, and *z* in the first three expressions of Eq. (4.136) are produced through the elastic deformations of the respective flexure hinges; therefore, they depend on those deformations. The main point here is not specifically to define precise relationships between elastic deformations and displacement, but to acknowledge the above-mentioned dependency. It is clear now that Eq. (4.136) can iteratively be written $n - 1$ times, which amounts to $6(n - 1)$ constraint equations between the physical coordinates of the whole system. As a consequence, the number of generalized coordinates that completely define the motion of the spatial parallel mechanism will be the difference between $6n$ and $6(n - 1)$:

$$DOF = 6 \tag{4.137}$$

It would again be convenient to select the displacement components of the center of mass of the output platform as generalized coordinates, on the condition that all other physical coordinates can be expressed in terms of the generalized coordinates. Based on Figure 4.9 and on the reasoning presented when analyzing the planar parallel case, the following relationships can be formulated:

$$\begin{cases} u_{ix_i} = u_{Cx}\sin\varphi_{ixy} + u_{Cy}\cos\varphi_{ixy} + [(1-\cos\theta_{Cxy})\sin\varphi_{ixy} - \sin\theta_{Cxy}\cos\varphi_{ixy}]s_{ixy} \\ u_{iy_i} = u_{Cx}\cos\varphi_{ixy} - u_{Cy}\sin\varphi_{ixy} + [(1-\cos\theta_{Cxy})\cos\varphi_{ixy} + \sin\theta_{Cxy}\sin\varphi_{ixy}]s_{ixy} \\ u_{iz_i} = u_{Cx}\cos\varphi_{izxy} - u_{Cz}\sin\varphi_{izx} + [(1-\cos\theta_{Czx})\cos\varphi_{izx} + \sin\theta_{Czx}\sin\varphi_{izx}]s_{izx} \\ \theta_{ix} = \theta_{Cx} \\ \theta_{iy} = \theta_{Cz} \\ \theta_{iz} = \theta_{Cz} \end{cases} \tag{4.138}$$

where the last three equations indicate that the angle of rotations of each flexure hinge (at their tip which is attached to the output platform) is equal to the rotation angles of the platform, in terms of the global reference frame. Eq. (4.138) offers the transformation relationship that enables expressing the individual physical coordinates of the flexure hinges as functions of the displacement components of the output platform center of mass. As a consequence, only six Lagrange's equations are necessary, namely:

$$\begin{cases} \dfrac{d}{dt}\left(\dfrac{\partial T}{\partial \dot{u}_{Cx}}\right) - \dfrac{\partial T}{\partial u_{Cx}} + \dfrac{\partial U}{\partial u_{Cx}} = 0 \\ \dfrac{d}{dt}\left(\dfrac{\partial T}{\partial \dot{u}_{Cy}}\right) - \dfrac{\partial T}{\partial u_{Cy}} + \dfrac{\partial U}{\partial u_{Cy}} = 0 \\ \dfrac{d}{dt}\left(\dfrac{\partial T}{\partial \dot{u}_{Cz}}\right) - \dfrac{\partial T}{\partial u_{Cz}} + \dfrac{\partial U}{\partial u_{Cz}} = 0 \\ \dfrac{d}{dt}\left(\dfrac{\partial T}{\partial \dot{\theta}_{Cx}}\right) - \dfrac{\partial T}{\partial \theta_{Cx}} + \dfrac{\partial U}{\partial \theta_{Cx}} = 0 \\ \dfrac{d}{dt}\left(\dfrac{\partial T}{\partial \dot{\theta}_{Cy}}\right) - \dfrac{\partial T}{\partial \theta_{Cy}} + \dfrac{\partial U}{\partial \theta_{Cy}} = 0 \\ \dfrac{d}{dt}\left(\dfrac{\partial T}{\partial \dot{\theta}_{Cz}}\right) - \dfrac{\partial T}{\partial \theta_{Cz}} + \dfrac{\partial U}{\partial \theta_{Cz}} = 0 \end{cases} \tag{4.139}$$

Lagrange's equations, Eq. (4.139), must be used in conjunction with Eq. (4.138), which provides the necessary connections between the individual deformations of the flexure hinges (which input terms of potential and kinetic energy, as detailed previously) and the six generalized coordinates. As previously mentioned, the nonlinear terms resulted by applying the partial derivations required by Lagrange's equations process will be neglected.

4.4.3.3 Hybrid Compliant Mechanisms

The spatial hybrid flexure-based compliant mechanism is a serial–parallel combination, as such a mechanism is formed by connecting n serial chains in parallel to an output platform at one end and fixed at the opposite end. Each serial chain contains n_i three-dimensional (revolute) flexure hinges. The same argument that was developed when discussing planar hybrid mechanisms applies in this case also; therefore, it can be shown that a spatial hybrid mechanism in the configuration mentioned here possesses a total number of degrees of freedom of:

$$DOF = 6n_i n - 6(n-1) \tag{4.140}$$

because the $6n_i n$ physical coordinates (equal to the total number of deformations collected from all flexure hinges) are subject to $6(n-1)$ constraint equations (due to the parallel side of such a mechanism), so the number of generalized coordinates that completely define the state of the mechanism is the difference of these two numbers:

$$DOF = 6n(n_i - 1) + 6 \tag{4.141}$$

Equation (4.141) highlights the fact that the generalized coordinates can be selected from two different categories: $6n(n_i - 1)$ DOFs represent the elastic deformations (deflections and slopes) of the first $(n_i - 1)$ flexure hinges from each of the n serial chains (when counting starts from the fixed flexure hinge and continues towards the output platform), and the remaining six DOFs, which are individualized in Eq. (4.141), are the translational and rotary displacements of the output plate. It would definitely be a serious undertaking and well beyond the scope of this work to explicitly formulate Lagrange's equations for a generic spatial hybrid flexure-based compliant mechanism, and such an elaboration will be not approached here.

4.5 Damping Effects

4.5.1 Introduction

Damping is generally defined as energy dissipation under cyclic loading and the resulting stress. During vibration, damping might add in factors that seriously alter the dynamic response of a flexure-based compliant mechanism through either internal or external friction effects. The dynamics of

such compliant mechanisms has been studied so far in this chapter without including damping in the mathematical model, as this topic might not have been of specific interest for a first-hand evaluation of such a system response in either the static or dynamic ranges (through undamped models), but now the damping is taken into consideration and discussed. Details regarding specific damping aspects can be found in the specialty textbooks of Nashif et al.,[27] Lazan,[28] and Rivin,[29] or in the works by Goodman[30] and Jones.[31] Very good incorporation of the damping phenomenon into the general treatment of vibrations can be found in the books of Thomson[18] and Inman.[19]

Internal (also called structural or material) damping can be a very important issue, especially when vibrations occur in the vicinity of a resonant frequency, and at least two major factors impede the accurate evaluation of structural damping, as mentioned by Kareem and Gurley.[32] One factor pertains to the nonreplicating nature of several parameters involved in damping, such as material properties, manufacturing processes, or the experimental environment. The other factor refers to an intrinsic conflict of scales because material damping is incepted at a molecular level and structural dynamics focuses on the macroscale behavior of systems.

Other important considerations also complicate the process of theoretical modeling of the damping phenomenon. The damping process might be desirable when issues related to the resonant behavior of mechanisms or structures are important, such as reducing the peak stresses or prolonging the fatigue life of a system. Damping is, however, a hampering factor in structures and systems where the associated heat generated through energy dissipation impedes the functional precision of a given device. For a large category of mechanical components constructed of metallic or nonmetallic materials, damping is usually attributed to the phenomenon of hysteresis, through which the loading and unloading curves do not coincide over time, due to energy losses, as pictured in Figure 4.10.

The area enclosed by the loading–relieving curves of Figure 4.10 is proportional to the energy lost through material damping during one excitation cycle.

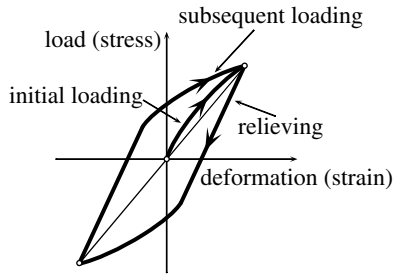

FIGURE 4.10
Hysteresis loop for a generic nonlinear material with damping.

It should be mentioned here that the so-called passive damping, named in such a way to contrast with the active damping that accounts for the energy that dissipates through external devices (such as actuators, for instance), corresponds to losses in structural joints and supports and internal losses and can also be produced by isolator-type devices. Of those three macroscopic sources, internal (material) damping amounts to no more than 10%, as shown by Jones.[31] This aspect is particularly important in flexure-based compliant mechanisms that are built in a monolithic manner, as such devices present virtually no losses though joints.

Lazan[28] enumerated several microscopic sources that contribute to damping, such as constituent defects, grain boundary viscosity, microthermal currents due to internal friction, or eddy currents produced through coupled mechanical–magnetic internal interactions. Among the most important factors that generate damping in beam-type structures, Lazan[28] mentioned a macrothermoelastic phenomenon that manifests itself as a relaxation process of alternative heat generation and conduction through the beam thickness. This process is treated in more detail by Crandall,[33] who analyzed the vibration and vibration damping of an aluminum beam suspended by two wires at its ends. Besides the energy that is dissipated through acoustic radiation and radiation through the supporting strings, most of the losses are due to internal dissipation by a thermoelastic phenomenon. Lobontiu et al.[21] followed a similar approach in assessing the equivalent internal damping present in a thin cantilever beam with piezoelectric patches attached to it. The theoretical damping model was verified experimentally, and the results of the two procedures were in good agreement.

One of the most commonly utilized damping models that apply to both metallic and nonmetallic materials assumes that the process of losing energy through internal dissipation is essentially viscous and that the force generated through this type of damping is proportional to velocity, in the form:

$$F_d = cv \tag{4.142}$$

where c is a proportionality coefficient.

Similar to the manner of allocating stiffness and inertia properties to the degrees of freedom defining the lumped-parameter dynamic model of the three different categories of flexure hinges (single-, multiple-, and two-axis configurations), an attempt will be made here to discretize the internal (and then external) damping characteristics of those flexure hinges about the same degrees of freedom to allow consistent formulation of a damped dynamic model. The reason for proceeding this way is that formulation of the following dynamic equations becomes possible for the one-DOF translatory motion:

$$m\frac{d^2u}{dt^2} + c_{tr}\frac{du}{dt} + k_{tr}u = F \tag{4.143}$$

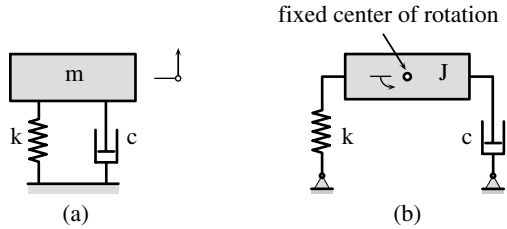

FIGURE 4.11
One-DOF mass–dashpot systems with viscous (Voigt model) damping: (a) translatory system; (b) rotary system.

For rotary degrees of freedom, the corresponding dynamic equation for a damped system is:

$$J\frac{d^2\theta}{dt^2} + c_{rot}\frac{d\theta}{dt} + k_{rot}\theta = M \tag{4.144}$$

Figure 4.11 shows the schematic representation of a translation and rotation mass–dashpot elements with viscous damping (also called Voigt model damping). The lumped stiffness k and inertia m and J properties in the equations above were already dealt with in Chapters 2 and 3, respectively. Variable c, also called the damping coefficient or dashpot parameter, corresponds to the damped motion of the respective degrees of freedom. Equations (4.143) and (4.144) give the mathematical model of a forced one-DOF dynamic system but also depicts the free response of the same system when $F = 0$ or $M = 0$. The damping coefficient is usually related to the critical damping coefficient c_c by means of the damping ratio ζ, as shown by Thomson[18] or Inman,[19] according to:

$$c = \zeta c_c \tag{4.145}$$

where the critical damping coefficient is defined as:

$$c_c = 2\pi\sqrt{mk} \tag{4.146}$$

so that, clearly, the critical damping coefficient can be evaluated when the discretized inertia and stiffness of the motion about the analyzed DOF are already determined, which is perfectly possible, as shown in Chapters 2 and 3. Another important parameter that defines damping is the loss factor η, which represents the energy fraction lost during one vibration cycle and relates to the damping ratio according to:

$$\eta = 2\zeta \tag{4.147}$$

An experimental procedure of evaluating the damping ratio ζ, and therefore the damping coefficient c, is to determine the so-called logarithmic decrement that represents the logarithm of the ratio of two consecutive amplitudes, as measured in a damped vibration (see, for example, Thomson[18] or Inman[19]). The logarithmic decrement, denoted by δ, is connected to the damping ratio by means of the relation:

$$\delta = \frac{2\pi\varsigma}{\sqrt{1-\varsigma^2}} \tag{4.148}$$

As previously mentioned, the damping ratio about a particular DOF can be determined according to a procedure first mentioned by Crandall,[33] who made the assumption, later confirmed by experimental test results, that a linear relaxation process that involves a transverse heat flow from the warmer in-compression fibers to the cooler in-tension fibers of a beam is mainly responsible for the vibration energy that is being lost through damping at room temperature. Crandall[33] showed that the loss factor can therefore be expressed in terms of thermal material properties in the form:

$$\eta = \frac{\alpha^2 E}{c_v} T \frac{\frac{f}{f_r}}{1+\left(\frac{f}{f_r}\right)^2} \tag{4.149}$$

where f is the undamped resonant frequency, calculated as:

$$f = \frac{1}{2\pi}\sqrt{\frac{k}{m}} \tag{4.150}$$

and f_r is the so-called relaxation frequency, defined as:

$$f_r = \frac{\pi}{2}\frac{\kappa}{c_v t^2} \tag{4.151}$$

The above formulation is applicable to the bending of beams where the upper and lower fibers are permanently in opposed conditions, either being in tension or compression, a situation that accounts for the thermal radiation, resulting in internal damping, between the warmer compressed fibers and the cooler tensioned fibers.

A quantifier that evaluates the energy lost during one oscillation cycle is the specific damping energy, which for translation is defined as:

$$D_s = \int_0^{\frac{2\pi}{w}} F_d v \, dt \tag{4.152}$$

In the case of rotary degrees of freedom, Eq. (4.152) will utilize moment M_d instead of damping force F_d and angular velocity ω instead of the linear velocity, v. Lazan[28] showed that this damping energy can be expressed as:

$$D = J\sigma_a^n \tag{4.153}$$

where σ_a is the stress amplitude and J and n are material-dependent coefficients. The linear damping model specified by Lazan[28] takes a value of n = 2 and considers that the shape of the hysteresis loop of Figure 4.10 is an ellipse. Given this set of conditions, Lazan[28] derived the following expression for the loss factor of a viscous material:

$$\eta = \frac{JE}{\pi} \tag{4.154}$$

In several occasions, the external damping can also have an important contribution to the overall energy dissipation. Backer et al.[34] conducted research on the contribution of the external damping as generated by friction of a mechanical member with the surrounding air. They concluded that the damping force applicable to this situation is also proportional to the velocity of that member in the form:

$$F_{d,ext} = c_{ext} v \tag{4.155}$$

Again, Eq. (4.155) is valid, with the corresponding modifications in load and type of deformation, for rotary degrees of freedom, as well. In the equation above, the damping coefficient can be expressed, according to Baker et al.[34] as:

$$c_{ext} = \frac{1}{2}\rho A C_{drag} \tag{4.156}$$

where ρ is the density of the external friction environment (air, in the majority of cases), A is the area of the mechanical member that is normally exposed to friction, and C_{drag} is a drag coefficient.

By analyzing both the internal and external damping it can be seen that the damping forces produced by the two different sources add up to yield in an overall (resultant) damping force whose damping coefficient is:

$$c_r = c + c_{ext} \tag{4.157}$$

so that c_r can be utilized in the dynamic equation of a single DOF system instead of the internal damping coefficient c of Eq. (4.143), for instance.

The damping properties will be now discretized for single-, multiple-, and two-axis flexure hinges in order to enable formulation of the following lumped-parameter dynamic equations expressing either the free response:

$$[M]\left\{\frac{d^2u}{dt^2}\right\}+[c]\left\{\frac{du}{dt}\right\}+[K]\{u\}=\{0\} \tag{4.158}$$

or the forced response:

$$[M]\left\{\frac{d^2u}{dt^2}\right\}+[c]\left\{\frac{du}{dt}\right\}+[K]\{u\}=\{F\} \tag{4.159}$$

where $[c]$ is a diagonal damping matrix, defined specifically for each of the previously mentioned flexure hinge types. The criterion of deriving the discretized damping properties is based on equalizing the energy lost through damping by the real distributed-parameter flexure hinge during a particular type of vibration (axial, bending, or torsional) and the equivalent damping energy of a lumped-parameter system subject to the same type of vibration. This derivation will closely follow the path set when determining the equivalent lumped-parameter inertia properties for the three types of flexure hinges, as previously shown in this chapter. Again, the axial, bending, and torsional effects are considered as taking place independently, according to the small-displacement theory provisions. Because the energy lost through damping is defined in terms of the velocity field, the Rayleigh method is again utilized in a fashion similar to that for deriving the lumped inertia properties—by formulating damping properties for both Euler–Bernoulli and Timoshenko beam models.

4.5.2 Damping Properties of Flexure Hinges as Long (Euler–Bernoulli) Members

The main assumptions of the Euler–Bernoulli beam model were mentioned in both Chapters 2 and 3. The distributed damping properties of a vibrating flexure hinge are transformed into equivalent lumped damping properties corresponding to the discretized elastic and inertia properties that were already derived and located at one end of the respective flexure hinge.

4.5.2.1 Single-Axis Flexure Hinges

As shown when treating the problem of discretizing stiffness (compliance) and inertia properties, a single-axis flexure hinge has mainly three DOFs: two translations (one axial and the other deflectional) and one rotation at its

free end. The damping matrix will also need to be three dimensional, and a simple way to define it is in a diagonal form, as:

$$[c] = \begin{bmatrix} c_{u_x} & 0 & 0 \\ 0 & c_{u_y} & 0 \\ 0 & 0 & c_{\theta_z} \end{bmatrix} \tag{4.160}$$

where the damping coefficient c_{u_x} corresponds to axial vibrations, c_{u_y} is generated through deflectional bending, and c_{θ_z} is connected to rotational bending. As previously mentioned, the Rayleigh method assumes that the velocity distribution of a vibrating system is identical to the corresponding displacement (deformation) field of the same system, and this principle was mathematically expressed by Eqs. (3.4) and (3.5).

For axial vibrations, the specific energy lost in one second through damping of an elemental portion, as pictured in Figure 4.2 and based on combining Eqs. (4.145) and (4.155), can be expressed as:

$$dD_a = v_x^2 \, dc_a \tag{4.161}$$

where the subscript a denotes the axial degrees of freedom. If the damping properties are assumed to be constant over the entire flexure hinge, which means that:

$$dc_a = c_a \, dx \tag{4.162}$$

it follows that the total energy lost through damping in the axial vibration in 1 second will be:

$$D_a = c_a \int_0^l v_x^2 \, dx \tag{4.163}$$

The Rayleigh hypothesis gives the velocity v_x (at a given abscissa) in terms of the velocity at the tip of the flexure v_{1x}, according to Eq. (4.35), so that Eq. (4.163) can be transformed into:

$$D_a = c_a v_{1x}^2 \int_0^l f_a^2(x) \, dx \tag{4.164}$$

The corresponding damping energy of the equivalent system in axial vibration is:

$$D_{ae} = c_{u_x} v_x^2 \tag{4.165}$$

and, because the assumption has been made that the real and equivalent lumped-parameter systems should dissipate the same amount of energy through damping, it follows from Eqs. (4.163) and (4.165) that the equivalent damping coefficient in axial vibration is:

$$c_{u_x} = c_a \int_0^l f_a^2(x)\,dx \tag{4.166}$$

A similar reasoning will allow expressing the equivalent lumped-parameter damping properties generated through bending, and the corresponding damping coefficients are:

$$c_{u_y} = c_b \int_0^l f_{by}^2(x)\,dx \tag{4.167}$$

and:

$$c_{\theta_z} = c_b \int_0^l f_{b\theta_z}^2(x)\,dx \tag{4.168}$$

where the subscript b indicates the bending degrees of freedom. The distribution function $f_{by}(x)$ was given in Eqs. (4.45) and (4.48), whereas the distribution function $f_{b\theta_z}(x)$ is expressed in Eq. (4.58).

4.5.2.2 Multiple-Axis Flexure Hinges

For multiple-axis flexure hinge configurations (with revolute geometry) that have been discretized as six-DOF systems in terms of their stiffness (compliance) and inertia properties, the corresponding lumped-parameter damping matrix will be a diagonal matrix of dimension 6 with the following nonzero components:

$$\begin{cases} c_{11} = c_{u_x} \\ c_{22} = c_{33} = c_{u_y} \\ c_{44} = c_{\theta_x} \\ c_{55} = c_{66} = c_{\theta_y} \end{cases} \tag{4.169}$$

The damping fractions c_{u_x}, c_{u_y}, and c_{θ_z} are formally identical to the ones that were already determined for single-axis flexure hinges in the previous discussion. The damping parameter c_{θ_x} of Eq. (4.169) is produced through

torsion effects and can be derived similarly to other damping coefficients as:

$$c_{\theta_x} = c_t \int_0^l f_t^2(x)\,dx \tag{4.170}$$

where the subscript t denotes the torsional degrees of freedom and the distribution function $f_t(x)$ is given in Eq. (4.68).

4.5.2.3 Two-Axis Flexure Hinges

It was shown in Chapter 3 that the displacement vector of a two-axis flexure hinge has the dimension five; therefore, the diagonal lumped-parameter damping matrix will be of 5×5 dimension in order to enable dynamic modeling that is consistent with the dimensions of the stiffness and inertia matrices corresponding to this type of flexure hinge. The nonzero components of the damping matrix are:

$$\begin{cases} c_{11} = c_{u_x} \\ c_{22} = c_{u_y} \\ c_{33} = c_{u_z} \\ c_{44} = c_{\theta_y} \\ c_{55} = c_{\theta_z} \end{cases} \tag{4.171}$$

The newly introduced damping coefficients of Eq. (4.171) can be calculated similarly to the procedure developed when analyzing the bending of single-axis flexure hinges and the efficient (equivalent) damping coefficients in this case are:

$$c_{u_z} = c_b \int_0^l f_{bz}^2(x)dx \tag{4.172}$$

and:

$$c_{\theta_y} = c_b \int_0^l f_{b\theta_y}^2(x)\,dx \tag{4.173}$$

where the distribution functions f_{bz} and $f_{b\theta_y}$ of Eqs. (4.172) and (4.173) are calculated according to Eqs. (4.80), (4.81), and (4.83), respectively.

4.5.3 Damping Properties of Flexure Hinges as Short (Timoshenko) Members

As previously discussed, the Timoshenko beam model offers a better description for short beams, compared to the Euler–Bernoulli beam model, because the former takes into account shearing and rotary effects that are manifest in short members. The corrections that have to be introduced when utilizing the Timoshenko model will only affect the damping coefficients that are bending connected and will leave unaffected the damping properties that are generated through either axial or torsional vibration. As a consequence, following the reasoning presented within this section and coupling it with the remarks made when deriving the inertia properties, the lumped-parameter damping coefficient for a single-axis flexure hinge that is modified by working under the Timoshenko beam model assumptions is expressed as:

$$c^s_{u_y} = c_b \int_0^l [f^s_{by}(x)]^2 dx \tag{4.174}$$

The superscript *s* in the above equation denotes again the presence of shearing effects in a Timoshenko model. The distribution function of Eq. (4.174) has originally been introduced in Eq. (4.88). Simple changes in the subscript notation will enable calculating the other lumped-parameter damping coefficients that define the multiple- and two-sensitive-axis flexure hinge designs.

References

1. Shabana, A.A., *Dynamics of Multibody Systems*, Cambridge University Press, New York, 1998.
2. Meirovitch, L., *Principles and Techniques of Vibrations*, Prentice-Hall, Englewood Cliffs, NJ, 1997.
3. Gao, X., Solution methods for dynamic response of flexible mechanisms, in *Modern Kinematics: Developments in the Last Forty Years*, A.G. Erdman, Ed., John Wiley & Sons, New York, 1993.
4. Bagci, C. and Streit, D.A., Flexible manipulators, in *Modern Kinematics: Developments in the Last Forty Years*, A.G. Erdman, Ed., John Wiley & Sons, New York, 1993.
5. Boutaghou, Z.-E. and Erdman, A.G., On various nonlinear rod theories for the dynamic analysis of multibody systems, in *Modern Kinematics: Developments in the Last Forty Years*, A.G. Erdman, Ed., John Wiley & Sons, New York, 1993.
6. Simo, J.C. and Vu-Quoc, L., On the dynamics of flexible beams under large overall motions—the plane case, parts 1 and 2, *ASME Journal of Applied Mechanics*, 53, 849, 1986.
7. McPhee, J.J., Automatic generation of motion equations for planar mechanical systems using the new set of "branch coordinates," *Mechanism and Machine Theory*, 33(6), 805, 1998.

8. Liew, K.M., Lee, S.E., and Liu, A.Q., Mixed-interface substructures for dynamic analysis of flexible multibody systems, *Engineering Structures*, 18(7), 495, 1996.
9. Engstler, C. and Kaps, P., A comparison of one-step methods for multibody system dynamics in descriptor and state space form, *Applied Numerical Mathematics*, 24, 457, 1997.
10. Cui, K. and Haque, I., Symbolic equations of motion for hybrid multibody systems using a matrix-vector formulation, *Mechanism and Machine Theory*, 32(6), 743, 1997.
11. Boyer, F. and Coiffet, P., Symbolic modeling of a flexible manipulator via assembling of its generalized Newton–Euler model, *Mechanism and Machine Theory*, 31(1), 45, 1996.
12. Vibet, C., Dynamics modeling of Lagrangian mechanisms from inertial matrix elements, *Computer Methods in Applied Mechanical Engineering*, 123, 317, 1995.
13. Surdilovic, D. and Vukobratovic, M., One method for efficient dynamic modeling of flexible manipulators, *Mechanism and Machine Theory*, 31(3), 297, 1996.
14. Yu, W., Mathematical modeling of a class of flexible robot, *Applied Mathematical Modelling*, 19, 537, 1995.
15. Indri, M. and Tornambe, A., Lyapunov analysis of the approximate motion equations of flexible structures, *Systems & Control Letters*, 28, 31, 1996.
16. Lyon, S.M. et al., Prediction of the first modal frequency of compliant mechanisms using the pseudo-rigid-body model, *ASME Journal of Mechanical Design*, 121(2), 309, 1999.
17. Smith, S.T., *Flexures: Elements of Elastic Mechanisms*, Gordon & Breach, Amsterdam, 2000.
18. Thomson, W.T., *Theory of Vibration with Applications*, 3rd ed., Prentice-Hall, Englewood Cliffs, NJ, 1988.
19. Inman, D.J., *Engineering Vibrations*, Prentice-Hall, Englewood Cliffs, NJ, 1994.
20. Weaver, W., Jr., Timoshenko, S.P., and Young, D.H., *Vibration Problems in Engineering*, 5th ed., John Wiley & Sons, New York, 1990.
21. Lobontiu, N., Goldfarb, M., and Garcia, E., Achieving maximum tip displacement during resonant excitation of piezoelectrically actuated beams, *Journal of Intelligent Material Systems and Structures*, 10, 900, 1999.
22. Lee, S.Y., Ke, H.Y., and Kuo, Y.H., Analysis of non-uniform beam vibration, *Journal of Sound and Vibration*, 142(1), 15, 1990.
23. Lee, S.Y., Wang, W.R., and Chen, T.Y., A general approach on the mechanical analysis of non-uniform beams with nonhomogeneous elastic boundary conditions, *ASME Journal of Vibration and Acoustics*, 120, 164, 1998.
24. Lobontiu, N., Distributed-parameter dynamic model and optimized design of a four-link pendulum with flexure hinges, *Mechanism and Machine Theory*, 36(5), 653, 2001.
25. Wood, W.L., *Practical Time Stepping Schemes*, Clarendon Press, London, 1990.
26. Beer, F.P. and Johnston, E.R., *Vector Mechanics for Engineers: Dynamics*, 6th ed., McGraw-Hill, New York, 1997.
27. Nashif, A.D., Jones, D.I.G., and Henderson, J.P., *Vibration Damping*, Wiley-Interscience, New York, 1985.
28. Lazan, B.J., *Damping of Materials and Members in Structural Mechanics*, Pergamon Press, Oxford, 1968.
29. Rivin, E.I., *Stiffness and Damping in Mechanical Design*, Marcel Dekker, New York, 1999.

30. Goodman, L.E., Material damping and slip damping, in *Shock and Vibration Handbook*, C.M. Harris, Ed., McGraw-Hill, New York, 1996, p. 36.1.
31. Jones, D.G.I., Applied damping treatments, in *Shock and Vibration Handbook*, C.M. Harris, Ed., McGraw-Hill, New York, 1996, p. 37.1.
32. Kareem, A. and Gurley, K., Damping in structures: its evaluation and treatment of uncertainty, *Journal of Wind Engineering and Industrial Aerodynamics*, 59, 131, 1996.
33. Crandall, S.H., The role of damping in vibration theory, *Journal of Sound and Vibration*, 11(1), 3, 1970.
34. Baker, W.E., Woolam, W.E., and Young, D., Air and internal damping of thin cantilever beams, *International Journal of Mechanical Sciences*, 9, 743, 1967.

5

Finite-Element Formulation for Flexure Hinges and Flexure-Based Compliant Mechanisms

5.1 Introduction

The finite-element technique, through several commercially available software programs, is a favorite tool for modeling and analyzing the behavior of compliant mechanisms. A few reasons for the preference given to the finite-element procedure in both industry and research or academia include the speed of analysis, wide choice of analysis types (static, modal, dynamic, thermal, and mixed/coupled-field are the basic modules currently incorporated in professional finite-element software), and direct interaction with related CAD tools that provide the geometry of oftentimes complex shapes or the relative (at least apparent) ease of use. Several levels of complexity for modeling and analyzing flexure-based compliant mechanisms are provided by the finite-element software codes. The most basic approach to a given application starts with a specified geometry that is utilized to perform the desired analysis in order to find the state of stress and deformation or the modal response, for instance. Because all the parameters are predetermined, the insight that can be gained by running a finite-element analysis is limited to the particular geometry that has originally been selected. Several CAD programs are currently designed to connect interactively with a finite-element module and enable the parametric design or drawing of a part or subassembly. As a consequence, it is possible to quickly model and analyze more geometry configurations by simply changing the numerical values of the geometric parameters of interest, and the procedure this way actually becomes an optimization tool that performs a sequential search over the design subspace of interest. Most of the finite-element programs also have the capability of running a real optimization module based on a start design whose parameters are subsequently varied through algorithms that are internal to the software until the local optimum response is reached.

Whereas general-use finite-element software programs are involved in solving compliant mechanism applications (especially at the microelectromechanical system [MEMS] level) through their normal routines and element libraries, approaching the flexure hinges and the flexure-based compliant mechanisms by means of dedicated finite-element software with a minimal library containing special elements represents a direction that will probably receive more attention in the future. In a recent monograph, Gerardin and Cardona[1] treated the subject of dynamics of flexible multibody systems by utilizing a finite-element approach whereby the total motion of such systems is modeled in a unitary fashion by referring both the elastic deformation and rigid body motion to an inertial frame. Their book also presents dedicated software and a corresponding element library that includes models for both elastic and rigid members, with provisions for handling large deformations in dynamic applications from aircraft, vehicle, and other mechanical systems. Although the book mentions flexible hinges, the topic of flexure hinges and their modeling aspects are not specifically addressed.

In their finite-element monograph, Zienkiewicz and Taylor[2] offer a comprehensive set of data, at both the theoretical and application levels, of the finite-element method for a vast array of engineering applications, with many detailed insights into advanced topics such as material, deformation, and contact nonlinearities or mixed problems. Probably the work that best approaches the problem of modeling a flexure (notch) hinge through the finite-element technique is a recent paper written by Zhang and Fasse,[3] in which six nondimensional stiffness parameters (in terms of three translations and three rotations) are derived for the so-called center of stiffness (actually the centroid) of a circular notch hinge of constant width. A similar work is the monograph of Koster,[4] which, among other discussed topics, analyzes a circular flexure hinge by means of only five such nondimensional stiffness parameters. More recently, Murin and Kutis[5] have formulated a three-dimensional beam element for which the cross-section dimensions varied continuously. The stiffness matrix and nodal forces are formulated and their components solved numerically.

In another recent work, Wang and Wang[6] have developed a finite-element scheme for the dynamic analysis of mechanisms that include elastic joints. Specifically, the elastic joints were modeled as linear contact springs that connect the pin and the journal of the joint by formulating a set of constitutive equations that couple the differential equations for the rigid links. Saxena and Ananthasuresh[7] approach the nonlinearities introduced by large displacements in compliant mechanism members and analyze them by means of the finite-element approach. The effect of the geometric parameters of a rectangular cross-section flexible link on the frequency response planar mechanisms is investigated by Yu and Smith,[8] who studied several modalities of reducing the inertia forces without changing the mass of the respective flexible link.

An excellent account of the state of the art in the domain of finite-element analysis of mechanisms is given by Thompson and Sung[9] for the situation that existed in 1985. The paper presents a list of all relevant research dedicated

to highlighting the main phenomena, design functions, element selection, and formulation, as well as solution procedures employed in studying planar mechanisms by means of the finite-element approach. A summary of the factors involved in designing and analyzing flexible linkages, especially those operating at high speeds, is provided by Sung and Thompson,[10] who present various aspects of material selection. Specifically, the authors performed a parametric study based on finite-element modeling by analyzing the dynamic response of four-bar linkages constructed on high-strength, fiber-reinforced composites. Hac and Osinski[11] developed a finite-element model that is capable of capturing the rigid-body motion of flexible members. A special shape function is integrated within the stiffness and mass matrices of a bar element to account for rigid-body displacements. The results of this procedure are validated by comparison to classical analyses of rigid bodies, based on discussion of several applications. In a continuation of this approach, Hac[12] developed a finite-element model for flexible planar linkages by deriving the elemental properties of truss-type elements that combine axial elastic deformation and rigid-body displacement capabilities to model large mechanism displacement.

The finite-element dynamic response of flexible-link mechanisms was formulated by Sriram and Mruthyunjaya,[13] who proposed a modeling and solution scheme whereby the elastic deformations and rigid body motions are integrally captured by utilizing planar beam elements in a co-rotational formulation and an incremental iterative solution procedure based on the Newmark integration scheme and the Newton–Raphson method. Al-Bedoor and Khulief[14] formulated the finite-element model of a translating and rotating flexible link by also introducing a transition element with variable stiffness to model the time-dependent boundary conditions at the prismatic joint. Liew et al.[15] analyzed elastic structures as flexible multibody systems by following a mixed-interface substructuring technique, capable of modeling both the free and fixed interfaces between adjoining flexible/rigid bodies and to reduce the number of elastic coordinates of the entire system.

Transforming the elemental properties from local to global coordinates is a necessary but costly step in the finite-element analysis. To circumvent this drawback, Fallahi[16] developed a finite-element approach based on implicitly eliminating the dependent generalized coordinates in Lagrange's equations for flexible Bernoulli beam elements. The frequency response is fundamental in assessing the dynamic behavior of flexible-link mechanisms. Closed flexible mechanisms and their frequency response were analyzed by Xianmin et al.[17] by means of a finite-element procedure centered on substructuring the entire system, developing a modal basis, and producing the required coupling equations for planar and spatial multibar structures. The resonant response of flexible linkages was studied by Wang,[18] who proposed a finite-element technique designed to model geometric nonlinearities produced by large deformations of links and thus to detect multifrequency resonances such as superharmonic and combination resonances that are shown to be intimately related to the critical speeds of the mechanism.

The classical approach of superimposing rigid-body motion (possibly nonlinear) on small elastic deformations was followed by Chen,[19] who analyzed the finite-element dynamic response of multilink flexible manipulators through a Lagrange procedure whereby the rigid-body and elastic deformation components are decoupled by linearization of the motion equations around the so-called rigid-body reference trajectory. Wang and Wang[6] introduced the finite-element model of elastic joints to describe the link interconnection in elastic mechanisms. They formulated the governing equations of motion of individual links in local coordinates and then coupled these equations with those corresponding to the elastic joints in order to characterize the steady-state solutions of vibrating elastic mechanisms. Besseling and Gong[20] presented a finite-element method for simulating the kinematic or dynamic response of spatial elastic mechanisms by relating the nodal coordinates to element deformation and relative motion through a technique based on the principle of virtual power. Fallahi[21] has proposed a finite-element formulation of Timoshenko beam elements that incorporates the nonlinear effect of geometric stiffening by introducing a tensor to replace the customary elemental matrices, thus generalizing the finite-element approach.

Li[22] has provided the formulation of a two-dimensional beam element that is capable of overpowering restrictions generally posed through the regular assumptions of the linear finite-element theory such as: small displacements, small strains, and small loading steps. A large list of the finite-element approaches to flexible mechanisms is given by Gao.[23] Included are research results treating modal analysis of flexible mechanisms, including those of Imam et al.,[24] Midha et al.,[25,26] and Turcic and Midha,[27] who developed various finite-element modal schemes. The dynamic response of flexible mechanisms, either steady state or transient, has been studied through finite-element techniques by Gear,[28] Chu and Pan,[29] Song and Haug,[30] and Gao et al.,[31] among others. Sekulovic and Salatic[32] have analyzed the plane frames with flexible connections and proposed the stiffness matrix for a beam element with flexible eccentric connections by means of a derivation that utilized the analytical solution of second-order equations.

This chapter approaches the flexure hinges and the flexure-based compliant mechanisms from the viewpoint of the finite-element method (in the stiffness approach) by developing a formulation whereby the flexure hinges are modeled as three-node line elements. It is thus possible to reduce by one the dimensionality of a compliant mechanism problem that is usually solved through existing finite-element software, as it is known that classical modeling through commercially available finite-element software of a single-axis flexure hinge, for instance, requires at least two-dimensional elements because of the geometry variation. Elemental stiffness and mass matrices are formulated in generic (integral) form for single-, multiple-, and two-axis flexure hinges by considering them to be long Euler–Bernoulli members subject to small deformations. Two-node elements are also formulated to model the rigid links for both planar and spatial quasi-rigid links by providing

them with a number of nodal degrees of freedom equal to the number of degrees of freedom of the flexure hinge to which they are connected in a practical application. Explicit formulas are given for the elemental stiffness and mass matrices of single-axis, corner-filleted flexure hinges. These formulas are checked against the corresponding formulas for constant cross-section flexure hinges by considering that the fillet radius reaches the zero limit value. An example is solved by means of the formulation developed in this chapter, by performing both static and modal analysis, and the results are in agreement with those obtained when solving the same problem by a commercially available finite-element code.

The elements presented within this chapter are basic and therefore minimal, as they do not include more advanced topics such as material or large-deformation nonlinearities, shearing, and rotary inertia or stress stiffening effects. The aim here is to give a brief introduction to analyzing the flexure hinges by means of the classical finite-element method and to outline the algorithmic fundamentals that allow formulation of the elemental matrices for other flexure hinge configurations not covered here. The interested reader could attempt to directly employ the explicit formulas that are given in this chapter for single-axis flexure hinges of corner-filleted profile and implement them in finite-element software that permits external addition of elemental matrices in order to further test the formulations.

5.2 Generic Formulation

The finite-element modeling analysis is a tool utilized to determine an approximate solution to a continuum-type field differential problem. In structural statics, for instance, the finite-element technique goes over the following generic steps in a regular stiffness formulation:

- Discretization of the continuum problem into a finite-element mesh—The real geometry of the continuum is divided through surfaces or lines into several conveniently shaped subregions, called finite elements, which are connected at nodes (their adjoining points); this step constitutes the first approximation introduced by the finite-element procedure.
- Formulation of a displacement model—It is assumed that the distribution of the unknown quantity (which is also the main dependent variable) is relatively simple inside each finite element and is determined by interpolating the nodal values of that unknown (also called coordinates or generalized coordinates) through some shape or distribution function (usually of polynomial form); this step constitutes the second approximation introduced by the finite-element method.

- Transformation of the original continuous problem into a discrete one (possessing a finite number of degrees of freedom) by utilizing the two approximations mentioned previously and by applying a principle or statement that is adequate for the studied problem (for instance, the minimization of the total potential energy in static situations).
- Solution of the resulting algebraic equations (which may be derived directly or as a result of additional conditioning, such as linearization or condensation) for the nodal unknowns and further calculation of other quantities related to the already-determined principal unknowns that are either nodal or reside inside the finite elements.

All the steps mentioned above also permit solving modal and frequency-response problems in structural dynamics, where time does not explicitly enter the mathematical formulation. These problems are inscribed into the space-domain discretization class, as illustrated in Figure 5.1.

Another distinct class of problems must account for time dependency; therefore, an additional division, time discretization, which is independent of the previous space discretization, has to be used. Problems of steady-state and transient response are usually treated by solution techniques that combine space and time discretization algorithms, as indicated in Figure 5.1. Details will be given in the following discussion of the space and time semidiscretization processes involved in a dynamic finite-element analysis of structures.

Technically, the space-discretization process, which is common to all types of finite-element analyses, is composed of two main subphases:

- Formulation of the elemental matrix equation and its corresponding matrix and vectors

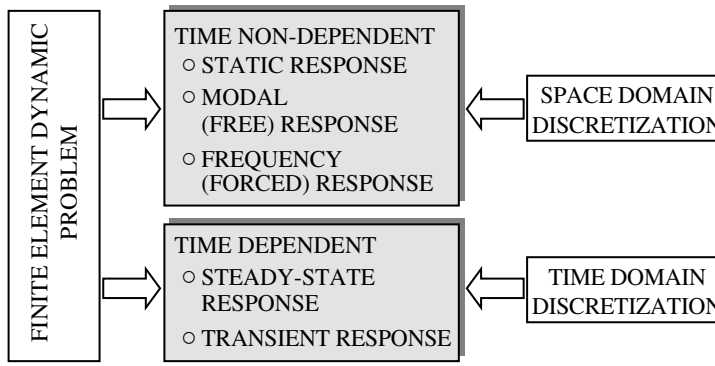

FIGURE 5.1
Main problems and features in the finite-element analysis of flexure-based compliant mechanisms.

- Formulation of the global matrix equation that encompasses all elements of the discretized structure, by means of the assembling process

These steps that are necessary in formulating the elemental matrices and in assembling the global finite-element equations will be discussed next.

5.2.1 Elemental Matrix Equation

Approaches to determine the elemental matrix equation of a structural dynamics problem include Lagrange's equations, Hamilton's principle, the kinetostatic method, and virtual work. The elemental equation is of the form:

$$\{r^e\} = [M^e]\frac{d^2}{dt^2}\{u_n^e\} + [C^e]\frac{d}{dt}\{u_n^e\} + [K^e]\{u_n^e\} + \{f^e\} \tag{5.1}$$

where the superscript e denotes an element and $\{u_n^e\}$ is the element nodal displacement vector.

Details of the derivation of this equation can be found in specialized finite-element work, such as that of Zienkiewicz and Taylor.[2] As mentioned previously, the first approximation in a finite-element problem is involved with space discretization and assumes a given distribution of the problem's unknown (displacement in this case) inside the element in terms of the nodal unknown (nodal displacement here) by means of shape functions, in the form:

$$\{u^e\} = [N]\{u_n^e\} \tag{5.2}$$

In Eq. (5.1), $\{r^e\}$ is the elemental nodal reaction vector, and:

- $[M^e]$ is the mass matrix, defined as:

$$[M^e] = \int_{V_e} [N]^T[\rho][N]\,dV \tag{5.3}$$

  where $[\rho]$ is the density matrix.
- $[C^e]$ is the damping matrix, defined as:

$$[C^e] = \int_{V_e} [N]^T[\mu][N]\,dV \tag{5.4}$$

where $[\mu]$ is the viscosity matrix.

- $[K^e]$ is the stiffness matrix, defined as:

$$[K^e] = \int_{V_e} [B]^T [D][B]\, dV \tag{5.5}$$

where $[D]$ is the elastic matrix.

The accepted definition of the strain vector, according to any classical finite-element textbook, assumes a linear relationship between the strain and nodal displacement vectors:

$$\{\varepsilon^e\} = [B]\{u_n^e\} \tag{5.6}$$

and a similar linear relationship can be cast between the same strain vector and the overall elemental displacement vector:

$$\{\varepsilon^e\} = [S]\{u^e\} \tag{5.7}$$

where $[S]$ is a differential operator that will be explicitly formulated at the element level based on the theory of elasticity considerations.

Combining Eqs. (5.6) and (5.7) results in the following expression for the matrix $[B]$:

$$[B] = [S][N] \tag{5.8}$$

- $\{f^e\}$ is a forcing vector generically defined as:

$$\{f^e\} = -\int_{V_e} [B]^T [D]\{\varepsilon_0\}\, dV + \int_{V_e} [B]^T \{\sigma_0\}\, dV - \int_{V_e} [N]^T \{b\}\, dV - \int_{A_e} [N]^T \{t\}\, dA \tag{5.9}$$

The first term in the right-hand side of Eq. (5.9) represents the initial strain force vector, the second term is the initial stress force vector, the next term takes into consideration volume or body forces, and the last term is a force vector generated by surface effects. More details on elemental matrices will be given when deriving the required terms for different types of elements.

5.2.2 Global Matrix Equation (Assembly Process)

As evident in all the elemental equations presented, no external loading has been introduced so far. However, external loading is likely to act on a structure, and the finite-element procedure usually introduces an external force

or moment vector at a generic node i (of the n-node finite-element mesh), in the form:

$$\{r_i^{ex}\} = \sum_{e=1}^{m} \{r_i^e\} \tag{5.10}$$

The sum in the right-hand side of Eq. (5.10) represents all nodal reactions that are adjacent to the generic node i (it is assumed that m such adjacent nodes do exist). By combining Eq. (5.10) with Eq. (5.1) (written for all the elements of the structure) and after performing simple calculations, the following equation is produced:

$$[M]\frac{d^2}{dt^2}\{u_n\} + [C]\frac{d}{dt}\{u_n\} + [K]\{u_n\} = \{r_{ex}\} - \{f\} \tag{5.11}$$

In the equation above, several global matrices and vectors were introduced as explained next:

- $[M]$ is the $n \times n$ mass matrix with its generic ij term defined as:

$$M_{ij} = \sum_{e=1}^{m} M_{ij}^e \tag{5.12}$$

- $[C]$ is the $n \times n$ damping matrix with its generic ij term defined as:

$$C_{ij} = \sum_{e=1}^{m} C_{ij}^e \tag{5.13}$$

- $[K]$ is the $n \times n$ stiffness matrix with its generic ij term defined as:

$$K_{ij} = \sum_{e=1}^{m} K_{ij}^e \tag{5.14}$$

- $\{f\}$ is the n-dimension internal force vector with its generic i term defined as:

$$f_i = \sum_{e=1}^{m} f_i^e \tag{5.15}$$

The displacement vector $\{u_n\}$ comprises the displacements (degrees of freedom) of all the n nodes of the discretized structure. Following are a few general remarks regarding the global matrices of Eq. (5.11):

- The mass matrix [M] is:
  - Symmetric and positive definite.
  - Known under the name of consistent mass matrix when calculated by means of Eq. (5.12). Another variant of formulating the mass matrix lumps the total mass of one element at nodes according to a predefined criterion, which leads to a diagonal lumped matrix. In the case of a two-node line element, for instance, the mass can be divided into two parts, each placed at one node; for a three-node plane triangular element, the total mass can be partitioned into three equal nodal submasses, and so forth. Utilizing a lumped mass matrix instead of a consistent one greatly simplifies any further calculations.

- The stiffness matrix [K] is:
  - Symmetric and positive definite.
  - A band matrix, because the finite-element method connects one element with only its neighboring elements (thus the method is a "piecewise" one); therefore, its nonzero elements are located in a region that includes the main diagonal. All efforts directed at simplifying the implementation of and further calculations based on the stiffness matrix attempt to minimize the width of the semi-band (because the stiffness matrix is symmetric), and this is generally achieved by minimizing the numeric difference between neighboring nodes and by an adequate rearranging/renumbering algorithm.

- The damping matrix [C] is:
  - Generally cumbersome based on the definition Eq. (5.13).
  - Introduced often-times as a Rayleigh-type linear combination between the mass and stiffness matrices, in the form:

$$[C] = \alpha[M] + \beta[K] \tag{5.16}$$

Full-form Eq. (5.11) is utilized to evaluate the forced transient response of a dynamic system in cases where the initial conditions must be taken into account or when the forcing terms are not periodic. In such situations, various time-stepping integration schemes have to be applied to solve the said equation in the time domain. Essentially, the time is fractioned into n subintervals, and two successive time stations, k and $k + 1$, are connected by means of a time step Δt_k (which can vary to allow for increased solving accuracy) as:

$$t_{k+1} = t_k + \Delta t_k \tag{5.17}$$

An integration method is iteratively applied for each time step that connects two successive time stations, coupled with the initial conditions of the analyzed problem, in order to solve for the unknown nodal displacements of Eq. (5.11).

Such an application makes use of both the space and time semidiscretizations, and more details will be provided when dealing with this issue at a later stage.

For long-transient dynamic problems, simpler time integration schemes are developed to solve for the forced response, as also mentioned in Chapter 4. The modal decomposition technique is most often used due to its relative simplicity and to the fact that the modal response is sought. An alternative procedure for economically solving long-transient problems is to utilize a Ritz vector instead of the modal vector.

The modal response that was just mentioned seeks to solve for either the undamped free response expressed by the equation:

$$[M]\frac{d^2}{dt^2}\{u_n\} + [K]\{u_n\} = \{0\} \tag{5.18}$$

or the free damped response given by the equation:

$$[M]\frac{d^2}{dt^2}\{u_n\} + [C]\frac{d}{dt}\{u_n\} + [K]\{u_n\} = \{0\} \tag{5.19}$$

Problems that are described by either Eq. (5.18) or (5.19) are solved without it being necessary to use time-stepping schemes, usually by applying the substitution:

$$\{u_n\} = \{\Phi_n\}e^{iwt} \tag{5.20}$$

Through this substitution, Eq. (5.19), for instance, will transform into:

$$(-\omega^2[M] + \omega[C] + [K])\{\Phi_n\} = \{0\} \tag{5.21}$$

which is a typical eigenvalue formulation corresponding to a damped free dynamic response situation. When the free response is undamped, the eigenvalue formulation will be:

$$(-\omega^2[M] + [K])\{\Phi_n\} = \{0\} \tag{5.22}$$

For both Eqs. (5.21) and (5.22), $\{\Phi_n\}$ is the eigenvector and ω is the natural frequency of the system. The solution to a free-response dynamic application involves evaluation of the eigenvalues defined as:

$$\lambda = 1/\omega^2 \tag{5.23}$$

through specific techniques, followed by solution to determine the eigenvectors.

A static finite-element problem is governed by the equation:

$$[K]\{u_n\} = \{r_{ex}\} - \{f\} \tag{5.24}$$

whose solution is:

$$\{u_n\} = [K]^{-1}[\{r_{ex}\} - \{f\}] \tag{5.25}$$

5.3 Elemental Matrices for Flexure Hinges

Instead of treating the flexure hinge with its full two- or three-dimensional geometric details (by using two- or three-dimensional finite elements), as the commercially available finite-element software would do, the approach presented here reduces the problem dimensionality by defining the flexure hinge as a three-node line element. Elemental stiffness and mass matrices are presented for single-, multiple-, and two-axis flexure types in a generic (integral) form that enables specific solutions to be found for different flexure hinge geometries. Explicit formulas are given for the elemental stiffness and mass matrices of single-axis, corner-filleted flexure hinges. Special elements will also be formulated to model the rigid links that are connected by flexure hinges in both two- and three-dimensional applications, as detailed next, in order to enable studying the finite-element static, modal, and dynamic responses of flexure-based compliant mechanisms.

Figure 5.2 shows the basic function of modeling a flexure hinge as a three-node finite element as compared to the classical approach of a commercially available finite-element code of meshing the geometric region of an actual flexure hinge with many two- or three-dimensional finite elements. The choice of having an extra node at the midpoint of a flexure hinge element, in addition to the two end nodes, enhances the capacity of these elements to better describe the behavior of a real flexure where, as seen in Chapter 2, the midpoint (or center of rotation of the flexure hinge) is extremely important in terms of quantifying the precision of motion and sensitivity to parasitic effects.

The elemental matrices will be formulated next for single-axis flexure hinges (for two-dimensional applications, as defined in Chapter 2), multiple-axis

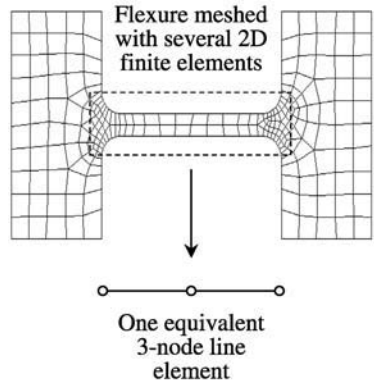

FIGURE 5.2
Flexure hinge as a single, three-node, finite element replacing the multiple-element classical meshing produced through commercial finite-element software.

flexure hinges (revolute), and two-axis flexure hinges (for three-dimensional applications, according to the same definition of Chapter 2).

5.3.1 Single-Axis Flexure Hinge Finite Element for Two-Dimensional Applications

The elemental stiffness and mass matrices will be formulated first for single-axis flexure hinges that are geometrically constant-width members. Figure 5.3 illustrates a three-node line element with three degrees of freedom (DOFs) per node that can serve as a model for any single-axis flexure hinge. The elemental stiffness matrix is calculated according to Eq. (5.5), as discussed in the general presentation of this chapter. For a three-DOF-per-node element, the elastic matrix introduced in Eq. (5.5) is defined as:

$$[D] = E\begin{bmatrix} A(x) & 0 \\ 0 & I_z(x) \end{bmatrix} \tag{5.26}$$

where the variable cross-section area $A(x)$ and moment of inertia about the z-axis $I_z(x)$ are:

$$\begin{aligned} A(x) &= wt(x) \\ I_z(x) &= \frac{wt(x)^3}{12} \end{aligned} \tag{5.27}$$

The strain-displacement of a finite element that is sensitive to axial loading and bending can be put in the following differential form:

$$\begin{Bmatrix} \varepsilon_a \\ \varepsilon_b \end{Bmatrix} = \begin{bmatrix} \dfrac{d}{dx} & 0 \\ 0 & \dfrac{d^2}{dx^2} \end{bmatrix} \begin{Bmatrix} u_x \\ u_y \end{Bmatrix} \tag{5.28}$$

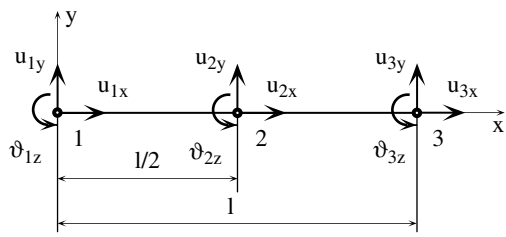

FIGURE 5.3
Three-node, three-DOF-per-node beam element modeling a single-axis flexure hinge.

where the subscripts *a* and *b* stand for axial and bending, respectively. It follows that the [*S*] matrix defined in Eq. (5.7) and relating strain to deformation is:

$$[S] = \begin{bmatrix} \dfrac{d}{dx} & 0 \\ 0 & \dfrac{d^2}{dx^2} \end{bmatrix} \tag{5.29}$$

As shown earlier in this chapter, the internal displacements of a finite element are related to the nodal displacements of the same element by means of shape functions, and in the case of the element shown in Figure 5.3 this relationship is:

$$\begin{cases} u_x = N_{u1x}u_{1x} + N_{u2x}u_{2x} + N_{u3x}u_{3x} \\ u_y = N_{u1y}u_{1y} + N_{u2y}u_{2y} + N_{u3y}u_{3y} + N_{\theta 1z}\theta_{1z} + N_{\theta 2z}\theta_{2z} + N_{\theta 3z}\theta_{3z} \end{cases} \tag{5.30}$$

In order to ensure that the three-node finite element is conformal, which means that it provides continuity of axial displacements as well as continuity of deflection and slope for bending effects, a second-degree polynomial meets this requirements for the intra-elemental axial displacements, and a fifth-degree polynomial fits the respective bending conditions, as defined below:

$$\begin{cases} u_x = a_0 + a_1 x + a_2 x^2 \\ u_y = b_0 + b_1 x + b_2 x^2 + b_3 x^3 + b_4 x^4 + b_5 x^5 \end{cases} \tag{5.31}$$

An explanation for the minimum degrees of the polynomials introduced by Eq. (5.30) is quite simple. Because the flexure hinge finite element has three nodes, one would have to be able to express three different boundary conditions for the axial displacement at each of the nodes (and this will be done in the following); as a consequence, a polynomial with a minimum of three coefficients (therefore of second degree, according to the first expression in Eq. (5.30)) is necessary. Similarly, six boundary conditions must be enforceable at each of the three element nodes in terms of bending effects (one for deflection and the other for the slope), so at least six coefficients in a fifth-degree polynomial would satisfy this condition, as shown in the second expression of Eq. (5.31). At the same time, it is well known from the study of the basic strength of materials that the slope of a beam-like member is the derivative of the deflection in terms of the local coordinate *x*, and the second expression in Eq. (5.31), which gives the deflection, will also give the slope as:

$$\theta_z = b_1 + 2b_2 x + 3b_3 x^2 + 4b_4 x^3 + 5b_5 x^4 \tag{5.32}$$

For a three-node line element, as the one discussed here, the nodal displacement vector is:

$$\{u_n\} = \{u_{1x}, u_{1y}, \theta_{1z}, u_{2x}, u_{2y}, \theta_{2z}, u_{3x}, u_{3y}, \theta_{3z}\}^T \tag{5.33}$$

whereas the shape function matrix is:

$$[N]=\begin{bmatrix} N_{u1x} & 0 & 0 & N_{u2x} & 0 & 0 & N_{u3x} & 0 & 0 \\ 0 & N_{u1y} & N_{\theta 1z} & 0 & N_{u2y} & N_{\theta 2z} & 0 & N_{u3y} & N_{\theta 3z} \end{bmatrix} \tag{5.34}$$

By using the following boundary conditions for axial deformation, deflection, and slope at the three nodes of the finite element:

$$\begin{cases} u = u_i \\ v = v_i \\ \theta = \theta_i \end{cases} \quad \text{for } i = 1,2,3 \quad \text{and } x = \begin{cases} 0, & \text{for } i = 1 \\ \dfrac{l}{2}, & \text{for } i = 2 \\ l, & \text{for } i = 3 \end{cases} \tag{5.35}$$

the shape functions of Eq. (5.30) can be determined by utilizing Eqs. (5.31) in the form:

$$\begin{cases} N_{u1x} = 1 - 3\dfrac{x}{l} + 2\dfrac{x^2}{l^2} \\ N_{u2x} = 4\dfrac{x}{l}\left(1 - \dfrac{x}{l}\right) \\ N_{u3x} = \dfrac{x}{l}\left(2\dfrac{x}{l} - 1\right) \\ N_{u1y} = 1 - \dfrac{387}{69}\dfrac{x^2}{l^2} + \dfrac{214}{23}\dfrac{x^3}{l^3} - \dfrac{156}{23}\dfrac{x^4}{l^4} + \dfrac{144}{69}\dfrac{x^5}{l^5} \\ N_{u2y} = \dfrac{416}{69}\dfrac{x^2}{l^2} - \dfrac{192}{23}\dfrac{x^3}{l^3} - \dfrac{32}{23}\dfrac{x^4}{l^4} + \dfrac{256}{69}\dfrac{x^5}{l^5} \\ N_{u3y} = -\dfrac{29}{69}\dfrac{x^2}{l^2} - \dfrac{22}{23}\dfrac{x^3}{l^3} + \dfrac{188}{23}\dfrac{x^4}{l^4} - \dfrac{400}{69}\dfrac{x^5}{l^5} \\ N_{\theta 1z} = x - \dfrac{168}{69}\dfrac{x^2}{l} + \dfrac{51}{23}\dfrac{x^3}{l^2} - \dfrac{26}{23}\dfrac{x^4}{l^3} + \dfrac{24}{69}\dfrac{x^5}{l^4} \\ N_{\theta 2z} = -\dfrac{16}{69}\dfrac{x^2}{l} + \dfrac{64}{23}\dfrac{x^3}{l^2} - \dfrac{112}{23}\dfrac{x^4}{l^3} + \dfrac{160}{69}\dfrac{x^5}{l^4} \\ N_{\theta 3z} = \dfrac{5}{69}\dfrac{x^2}{l} + \dfrac{3}{23}\dfrac{x^3}{l^2} - \dfrac{34}{23}\dfrac{x^4}{l^3} + \dfrac{88}{69}\dfrac{x^5}{l^4} \end{cases} \tag{5.36}$$

5.3.1.1 Stiffness Matrix

The nonzero stiffness terms in the symmetric 9×9 stiffness matrix are given next. The terms that are connected to axial deformation are located on lines 1, 4, and 7, according to the manner of allocating the degrees of freedom of the three nodes of the line element shown in Figure 5.3, and their generic equations are given as:

$$K_{1,1} = wE\int_l t(x)\left(\frac{dN_{u1x}}{dx}\right)^2 dx \tag{5.37}$$

$$K_{1,4} = wE\int_l t(x)\left(\frac{dN_{u1x}}{dx}\right)\left(\frac{dN_{u2x}}{dx}\right)dx \tag{5.38}$$

$$K_{1,4} = wE\int_l t(x)\left(\frac{dN_{u1x}}{dx}\right)\left(\frac{dN_{u3x}}{dx}\right)dx \tag{5.39}$$

$$K_{4,4} = wE\int_l t(x)\left(\frac{dN_{u2x}}{dx}\right)^2 dx \tag{5.40}$$

$$K_{4,7} = wE\int_l t(x)\left(\frac{dN_{u2x}}{dx}\right)\left(\frac{dN_{u3x}}{dx}\right)dx \tag{5.41}$$

$$K_{7,7} = wE\int_l t(x)\left(\frac{dN_{u3x}}{dx}\right)^2 dx \tag{5.42}$$

The direct-bending stiffness terms (connecting either force to deflection or moment to slope) are:

$$K_{2,2} = \frac{w}{12}E\int_l t(x)^3\left(\frac{d^2N_{u1y}}{dx^2}\right)^2 dx \tag{5.43}$$

$$K_{2,5} = \frac{w}{12}E\int_l t(x)^3\left(\frac{d^2N_{u1y}}{dx^2}\right)\left(\frac{d^2N_{u2y}}{dx^2}\right)dx \tag{5.44}$$

$$K_{2,8} = \frac{w}{12}E\int_l t(x)^3\left(\frac{d^2N_{u1y}}{dx^2}\right)\left(\frac{d^2N_{u3y}}{dx^2}\right)dx \tag{5.45}$$

$$K_{3,3} = \frac{w}{12}E\int_l t(x)^3\left(\frac{d^2N_{\theta 1z}}{dx^2}\right)^2 dx \tag{5.46}$$

$$K_{3,6} = \frac{w}{12} E \int_l t(x)^3 \left(\frac{d^2 N_{\theta 1z}}{dx^2} \right) \left(\frac{d^2 N_{\theta 2z}}{dx^2} \right) dx \tag{5.47}$$

$$K_{3,9} = \frac{w}{12} E \int_l t(x)^3 \left(\frac{d^2 N_{\theta 1z}}{dx^2} \right) \left(\frac{d^2 N_{\theta 3z}}{dx^2} \right) dx \tag{5.48}$$

$$K_{4,4} = \frac{w}{12} E \int_l t(x)^3 \left(\frac{d^2 N_{u2y}}{dx^2} \right)^2 dx \tag{5.49}$$

$$K_{4,7} = \frac{w}{12} E \int_l t(x)^3 \left(\frac{d^2 N_{u2y}}{dx^2} \right) \left(\frac{d^2 N_{u3y}}{dx^2} \right) dx \tag{5.50}$$

$$K_{6,6} = \frac{w}{12} E \int_l t(x)^3 \left(\frac{d^2 N_{\theta 2z}}{dx^2} \right)^2 dx \tag{5.51}$$

$$K_{6,9} = \frac{w}{12} E \int_l t(x)^3 \left(\frac{d^2 N_{\theta 2z}}{dx^2} \right) \left(\frac{d^2 N_{\theta 3z}}{dx^2} \right) dx \tag{5.52}$$

$$K_{8,8} = \frac{w}{12} E \int_l t(x)^3 \left(\frac{d^2 N_{u3y}}{dx^2} \right)^2 dx \tag{5.53}$$

$$K_{9,9} = \frac{w}{12} E \int_l t(x)^3 \left(\frac{d^2 N_{\theta 3z}}{dx^2} \right)^2 dx \tag{5.54}$$

The cross-bending stiffness terms (that connect either force to slope or moment to deflection) are:

$$K_{2,3} = \frac{w}{12} E \int_l t(x)^3 \left(\frac{d^2 N_{u1y}}{dx^2} \right) \left(\frac{d^2 N_{\theta 1z}}{dx^2} \right) dx \tag{5.55}$$

$$K_{2,6} = \frac{w}{12} E \int_l t(x)^3 \left(\frac{d^2 N_{u1y}}{dx^2} \right) \left(\frac{d^2 N_{\theta 2z}}{dx^2} \right) dx \tag{5.56}$$

$$K_{2,9} = \frac{w}{12} E \int_l t(x)^3 \left(\frac{d^2 N_{u1y}}{dx^2} \right) \left(\frac{d^2 N_{\theta 3z}}{dx^2} \right) dx \tag{5.57}$$

$$K_{3,5} = \frac{w}{12} E \int_l t(x)^3 \left(\frac{d^2 N_{\theta 1z}}{dx^2} \right) \left(\frac{d^2 N_{u2y}}{dx^2} \right) dx \tag{5.58}$$

$$K_{3,8} = \frac{w}{12} E \int_l t(x)^3 \left(\frac{d^2 N_{\theta 1z}}{dx^2} \right) \left(\frac{d^2 N_{u3y}}{dx^2} \right) dx \tag{5.59}$$

$$K_{5,6} = \frac{w}{12} E \int_l t(x)^3 \left(\frac{d^2 N_{u2y}}{dx^2} \right) \left(\frac{d^2 N_{\theta 2z}}{dx^2} \right) dx \tag{5.60}$$

$$K_{5,9} = \frac{w}{12} E \int_l t(x)^3 \left(\frac{d^2 N_{u2y}}{dx^2} \right) \left(\frac{d^2 N_{\theta 3z}}{dx^2} \right) dx \tag{5.61}$$

$$K_{8,9} = \frac{w}{12} E \int_l t(x)^3 \left(\frac{d^2 N_{\theta 3z}}{dx^2} \right) \left(\frac{d^2 N_{u3y}}{dx^2} \right) dx \tag{5.62}$$

$$K_{8,9} = \frac{w}{12} E \int_l t(x)^3 \left(\frac{d^2 N_{\theta 3z}}{dx^2} \right) \left(\frac{d^2 N_{u3y}}{dx^2} \right) dx \tag{5.63}$$

In the equations above, the geometry of the cross-section of the flexure is defined by means of the constant width w and variable thickness $t(x)$ as given in Eq. (5.27).

5.3.1.2 Mass Matrix

The elemental mass matrix was generically introduced in Eq. (5.3). For a homogeneous and isotropic material, the density is constant, and the stiffness matrix defining the mass matrix that is symmetric simplifies. The nonzero components of the diagonal mass matrix that are attributed to axial effects are:

$$M_{1,1} = \rho w \int_l t(x) N_{u1x}^2 \, dx \tag{5.64}$$

$$M_{1,4} = \rho w \int_l t(x) N_{u1x} N_{u2x} \, dx \tag{5.65}$$

$$M_{1,7} = \rho w \int_l t(x) N_{u1x} N_{u3x} \, dx \tag{5.66}$$

$$M_{4,4} = \rho w \int_l t(x) N_{u2x}^2 \, dx \tag{5.67}$$

$$M_{4,7} = \rho w \int_l t(x) N_{u2x} N_{u3x} \, dx \tag{5.68}$$

$$M_{7,7} = \rho w \int_l t(x) N_{u3x}^2 \, dx \tag{5.69}$$

The similar components of the elemental mass matrix that are produced through direct bending are:

$$M_{2,2} = \rho w \int_l t(x) N_{u1y}^2 \, dx \tag{5.70}$$

$$M_{2,5} = \rho w \int_l t(x) N_{u1y} N_{u2y} \, dx \tag{5.71}$$

$$M_{2,8} = \rho w \int_l t(x) N_{u1y} N_{u3y} \, dx \tag{5.72}$$

$$M_{3,3} = \rho w \int_l t(x) N_{\theta 1z}^2 \, dx \tag{5.73}$$

$$M_{3,6} = \rho w \int_l t(x) N_{\theta 1z} N_{\theta 2z} \, dx \tag{5.74}$$

$$M_{3,6} = \rho w \int_l t(x) N_{\theta 1z} N_{\theta 3z} \, dx \tag{5.75}$$

$$M_{5,5} = \rho w \int_l t(x) N_{u2y}^2 \, dx \tag{5.76}$$

$$M_{5,8} = \rho w \int_l t(x) N_{u2y} N_{u3y} \, dx \tag{5.77}$$

$$M_{6,6} = \rho w \int_l t(x) N_{\theta 2z}^2 \, dx \tag{5.78}$$

$$M_{6,9} = \rho w \int_l t(x) N_{\theta 2z} N_{\theta 3z} \, dx \tag{5.79}$$

$$M_{8,8} = \rho w \int_l t(x) N_{u3y}^2 \, dx \tag{5.80}$$

$$M_{9,9} = \rho w \int_l t(x) N_{\theta 3z}^2 \, dx \tag{5.81}$$

The cross-bending mass terms can be determined by means of the following equations:

$$M_{2,3} = \rho w \int_l t(x) N_{u1y} N_{\theta 1z} \, dx \tag{5.82}$$

$$M_{2,6} = \rho w \int_l t(x) N_{u1y} N_{\theta 2z} \, dx \tag{5.83}$$

$$M_{2,9} = \rho w \int_l t(x) N_{u1y} N_{\theta 3z} \, dx \tag{5.84}$$

$$M_{3,5} = \rho w \int_l t(x) N_{\theta 1z} N_{u2y} \, dx \tag{5.85}$$

$$M_{3,8} = \rho w \int_l t(x) N_{\theta 1z} N_{u3y} \, dx \tag{5.86}$$

$$M_{5,6} = \rho w \int_l t(x) N_{u2y} N_{\theta 2z} \, dx \tag{5.87}$$

$$M_{5,9} = \rho w \int_l t(x) N_{u2y} N_{\theta 3z} \, dx \tag{5.88}$$

$$M_{6,8} = \rho w \int_l t(x) N_{\theta 2z} N_{u3y} \, dx \tag{5.89}$$

$$M_{8,9} = \rho w \int_l t(x) N_{u3y} N_{\theta 3z} \, dx \tag{5.90}$$

At the end of this chapter, in the appendix, the elemental stiffness and mass matrices are explicitly given for a three-node, three-DOF-per-node finite

element corresponding to a single-axis, corner-filleted flexure hinge, as well as for a similar constant cross-section element.

5.3.2 Multiple-Axis Flexure Hinge Finite Element for Three-Dimensional Applications

Revolute multiple-axis finite elements are given a generic formulation, similar to the development described for single-axis flexure hinges. Figure 5.4 illustrates a three-node, six-DOF-per-node finite element that models a generic revolute flexure hinge.

5.3.2.1 Stiffness Matrix

The elemental stiffness matrix is formulated first for a three-dimensional finite element that also possesses torsion capability, in addition to being sensitive to axial and bending effects. The bending, as shown in Figure 5.4, is now double, as independent actions can be handled in bending about either the y or z principal axes of the finite element. The only new aspect is therefore the torsion and the shape function associated with it. Torsion is formally similar to axial loading, which allows introducing the corresponding shape function as a second-degree polynomial, because three nodal boundary conditions must be complied with. However, the newly introduced shape functions are expressed in terms of the nodal coordinates as:

$$\begin{cases} u_z = N_{u1z}u_{1z} + N_{u2z}u_{2z} + N_{u3z}u_{3z} + N_{\theta 1y}\theta_{1y} + N_{\theta 2y}\theta_{2y} + N_{\theta 3y}\theta_{3y} \\ \theta_x = N_{\theta 1x}\theta_{1x} + N_{\theta 2x}\theta_{2x} + N_{\theta 3x}\theta_{3x} \end{cases} \tag{5.91}$$

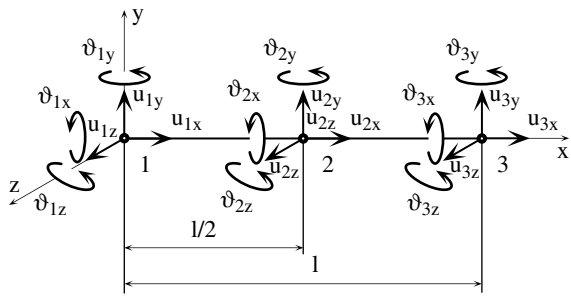

FIGURE 5.4
Three-node, six-DOF-per-node beam element modeling a multiple-axis flexure hinge.

The shape function matrix [N] in this case is a 4×18 matrix with nontrivial terms:

$$\begin{cases} N_{1,1} = N_{4,4} = N_{u1x} \\ N_{1,7} = N_{4,10} = N_{u2x} \\ N_{1,13} = N_{4,16} = N_{u3x} \\ N_{2,2} = N_{3,3} = N_{u1y} \\ N_{2,6} = N_{3,5} = N_{\theta 1z} \\ N_{2,8} = N_{3,9} = N_{u2y} \\ N_{2,12} = N_{3,11} = N_{\theta 1z} \\ N_{2,14} = N_{3,15} = N_{u3y} \\ N_{2,18} = N_{3,17} = N_{\theta 3z} \end{cases} \tag{5.92}$$

Obviously, the shape functions of this equation are the ones already introduced when dealing with the generic formulation of single-axis flexure hinge finite elements. The generalized strain–deformation relationship for a multiple-axis flexure hinge finite element is of the form:

$$\begin{Bmatrix} \varepsilon_a \\ \varepsilon_{by} \\ \varepsilon_{bz} \\ \gamma_t \end{Bmatrix} = \begin{bmatrix} \frac{d}{dx} & 0 & 0 & 0 \\ 0 & \frac{d^2}{dx^2} & 0 & 0 \\ 0 & 0 & \frac{d^2}{dx^2} & 0 \\ 0 & 0 & 0 & \frac{d}{dx} \end{bmatrix} \begin{Bmatrix} u_x \\ u_y \\ u_z \\ \theta_x \end{Bmatrix} \tag{5.93}$$

which, according to the definition of Eq. (5.7), suggests that the [S] matrix is:

$$[S] = \begin{bmatrix} \frac{d}{dx} & 0 & 0 & 0 \\ 0 & \frac{d^2}{dx^2} & 0 & 0 \\ 0 & 0 & \frac{d^2}{dx^2} & 0 \\ 0 & 0 & 0 & \frac{d}{dx} \end{bmatrix} \tag{5.94}$$

The generalized stress–strain relationship for an element that captures axial, double bending, and torsion can be written as:

$$\begin{Bmatrix} N \\ M_{by} \\ M_{bz} \\ M_t \end{Bmatrix} = \begin{bmatrix} EA(x) & 0 & 0 & 0 \\ 0 & EI(x) & 0 & 0 \\ 0 & 0 & EI(x) & 0 \\ 0 & 0 & 0 & GI_p(x) \end{bmatrix} \begin{Bmatrix} \varepsilon_a \\ \varepsilon_{by} \\ \varepsilon_{bz} \\ \gamma_t \end{Bmatrix} \tag{5.95}$$

This generic formulation suggests that the elasticity matrix introduced in Eq. (5.5) is:

$$[D] = \begin{bmatrix} EA(x) & 0 & 0 & 0 \\ 0 & EI(x) & 0 & 0 \\ 0 & 0 & EI(x) & 0 \\ 0 & 0 & 0 & GI_p(x) \end{bmatrix} \tag{5.96}$$

In the equations above, the geometry of the cross-section of the flexure is defined by means of the area, $A(x)$; the moment of inertia about either the y or z axis, $I(x)$; and the polar moment of inertia, $I_p(x)$ as:

$$\begin{cases} A(x) = \dfrac{\pi\, t(x)^2}{4} \\ I(x) = \dfrac{\pi\, t(x)^4}{64} \\ I_p(x) = \dfrac{\pi\, t(x)^4}{32} \end{cases} \tag{5.97}$$

All the elements that are necessary to calculate the components of the elemental symmetric stiffness matrix, according to Eq. (5.5), are now available. The stiffness components that are related to axial effects can be calculated as:

$$K_{1,1} = \frac{\pi}{4} E \int_l t(x)^2 \left(\frac{dN_{u1x}}{dx} \right)^2 dx \tag{5.98}$$

$$K_{1,7} = \frac{\pi}{4} E \int_l t(x)^2 \left(\frac{dN_{u1x}}{dx} \right) \left(\frac{dN_{u2x}}{dx} \right) dx \tag{5.99}$$

$$K_{1,13} = \frac{\pi}{4} E \int_l t(x)^2 \left(\frac{dN_{u1x}}{dx} \right) \left(\frac{dN_{u3x}}{dx} \right) dx \tag{5.100}$$

$$K_{7,7} = \frac{\pi}{4} E \int_l t(x)^2 \left(\frac{dN_{u2x}}{dx} \right)^2 dx \tag{5.101}$$

$$K_{7,13} = \frac{\pi}{4} E \int_l t(x)^2 \left(\frac{dN_{u2x}}{dx} \right) \left(\frac{dN_{u3x}}{dx} \right) dx \tag{5.102}$$

$$K_{13,13} = \frac{\pi}{4} E \int_l t(x)^2 \left(\frac{dN_{u3x}}{dx} \right)^2 dx \tag{5.103}$$

The direct-bending stiffness terms are given by the following equations:

$$K_{2,2} = K_{3,3} = \frac{\pi}{64} E \int_l t(x)^4 \left(\frac{d^2 N_{u1y}}{dx^2} \right)^2 dx \tag{5.104}$$

$$K_{2,8} = K_{3,9} = \frac{\pi}{64} E \int_l t(x)^4 \left(\frac{d^2 N_{u1y}}{dx^2} \right) \left(\frac{d^2 N_{u2y}}{dx^2} \right) dx \tag{5.105}$$

$$K_{2,14} = K_{3,15} = \frac{\pi}{64} E \int_l t(x)^4 \left(\frac{d^2 N_{u1y}}{dx^2} \right) \left(\frac{d^2 N_{u3y}}{dx^2} \right) dx \tag{5.106}$$

$$K_{5,5} = K_{6,6} = \frac{\pi}{64} E \int_l t(x)^4 \left(\frac{d^2 N_{\theta 1z}}{dx^2} \right)^2 dx \tag{5.107}$$

$$K_{5,11} = K_{6,12} = \frac{\pi}{64} E \int_l t(x)^4 \left(\frac{d^2 N_{\theta 1z}}{dx^2} \right) \left(\frac{d^2 N_{\theta 2z}}{dx^2} \right) dx \tag{5.108}$$

$$K_{5,17} = K_{6,18} = \frac{\pi}{64} E \int_l t(x)^4 \left(\frac{d^2 N_{\theta 1z}}{dx^2} \right) \left(\frac{d^2 N_{\theta 3z}}{dx^2} \right) dx \tag{5.109}$$

$$K_{8,8} = K_{9,9} = \frac{\pi}{64} E \int_l t(x)^4 \left(\frac{d^2 N_{u2y}}{dx^2} \right)^2 dx \tag{5.110}$$

$$K_{8,14} = K_{9,15} = \frac{\pi}{64} E \int_l t(x)^4 \left(\frac{d^2 N_{u2y}}{dx^2} \right) \left(\frac{d^2 N_{u3y}}{dx^2} \right) dx \tag{5.111}$$

$$K_{11,11} = K_{12,12} = \frac{\pi}{64} E \int_l t(x)^4 \left(\frac{d^2 N_{\theta 2z}}{dx^2} \right)^2 dx \tag{5.112}$$

$$K_{11,17} = K_{12,18} = \frac{\pi}{64} E \int_l t(x)^4 \left(\frac{d^2 N_{\theta 2z}}{dx^2} \right) \left(\frac{d^2 N_{\theta 3z}}{dx^2} \right) dx \tag{5.113}$$

$$K_{14,14} = K_{15,15} = \frac{\pi}{64} E \int_l t(x)^4 \left(\frac{d^2 N_{u3y}}{dx^2} \right)^2 dx \tag{5.114}$$

$$K_{17,17} = K_{18,18} = \frac{\pi}{64} E \int_l t(x)^4 \left(\frac{d^2 N_{\theta 3z}}{dx^2} \right)^2 dx \tag{5.115}$$

The cross-bending stiffness terms can be calculated for a given longitudinal profile of a revolute flexure hinge by means of the equations:

$$K_{2,6} = K_{3,5} = \frac{\pi}{64} E \int_l t(x)^4 \left(\frac{d^2 N_{u1y}}{dx^2} \right) \left(\frac{d^2 N_{\theta 1z}}{dx^2} \right) dx \tag{5.116}$$

$$K_{2,12} = K_{3,11} = \frac{\pi}{64} E \int_l t(x)^4 \left(\frac{d^2 N_{u1y}}{dx^2} \right) \left(\frac{d^2 N_{\theta 2z}}{dx^2} \right) dx \tag{5.117}$$

$$K_{2,18} = K_{3,17} = \frac{\pi}{64} E \int_l t(x)^4 \left(\frac{d^2 N_{u1y}}{dx^2} \right) \left(\frac{d^2 N_{\theta 3z}}{dx^2} \right) dx \tag{5.118}$$

$$K_{5,9} = K_{6,8} = \frac{\pi}{64} E \int_l t(x)^4 \left(\frac{d^2 N_{\theta 1z}}{dx^2} \right) \left(\frac{d^2 N_{u2y}}{dx^2} \right) dx \tag{5.119}$$

$$K_{5,15} = K_{6,14} = \frac{\pi}{64} E \int_l t(x)^4 \left(\frac{d^2 N_{\theta 1z}}{dx^2} \right) \left(\frac{d^2 N_{u3y}}{dx^2} \right) dx \tag{5.120}$$

$$K_{8,12} = K_{9,11} = \frac{\pi}{64} E \int_l t(x)^4 \left(\frac{d^2 N_{u2y}}{dx^2} \right) \left(\frac{d^2 N_{\theta 2z}}{dx^2} \right) dx \tag{5.121}$$

$$K_{8,18} = K_{9,17} = \frac{\pi}{64} E \int_l t(x)^4 \left(\frac{d^2 N_{u2y}}{dx^2} \right) \left(\frac{d^2 N_{\theta 3z}}{dx^2} \right) dx \tag{5.122}$$

$$K_{11,15} = K_{12,14} = \frac{\pi}{64} E \int_l t(x)^4 \left(\frac{d^2 N_{\theta 2z}}{dx^2} \right) \left(\frac{d^2 N_{u3y}}{dx^2} \right) dx \tag{5.123}$$

$$K_{14,18} = K_{15,17} = \frac{\pi}{64} E \int_l t(x)^4 \left(\frac{d^2 N_{u3y}}{dx^2} \right) \left(\frac{d^2 N_{\theta 3z}}{dx^2} \right) dx \tag{5.124}$$

The stiffness terms that are torsion related can be calculated as:

$$K_{4,4} = \frac{\pi}{32} G \int_l t(x)^4 \left(\frac{dN_{u1x}}{dx} \right)^2 dx \tag{5.125}$$

$$K_{4,10} = \frac{\pi}{32} G \int_l t(x)^4 \left(\frac{dN_{u1x}}{dx} \right) \left(\frac{dN_{u2x}}{dx} \right) dx \tag{5.126}$$

$$K_{4,16} = \frac{\pi}{32} G \int_l t(x)^4 \left(\frac{dN_{u1x}}{dx} \right) \left(\frac{dN_{u3x}}{dx} \right) dx \tag{5.127}$$

$$K_{10,10} = \frac{\pi}{32} G \int_l t(x)^4 \left(\frac{dN_{u2x}}{dx} \right)^2 dx \tag{5.128}$$

$$K_{10,16} = \frac{\pi}{32} G \int_l t(x)^4 \left(\frac{dN_{u2x}}{dx} \right) \left(\frac{dN_{u3x}}{dx} \right) dx \tag{5.129}$$

$$K_{16,16} = \frac{\pi}{32} G \int_l t(x)^4 \left(\frac{dN_{u3x}}{dx} \right)^2 dx \tag{5.130}$$

5.3.2.2 Mass Matrix

The elemental matrix of Eq. (5.3) can be rewritten in the following form:

$$[M^e] = \frac{\pi \rho}{4} \int_l t(x)^2 [N]^T [N] dx \tag{5.131}$$

where it has been taken into account that the flexure hinge is constructed of homogeneous material, thus the density matrix of generic Eq. (5.3) reduces to the constant factor ρ. By carrying on the matrix multiplication of the previous equation, the components of the symmetric elemental mass matrix of a generic revolute flexure hinge whose variable diameter is $t(x)$ can be found. The nonzero mass terms that are related to axial and torsional effects are:

$$M_{1,1} = M_{4,4} = \frac{\pi\rho}{4}\int_l t(x)^2 N_{u1x}^2\, dx \tag{5.132}$$

$$M_{1,7} = M_{4,10} = \frac{\pi\rho}{4}\int_l t(x)^2 N_{u1x} N_{u2x}\, dx \tag{5.133}$$

$$M_{1,13} = M_{4,16} = \frac{\pi\rho}{4}\int_l t(x)^2 N_{u1x} N_{u3x}\, dx \tag{5.134}$$

$$M_{7,7} = M_{10,10} = \frac{\pi\rho}{4}\int_l t(x)^2 N_{u2x}^2\, dx \tag{5.135}$$

$$M_{7,13} = M_{10,16} = \frac{\pi\rho}{4}\int_l t(x)^2 N_{u2x} N_{u3x}\, dx \tag{5.136}$$

$$M_{13,13} = M_{16,16} = \frac{\pi\rho}{4}\int_l t(x)^2 N_{u3x}^2\, dx \tag{5.137}$$

The components of the elemental mass matrix that are associated with direct-bending effects are:

$$M_{2,2} = M_{3,3} = \frac{\pi\rho}{4}\int_l t(x)^2 N_{u1y}^2\, dx \tag{5.138}$$

$$M_{2,8} = M_{3,9} = \frac{\pi\rho}{4}\int_l t(x)^2 N_{u1y} N_{u2y}\, dx \tag{5.139}$$

$$M_{2,14} = M_{3,15} = \frac{\pi\rho}{4}\int_l t(x)^2 N_{u1y} N_{u3y}\, dx \tag{5.140}$$

$$M_{5,5} = M_{6,6} = \frac{\pi\rho}{4}\int_l t(x)^2 N_{\theta 1z}^2\, dx \tag{5.141}$$

$$M_{5,11} = M_{6,12} = \frac{\pi\rho}{4}\int_l t(x)^2 N_{\theta 1z} N_{\theta 2z}\, dx \tag{5.142}$$

$$M_{5,17} = M_{6,18} = \frac{\pi\rho}{4}\int_l t(x)^2 N_{\theta 1z} N_{\theta 3z}\, dx \tag{5.143}$$

$$M_{8,8} = M_{9,9} = \frac{\pi\rho}{4}\int_l t(x)^2 N_{u2y}^2\, dx \tag{5.144}$$

$$M_{8,14} = M_{9,15} = \frac{\pi\rho}{4}\int_l t(x)^2 N_{u2y} N_{u3y}\, dx \tag{5.145}$$

$$M_{11,11} = M_{12,12} = \frac{\pi\rho}{4}\int_l t(x)^2 N_{\theta 2z}^2\, dx \tag{5.146}$$

$$M_{11,17} = M_{12,18} = \frac{\pi\rho}{4}\int_l t(x)^2 N_{\theta 2z} N_{\theta 3z}\, dx \tag{5.147}$$

$$M_{14,14} = M_{15,15} = \frac{\pi\rho}{4}\int_l t(x)^2 N_{u3y}^2\, dx \tag{5.148}$$

The components of the elemental mass matrix that are produced by cross-bending effects are:

$$M_{2,6} = M_{3,5} = \frac{\pi\rho}{4}\int_l t(x)^2 N_{u1y} N_{\theta 1z}\, dx \tag{5.149}$$

$$M_{2,12} = M_{3,11} = \frac{\pi\rho}{4}\int_l t(x)^2 N_{u1y} N_{\theta 2z}\, dx \tag{5.150}$$

$$M_{2,18} = M_{3,17} = \frac{\pi\rho}{4}\int_l t(x)^2 N_{u1y} N_{\theta 3z}\, dx \tag{5.151}$$

$$M_{5,9} = M_{6,8} = \frac{\pi\rho}{4}\int_l t(x)^2 N_{\theta 1z} N_{u2y}\, dx \tag{5.152}$$

$$M_{5,15} = M_{6,14} = \frac{\pi\rho}{4}\int_l t(x)^2 N_{\theta 1z} N_{u3y}\, dx \tag{5.153}$$

$$M_{8,12} = M_{9,11} = \frac{\pi\rho}{4}\int_l t(x)^2 N_{u2y} N_{\theta 2z}\, dx \tag{5.154}$$

$$M_{8,18} = M_{9,17} = \frac{\pi\rho}{4}\int_l t(x)^2 N_{u2y} N_{\theta 3z}\, dx \tag{5.155}$$

$$M_{11,15} = M_{12,14} = \frac{\pi\rho}{4}\int_l t(x)^2 N_{\theta 2z} N_{u3y}\, dx \tag{5.156}$$

$$M_{14,18} = M_{15,17} = \frac{\pi\rho}{4}\int_l t(x)^2 N_{u3y} N_{\theta 3z}\, dx \tag{5.157}$$

5.3.3 Two-Axis Flexure Hinge Finite Element for Three-Dimensional Applications

Developed here are the stiffness and mass matrices of a generic two-axis finite element for three-dimensional applications. Such a flexure hinge configuration was introduced in Chapter 2, where the full set of compliances was formulated based the parameters defining the geometry of this flexure configuration. Figure 5.5 illustrates a generic three-node, five-DOF-per-node generic finite element that represents a two-axis flexure hinge. As mentioned in Chapter 2, this flexure type is expected to be capable of responding to bending about two perpendicular axes and axial loading, but not to torsion, and this is the reason for the finite element being described by five DOFs per node.

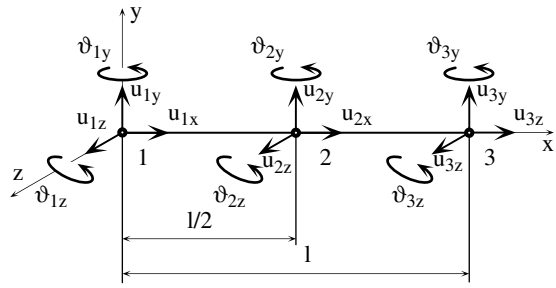

FIGURE 5.5
Three-node, five-DOF-per-node beam element modeling a two-axis flexure hinge.

5.3.3.1 Stiffness Matrix

Considerations similar to the ones discussed for a multiple-axis flexure hinge finite element allow us to formulate the shape functions and corresponding 3×15 shape function matrix with the following nonzero components:

$$\begin{cases} N_{1,1} = N_{u1x} \\ N_{1,6} = N_{u2x} \\ N_{1,11} = N_{u3x} \\ N_{2,2} = N_{3,3} = N_{u1y} \\ N_{2,5} = N_{3,4} = N_{\theta 1z} \\ N_{2,7} = N_{3,8} = N_{u2y} \\ N_{2,10} = N_{3,9} = N_{\theta 1z} \\ N_{2,12} = N_{3,13} = N_{u3y} \\ N_{2,15} = N_{3,14} = N_{\theta 3z} \end{cases} \tag{5.158}$$

The [S] matrix is similar to that of a multiple-axis flexure hinge finite element and is derived following similar reasoning in the form:

$$[S] = \begin{bmatrix} \dfrac{d}{dx} & 0 & 0 \\ 0 & \dfrac{d^2}{dx^2} & 0 \\ 0 & 0 & \dfrac{d^2}{dx^2} \end{bmatrix} \tag{5.159}$$

The elasticity matrix [D] is similarly formulated as:

$$[D] = \begin{bmatrix} EA(x) & 0 & 0 \\ 0 & EI_y(x) & 0 \\ 0 & 0 & EI_z(x) \end{bmatrix} \tag{5.160}$$

where the variable cross-section area $A(x)$ and moments of inertia $I_y(x)$ and $I_z(x)$ are:

$$\begin{cases} A(x) = w(x)t(x) \\ I_y(x) = \dfrac{w(x)^3 t(x)}{12} \\ I_z(x) = \dfrac{w(x)t(x)^3}{12} \end{cases} \tag{5.161}$$

Having defined the matrices [*N*], [*S*], and [*D*], the elemental symmetric stiffness matrix can be calculated by utilizing generic Eq. (5.5). The axial stiffness components are:

$$K_{1,1} = E\int_l t(x)w(x)\left(\frac{dN_{u1x}}{dx}\right)^2 dx \tag{5.162}$$

$$K_{1,6} = E\int_l t(x)w(x)\left(\frac{dN_{u1x}}{dx}\right)\left(\frac{dN_{u2x}}{dx}\right)dx \tag{5.163}$$

$$K_{1,11} = E\int_l t(x)w(x)\left(\frac{dN_{u1x}}{dx}\right)\left(\frac{dN_{u3x}}{dx}\right)dx \tag{5.164}$$

$$K_{6,6} = E\int_l t(x)w(x)\left(\frac{dN_{u2x}}{dx}\right)^2 dx \tag{5.165}$$

$$K_{6,11} = E\int_l t(x)w(x)\left(\frac{dN_{u2x}}{dx}\right)\left(\frac{dN_{u3x}}{dx}\right)dx \tag{5.166}$$

$$K_{6,6} = E\int_l t(x)w(x)\left(\frac{dN_{u3x}}{dx}\right)^2 dx \tag{5.167}$$

The stiffness terms that express the direct bending are:

$$K_{2,2} = K_{3,3} = \frac{E}{12}\int_l t(x)w(x)^3\left(\frac{d^2N_{u1y}}{dx^2}\right)^2 dx \tag{5.168}$$

$$K_{2,7} = K_{3,8} = \frac{E}{12}\int_l t(x)w(x)^3\left(\frac{d^2N_{u1y}}{dx^2}\right)\left(\frac{d^2N_{u2y}}{dx^2}\right)dx \tag{5.169}$$

$$K_{2,12} = K_{3,13} = \frac{E}{12}\int_l t(x)w(x)^3\left(\frac{d^2N_{u1y}}{dx^2}\right)\left(\frac{d^2N_{u3y}}{dx^2}\right)dx \tag{5.170}$$

$$K_{4,4} = K_{5,5} = \frac{E}{12}\int_l t(x)^3w(x)\left(\frac{d^2N_{\theta 1z}}{dx^2}\right)^2 dx \tag{5.171}$$

$$K_{4,9} = K_{5,10} = \frac{E}{12}\int_l t(x)^3w(x)\left(\frac{d^2N_{\theta 1z}}{dx^2}\right)\left(\frac{d^2N_{\theta 2z}}{dx^2}\right)dx \tag{5.172}$$

$$K_{4,14} = K_{5,15} = \frac{E}{12}\int_l t(x)^3 w(x)\left(\frac{d^2N_{\theta 1z}}{dx^2}\right)\left(\frac{d^2N_{\theta 3z}}{dx^2}\right)dx \tag{5.173}$$

$$K_{7,7} = K_{8,8} = \frac{E}{12}\int_l t(x)w(x)^3\left(\frac{d^2N_{u2y}}{dx^2}\right)^2 dx \tag{5.174}$$

$$K_{7,12} = K_{8,13} = \frac{E}{12}\int_l t(x)w(x)^3\left(\frac{d^2N_{u2y}}{dx^2}\right)\left(\frac{d^2N_{u3y}}{dx^2}\right)dx \tag{5.175}$$

$$K_{9,9} = K_{10,10} = \frac{E}{12}\int_l t(x)^3 w(x)\left(\frac{d^2N_{\theta 2z}}{dx^2}\right)^2 dx \tag{5.176}$$

$$K_{9,14} = K_{10,15} = \frac{E}{12}\int_l t(x)^3 w(x)\left(\frac{d^2N_{\theta 2z}}{dx^2}\right)\left(\frac{d^2N_{\theta 3z}}{dx^2}\right)dx \tag{5.177}$$

$$K_{12,12} = K_{13,13} = \frac{E}{12}\int_l t(x)w(x)^3\left(\frac{d^2N_{u3y}}{dx^2}\right)^2 dx \tag{5.178}$$

$$K_{14,14} = K_{15,15} = \frac{E}{12}\int_l t(x)^3 w(x)\left(\frac{d^2N_{\theta 3z}}{dx^2}\right)^2 dx \tag{5.179}$$

The cross-bending stiffness terms are:

$$K_{2,5} = K_{3,4} = \frac{E}{12}\int_l t(x)w(x)^3\left(\frac{d^2N_{u1y}}{dx^2}\right)\left(\frac{d^2N_{\theta 1z}}{dx^2}\right)dx \tag{5.180}$$

$$K_{2,10} = K_{3,9} = \frac{E}{12}\int_l t(x)w(x)^3\left(\frac{d^2N_{u1y}}{dx^2}\right)\left(\frac{d^2N_{\theta 2z}}{dx^2}\right)dx \tag{5.181}$$

$$K_{2,15} = K_{3,14} = \frac{E}{12}\int_l t(x)w(x)^3\left(\frac{d^2N_{u1y}}{dx^2}\right)\left(\frac{d^2N_{\theta 3z}}{dx^2}\right)dx \tag{5.182}$$

$$K_{4,8} = K_{5,7} = \frac{E}{12}\int_l t(x)^3 w(x)\left(\frac{d^2N_{\theta 1z}}{dx^2}\right)\left(\frac{d^2N_{u2y}}{dx^2}\right)dx \tag{5.183}$$

$$K_{4,13} = K_{5,12} = \frac{E}{12}\int_l t(x)^3 w(x)\left(\frac{d^2N_{\theta 1z}}{dx^2}\right)\left(\frac{d^2N_{u3y}}{dx^2}\right)dx \tag{5.184}$$

$$K_{7,10} = K_{8,9} = \frac{E}{12}\int_l t(x)w(x)^3\left(\frac{d^2N_{u2y}}{dx^2}\right)\left(\frac{d^2N_{\theta 2z}}{dx^2}\right)dx \tag{5.185}$$

$$K_{7,15} = K_{8,14} = \frac{E}{12}\int_l t(x)w(x)^3\left(\frac{d^2N_{u2y}}{dx^2}\right)\left(\frac{d^2N_{\theta 3z}}{dx^2}\right)dx \tag{5.186}$$

$$K_{9,13} = K_{10,12} = \frac{E}{12}\int_l t(x)^3 w(x)\left(\frac{d^2N_{\theta 2z}}{dx^2}\right)\left(\frac{d^2N_{u3y}}{dx^2}\right)dx \tag{5.187}$$

$$K_{12,15} = K_{13,14} = \frac{E}{12}\int_l t(x)w(x)^3\left(\frac{d^2N_{u3y}}{dx^2}\right)\left(\frac{d^2N_{\theta 3z}}{dx^2}\right)dx \tag{5.188}$$

5.3.3.2 Mass Matrix

The nonzero components of the symmetric mass matrix are derived similarly to the ones corresponding to a revolute flexure finite element. The axial-related components are:

$$M_{1,1} = \rho\int_l t(x)w(x)N_{u1x}^2\,dx \tag{5.189}$$

$$M_{1,6} = \rho\int_l t(x)w(x)N_{u1x}N_{u2x}\,dx \tag{5.190}$$

$$M_{1,11} = \rho\int_l t(x)w(x)N_{u1x}N_{u3x}\,dx \tag{5.191}$$

$$M_{6,6} = \rho\int_l t(x)w(x)N_{u2x}^2\,dx \tag{5.192}$$

$$M_{6,11} = \rho\int_l t(x)w(x)N_{u2x}N_{u3x}\,dx \tag{5.193}$$

$$M_{11,11} = \rho\int_l t(x)w(x)N_{u3x}^2\,dx \tag{5.194}$$

The mass components that are related to direct bending are:

$$M_{2,2} = M_{3,3} = \rho \int_l t(x) w(x) N_{u1y}^2 \, dx \tag{5.195}$$

$$M_{2,7} = M_{3,8} = \rho \int_l t(x) w(x) N_{u1y} N_{u2y} \, dx \tag{5.196}$$

$$M_{2,12} = M_{3,13} = \rho \int_l t(x) w(x) N_{u1y} N_{u3y} \, dx \tag{5.197}$$

$$M_{4,4} = M_{5,5} = \rho \int_l t(x) w(x) N_{\theta 1z}^2 \, dx \tag{5.198}$$

$$M_{4,9} = M_{5,10} = \rho \int_l t(x) w(x) N_{\theta 1z} N_{\theta 2z} \, dx \tag{5.199}$$

$$M_{4,14} = M_{5,15} = \rho \int_l t(x) w(x) N_{\theta 1z} N_{\theta 3z} \, dx \tag{5.200}$$

$$M_{7,7} = M_{8,8} = \rho \int_l t(x) w(x) N_{u2y}^2 \, dx \tag{5.201}$$

$$M_{7,12} = M_{8,13} = \rho \int_l t(x) w(x) N_{u2y} N_{u3y} \, dx \tag{5.202}$$

$$M_{9,9} = M_{10,10} = \rho \int_l t(x) w(x) N_{\theta 2z}^2 \, dx \tag{5.203}$$

$$M_{9,14} = M_{10,15} = \rho \int_l t(x) w(x) N_{\theta 2z} N_{\theta 3z} \, dx \tag{5.204}$$

$$M_{12,12} = M_{13,13} = \rho \int_l t(x) w(x) N_{u3y}^2 \, dx \tag{5.205}$$

$$M_{14,14} = M_{15,15} = \rho \int_l t(x) w(x) N_{\theta 3z}^2 \, dx \tag{5.206}$$

The cross-bending mass components are:

$$M_{2,5} = M_{3,4} = \rho \int_l t(x) w(x) N_{u1y} N_{\theta 1z} \, dx \tag{5.207}$$

$$M_{2,10} = M_{3,9} = \rho \int_l t(x)w(x)N_{u1y}N_{\theta 2z}\,dx \tag{5.208}$$

$$M_{2,15} = M_{3,14} = \rho \int_l t(x)w(x)N_{u1y}N_{\theta 3z}\,dx \tag{5.209}$$

$$M_{4,8} = M_{5,7} = \rho \int_l t(x)w(x)N_{\theta 1z}N_{u2y}\,dx \tag{5.210}$$

$$M_{4,13} = M_{5,12} = \rho \int_l t(x)w(x)N_{\theta 1z}N_{u3y}\,dx \tag{5.211}$$

$$M_{7,10} = M_{8,9} = \rho \int_l t(x)w(x)N_{u2y}N_{\theta 2z}\,dx \tag{5.212}$$

$$M_{7,15} = M_{8,14} = \rho \int_l t(x)w(x)N_{u2y}N_{\theta 3z}\,dx \tag{5.213}$$

$$M_{9,13} = M_{10,12} = \rho \int_l t(x)w(x)N_{\theta 2z}N_{u3y}\,dx \tag{5.214}$$

5.4 Elemental Matrices for Rigid Links

5.4.1 Two-Dimensional Rigid Link Modeled as a Two-Node Line Element

In a compliant mechanism, the flexure hinges connect several links that are quasi-rigid and carry out the effective motion the mechanism was designed to produce. Although it would be attractive to treat these quasi-rigid links as completely rigid, as was the case in Chapter 3, the fact that they are compliant to some degree is advantageous for their modeling by means of the finite-element technique, which qualifies the stiffness of a finite element by means of its stiffness matrix $[K^e]$. Each component of $[K^e]$ is basically of the form:

$$K^e_{i,j} = Ef_{i,j}(element\ \ geometry) \tag{5.215}$$

when only axial and bending effects are considered.

Therefore, to achieve an infinite stiffness component, it is necessary that either the Young's modulus (or the transverse modulus, for shearing and torsion) or some dimensions of the physical component go to infinity, which

is practically impossible. In principle, there might be three different approaches of realistically modeling such a quasi-rigid link through finite elements.

If the assumption is made that the element is technically rigid (and therefore the compliance of a mechanism resides entirely in its flexible joints—the flexure hinges), one can select as simple an element as possible—for instance, a line element with only two nodes. It is then possible to artificially increase the material elastic moduli such that the corresponding stiffness is considerably large and the finite element practically acts as a quasi-rigid member.

The shape functions of a finite element can be designed or selected conveniently such that they incorporate the rigid-body motion capability in a direct manner, as mentioned by Hac and Osinski[11] or Hac.[12]

A third variant would enable utilizing a finite element that sensibly captures the real deformations of a quasi-rigid link by defining elements that better model the real geometry and loading of that specific link as needed. If the compliant mechanism is planar, a plate element with in-plane deformation capabilities (Kirchhoff plate element, as indicated in Zienkiewicz and Taylor,[2] for instance) would be an appropriate selection. In the case of three-dimensional compliant mechanisms, a plate element with in- and out-of-plane deformation capabilities (a Reissner–Mindlin plate element, as also mentioned by Zienkiewicz and Taylor[2]) would have the necessary features. Such elements come, of course, with a higher number of nodes, and the dimensionality and complexity of the problem would increase unnecessarily. However, in mechanisms where ignoring the compliance of members that are customarily considered rigid might affect the overall precision or other key output parameters, this avenue might be the correct one to chose.

Our discussion here, however, will take the simpler route as indicated in the first approach outlined previously, whereby a two-node line element is considered for modeling a quasi-rigid member, a choice that covers the vast majority of flexure-based compliant mechanisms. In a serial mechanism (or in the serial leg of a hybrid one), such an element matches the geometry pattern by connecting with adjacent members at its terminal nodes, but the element is also amenable to parallel applications. A situation of a quasi-rigid link that connects to three adjacent flexure hinges is pictured in Figure 5.6a.

As shown in Figure 5.6b, it is possible to divide the real quasi-rigid member into two line elements by following the directions between the end nodes of the flexure elements. Figure 5.6 illustrates a planar situation, but the discussion is also valid for the three-dimensional case. It is, however, necessary for each of these two nodes of the quasi-rigid element to possess the same degrees of freedom as the flexure hinge finite element it connects to, in order to ensure inter-element compatibility. Because a single-axis flexure hinge finite element was already defined with three DOFs per node, a similar assumption is introduced for the two-node line element illustrated in Figure 5.7.

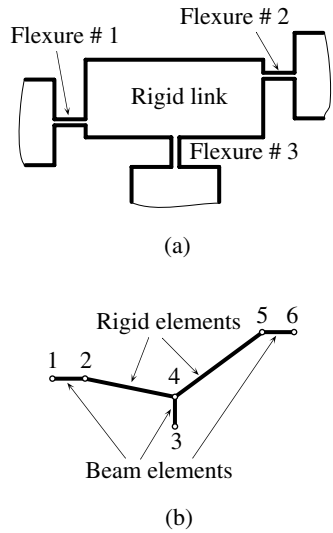

FIGURE 5.6
Rigid link connected to several flexure hinges in a two-dimensional compliant mechanism: (a) geometry of connection; (b) finite-element model.

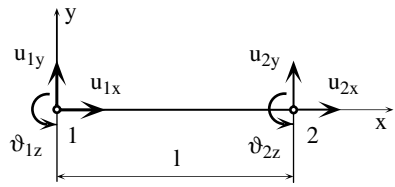

FIGURE 5.7
Two-node, three-DOF-per-node element modeling a quasi-rigid link for planar compliant mechanism applications.

In order to keep the development simple, the assumption is also made that the cross-section of this element is constant; therefore, the cross-sectional area A and moment of inertia I_z are also constant. The stiffness and mass matrices are formulated next.

5.4.1.1 Stiffness Matrix

The derivation is similar to the several derivations that have already been presented within this chapter; such an element is quite standard and can be found in any finite-element textbook. The shape functions for the axial deformation are first-degrees polynomials, while the shape functions for the bending deflections must be third-degree polynomials in order to allow expressing

the necessary boundary conditions at the two end nodes of the element. The shape functions are:

$$\begin{cases} N_{u1x} = 1 - \dfrac{x}{l} \\ N_{u2x} = \dfrac{x}{l} \\ N_{u1y} = 1 - 3\dfrac{x^2}{l^2} + 2\dfrac{x^3}{l^3} \\ N_{u2y} = \dfrac{x^2}{l^2}\left(3 - 2\dfrac{x}{l}\right) \\ N_{\theta 1z} = x\left(1 - 2\dfrac{x}{l} + \dfrac{x^2}{l^2}\right) \\ N_{\theta 2z} = \dfrac{x^2}{l}\left(-1 + \dfrac{x}{l}\right) \end{cases} \tag{5.216}$$

The 2×6 shape function matrix $[N]$ is:

$$[N] = \begin{bmatrix} N_{u1x} & 0 & 0 & N_{u1y} & 0 & 0 \\ 0 & N_{u1y} & N_{\theta 1z} & 0 & N_{u2y} & N_{\theta 2z} \end{bmatrix} \tag{5.217}$$

The $[S]$ matrix, in this case, is a 2×2 matrix defined as:

$$[S] = \begin{bmatrix} \dfrac{d}{dx} & 0 \\ 0 & \dfrac{d^2}{dx^2} \end{bmatrix} \tag{5.218}$$

while the elasticity matrix $[D]$ can similarly be formulated as:

$$[D] = \begin{bmatrix} EA & 0 \\ 0 & EI_z \end{bmatrix} \tag{5.219}$$

where A and I_z denote the cross-sectional area and moment of inertia that are considered constant.

By following the standard definitions, the elemental stiffness matrix can be found. The axial-connected terms of the stiffness matrix are:

$$K_{1,1} = EA \int_l \left(\frac{dN_{u1x}}{dx}\right)^2 dx \tag{5.220}$$

$$K_{1,4} = EA\int_l \left(\frac{dN_{u1x}}{dx}\right)\left(\frac{dN_{u2x}}{dx}\right)dx \tag{5.221}$$

$$K_{4,4} = EA\int_l \left(\frac{dN_{u2x}}{dx}\right)^2 dx \tag{5.222}$$

The stiffness components that are connected to direct-bending effects are:

$$K_{2,2} = EI_z\int_l \left(\frac{d^2N_{u1y}}{dx^2}\right)^2 dx \tag{5.223}$$

$$K_{2,5} = EI_z\int_l \left(\frac{d^2N_{u1y}}{dx^2}\right)\left(\frac{d^2N_{u2y}}{dx^2}\right)dx \tag{5.224}$$

$$K_{3,3} = EI_z\int_l \left(\frac{d^2N_{\theta 1z}}{dx^2}\right)^2 dx \tag{5.225}$$

$$K_{3,6} = EI_z\int_l \left(\frac{d^2N_{\theta 1z}}{dx^2}\right)\left(\frac{d^2N_{\theta 2z}}{dx^2}\right)dx \tag{5.226}$$

$$K_{5,5} = EI_z\int_l \left(\frac{d^2N_{u2y}}{dx^2}\right)^2 dx \tag{5.227}$$

$$K_{6,6} = EI_z\int_l \left(\frac{d^2N_{\theta 2z}}{dx^2}\right)^2 dx \tag{5.228}$$

The stiffness components that are related to cross-bending effects are:

$$K_{2,3} = EI_z\int_l \left(\frac{d^2N_{u1y}}{dx^2}\right)\left(\frac{d^2N_{\theta 1z}}{dx^2}\right)dx \tag{5.229}$$

$$K_{2,6} = EI_z\int_l \left(\frac{d^2N_{u1y}}{dx^2}\right)\left(\frac{d^2N_{\theta 2z}}{dx^2}\right)dx \tag{5.230}$$

$$K_{3,5} = EI_z \int_l \left(\frac{d^2 N_{\theta 1z}}{dx^2} \right) \left(\frac{d^2 N_{u2y}}{dx^2} \right) dx \tag{5.231}$$

$$K_{5,6} = EI_z \int_l \left(\frac{d^2 N_{u2y}}{dx^2} \right) \left(\frac{d^2 N_{\theta 2z}}{dx^2} \right) dx \tag{5.232}$$

5.4.1.2 Mass Matrix

The mass matrix components that are produced through axial effects are:

$$M_{1,1} = \rho A \int_l N_{u1x}^2 \, dx \tag{5.233}$$

$$M_{1,4} = \rho A \int_l N_{u1x} N_{u2x} \, dx \tag{5.234}$$

$$M_{4,4} = \rho A \int_l N_{u2x}^2 \, dx \tag{5.235}$$

The mass terms that are connected to direct-bending effects are:

$$M_{2,2} = \rho A \int_l N_{u1y}^2 \, dx \tag{5.236}$$

$$M_{2,5} = \rho A \int_l N_{u1y} N_{u2y} \, dx \tag{5.237}$$

$$M_{3,3} = \rho A \int_l N_{\theta 1z}^2 \, dx \tag{5.238}$$

$$M_{3,6} = \rho A \int_l N_{\theta 1z} N_{\theta 2z} \, dx \tag{5.239}$$

$$M_{5,5} = \rho A \int_l N_{u2y}^2 \, dx \tag{5.240}$$

$$M_{6,6} = \rho A \int_l N_{\theta 2z}^2 \, dx \tag{5.241}$$

The cross-bending mass terms are:

$$M_{2,3} = \rho A \int_l N_{u1y} N_{\theta 1z}\, dx \tag{5.242}$$

$$M_{2,6} = \rho A \int_l N_{u1y} N_{\theta 2z}\, dx \tag{5.243}$$

$$M_{3,5} = \rho A \int_l N_{\theta 1z} N_{u2y}\, dx \tag{5.244}$$

$$M_{5,6} = \rho A \int_l N_{u2y} N_{\theta 2z}\, dx \tag{5.245}$$

5.4.2 Three-Dimensional Rigid Link Modeled as a Two-Node Line Element

The stiffness and mass matrices are now formulated for a similar two-node line element as a model for quasi-rigid links that are part of compliant mechanisms in three-dimensional applications. Figure 5.8 illustrates the element and its six DOFs per node. Because the flexure hinge finite elements that have been developed so far have had six DOFs, the same feature is transferred to this element in order to provide for inter-element compatibility.

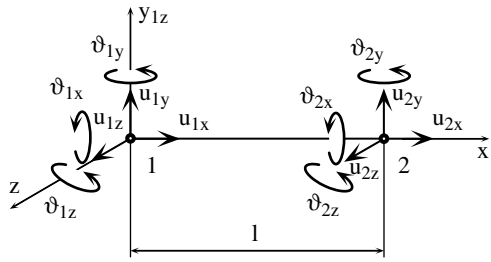

FIGURE 5.8
Two-node, six-DOF-per-node element modeling a quasi-rigid link for spatial compliant mechanism applications.

5.4.2.1 Stiffness Matrix

The shape function matrix [*N*] is a 4×12 matrix with the nonzero components:

$$\begin{cases} N_{1,1} = N_{4,4} = N_{u1x} \\ N_{1,7} = N_{4,10} = N_{u2x} \\ N_{2,2} = N_{3,3} = N_{u1y} \\ N_{2,6} = N_{3,5} = N_{\theta 1z} \\ N_{2,8} = N_{3,9} = N_{u2y} \\ N_{2,12} = N_{3,11} = N_{\theta 2z} \end{cases} \tag{5.246}$$

where the shape functions in Eq. (5.246) are identical to the ones already introduced for the two-dimensional quasi-rigid finite element. The [*S*] matrix is the 4×4 one defined in Eq. (5.94) for a multiple-axis flexure hinge finite element. The elasticity matrix is also 4×4 and, similar to the corresponding three-dimensional revolute flexure hinge element, is defined as:

$$[E] = \begin{bmatrix} EA & 0 & 0 & 0 \\ 0 & EI_y & 0 & 0 \\ 0 & 0 & EI_z & 0 \\ 0 & 0 & 0 & GI_t \end{bmatrix} \tag{5.247}$$

As indicated in Eq. (5.247), it is assumed again that the rectangular cross-section of the quasi-rigid finite element is constant and therefore also constant are its cross-sectional area A, moments of inertia I_y and I_z, and the conventional moment of inertia in torsion, I_t.

The elemental stiffness components that are related to axial effects are:

$$K_{1,1} = EA \int_l \left(\frac{dN_{u1x}}{dx} \right)^2 dx \tag{5.248}$$

$$K_{1,7} = EA \int_l \left(\frac{dN_{u1x}}{dx} \right) \left(\frac{dN_{u2x}}{dx} \right) dx \tag{5.249}$$

$$K_{7,7} = EA \int_l \left(\frac{dN_{u2x}}{dx} \right)^2 dx \tag{5.250}$$

The stiffness terms that are produced through direct-bending effects can be calculated as:

$$K_{2,2} = EI_y \int_l \left(\frac{d^2 N_{u1y}}{dx^2} \right)^2 dx \tag{5.251}$$

$$K_{2,8} = EI_y \int_l \left(\frac{d^2 N_{u1y}}{dx^2} \right) \left(\frac{d^2 N_{u2y}}{dx^2} \right) dx \tag{5.252}$$

$$K_{3,3} = EI_z \int_l \left(\frac{d^2 N_{u1y}}{dx^2} \right)^2 dx \tag{5.253}$$

$$K_{3,9} = EI_z \int_l \left(\frac{d^2 N_{u1y}}{dx^2} \right) \left(\frac{d^2 N_{u2y}}{dx^2} \right) dx \tag{5.254}$$

$$K_{5,5} = EI_z \int_l \left(\frac{d^2 N_{\theta 1z}}{dx^2} \right)^2 dx \tag{5.255}$$

$$K_{5,11} = EI_z \int_l \left(\frac{d^2 N_{\theta 1z}}{dx^2} \right) \left(\frac{d^2 N_{\theta 2z}}{dx^2} \right) dx \tag{5.256}$$

$$K_{6,6} = EI_y \int_l \left(\frac{d^2 N_{\theta 1z}}{dx^2} \right)^2 dx \tag{5.257}$$

$$K_{6,12} = EI_y \int_l \left(\frac{d^2 N_{\theta 1z}}{dx^2} \right) \left(\frac{d^2 N_{\theta 2z}}{dx^2} \right) dx \tag{5.258}$$

$$K_{8,8} = EI_y \int_l \left(\frac{d^2 N_{u2y}}{dx^2} \right)^2 dx \tag{5.259}$$

$$K_{9,9} = EI_z \int_l \left(\frac{d^2 N_{u2y}}{dx^2} \right)^2 dx \tag{5.260}$$

$$K_{11,11} = EI_z \int_l \left(\frac{d^2 N_{\theta 2z}}{dx^2} \right)^2 dx \tag{5.261}$$

$$K_{12,12} = EI_y \int_l \left(\frac{d^2 N_{\theta 2z}}{dx^2} \right)^2 dx \tag{5.262}$$

The stiffness components that are related to cross-bending effects are:

$$K_{2,6} = EI_y \int_l \left(\frac{d^2 N_{u1y}}{dx^2} \right) \left(\frac{d^2 N_{\theta 1z}}{dx^2} \right) dx \tag{5.263}$$

$$K_{2,12} = EI_y \int_l \left(\frac{d^2 N_{u1y}}{dx^2} \right) \left(\frac{d^2 N_{\theta 2z}}{dx^2} \right) dx \tag{5.264}$$

$$K_{3,5} = EI_z \int_l \left(\frac{d^2 N_{u1y}}{dx^2} \right) \left(\frac{d^2 N_{\theta 1z}}{dx^2} \right) dx \tag{5.265}$$

$$K_{3,11} = EI_z \int_l \left(\frac{d^2 N_{u1y}}{dx^2} \right) \left(\frac{d^2 N_{\theta 2z}}{dx^2} \right) dx \tag{5.266}$$

$$K_{5,9} = EI_z \int_l \left(\frac{d^2 N_{\theta 1z}}{dx^2} \right) \left(\frac{d^2 N_{u2y}}{dx^2} \right) dx \tag{5.267}$$

$$K_{6,8} = EI_y \int_l \left(\frac{d^2 N_{\theta 1z}}{dx^2} \right) \left(\frac{d^2 N_{u2y}}{dx^2} \right) dx \tag{5.268}$$

$$K_{8,12} = EI_y \int_l \left(\frac{d^2 N_{u2y}}{dx^2} \right) \left(\frac{d^2 N_{\theta 2z}}{dx^2} \right) dx \tag{5.269}$$

$$K_{9,11} = EI_z \int_l \left(\frac{d^2 N_{u2y}}{dx^2} \right) \left(\frac{d^2 N_{\theta 2z}}{dx^2} \right) dx \tag{5.270}$$

The elemental stiffness components that are torsion generated can be calculated by means of the following equations:

$$K_{4,4} = GI_t \int_l \left(\frac{dN_{u1x}}{dx} \right)^2 dx \tag{5.271}$$

$$K_{4,10} = GI_t \int_l \left(\frac{dN_{u1x}}{dx} \right) \left(\frac{dN_{u2x}}{dx} \right) dx \tag{5.272}$$

$$K_{10,10} = GI_t \int_l \left(\frac{dN_{u2x}}{dx} \right)^2 dx \tag{5.273}$$

5.4.2.2 Mass Matrix

The axial- and torsional-related mass matrix components are:

$$M_{1,1} = M_{4,4} = \rho A \int_l N_{u1x}^2 \, dx \tag{5.274}$$

$$M_{1,7} = M_{4,10} = \rho A \int_l N_{u1x} N_{u2x} \, dx \tag{5.275}$$

$$M_{7,7} = M_{10,10} = \rho A \int_l N_{u2x}^2 \, dx \tag{5.276}$$

The mass components that are related to direct-bending effects are:

$$M_{2,2} = M_{3,3} = \rho A \int_l N_{u1y}^2 \, dx \tag{5.277}$$

$$M_{2,8} = M_{3,9} = \rho A \int_l N_{u1y} N_{u2y} \, dx \tag{5.278}$$

$$M_{5,5} = M_{6,6} = \rho A \int_l N_{\theta 1z}^2 \, dx \tag{5.279}$$

$$M_{5,11} = M_{6,12} = \rho A \int_l N_{\theta 1z} N_{\theta 2z} \, dx \tag{5.280}$$

$$M_{8,8} = M_{9,9} = \rho A \int_l N_{u2y}^2 \, dx \tag{5.281}$$

$$M_{11,11} = M_{12,12} = \rho A \int_l N_{\theta 2z}^2 \, dx \tag{5.282}$$

The cross-bending mass terms are:

$$M_{2,6} = M_{3,5} = \rho A \int_l N_{u1y} N_{\theta 1z} \, dx \tag{5.283}$$

$$M_{5,9} = M_{6,8} = \rho A \int_l N_{\theta 1z} N_{u2y} \, dx \tag{5.284}$$

$$M_{8,12} = M_{9,11} = \rho A \int_l N_{u2y} N_{\theta 2z} \, dx \tag{5.285}$$

5.5 Application Example

In order to further test the finite-element formulation that has been developed within this chapter, a simple example was analyzed in the form of a two-link planar serial compliant mechanism, as pictured in Figure 5.9. The flexible link is a single-axis flexure hinge that is connected to a massive quasi-rigid link with the flexure hinge being fixed at its end, as shown in Figure 5.9a. According to the procedure developed here, each link can be represented as a three-DOF-per-node line element; that is, the flexure hinge is defined as a three-node element, whereas the quasi-rigid link is represented by a two-node quasi-rigid element, as shown in Figure 5.9b. The mechanism is considered to be constructed monolithically from steel with a Young's modulus of E = 200 GPa and a Poisson's ratio of 0.3. The width of the mechanism is constant and equal to 0.004 m. The other geometric parameters are, according to the variables provided in Figure 5.9a, l_1 = 0.006 m, t_1 = 0.001 m, and r = 0.0005 m (all these parameters define the longitudinal profile of the flexure hinge); also, $l_2 = t_2$ = 0.015 m (for the end bloc).

Solution

Finite-element simulations have studied the static response of mechanisms under various externally applied loads and the modal response, as well. The results obtained by applying the simple derivation presented in this chapter were checked by running the corresponding simulations on an identical physical model aided by the ANSYS finite-element software.

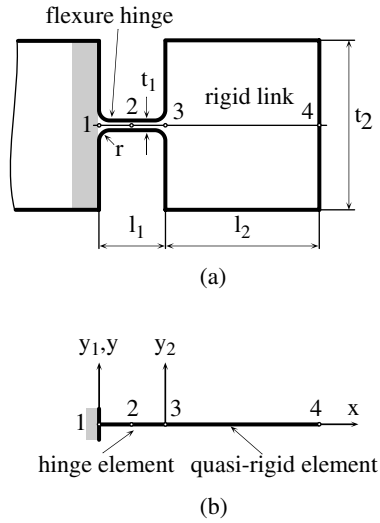

FIGURE 5.9
Finite-element models of a two-link, serial, compliant mechanism including a single-axis, corner-filleted flexure hinge: (a) classical two-dimensional finite-element model; (b) model based on line elements.

The first set of tests, as mentioned, was static and consisted of applying different loads and determining the produced displacements at points of interest. Utilizing the ANSYS finite-element code makes this a straightforward task but, when approaching a simulation by means of the procedure presented here all the steps that were hidden in the commercial code must be tackled explicitly. Equation (5.25) indicates that the displacement field in a static finite-element problem can be determined by multiplying the inverse of the global stiffness matrix by the load vector. Although not detailed here, the subject of assembling the global matrices and vectors will briefly be discussed.

In a raw, standard finite-element procedure, the first steps are defining the finite elements by means of their matrices and numbering the nodes, which, as mentioned in the introduction to this chapter, reduces the bandwidth of the global stiffness matrix and therefore the number of equations that ultimately have to be solved. In the present example, the elemental stiffness and mass matrices have been defined for both the single-axis, corner-filleted flexure element and the quasi-rigid element utilized in two-dimensional applications. Numbering the nodes is a straightforward procedure because the two elements are serially connected and, as a consequence, the mechanism will be defined by four nodes, as indicated in Figure 5.9b. The next step following node numbering transforms the elemental matrices and vectors from the local reference frame to the global one by means of transformation

matrices that account for the relative position of the two reference frames. This step is unnecessary with this example because the local reference frames of the two elements and the global frame *xy* (as illustrated in Figure 5.9b) are parallel.

The last preparatory step is assembling the global matrices and vectors from the corresponding elemental counterparts. In solving this problem, the principle of superposition is employed, which basically states that the total reaction load at a node where two or more elements meet is the sum of the partial reaction loads pertaining to each of the concurrent elements. This principle enables defining the stiffness or mass terms in their corresponding assembled matrices as the sum of stiffness or mass terms corresponding to the adjoining elements. In our case, the displacement vector of the entire structure has the following form:

$$\{u_n\} = \{u_{1x}, u_{1y}, \theta_{1z}, u_{2x}, u_{2y}, \theta_{2z}, u_{3x}, u_{3y}, \theta_{3z}, u_{4x}, u_{4y}, \theta_{4z}\}^T \qquad (5.286)$$

and the load vector will have a similar expression. As a consequence, both the overall (assembled) stiffness and mass matrices will be of dimension 12×12. Because node 3 is the junction node that connects the flexure element to the quasi-rigid element, the summation previously mentioned will apply to its three DOFs. Figure 5.10 is a graphical representation of the assembling process for the particular problem of either global stiffness or the global mass matrix.

The light-gray shade designates the 9×9 elemental matrix of the flexure hinge element, and the slightly darker gray shade indicates the 6×6 elemental matrix of the quasi-rigid finite element. The letter *T* stands for either

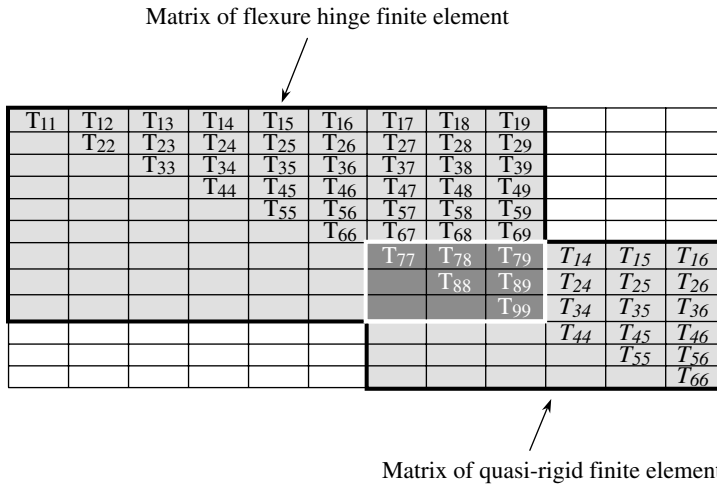

FIGURE 5.10
Matrix representation of the assembling process.

stiffness or mass terms and, because the referred matrices are symmetric, only the terms in the upper diagonal sector have been input. The dark gray intersection area and the white lettering symbolize the terms that have to be calculated by adding up the individual contributions from both elements. The terms of the flexure finite element that are denoted on the light-gray shaded area are also the real terms of the assembled matrix (going with the same subscript notation), but for the terms of the quasi-rigid finite element the elemental order notation has been used in order to indicate the original significance of those terms. In the assembled form, their subscripts will change to reflect the position in the 12×12 overall matrix. The mixed terms in the assembled stiffness matrix, for instance, are calculated as:

$$\begin{cases} K_{77} = K_{77}^1 + K_{11}^2 \\ K_{78} = K_{78}^1 + K_{12}^2 \\ K_{79} = K_{79}^1 + K_{13}^2 \\ K_{88} = K_{88}^1 + K_{22}^2 \\ K_{89} = K_{89}^1 + K_{23}^2 \\ K_{99} = K_{99}^1 + K_{33}^2 \end{cases} \tag{5.287}$$

and the corresponding superimposed terms of the assembled mass matrix are calculated similarly. The superscripts 1 and 2 have been used in Eq. (5.287) to indicate the first element (the flexure hinge) and the second one (the quasi-rigid link), respectively.

The static finite-element simulation consists of two different subsets. In the first simulation, a force of 10 N has been applied along the x direction at node 3, and the corresponding x displacements were calculated by means of the finite-element procedure presented here and also determined by means of the ANSYS code at nodes 2 and 3. The results follow:

- For x displacement at node 2:
  - 3.4×10^{-8} m, by means of the dedicated finite-element procedure
  - 3.2×10^{-8} m, by means of the ANSYS software
- For x displacement at node 3:
  - 6.8×10^{-8} m, by means of the dedicated finite-element procedure
  - 6.4×10^{-8} m, by means of the ANSYS software

The second subset of numerical simulations consists of applying a force of 10 N at the same node 3 about the y direction and calculating the deflections

at points 2 and 3 about the same direction by means of the above-mentioned procedures. The results follow:

- For y displacement at node 2:
  - 1.7×10^{-8} m, by means of the dedicated finite-element procedure
  - 1.6×10^{-8} m, by means of the ANSYS software
- For y displacement at node 3:
  - 5.1×10^{-8} m, by means of the dedicated finite-element procedure
  - 4.9×10^{-8} m, by means of the ANSYS software

The errors between the results produced by the two finite-element procedures were less than 6%, with the displacements determined by means of the ANSYS code being always smaller than the ones predicted by the model developed in this chapter, as the model generated by the commercially available code is stiffer due to the larger number of finite elements that introduce additional internal constraints.

A modal analysis was also performed by both finite-element procedures and the first three modal frequencies were determined for the planar serial compliant mechanism of Figure 5.9. In Chapter 4, which treated the dynamic response of flexure-based compliant mechanisms, the algorithm that is generally used to determine the modal frequencies was detailed and will not be explained again here. Briefly, the dynamic matrix for the system of Figure 5.9 was calculated, according to this algorithm, based on the assembled stiffness and mass matrices, which enabled calculation of the eigenvalues λ_1, λ_2, and λ_3. The modal frequencies were then calculated from the corresponding eigenvalues by means of the definition equation:

$$f_i = \frac{\sqrt{\lambda_i}}{2\pi}, \; i = 1, 2, 3 \tag{5.288}$$

The results of the two groups of finite-element simulations are noted below:

- For the first mode (regular bending of the flexure element with the rigid link following the flexure without any rotation):
  - 920-Hz resonant frequency by means of the dedicated finite-element procedure
  - 946-Hz resonant frequency by means of the ANSYS software
- For the second mode (bending of the flexure element with the rigid link having its own rotation relative to the flexure hinge element):
  - 10,350-Hz resonant frequency by means of the dedicated finite-element procedure
  - 10,583-Hz resonant frequency by means of the ANSYS software

- For the third mode (pure axial vibration of the entire system due to axial deformation of the flexure hinge element):
  - 23,260-Hz resonant frequency by means of the dedicated finite-element procedure
  - 23,512-Hz resonant frequency by means of the ANSYS software

As the results of the modal finite-element simulations indicate, the errors between the two procedures were less than 3% and the higher resonant frequencies predicted by the ANSYS code are, again, normal because of the denser mesh that introduces more constraints (model is stiffer), compared to the procedure of this chapter where, for the analyzed problem, only two elements were utilized.

References

1. Gerardin M. and Cardona A., *Flexible Multibody Dynamics: A Finite-Element Approach*, John Wiley & Sons, Chichester, 2001.
2. Zienkiewicz, O.C. and Taylor R.L., *The Finite-Element Method*, McGraw-Hill, London, 1993.
3. Zhang, S. and Fasse, E.D., A finite-element-based method to determine the spatial stiffness properties of a notch hinge, *ASME Journal of Mechanical Design*, 123(1), 141, 2001.
4. Koster, M., *Constructieprincipies voor het Nauwkeurig Bewegen en Positioneren*, Twente University Press, 1998.
5. Murin, J. and Kutis, V., 3D-beam element with continuous variation of the cross-sectional area, *Computers and Structures*, 80(3–4), 329, 2002.
6. Wang, Y. and Wang, Z., A time finite-element method for dynamic analysis of elastic mechanisms in link coordinate systems, *Computers and Structures*, 79(2), 223, 2001.
7. Saxena, A. and Ananthasuresh, G.K., Topology synthesis of compliant mechanisms for non-linear forced-deflection and curved path specifications, *ASME Journal of Mechanical Design*, 123(1), 33, 2001.
8. Yu, Y.-Q. and Smith, M.R., The effect of cross-sectional parameters on the dynamics of elastic mechanisms, *Mechanism and Machine Theory*, 31(7), 947, 1996.
9. Thompson, B.S. and Sung, C.K., A survey of finite-element techniques for mechanism design, *Mechanism and Machine Theory*, 21(4), 351, 1986.
10. Sung, C.K. and Thompson, B.S., Material selection: an important parameter in the design of high-speed linkages, *Mechanism and Machine Theory*, 19(4/5), 389, 1984.
11. Hac, M. and Osinski, J., Finite element formulation of rigid body motion in dynamic analysis of mechanisms, *Computers and Structures*, 57(2), 213, 1995.
12. Hac, M., Dynamics of flexible mechanisms with mutual dependence between rigid body motion and longitudinal deformation of links, *Mechanism and Machine Theory*, 30(6), 837, 1995.

13. Sriram, B.R. and Mruthyunjaya, T.S., Dynamics of flexible-link mechanisms, *Computers and Structures*, 56(6), 1029, 1995.
14. Al-Bedoor, B.O. and Khulief, Y.A., Finite element dynamic modeling of a translating and rotating flexible link, *Computer Methods in Applied Mechanical Engineering*, 131, 173, 1996.
15. Liew, K.M., Lee, S.E., and Liu, A.Q., Mixed-interface substructures for dynamic analysis of flexible multibody systems, *Engineering Structures*, 18(7), 495, 1996.
16. Fallahi, B., An enhanced computational scheme for the analysis of elastic mechanisms, *Computers and Structures*, 62(2), 369, 1997.
17. Xianmin, Z., Jike, L., and Yunwen, S., A high frequency analysis method for closed flexible mechanism systems, *Mechanism and Machine Theory*, 33(8), 1117, 1998.
18. Wang, Y.-X., Multifrequency resonances of flexible linkages, *Mechanism and Machine Theory*, 33(3), 255, 1998.
19. Chen, W., Dynamic modeling of multi-link flexible robotic manipulators, *Computers and Structures*, 79(2), 183, 2001.
20. Besseling, J.F. and Gong, D.G., Numerical simulation of spatial mechanisms and manipulators with flexible links, *Finite Element in Analysis and Design*, 18, 121, 1994.
21. Fallahi, B., A non-linear finite-element approach to kineto-static analysis of elastic beams, *Mechanisms and Machine Theory*, 31(3), 353, 1996.
22. Li, M., The finite deformation theory for beam, plate and shell. Part I. The two-dimensional beam theory, *Computer Methods in Applied Mechanical Engineering*, 146, 53, 1997.
23. Gao, X., Solution methods for dynamic response of flexible mechanisms, in *Modern Kinematics: Developments in the Last Forty Years*, A.G. Erdman, Ed., John Wiley & Sons, New York, 1993.
24. Imam, I., Sandor, G.N., and Kramer, S.N., Deflection and stress analysis in high-speed planar mechanisms with elastic links, *ASME Journal of Engineering for Industry*, 94B, 541, 1973.
25. Midha, A., Erdman, A.G., and Frohrib, D.A., A computationally efficient numerical algorithm for the transient response of high-speed elastic linkages, *ASME Journal of Mechanical Design*, 101, 138, 1979.
26. Midha, A., Erdman, A.G., and Frohrib, D.A., A closed form numerical algorithm for the periodic response of high-speed elastic linkages, *ASME Journal of Mechanical Design*, 101, 154, 1979.
27. Turcic, D.A. and Midha, A., Dynamic analysis of elastic mechanism systems, Part 1. Applications, *ASME Journal of Dynamic Systems, Measurement and Control*, 106, 249. 1984.
28. Gear, C.W., *Numerical Initial Value problems in Ordinary Differential Equations*, Prentice-Hall, Englewood Cliffs, NJ, 1971.
29. Chu, S.C. and Pan, K.C., Dynamic response of high-speed slider-crank mechanism with an elastic connecting rod, *ASME Journal of Engineering for Industry*, 97(2), 542, 1975.
30. Song, J.O. and Haug, E.J., Dynamic analysis of planar flexible mechanisms, *Computer Methods in Applied Mechanics and Engineering*, 24, 358, 1980.
31. Gao, X.C., King, Z.Y., and Zhang, Q.X., A closed-form linear multi-step algorithm for the steady-state response of high-speed flexible mechanisms, *Mechanism and Machine Theory*, 23(5), 361, 1988.
32. Sekulovic, M. and Salatic, R., Nonlinear analysis of frames with flexible connections, *Computers and Structures*, 79(11), 1097, 2001.

Appendix: Stiffness and Mass Matrices for Single-Axis, Corner-Filleted Flexure Hinge Finite Elements

The stiffness and mass matrices are explicitly given here for a three-node, three-DOF-per-node finite element that models single-axis, corner-filleted flexure hinges. The geometry of such a flexure was defined in Chapter 2, where it was shown that the longitudinal geometry of such a flexure is characterized by the following parameters: the total length of the flexure, l; its minimum thickness, t, the fillet radius, r; and the constant width, w, of the flexure.

Elemental Stiffness Matrix

The components of the elemental stiffness matrix are given here explicitly. It is clear that by taking $r = 0$ in all subsequent equations, the corresponding stiffness components of a simple nonfilleted strip flexure hinge can be obtained simply. The * superscript indicates the stiffness components of such a flexure hinge. The stiffness terms of a constant cross-section flexure hinge of minimum thickness t were also calculated separately in order to check the results derived by taking $r \to 0$ in the stiffness components of a generic flexure hinge, and the limit results confirmed the stiffness equations for the constant cross-section flexures. Similar verifications were also performed successfully for the mass terms of a corner-filleted flexure hinge.

The terms corresponding to axial effects (located on lines 1, 4, and 7 of the elemental stiffness matrix) are presented first:

$$K_{1,1} = K_{7,7} = \frac{Ew}{3l^4}[4r^4(48-15\pi) - 16r^3l(10-3\pi) + 15r^2l^2(4-\pi) + 7l^3t] \quad \text{(A.1)}$$

$$K^*_{1,1} = \frac{7Ewt}{3l} \quad \text{(A.2)}$$

$$K_{1,4} = K_{4,7} = -\frac{8Ew}{3l^4}[r^4(48-15\pi) - 4r^3l(10-3\pi) + 3r^2l^2(4-\pi) + l^3t] \quad \text{(A.3)}$$

$$K^*_{1,4} = -\frac{8Ewt}{3l} \quad \text{(A.4)}$$

$$K_{1,7} = \frac{Ew}{3l^4}[4r^4(48-15\pi) - 16r^3l(10-3\pi) + 9r^2l^2(4-\pi) + l^3t] \quad \text{(A.5)}$$

$$K_{1,7}^{*} = \frac{Ewt}{3l} \tag{A.6}$$

$$K_{4,4} = -2K_{1,4} \tag{A.7}$$

The terms that are located on the other lines of the elemental stiffness matrix are produced through bending, either direct or crossed:

$$K_{22} = \frac{144}{18515Ewl^{10}}(22499l^7t^3 - 420l^6r^2K_{22,1} - 168l^5K_{22,2} + 28l^4r^3K_{22,3} - 24l^3r^4K_{22,4} + 48l^2r^5K_{22,5} - 800lr^6K_{22,6} + 51200r^7K_{22,7}) \tag{A.8}$$

with:

$$K_{22,1} = 30(93\pi - 442)r^2 + 2(1116\pi - 5525)rt + 3(186\pi - 1105)t^2 \tag{A.9}$$

$$K_{22,2} = (184310 - 73800\pi)r^5 + [126384r + (144815 - 59040\pi)t]r^4 + 5[21064r + (13165 - 2952\pi)t]r^3t \tag{A.10}$$

$$K_{22,3} = -74(28755\pi - 41956)r^3 - 12(143775\pi - 199291)r^2t + 15[335648r + (41956 - 28755\pi)t]rt + 251736(24r^2 + 5t^2)r \tag{A.11}$$

$$K_{22,4} = (5881792 - 6565230\pi)r^3 - 28(193095\pi - 160312)r^2t + 7[3007232r + (165840 - 193095\pi)t]rt + 44224(568r^2 + 119t^2)r \tag{A.12}$$

$$K_{22,5} = -27(175875\pi - 108224)r^3 + 8(277324 - 496125\pi)r^2t + 14[1515136r + (40584 - 70875\pi)t]rt + 108224(232r^2 + 49t^2)r \tag{A.13}$$

$$K_{22,6} = (104640 - 176715\pi)r^3 - 792(189\pi - 100)r^2t + 18[82688r + (1120 - 2079\pi)t]rt + 128(13640r^2 + 2907t^2)r \tag{A.14}$$

$$K_{22,7} = 470r^3 + 355r^2t + 6(2152r + 15t)rt + 4(3752r^2 + 807t^2)r \tag{A.15}$$

$$K_{22}^{*} = \frac{269988t^3}{18515Ewl^3} \tag{A.16}$$

$$K_{23} = \frac{24}{18515Ewl^9}(59529l^7t^3 - 735l^6r^2K_{23,1} - 42l^5K_{23,2} + 252l^4r^3K_{23,3} - 72l^3r^4K_{23,4} + 48l^2r^5K_{23,5} - 800lr^6K_{23,6} + 51200r^7K_{22,7}) \quad \text{(A.17)}$$

with:

$$K_{23,1} = 3(1435\pi - 6416)r^2 + 4(861\pi - 4010)rt + 3(287\pi - 1604)t^2 \quad \text{(A.18)}$$

$$K_{23,2} = -35(16665\pi - 43144)r^5 + 4[258864r + (296615 - 116655\pi) + 5[172576r + (107860 - 23331\pi)t]r^3t \quad \text{(A.19)}$$

$$K_{23,3} = -74(4805\pi - 7524)r^3 - 12(24025\pi - 35739)r^2t + 15[60192r + (7524 - 4805\pi)t]rt + 45144(24r^2 + 5t^2)r \quad \text{(A.20)}$$

$$K_{23,4} = 14(186656 - 183685\pi)r^3 - 28(75635\pi - 71224)r^2t + 7[1336064r + (73680 - 75635\pi)t]rt + 19648(568r^2 + 119t^2)r \quad \text{(A.21)}$$

$$K_{23,5} = -27(175875\pi - 122944)r^3 + 8(315044 - 496125\pi)r^2t + 14[1721216r + (46104 - 70875\pi)t]rt + 122944(232r^2 + 49t^2)r \quad \text{(A.22)}$$

$$K_{23,6} = K_{22,6} \quad \text{(A.23)}$$

$$K_{23}^* = \frac{1428696t^3}{18515Ewl^2} \quad \text{(A.24)}$$

$$K_{25} = \frac{768}{55545Ewl^{10}}(-7608l^7t^3 + 210l^6r^2K_{25,1} + 336l^5K_{25,2} + 21l^4r^3K_{25,3} - 18l^3r^4K_{25,4} + 12l^2r^5K_{25,5} - 200lr^6K_{25,6} + 51200r^7K_{22,7}) \quad \text{(A.25)}$$

with:

$$K_{25,1} = 15(479\pi - 256)r^2 + 4(1437\pi - 800)rt + 3(479\pi - 320)t^2 \quad \text{(A.26)}$$

$$K_{25,2} = -5(8835\pi - 1372)r^5 + 2[2352r + (2695 - 17670\pi)t]r^4 + 5[784r + (490 - 1767\pi)t]r^3t \quad \text{(A.27)}$$

$$K_{25,3} = 74(41355\pi + 4544)r^3 + 12(206775\pi + 21584)r^2t + 15[36352r + (4544 + 41355\pi)t]rt + 27264(24r^2 + 5t^2)r \quad \text{(A.28)}$$

$$K_{25,4} = 14(215232 + 608345\pi)r^3 + 28(250495\pi + 82128)r^2t + 7[1540608r + (84960 + 250495\pi)t]rt + 22656(568r^2 + 119t^2)r \quad \text{(A.29)}$$

$$K_{25,5} = 27(644875\pi + 323968)r^3 + 8(830168 + 1819125\pi)r^2t + 14[4535552r + (121488 + 259875\pi)t]rt + 323968(232r^2 + 49t^2)r \quad \text{(A.30)}$$

$$K_{25,6} = 15(27904 + 43197\pi)r^3 + 792(693\pi + 400)r^2t + 18[330752r + (480 + 7632\pi)t]rt + 512(13640r^2 + 2907t^2)r \quad \text{(A.31)}$$

$$K_{25}^{*} = \frac{-162304t^3}{18515Ewl^3} \quad \text{(A.32)}$$

$$K_{26} = \frac{768}{55545Ewl^9}(-408l^7t^3 + 420l^6r^2K_{26,1} - 84l^5K_{26,2} + 42l^4r^3K_{26,3} - 36l^3r^4K_{26,4} + 21l^2r^5K_{26,5} - 50lr^6K_{26,6} + 32000r^7K_{22,7}) \quad \text{(A.33)}$$

with:

$$K_{26,1} = 12(20\pi + 107)r^2 + 2(96\pi + 535)rt + 3(16\pi + 107)t^2 \quad \text{(A.34)}$$

$$K_{26,2} = 10(435\pi + 6979)r^5 + [47856r + (54835 + 3480\pi)t]r^4 + 5[7976r + (4985 + 174\pi)t]r^3t \quad \text{(A.35)}$$

$$K_{26,3} = -74(855\pi - 8044)r^3 - 228(225\pi - 2011)r^2t + 15[64352r + (8044 - 855\pi)t]rt + 48264(24r^2 + 5t^2)r \quad \text{(A.36)}$$

$$K_{26,4} = (1602384 - 484330\pi)r^3 - 28(14245\pi - 43674)r^2t + 7[819264r + (45180 - 14245\pi)t]rt + 12048(568r^2 + 119t^2)r \quad \text{(A.37)}$$

$$K_{26,5} = -27(58625\pi - 132736)r^3 + 8(340136 - 165375\pi)r^2t + 14[1858304r + (49776 - 23625\pi)t]rt + 132736(232r^2 + 49t^2)r \quad \text{(A.38)}$$

$$K_{26,6} = 15(69760 - 27489\pi)r^3 - 792(441\pi - 1000)r^2t + 18[826880r + (11200 - 4851\pi)t]rt + 1280(13640r^2 + 2907t^2)r \quad \text{(A.39)}$$

$$K_{26}^{*} = -\frac{870t^3}{18515Ewl^2} \quad \text{(A.40)}$$

$$K_{28} = -\frac{48}{55545Ewl^{10}}(80763l^7t^3 + 420l^6r^2K_{28,1} - 168l^5K_{28,2} + 84l^4r^3K_{28,3} - 72l^3r^4K_{28,4} + 48l^2r^5K_{28,5} - 800lr^6K_{28,6} + 1280000r^7K_{22,7}) \quad \text{(A.41)}$$

with:

$$K_{28,1} = 30(1079\pi + 2954)r^2 + 2(12948\pi + 36925)rt + 3(2158\pi + 7385)t^2 \quad \text{(A.42)}$$

$$K_{28,2} = 10(74940\pi + 143927)r^5 + [986928r + (1130855 + 599520\pi)t]r^4 + 5[164488r + (102805 + 29976\pi)t]r^3t \quad \text{(A.43)}$$

$$K_{28,3} = 74(79155\pi + 144044)r^3 + 12(395775\pi + 684209)r^2t + 15[1152352r + (144044 + 79155\pi)t]rt + 864264(24r^2 + 5t^2)r \quad \text{(A.44)}$$

$$K_{28,4} = 14(2121312 + 1026545\pi)r^3 + 28(422695\pi + 809448)r^2t + 7[15184128r + (837360 + 422695\pi)t]rt + 223296(568r^2 + 119t^2)r \quad \text{(A.45)}$$

$$K_{28,5} = 27(996625\pi + 2269888)r^3 + 8(5816588 + 2811375\pi)r^2t + 14[31778432r + (851208 + 401625\pi)t]rt + 2269888(232r^2 + 49t^2)r \quad \text{(A.46)}$$

$$K_{28,6} = 15(174400 + 66759\pi)r^3 + 792(1071\pi + 2500)r^2t + 18[2067200r + (28000 + 11781\pi)t]rt + 3200(13640r^2 + 2907t^2)r \quad \text{(A.47)}$$

$$K_{28}^{*} = -\frac{107684t^3}{18515Ewl^3} \tag{A.48}$$

$$K_{29} = -\frac{24}{55545Ewl^9}(117723l^7t^3 + 525l^6r^2K_{29,1} - 42l^5K_{29,2} + 84l^4r^3K_{29,3} - 72l^3r^4K_{29,4} + 48l^2r^5K_{29,5} - 8800lr^6K_{29,6} + 563200r^7K_{22,7}) \tag{A.49}$$

with:

$$K_{29,1} = 3(5915\pi + 17552)r^2 + 4(3459\pi + 10970)rt + 3(1183\pi + 4388)t^2 \tag{A.50}$$

$$K_{29,2} = 5(362445\pi + 679112)r^5 + 4[582096r + (666985 + 362445\pi)t]r^4 + 5[388064r + (242540 + 72489\pi)t]r^3t \tag{A.51}$$

$$K_{29,3} = 74(49815\pi + 73492)r^3 + 12(249075\pi + 349087)r^2t + 15[587936r + (73492 + 49815\pi)t]rt + 440952(24r^2 + 5t^2)r \tag{A.52}$$

$$K_{29,4} = 14(990432 + 724285\pi)r^3 + 28(298235\pi + 377928)r^2t + 7[7089408r + (390960 + 298235\pi)t]rt + 104256(568r^2 + 119t^2)r \tag{A.53}$$

$$K_{29,5} = 27(762125\pi + 1016768)r^3 + 8(2605468 + 2149875\pi)r^2t + 14[14234752r + (381288 + 307125\pi)t]rt + 1016768(232r^2 \tag{A.54}$$

$$K_{29,6} = 15(6976 + 4641\pi)r^3 + 72(819\pi + 1100)r^2t + 18[82688r + (1120 + 819\pi)t]rt + 128(13640r^2 + 2907t^2)r \tag{A.55}$$

$$K_{29}^{*} = -\frac{74482t^3}{18515Ewl^2} \tag{A.56}$$

$$K_{33} = \frac{24}{55545Ewl^8}(113082l^7t^3 - 5145l^6r^2K_{33,1} - 2646l^5K_{33,2} + 210l^4r^3K_{33,3} - 12l^3r^4K_{33,4} + 216l^2r^5K_{33,5} - 400lr^6K_{22,6} + 25600r^7K_{22,7}) \tag{A.57}$$

with:

$$K_{33,1} = 3(275\pi - 1168)r^2 + 20(33\pi - 146)rt + 3(55\pi - 292)t^2 \tag{A.58}$$

$$K_{33,2} = (22820 - 8175\pi)r^5 + 2[7824r + (8965 - 3270\pi)t]r^4 + 5[2608r + (1630 - 327\pi)t]r^3t \tag{A.59}$$

$$K_{33,3} = -74(3849\pi - 6796)r^3 - 12(19245\pi - 32281)r^2t + 15[54368r + (6796 - 3849\pi)t]rt + 40776(24r^2 + 5t^2)r \tag{A.60}$$

$$K_{33,4} = (9797312 - 8864310\pi)r^3 - 28(260715\pi - 267032)r^2t + 7[5009152r + (276240 - 260715\pi)t]rt + 73664(568r^2 + 119t^2)r \tag{A.61}$$

$$K_{33,5} = (412992 - 527625\pi)r^3 + 8(39196 - 55125\pi)r^2t + 14[214144r + (5736 - 7875\pi)t]rt + 15296(232r^2 + 49t^2)r \tag{A.62}$$

$$K_{33}^{*} = \frac{75388t^3}{18515Ewl} \tag{A.63}$$

$$K_{35} = \frac{384}{166635Ewl^9}(-7608l^7t^3 + 1470l^6r^2K_{35,1} + 4536l^5K_{35,2} + 21l^4r^3K_{35,3} - 6l^3r^4K_{35,4} + 36l^2r^5K_{35,5} - 200lr^6K_{35,6} + 25600r^7K_{22,7}) \tag{A.64}$$

with:

$$K_{35,1} = (2505\pi - 1968)r^2 + 4(501\pi - 410)rt + 3(167\pi - 164)t^2 \tag{A.65}$$

$$K_{35,2} = (210 - 6850\pi)r^5 + [144r + (165 - 5480\pi)t]r^4 + 5[24r + (15 - 274\pi)t]r^3t \tag{A.66}$$

$$K_{35,3} = 74(69645\pi + 24784)r^3 + 12(348225\pi + 117724)r^2t + 15[198272r + (24784 + 69645\pi)t]rt + 148704(24r^2 + 5t^2)r \quad \text{(A.67)}$$

$$K_{35,4} = 14(1205056 + 2305965\pi)r^3 + 28(949515\pi + 459824)r^2t + 7[8625664\,r + (475680 + 949515\pi)t]rt + 126848(568r^2 + 119t^2)r \quad \text{(A.68)}$$

$$K_{35,5} = 9(382848 + 644875\pi)r^3 + 8(327016 + 606375\pi)r^2t + 14[1786624\,r + (47856 + 86625\pi)t]rt + 127616(232r^2 + 49t^2)r \quad \text{(A.69)}$$

$$K_{35,6} = 15(27904 + 43197\pi)r^3 + 792(693\pi + 400)r^2t + 18[330752\,r + (4480 - 7623\pi)t]rt + 512(13640r^2 + 2907t^2)r \quad \text{(A.70)}$$

$$K_{35}^{*} = -\frac{81152t^3}{55545Ewl} \quad \text{(A.71)}$$

$$K_{36} = \frac{192}{166635Ewl^8}(-816l^7t^3 + 1470l^6r^2K_{36,1} - 1512l^5K_{36,2} + 21l^4r^3K_{36,3} - 42l^3r^4K_{36,4} + 18l^2r^5K_{36,5} - 100lr^6K_{36,6} + 64000r^7K_{22,7}) \quad \text{(A.72)}$$

with:

$$K_{36,1} = 15(19\pi + 112)r^2 + 4(57\pi + 350)rt + 3(19\pi + 140)t^2 \quad \text{(A.73)}$$

$$K_{36,2} = 5(3626 + 135\pi)r^5 + [12432r + (14245 + 540\pi)t]r^4 + 5[2072r + (1295 + 27\pi)t]r^3t \quad \text{(A.74)}$$

$$K_{36,3} = -74(3765\pi - 63824)r^3 + 12(-18825\pi + 303164)r^2t + 15[510592r + (63824 - 3765\pi)t]rt + 382944(24r^2 + 5t^2)r \quad \text{(A.75)}$$

$$K_{36,4} = (4145344 - 842010\,\pi)r^3 - 28(24765\,\pi - 112984)\,r^2t + 7[2119424\,r + (116880 - 24765\,\pi)\,t]rt + 31168(568r^2 + 119\,t^2)r \quad \text{(A.76)}$$

$$K_{36,5} = (9687168 - 3693375\pi)r^3 + 8(919384 - 385875\pi)r^2t + 14[5022976r + (134544 - 55125\pi)t]rt + 358784(232r^2 + 49t^2)r \quad \text{(A.77)}$$

$$K_{36,6} = 15(69760 - 27489\pi)r^3 - 792(441\pi - 1000)r^2t + 18[826880r + (11200 - 4851\pi)t]rt + 1280(13640r^2 + 2907t^2)r \quad \text{(A.78)}$$

$$K_{36}^{*} = -\frac{4352t^3}{55545Ewl} \quad \text{(A.79)}$$

$$K_{38} = -\frac{24}{166635Ewl^9}(4140331l^7t^3 + 735l^6r^2K_{38,1} - 378l^5K_{38,2} + 84l^4r^3K_{38,3} - 24l^3r^4K_{38,4} + 144l^2r^5K_{38,5} - 800lr^6K_{38,6} + 1280000r^7K_{22,7}) \quad \text{(A.80)}$$

with:

$$K_{38,1} = 3(13805\pi + 36752)r^2 + 4(8283\pi + 22970)rt + 3(2761\pi + 9188)t^2 \quad \text{(A.81)}$$

$$K_{38,2} = 5(293944 + 146385\pi)r^5 + 4[251952r + (288695 + 146385\pi)t]r^4 + 5[167968r + (104980 + 29277\pi)t]r^3t \quad \text{(A.82)}$$

$$K_{38,3} = 74(148845\pi + 302284)r^3 + 12(744225\pi + 1435849)r^2t + 15[2418272r + (302284 + 148845\pi)t]rt + 1813704(24r^2 + 5t)r \quad \text{(A.83)}$$

$$K_{38,4} = 14(9859936 + 4264365\pi)r^3 + 28(1755915\pi + 3762344)r^2t + 7[70576384r + (3892080 + 1755915\pi)t]rt + 1037888(568r^2 + 119t^2)r \quad \text{(A.84)}$$

$$K_{38,5} = 9(2637888 + 996625\pi)r^3 + 8(2253196 + 937125\pi)r^2t + 14[12310144r + (329736 + 133875\pi)t]rt + 879296(232r^2 + 49t^2)r \quad \text{(A.85)}$$

$$K_{38,6} = 15(174400 + 66759\pi)r^3 + 792(1071\pi + 2500)r^2t + 18[2067200r + (28000 + 11781\pi)t]rt + 3200(13640r^2 + 2907t^2)r \quad \text{(A.86)}$$

$$K_{38}^{*} = -\frac{276022t^3}{55545Ewl^2} \tag{A.87}$$

$$K_{39} = \frac{24}{166635Ewl^8}(142179l^7t^3 + 14700l^6r^2K_{39,1} - 11340l^5K_{39,2} + 42l^4r^3K_{39,3} - 12l^3r^4K_{39,4} + 504l^2r^5K_{39,5} - 4400lr^6K_{39,6} + 281600) \tag{A.88}$$

with:

$$K_{39,1} = 3(235\pi + 688)r^2 + 4(141\pi + 430)rt + 3(47\pi + 172)t^2 \tag{A.89}$$

$$K_{39,2} = 10(1435 + 748\pi)r^5 + [9840r + (11275 + 5984\pi)t]r^4 + [8200r + (6125 + 1496\pi)t]r^3t \tag{A.90}$$

$$K_{39,3} = 74(91905\pi + 148196)r^3 + 12(459525\pi + 703931)r^2t + 15[1185568r + (148196 + 91925\pi)t]rt + 889176(24r^2 + 5t)r \tag{A.91}$$

$$K_{39,4} = 14(4509536 + 2888385\pi)r^3 + 28(1189335\pi + 1720744)r^2t + 7[32278784r + (1780080 + 1189335\pi)t]rt + 474688(568r^2 + 119t^2)r \tag{A.92}$$

$$K_{39,5} = 9(168384 + 108875\pi)r^3 + 8(143828 + 102375\pi)r^2t + 14[785792r + (21048 + 14625\pi)t]rt + 56128(232r^2 + 49t^2)r \tag{A.93}$$

$$K_{39,6} = 15(6976 + 4641\pi)r^3 + 72(819\pi + 1100)r^2t + 18[82688r + (1120 + 819\pi)t]rt + 128(13640r^2 + 2907t^2)r \tag{A.94}$$

$$K_{39}^{*} = \frac{94786t^3}{55545Ewl} \tag{A.95}$$

$$K_{55} = -\frac{73728}{4932562635\,Ewl^{15}}\{9867l^5[24(l-2r)K_{55,1} + r(400r^6K_{55,2}$$
$$- 240lr^5K_{55,3} - 6237l^2r^4K_{55,4} + 12072\ l^3r^3K_{55,5} + 17136l^4r^2K_{55,6}$$
$$- 117936l^5rK_{55,7} + 70980\ l^6K_{55,8})] + 32r(1112431320\ l^9K_{55,9}$$
$$- 4767562800l^8rK_{55,10} + 3425834412\ l^7r^2K_{55,11} - 6586557120l^6r^3K_{55,12}$$
$$+ 4204605834l^5r^4K_{55,13} - 710604180l^4r^5K_{55,14} + 488492433l^3r^6K_{55,15}$$
$$- 23900760l^2r^7K_{55,16} + 1154400lr^8K_{55,17} - 3200r^9K_{55,18})\} \quad \text{(A.96)}$$

with:

$$K_{55,1} = 2103l^6 - 17144l^5r + 100532l^4r^2 - 198776l^3r^3 + 179388l^2r^4$$
$$- 96000lr^5 + 32000r^6 \quad \text{(A.97)}$$

$$K_{55,2} = (-1981184 + 630630\pi)r^3 + 4(-424544 + 135135\pi)r^2t$$
$$+ 21(-20224 + 6435\pi)rt^2 - 1920t^3 \quad \text{(A.98)}$$

$$K_{55,3} = 5(-185056 + 58905\,\pi)r^3 + 72\,(-10886 + 3465\,\pi)r^2t$$
$$+ 54(-3632 + 1155\,\pi)rt^2 - 1680t^3 \quad \text{(A.99)}$$

$$K_{55,4} = 7(-9472 + 3015\,\pi)r^3 + 8[-6928 + 2205\pi)r^2t$$
$$+ 14\,(-992 + 315\,\pi)rt^2 - 224\,t^3 \quad \text{(A.100)}$$

$$K_{55,5} = (-11216 + 3570\pi)r^3 + 420\,[-22 + 7\pi)r^2t$$
$$+ 7(-332 + 105\pi)rt^2 - 70t^3 \quad \text{(A.101)}$$

$$K_{55,6} = (-3488 + 1110\pi)r^3 + 12(-236 + 75\pi)r^2t$$
$$+ 45(-16 + 5\pi)rt^2 - 40t^3 \quad \text{(A.102)}$$

$$K_{55,7} = (-236 + 75\pi)r^3 + 10(-19 + 6\pi)r^2t$$
$$+ 5(-10 + 3\pi)rt^2 - 5\,t^3 \quad \text{(A.103)}$$

$$K_{55,8} = 3(-16+5\pi)r^3 + 4(-10+3\pi)r^2t + 3(-4+\pi)rt^2 - 2t^3 \quad \text{(A.104)}$$

$$K_{55,9} = 3(16+5\pi)r^3 + 4(10+3\pi)r^2t + 3(4+\pi)rt^2 + 2t^3 \quad \text{(A.105)}$$

$$K_{55,10} = (236+75\pi)r^3 + 10(19+6\pi)r^2t + 5(10+3\pi)rt^2 + 5t^3 \quad \text{(A.106)}$$

$$K_{55,11} = (3488+1110\pi)r^3 + 12(236+75\pi)r^2t + 45(16+5\pi)rt^2 + 40t^3 \quad \text{(A.107)}$$

$$K_{55,12} = (11216+3570\pi)r^3 + 420(22+7\pi)r^2t + 7(332+105\pi)rt^2 + 70t^3 \quad \text{(A.108)}$$

$$K_{55,13} = 7(9472+3015\pi)r^3 + 8(6928+2205\pi)r^2t + 14(992+315\pi)rt^2 + 224t^3 \quad \text{(A.109)}$$

$$K_{55,14} = 5(185056+58905\pi)r^3 + 72(10886+3465\pi)r^2t + 54(3632 + 1155\pi)rt^2 + 1680t^3 \quad \text{(A.110)}$$

$$K_{55,15} = (1981184+630630\pi)r^3 + 4(424544+135135\pi)r^2t + 21(20224+6435\pi)rt^2 + 1920t^3 \quad \text{(A.111)}$$

$$K_{55,16} = 30(1198144+381381\pi)r^3 + 132(235856+75075\pi)r^2t + 55(141536+45045\pi)rt^2 + 18480t^3 \quad \text{(A.112)}$$

$$K_{55,17} = 165(2201600+700791\pi)r^3 + 36(8820992+2807805\pi)r^2t + 33(2405888+765765\pi)rt^2 + 98560t^3 \quad \text{(A.113)}$$

$$K_{55,18} = 5(539362816+171684513\pi)r^3 + 52(45708736+14549535\pi)r^2t + 845(703232+223839\pi)rt^2 + 384384t^3 \quad \text{(A.114)}$$

$$K_{55}^{*} = \frac{2871296\,t^3}{55545\,Ewl^3} \quad \text{(A.115)}$$

$$K_{56} = \frac{6144}{499905\,Ewl^9}(6912l^7t^3 + 420l^6r^2K_{56,1} - 4536l^5K_{56,2} + 756l^4r^3K_{56,3} - 48l^3r^4K_{56,4} + 94l^2r^5K_{56,5} - 50lr^6K_{56,6} + 64000r^7K_{22,7}) \quad \text{(A.116)}$$

with:

$$K_{56,1} = 3(505\pi + 1408)r^2 + 4(303\pi + 880)rt + 3(101\pi + 352)t^2 \quad \text{(A.117)}$$

$$K_{56,2} = 5(672 + 505\pi)r^5 + 4[576r + (660 + 505\pi)t]r^4 + 5[384r + (240 + 101\pi)t]r^3t \quad \text{(A.118)}$$

$$K_{56,3} = 74(1515\pi + 1088)r^3 + 12(7575\pi + 5168)r^2t + 15[8704r + (1088 + 1515\pi)t]rt + 6528(24r^2 + 5t)r \quad \text{(A.119)}$$

$$K_{56,4} = 14(190912 + 437835\,\pi)r^3 + 28(180285\pi + 72848)\,r^2t + 7[1366528\,r + (75360 + 180285\pi)t]rt + 20096(568r^2 + 119\,t^2)r \quad \text{(A.120)}$$

$$K_{56,5} = 9(1923072 + 5921125\,\pi)r^3 + 8(1642624 + 5567625\,\pi)r^2t + 14[8974336r + (240384 + 795375\,\pi)t]rt + 641024\,(232r^2 + 49\,t^2)r \quad \text{(A.121)}$$

$$K_{56,6} = 15(139520 + 396627\pi)r^3 + 792(6363\,\pi + 2000)r^2t + 18[1653760\,r + (22400 + 69993\,\pi)t]rt + 2560(13640\,r^2 + 2907t^2)r \quad \text{(A.122)}$$

$$K_{56}^{*} = \frac{131072\,t^3}{18515\,Ewl^2} \quad \text{(A.123)}$$

$$K_{58} = -\frac{768}{499905\,Ewl^{10}}(335304\,l^7t^3 + 210\,l^6r^2K_{58,1} - 3024\,l^5K_{58,2} + 63\,l^4r^3K_{58,3} - 6\,l^3r^4K_{58,4} + 36\,l^2r^5K_{58,5} - 200\,lr^6K_{58,6} + 1280000\,r^7K_{22,7}) \quad \text{(A.124)}$$

with:

$$K_{58,1} = 15\,(8663\,\pi + 28928)r^2 + 4\,(25989\,\pi + 90400)rt + 3\,(8663\,\pi + 36160)t^2 \quad \text{(A.125)}$$

$$K_{58,2} = 5(46564 + 25155\pi)r^5 + [159648r + (182930 + 100620\pi)t]r^4 + 5[26608r + (16630 + 5031\pi)t]r^3t \quad \text{(A.126)}$$

$$K_{58,3} = 74(515745\pi + 501056)r^3 + 12(2578725\pi + 2380016)r^2t + 15[4008448r + (501056 + 515745\pi)t]rt + 3006336(24r^2 + 5t)r \quad \text{(A.127)}$$

$$K_{58,4} = 14(45900352 + 91888995\pi)r^3 + 28(37836645\pi + 17514608)r^2t + 7[328549888r + (18118560 + 37836645\pi)t]rt + 4831616(568r^2 + 119t^2)r \quad \text{(A.128)}$$

$$K_{58,5} = 9(11231616 + 37695875\pi)r^3 + 8(9593672 + 35445375\pi)r^2t + 14[52414208r + (1403952 + 5063625\pi)t]rt + 3743872(232r^2 + 49t^2)r \quad \text{(A.129)}$$

$$K_{58,6} = 15(697600 + 2525061\pi)r^3 + 792(40509\pi + 10000)r^2t + 18[8268800r + (112000 + 445599\pi)t]rt + 12800(13640r^2 + 2907t^2)r \quad \text{(A.130)}$$

$$K_{58}^{*} = -\frac{2384384\,t^3}{55545\,Ewl^3} \quad \text{(A.131)}$$

$$K_{59} = \frac{384}{499905\,Ewl^9}(179064\,l^7t^3 + 1050\,l^6r^2K_{59,1} - 4536\,l^5K_{59,2} + 63\,l^4r^3K_{59,3} - 6\,l^3r^4K_{59,4} + 36\,l^2r^5K_{59,5} - 2200\,lr^6K_{59,6} + 563200\,r^7K_{22,7}) \quad \text{(A.132)}$$

with:

$$K_{59,1} = 3(6235\pi + 20368)r^2 + 4(3741\pi + 12730)rt + 3(1247\pi + 5092)t^2 \quad \text{(A.133)}$$

$$K_{59,2} = 10(9751 + 5235\pi)r^5 + [66864r + (76615 + 41880\pi)t]r^4 + 5[11144r + (6965 + 2094\pi)t]r^3t \quad \text{(A.134)}$$

$$K_{59,3} = 74(279285\pi + 281008)r^3 + 12(1396425\pi + 1334788)r^2t + 15[2248064r + (281008 + 279285\pi)t]rt + 1686048(24r^2 + 5t)r \quad \text{(A.135)}$$

$$K_{59,4} = 14(23659712 + 45353535\pi)r^3 + 812(643965\pi + 311312)r^2t + 7[169353728r + (9339360 + 18674985\pi)t]rt + 2490496(568r^2 + 119t^2)r \quad \text{(A.136)}$$

$$K_{59,5} = 9(5306496 + 17880625\pi)r^3 + 8(4532632 + 16813125\pi)r^2t + 14$$
$$[24763648r + (663312 + 2401875\pi)t]rt + 1768832(232r^2 + 49t^2)r \quad \text{(A.137)}$$

$$K_{59,6} = 15(27904 + 108885\pi)r^3 + 360(3843\pi + 880)r^2t + 18$$
$$[330752r + (4480 + 19215\pi)t]rt + 512(13640r^2 + 2907t^2)r \quad \text{(A.138)}$$

$$K_{59}^* = \frac{212224t^3}{18515Ewl^2} \quad \text{(A.139)}$$

$$K_{66} = \frac{12288}{499905Ewl^8}(711l^7t^3 + 420l^6r^2K_{66,1} - 3024l^5K_{66,2} + 504l^4r^3K_{66,3}$$
$$- 24l^3r^4K_{66,4} + 18l^2r^5K_{66,5} - 500lr^6K_{66,6} + 20000r^7K_{22,7}) \quad \text{(A.140)}$$

with:

$$K_{66,1} = 6(25\pi + 82)r^2 + 10(12\pi + 41)rt + 3(10\pi + 41)t^2 \quad \text{(A.141)}$$

$$K_{66,2} = 5(154 + 75\pi)r^5 + [528r + (605 + 300\pi)t]r^4$$
$$+ 5[88r + (55 + 15\pi)t]r^3t \quad \text{(A.142)}$$

$$K_{66,3} = 74\ (225\pi + 326)r^3 + 6(2250\pi + 3097)r^2t + 15$$
$$\times[2608r + (326 + 225\pi)t]rt + 1956(24r^2 + 5t)r \quad \text{(A.143)}$$

$$K_{66,4} = 28(47861 + 43350\pi)r^3 + 14(71400\pi + 73051)r^2t$$
$$+ 7[685168r + (37785 + 35700\pi)t]rt + 10076(568r^2 + 119t^2)r \quad \text{(A.144)}$$

$$K_{66,5} = 9(280608 + 293125\pi)r^3 + 8(239686 + 275625\pi)r^2t$$
$$+ 14[1309504r + (35076 + 39375\pi)t]rt + 93536(232r^2 + 49t^2)r \quad \text{(A.145)}$$

$$K_{66,6} = 15(4360 + 3927\pi)r^3 + 396(126\pi + 125)r^2t$$
$$+ 18[51680r + (700 + 693\pi)t]rt + 80(13640r^2 + 2907t^2)r \quad \text{(A.146)}$$

$$K_{66}^* = \frac{80896t^3}{55545Ewl} \quad \text{(A.147)}$$

$$K_{68} = -\frac{768}{499905Ewl^9}(51624l^7t^3 + 420l^6r^2K_{68,1} - 756l^5K_{68,2} + 1134l^4r^3K_{68,3} - 12l^3r^4K_{68,4} + 9l^2r^5K_{68,5} - 250lr^6K_{68,6} + 800000r^7K_{22,7}) \quad (A.148)$$

with:

$$K_{68,1} = 12(1190\pi + 3779)r^2 + 2(5712\pi + 18895)rt + 3(952\pi + 3779)t^2 \quad (A.149)$$

$$K_{68,2} = 10(23107 + 12555\pi)r^5 + [158448r + (181555 + 100440\pi)t]r^4 + 5[26408r + (16505 + 5022\pi)t]r^3t \quad (A.150)$$

$$K_{68,3} = 74(7795\pi + 8484)r^3 + 12(38975\pi + 40299)r^2t + 15[67872r + (8484 + 7795\pi)t]rt + 50904(24r^2 + 5t)r \quad (A.151)$$

$$K_{68,4} = 266(484184 + 688245\pi)r^3 + 28(5384505\pi + 3510334)r^2t + 7[65849024r + (3631380 + 5384505\pi)t]rt + 968368(568r^2 + 119t^2)r \quad (A.152)$$

$$K_{68,5} = 603(354432 + 651875\pi)r^3 + 8(20283848 + 41068125\pi)r^2t + 14[110819072r + (2968368 + 5866875\pi)t]rt + 7915648(232r^2 + 49t^2)r \quad (A.153)$$

$$K_{68,6} = 15(348800 + 585123\pi)r^3 + 792(9387\pi + 5000)r^2t + 18[4134400r + (56000 + 103257\pi)t]rt + 6400(13640r^2 + 2907t^2)r \quad (A.154)$$

$$K_{68}^{*} = -\frac{122368t^3}{18515Ewl^2} \quad (A.155)$$

$$K_{69} = \frac{192}{499905Ewl^8}(52848l^7t^3 + 1050l^6r^2K_{69,1} - 1512l^5r^3K_{69,2} + 189l^4r^4K_{69,3} - 6l^3r^5K_{69,4} + 126l^2r^6K_{69,5} - 1100lr^7K_{69,6} + 704000r^8K_{69,7}) \quad (A.156)$$

with:

$$K_{69,1} = 3(8624 + 2705\pi)r^2 + 4(5390 + 1623\pi)rt + 3(2156 + 541\pi)t^2 \quad (A.157)$$

$$K_{69,2} = (249334 + 79875\pi)r^2 + 5(40147 + 12780\pi)rt + 25(2113 + 639\pi)t^2 \tag{A.158}$$

$$K_{69,3} = 2(6220848 + 1960075\,\pi)r^2 + 12(841812 + 264875\,\pi)rt + 15\,(171216 + 52975\,\pi)t^2 \tag{A.159}$$

$$K_{69,4} = 2(680205536 + 193467225\pi)r^2 + 420(2668424 + 758695\pi)rt + 7(40268944 + 11380425\pi)t^2 \tag{A.160}$$

$$K_{69,5} = (134696576 + 28868625\pi)r^2 + 8(14074232 + 3016125\pi)rt + 14(2015248 + 430875\pi)t^2 \tag{A.161}$$

$$K_{69,6} = 5(3701120 + 410193\pi)r^2 + 72(217720 + 24129\pi)rt + 54(72640 + 8043\pi)t^2 \tag{A.162}$$

$$K_{69,7} = 15478r^2 + 13267rt + 3318\,t^2 \tag{A.163}$$

$$K_{69}^{*} = \frac{1127424\,t^3}{55545Ewl} \tag{A.164}$$

$$K_{88} = \frac{48}{499905\,Ewl^{10}}(6091731l^7t^3 + 420\,l^6r^2K_{88,1} - 4536\,l^5K_{88,2} + 252\,l^4r^3 K_{88,3} - 168\,l^3r^4K_{88,4} + 144\,l^2r^5K_{88,5} - 20000\,lr^6K_{88,6} + 32000000r^7K_{22,7}) \tag{A.165}$$

with:

$$K_{88,1} = 30(44363\,\pi + 142298)r^2 + 2\,(532356\pi + 1778725)rt + 3(88726\,\pi + 355745)t^2 \tag{A.166}$$

$$K_{88,2} = 10(296317 + 159140\pi)r^5 + [2031888\,r + (2328205 + 127312\,\pi)t]r^{\cdot} + 5[338648\,r + (211655 + 63656\,\pi)t]r^3t \tag{A.167}$$

$$K_{88,3} = 74(2300445\pi + 2436356)r^3 + 12(11502225\pi + 11572691)r^2t + 15$$
$$[19490848\,r + (2436356 + 2300445\,\pi)t]rt + 14618136\,(24r^2 + 5t)r \quad \text{(A.168)}$$

$$K_{88,4} = (481753664 + 790545390\,\pi)r^3 + 28(23251335\,\pi + 13130504)r^2t$$
$$+ 7[246310144r + (13583280 + 23251335\,\pi)t]rt$$
$$+ 3622208\,(568r^2 + 119t^2)r \quad \text{(A.169)}$$

$$K_{88,5} = 9\,(6535456 + 159753125\ \pi)r^3 + 8\,(55824452 + 150215625\,\pi)r^2t$$
$$+ 14\,[304992128\,r + (8169432 + 21459375\,\pi)t]rt$$
$$+ 21785152\,(232r^2 + 49\,t^2)r \quad \text{(A.170)}$$

$$K_{88,6} = 1635(1600 + 3927\pi)r^3 + 792(6867\pi + 2500)r^2t + 18$$
$$[2067200r + (28000 + 75537\pi)t]rt + 3200(13640r^2 + 2907t^2)r \quad \text{(A.171)}$$

$$K_{88}^{*} = \frac{2707436\,t^3}{55545\,Ewl^3} \quad \text{(A.172)}$$

$$K_{89} = -\frac{24}{499905Ewl^9}(3924531l^7t^3 + 525l^6r^2K_{89,1} - 378l^5K_{89,2} + 252l^4r^3K_{89,3}$$
$$- 264l^3r^4K_{89,4} + 144l^2r^5K_{89,5} - 8800lr^6K_{89,6} + 14080000r^7K_{22,7}) \quad \text{(A.173)}$$

with:

$$K_{89,1} = 3(252755\,\pi + 809744)r^2 + 4(151653\,\pi + 506090)rt$$
$$+ 3(50551\,\pi + 202436)t^2 \quad \text{(A.174)}$$

$$K_{89,2} = 35(631928 + 338955\,\pi)r^5 + 4\,[3791568\,r + (4344505 + 2372685\,\pi)t]r^4$$
$$+ 5[2527712\,r + (1579820 + 474537\,\pi)t]r^3t \quad \text{(A.175)}$$

$$K_{89,3} = 74\,(1266585\,\pi + 1344508)r^3 + 12(6332925\,\pi + 6386413)r^2t + 15$$
$$[10756064\,r + (1344508 + 1266585\,\pi)t]rt + 8067048\,(24r^2 + 5t^2)r \quad \text{(A.176)}$$

$$K_{89,4} = 14(11034592 + 18269985\pi)r^3 + 28(7522935\pi + 4210568)r^2t + 7[78984448r + (4355760 + 7522935\pi)t]rt + 1161536(568r^2 + 119t^2)r \tag{A.177}$$

$$K_{89,5} = 9(30376896 + 78381625\pi)r^3 + 8(25946932 + 73702125\pi)r^2t + 14[141758848r + (3797112 + 10528875\pi)t]rt + 10125632(232r^2 + 49t^2)r \tag{A.178}$$

$$K_{89,6} = 15(174400 + 477309\pi)r^3 + 72(84231\pi + 27500)r^2t + 18[2067200r + (28000 + 84231\pi)t]rt + 3200(13640r^2 + 2907t^2)r \tag{A.179}$$

$$K_{89}^{*} = -\frac{290706t^3}{18515Ewl^2} \tag{A.180}$$

$$K_{99} = \frac{24}{499905Ewl^8}(16426981l^7t^3 + 2625l^6r^2K_{99,1} - 1890l^5K_{99,2} + 126l^4r^3 K_{99,3} - 84l^3r^4K_{99,4} + 72l^2r^5K_{99,5} - 48400lr^6K_{99,6} + 3097600r^7K_{22,7}) \tag{A.181}$$

with:

$$K_{99,1} = 3(17995\pi + 57616)r^2 + 4(10797\pi + 36010)rt + 3(3599\pi + 14404)t^2 \tag{A.182}$$

$$K_{99,2} = 5(269276 + 144345\pi)r^5 + [923232r + (1057870 + 577380\pi)t]r^4 + 5[153872r + (96170 + 28869\pi)t]r^3t \tag{A.183}$$

$$K_{99,3} = 74(688425\pi + 731924)r^3 + 12(3442125\pi + 3476639)r^2t + 15[5855392r + (731924 + 688425\pi)t]rt + 4391544(24r^2 + 5t^2)r \tag{A.184}$$

$$K_{99,4} = 238(511328 + 851325\pi)r^3 + 28(5959275\pi + 3316904)r^2t + 7[62220544r + (3431280 + 5959275\pi)t]rt + 915008(568r^2 + 119t^2)r \tag{A.185}$$

$$K_{99,5} = 9(14149056 + 38047625\pi)r^3 + 8(12085652 + 35776125\pi)r^2t + 14[66028928r + (1768632 + 5110875\pi)t]rt + 4716352(232r^2 + 49t^2)r \quad \text{(A.186)}$$

$$K_{99,6} = 15(6976 + 21063\pi)r^3 + 72(3717\pi + 1100)r^2t + 18[82688r + (1120 + 3717\pi)t]rt + 128(13640r^2 + 2907t^2)r \quad \text{(A.187)}$$

$$K_{99}^* = \frac{365044\,t^3}{55545\,Ewl} \quad \text{(A.188)}$$

Elemental Mass Matrix

The mass terms that correspond to the axial-deformation degrees of freedom are:

$$m_{11} = m_{77} = \frac{\rho w}{60l^4}[2r^6(992 - 315\pi) - 8r^5l(332 - 105\pi) + 35r^4l^2(48 - 15\pi) - 60r^3l^3(10 - 3\pi) + 30r^2l^4(4 - \pi) + 8l^5t] \quad \text{(A.189)}$$

$$m_{11}^* = \frac{2}{15}m \quad \text{(A.190)}$$

$$m_{14} = -2m_{17} = -m_{47} = \frac{\rho w}{30l^4}[-2r^6(992 - 315\pi) + 8r^5l(332 - 105\pi) - 25r^4l^2(48 - 15\pi) + 20r^3l^3(10 - 3\pi) + 2l^5t] \quad \text{(A.191)}$$

$$m_{14}^* = \frac{1}{15}m \quad \text{(A.192)}$$

$$m_{44} = \frac{2\rho w}{15l^4}[r^6(992 - 315\pi) - 4r^5l(332 - 105\pi) + 10r^4l^2(48 - 15\pi) + 4l^5t] \quad \text{(A.193)}$$

$$m_{44}^* = \frac{8}{15}m \quad \text{(A.194)}$$

The bending-related mass terms are:

$$m_{22} = \frac{\rho w}{9775920 l^{10}} \{128 r^4 (2r - l)[1142295 l^7 - 936859 l^6 r - 8726564 l^5 r^2$$
$$+ 36715910 l^4 r^3 - 75287520 l^3 r^4 + 90184160 l^2 r^5 - 704056321 l r^6 + 29936256 r^7]$$
$$+ 7r^2 [698280(4 - \pi) l^{10} + 652740(15\pi - 16) l^8 r^2 - 3248520(7\pi - 4) l^7 r^3$$
$$- 419562(105\pi - 32) l^6 r^4 + 3354120(99\pi - 16) l^5 r^5 - 296175(3003\pi - 256) l^4 r^6$$
$$+ 1987920(715\pi - 32) l^3 r^7 - 67210(21789\pi - 512) l^2 r^8 + 47520(20995\pi - 256) l r^9$$
$$- 1080(323323\pi - 2048) r^{10}] + 3095792 l^{11} t\} \tag{A.195}$$

$$m_{22}^* = \frac{27641 \rho w l t}{87285} \tag{A.196}$$

$$m_{23} = \frac{\rho w}{29327760 l^9} \{32 r^3 (2r - l)[-610995 l^8 + 1753290 l^7 t + 10551618 l^6 r^2$$
$$- 61331424 l^5 r^3 + 143556336 l^4 r^4 - 219941568 l^3 r^5 + 218128064 l^2 r^6$$
$$- 140811264 l r^7 + 59872512 r^8] + 35 r^3 [418968(\pi - 2) l^9 + 85008(15\pi - 16) l^8 r$$
$$+ 355212(7\pi - 4) l^7 r^2 - 252351(105\pi - 32) l^6 r^3 + 824208(99\pi - 16) l^5 r^4$$
$$- 50490(3003\pi - 256) l^4 r^5 + 271656(715\pi - 32) l^3 r^6 - 7733(21789\pi - 512) l^2 r^7$$
$$+ 4752(20995\pi - 256) l r^8 + 108(323323\pi - 2048) r^9] + 1236200 l^{11} t\} \tag{A.197}$$

$$m_{23}^* = \frac{4415 \rho w l^2 t}{104742} \tag{A.198}$$

$$m_{25} = \frac{\rho w}{5498955 l^{10}} \{r^4 [-4144140(5\pi - 16) l^8 + 382536(105\pi$$
$$- 332) l^7 r + 253638(315\pi - 992) l^6 r^2 - 191664(1155\pi - 3632) l^5 r^3$$
$$- 108570(6435\pi - 20224) l^4 r^4 + 89320(45045\pi - 141536) l^3 r^5$$
$$- 10153(765765\pi - 2405888) l^2 r^6 + 31200(223839\pi - 703232) l r^7$$
$$- 1848(1322685\pi - 4155392) r^8] + 584008 l^{11} t\} \tag{A.199}$$

$$m_{25}^{*} = \frac{584008\rho wlt}{5498955} \tag{A.200}$$

$$m_{26} = \frac{\rho w}{21995820 l^9}\{r^4[637560(5\pi - 16)l^8 - 510048(105\pi - 332)l^7 r - 146916(315\pi - 992)l^6 r^2 + 1488168(1155\pi - 3632)l^5 r^3 - 1132131(6435\pi - 20224)l^4 r^4 + 359920(45045\pi - 141536)l^3 r^5 - 28798(765765\pi - 2405888)l^2 r^6 + 78000(223839\pi - 703232)lr^7 - 4620(1322685\pi - 4155392)r^8] + 212224\, l^{11} t\} \tag{A.201}$$

$$m_{26}^{*} = \frac{53056\rho wl^2 t}{5498955} \tag{A.202}$$

$$m_{28} = \frac{\rho w}{87983280 l^{10}}\{r^4[22633380(5\pi - 16)l^8 + 2932776(105\pi - 332)l^7 r + 5900202(315\pi - 992)l^6 r^2 - 15045624(1155\pi - 3632)l^5 r^3 + 10444665(6435\pi - 20224)l^4 r^4 - 3417040(45045\pi - 141536)l^3 r^5 + 283426(765765\pi - 2405888)l^2 r^6 - 780000(223839\pi - 703232)lr^7 + 46200(1322685\pi - 4155392)r^8] + 2194952\, l^{11} t\} \tag{A.203}$$

$$m_{28}^{*} = \frac{274369\rho wlt}{10997910} \tag{A.204}$$

$$m_{29} = \frac{\rho w}{7998480 l^9}\{r^4[-72450(5\pi - 16)l^8 + 156492(105\pi - 332)l^7 r - 397719(315\pi - 992)l^6 r^2 + 470520(1155\pi - 3632)l^5 r^3 - 251349(6435\pi - 20224)l^4 r^4 + 73640(45045\pi - 141536)l^3 r^5 - 5801(765765\pi - 2405888)l^2 r^6 + 15600(223839\pi - 703232)lr^7 - 924(1322685\pi - 4155392)r^8] - 27604\, l^{11} t\} \tag{A.205}$$

$$m_{29}^{*} = -\frac{6901\rho wl^2 t}{1999620} \tag{A.206}$$

$$m_{33} = \frac{\rho w}{117311040 l^8}\{r^4[-14663880(5\pi - 16) l^8 + 4760448(105\pi$$
$$- 332) l^7 r - 5472852(315\pi - 992) l^6 r^2 + 3184632(1155\pi - 3632) l^5 r^3$$
$$- 831369(6435\pi - 20224) l^4 r^4 + 127600(45045\pi - 141536) l^3 r^5 \qquad \text{(A.207)}$$
$$- 5830(765765\pi - 2405888) l^2 r^6 + 10400(223839\pi - 703232) l r^7$$
$$- 616(1322685\pi - 4155392) r^8] + 895648 l^{11} t\}$$

$$m_{33}^* = \frac{27989 \rho w l^3 t}{3665970} \qquad \text{(A.208)}$$

$$m_{35} = \frac{\rho w}{219958320 l^9}\{r^5[-1105104\ (105\pi - 332) l^7 + 1295448(315\pi - 992) l^6 r$$
$$+ 11880(1155\pi - 3632) l^5 r^2 - 350427(6435\pi - 20224) l^4 r^3$$
$$+ 113520(45045\pi - 141536) l^3 r^4 - 8118(765765\pi - 2405888) l^2 r^5$$
$$+ 20800(223839\pi - 703232) l r^6 - 1232(1322685\pi - 4155392) r^7] + 532368 l^{11} t\} \qquad \text{(A.209)}$$

$$m_{35}^* = \frac{14788 \rho w l^2 t}{610995} \qquad \text{(A.210)}$$

$$m_{36} = \frac{\rho w}{43991640 l^8}\{r^5[85008(105\pi - 332) l^7 - 962808(315\pi - 992) l^6 r$$
$$+ 1613304(1155\pi - 3632) l^5 r^2 - 816585(6435\pi - 20224) l^4 r^3$$
$$+ 187440(45045\pi - 141536) l^3 r^4 - 11286(765765\pi - 2405888) l^2 r^5$$
$$+ 26000(223839\pi - 703232) l r^6 - 1540\ (1322685\pi - 4155392) r^7] + 109872 l^{11} t\} \qquad \text{(A.211)}$$

$$m_{36}^* = \frac{218 \rho w l^3 t}{87285} \qquad \text{(A.212)}$$

$$m_{38} = \frac{\rho w}{87983280 l^9}\{r^4[-10041570(5\pi - 16) l^8 + 1168860(105\pi - 332) l^7 r$$
$$+ 3841761(315\pi - 992) l^6 r^2 - 7465392(1155\pi - 3632) l^5 r^3$$

$$+3875718(6435\pi-20224)l^4r^4-906840(45045\pi-141536)l^3r^5$$
$$+55671(765765\pi-2405888)l^2r^6-130000(223839\pi-703232)lr^7$$
$$+7700(1322685\pi-4155392)r^8]+728796l^{11}t\} \quad \text{(A.213)}$$

$$m_{38}^{*}=\frac{60733\rho wl^2t}{7331940} \quad \text{(A.214)}$$

$$m_{39}=\frac{\rho w}{31993920l^8}\{r^5[224112(105\pi-332)l^7-679560(315\pi-992)l^6r$$
$$+783432(1155\pi-3632)l^5r^2-345471(6435\pi-20224)l^4r^3$$
$$+76080(45045\pi-141536)l^3r^4-4542(765765\pi-2405888)l^2r^5$$
$$+10400(223839\pi-703232)lr^6-616(1322685\pi-4155392)r^7]-35760l^{11}t\} \quad \text{(A.215)}$$

$$m_{39}^{*}=-\frac{149\rho wl^3t}{133308} \quad \text{(A.216)}$$

$$m_{55}=\frac{\rho w}{16496865l^{10}}\{8r^6[-1127280(315\pi-992)l^6$$
$$+2033856(1155\pi-3632)l^5r-9933001(6435\pi-20224)l^4r^2$$
$$+204600(45045\pi-141536)l^3r^3-10395(765765\pi-2405888)l^2r^4$$
$$+20800(223839\pi-703232)lr^5-1232(1322685\pi-4155392)r^6]+1635840l^{11}t\} \quad \text{(A.217)}$$

$$m_{55}^{*}=\frac{36352\rho wlt}{366597} \quad \text{(A.218)}$$

$$m_{56}=\frac{\rho w}{16496865l^9}\{16r^6[-81312(315\pi-992)l^6$$
$$+171072(1155\pi-3632)l^5r-107184(6435\pi-20224)l^4r^2$$
$$+31680(45045\pi-141536)l^3r^3-2442(765765\pi-2405888)l^2r^4$$
$$+6500(223839\pi-703232)lr^5-385(1322685\pi-4155392)r^6]+196608l^{11}t\} \quad \text{(A.219)}$$

$$m_{56}^{*} = \frac{65536\rho wl^2t}{5498955} \tag{A.220}$$

$$m_{58} = \frac{\rho w}{16496865l^{10}}\{r^4[-20083140(5\pi-16)l^8 + 3187800(105\pi - 332)l^7r + 7173474(315\pi-992)l^6r^2 - 15695856\ (1155\pi-3632)l^5r^3 + 8272110(6435\pi-20224)l^4r^4 - 1904760\ (45045\pi-141536)l^3r^5 + 113619(765765\pi-2405888)l^2r^6 - 260000\ (223839\pi-703232)lr^7 + 15400(1322685\pi-4155392)r^8] + 947544l^{11}t\} \tag{A.221}$$

$$m_{58}^{*} = \frac{315848\rho wlt}{5498955} \tag{A.222}$$

$$m_{59} = \frac{\rho w}{5998860l^9}\{r^5[486864(105\pi-332)l^7 - 1648920(315\pi-992)l^6r + 1989144(1155\pi-3632)l^5r^2 - 867237(6435\pi-20224)l^4r^3 + 179760(45045\pi-141536)l^3r^4 - 9774(765765\pi-2405888)l^2r^5 + 20800(223839\pi-703232)lr^6 - 1232(1322685\pi-4155392)r^7] - 43920l^{11}t\} \tag{A.223}$$

$$m_{59}^{*} = -\frac{244\rho wl^2t}{33327} \tag{A.224}$$

$$m_{66} = \frac{\rho w}{16496865l^8}\{16r^6[3696(1575\pi+5084)l^6 - 104544(525\pi+1816)l^5r + 924(225225\pi+942944)l^4r^2 - 5280(75075\pi+429031)l^3r^3 + 33(11486475\pi+104355392)l^2r^4 - 650(223839\pi+4395200)lr^5 + 999891200r^6] + 25728l^{11}t\} \tag{A.225}$$

$$m_{66}^{*} = \frac{8576\rho wl^3t}{5498955} \tag{A.226}$$

$$m_{68} = \frac{\rho w}{65987460 l^9}\{r^4[-17214120\ (5\pi - 16)l^8 + 3570336(105\pi - 332)l^7 r + 5134668(315\pi - 992)l^6 r^2 - 15413112(1155\pi - 3632)l^5 r^3 + 10256169(6435\pi - 20224)l^4 r^4 - 3107280\ (45045\pi - 141536)l^3 r^5 + 242682(765765\pi - 2405888)l^2 r^6 - 650000\ (223839\pi - 703232)lr^7 + 38500(1322685\pi - 4155392)r^8] + 617088 l^{11} t\} \quad \text{(A.227)}$$

$$m_{68}^* = \frac{51424\rho w l^2 t}{5498955} \quad \text{(A.228)}$$

$$m_{69} = \frac{\rho w}{11997720 l^8}\{r^5[208656(105\pi - 332)l^7 - 777336(315\pi - 992)l^6 r + 1056888(1155\pi - 3632)\ l^5 r^2 - 546105(6435\pi - 20224)l^4 r^3 + 143280(45045\pi - 141536)l^3 r^4 - 10182(765765\pi - 2405888)l^2 r^5 + 26000(223839\pi - 703232)\ lr^6 - 1540(1322685\pi - 4155392)r^7] - 13776 l^{11} t\} \quad \text{(A.229)}$$

$$m_{69}^* = -\frac{82\rho w l^3 t}{71415} \quad \text{(A.230)}$$

$$m_{88} = \frac{\rho w}{263949840 l^{10}}\{r^4[806194620(5\pi - 16)l^8 - 115398360\ (105\pi - 332)l^7 r - 118577382(315\pi - 992)l^6 r^2 + 296270568(1155\pi - 3632)\ l^5 r^3 - 163687755(6435\pi - 20224)l^4 r^4 + 40727280\ (45045\pi - 141536)\ l^3 r^5 - 2668182(765765\pi - 2405888)l^2 r^6 + 6500000\ (223839\pi - 703232)\ lr^7 - 385000(1322685\pi - 4155392)r^8] + l^{10}[131974920\ (4 - \pi)r^2 + 54634128\, lt]\} \quad \text{(A.231)}$$

$$m_{88}^* = \frac{1138211\rho w l t}{5498955} \quad \text{(A.232)}$$

$$m_{89} = \frac{\rho w}{23995440 l^9}\{r^3[3999240(3\pi - 10)l^9 - 13041000(5\pi - 16)l^8 r$$
$$- 1049076(105\pi - 332)l^7 r^2 + 744687(315\pi - 992)l^6 r^3 - 9368136(1155\pi$$
$$- 3632)l^5 r^4 + 4222995(6435\pi - 20224)l^4 r^5 - 939960(45045\pi - 141536)l^3 r^6$$
$$+ 56499(765765\pi - 2405888)l^2 r^7 - 130000(223839\pi - 703232)lr^8$$
$$+ 7700(1322685\pi - 4155392)r^9] - 373272 l^{11} t\} \tag{A.233}$$

$$m_{89}^* = -\frac{15553\rho w l^2 t}{999810} \tag{A.234}$$

$$m_{99} = \frac{\rho w}{95981760 l^8}\{r^4[-11997720(5\pi - 16)l^8 + 6955200(105\pi$$
$$- 332)l^7 r - 13137852(315\pi - 992)l^6 r^2 + 12065544(1155\pi - 3632)l^5 r^3$$
$$- 4676343(6435\ \pi - 20224)l^4 r^4 + 947280(45045\pi - 141536)l^3 r^5$$
$$- 52722(765765\pi - 2405888)l^2 r^6 + 114400(223839\pi - 703232)lr^7$$
$$- 6776(1322685\pi - 4155392)r^8] + 144288 l^{11} t\} \tag{A.235}$$

$$m_{99}^* = \frac{167\rho w l^3 t}{111090} \tag{A.236}$$

6

Topics Beyond the Minimal Modeling Approach to Flexure Hinges

This chapter presents a few topics that are important in analyzing the behavior of flexure hinges under circumstances that extend over the minimal set of conditions studied previously. Discussed will be aspects connected to large deformations, buckling, torsion of noncircular cross-section flexures, composite flexure hinges, thermal effects, shape optimization, materials and fabrication technologies for macro- and MEMS applications.

6.1 Large Deformations

The classic theory of deformations assumes that all deformations within an elastic body are small. This hypothesis is consistent, on one hand, with the real-world character of deformations or strains sustained by the vast majority of mechanical components that are subject to loads below levels that would cause failure. On the other hand, the small displacement theory allows us to develop and apply a relatively simple mathematical apparatus, whose main virtue stems from its linear character, which further enables convenient calculations to be carried out. Mathematically speaking, the distinction between small and large displacement theory lies in the way in which the strains are expressed in terms of displacements. It is known from the theory of elasticity that strains can be formulated as functions of the partial derivatives of the displacement functions, and that higher-order partial derivatives are usually involved. When neglecting partial derivatives that have an order or power greater than one, the corresponding simplification leads to the so-called small displacement theory (see, for instance, Freudenthal[1]). When these simplifications are not applied, the resulting theory is a large displacement one. More specifically, in the case of members that are subject to bending, the small displacement theory assumes that a bent element of length ds is approximately equal to its projection on the x axis, as shown in Figure 6.1.

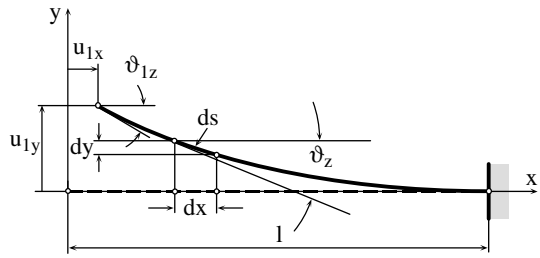

FIGURE 6.1
Real and projected bending deformations as sources for small vs. large displacement theory.

In actuality, according to basic differential geometry, the length of a curved element taken from the bent beam is expressed as:

$$ds = \sqrt{1+\left(\frac{dy}{dx}\right)^2}\,dx \tag{6.1}$$

At the same time, the exact equation that gives the curvature of a beam is:

$$\rho = \frac{1}{R} = \frac{\frac{d^2y}{dx^2}}{\sqrt{\left[1+\left(\frac{dy}{dx}\right)^2\right]^3}} \tag{6.2}$$

However, when neglecting powers higher than one, as mentioned previously (which, in the bending case, pertains to the second power of the slope), Eq. (6.1) is simplified for the small displacement case to:

$$ds \cong dx \tag{6.3}$$

which also simplifies Eq. (6.2) to:

$$\rho \cong \frac{d^2y}{dx^2} \tag{6.4}$$

Equation (6.4) is the basis for all subsequent linear or small deformation modeling for beam members because the bending moment, for instance, is connected to curvature according to:

$$M_b = EI\rho \tag{6.5}$$

Shanley[2] mentions that, for beams where the deflection-to-length ratio is less than 0.2, the errors induced by applying the approximation of Eq. (6.4) are less than 6%, but at such deformation levels the appreciable bending stresses could cause failure of the mechanical member, or, in the best-case scenario, a situation is created where the elastic limit is exceeded. As a consequence, as underscored by Shanley,[2] the large deflection theory is of only academic interest, unless the member has specifically been designed to operate as a large deflection one.

Wang et al.[3] focus on an end-supported beam that is subject to a midpoint load under the assumption of large deformations. The solution to the problem is provided by both elliptical integrals and the shooting-optimization technique. Dado[4] treats the problem of large deflection beams with end loads by using the pseudo-rigid-body model as connectors in compliant mechanisms by developing a parameterized model. Lee[5] studied cantilever beams constructed of nonlinear materials and simultaneously subjected to a uniformly distributed load and a tip load. The governing equations of the deflected member were derived by using a shearing-force-based formulation and were further solved by a Runge–Kutta type of numerical algorithm. Ohtsuki and Ellyn[6] studied frames where large deformations must be accounted for. Elliptical integrals are utilized to obtain the solution to the problem, and the results are compared to similar experimental data. Hamdouni[7] presents a decomposition technique that allows derivation of the compatibility equations corresponding to large deformations of elastic members.

Pai and Palazotto[8] utilized a multiple-shooting technique to solve the problem of flexible beams undergoing large three-dimensional deformations, such that the resulting nonlinear model gives exact solutions. In an extension of this work, Gummadi and Palazotto[9] address the problem of laminated composite beams and arches that are subject to large strains. The large strain–load characteristics are studied for both isotropic and laminated structures. Wriggers and Reese[10] have investigated the strain-enhanced elements and their suitability of representing large deformations in both bending and compressive situations by means of the finite element method. Zelenina and Zubov[11] analyzed the bending of prismatic beams that are subject to large deformations by using a semi-inverse method whereby a two-dimensional, nonlinear, boundary-value model is obtained. The solution is produced in both displacements and stresses by using the Ritz method.

Oguibe and Webb[12] have developed an approximate theoretical model for the analysis of large deflections of multilayer cantilever beams that are subject to impulse loading. The numerical results of this model are in agreement with the corresponding experimental data. Fortune and Vallee[13] detail the Bianchi identities for three-dimensional continua undergoing large deformations, which are explicit formulations of the compatibility equations. Howell and Midha[14] introduce the pseudo-rigid-body method of describing compliant mechanisms that include small-length flexural pivots capable of large displacements whereby the flexible members are modeled as discrete torsional

springs attached to the rigid links. An extension of this approach is pursued by Howell and Midha,[15] who utilize the pivot-as-torsional-spring concept within the rigid-body modeling of compliant mechanisms that incorporate initially curved, large deflection beams.

Described next are several applications where flexible members of compliant mechanisms are specifically designed to sustain large deformations in order to fulfill their functional role. In a survey paper, Shoup and McLarnan[16] presented the methodologies utilized for deriving flexible-link mechanisms from their rigid-link counterparts, and, specifically, they focus on single-loop, closed-loop plane flexible mechanisms with lower pairs. Shoup and McLarnan[17] and Shoup[18] investigated the problems related to undulating and nodal elastica curves, which denote shapes that can be taken by flexible members (strips) undergoing large deformations. Models are derived for both cases and approximate solutions are given that allow evaluation of several parameters useful in the design of such members. Saggere and Kota,[19] in the context of analyzing the motions produced by planar, compliant, four-bar mechanisms, approach the inverse elastica problem by determining the shape that a flexible component which is capable of large deformations must take in terms of its prescribed end displacements and when the loading acting on it is known.

Shoup and McLarnan[20] present the main equations that govern the static response of a doubly clamped flexible strip that can be utilized as a nonlinear spring in flexible mechanisms. Jensen et al.[21] investigated a Young-type bistable mechanism that includes two compliant members capable of large deformations. The pseudo-rigid-body approach is again employed to model this mechanism. Edwards et al.[22] utilized the same concept of pseudo-rigid-body to model an initially curved pinned–pinned flexible member capable of large deflections and that behaves almost like a translatory spring in compliant mechanisms. Saxena and Anathasuresh[23] applied the large deformation capability of flexural members that are part of compliant mechanisms to commercially available finite-element software and analyzed several frame-type applications.

From a practical standpoint, it would be of interest to establish how much error is introduced by carrying out calculations according to the small displacement (linear) theory instead of the nonlinear large displacement theory. Consider a constant cross-section (dimensions w and t) cantilever beam of length l that is constructed of homogeneous, isotropic material with a Young's modulus of E that is subject to bending moment M at its free end. The goal is to express the tip slope in terms of the applied bending moment in the case of large displacements. The differential equation that takes into account large deformations and is given in Eqs. (6.2) and (6.5) can be put into the form:

$$\frac{d^2y}{dx^2} - k\sqrt{\left[1+\left(\frac{dy}{dx}\right)^2\right]^3} = 0 \tag{6.6}$$

which is a nonlinear homogeneous equation in *y*. In the equation above:

$$k = \frac{M}{EI} \tag{6.7}$$

By applying the substitution:

$$\frac{dy}{dx} = \tan z \tag{6.8}$$

where z is an unknown function depending on x, the following solution is obtained after basic calculations, back substitution for the original unknown function y, and consideration of the zero-slope boundary condition for $x = l$ (see Figure 6.1):

$$\frac{dy}{dx} = k\frac{(x-l)}{\sqrt{1-k^2(x-l)^2}} \tag{6.9}$$

The maximum slope is found at the free end, so by taking $x = 0$ in Eq. (6.9), the maximum slope for large displacements is:

$$\theta_1^l = \frac{kl}{\sqrt{1-k^2l^2}} \tag{6.10}$$

However, it is known that the maximum slope of the same cantilever beam, when the deformations are assumed small, is given by the equation:

$$\theta_1 = kl \tag{6.11}$$

By comparing Eqs. (6.10) and (6.11), the following relationship can be formulated:

$$\theta_1^l = \frac{\theta_1}{\sqrt{1-\theta_1^2}} \tag{6.12}$$

Through simple inspection of Eq. (6.12) it can be seen that the end slope for large displacements is always greater than the one corresponding to small displacements. The relative error between large and small displacement end slopes is defined as:

$$\text{error} = \frac{\theta_1^l - \theta_1}{\theta_1^l} = 1 - \sqrt{1-\theta_1^2} \tag{6.13}$$

In allowing large displacement to take place, it is of primary importance that the stresses set in the mechanical component do not exceed a maximum limit, say σ_{max}. For a constant rectangular cross-section beam, the maximum stress occurs on the outer fibers of the cantilever beam and is given by the equation:

$$\sigma_{max} = \frac{Mt}{2I} \tag{6.14}$$

Combining Eqs. (6.7), (6.11), and (6.14) yields:

$$\theta_1 = 2\frac{\sigma_{max}}{E}\frac{l}{t} \tag{6.15}$$

Clearly, Eq. (6.15) shows that for a given length-to-thickness ratio l/t, the maximum tip slope is limited by material properties. Equation (6.15) was utilized to plot the relative error functions, as given in Eq. (6.13), for three different materials: regular steel, aluminum, and titanium alloys, as illustrated in Figure 6.2. Some average and conservative values were taken for the maximum strength and Young's modulus of the three materials, namely: for steel, $\sigma_{max} = 3 \times 10^8$ N/m^2 and $E = 2 \times 10^{11}$ N/m^2; for aluminum, $\sigma_{max} = 1.5 \times 10^8$ N/m^2 and $E = 0.7 \times 10^{11}$ N/m^2; and, for titanium, $\sigma_{max} = 4.5 \times 10^8$ N/m^2 and $E = 1.1 \times 10^{11}$ N/m^2. Figure 6.2 is quite indicative of the differences between large and small deformations in calculating the tip slope of a cantilever

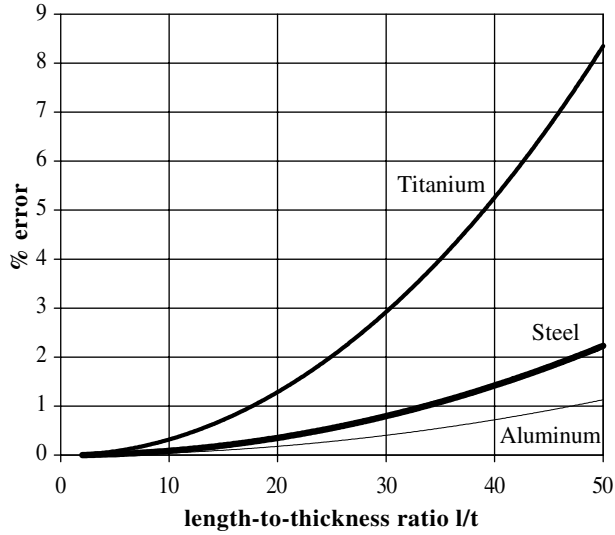

FIGURE 6.2
Relative errors of large vs. small displacement theory slope at the free end of a cantilever beam subjected to a tip bending moment.

beam under a tip moment load. For length-to-thickness ratios less than 10, for instance, the relative errors are less than 0.3% for all three materials that were investigated (for steel and aluminum the errors are less than 0.1%), as shown in Figure 6.2. In the great majority of engineering applications that utilize regular flexure hinges for displacement amplification or force reduction (in precision mechanisms or microelectromechanical systems, or MEMS, for instance), the length-to-thickness ratio is kept well under the threshold value of 10, so the errors implied by assuming small displacements are negligible, as also pointed out by Shanley[2] after analyzing the tip deflection of a cantilever beam. The exercise that was just carried out is a simple one, as it took into consideration only a tip moment. When axial and shearing forces are also present, the formulation is further complicated and the solution to the resulting differential equation can be obtained by means of elliptical integrals. The works of Shoup and McLarnan[16] and Shoup,[18] for instance, provide details on the respective derivation and solution. The displacement (deformation)–load relationships, however, are highly nonlinear, and, as underscored by the simple example presented earlier, it is impossible to find out a solution to the differential equation of equilibrium of the form:

$$u = CL \tag{6.16}$$

where u and L denote generic displacement (deformation) and load components, respectively, and C stands for the corresponding compliance factor.

Applications exist, however, where the flexible members that are expected to undergo large deformations must be accordingly designed and where the small-deformation model definitely might not be a suitable tool. The example of the constant cross-section cantilever beam shown in Figure 6.1 will be analyzed when its free tip is under the action of two forces, F_{1x} and F_{1y}, and a moment, M_{1z}. The aim is to determine the tip displacements u_{1x}, u_{1y}, and rotation θ_{1z} in terms of the load. The path followed in the corresponding derivation is the one proposed by Shoup and McLarnan[17] to solve a similar problem. The large deformation aspect in this case is included by taking into consideration the combined bending effect of the three end loads, as it is well known that the small displacement theory disregards the contribution of the axial force to bending. The bending moment about the z-axis a generic point of abscissa x is:

$$M = M_{1z} + F_{1y}x + F_{1x}(u_{1y} - u_y) \tag{6.17}$$

where u_y represents the deflection at the generic point under consideration. The Euler–Bernoulli theory (for long beam-like members) gives the following basic differential equation:

$$M = EI_z \frac{d\theta_z}{ds} \tag{6.18}$$

By combining Eqs. (6.17) and (6.18) and differentiating the resulting equation in terms of s, we obtain:

$$EI_z \frac{d^2\theta_z}{ds^2} = -F_{1x} \sin\theta_z + F_{1y} \cos\theta_{1z} \tag{6.19}$$

Because the following identities are valid for an element of the deflected cantilever beam:

$$\begin{cases} \sin\theta_z = \dfrac{du_y}{ds} \\ \cos\theta_z = \dfrac{dx}{ds} \end{cases} \tag{6.20}$$

Eq. (6.19) can then be reformulated as:

$$EI_z d\left[\left(\frac{d\theta_z}{ds}\right)^2\right] = 2(-F_{1x} \sin\theta_z + F_{1y} \cos\theta_z) d\theta_z \tag{6.21}$$

for which the solution is:

$$\frac{d\theta_z}{ds} = \sqrt{\frac{2(F_{1x} \cos\theta_z + F_{1y} \sin\theta_z + C)}{EI_z}} \tag{6.22}$$

which is, of course, the solution indicated by Shoup and McLarnan.[17] Combining Eqs. (6.17), (6.18), and (6.22) produces the following relationship:

$$\sqrt{2EI_z(F_{1x} \cos\theta_z + F_{1y} \sin\theta_z + C)} = M_{1z} + F_{1y}x + F_{1x}(u_{1y} - u_y) \tag{6.23}$$

By utilizing the following boundary conditions in Eq. (6.23):

$$\begin{cases} \theta_z = 0 \quad \text{and} \quad u_y = 0 \quad \text{for } x = l \\ \theta_z = \theta_{1z} \quad \text{and} \quad u_y = u_{1y} \quad \text{for } x = 0 \end{cases} \tag{6.24}$$

the following two equations can be written:

$$\begin{cases} \sqrt{2EI_z(F_{1x} \cos\theta_{1z} + F_{1y} \sin\theta_{1z} + C)} = M_{1z} \\ \sqrt{2EI_z(F_{1x} + C)} = M_{1z} + F_{1y}l + F_{1x}u_{1y} \end{cases} \tag{6.25}$$

Two more equations can be formulated to express the horizontal and vertical displacement of the free end 1, again according to Shoup and McLarnan,[17] as:

$$\begin{cases} u_{1y} = \int_0^l \sin\theta_z \, ds \\ u_{1x} = l - \int_0^l \cos\theta_z \, ds \end{cases} \tag{6.26}$$

Equation (6.26) can be transformed, by taking into account Eq. (6.22), into the equivalent form:

$$\begin{cases} u_{1y} = \sqrt{\dfrac{EI_z}{2}} \displaystyle\int_{\theta_{1z}}^0 \frac{\sin\theta_z}{\sqrt{F_{1x}\cos\theta_z + F_{1y}\sin\theta_z + C}} \, d\theta_z \\ u_{1x} = l - \sqrt{\dfrac{EI_z}{2}} \displaystyle\int_{\theta_{1z}}^0 \frac{\cos\theta_z}{\sqrt{F_{1x}\cos\theta_z + F_{1y}\sin\theta_z + C}} \, d\theta_z \end{cases} \tag{6.27}$$

Equations (6.25) and (6.27) form a system of four equations with four unknowns, namely: the integration constant, C, and the free end displacements, u_{1x}, u_{1y}, and θ_{1z}. If one of the two expressions in Eq. (6.25) is used to express C, and the resulting expression for C is substituted into the other expression of Eq. (6.25), as well as into Eq. (6.27), a system of three equations is formed, with the unknowns being the free end displacements of the cantilever. There is no solution through elementary functions to this system because the integrals composing it are elliptical integrals of the first and second kind. These integrals can either be solved by using a numerical integration technique or, alternatively, can be series-expanded and therefore approximated through a sufficient number of elementary function terms. Whatever the course taken to solve the above-mentioned integrals, the solution to the resulting equation system is of the form:

$$\begin{cases} u_{1x} = f_1(F_{1x}, F_{1y}, M_{1z}) \\ u_{1y} = f_2(F_{1x}, F_{1y}, M_{1z}) \\ \theta_{1z} = f_3(F_{1x}, F_{1y}, M_{1z}) \end{cases} \tag{6.28}$$

where the functions of Eq. (6.28) are nonlinear in the load components F_{1x}, F_{1y}, and M_{1z}, and, as a consequence, no factors express each displacement as a linear combination of the corresponding loads, so no compliances can be individualized in this large displacement case.

The case previously analyzed was relatively simple because the large deformation capability was reflected only through the inclusion of the axial force into the bending effects. Further complications are expected for the case where the axial deformation of the member is taken into account and combined with the bending-produced deformations. Moreover, when shearing has to be taken into consideration for relatively short flexures, the Euler–Bernoulli model must be dropped in favor of the Timoshenko model, which can accommodate such shearing effects, as detailed in the discussion dedicated to short flexures in Chapters 2 and 4. Adding to the complexity of the problem is the fact that, for flexure hinges with non-constant cross-section dimensions (as in the case for the configurations that have been studied throughout this work), solving for the unknown tip displacements in terms of loads must progress through the step of solving nonlinear differential equations, because the inertia moment is no longer constant. However, all these aspects are probably beyond the scope of the majority of current engineering applications and will not be addressed further in this work.

6.2 Buckling

In a broad sense, the buckling is defined as a phenomenon of structural instability characterized by a loss of the equilibrium state when the external loading reaches a critical stage. The flexure hinges in compliant mechanisms can experience buckling, especially when their configuration is slender (relatively high ratio for length to cross-section dimensions), and the axial loading is compressive. In such cases, the flexure hinge can be treated as a column, which is defined as a member that can carry axial compressive forces. Figure 6.3 shows a fixed–free column-type flexure hinge that is under compressive load.

Several excellent monographs on buckling are available, such as those of Timoshenko and Gere,[24] Allen and Bulson,[25] or Chen and Lui,[26] to name just a few. Historically, the elastic (or reversible) buckling of columns (or struts) was the first buckling topic, and Euler, as early as 1757 (see, for example,

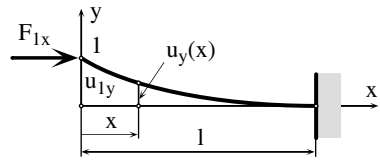

FIGURE 6.3
Schematic of buckling for a fixed–free column.

Timoshenko and Gere,[24] Shanley,[2] or Timoshenko[27]), proposed the mathematical model of the elastic buckling of columns that is still valid today. According to this model, the minimum axial load, or critical force, that would cause a constant cross-section column to bend (or buckle) is given by the following equation:

$$P_{cr} = \frac{\pi^2 E I_{min}}{l_{cr}^2} \tag{6.29}$$

In this equation, it is acknowledged that a minimum moment of inertia for the column cross-section must be taken in order to calculate the critical force. The critical length, l_{cr}, in the same equation takes into account the different types of end support. Classical strength of materials textbooks give details and values of those lengths in terms of the real length l of a column with a specific set of boundary conditions. Generically, the critical length is calculated by multiplying the physical length of a column by a specific coefficient, namely:

$$l_{cr} = kl \tag{6.30}$$

where the coefficient k takes values ranging from 0.5 (for a fixed–fixed column) to 2 (for a fixed–free column, which is also the case of the assumed boundary conditions for a flexure hinge). It is clear that the fixed–free conditions will generate the lowest critical force when compared to all boundary condition situations. The stress that is generated through buckling in the moment immediately before the lateral deformation (bending) generated by the axial load occurs is:

$$\sigma_{cr} = \frac{P_{cr}}{A} = \frac{\pi^2 E}{\lambda^2} \tag{6.31}$$

where λ is the slenderness ratio and is defined as:

$$\lambda = \frac{l_{cr}}{i_{min}} \tag{6.32}$$

with i_{min} being the minimum radius of gyration, given by:

$$i_{min} = \sqrt{\frac{I_{min}}{A}} \tag{6.33}$$

Apart from the elastic situation, there is another buckling type, where the bending produced through axial loading enters the inelastic (plastic) domain. In such cases, the critical stresses (and associated critical force) cannot be calculated by the Euler model. Several models treat the problem of inelastic buckling

and, again, the monographs of Timoshenko and Gere,[24] Allen and Bulson,[25] Chen and Lui,[26] or Shanley[2] are excellent sources for information in this area. The earliest explanation of the inelastic buckling phenomenon was provided by Engesser in 1889, when he proposed a slight modification of the Euler equations by utilizing the tangent modulus E_t instead of the Young's modulus E. The tangent modulus is defined as the ratio:

$$E_t = \frac{d\sigma}{d\varepsilon} \tag{6.34}$$

and can be calculated from the experimental compression tests that allow plotting the respective stress–strain curves. The work of Engesser, who calculated critical stresses for several materials that either do not obey Hooke's law or are loaded beyond their elastic limit, was continued, among other researchers, by Tetmajer and Jasinsky. Tetmajer, for instance, conducted a large number of experiments on short columns and concluded that Euler's formula is valid for slenderness ratios larger than 110 (see Timoshenko[27] for an interesting account of the buckling research and also Den Hartog[28,29] and Boresi et al.[30]). Jasinsky continued the experimental work of Tetmajer and provided sets of tabular data with critical stresses corresponding to various slender ratios. The work of the two researchers is concentrated in an equation that bears their name and that gives the approximate equation of the critical stress in terms of the slenderness ratio in the inelastic domain as:

$$\sigma_{cr} = a - b\lambda \tag{6.35}$$

with a and b being functions of the column material. In such cases, the critical force that produces inelastic buckling is:

$$P_{cr} = (a - b\lambda)A \tag{6.36}$$

It is apparent that longer columns are prone to elastic buckling while shorter columns might still buckle but more probably it will occur in the inelastic domain. Very short columns, though, do not buckle and, as expected, they can only fail through regular compression, and the corresponding stresses are simply:

$$\sigma = \frac{P}{A} \tag{6.37}$$

Figure 6.4 illustrates a plot that provides a visual representation of the three possible situations just mentioned: elastic (Euler) buckling, inelastic (plastic) buckling, and pure compression by representing the critical stress σ_{cr} as a function of the slenderness ratio λ. It can be seen that, for values larger than

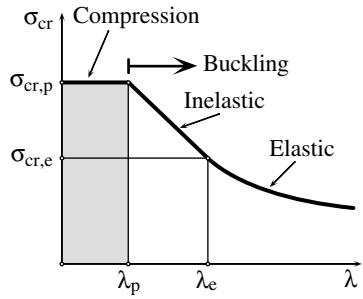

FIGURE 6.4
Critical stress–slenderness ratio plot as a decision tool for buckling/compression load.

a limit value of the slenderness ratio λ_e, the buckling is elastic, while for value less than λ_e but larger than λ_p (the subscript e stands for elastic and p for plastic) the buckling is inelastic (or plastic). For slenderness ratios smaller than λ_p, there is no buckling and the column is subject only to simple compression. In problems where the flexure hinges of a compliant mechanism have already been designed, it is useful to check the type of bending the flexures might be subject to, if any, by calculating the effective (actual) slenderness ratio λ of the specific flexure configuration and comparing it with the flag values λ_e and λ_p of Figure 6.4.

As for any problem regarding strength of materials, buckling is three faceted, as any of the following aspects can be addressed: verifying (checking), dimensioning, or calculation of the maximum safe load. Figure 6.5 provides a flowchart with the main steps involved in calculating a flexure hinge that might be subject to buckling. The verifying or checking step looks at an already existing flexure design with a defined geometry and material properties. After calculating the slenderness ratio by means of Eq. (6.32), the critical force can be determined through the equation that applies for elastic or inelastic buckling or pure compression, as given in Eqs. (6.31), (6.35), and (6.37), respectively. It is customary to calculate an effective (or actual) safety coefficient, c_{eff}, and compare it to a maximum allowable safety coefficient, c_a, according to:

$$c_{eff} = \frac{P_{cr}}{P_{eff}} \tag{6.38}$$

where P_{eff} is the axial compressive load that acts on the flexure hinge. In the case:

$$c_{eff} > c_a \tag{6.39}$$

the flexure will not be subject to the type of buckling it qualified for by virtue of its corresponding slenderness ratio.

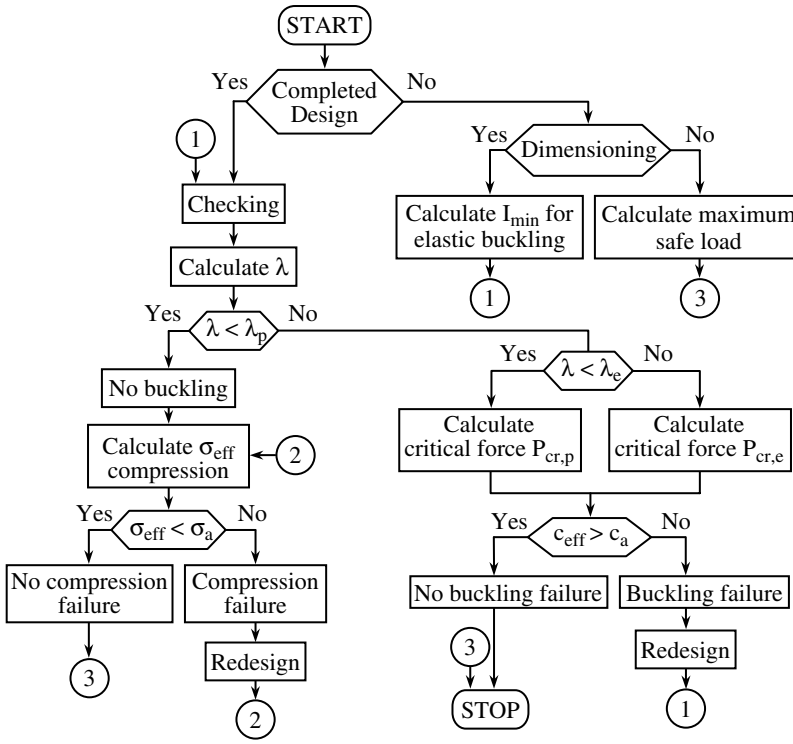

FIGURE 6.5
Flowchart of antibuckling approach to flexure hinges treated as columns.

The dimensioning problem in buckling is not so straightforward as it would be necessary to first decide which of the three possible categories apply for the analyzed case. This, however, is not possible to do because the slenderness ratio is not known in advance (determining some or all of the geometric parameters that define a flexure hinge is the very subject of dimensioning). The practical procedure usually assumes that in the worst-case scenario the flexure will be subject only to elastic buckling (which will at least preserve the physical integrity of the flexure after the load is removed). As a consequence, the minimum moment of inertia I_{min} can be calculated from Eqs. (6.31) through (6.33), under the assumption that the elastic properties of the flexure material are known, and proper cross-sectional dimensions can subsequently be selected to give the calculated minimum moment of inertia. The effective geometry is then used to actually check if buckling does occur, under the effective axial compressive load, according to the procedure previously exposed.

A third problem in buckling, as mentioned, is determining the maximum safety load, which is the axial load that can be carried by a particular flexure hinge without the peril of subjecting the flexure to buckling. Because the flexure hinge is already designed, it is known what type of loading it might

be subject to. As a consequence, the corresponding critical force can easily be calculated, and the maximum safety load under a specified maximum safety coefficient is given by:

$$P_a = \frac{P_{cr}}{c_a} \tag{6.40}$$

In deriving the critical force for a given constant cross-section column, the following steps have to be followed:

- Formulate the column deflection differential equation.
- Solve the differential equation (finding the function $u_y(x)$).
- Apply the boundary conditions and determine the critical force as the minimum-valued axial compressive force which is capable of preserving the shape of the first-order deflected curve, as given by the solution found according to the previous point.

The derivation of the critical force is briefly presented next for a fixed–free column under an axial load, as shown in Figure 6.3. It is well known from basic strength of materials principles that the bending-generated deflected curve $u_y(x)$ is solution to the differential equation:

$$EI\frac{d^2u_y}{dx^2} = -M_b \tag{6.41}$$

In the case shown in Figure 6.3, the bending moment, M_b, is produced through the action of the axial force, F_{1x}, and, at a current position x, this moment is:

$$M_b = F_{1x}(u_{1y} - u_y) \tag{6.42}$$

By substituting Eq. (6.42) into Eq. (6.41) and after rearranging factors, the differential equation of the deflected column becomes:

$$\frac{d^2u_y}{dx^2} - \omega^2 u_y = -\omega^2 u_{1y} \tag{6.43}$$

with:

$$\omega = \frac{F_{1x}}{EI} \tag{6.44}$$

Equation (6.43) is a nonhomogeneous second-order differential equation with constant coefficients, and its solution is expressed as the sum of the

solution of the homogeneous equation (zero in the right-hand side of Eq. (6.43)) and a particular solution of the nonhomogeneous equation. This solution, in this case, can be taken as:

$$u_y = -A\sin(\omega x) - B\cos(\omega x) + u_{1y} \tag{6.45}$$

where the constants A and B are determined, while the particular solution part is the deflection at the free end of the column u_{1y}. By applying the following boundary conditions:

$$\begin{cases} u_y(0) = u_{1y} \\ \left.\dfrac{du_y}{dx}\right|_{x=l} = 0 \end{cases} \tag{6.46}$$

we obtain the buckling condition:

$$\omega l = k\frac{\pi}{2}, \quad k = 1, 2, \ldots \tag{6.47}$$

Equation (6.47) combined with Eq. (6.44) will give the critical force as:

$$P_{cr} = F_{1x,min} = \frac{\pi^2 E I_{min}}{(2l)^2} \tag{6.48}$$

which, of course, coincides with the critical force of a fixed–free column as previously given. Taking into consideration the definition of the moment of inertia, the critical force for a constant rectangular cross-section, one-sensitivity-axis flexure hinge is:

$$P_{cr} = \frac{\pi^2 E w t^3}{48 l^2} \tag{6.49}$$

whereas for a multiple-axis (cylindrical) flexure hinge of diameter t the critical force is:

$$P_{cr} = \frac{\pi^3 E t^4}{256 l^2} \tag{6.50}$$

For all the other flexure hinge configurations dealt with so far in this book, the cross-section is not constant, and as a consequence the moment of inertia is not constant, so that the differential equation, Eq. (6.43), is of the general form:

$$\frac{d^2 u_y}{dx^2} - \omega(x)^2 u_y = -\omega(x)^2 u_{1y} \tag{6.51}$$

where:

$$\omega(x) = \frac{F_{1x}}{EI(x)} \tag{6.52}$$

The solution to the homogeneous part of this second-order differential equation with non-constant coefficients is of the form (as indicated, for example, by Tenenbaum and Pollard[31]):

$$u_{yh}(x) = C_1 u_{y1}(x) + C_2 u_{y2}(x) \tag{6.53}$$

where C_1 and C_2 are constants and $u_{y1}(x)$ and $u_{y2}(x)$ are two solutions. Provided that one solution is known (say, $u_{y1}(x)$), the theory shows that the other one can be found by means of the equation:

$$u_{y2}(x) = u_{y1}(x) \int \frac{e^{\int \frac{F_{1x}}{EI(x)}}}{u_{y1}^2(x)} dx \tag{6.54}$$

The double integration that is part of Eq. (6.54) can rarely be carried out through elementary functions so that the problem of finding the solutions of Eq. (6.51) has to be solved by means of approximate numerical procedures. A brief account of the methods that can be utilized to find the critical force in buckling for the case of variable cross-section columns is given by Timoshenko,[27] while a more detailed presentation can be found in the works of Timoshenko and Gere,[24] Allen and Bulson,[25] or Chen and Lui.[26] Fundamentally, two method categories are dedicated to solving this problem: the energy category and the numerical integration category. Energy methods, such as the Rayleigh–Ritz method developed and implemented by Timoshenko, the Galerkin method, or the Trefftz method, start by assuming a deflection curve that satisfies certain constraints (the boundary conditions of the real problem, most often) and then proceed by equating the strain energy that is stored through buckling and the work done through axial compression. It is thus possible to determine a critical force that is always greater than the real one because, by assuming a deflection curve, additional constraints are introduced to ensure that no other shape is taken by the deformed column, other than the assumed one. A relaxation of this procedure that reduces the value of the approximate critical force, as shown by Timoshenko,[27] can be achieved by selecting various assumed deflection curves in terms of several parameters that can conveniently be adjusted to minimize the critical load.

The second category of methods, which includes the Newmark procedure and the step-by-step numerical integration technique, is specifically suited to buckling applications where the cross-section is variable. In addition, as detailed by Allen and Bulson,[25] the Newmark method, for instance, can be utilized for inelastic buckling situations. This category of methods also

assumes a deflected shape of the column and then divides the length of the column into several partitions, bounded by so-called stations. Two numerical integrations are subsequently performed that permit evaluating the critical force. In the methods where an assumed deflection curve is considered *a priori*, of the generic form:

$$u_y(x) = f(x) \tag{6.55}$$

twice integrating the differential equations of the deflected column leads to a solution whereby the critical force is of the form:

$$P_{cr} = \frac{Ef(x)}{\int_0^l \left[\int \frac{f(x)}{I(x)} dx \right] dx} \tag{6.56}$$

Usually, assumed deflection functions are sine, parabolic, or cubic polynomials, as indicated by Allen and Bulson[25] or Chen and Li,[26] but even so, performing the integrations of Eq. (6.56) cannot be achieved by means of elementary functions so numerical integration is necessary in the majority of cases. Numerical integration can be carried out through several algorithms, and the work of Demidovich and Maron[32] (among the many other available monographs dedicated to this topic) is a very good source in this sense. Current-day mathematical software such as Mathematica, Matlab, Mathcad, or Mapple will easily solve numerical integration problems through dedicated routines; however, it is instructive and relatively easy to implement an existing numerical algorithm to solve this specific buckling application. The numerical integration can be stated as follows: Given the values of a function y_i at several locations x_i within its definition domain, find the numerical value of the integral:

$$I = \int_0^l f(x)\, dx \tag{6.57}$$

subject to the condition:

$$f(x_i) = y_i, \quad i = 1, 2, \ldots, n \tag{6.58}$$

where the values y_i are known on the n distinct locations of the definition domain. The best known integration methods, also known as quadrature formulas, include the Newton–Cotes', trapezoidal, Simpson's, Chebyshev's, Gauss', and Richardson's methods. A numerical integration algorithm based on Simpson's rule is developed and utilized here, in order to perform the double integration that is part of Eq. (6.56). Simpson's rule, as indicated by

Demodovich and Maron,[32] for example, assumes a parabolic interpolation polynomial is connecting a group of three consecutive values of a function, y_{i-1}, y_i, and y_{i+1}, according to the equation:

$$\int_{x_{i-1}}^{x_{i+1}} y dx = \frac{h}{3}(y_{i-1} + 4y_i + y_2) \tag{6.59}$$

Simpson's integration rule is quite accurate for a relatively small number of division points, as its remainder, R, defined as:

$$R = \int_{x_{i-1}}^{x_{i+1}} f(x)dx - \int_{x_{i-1}}^{x_{i+1}} y dx \tag{6.60}$$

is proportional to h^5, with h being the step distance (distance between any two consecutive division points). Because the numerical integration that will be used here requires calculation of n consecutive areas (integrals) by means of Eq. (6.59), it is clear that $2n - 1$ division points will be necessary, given the fact that Simpson's rule requires three consecutive points to evaluate one integral.

A Newmark-type algorithm is presented next, based on Eq. (6.56), together with a numerical integration procedure, and an example of a specific flexure hinge configuration is then detailed. The following steps are involved in finding the critical force by means of this numerical procedure:

- Divide the length of the fixed–free flexure hinge into n equally spaced subintervals by means of $2n - 1$ points (station), as explained previously, with the integration step (distance between two consecutive points) being h.
- Select an assumed-shape function $f(x)$ to approximate the unknown deflection curve of the fixed–free flexure hinge.
- Calculate the ratio $f(x)/I(x)$ of Eq. (28) for the given geometry of the analyzed flexure hinge ($I(x)$) and the assumed-shape function, $f(x)$.
- Calculate the discrete values of this ratio function at the $2n - 1$ stations.
- Apply Simpson's numerical integration rule twice, as necessary, in Eq. (28) and calculate the corresponding critical (buckling) force, according to the same equation, for each of the n consecutive divisions.
- Calculate the average critical force P_{cr}.

An example of calculating the buckling force is presented and solved next for a better understanding of the steps that were presented generically above.

Example

Determine the critical buckling force that corresponds to a single-axis flexure hinge of symmetric parabolic profile that is constructed of steel (E = 200 GPa) and is defined by the geometric parameters l = 0.01 m, t = 0.001 m, c = 0.002 m, and w = 0.003 m by using 10 integration divisions.

Solution

Because the number of integration divisions is n = 10, the total number of stations that are necessary to apply Simpson's rule will be $2n - 1 = 19$, which means that the value of the step is:

$$h = \frac{l}{2(n-1)} \tag{6.61}$$

In order to check how the final result is affected by the type of the assumed-deflection function $f(x)$, two different functions will be analyzed, one sinusoidal and the other parabolic. Both functions must comply with the fixed–free boundary condition of the flexure hinge. The equation of the sinusoidal assumed-shape function is:

$$f(x) = 1 - \sin\left(\frac{\pi}{2l}x\right) \tag{6.62}$$

where an amplitude of 1 was taken arbitrarily, as this will not affect the deflection distribution over the length of the flexure hinge. The equation of the parabolic assumed-deflection function is selected as:

$$f(x) = \frac{1}{10}(l-x)^2 \tag{6.63}$$

where, again, a value of 1/10 was arbitrarily chosen for the coefficient of x^2. For a parabolic flexure hinge, the variable moment of inertia is:

$$I(x) = \frac{w}{12}\left[t + 2c\left(1 - 2\frac{x}{l}\right)^2\right]^3 \tag{6.64}$$

The $f(x)/I(x)$ ratio that enters Eq. (6.56) can now simply be formulated by combining Eq. (6.64) with either Eq. (6.62) or Eq. (6.63), which enables calculation of the real values of this ratio at the 19 stations in this problem. This makes it possible to apply Simpson's numerical integration rule, according to Eq. (6.59), two times consecutively and to find the corresponding critical force of Eq. (6.56) at each of the 10 consecutive divisions for the sinusoidal or the parabolic assumed-deflection functions. In the case of the sinusoidal function of Eq. (6.62), the average value of the critical force was 3694 N,

whereas for the parabolic function defined in Eq. (6.63) the average value of the critical force was 3712 N.

6.3 Torsion of Noncircular Cross-Section Flexure Hinges

In Chapter 2, the torsional loading was considered and quantified only for flexure hinges of rotational symmetry (multiple-axis or revolute flexures) because these members are designed to be implemented in three-dimensional applications where, due to spatial loading, torsion is expected to be applied. In such cases, deriving the corresponding compliance factor, $C_{1,\theta x-Mx}$, that connects the torsion angle to the corresponding torque was relatively simple because of the formulation pertaining to circular cross-sections. No torsion compliance was derived for one- and two-axis flexure hinges because these types are assumed to work through bending, about either one or two axes in such way that torsion is not involved. For noncircular cross-sections such as for these two types of flexure hinges, the torsion phenomenon does yield load-deformation solutions that, for most of the cases, are not straightforward; therefore, approximations must be applied in order to obtain formulas that can be used in engineering applications within acceptable error limits. One such case is the rectangular cross-section, which does not produce a load-deformation solution that can be expressed by means of an exact closed-form equation. The situation applies to both single- and two-axis flexure hinges, as presented in Chapter 2, where the rectangular cross-section contains one or two dimensions that vary continuously over the length of the flexure hinge. More details on the torsion of noncircular cross-section members, in general, and on rectangular cross-section members, in particular, can be found in Shanley,[2] Timoshenko,[27] Den Hartog,[29] or Boresi et al.,[30] to cite just a few references.

Young[33] gives an approximate equation (with errors less than 4%) that connects the deformation angle to the torsion moment for a constant rectangular cross-section shaft that is fixed at one end, while the torsion moment is applied at the opposite free end. The respective equation is of the form:

$$\theta_{1x} = \frac{M_{1x} l}{G I_t} \tag{6.65}$$

where I_t is the approximate torsional moment of inertia. Equation (6.65) is also valid for a member whose length is infinitesimal, say dx, in which case it transforms into:

$$d\theta_x = \frac{M_{1x}}{G I_t(x)} dx \tag{6.66}$$

where $I_t(x)$ for a single-axis flexure hinge and when $t(x) > w$ is defined (according to the approximation mentioned by Young[33]) as:

$$I_t(x) = w^3 t(x)\left[a - b\frac{t(x)}{w}\right] \tag{6.67}$$

with the constants a and b defined as:

$$\begin{cases} a = 0.333 \\ b = 0.21 \end{cases} \tag{6.68}$$

For a two-axis flexure hinge, the equation for $I_t(x)$ is similar to Eq. (6.67), the only difference being in the width, w, which is a function of x and so will be denoted as $w(x)$. The total angle of torsion of a variable rectangular cross-section can be found by adding up all angular deformations of the infinitesimal-length constant cross-section portions:

$$\theta_{1,x-M_x} = \int_o^l d\theta_{x-M_x} \tag{6.69}$$

By combining Eqs. (6.66), (6.67), and (6.69), the compliance factor that corresponds to the torsion is defined as:

$$\theta_{1x} = C_{1,\theta_x - M_x} M_{1x} \tag{6.70}$$

and is of the form:

$$C_{1,\theta_x - M_x} = \frac{I_1}{w^3 G} \tag{6.71}$$

for a single-axis flexure hinge and of the form:

$$C_{1,\theta_x - M_x} = \frac{1}{G} I_2 \tag{6.72}$$

for a two-axis flexure hinge where I_1 and I_2 are integrals defined as:

$$I_1 = \int_0^l \frac{dx}{at(x) - bw} \tag{6.73}$$

and:

$$I_2 = \int_0^l \frac{dx}{w(x)^3[at(x) - bw(x)]} \tag{6.74}$$

Equations (6.71) through (6.74) were utilized to formulate the approximate equations of the compliance factor for the various single-axis flexure configurations introduced in Chapter 2, as well as for the specific two-axis flexure hinge also presented in Chapter 2.

For a constant rectangular cross-section flexure hinge, the torsional compliance is:

$$C_{1,\theta_x - M_x} = \frac{w^3 G}{l}(at - bw) \tag{6.75}$$

6.3.1 Symmetric Single-Axis Flexure Hinges

The torsional compliance factors are given first for symmetric single-axis flexure hinges. The torsional compliance of a circular flexure hinge is:

$$C_{1,\theta_x - M_x} = \frac{1}{2aw^3 G}\left\{\frac{a(2r+t) - bw}{\sqrt{(at - bw)[a(4r+t) - bw]}} \times \left[2\text{Arc}\tan\frac{2ar}{\sqrt{(at - bw)[a(4r+t) - bw]}} + \pi\right] - \pi\right\} \tag{6.76}$$

For a corner-filleted flexure hinge, the torsional compliance is:

$$C_{1,\theta_x - M_x} = \frac{1}{2aw^3 G}\left\{\frac{2a(l-2r)}{at - bw} + \frac{4[a(2r+t) - bw]}{\sqrt{[a(4r+t) - bw](at - bw)}} \times \text{Arc}\tan\sqrt{\frac{a(4r+t) - bw}{at - bw}} - \pi\right\} \tag{6.77}$$

The torsional compliance for an elliptic flexure hinge is:

$$C_{1,\theta_x - M_x} = \frac{l}{4acw^3 G}\left\{\frac{a(2c+t) - bw}{\sqrt{[a(4c+t) - bw](at - bw)}} \times \left[\pi + 2\text{Arc}\tan\frac{2ac}{\sqrt{[a(4c+t) - bw](at - bw)}}\right] - \pi\right\} \tag{6.78}$$

The torsional compliance of a parabolic flexure hinge is:

$$C_{1,\theta_x-M_x} = \frac{l}{w^3 G} \frac{\text{Arc tan}\sqrt{2ac/(at-bw)}}{\sqrt{2ac(at-bw)}} \tag{6.79}$$

The torsional compliance for a hyperbolic flexure hinge is:

$$C_{1,\theta_x-M_x} = \frac{l}{2a\sqrt{c(c+t)}w^3 G}\left[\text{Log}\frac{2c+t-2\sqrt{c(c+t)}}{t} - \frac{2bw}{\sqrt{a^2t^2-b^2w^2}}\right.$$
$$\left.\times \text{Arc tan}\sqrt{\frac{c(at+bw)}{(c+t)(at-bw)}}\right] \tag{6.80}$$

The torsional compliance of a flexure hinge with symmetric inverse parabolic profile is:

$$C_{1,\theta_x-M_x} = \frac{l}{bw^4 G}\left\{\frac{4aa_1 \text{Arc tan}\left[\frac{l}{2}\sqrt{\frac{bw}{2aa_1-bb_1^2w}}\right]}{l\sqrt{bw(2aa_1-bb_1^2w)}} - 1\right\} \tag{6.81}$$

where a_1 and b_1 were introduced in Eq. (2.283) of Chapter 2.

The torsional compliance of a secant-profile flexure hinge is:

$$C_{1,\theta_x-M_x} = \frac{l}{bw^4 G}\left[1 - \frac{2at\,\text{Arc tan}\sqrt{\frac{c(at+bw)}{(c+t)(at-bw)}}}{\sqrt{a^2t^2-b^2w^2}\,\text{Arc cos}\frac{t}{2c+t}}\right] \tag{6.82}$$

Several limit calculations were also performed to check whether the torsional compliance equations of the different symmetric one-sensitivity-axis flexure hinges that were derived here reach certain particular expressions when the geometry is conveniently altered. For instance, for all the *c* flexures (as introduced in Chapter 2, where this denomination covered the elliptic, parabolic, hyperbolic, inverse parabolic, and secant configurations) the particular expressions taken by the corresponding torsional compliances were checked when the parameter *c* was forced to converge to zero. It was seen that Eqs. (6.78) through (6.82) became identical to Eq. (6.75), which describes the torsional compliance of a constant rectangular cross-section flexure hinge for $c \to 0$, as is normal. A similar limit was performed for the torsional compliance of a corner-filleted flexure hinge by taking $r \to 0$ in Eq. (6.77), and again the

torsional compliance of a constant rectangular cross-section flexure (Eq. (6.75)) was retrieved. Additionally, $l \to 2r$ was also taken in the same equation of the corner-filleted flexure hinge to check whether, indeed, the torsional compliance would become that of a circular flexure hinge. The calculations showed that, indeed, by taking the limit mentioned above, Eq. (6.76), which describes the torsional characteristics of a circular flexure hinge, was retrieved.

6.3.2 Nonsymmetric Single-Axis Flexure Hinges

Similar expressions are now given for single-axis flexure hinges that are axially nonsymmetric, of the types discussed in Chapter 2. Their axial cross-section is formed by a straight line on one side of the longitudinal axis and a specific curve (circle, ellipse, parabola, hyperbola, etc.) on the other. The torsional compliance of a circular flexure hinge is:

$$C_{1,\theta_x-M_x} = \frac{1}{aw^3G}\left\{\frac{a(r+t)-bw}{\sqrt{(at-bw)[a(2r+t)-bw]}} \times\left[2\,\mathrm{Arc\,tan}\frac{ar}{\sqrt{(at-bw)[a(2r+t)-bw]}}-\pi\right]-\pi\right\} \tag{6.83}$$

The torsional compliance of a corner-filleted flexure hinge is:

$$C_{1,\theta_x-M_x} = \frac{1}{aw^3G}\left\{\frac{a(l-2r)}{at-bw}+\frac{4[a(r+t)-bw]}{\sqrt{[a(2r+t)-bw](at-bw)}} \times\mathrm{Arc\,tan}\sqrt{\frac{a(2r+t)-bw}{at-bw}}-\pi\right\} \tag{6.84}$$

The torsional compliance of an elliptical flexure hinge is:

$$C_{1,\theta_x-M_x} = \frac{l}{2acw^3G}\left\{\frac{a(c+t)-bw}{\sqrt{[a(2c+t)-bw](at-bw)}} \times\left[\pi+2\,\mathrm{Arc\,tan}\frac{ac}{\sqrt{[a(2c+t)-bw](at-bw)}}\right]-\pi\right\} \tag{6.85}$$

The torsional compliance of a parabolic flexure hinge is:

$$C_{1,\theta_x-M_x} = \frac{l}{w^3G}\frac{\mathrm{Arc\,tan}\sqrt{ac/(at-bw)}}{\sqrt{ac(at-bw)}} \tag{6.86}$$

The torsional compliance of a hyperbolic flexure hinge is:

$$C_{1,\theta_x-M_x} = \frac{l}{a\sqrt{c(c+t)}w^3G}\left[\text{Log}\frac{2c+t-2\sqrt{c(c+t)}}{t} + \frac{at-2bw}{\sqrt{bw(at-bw)}} \times \text{Arc tan}\sqrt{\frac{bcw}{(c+t)(at-bw)}}\right] \tag{6.87}$$

The torsional compliance of an inverse parabolic flexure hinge is:

$$C_{1,\theta_x-M_x} = \frac{2l}{(at-2bw)w^3G}\left\{1+\frac{4aa_1\text{Arc tan}\left[\frac{l}{2}\sqrt{\frac{at-2bw}{b_1^2(2bw-at)-2aa_1}}\right]}{l\sqrt{(at-2bw)[b_1^2(2bw-at)-2aa_1]}}\right\} \tag{6.88}$$

The torsional compliance of a secant flexure hinge is:

$$C_{1,\theta_x-M_x} = \frac{2l}{(at-2bw)w^3G}\left[1-\frac{at\,\text{Arc tan}\sqrt{\frac{bwc}{(c+t)(at-bw)}}}{\sqrt{bw(at-bw)}\,\text{Arc cos}\frac{t}{2c+t}}\right] \tag{6.89}$$

Just as for symmetric configurations, the same checks were performed for the torsional compliances of the nonsymmetric flexure hinges discussed here. The torsional compliance equation of a constant rectangular cross-section flexure was retrieved for c flexures when taking $c \to 0$, as well for corner-filleted flexures for $r \to 0$. In addition, the corner-filleted flexure hinge gave a torsional stiffness that was identical to that of a circular flexure hinge when $l \to 2r$.

6.3.3 Parabolic-Profile Two-Axis Flexure Hinges

For a two-axis flexure hinge, both cross-sectional dimensions vary in a continuous fashion as a function of x. In Chapter 2 the closed-form compliance equations were derived for a two-axis flexure hinge of double inverse parabolic profile which meant that both $t(x)$ and $w(x)$ were in the form of inverse parabolic functions as defined in Chapter 2. The torsional compliance of a two-axis flexure hinge with double parabolic profile is derived here following the procedure that was already outlined and applied for single-axis flexures. As previously done, it is assumed that the two symmetric profiles

are extending over the same length, l. The torsional compliance of this particular type of flexure hinge is:

$$C_{1,\theta_x-M_x} = \frac{l}{32G}\left\{\frac{8c_w}{aw(2c_w+w)^2(c_wt-c_tw)} + \frac{4c_w[c_w(3at+4bw)-7ac_tw]}{a^2w^2(2c_w+w)(c_wt-c_tw)^2}\right.$$

$$+\left[2\sqrt{2c_w}(8b^2c_w^2w^2+4abc_ww(c_wt-5c_tw)+a^2(3c_w^2t^2-10c_tc_wtw+15c_t^2w^2))\right.$$

$$\left.\times \operatorname{Arctan}\sqrt{\frac{2c_w}{w}}\right]/[a^3(c_wt-c_tw)^3\sqrt{w^5}] + \frac{16\sqrt{2(ac_t-bc_w)^5}}{a^3(c_tw-c_wt)^3\sqrt{at-bw}}$$

$$\left.\times \operatorname{Arctan}\sqrt{\frac{2(ac_t-bc_w)}{at-bw}}\right\} \tag{6.90}$$

Equation (6.90) was checked for the limit case when both $c_t \to 0$ and $c_w \to 0$. Equation (6.75) was obtained, which gives the torsional compliance of a constant rectangular cross-section flexure hinge.

6.4 Composite Flexure Hinges

All the modeling effort so far in terms of stiffness (compliance), inertia, and damping discretization for different types of flexure hinges has focused on flexure members constructed of isotropic materials. In some situations, however, the flexure hinges are built of several materials and of members with possibly nonidentical geometries that are attached together to form a composite flexure hinge. The MEMS domain, particularly, offers examples of composite flexure hinges. In his excellent monograph on MEMS, Maluf[34] provides examples of several such flexure designs, including radiofrequency (RF) switches that are realized from silicon and aluminum sandwiched together, piezoresistive write/read cantilevers that contain a piezoresistive layer glued atop a silicon substrate, or the special-configuration flexures that compose the so-called grating light valve device and are made up of two layers of aluminum and silicon nitride. All of these configurations and several others that can be found in MEMS applications are essentially single-axis flexure hinges that are built of at least two different materials. In our discussion here, we approach the problem of deriving adequate compliance, inertia, and damping properties of composite single-axis flexure hinges. This problem is extremely important as such applications are usually intended to function in a resonant regime, oftentimes in a narrow and very well-defined resonant frequency range. As a consequence, being able to correctly predict the stiffness (compliance), inertia, and damping properties of such systems is crucial.

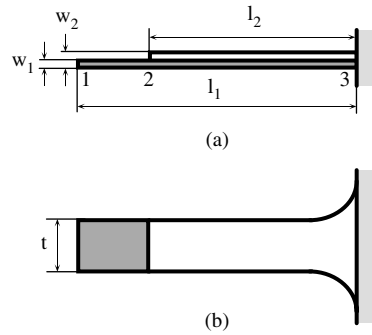

FIGURE 6.6
Composite flexure hinge made up of two members of different materials and geometry.

Figure 6.6 is an illustration of a composite flexure hinge that is built of two components having different lengths and thicknesses but which are identical in width. The two components are constructed of different materials that, for the sake of tractability, are assumed to be isotropic.

A procedure is explained in the following text that allows transformation of the composite flexure hinge in an equivalent flexure that is uniquely defined by unique compliance (stiffness), inertia, and damping properties that will permit, ultimately, analysis of the static and dynamic behavior of a single-axis flexure hinge with three degrees of freedom (DOFs). A somewhat similar procedure was followed by Lobontiu et al.[36] who transformed a composite beam of a sandwich configuration composed of two piezoelectric patches and a metallic substrate into an equivalent one-DOF beam in terms of mass, stiffness, damping, and forcing agents. From a connection viewpoint, it can be considered that we have two flexure segments attached in series: (1) one segment that extends over the length ($l_1 - l_2$) between points 1 and 2 in Figure 6.6 and consists of the material and geometry denoted by 2, and (2) another mixed segment that lies between points 2 and 3 over the length l_2, as also shown in Figure 6.6. This second part is made up of two members that are geometrically identical but fabricated of different materials, and it can be considered that these two flexure segments are connected in parallel. As a consequence, all subsequent equivalence calculations will go through two steps:

- Calculation of the partial equivalent properties over length l_2 by considering that the two sandwiched geometrically identical flexure portions are connected in parallel
- Calculation of the final equivalent properties of the composite flexure by taking the series combination of the flexure segment which lies between points 1 and 2 in Figure 6.6 (material 1) and the composite flexure segment extending over length l_2 and whose properties were already determined at the previous step

6.4.1 Compliance Properties

The equivalent axial compliance will be derived first, and then the other three equivalent compliances that define the in-plane flexible behavior of a single-axis flexure hinge will similarly be formulated. As a reminder, the number in the subscript notation of a compliance factor denotes the point that is considered free and actually gives a specific compliance of that point with respect to the opposite fixed point of the analyzed flexure segment. As a consequence, the number 2 in the subscript of the compliance indicates, in the case pictured in Figure 6.6, that segment 2–3 is targeted (with point 2 considered free and point 3 fixed), while the number 1 signals that homogeneous segment 1–2 is under scrutiny (point 1 is free and point 2 is considered fixed). The axial compliance of composite segment 2–3 can be found according to the parallel-connection formula:

$$C_{2,x-F_x} = \frac{C^1_{2,x-F_x} C^2_{2,x-F_x}}{C^1_{2,x-F_x} + C^2_{2,x-F_x}} \tag{6.90}$$

where the superscripts indicate the material. The equivalent axial compliance corresponding to the entire composite flexure combines the compliance of Eq. (6.90) with that of segment 1–2 by means of a series-connection situation, and the final compliance value is:

$$C^e_{1,x-F_x} = C_{1,x-F_x} + \frac{C^1_{2,x-F_x} C^2_{2,x-F_x}}{C^1_{2,x-F_x} + C^2_{2,x-F_x}} \tag{6.91}$$

where the superscript e has been utilized to denote the equivalent value. The other compliances that are meaningful to the in-plane behavior of the composite single-axis flexure hinge are calculated similarly, and their equations are:

$$\begin{cases} C^e_{1,y-F_y} = C_{1,y-F_y} + \dfrac{C^1_{2,y-F_y} C^2_{2,y-F_y}}{C^1_{2,y-F_y} + C^2_{2,y-F_y}} \\ C^e_{1,y-M_z} = C_{1,y-M_z} + \dfrac{C^1_{2,y-M_z} C^2_{2,y-M_z}}{C^1_{2,y-M_z} + C^2_{2,y-M_z}} \\ C^e_{1,\theta_z-M_z} = C_{1,\theta_z-M_z} + \dfrac{C^1_{2,\theta_z-M_z} C^2_{2,\theta_z-M_z}}{C^1_{2,\theta_z-M_z} + C^2_{2,\theta_z-M_z}} \end{cases} \tag{6.92}$$

All individual compliances that appear in Eqs. (6.91) and (6.92) can be calculated by the explicit formulations that were given in Chapter 2 for the flexure geometry that is of interest. If torsion is also important, as is the situation with many MEMS applications, the equivalent torsional compliance of the

composite flexure can be computed following the same format, according to the equation:

$$C^{e}_{1,\theta_x-M_x} = C_{1,\theta_x-M_x} + \frac{C^{1}_{2,\theta_x-M_x} C^{2}_{2,\theta_x-M_x}}{C^{1}_{2,\theta_x-M_x} + C^{2}_{2,\theta_x-M_x}} \tag{6.93}$$

where the individual torsional compliances were approximately calculated within this chapter.

6.4.2 Inertia Properties

The discretized inertia properties of the composite flexure of Figure 6.6 are calculated in a similar manner. It was shown previously that a three-DOF single-axis flexure hinge is associated with a basic diagonal 3×3 inertia matrix that accounts for axial and bending effects. If torsion is also taken into account, the basic 3×3 matrix can be extended to a 4×4 configuration by diagonally adding the torsion inertia on the last row and column. The details given within Chapter 4 with regard to inertia calculations that were aimed at transforming the original distributed-inertia flexure hinge into a lumped-parameter one highlighted the point that, for each of the main vibrations of the fixed–free element, an inertia parameter can be calculated and located at the free end. Applied to the specific problem of Figure 6.6, this general statement amounts to initially finding three inertia properties for each type of vibrational motion corresponding to the three different segments: material 1 over length $l_1 - l_2$, the same material over length l_2, and material 2 over length l_2. The total kinetic energy produced by, say, their axial (along the x axis) vibration should be equal to the kinetic energy of an equivalent (unknown as yet) mass that is located at free end 1 and also vibrates axially. The equation that corresponds to this statement is:

$$\frac{1}{2} m_{1x} v_{1x}^2 + \frac{1}{2} m_{2x}^1 v_{2x}^2 + \frac{1}{2} m_{2x}^2 v_{2x}^2 = \frac{1}{2} m_{1x}^e v_{1x}^2 \tag{6.94}$$

It was shown that the velocity field in a vibrating beam is distributed according to a specific law so the velocities at points 1 and 2 are connected, according to:

$$v_{2x} = f_a^{1-2}(x) v_{1x} \tag{6.95}$$

where the distribution function $f_a(x)$ was given in Chapter 4 in generic form but is also valid in this situation when calculated for segment 1–2. By substituting Eq. (6.95) into Eq. (6.94), the unknown equivalent mass that represents the axial vibration inertia properties of the entire composite flexure hinge can be calculated as:

$$m_{1x}^e = m_{1x} + [f_a^{1-2}(x)]^2 (m_{2x}^1 + m_{2x}^2) \tag{6.96}$$

The individual masses involved in Eq. (6.96) can be calculated by means of the equations that have been given in Chapter 4. Similarly, the distribution function $f_a(x)$ can be calculated by means of the formulation also given in Chapter 4 by making the modifications required for its specific application to segment 1–2 of Figure 6.6. Similar reasoning and calculation result in the following equivalent inertia properties for the remaining degrees of freedom:

$$\begin{cases} m_{1y}^{e} = m_{1y} + [f_{by}^{1-2}(x)]^2 (m_{2y}^{1} + m_{2y}^{2}) \\ J_{1\theta_z}^{e} = J_{1\theta_z} + [f_{b\theta_z}^{1-2}(x)]^2 (J_{2\theta_z}^{1} + J_{2\theta_z}^{2}) \end{cases} \tag{6.97}$$

Again, all individual inertia properties, together with the corresponding distribution functions f_{by} and $f_{b\theta z}$, were given in Chapter 4, and they only have to be calculated for the specific intervals and corresponding geometry. When torsion is taken into account, a similar equation can be written to express the equivalent torsional inertia of the composite beam, in the form:

$$J_{1\theta_x}^{e} = J_{1\theta_x} + [f_t^{1-2}(x)]^2 (J_{2\theta_x}^{1} + J_{2\theta_x}^{2}) \tag{6.98}$$

However, calculating the individual torsional moment of inertias and corresponding distribution function $f_t(x)$ of Eq. (6.98) is beyond the scope of this work.

6.4.3 Damping Properties

Establishing the discretized damping properties of the composite flexure hinge pictured in Figure 6.6 follows the path taken in deriving the similar inertia properties, as done previously. The damping matrix is also diagonal and has a dimension of 3×3 when the regular in-plane vibratory motions are considered but it can only be a 4×4 diagonal matrix when torsion is added to the regular axial and bending motions. The similarity with the inertia properties also resides in the fact that viscous damping, as described so far, depends on velocity, in the sense that the energy dissipated through damping is proportional to the square of the velocity corresponding to a given motion. The original composite beam is made up of three individual homogeneous segments, as explained when treating inertia equivalence; therefore, they will all contribute to the equivalent overall damping energy produced by an equivalent dashpot. The equation giving the damping energy equality between the original and the equivalent systems is of the form:

$$c_{1x} v_{1x}^2 + c_{2x}^1 v_{2x}^2 + c_{2x}^2 v_{2x}^2 = c_{1x}^e v_{1x}^2 \tag{6.99}$$

The velocities of Eq. (6.99) are connected according to Eq. (6.95); therefore, the equivalent dashpot parameter corresponding to axial vibrations is:

$$c_{1x}^{e} = c_{1x} + [f_a^{1-2}(x)]^2 (c_{2x}^1 + c_{2x}^2) \tag{6.100}$$

where the individual dashpot parameters can be calculated by means of the formulation given in Chapter 4. The equivalent dashpot parameters corresponding to bending can similarly be formulated as:

$$\begin{cases} c_{1y}^{e} = c_{1y} + [f_{by}^{1-2}(x)]^2 (c_{2y}^1 + c_{2y}^2) \\ c_{1\theta_z}^{e} = c_{1\theta_z} + \left[f_{b\theta_z}^{1-2}(x)\right]^2 \left(c_{2\theta_z}^1 + c_{2\theta_z}^2\right) \end{cases} \tag{6.101}$$

where again the individual damping coefficients can be calculated by means of the corresponding equations developed in Chapter 4. When torsion is taken into consideration, its equivalent dashpot parameter can be calculated similarly as:

$$c_{1\theta_x}^{e} = c_{1\theta_x} + [f_t^{1-2}(x)]^2 \left(c_{2\theta_x}^1 + c_{2\theta_x}^2\right) \tag{6.102}$$

where again the individual damping coefficients and corresponding distribution function are not explicitly given here.

6.5 Thermal Effects

For the vast majority of isotropic materials, linear dimensions of mechanical members expand with increasing temperature according to the well-known formula:

$$\Delta d = \alpha\, d \Delta T \tag{6.103}$$

where d is the initial value of a given dimension, while α is the coefficient of thermal expansion, and ΔT is the temperature increase.

6.5.1 Errors in Compliance Factors Induced through Thermal Effects

An interesting problem would be to determine how compliance properties change for the different flexure hinge configurations that have been treated so far with changes in the temperature in the fixed–free boundary condition. Directly related to this aspect is evaluation of the displacement errors that are induced by temperature variations. This issue is discussed here for

one-, multiple-, and two-axis flexure hinges by considering the Euler–Bernoulli (long-beam) model and then the Timoshenko (short-beam) model. It will be also assumed that the change in temperature is quasi-static and constant for the entire flexure hinge.

6.5.1.1 Euler–Bernoulli Beams

6.5.1.1.1 Single-Axis Flexure Hinges

For a constant-width single-axis flexure hinge, the final dimensions, after a temperature increase of ΔT, are:

$$\begin{cases} l_f = (1+\alpha\Delta T)l \\ w_f = (1+\alpha\Delta T)w \\ t(x)_f = (1+\alpha\Delta T)t(x) \end{cases} \tag{6.104}$$

According to its definition, the axial compliance is calculated by means of the equations given in Chapter 2 and, in the case of thermal expansion, will be given by:

$$C^{th}_{1,x-F_x} = \frac{E}{w(1+\alpha\Delta T)^2}\int_0^{l_f}\frac{dx}{t(x)} \tag{6.105}$$

It can easily be shown that the compliance that takes into consideration the thermal effects is related to the regular corresponding compliance as:

$$C^{th}_{1,x-F_x} = \frac{1}{(1+\alpha\Delta T)^2}\left[C_{1,x-F_x} + \frac{1}{Ew}\int_l^{l_f}\frac{dx}{t(x)}\right] \tag{6.106}$$

In a similar manner, the other compliances that define the in-plane flexible behavior of single-axis flexure hinges are:

$$C^{th}_{1,y-F_y} = \frac{1}{(1+\alpha\Delta T)^4}\left[C_{1,y-F_y} + \frac{12}{Ew}\int_l^{l_f}\frac{x^2dx}{t(x)^3}\right] \tag{6.107}$$

$$C^{th}_{1,y-M_z} = \frac{1}{(1+\alpha\Delta T)^4}\left[C_{1,y-M_z} + \frac{12}{Ew}\int_l^{l_f}\frac{xdx}{t(x)^3}\right] \tag{6.108}$$

$$C^{th}_{1,\theta_z-M_z} = \frac{1}{(1+\alpha\Delta T)^4}\left[C_{1,\theta_z-M_z} + \frac{12}{Ew}\int_l^{l_f}\frac{dx}{t(x)^3}\right] \tag{6.109}$$

Relative errors can now be defined to check how temperature effects account for changes in the compliant response of this type of flexure hinges. The error in the axial compliance can be defined simply as:

$$\text{error} \quad (C_{1,x-F_x}) = \frac{\left| C_{1,x-F_x} - C^{th}_{1,x-F_x} \right|}{C_{1,x-F_x}} \tag{6.110}$$

where the temperature-corrected axial compliance is given in Eq. (6.106) and the regular one is expressed in Chapter 2. Similar error functions can be defined for the other three in-plane compliance factors.

6.5.1.1.2 Multiple-Axis Flexure Hinges

An approach similar to the one just detailed yields the following temperature-corrected compliance factors for multiple-axis (revolute) flexure hinges:

$$C^{th}_{1,x-F_x} = \frac{1}{(1+\alpha\Delta T)^2}\left[C_{1,x-F_x} + \frac{4}{\pi E}\int_l^{l_f} \frac{dx}{t(x)^2} \right] \tag{6.111}$$

$$C^{th}_{1,y-F_y} = \frac{1}{(1+\alpha\Delta T)^4}\left[C_{1,y-F_y} + \frac{64}{\pi E}\int_l^{l_f} \frac{x^2 dx}{t(x)^4} \right] \tag{6.112}$$

$$C^{th}_{1,y-M_z} = \frac{1}{(1+\alpha\Delta T)^4}\left[C_{1,y-M_z} + \frac{64}{\pi E}\int_l^{l_f} \frac{x dx}{t(x)^4} \right] \tag{6.113}$$

$$C^{th}_{1,\theta_y-M_y} = \frac{1}{(1+\alpha\Delta T)^4}\left[C_{1,\theta_y-M_y} + \frac{64}{\pi E}\int_l^{l_f} \frac{dx}{t(x)^4} \right] \tag{6.114}$$

$$C^{th}_{1,\theta_x-M_x} = \frac{1}{(1+\alpha\Delta T)^4}\left[C_{1,\theta_x-M_x} + \frac{32}{\pi G}\int_l^{l_f} \frac{dx}{t(x)^4} \right] \tag{6.115}$$

The regular compliance factors that go into Eqs. (6.111) through (6.115) are given for specific flexure geometries in Chapter 2. Errors that are present when thermal effects are considered with respect to the situation when they are ignored can be evaluated by means of error functions that can be formulated similarly to Eq. (6.110).

6.5.1.1.3 Two-Axis Flexure Hinges

As defined in Chapter 2, two-axis flexure hinge configurations have a rectangular cross-section that is variable in terms of both parameters t and w.

In this case, the relevant compliance factors are:

$$C^{th}_{1,x-F_x} = \frac{1}{(1+\alpha\Delta T)^2}\left[C_{1,x-F_x} + \frac{1}{E}\int_l^{l_f}\frac{dx}{t(x)w(x)}\right] \tag{6.116}$$

$$C^{th}_{1,y-F_y} = \frac{1}{(1+\alpha\Delta T)^4}\left[C_{1,y-F_y} + \frac{12}{E}\int_l^{l_f}\frac{x^2dx}{t(x)^3w(x)}\right] \tag{6.117}$$

$$C^{th}_{1,y-M_z} = \frac{1}{(1+\alpha\Delta T)^4}\left[C_{1,y-M_z} + \frac{12}{E}\int_l^{l_f}\frac{xdx}{t(x)^3w(x)}\right] \tag{6.118}$$

$$C^{th}_{1,\theta_z-M_z} = \frac{1}{(1+\alpha\Delta T)^4}\left[C_{1,\theta_z-M_z} + \frac{12}{E}\int_l^{l_f}\frac{dx}{t(x)^3w(x)}\right] \tag{6.119}$$

$$C^{th}_{1,z-F_z} = \frac{1}{(1+\alpha\Delta T)^4}\left[C_{1,z-F_z} + \frac{12}{E}\int_l^{l_f}\frac{x^2dx}{t(x)w(x)^3}\right] \tag{6.120}$$

$$C^{th}_{1,z-M_y} = \frac{1}{(1+\alpha\Delta T)^4}\left[C_{1,z-M_y} + \frac{12}{E}\int_l^{l_f}\frac{xdx}{t(x)w(x)^3}\right] \tag{6.121}$$

$$C^{th}_{1,\theta_y-M_y} = \frac{1}{(1+\alpha\Delta T)^4}\left[C_{1,\theta_y-M_y} + \frac{12}{E}\int_l^{l_f}\frac{dx}{t(x)w(x)^3}\right] \tag{6.122}$$

As a reminder, Eqs. (6.117) through (6.119) give the direct- and cross-bending compliances about the primary bending axis, while Eqs. (6.120) through (6.122) give the direct- and cross-bending compliances about the secondary bending axis. Again, error functions can be formulated following the example with single-axis flexure hinges, Eq. (6.110), in order to assess the errors introduced through consideration of the thermal effects.

6.5.1.2 Timoshenko Beams

Chapter 2 treated the problem of short beams by introducing corrections to the corresponding compliance factors, according to the Timoshenko (short beam) model that takes into account the shearing effects. It was demonstrated in Chapter 2 that the only changes that need to be operated in order to account for shearing effects are in the direct-bending compliance factors that are related to deflection. As a consequence, the same change has to be implemented when analyzing the thermal effects on short flexure hinges. Formally, it is necessary to utilize $C^{s}_{1,y-Fy}$ as expressed in Chapter 2 for one-, multiple-, and two-axis flexures, instead of $C_{1,y-Fy}$ in the equations corresponding

to the Euler–Bernoulli model. The same modification has to be operated for the secondary bending axis z and its corresponding direct-bending deflection compliance, $C_{1,z-Fz}$, for two-axis flexure hinge configurations. Error functions can again be constructed on the model developed for Euler–Bernoulli one-axis flexures.

6.5.2 Compliance Aspects for Nonuniform Temperature Change: Castigliano's Displacement Theorem for Thermal Effects

It was relatively simple to determine the alterations in the compliance factors of various flexure hinge configurations when they were subjected to a change in temperature that was constant for the entire flexure hinge. Things change slightly when the temperature varies, potentially both over the flexure's length and thickness or width. In such instances, an extension of Castigliano's displacement theorem to include thermal effects (as detailed by Burgreen,[37] for instance) can successfully be utilized to determine load–deflection relationships. The method presented by Burgreen[37] essentially adds a strain-equivalent thermal energy to the regular strain energy being produced through elastic deformations of a mechanical member. The total strain energy can be expressed, in the case of a single-axis flexure hinge where only in-plane deformations are considered, as:

$$U_t = \frac{1}{2E}\int_0^l \frac{M_{b,t}^2}{I_z(x)}dx + \frac{1}{2E}\int_0^l \frac{N_t^2}{A(x)}dx \tag{6.123}$$

where the subscript t indicates total. The total bending moment, $M_{b,t}$, of Eq. (6.123) is expressed as follows:

$$M_{b,t} = M_b + E\alpha M_{b,th} \tag{6.124}$$

where M_b is the regular elastic bending moment and $M_{b,th}$ is an equivalent bending moment that is generated through thermal effects and is calculated as:

$$M_{b,th} = \int_{A(x)} yT(x,y)\,dA(x) \tag{6.125}$$

In the equation above, the temperature is assumed to vary both with x (over the flexure length) and y (over the flexure thickness); y also represents the distance measured parallel with the thickness (the y axis) from the neutral axis. Likewise, the total axial load N_t of Eq. (6.123) sums up the actual normal elastic load N and a normal component formulated based upon a factor N_{th} that is generated through thermal effects, namely:

$$N_t = N + E\alpha N_{th} \tag{6.126}$$

where:

$$N_{th} = \int_{A(x)} T(x,y)\, dA(x) \tag{6.127}$$

By substituting Eqs. (6.124) through (6.127) into Eq. (6.123) it is possible to calculate axial deformation, deflection, and slope at the free end of the flexure hinge by the regular procedure implied by the regular Castigliano's displacement theorem.

Example

Discussing all the variable-temperature aspects regarding each flexure configuration that has been presented so far is beyond the scope of this work, but an example is briefly discussed here to outline the main features of applying the extended form of Castigliano's displacement theorem. Consider that a given variable temperature $T(x,y)$ is applied to a single-axis flexure hinge. The axial displacement, deflection, and slope at the free end of the flexure must be determined when a static load composed of two tip forces, F_{1x} and F_{1y}, and a moment, M_{1z}, are also applied.

Solution

The axial displacement can be found, according to Castigliano's displacement theorem, as:

$$u_{1x} = \frac{\partial U_t}{\partial F_{1x}} \tag{6.128}$$

By following the calculation procedure exposed in Eqs. (6.124) through (6.127) it follows that the tip axial displacement can be expressed as:

$$u_{1x} = C_{1,x-F_x} F_{1x} - \alpha \int_0^l \frac{\int_{A(x)} T(x,y)\, dA(x)}{A(x)}\, dx \tag{6.129}$$

The minus sign in Eq. (6.129) shows that the thermal expansion opposes the elastic deformation according to the convention utilized so far that considers the compressive axial force is positive. Similar calculations can be made to determine the deflection u_{1y} and slope θ_{1z}. The free-end deflection is calculated as:

$$u_{1y} = \frac{\partial U_t}{\partial F_{1y}} \tag{6.130}$$

and it can be shown that its final expression is:

$$u_{1y} = C_{1,y-F_y} F_{1y} + C_{1,y-M_z} M_{1z} + \alpha \int_0^l \frac{\int_{A(x)} yT(x,y)dA(x)}{I_z(x)} dx \tag{6.131}$$

Similarly, the free-end slope is given by Castigliano's displacement theorem in the generic form:

$$\theta_{1z} = \frac{\partial U_t}{\partial M_{1z}} \tag{6.132}$$

and its final equation is:

$$\theta_{1z} = C_{1,y-M_z} F_{1y} + C_{1,\theta_z-M_z} M_{1z} + \alpha \int_0^l \frac{\int_{A(x)} yT(x,y)\,dA(x)}{I_z(x)} dx \tag{6.133}$$

6.6 Shape Optimization

Optimizing the shape of mechanical or structural components has been a topic of great interest over the last several decades, and the research results of either analytical or finite-element analysis (or other numerical techniques) have been presented in numerous works. The monographs of Kirsch,[38] Rozvany,[39] and Haftka et al.[40] are just a few examples that systematically present aspects of shape optimization of structural members and the associated modeling and solving methods that appeal to analytical procedures, while the work edited by Bennett and Botkin[41] gathers significant papers that treat the shape optimization topic by means of finite-element techniques. Another classical textbook that treats problems of optimization tailored to mechanical members and systems is that of Vanderplaats.[42] Relatively few works deal directly with shape optimization of flexure hinges; representative of this area, however, is the paper by Takaaki and Toshihiko,[43] which applies finite-element modeling and analysis to study the optimum profile of flexure hinges. The objective of this approach is to identify those configurations that present high bending flexibility (compliance) and high axial stiffness concomitantly.

Optimum profiles have been identified that are capable of taking a uniformly distributed stress whose performance was compared to circular, elliptic, and flat flexure hinges. In a paper by Silva et al.,[44] the homogenization

method is utilized to design the optimum configuration of so-called flextensional transducers, which are actually devices aimed at amplifying the output displacement of a piezoelectric actuator by means of a compliant flexure-based frame. The problem is treated in the dynamic domain by considering inertia properties, in addition to those for stiffness, and the result consists of an optimized piezoelectric-coupled structure whose specified mode shape is located in a predefined resonant frequency range. The work of Bendsoe[45] is dedicated entirely to optimizing structural material, shape, and topology by means of the homogenization method, which fundamentally assumes a structure to be composed of a mosaic of material regions with nonzero dimensions interspersed with voids. Alternatively, the density might be utilized to discriminate between material regions and voids. The optimum structure in terms of an objective function can thus be obtained by application of a so-called homogenization relationship. Haftka and Grandhi[46] present a collection of the most relevant research results in the domain of structural shape optimization. Belegundu[47] provides an excellent primer in shape optimization problems as approached by finite elements.

Several recently published papers approach various optimization techniques as applied to compliant mechanisms. Frecker et al.,[48] for instance, deal with the topological synthesis of compliant mechanisms through multicriteria optimization and by utilizing the concept of "design for required deflection." Several other research papers report results of optimizing compliant mechanisms in a fully blown procedure by analyzing the entire compliant mechanism in terms of both design variables and topology. Representative to this approach are the papers of Nishiwaki et al.,[49–51] in which multi-objective functions are formulated based on the mutual energy and a homogenization procedure to study the optimum configuration of several compliant mechanism applications. Hetrick et al.[52] study the robustness of several optimization formulations that are dedicated to compliant mechanisms, while Hetrick and Kota[53] propose an optimization technique that is energy based and designed to maximize the energy throughput for linear compliant mechanisms in the static domain. Sigmund[54] develops a methodology for the optimal design of compliant mechanism topologies by means of a continuum-type technique that constrains the input displacement and determines the mechanism configurations, which are able to maintain the stress levels within controlled limits. Tai and Chee[55] approach the topology and shape optimization of compliant structures by means of genetic algorithms, whereby geometric characteristics are transmitted across generations in an evolutionary process. Saxena and Anathasuresh[56] propose an optimization scheme for compliant mechanisms by formulating a nonlinear finite-element model capable of incorporating large deformation effects and that allows calculation of the design sensitivities analytically.

Chapter 2 introduced several flexure hinge configurations for both two- and three-dimensional compliant mechanism applications that were defined as fully compliant multiple-spring members by giving compliance closed-form equations for various motions (deformations). At the same time, trends

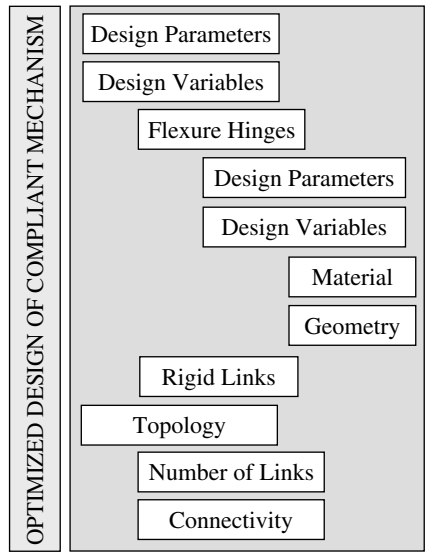

FIGURE 6.7
Main components in the optimized design of a compliant mechanism.

were indicated for the ways in which a particular compliance can be increased or reduced through corresponding variations of the defining geometric parameters. In a similar manner, Chapter 4 included a segment where the corresponding inertia properties of flexure hinges were derived, such that their behavior can be studied in both the static (or quasi-static) and dynamic ranges. An attempt will be made here to analyze the conditions under which the response of a given flexure hinge can be optimized, with regard to either the static and dynamic response of a given flexure hinge. A major research effort has been directed lately at optimizing the compliant mechanism in its entirety, but little research has targeted optimizing flexure hinges, as basic components, before attacking the full system of a compliant mechanism. Figure 6.7 describes the main aspects that are involved in the process of optimizing a compliant mechanism.

It is known that the optimized design of a structural system defines first its design parameters (quantities that usually remain unaltered during optimization) and its design variables (quantities that need to be determined in order to render a design optimal). For a compliant mechanism, a flexure hinge component can be regarded as a design subsystem that requires optimization at its own level, as indicated in Figure 6.7, before proceeding with optimization for the entire compliant mechanism system. This approach, compared to the current procedures that attempt full-blown optimization of a compliant mechanism, has its advantages. For example, it allows for better, more intimate analysis of a flexure hinge, at its individual performance level, which is most often not the case with the classic approach, which tends to divide its

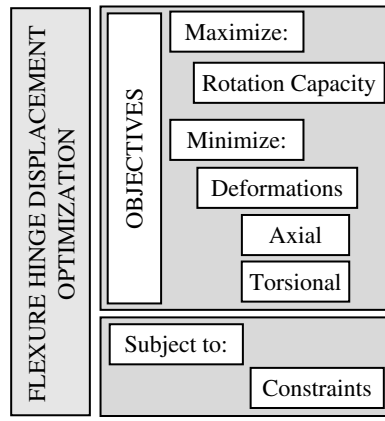

FIGURE 6.8
Generic optimization problem for flexure hinges.

solving resources on an even basis between the components of the compliant system, be they compliant or rigid. In doing so, it is possible to avoid the great effort required to analyze the rigid links that are merely connectors and followers of the flexure hinges. Optimizing a flexure hinge basically requires maximizing the relative rotation between two adjacent rigid members, while minimizing all other (or as many as possible of the) undesired motions under given design restrictions or constraints, as pictured in Figure 6.8.

As mentioned by Kirsch,[38] for example, it is necessary to discriminate between *design constraints*, which are mainly defined through geometric limitations that have to be imposed by the very nature of the design (for instance, the length of a flexure hinge cannot exceed a maximum value but, at the same time, obviously must be nonzero), and *behavior constraints*, which denote limitations placed by maximum levels of stresses (to avoid excessive loading), critical axial loading (to prevent buckling), displacement (to stay within predefined bounds), or natural frequencies (to avoid or provoke the resonant response). The mathematical formulation of a generic optimization problem can be stated as:

$$\begin{cases} Minimize \;\; f(\{X\}) \\ Subject\ to\text{:}\; g_j(\{X\}), \quad for\ j = 1 \rightarrow m \end{cases} \tag{6.134}$$

where f is the *objective function* defined in terms of the *design vector* $\{X\}$, and g_j are constraint functions, also defined in terms of $\{X\}$. The design vector $\{X\}$ has n design variables, namely:

$$\{X\} = \{X_1\ X_2 \cdots X_n\}^T \tag{6.135}$$

Several methods are available for mathematically treating an optimization problem, but one of the most reliable and used methods is the Lagrange's multipliers method coupled with the Kuhn–Tucker conditions, as mentioned in such works as those of Kirsch,[38] Rozvany,[39] or Vanderplaats,[42] to cite just a few. Lagrange's function Φ is introduced and depends on the objective function f, the constraint functions g_j, and several undetermined parameters, θ_j:

$$\Phi(\{X\},\{\lambda\}) = f(\{X\}) + \sum_{j}^{j_a} \lambda_j g_j(\{X\}) \tag{6.136}$$

where:

$$\{\lambda\} = \{\lambda_1\ \lambda_2 \cdots \lambda_{j_a}\}^T \tag{6.137}$$

and j_a denotes the number of active constraints (i.e., constraints that effectively influence the design variables). The necessary conditions for a minimum point in the design space $\{X\}$ for the function of Eq. (6.136) are:

$$\begin{cases} \dfrac{\partial \Phi}{\partial X_i} = 0,\ i = 1 \to n \\ \dfrac{\partial \Phi}{\partial \lambda_j} = 0,\ j = 1 \to j_a \end{cases} \tag{6.138}$$

The solutions of the optimized problem are among those identified by applying Eqs. (6.137) and, of those, only the ones that comply with the Kuhn–Tucker conditions:

$$\begin{cases} \{\nabla f\} + [\nabla g]\{\lambda\} = 0 \\ \lambda_j \geq 0,\ j = 1 \to j_a \end{cases} \tag{6.139}$$

where the newly introduced differential operator is defined for a given vector $\{V\}$ that depends on the variables X_i as:

$$\{\nabla V\} = \left\{ \frac{\partial V}{\partial X_1} \frac{\partial V}{\partial X_2} \cdots \frac{\partial V}{\partial X_n} \right\}^T \tag{6.140}$$

The same operator applied in matrix form to the constraint functions g_j is defined as:

$$[\nabla g] = [\{\nabla g_1\}\{\nabla g_2\} \cdots \{\nabla g_{j_a}\}] \tag{6.141}$$

The usefulness of an approach that combines Lagrange's function and Kuhn–Tucker conditions resides in the fact that it incorporates the constraint inequalities in a single function alongside the objective function.

A displacement-related optimization study is performed next that addresses each group of flexure hinges, as previously defined, followed by examples from each category. For single-axis flexure hinges, the objective functions (that must be either maximized or minimized) are formulated in terms of compliances and can be stated as:

$$Maximize: C_{1,\theta_z-M_z} \; and \; / \; or \; C_{1,\theta_z-F_y} \tag{6.142}$$

because each of the above-mentioned compliances defines the capacity of rotation of a specific flexure hinge. Coupled to Eq. (6.142), either of the following statements are also desirable:

$$Minimize: C_{1,x-F_x} \; and/or \; C_{1,z-F_z} \; and/or \; C_{1,z-M_y} and/or \; C_{1,\theta_x-M_x} \; and/or \; C_{1,\theta_y-M_y} \; and/or \; C_{1,\theta_y-F_z} \tag{6.143}$$

The compliances of Eq. (6.143) denote effects that must be minimized, such as axial, out-of-plane bending and torsion, because they are detrimental to the functional output of a flexure hinge. Instead of treating each of the statements of Eqs. (6.142) and (6.143) individually, a mixed objective function can be constructed of the form:

$$f = C_{1,x-F_x} + C_{1,z-F_z} + C_{1,z-M_y} + C_{1,\theta_x-M_x} + C_{1,\theta_y-M_y} + C_{1,\theta_y-F_z} - (C_{1,\theta_z-M_z} + C_{1,\theta_z-F_y}) \tag{6.144}$$

which must be minimized. For multiple-axis flexure hinges, the compliances that have to be maximized are the ones enumerated in Eq. (6.142), while the ones that must be minimized are:

$$Minimize: C_{1,x-F_x} \; and \; / \; or \; C_{1,\theta_x-M_x} \tag{6.145}$$

As a result, a composite objective function of the following form can be constructed in order to be minimized:

$$f = C_{1,x-F_x} + C_{1,\theta_x-M_x} - (C_{1,\theta_z-M_z} + C_{1,\theta_z-F_y}) \tag{6.146}$$

For two-axis flexure hinges, the minimum and maximum conditions, as well as the form of composite objective function, *f*, are similar to those expressed in

Eq. (6.145) although a more detailed discussion, not developed here, is necessary in order to comply with the restrictions in compliance about the primary and secondary sensitive axes.

With respect to constraints, in a displacement-based optimization approach to flexures, a reasonable set of conditions for a single-sensitive axis flexure hinges will place constraints upon the length, l; minimum thickness, t; and parameter c (for elliptic, parabolic, hyperbolic, inverse parabolic, and secant configurations, as detailed in Chapter 2) or fillet radius r (for corner-filleted configurations) in the bounding form:

$$\begin{cases} l_{min} \le l \le l_{max} \\ t_{min} \le t \le t_{max} \\ c_{min} \le c \le c_{max} \end{cases} \tag{6.147}$$

For this type of flexure hinge, it is considered that width w is constant. Equation (6.147) can be rewritten in the form required by the generic constraint expression of Eq. (6.134), namely:

$$\begin{cases} g_1 = l_{min} - l \\ g_2 = l - l_{max} \\ g_3 = t_{min} - t \\ g_4 = t - t_{max} \\ g_5 = c_{min} - c \\ g_6 = c - c_{max} \end{cases} \tag{6.148}$$

According to this form, six parameters, θ_j, will be necessary to complete the Kuhn–Tucker conditions given in Eq. (6.139). Constraints that are identical to this flexure category must be formulated for multiple-sensitivity flexure hinges. For two-dimensional flexures, where the width is variable, a condition in addition to those of Eq. (6.148) must be applied:

$$w_{min} \le w \le w_{max} \tag{6.149}$$

which generates two additional standard constraint functions:

$$\begin{cases} g_7 = w_{min} - w \\ g_8 = w - w_{max} \end{cases} \tag{6.150}$$

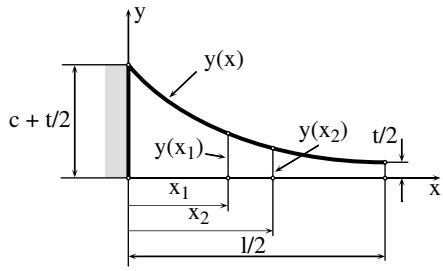

FIGURE 6.9
Quarter-model of flexure hinge with unknown thickness variation.

and, as a consequence, two more θ_j parameters (j = 7, 8) will be needed in the Kuhn–Tucker conditions.

The displacement-based optimization of different flexure hinges has focused so far on known configurations, in the sense that the longitudinal profiles and the associated compliances were explicit functions. The question arises as to whether there are other profiles that have not been investigated so far but which can lead to better results, compared to the definite-profile flexures previously analyzed, in terms of the objective functions. In other words, the optimization problem might be stated as: Find the thickness of a flexure hinge in order to minimize a compliance-based objective function. In this case, the compliances that would enter the objective functions are unknown because they depend on the unknown thickness. Figure 6.9 illustrates the quarter model of a flexure hinge with unknown variation of its thickness.

The geometric constraints that would apply to this particular optimization problem are:

$$\begin{cases} y(x_2) \le y(x_1) \text{ for } x_2 \ge x_1 \\ y(0) = c + \dfrac{t}{2} \\ y\left(\dfrac{l}{2}\right) = \dfrac{t}{2} \\ \left.\dfrac{dy}{dx}\right|_{x=\frac{l}{2}} = 0 \end{cases} \tag{6.151}$$

It is beyond the scope of this discussion to go into more detail with the shape optimization of a flexure hinge by means of the general formulation previously stated.

6.7 Means of Actuation

Actuation is an extremely important topic in assessing the overall behavior of flexure-based compliant mechanisms. Various means of actuation will briefly be analyzed pertaining to either macroscale or microscale (MEMS) applications.

6.7.1 Macro-Actuation

Several types of actuation can be utilized for macroscale flexure-based compliant mechanisms, depending upon the specific functions the mechanism was designed to accomplish. An entire class of materials and actuators is implemented in various compliant mechanism applications because they share a common trait. Those materials are often encountered under the common label of "smart materials" in the sense that they are capable of changing their shape and geometrical dimensions in a meaningful and, often-times, controllable fashion when subject to a specific input to which they are sensitive. Examples of such materials or components take advantage of their sensitivity to an electric, magnetic, or thermal stimulus that prompts energy conversion and produces mechanical work output. These special actuators are briefly described in the following text, alongside more common types of actuators that are being employed in macroscale flexure-based compliant mechanisms.

6.7.1.1 Induced-Strain Actuators

Induced-strain actuators are also called solid-state, strain-induced actuators as they can generate mechanical output from either electrical or magnetic input energy. Included in this category are piezoelectric, electrostrictive (these two subsets are also called electroactive), and magnetostrictive (also called magnetoactive) materials. They all produce relatively small output displacement but high output force. Giurgiutiu and Rogers[57] have given a comparative account of the performance of the strain-induced actuators, and a general view of the electroceramic materials can be found in the work of Moulson and Herbert,[58] as well as in a paper by Haertling.[59] A brief presentation of each of the above-mentioned types will be presented next.

6.7.1.1.1 Piezoelectric Ceramics

These materials are usually composed of lead, zirconium, and titanium (denoted by PZT) or of lead, lanthanum, zirconium, and titanium (simply denoted by PLZT). They are ferroelectric ceramics that are reciprocally electroactive, as they can change their dimensions when an electrical field is applied to them and, conversely, generate an electric output when acted upon by an external mechanical pressure. Piezoelectric materials accept reversed polarity in a proportion of up to 30% and display a hysteretic characteristic that is quasi-linear up to an approximately 0.15% strain. The classical PZT

equations (ANSI/IEE Standard 176–1987) connect mechanical to electrical amounts in the following form:

$$\begin{cases} S_{ij} = s^{E}_{ijkl} T_{kl} + d_{kij} E_k \\ D_j = d_{jkl} T_{kl} + \varepsilon^{T}_{jk} E_k \end{cases} \tag{6.152}$$

where S is the mechanical strain, T is the mechanical stress, E denotes the electrical field, D represents the electrical displacement, s is the mechanical compliance of the material at zero electrical field ($E = 0$), ε is the dielectric permitivity at zero mechanical stress ($T = 0$), and d denotes the piezoelectric coupling factor between electrical and mechanical properties. It is worth noting that in a piezoelectric material, the strains developed under an applied electrical field are proportional to the voltage. In a PZT plate, for example, that is subject to voltage V and has thickness t, the free strain that is produced is expressed as:

$$\varepsilon = d \frac{V}{h} \tag{6.153}$$

where d is the piezoelectric charge constant.

PZT ceramics achieve a high performance actuation because of their morphotropic composition, being situated between the tetragonal and rhombohedral phases, which allows easy coupling between the two phases and, therefore, produces high piezoelectric properties through enhanced polarizability, as mentioned by Park and Shrout.[63] The piezoelectric properties are further increased by reducing the Curie temperature, which dictates the phase transformation for a PZT. Unfortunately, this leads to more sensitivity to temperature and increased exposure to aging effects and less piezoelectric activity. Such soft ceramic PZTs (the proptotype being the PZT-5H composition, also known as Navy type VI) could reach values of the piezoelectric coefficient as high as 700 pC/N and strain levels of up to 0.1%, at the expense of high hysteresis and poor temperature stability, which restrict the application domain to low-frequency ones. Reducing the hysteretic losses can be achieved through material enhancements such as in the hard PZTs such as PZT-8 (Navy type III), for instance, but this improvement substantially reduces the piezoelectric coefficient to maximum values of 300 pC/N.

Piezoelectric actuators are fabricated in various forms, and Figure 6.10 illustrates a few configurations. A very common design is the stacked PZT, which is realized by gluing, pressing, and sintering together several piezoelectric patches to form a bloc, as illustrated in Figure 6.10a. By applying an electrical field, the PZT stack either contracts or expands, thus producing the output linear motion. The stack PZT is a commonly utilized actuator in small- to medium-scale compliant mechanisms that are designed as precision positioning systems, for instance. Another application is the PZT bender that can be constructed in a dome configuration, as sketched in Figure 6.10b,

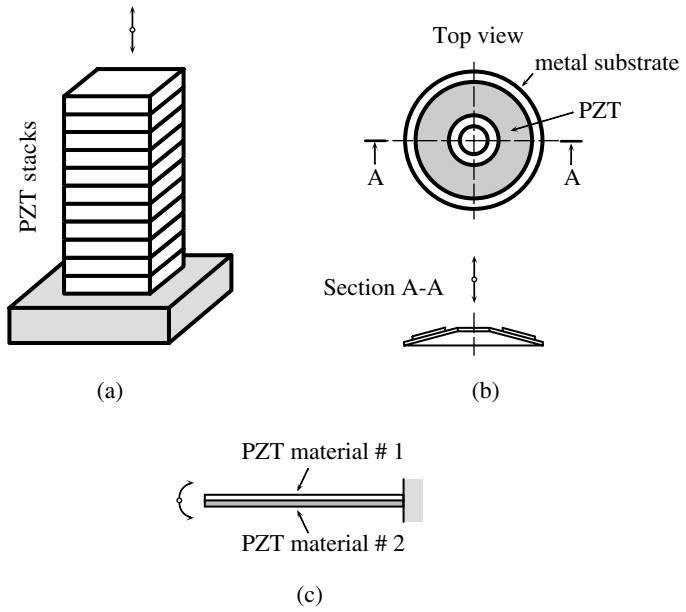

FIGURE 6.10
Some configurations of strain-induced actuators: (a) linear PZT stack; (b) unimorph dome (THUNDER variant); (c) bimorph bender.

or in an initially planar shape as shown in Figure 6.10c. The domed design is encountered in commercially available products such as THUNDER (developed by Face® International Corp.). Other disk-shaped configurations are MOONIE and RAINBOW. In such designs, the PZT wafer is attached to a metal substrate and specific heat treatment induces stresses that bend the entire structure in the absence of external loading or an electrical field. More details on the particular geometry and operating features of these types of commercially available actuators can be found in the papers of Li et al.,[60–62] to cite just a few. Such constructions, in either bent or straight designs, are called *unimorph piezoelectrics*, whereas the configurations that utilize different pizoelectric materials glued together are called *bimorphs*. Apart from these composite actuators, companies that are involved with piezoelectric materials, such as Morgan Matroc, Inc., for instance, also develop actuators in more common shapes, including blocks, discs, tubes, rings, or hemispheres.

6.7.1.1.2 Electrostrictive (PMN) Materials

The main constituents of electrostrictive materials are lead, magnesium, and niobium (PMN). These electroactive ceramic also manifest reciprocal piezoelectric properties by being able to convert the electric energy into mechanical energy and vice versa; however, they do not accept reversed polarity.

The strain produced by electrostrictive actuators is proportional to the square of polarization, according to the general equation:

$$\varepsilon = cV^2 \tag{6.154}$$

where c is a constant that incorporates both geometrical and material properties of the electrostrictive component.

The dielectric performance of commercially available electrostrictive materials rivals the performance of soft PZTs, as strain levels of up to 0.15% can be achieved, and the d_{33} coefficient can reach values of 800 pC/N. Like hard PZTs, the PMN materials are limited in their maximum strain levels by polarization saturation and dielectric breakdown strength, which are inherent material barriers. At the same time, electrostrictive materials exhibit low hysteresis. Those good properties are only obtainable over a narrow electric field and temperature domains, unfortunately. Electrostrictive polymers mimicking natural muscle functions have recently been developed to be utilized in robotic and microrobotic actuation. As mentioned by Kornbluh et al.[65] and Pelrine et al.,[66] for instance, such actuators are capable of producing strains of up to 30% and stresses in an axial (linear actuator) loading of up to 1.9 MPa. The paper by Kornbluh et al.[65] presents a comparative synthesis of different types of actuation in terms of various performance criteria, such as maximum attainable strain, maximum stress (pressure), maximum energy density, or relative speed. It is shown that the piezoelectric actuators are performing the best in terms of the output force (pressure), whereas the artificial muscle actuator delivers the best maximum strain (30%, as mentioned previously). A similar class of actuators is based on gel polymers or film piezoelectric/electrostrictive layers that can be configured in various shapes and therefore can be custom-designed to specific applications that present spatial constraints where other actuators, built on a more standard basis, cannot be utilized.

6.7.1.1.3 Relaxor-Based Ferroelectric Single Crystals

More recently, relaxor-based ferroelectric single crystals have demonstrated real potential in terms of actuation performance, as Park and Shrout[63] mention in their paper. Materials such as PMN-PT (lead, magnesium, niobate, and lead titanate) and PZN-PT (lead, zinc, niobate, and lead titanate) present excellent properties in terms of the levels of strain, where they have produced up to 1.7% (which is one order of magnitude larger than those available from conventional piezoelectric or electrostrictive ceramics); electromechanical coupling, as they have shown coupling coefficients k_{33} in excess of 90%; and very low hysteresis through dielectric losses, less than 1%. Park and Shrout[63] provide the following equation which relates the maximum strain energy density to the maximum strain level, ε_{max}; the material density, ρ; and Young's elastic modulus, E:

$$U_s = \frac{1}{16\rho} E\varepsilon_{max}^2 \tag{6.155}$$

which indicates that the energy performance of a relaxor-based single crystal actuator depends on the level of strain, taking into account that density and Young's modulus vary little between different materials. At reasonable electric fields that do not exceed 50 kV/cm, the piezoelectric coefficient d_{33} is ultrahigh compared to regular piezoelectric materials, and this accounts for the elevated performance of this type of actuator material. Piezoelectric coefficients with values nearing 2500 pC/N have been produced at strain levels of 0.6 to 1.7% with relatively low hysteresis, as mentioned by Park and Shrout.[63] The optimum crystallographic configuration is pseudocubic in rhombohedral crystals or rhombohedral-tetragonal crystals.

6.7.1.1.4 Magnetostrictive (TERFENOL) Materials

Magnetostrictive materials deform under the action of an external magnetic field and are also termed TERFENOL, an acronym that combines the main constituents, terbium and iron (Fe), and their development source, which is NOL (Naval Ordinance Laboratory). These materials are piezomagnetic (magnetoactive; converting magnetic energy into mechanical energy). Such materials behave quasi-linearly within a range of up to 0.1% strain levels. The basic equations that govern the magnetic–mechanical phenomena are similar to those describing the piezoelectric effect, namely:

$$\begin{cases} S_{ij} = s^{E}_{ijkl} T_{kl} + d_{kij} H_k \\ D_j = d_{jkl} T_{kl} + \mu^{T}_{jk} H_k \end{cases} \tag{6.156}$$

where H is the magnetic field and μ is the magnetic permeability under constant stress. Clephas and Janocha[64] recently described the possibility of combining piezoelectric and magnetostrictive materials into a hybrid actuator that would present the advantage of functioning under both the capacitive and inductive regimens, thus increasing the power efficiency, which for either piezoelectrics or magnetostricters, taken individually, is rather low.

6.7.1.2 Thermal Actuators

Thermal actuators utilize their temperature-related deformation to act as linear actuators. The two basic types of thermal actuators are metal thermostats and wax actuators. The metal thermostats consist of several metal sheets that are bonded in a sandwich fashion and constructed of materials with different thermal expansion coefficients. The same amount of temperature variation will cause each of the sheets to deform differently and, because of the subsequent prevented expansion/contraction, the sandwiched beam will bend and produce output motion or force. The output effects are generally modest because they are proportional to the temperature variation. Wax actuators are capable of producing larger output displacements, as their

effect is based on either large thermal expansion coefficients or a liquid–solid phase change. Such actuators can only generate a slow response because the wax has a low thermal conductivity. Both categories of thermal actuators can be utilized only in linear applications.

6.7.1.3 Shape-Memory Alloys

Shape-memory alloy (SMA) actuators use the same basic mechanism as the thermal actuators, as they utilize the shape-memory effect to convert thermal energy into mechanical output. The basic phenomenon that generates this energy conversion (as shown by Otsuka and Wayman,[67] for instance) is the reversible martensitic–austenitic solid-state phase transformation. Alloys such as those based on Ti–Ni, Au–Cd, In–Tl, Cu–Zn, or Cu–Al, among others, present two basic effects or properties: the shape-memory effect and the superelasticity, which are both based on the evidence that at low temperature they present a martensitic state, with atoms that can move easily through shearing-enabled mechanisms, while at higher temperatures, after passing through the so-called reverse transformation temperature, the dominant state is the austenite, which is more stable and therefore more difficult to alter. Figure 6.11 illustrates the force–displacement characteristics of an SMA linear spring that acts against an external load at two different temperatures. By lowering the temperature from a value T_1 that keeps the material within the austenitic (parent) phase to a value T_2 that defines the martensitic phase, a gain in displacement is achieved.

The SMA actuators take advantage of the fact that their operation principle enables compression/extension and torsion, as well as utilization in both linear and rotary applications. Compared to thermal actuators and voice coils (magnetic solenoids), the SMA actuators clearly perform better in terms of stroke-to-weight and output force-to-weight ratios, quietness of operation, and speed of motion or response at given temperatures. They are also advantageous in applications that are designed based on a two-way effect.

A related breed of actuators that have entered the actuation scene relatively recently is the shape memory polymer family, as discussed by Monkman.[68] Like their metallic counterparts, the shape-memory polymers are

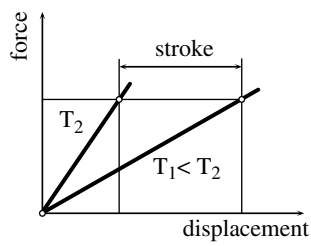

FIGURE 6.11
Force–displacement characteristic for a shape memory alloy in parent (austenitic) phase at a higher temperature T_2 versus the martensitic phase at the lower temperature T_1.

also based on a temperature effect that, through several phase transitions, changes the elastic properties of the structural component. The radical difference is due to the fact that the elastic modulus of a shape-memory polymer reduces with increasing temperature, unlike the metallic shape-memory alloys.

6.7.1.4 Classical Actuation

The hydraulic and pneumatic actuators provide high-output forces and large displacements and are often equipped with servo-control that allows frequency and stroke variation. They are less utilized in small-scale compliant mechanism applications because of a few drawbacks, such as the necessity for additional electric and hydraulic sources that increase their overall size. The magnetic or electromagnetic actuators, in their various embodiments (e.g., solenoids, moving coils, voice coils, linear and stepper motors, rotary motors), can be employed in compliant mechanism applications that require relatively low force capabilities. The magnetic motors are recognized for their versatility in covering wide spans in terms of performance. In a recent paper dedicated to magnetic actuation aspects, Howe[69] mentions that this type of actuation can produce displacements from microns to meters, accelerations that can be a few hundred times larger than the gravitational acceleration, highly accurate, and repeatable positioning.

6.7.2 MEMS Actuation

The means of actuation in compliant microelectromechanical systems (MEMS) must adapt to the very small scale of this type of device and, as a consequence, the actuators presented previously cannot be utilized here because they are too large. Microactuation must successfully deliver quantities of mechanical energy that are sufficient to the particular application. Because the primary means of microactuation transforms a certain type of energy into mechanical energy by intermediate storing of this energy, the amount of the stored energy must also be relatively high. This aspect can be quite difficult to overcome, as mentioned by Guckel,[70] among others researchers. The stored energy is the product of the energy density and the volume of the actuator; therefore, the small dimensions of a microactuator must be counteracted by a high value of the energy density. The energy density however is limited by the very of the nature of the process of converting one type of energy into mechanical energy. Electro- and magnetoactive materials are recognized as having good energy density properties, but unfortunately they cannot be fabricated at the microscale required by MEMS applications. Balancing this drawback is evidence that in the great majority of cases MEMS do not require high output forces although large output displacements might be desired. Nonetheless, large output displacements can be achieved through utilizing large displacement amplification devices that can take advantage of the important aspect that

silicon flexible members are only subject to fracture at stress levels that are substantially higher than those corresponding to bulk silicon members. As a consequence, such micromembers can deform more and deliver the desired levels in output displacement.

The main means of microactuation is discussed next, based on examples given by the MEMS literature. It is worth noting that only the primary means of actuation are presented here. The compound microactuators such as microsteppers or micro-inchworms are analyzed in the chapter dedicated to real-life MEMS applications (Chapter 7), as it is known that these actuators combine primary means of actuation with additional structures in order to gain the necessary output figures.

6.7.2.1 Electrostatic Actuation

This type of actuation is the most utilized in microelectromechanical systems. The main configuration of an electrostatic actuator is the comb drive, which is shown schematically in Figure 6.12. The comb drive is essentially a parallel-plate capacitor. It consists of several interdigitated plates that are placed on two supports, one of which is mobile, so that when a voltage is applied to them the electrostatic force that is generated causes the fingers of the mobile plate to move within the interstices created between the similar fingers of the fixed plate. Rotary variants of the comb drives are also implemented with the mobile plate, where the fingers move circularly within the spaces created by the similarly designed fixed plate.

6.7.2.2 Piezoelectric Actuation

Present-day piezoelectric technology enables the fabrication of small actuators that are capable of integrating with MEMS-type technology and applications. Commercially available piezoelectric stacks can be as small as 1 mm long with a 1-mm cross-section. Such PZT stacks were utilized by Cao et al.,[71] for instance, to design and fabricate a PZT-actuated micropump for drug delivery. Three small PZT actuators of the sizes mentioned above were implemented in a microhydraulic peristaltic pump that was capable of flow rates of up to 10 μl/min. The three PZTs were sequentially actuated to push against three

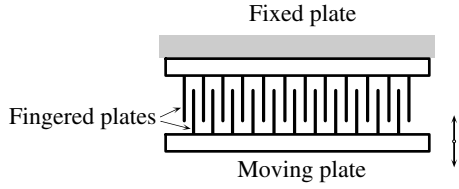

FIGURE 6.12
Schematic representation of a parallel-plate comb drive utilized as an electrostatic actuator in compliant MEMS.

elastic silicon membranes and produce the output peristaltic motion. A similar application that utilizes small-dimensions PZT wafers is presented by Roberts et al.,[72] who introduced a high-stiffness piezoelectric actuator for microhydraulic applications. The application employs one single piston that is acted upon by three small-size bar PZT actuators that are equally spaced radially and circumferentially.

6.7.2.3 Magnetostrictive Actuation

Small magnetostrictive actuators, of dimensions similar to the piezoelectric ones that were just presented, can also be utilized in MEMS-scale applications. An interesting alternative is reported by Quandt and Ludwig,[73] who present bending actuators realized by sputter-depositing multilayers of magnetostrictive TbFe/FeCo on a silicon substrate. Such cantilevers operate on the principle of prevented free-deformation of the magnetostrictive material when subject to an external magnetic field, which results in bending of the composite flexure. Such multilayered benders can operate favorably even at low magnetic fields because they provide a reduction of the magnetostrictive saturation, which translates to better deformation capability. A similar application of a magnetostrictive bimorph is presented by Garnier et al.,[74] who detail its utilization in optical scanners.

6.7.2.4 Electromagnetic Actuation

Electromagnetic actuation has also been implemented into the microworld. The work by Khoo and Liu,[75] for example, describes the design of a micromagnetic actuator capable of high torque and large output displacements. The microactuator consists of a highly flexible elastic-polymer membrane that is fixed on its edges over a through-hole cut in a silicon support. Several small-size magnetic flaps are embedded in the elastic membrane, and when an external magnetic field is applied the flaps tend to move, thus causing the membrane to deflect outside of its plane. A similar approach was pursued by Maekoba et al.,[76] who glued a patch of magnetic Permalloy at the free tip of a silicon cantilever to achieve deflection of the composite flexure under the action of an externally applied electromagnetic field. Such bimorph cantilevers are implemented in the construction of optical switches that are operating in a bistable condition.

6.7.2.5 Pneumatic Actuation

In a recent paper, Butefisch et al.[77] present the functional principles and concrete design, fabrication, and testing of a micropneumatic actuator that acted on a microgripper. Two different fabrication techniques were utilized: reactive ion etching (RIE) for the silicon parts and ultraviolet-depth lithography for the photoepoxy components. The micropneumatic actuator consists of a piston that is attached to its housing by means of two serpentine

multiflexure members that act as both return springs and sealing agents. The piston can move in its cavity bidirectionally when air under pressure is fed through the inlet. The actuator is capable of producing up to 600 μm output displacement at 120-mbar air pressure in quasi-static conditions. The operation frequency in the dynamic range has been measured up to 150 Hz, at which level output displacements of approximately 500 μm were obtained.

6.7.2.6 Thermal Actuation

Thermal actuation is also applicable at a microscale in a manner similar to macroscale actuation. Liew et al.[78] describe the main modeling aspects of thermal actuation in bulk-micromachined CMOS micromirrors. The thermal actuator is a multimorph member consisting of several layers of aluminum, silicon dioxide, and polysilicon that are stacked together in the form of a composite flexure. The entire structure is thermally isolated from the exterior environment. Very much like in macroscale applications, the flexure bends when thermal heating through an electrical resistor is applied, because of the different thermal expansion coefficients of the components. Modeling resulting from an analytic approach and finite-element analysis produced results that were similar. A prototype micromirror was also fabricated, and static as well as dynamic experimental measurements were taken. The actuator showed a very promising thermal response of the order of milliseconds which usually is the main impediment to using thermal actuators.

6.7.2.7 Thermopneumatic Actuation

In situations where subsequent effects are not key to the main process, thermopneumatic microactuation can be implemented to produce relatively large output displacements at low levels of applied voltage. Jeong and Yang[79] present the details of fabricating and the performances of such a thermopneumatic microactuator capable of delivering up to 6.25-μm/V output displacement when utilizing a corrugated diaphragm constructed of a p+ silicon film. The motion of the diaphragm (a flat configuration is also analyzed) is generated by ohmic heating and air cooling of the air, which is confined in a cavity enclosed on one side by the elastic diaphragm. The displacement/voltage characteristic demonstrates a very good linearity for both the corrugated and flat diaphragms.

6.7.2.8 Other Means of Microactuation

The so-called *carbon nanotubes*, presented, for instance, in the paper of Minett et al.,[80] are constructed as cantilevers that achieve their deflection by converting electrical energy into mechanical energy. The phenomenon of this energy transfer is the charge transfer that takes place under an externally

applied electric field at the carbon–carbon bond interface, which causes geometric expansion. The principles of quantum-mechanical actuation by means of the Casimir force in MEMS is explained in a paper by Chan et al.[81] The Casimir force is an attraction between two surfaces determined by the quantum-mechanical vacuum fluctuations of an electromagnetic field. It is thus possible to obtain relative rotation of one plate that is laterally supported by two torsional flexure hinges and is set parallel within nanometer distance from a fixed plate.

6.8 Fabrication

Selecting the adequate material and fabrication technology for a given application is clearly influenced by the scale of the flexure hinge or the flexure-based compliant mechanism, as illustrated in Figure 6.13. Macroscale applications are usually constructed of metallic materials using fabrication techniques that can handle machining at this scale, such as classical drilling, milling, or wire electrodischarge machining (EDM), as shown in the following text. On the other hand, microcompliant mechanisms are built on silicon and other materials that are deposited on the silicon substrate for which specific fabrication procedures such as LIGA or etching must be applied in order to realize the necessary microshapes.

Although fundamentally similar, macro- and micromachining present marked differences (as mentioned by Maluf,[34] for instance) due to the scale specificity of each procedure. While macromachining attempts to realize the finite part by sequential operations and is therefore a serial process, micromachining procedures, in order to be cost effective, proceed in a parallel fashion by applying a given operation to many "workpieces" (being placed on the same wafer, in the case of silicon, for instance) and therefore are batch procedures. Another contrast between the two machining categories is the minimum attainable dimensions. Macromachining can fabricate parts to the level of 20 to 25 μm, whereas micromachined components can be as small as 1 μm.

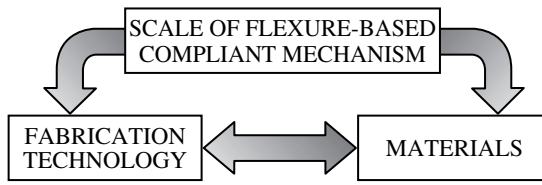

FIGURE 6.13
Schematic showing the interrelations between the scale of the flexure-based compliant mechanism and the corresponding fabrication technology and materials.

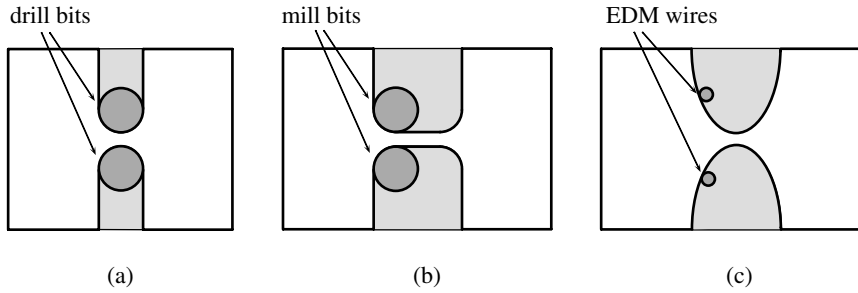

FIGURE 6.14
Possible macromachining procedures for three different flexure configurations: (a) circular flexure hinge machined by drilling; (b) corner-filleted flexure hinge machined by milling; (c) a more complex-shaped flexure hinge machined by wire-EDM.

6.8.1 Macroscale Fabrication

The procedures utilized for the fabrication of macroscale flexure hinges and flexure-based compliant mechanisms have evolved historically from simple ones, such as drilling or milling, to more complex ones, such as EDM, wire-EDM, electron/ion beam machining, water jet machining, and laser machining, to name just a few. Obviously, simple shapes can be obtained by simple machining procedures, while more sophisticated geometry configurations require adequate fabrication techniques.

Three simple examples are presented in Figure 6.14, which suggests the machining techniques that are applicable to a symmetric circular flexure hinge (Figure 6.14a), a corner-filleted hinge (Figure 6.14b), and a more complex shape flexure (Figure 6.14c). The circular flexure hinge can simply be machined by drilling two through-holes in a blank material, followed by cutting and removing the shaded portion of the workpiece. The corner-filleted flexure hinge requires at least milling so that the line–arc–line profile can be machined. The fillet radius at the corners is limited by the mill bits that are available; therefore, small flexures that require even smaller fillet radii cannot be machined by this procedure. Wire-EDM, however, can handle complex shapes with small curvature radii and is the preferred method of realizing such configurations.

6.8.1.1 Electrodischarge Machining

In a monograph dedicated to modern machining methods, McGeough[82] focuses upon the process of electrodischarge machining (EDM), which is one of the most utilized high-precision and relatively low-cost (therefore affordable) material removal procedures available today. The machining procedure is based on the phenomenon of metal erosion under spark discharges.

First noticed in the late 1700s, advances were not made until the 1940s when researchers B.R. Lazarenko and N.I. Lazarenko considered using the spark discharge process for machining materials that were difficult to machine by existing methods at that time, such as cutting by means of diamond tools. Fundamentally, the EDM process consists of a controlled sequence of spark discharges between two electrodes: the tool and the workpiece in a DC circuit within a dielectric environment. The sequence is made up of very short-duration discharges that repeat themselves at high frequency. During the EDM process, the spark reaches temperatures of 20,000°C; this intensity combined with its short lifetime results in local melting and vaporization of the workpiece metal, while imposing few side effects on the adjacent areas. The end result of all these localized sparks is a path that is cut in the workpiece and which is the approximate negative imprint of the tool shape.

The main roles of the dielectric are to keep the high energy of the spark very localized and to cool the electrodes while also helping to transport the tiny spherical metal debris (that resolidify in the dielectic) from the recently created cut region. The electrical resistance of the dielectric must be balanced between a minimum value that would produce a premature discharge and a maximum value that would not permit the spark to occur at all. Technically, a typical EDM process utilizes rectangular voltage pulses, oftentimes in the 50- to 150-V range, at frequencies in the range of 50 to 500 kHz. For high-quality surface finishes, relatively low energy and high frequencies are utilized, while for a rougher cut surface the reverse conditions must be applied in order to achieve high rates of material removal. In many situations, these two operations (rough cut and finish cut) are subsequently applied to ensure both productivity and quality in the process. The material removal rate will, of course, vary depending on the desired surface quality and the corresponding machining conditions. By increasing the current and reducing the frequency of the process, high removal rates on the order of 25 cm^3/hr can be obtained for rough machining.

A big advantage of the EDM technique over other material-removing procedures is that the machining speed is not influenced by the workpiece hardness. Superior surface finishes require lower material removal rates, as low as 0.05 cm^3/hr. Two different EDM procedures were discussed by McGeough[82] and Hatschek.[83] One method is drilling, which utilizes a hollow electrode in order to negatively copy its own shape into the workpiece. Very complex shapes, both in the depth of the workpiece and on the planes perpendicular to the direction of penetration of the tool, can be obtained. The other method is the wire-EDM technique currently in use on a wide scale, as it offers high-quality cut profiles and is implemented on CNC machines that can directly read the coordinates of a complicated contour from a CAD-generated drawing. The tool electrode is a wire that is recirculated continuously as it unwinds from one spool, passes through the workpiece by cutting a portion of the desired profile, and then rewinds on a second spool such that fresh portions of the wire are always in contact with

the workpiece. The direction of machining is realized by the motion of either the workpiece or the wire head. The wire-EDM technique enables machining of complex shapes that are equivalent to offsetting a planar profile through the thickness of the workpiece. Wire is usually constructed of copper or brass, and regular EDM machines can utilize wire diameters as small as 0.25 mm. When tungsten or molybdenum wires are utilized, the diameter can be reduced to 50 μm. The surface quality achieved by EDM techniques is very good, and the surface roughness can be of the order of 0.05 μm, as mentioned by McGeough.[82]

After machining a piece by EDM technology, the layers in the immediate vicinity of the surface suffer changes that are mainly produced by the thermal effects induced through the process. A thin epithaxial layer with a thickness less than 40 μm is formed at the workpiece surface because the material melts there and then is quickly hardened when it comes into contact with the cooling dielectric fluid. Underneath this layer is another heat-affected layer less than 250 μm thick which is subject to thermal stresses generated through heating, cooling, and material diffusion during machining. These layers particularly reduce the fatigue life of parts that are fabricated by EDM, and their presence is particularly undesirable in flexure hinges and flexure-based mechanisms.

Xiaowei et al.[84] reported on a combined EDM-based method for the fabrication of flexure hinges. By applying EDM with orbital (planetary) motion of the workpiece followed by stationary microsecond pulsed electrochemical machining (MPECM), the authors found that this process managed to eliminate the heat-affected superficial layers in the region of minimum thickness of the flexure hinge (the so-called subtle neck). Henein et al.[85] investigated the fatigue failure of flexure hinges that are machined by the EDM technology. They tested several very thin circular flexure hinges (50 μm in diameter) and compared the resulting experimental data with existing results for standard test specimens; they concluded that fatigue data found in the literature can be applied to EDM-produced flexure hinges without additional corrections.

6.8.1.2 Other Fabrication Procedures

Although electrodischarge machining is the predominant method, especially for fabrication of two-dimensional or nonrevolute flexure hinges, other machining methods are also applicable. For high-quality surfaces and dimensional precision, such as that required by flexure-based compliant mechanisms, advanced cutting methods that utilize tools constructed on monocrystalline diamond or fine-grit corundum must be supplemented by special lapping and polishing techniques. Unconventional machining techniques such as electrochemical, laser, plasma-arc, water-jet, or abrasive jet machining can also be applied to produce monolithic flexure-based compliant mechanisms, as well as precision molding or stamping, for the fabrication of three-dimensional revolute flexure hinges.

6.8.2 MEMS-Scale Fabrication

A summary presentation is given here on the fabrication technologies that apply to compliant MEMS. Detailed information into the general subject of MEMS fabrication and materials can be found in the monographs of Maluf[34] and Madou.[86]

Because the MEMS applications require several components that are assembled or glued together, similar to the spate of materials, the fabrication technologies necessary to construct these microsystems are also varied. Mechanically compliant microsystems are almost totally based on the use of the silicon as a backbone or supporting member, ensuring the overall deformation and resulting motion of such systems. Structurally, the silicon is a monocrystal that behaves like a brittle material. Although the reverse would have been expected from a brittle material, it is well known that silicon microstructural members that are subject to bending display excellent deformation qualities (see, for example, Lang[87]), and large deformations can be achieved in such members before the fracture limit of the material is reached.

An interesting comparison between silicon and titanium or steel can be performed in terms of the maximum deflection produced by a constant cross-section cantilever when an end moment is applied such that the ultimate strength of the respective material is reached. It can be shown that the tip deflection, under these circumstances, is given by the equation:

$$u_{y,max} = c_{mat} \frac{l^2}{t} \tag{6.157}$$

where l is the cantilever's length, t is the thickness of a constant rectangular cross-section, and c_{mat} is a material constant, defined as the ratio of the ultimate strength to the Young's modulus. If the comparison is run between two geometrically identical cantilevers made up of silicon and a regular titanium alloy, then the ratio of the maximum deflection of the two cantilevers is:

$$r_{u_{y,max}} = \frac{c_{silicon}}{c_{titanium}} \tag{6.158}$$

Average values for the two materials discussed indicate that for silicon the ultimate (fracture) strength is 7 GPa and the Young's modulus is 160 GPa, whereas for a titanium alloy the yield strength is approximately 1 GPa and the Young's modulus is 110 GPa. As a consequence, the ratio defined in Eq. (6.158) will have a value of 4.812, which basically indicates that a silicon cantilever can produce a deflection that is almost five times greater than the deflection produced by a geometrically identical cantilever that is constructed of a titanium alloy.

As a consequence, the compliant MEMS are designed almost exclusively based on this important property, and the output motion of these microsystems

is obtained by the elastic deformation (most often bending and torsion) of cantilever-like or double-clamped silicon members. Crystalline silicon of 4- or 6-inch diameter with corresponding thicknesses of 525 μm and 650 μm, respectively, that are commercially available are generally utilized as substrates for MEMS applications. The crystalline silicon wafers have mechanical properties that are very uniform and usually do not have internal stresses. In addition to the excellent deformational properties, silicon also has good thermal properties and preserves its mechanical properties up to approximately 500°C.

Realizing the final MEMS application, however, requires several other materials and components that would supplement the silicon flexible parts in order to solve the functional tasks of the microsystem. In a recent paper, Ehrfeld and Ehrfeld[88] have summarized several other materials that are utilized in constructing MEMS applications, including various metals, metal alloys, and nonmetallics. A more detailed picture of the materials that are utilized in constructing MEMS is provided by Maluf.[34] Amorphous silicon and polysilicon of different concentrations, for instance, are often deposited on the crystalline silicon wafers as thin films. Silicon oxides and nitrides form another group of materials that are used in MEMS fabrication, usually as thermal and electrical insulating layers or sacrificial layers in surface micromachining. Metal films such as aluminum, gold, titanium, tungsten, nickel, platinum, or copper are also used in combination with the silicon substrate in MEMS for different purposes mostly dedicated to electrical connectivity. Polymers such as photoresists or special-purpose resists are employed for patterned masks that further facilitate the etching of inner layers already deposited on the silicon backbone. Other materials tested in the construction of MEMS are glasses and quartz. They are usually used as substrate materials in applications where optical transparency and/or electrical insulation is required from a substrate component.

In a paper dedicated to looking into the future of microsystems, Lang[87] suggests that the large variety of MEMS applications directly translates into an equally extended pool of materials, technologies, and fabrication methods. Unlike the electronic chip industry, where the technology is quite standardized, in the silicon microworld an abundance of technological methods are in place, mainly having to do with performing three-dimensional structuring of the MEMS applications. Lang[87] cites the main processes that are utilized in fabricating microsystems as being wet chemical etching of silicon for three-dimensional micromachining and plasma/ion-beam dry etching for surface micromachining, as well as mechanical micromachining, microreplication, quartz-machining procedures, ion implantation, or thick and thin film deposition technology, in order to enable further fabrication of MEMS.

Figure 6.15 attempts to illustrate a sequence of the minimum number of various processes involved in fabricating a micromechanical system. The first group of fabrication methods includes deposition procedures that are designed to attach thin layers (films) of various materials to the silicon

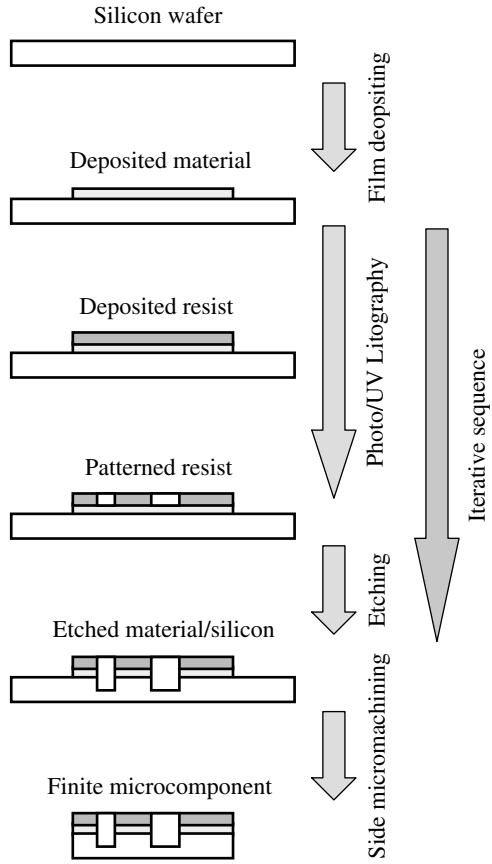

FIGURE 6.15
Minimal steps in the fabrication of micromechanical systems.

substrate or to already-deposited layers. Specific deposition techniques include epitaxy, sputter deposition, oxidation, evaporation, chemical vapor deposition (CVD), or spin-on methods, each subgroup being developed for different materials and physical conditions. The lithographic techniques usually follow the fabrication sequence and are intended for creating a protective masking layer that will serve for subsequent etching operations. The lithography itself is generally broken down into the following suboperations: A photoresist layer is first deposited on the previously fabricated microcomponent (which has an already-deposited layer on top of the silicon substrate). A process of optical exposure follows by which a pattern is transferred (printed) from a chromium-transparent glass mask to the photoresist layer. Eventually, either the exposed resist (if the resist substance is positive) or the unexposed portion (if the resist substance is negative) is dissolved such that the mask pattern is machined into the resist layer and completes the

lithography operation. An etching process is further applied that will selectively remove material from the thin films that have already been deposited and, possibly, from the silicon substrate as well. Wet and dry etching techniques can be employed depending on the precision required for the final product. The newly developed deep reactive ion etching technique (DRIE) can channel down to depths of 500 μm.

The LIGA process was considered until a few years ago to be the technology of choice for generating precision, high-aspect-ratio microcomponents. The LIGA acronym is derived from lithography, galvoplating, and injection molding (*abformung* in German; see Ehrfeld and Ehrfeld[88] and Guckel[70]) and is similar to a regular deposition–lithography–etching sequence, as previously described. The LIGA process is capable of utilizing resist layers that can be up to 1000 μm thick. Instead of using a photolithography operation, the LIGA technique utilizes collimated x-ray irradiation to create a deep mask in the resist layer. The process continues with an electroplating/molding phase where the cavities in the resist material are filled with materials such as gold, copper, aluminum, or nickel. The last phase removes the resist mold and frees the newly created micromechanical component. It is worth noting that microparts with very high aspect ratios can be obtained through the LIGA process.

References

1. Freudenthal, A.M., *Introduction to the Mechanics of Solids*, John Wiley & Sons, New York, 1966.
2. Shanley, F.R., *Strength of Materials*, McGraw-Hill, New York, 1957.
3. Wang, C.M., Lam, K.Y., He, X.Q., and Chucheepsakul, S., Large deflections of an end supported beam subjected to a point load, *International Journal of Non-Linear Mechanics*, 32(1), 63, 1997.
4. Dado, M.H., Variable parametric pseudo-rigid-body model for large deflection beams with end loads, *International Journal of Non-Linear Mechanics*, 36, 1123, 2001.
5. Lee, K., Large deflections of cantilever beams of non-linear elastic material under a combined loading, *International Journal of Non-Linear Mechanics*, 37, 430, 2002.
6. Ohtsuki, A. and Ellyn, F., Large deformation analysis of a square frame with rigid joints, *Thin-Walled Structures*, 38, 79, 2000.
7. Hamdouni, A., Interpretation geometrique de la decomposition des equations de compatibilite en grandes deformations, *Mecanique des Solides et des Structures*, 328, 709, 2000.
8. Pai, P.F. and Palazotto, A.N., Large-deformation analysis of flexible beams, *International Journal of Solids and Structures*, 33(9), 1335, 1996.
9. Gummadi, L.N.B. and Palazotto, A.N., Large strain analysis of beams and arches undergoing large rotations, *International Journal of Non-Linear Mechanics*, 33(4), 615, 1998.
10. Wriggers, P. and Reese, S., A note on enhanced strain methods for large deformations, *Computer Methods in Applied Mechanics and Engineering*, 135, 201, 1996.

11. Zelenina, A.A. and Zubov, L.M., The non-linear theory of the pure bending of prismatic elastic solids, *Journal of Applied Mathematics and Mechanics*, 64(3), 399, 2000.
12. Oguibe, C.N. and Webb, D.C., Large deflection analysis of multilayer cantilever beams subjected to impulse loading, *Computers and Structures*, 78(1), 537, 2000.
13. Fortune, D. and Vallee, C., Bianchi identities in the case of large deformations, *International Journal of Engineering Science*, 39(2), 113.
14. Howell, L.L. and Midha, A., A method for the design of compliant mechanisms with small-length flexural pivots, *ASME Journal of Mechanical Design*, 116, 280, 1994.
15. Howell, L.L. and Midha, A., Parametric deflection approximations for initially curved, large deflection beams in compliant mechanisms, in *Proc. of the 1996 ASME Design Engineering Technical Conferences and Computers in Engineering Conference*, 1996, p. 1.
16. Shoup, T.E. and McLarnan, C.W., A survey of flexible link mechanisms having lower pairs, *Journal of Mechanisms*, 6, 97, 1971.
17. Shoup, T.E. and McLarnan, C.W., On the use of the undulating elastica for the analysis of flexible link mechanisms, *ASME Journal of Engineering for Industry*, 93(1), 263, 1971.
18. Shoup, T.E., On the use of the nodal elastica for the analysis of flexible link devices, *ASME Journal of Engineering for Industry*, 94(3), 871, 1972.
19. Saggere, L. and Kota, S., Synthesis of planar, compliant four-bar mechanisms for compliant-segment motion generation, *ASME Journal of Mechanical Design*, 123, 535, 2001.
20. Shoup, T.E. and McLarnan, C.W., On the use of a doubly clamped flexible strip as a nonlinear spring, *ASME Journal of Applied Mechanics*, June, 559, 1971.
21. Jensen, B.D., Howell, L.L., and Salmon, L.G., Design of two-link, in-plane, bistable compliant micro-mechanisms, *ASME Journal of Mechanical Design*, 121, 416, 1999.
22. Edwards, B.T., Jensen, B.D., and Howell, L.L., A pseudo-rigid-body model for initially-curved pinned-pinned segments used in compliant mechanisms, *ASME Journal of Mechanical Design*, 123, 464, 2001.
23. Saxena, A. and Ananthasuresh, G.K., Topology synthesis of compliant mechanisms for non-linear force–deflection and curved path specifications, *ASME Journal of Mechanical Design*, 123, 33, 2001.
24. Timoshenko, S.P. and Gere, J.M., *Theory of Elastic Stability*, 2nd ed., McGraw-Hill, New York, 1961.
25. Allen, H.G. and Bulson, P.S., *Background to Buckling*, McGraw-Hill, London, 1980.
26. Chen, W.F. and Lui, E.M., *Structural Stability: Theory and Implementation*, Elsevier Science, New York, 1987.
27. Timoshenko, S.P., *History of Strength of Materials*, Dover, New York, 1983.
28. Den Hartog, J.P., *Strength of Materials*, Dover, New York, 1977.
29. Den Hartog, J.P., *Advanced Strength of Materials*, Dover, New York, 1987.
30. Boresi, A.P., Schmidt, R.J., and Sidebottom, O.M., *Advanced Mechanics of Materials*, 5th ed., John Wiley & Sons, New York, 1993.
31. Tenenbaum, M. and Pollard, H., *Ordinary Differential Equations*, Dover, New York, 1985.
32. Demidovich, B.P. and Maron, I.A., *Computational Mathematics*, MIR Publishers, Moscow, 1987.
33. Young, W.C., *Roark's Formulas for Stress and Strain*, 6th ed., McGraw-Hill, New York, 1989.

34. Maluf, N., *An Introduction to Microelectromechanical Systems Engineering*, Artech House, Boston, 2000.
35. Budynas, R.G., *Advanced Strength and Applied Stress Analysis*, McGraw-Hill, New York, 1977.
36. Lobontiu, N., Goldfarb, M., and Garcia, E., Achieving maximum tip displacement during resonant excitation of piezoelecrtically-actuated beams, *Journal of Intelligent Material Systems and Structures*, 10, 900, 1999.
37. Burgreen, D., *Elements of Thermal Stress Analysis*, first ed., C.P. Press, New York, 1971.
38. Kirsch, U., *Optimum Structural Design*, McGraw-Hill, New York, 1981.
39. Rozvany, G.I.N., *Structural Design via Optimality Criteria*, Kluwer Academic, Dordrecht, 1989.
40. Haftka, R.T., Gurdal, Z., and Kamat, M.P., *Elements of Structural Optimization*, Kluwer Academic, Dordrecht, 1990.
41. Bennett, J.A. and Botkin, M.E., Eds., *The Optimum Shape-Automated Structural Design*, Plenum Press, New York, 1986.
42. Vanderplaats, G.N., *Numerical Optimization Techniques for Engineering Design*, McGraw-Hill, New York, 1984.
43. Takaaki, O. and Toshihiko, S., Shape optimization for flexure hinges, *Journal of the Japan Society for Precision Engineering*, 63(10), 1454, 1997.
44. Silva, E.C.N., Nishiwaki, S., and Kikuchi, N., Design of flextensional transducers using the homogenization design method, unpublished data, 1999.
45. Bendsoe, M.P., *Optimization of Structural Topology*: *Shape and Material*, Springer-Verlag, Berlin, 1995.
46. Haftka, R.T. and Grandhi, R.V., Structural shape optimization: a survey, *Journal of Computer Methods in Applied Mechanics and Engineering*, 57, 91, 1986.
47. Belegundu, A.D., Optimizing the shapes of mechanical components, *Mechanical Engineering*, January, 44, 1993.
48. Frecker, M.I., Ananthasuresh, G.K., Nishiwaki, S., Kicuchi, N., and Kota, S., Topological synthesis of compliant mechanisms using multi-criteria optimization, *ASME Journal of Mechanical Design*, 119, 238, 1997.
49. Nishiwaki, S., Frecker, M.I., Min, S., and Kikuchi, N., Structural optimization considering flexibility: formulation of equation and application to compliant mechanisms, *JSME International Journal*, 63(612), 2657, 1997.
50. Nishiwaki, S., Frecker, M.I., Min, S., Susumu, E., and Kikuchi, N., Structural optimization considering flexibility: integrated design method for compliant mechanisms, *JSME International Journal*, 41(3), 476, 1998.
51. Nishiwaki, S., Frecker, M.I., Min, S., and Kikuchi, N., Topology optimization of compliant mechanisms using the homogenization method, *International Journal for Numerical Methods in Engineering*, 42(3), 535, 1998.
52. Hetrick, J.A., Kikuchi, N., and Kota, S., Robustness of compliant mechanism topology optimization formulation, proceedings of the 1999 Smart Structures and Materials: Mathematics and Control in Smart Structures, *Proc. SPIE Conference*, 3667, 244, 1999.
53. Hetrick, J.A. and Kota, S., Energy formulation for parametric size and shape optimization of compliant mechanisms, *ASME Journal of Mechanical Design*, 121(2), 229, 1999.
54. Sigmund, O., On the design of compliant mechanisms using topology optimization, *Mechanics of Structures and Machines*, 25(4), 493, 1997.
55. Tai, K. and Chee, T.H., Design of structures and compliant mechanisms by evolutionary optimization of morphological representations of topology, *ASME Journal of Mechanical Design*, 122, 560, 2000.

56. Saxena, A. and Ananthasuresh, G.K., Topology synthesis of compliant mechanisms for non-linear force–deflection and curved path specifications, *ASME Journal of Mechanical Design*, 123, 33, 2001.
57. Giurgiutiu, V. and Rogers, C.A., Power and energy characteristics of solid-state induced-strain actuators for static and dynamic applications, *Journal of Intelligent Material Systems and Structures*, 8(9), 738, 1997.
58. Moulson, A.J. and Herbert, J.M., *Electroceramics: Materials, Properties, Applications*, Chapman & Hall, London, 1991.
59. Haertling, G.H., Ferroelectric ceramics: history and technology, *Journal of the American Ceramic Society*, 82(4), 797, 1999.
60. Li, G., Furman, E., and Haertling, G.H., Stress-enhanced displacements in PLZT rainbow actuators, *Journal of the American Ceramic Society*, 80(6), 1382, 1997.
61. Li, X., Shih, W.Y., Aksay, I.A., and Shih, W.-H., Electromechanical behavior of PZT-brass unimorphs, *Journal of the American Ceramic Society*, 82(7), 1753, 1999.
62. Li, X., Artuli, J.S., Milius, D.L., Aksay, I.A., Shih, W.-Y., and Shih, W.-H., Electromechanical properties of a ceramic d_{31}-gradient flextensional actuator, *Journal of the American Ceramic Society*, 82(7), 1753, 1999.
63. Park, S.-E. and Shrout, T.R., Ultrahigh strain and piezoelectric behavior in relaxor based ferroelectric single crystals, *Journal of Applied Physics*, 82(4), 1804, 1997.
64. Clephas, B. and Janocha, H., New linear motor with hybrid actuator, *Proc. SPIE Conference*, 3041, 316, 1997.
65. Kornbluh, R., Eckerle, J., and Andeen, G., Electrostrictive polymer artificial muscle actuators, paper presented at the International Conference on Robotics and Automation, ICRA98, Leuven, Belgium, 1998.
66. Pelrine, R., Kornbluh, R., Joseph, J., Heydt, R., Pei, Q., and Chiba, S., High-field deformation of elastomeric dielectrics for actuators, *Materials Science and Engineering, Series C*, 11, 89, 2000.
67. Otsuka, K. and Wayman, C.M., Eds., *Shape Memory Materials*, Cambridge University Press, London, 1998.
68. Monkman, G.J., Advances in shape memory polymer actuation, *Mechatronics*, 10, 489, 2000.
69. Howe, D., Magnetic actuators, *Sensors and Actuators, Series A: Physical*, 81, 268, 2001.
70. Guckel, H., Micromechanisms, *Philosophical Transactions of the Royal Society: Physical Sciences and Engineering, Series A*, 1703, 355, 1995.
71. Cao, L., Mantell, S., and Polla, D., Design and simulation of implantable medical drug delivery system using microelectromechanical systems technology, *Sensors and Actuators, Series A: Physical*, 94, 117, 2001.
72. Roberts, D.C. et al., A high-frequency, high-stiffness piezoelectric actuator for microhydraulic applications, *Sensors and Actuators, Series A: Physical* (in press).
73. Quandt, E. and Ludwig, A., Magnetostrictive actuation in microsystems, *Sensors and Actuators, Series A: Physical*, 81, 275, 2000.
74. Garnier, A. et al., Magnetic actuation of bending and torsional vibrations for two-dimensional optical-scanner application, *Sensors and Actuators, Series A: Physical*, 84, 156, 2000.
75. Khoo, M. and Liu, C., Micro magnetic silicone elastomer membrane actuator, *Sensors and Actuators, Series A: Physical*, 89, 259, 2001.
76. Maekoba, H. et al., Self-aligned vertical mirror and V-grooves applied to an optical switch: modeling and optimization of bi-stable operation by electromagnetic actuation, *Sensors and Actuators, Series A: Physical*, 87, 172, 2001.

77. Butefisch, S., Seidemann, V., and Buttgenbach, S., Novel micro-pneumatic actuator for MEMS, *Sensors and Actuators, Series A: Physical* (in press).
78. Liew, L.-A., Tuantranont, A., and Bright, V.M., Modeling of thermal actuation in a bulk-micromachined CMOS micromirror, *Microelectronics Journal*, 31, 791, 2000.
79. Jeong, O.C. and Yang, S.S., Fabrication of a thermopneumatic microactuator with a corrugated p+ silicon diaphragm, *Sensors and Actuators, Series A: Physical*, 80, 62, 2002.
80. Minett, A. et al., Nanotube actuators for nanomechanics, *Current Applied Physics*, 2, 61, 2002.
81. Chan, H.B. et al., Quantum mechanical actuation of microelectromechanical systems by the Casimir force, *Science*, 29(5510), 1941, 2001.
82. McGeough, J.A., *Advanced Methods of Machining*, Chapman & Hall, London, 1988.
83. Hatschek, R.L., EDM update '84, *American Machinist*, March, 113, 1984.
84. Xiaowei, L., Zhixin, J., Jiaqi, Z., and Jinchun, L., A combined electrical machining process for the production of a flexure hinge, *Journal of Materials Processing Technology*, 71, 373, 1997.
85. Henein, S., Aymon, C., Bottinelli, S., and Clavel, R., Fatigue failure of thin wire-electrodischarge machined flexible hinges, proceedings of the 1999 Microrobotics and Microassembly, *Proc. SPIE Conference*, 3834, 110, 1999.
86. Madou, M., *Fundamentals of Microfabrication*, CRC Press, Boca Raton, FL, 1997.
87. Lang, W., Reflexions on the future of microsystems, *Sensors and Actuators, Series A: Physical*, 72, 1, 1999.
88. Ehrfeld, W. and Ehrfeld, U., Progress and profit through micro technologies: commercial applications of MEMS/MOEMS, in Reliability, Testing, and Characterization of MEMS/MOEMS, *Proc. of SPIE Conference*, 4558, 2001.

7

Applications of Flexure-Based Compliant Mechanisms

The preface to this book, as well as Chapter 1, underscored the importance of the increase in industrial applications that incorporate flexure hinges and flexure-based compliant mechanisms. The automotive, aeronautical, computer, telecommunications, optical, and medical industries, to name just a few, are utilizing both macroscale and microscale (microelectromechanical systems, or MEMS) compliant mechanisms in their applications. Presented here are a few application examples drawn from the multitude of flexure-based compliant mechanisms. The selection represents just a very small portion of the array of available applications and was definitely influenced by the ability to obtain reproduction permission as well as by subjectivity; therefore, apologies are extended, in advance, for the inevitable omissions. The chapter first describes several macroscale flexure-based compliant mechanisms and concludes with another section that is dedicated to examples from the MEMS world.

7.1 Macroscale Applications

The examples of macroscale flexure-based compliant mechanisms presented in this section are based on either actual photographs of the designs (when permission was obtained) or schematic line drawings, where the intention is to emphasize principles of operation that are common to several mechanism configurations.

The simplest flexure-based compliant mechanism is, naturally, the one that is composed of a single flexure hinge, as pictured in Figure 7.1. The relatively long flexure is constructed of carbon-based composite material with 60% fiber volume to ensure good thermal stability in addition to general high stiffness. The aspect ratio of the flexure was selected as shown in Figure 7.1 in order to complement the material elastic properties and to achieve very low lateral stiffness (in bending about the sensitive axis) and very high axial

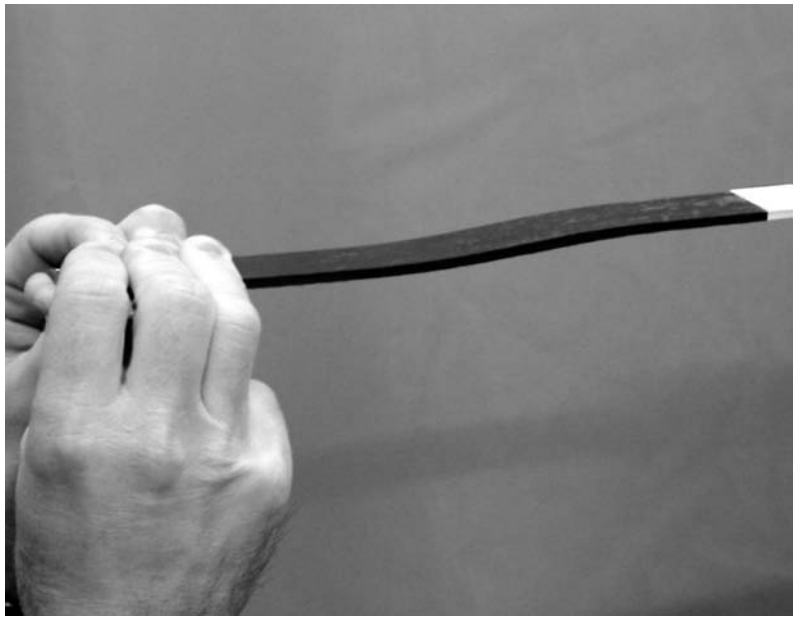

FIGURE 7.1
Composite flexure hinge for high lateral stiffness application. (Courtesy of Foster-Miller.)

stiffness such that the part could produce a precise lateral translation of another component.

The schematic of an optical mount is sketched in Figure 7.2, and the application serves as a device that allows orientation of an optical component (generally a mirror) that is fixed on the output plate. The two strip flexures are rather wide in this type of application to ensure low sensitivity in both torsion and bending about the nonsensitive axis. Basically, the device is a spatial serial compliant mechanism that is formed of three rigid links and two flexure hinges and operates by actuating the middle and output plates to produce a rotary motion with two degrees of freedom (DOFs) at the output plate. A downside of this design configuration is its thermal sensitivity, which, ironically, is created by the flexure hinges themselves, which are rather prone to thermal deformations; this aspect reduces the capacity of producing precise motion at the output port.

Precision flexure-based compliant mechanisms are frequently used in positioning/aligning applications in the optical, telecommunications, photonics, and laser industries where output motions at the nanometer or sub-nanometer levels are required. Tolbert[1] presented specific aspects of utilizing nano-alignment and nano-positioning in photonics manufacturing and discussed the primary factors that have an impact on these processes, such as resolution, repeatability, stability, automation, and software control. Basically, two motion modules can be designed and combined in various configurations

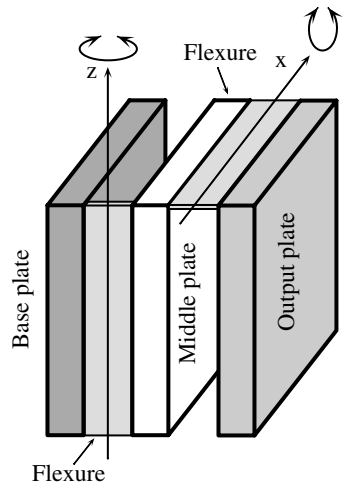

FIGURE 7.2
Optical mount as a two-DOF spatial serial flexure-based compliant mechanism.

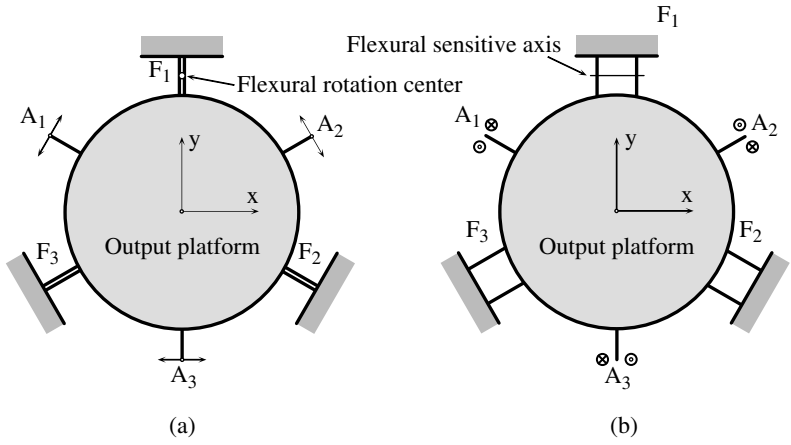

FIGURE 7.3
Flexure-based stages for precision positioning/alignment: (a) three-DOF planar mechanism; (b) three-DOF spatial mechanism.

in order to achieve high-precision motion capability at the output port; Figure 7.3 illustrates these two basic devices. The mechanism shown in Figure 7.3a, also known as an $xy\theta$ stage, is a planar parallel minimum configuration that can create two-dimensional motion. By combining the input of the three actuators, A_1, A_2, and A_3, it is possible to obtain individual translations about two arbitrary directions x and y, as well as pure rotation about an instantaneous center of rotation or other types of prescribed-path motions. The flexural chains, F_1, F_2, and F_3, are represented as single-flexure units but

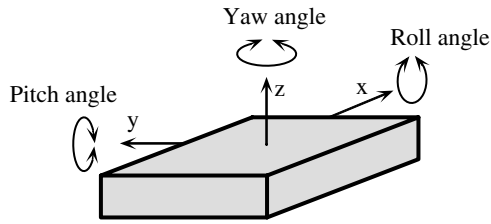

FIGURE 7.4
Output platform for spatial mechanism with main rotation angles.

they actually can encompass several flexures and rigid links in different topologies. Figure 7.3b shows the main features of another basic design that creates out-of-plane motion. In this case, the actuation must have components that are perpendicular to the plane of the output platform, as indicated in Figure 7.3b, in order to move this plate out of its own plane. In the situation pictured in Figure 7.3a, the flexure hinges are arranged with their sensitive axes perpendicular to the plane of the output platform, but for the compliant mechanism of Figure 7.3b the flexure hinges have their sensitive axes parallel to the plane of the output platform in order to produce the desired out-of-plane motion component. Similar to the distinct motions that the $xy\theta$ stage can generate, the stage of Figure 7.3b (also called a z stage) is capable of outputting a pure translation about the z axis and rotations about two arbitrary axes lying in the plane of the output platform or other mixed motions as a result of various combinations of these three basic motive options.

Each of the two compliant mechanisms described here behave as three-DOF systems, and their combination results in configurations that are capable of spanning the full six-dimensional space. An output platform that is actuated by such a six-DOF mechanism is illustrated in Figure 7.4, together with the roll, pitch, and yaw angles that are customarily used to specify the angular position of the output link.

Several designs shown in the following section of this chapter illustrate various configurations and output capabilities. Figure 7.5, for instance, shows a planar serial compliant device that serves to amplify the input motion from a piezoelectric stack actuator through two stages so that the output motion is parallel to the input motion. This mechanism contains both symmetric and nonsymmetric corner-filleted flexure hinges arranged with their longitudinal axis either parallel or perpendicular to the actuation source.

The planar hybrid amplification compliant mechanism pictured in Figure 7.6 presents a double symmetry. Nonsymmetric corner-filleted flexure hinges are employed in this configuration to amplify the input motion from two serially connected stack actuators to an output direction which is perpendicular to the input one. The stack actuators are precompressed by a wire, which also acts as a return spring.

Figure 7.7 shows a design that is a real-life application of the schematic representation of the $xy\theta$ stage of Figure 7.3b. The three stack actuators

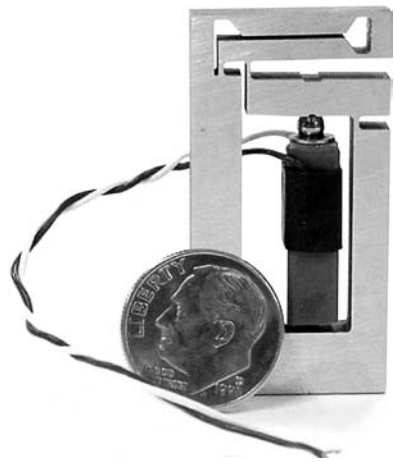

FIGURE 7.5
Two-stage planar serial flexure-based compliant mechanism with piezoelectric actuation. (Courtesy of Dynamic Structures and Materials.)

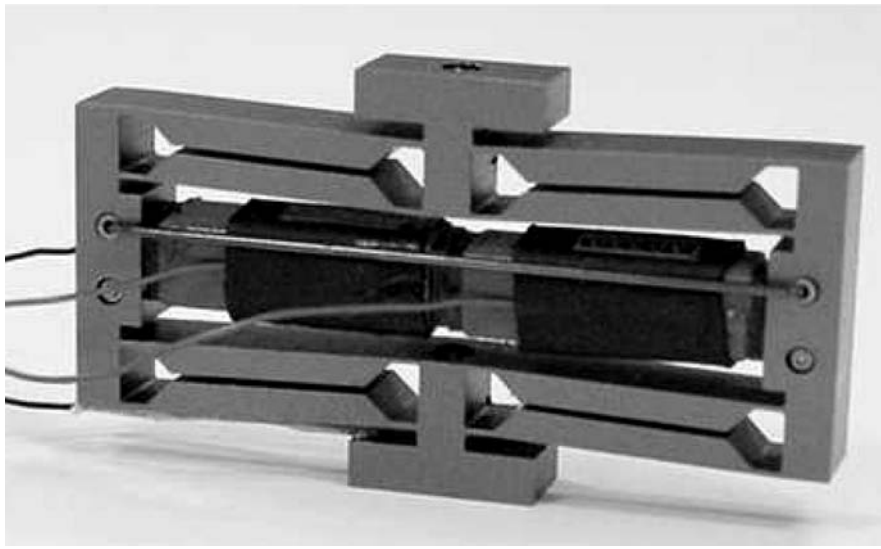

FIGURE 7.6
Planar hybrid amplification mechanism with piezoelectric actuation. (Courtesy of Dynamic Structures and Materials.)

provide the input motion through identical serial flexure-based chains that are designed to amplify the input. Various combinations of the actuator motion can produce different output paths.

The spatial flexure-based design illustrated in Figure 7.8 is of the type that has been described based on the principle drawing of Figure 7.3b. The input

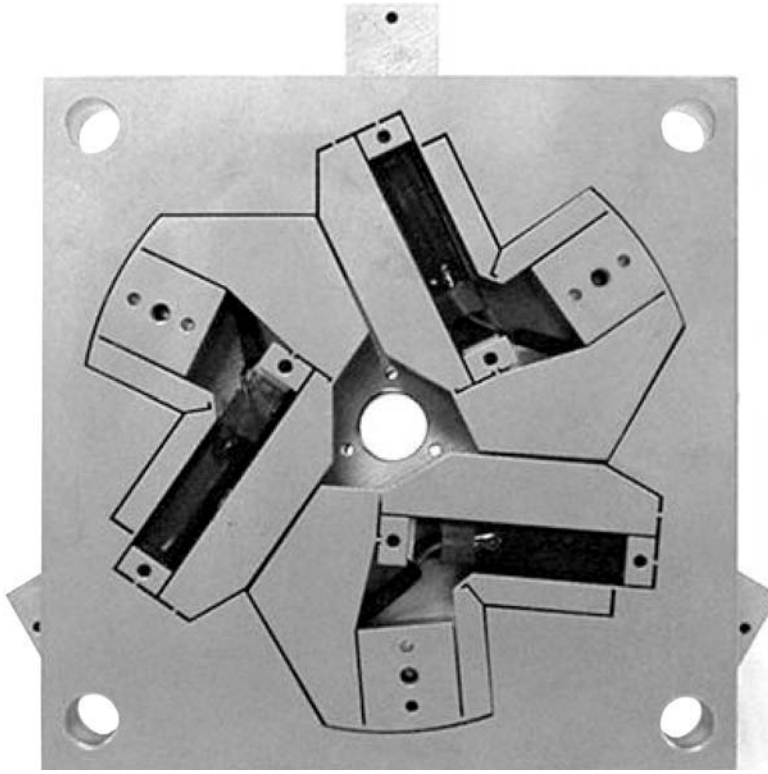

FIGURE 7.7
Three-actuator, planar, hybrid flexure-based platform for $xy\theta$ positioning. (Courtesy of Dynamic Structures and Materials.)

to this mechanism is the linear amplified motion generated from three piezo-driven devices of the type pictured in Figure 7.6. Identically actuating the three input units produces a purely vertical translation; inputing different motions from the three actuators results in a mixed output motion. The three stages of triangular rigid links shown in Figure 7.8 are interconnected by means of wire-like cylindrical flexure hinges that can handle bending, axial loading, and torsion.

The literature to date mentions various other flexure-based compliant mechanism configurations, and a few examples are mentioned next. Park et al.[2] presented the design of a compact displacement accumulation device (of the inchworm type) that has large displacement and force capabilities. King and Xu[3] designed two prototype piezoelectric-actuated flexure-based amplification mechanisms that serve as the basis for analysis regarding the performance of piezomotors. Xu and King[4] compared the performance of compliant mechanisms that are constructed by incorporating different types of flexure hinges such as circular, corner-filleted, and elliptical. Ryu et al.[5] developed a flexure-based $xy\theta$ stage that is actuated by three stack actuators.

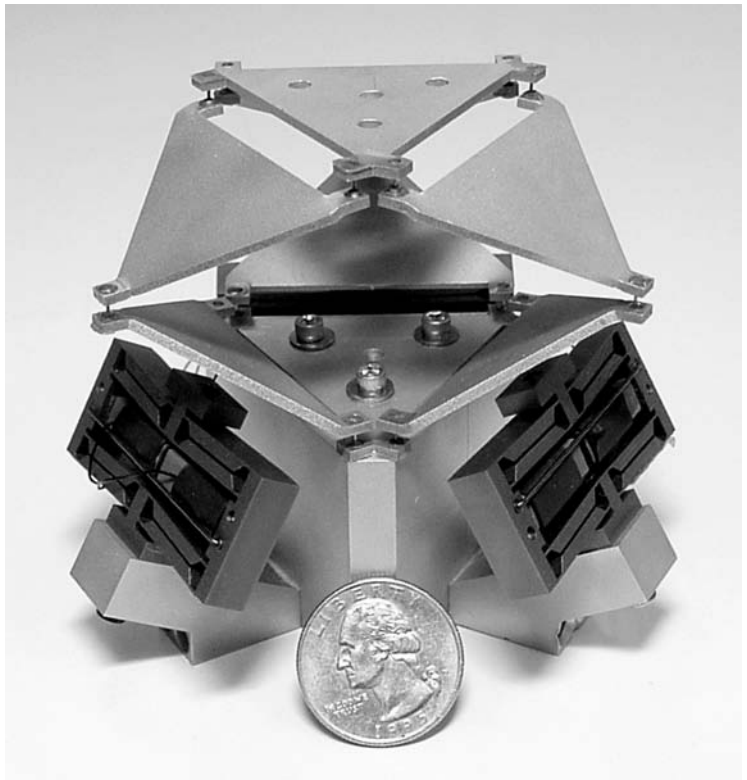

FIGURE 7.8
Spatial hybrid flexure-based compliant mechanism for complex positioning. (Courtesy of Dynamic Structures and Materials.)

A parameterized mathematical model of the static response of the mechanism was formulated that serves as a tool for performance optimization simulations. Renyi et al.[6] presented the design and characterization of a piezo-driven micropositioning stage utilizing an amplification chain that transforms the horizontal input motion into a vertical one at the output port. Chen et al.[7] designed and tested a flexure-based stage that is utilized to position a system of mirrors in synchrotron x-ray equipment. Choi et al.[8] presented the design of orientation stages that are employed in high-resolution step-and-flash imprint lithography machines.

Figure 7.9 illustrates a possible implementation of another flexure-based design that is utilized in suspensions, gyroscopes, and couplings allowing for misalignments of z stages of the type sketched in Figure 7.3b. The cylinder of Figure 7.9 is hollow, and the flexure hinges (which are symbolically represented) are realized by wire-EDM, for instance. The two axially opposite sections of the tube can move, one relative to the other, as this type of motion is enabled by the flexure hinges. Figure 7.10 illustrates a design based on

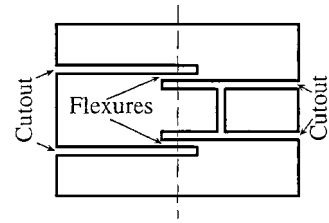

FIGURE 7.9
Flexure-based cylinder for out-of-plane operation.

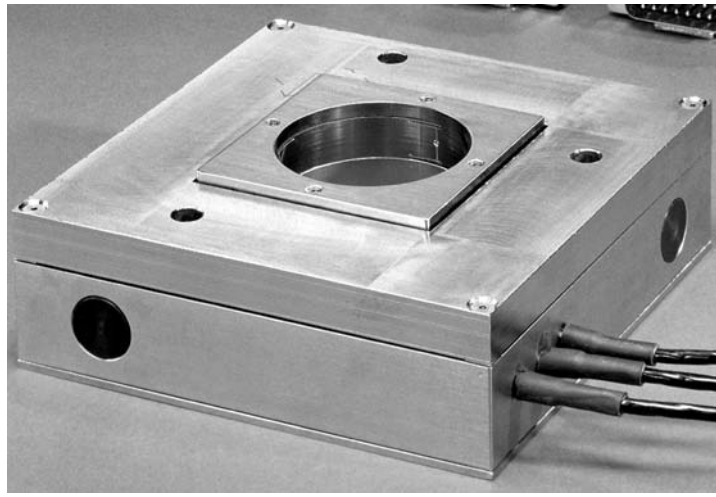

FIGURE 7.10
The z stage for out-of-plane positioning. (Courtesy of Piezomax Technologies.)

this principle and which can be utilized as a z stage mechanism of the type sketched in Figure 7.3b.

Another group of flexure-based compliant mechanisms includes the so-called flexural pivots or bearings that were first described and modeled by Weinstein.[9] Figure 7.11a shows the operating principle of a flexural pivot that is designed to produce limited relative rotation between two split tubes that are concentric. The flexure strip attaches to each of the two split tubes at its ends and, through flexing (which ideally occurs about the midpoint of the flexure that is collocated with the center of the two tubes), one tube can rotate with respect to the other. Two or more flexure hinges can be utilized and spaced axially in order to increase the load capacity of this system. Figure 7.11b shows another design of a flexural pivot that makes possible relative rotation between the base and the mobile part through either bending or torsion of the connecting flexure hinge. The cross-axis flexural pivot is illustrated in Figure 7.11c, and a modeling of its behavior was developed by Smith[10] and Jensen and Howell.[11]

Figure 7.12 provides a representation of a load cell that utilizes the Free-Flex® pivot developed at TRW Aeronautical Systems. This pivot is based on the

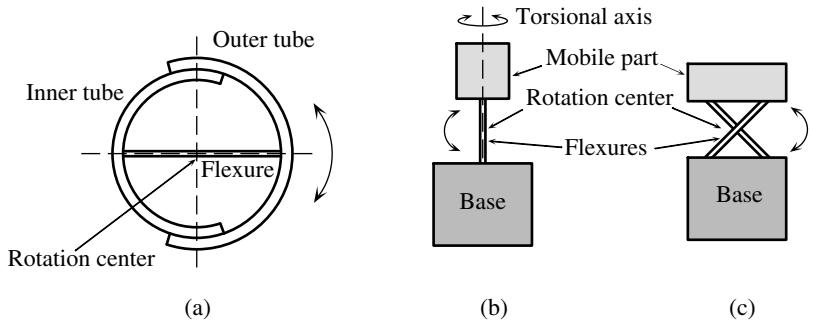

FIGURE 7.11
Flexural pivot design variants: (a) relative-rotation configuration with bending of the single flexure; (b) relative-rotation with bending/torsion of the single flexure; (c) cross-axis flexural pivot.

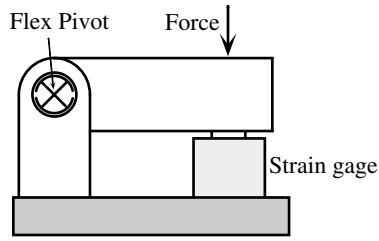

FIGURE 7.12
Load cell with Free-Flex® Pivot. (Adapted from TRW Aeronautical Systems.)

schematic of Figure 7.11 and incorporates two flexure hinges that are 90 degrees apart and also spaced axially.

Another variant of the flexural pivot, designed and modeled by Goldfarb and Speich,[12] is referred to as a split-tube flexure and is capable of producing a large relative rotation between its ends by accommodating both bending and torsion of its compliant sections.

An interesting application of the flexure hinge is presented by Carlson et al.,[13] who developed a double short flexure-type orthotic ankle joint to be used as a prosthesis. The design has the advantage that it is almost insensitive to axial and torsional loads and therefore is highly stable.

7.2 Microscale (MEMS) Applications

Several applications illustrating the use of flexure hinges and flexure-based compliant mechanisms in MEMS are presented in this section of the chapter. The applications are separated into single- and multiple-flexure compliant configurations.

7.2.1 Single-Flexure Microcompliant Mechanisms

7.2.1.1 Microcantilevers

Microcantilevers were originally utilized as ultra-precise means of sensing forces in atomic force microscopy (AFM). With dimensions that can go down to the micron level, this type of sensor is compact and lightweight and requires low levels of energy for operation. In AFM applications, as shown in Figure 7.13a, a tip is usually attached at the free tip of the cantilever in order to minimize the friction surface.

Several cantilever configurations are actually in operation, and Figure 7.13b–d illustrates a few of them. The most widely used geometry is the rectangular one shown in Figure 7.13b. A triangular configuration is shown in Figure 7.13c; the hollow variant is shown, but the solid configuration is also possible, especially in practical applications where it is expected that the cantilever will experience constant stresses along its length. The triangular shape is adopted in cases where torsional effects might have to be minimized in order not to blur the main bending operation mode of the cantilever. Figure 7.13d

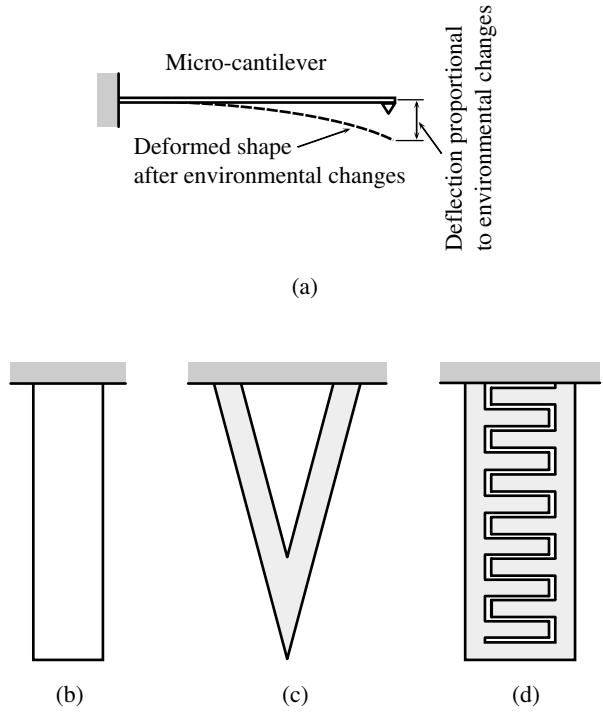

FIGURE 7.13
Operation and main geometry configurations of microcantilevers: (a) side view; (b) top view of rectangular configuration; (c) top view of triangular configuration; (d) top view of interdigitated configuration.

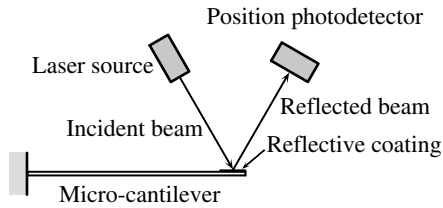

FIGURE 7.14
Principle of optical measurement with microcantilever.

shows a possible implementation of an interdigitated cantilever that is being used for optical measurements by means of diffraction.

As illustrated in Figure 7.14, the optical method of measuring the small tip deflections of microcantilevers usually consists of sending an incident light beam to the tip of a microcantilever, where a reflective coating is deposited in order to enable reflection of the incident light on a position photodetector device. The tip deflection of the microcantilever is monitored by the detection device in a proportional manner. According to the technique of capturing the reflected light beam, three different optical methods of measuring the tip deflection are available: the optical lever deflection method, where the reflected light beam is recorded by a photodetector device; the interferometric method, which reads an interference pattern created by the reflected light beam and another beam sent directly from the light source; and the diffraction-pattern method, which reads the diffraction created by means of an interdigitated microcantilever, similar to the one shown in Figure 7.13d.

In addition to the optical methods of measuring the tip deflection of microcantilevers, which are capable of sub-Angstrom resolutions, electrical principles and methods are also utilized for the same purpose. As mentioned by Raiteri et al.,[14] the microcantilever can operate as a capacitive transducer, as it can serve as the mobile armature of a capacitor whose capacitance varies through bending of the microactuator. The bending can also be quantified by electroresistive means when a resistive pattern is transferred on the microcantilever to sense deformations based on the Wheatstone bridge (strain gauge) principle. Another way of electrically monitoring the deformations of microcantilevers is to apply a piezoelectric film on the transducer such that the mechanical deformations of the compound sensor will be transformed in electrical signals through the associated piezoelectric effect.

The microcantilevers can be utilized either in static (quasi-static) mode, when the static deflections are measured, or in an oscillating mode, when the monitored quantity is the natural frequency of the vibrating system. Apart from being used as force sensors in (mainly) AFM applications, microcantilevers are also implemented in several other applications. A microcantilever can be conditioned to act as a thermal sensor by depositing a metal layer and taking advantage of the difference in thermal expansion coefficients between the component materials that force the microcantilever to

deflect upon absorbtion of thermal energy, as detailed in the discussion on actuation. Thermal sensitivity of bi-material microcantilever beams can be of the order of 10^{-5} K (see, for example, Raiteri et al.[14] and Oden et al.[15]). Other applications of microcantilevers in the thermal domain include calorimetry and photothermal spectroscopy of thin coats, where the sensor is capable of discerning energy levels down to atto-Joules. In phase-change situations, the microcantilevers are capable of detecting enthalpy changes of 500 pico-Joules for picogram quantities that adhere to the tip of the sensor.

The microcantilever can also be implemented for detection of the presence of very small quantities of material by monitoring changes in the vibratory response of the system. Small amounts of external damping can also be identified based on the same change in the natural frequency, in which case the microcantilever functions as a damping sensor. Oden et al.[15] describe a microcantilever application where the infrared (IR) radiation can be detected by means of the piezoelectric effect. The piezoelectric layer deposited over a silicon microcantilever beam reacts to the thermal energy gained upon IR exposure, and the composite beam bends, which causes a change in piezoresistance proportional to the absorbed heat. The authors conclude that utilizing such microcantilevers arranged in two-dimensional arrays may constitute an adequate tool for remote IR sensing.

In similar research, Wachter et al.[16] investigated the response of composite microcantilevers to both visible and mid-IR radiation that was frequency modulated by utilizing AFM measurements and several types of commercially available microcantilever configurations. Miyahara et al.[17] presented the design and testing of a piezoelectric microcantilever for AFM applications that integrates the functions of deflection sensing, actuation, and feedback. The system can be utilized successfully, according to the authors, in extreme environments such as low temperature or low vacuum, and it demonstrated atomic step resolution when tested on annealed alumina test surfaces. Lu et al.[18] analyzed surface effects on the mechanical (frequency) response of microcantilevers. Specifically, they investigated the changes in the natural frequency of a coated microcantilever as induced by surface stresses and the so-called Q factor.

The study demonstrated that the Q factor can be increased by placing the coating layer toward the tip of the vibrating beam and that surface stresses, such as those created in biosensing applications, will modify the natural frequency by either increasing it (for tensile stresses) or decreasing it (for compressive stresses).

The field of biosensing offers quite an impressive and spectacular range of applications. In a recent article, Raiteri et al.[14] discuss the implementation of microcantilevers in physical and biochemical detecting and sensing of very small amounts of materials. In these applications, the microcantilever must first be *functionalized*, which means that a receptor layer has to be deposited on one surface of the beam. This receptor layer is usually a noble material that should be thin enough (normally monolayer) so that it does not alter the mechanical characteristic of the microcantilever, but still sufficiently

strong as to be able to anchor incoming external material particles. This monolayer contains a substance that can act as marker and enable a specific reaction upon interaction with the external monitored agent. Upon capturing the foreign material, the mechanical properties of the microcantilever change and therefore can be detected by either static (modification of the tip deflection) or frequency (different natural frequencies) means. Raiteri et al.[14] also cite several biosensing applications that have used microcantilevers for detection or sensing. Applications include identifying the response to external agents of living cells that are directly cultured on microcantilevers, counting or weighing of bacteria absorbed by an antibody layer, and detection and quantification of markers for prostate cancer or of various herbicides. Equally spectacular is the report of DNA variation detection by means of the same microcantilevers. The DNA hybridization is monitored by measuring the differential deflection of two microcantilevers mounted in parallel in order to discriminate very slight differences in the DNA molecular structure.

Microcantilevers are also successfully implemented in disk data write/read applications, as discussed by Chui et al.[19] and Maluf.[20] Two geometrically similar but functionally different microcantilevers, each provided with a pointed tip at their free ends, are used for data writing (storage) and reading, respectively. The writing cantilever inscribes microindentations in a prescribed manner on a rotating polycarbonate disk by locally melting mini "craters" on it through tip vibrations. The reading microcantilever decodifies the information encoded in the already inscribed rotating disc piezoelectrically. The reading microcantilever must be more compliant than the writing microcantilever in order to be able to convert indentations of the order of a few tens of nanometers into a discernable electric signal output, and its mass must be almost meaningless in order to enable reading. Writing rates of 100 kbit/sec and reading rates three times higher were feasible with these write/read microcantilevers.

Another interesting application of microcantilevers, different from the sensing functions presented so far, is in nanoindentation, according to a procedure that has recently been introduced by the Veeco Metrology Group (Santa Barbara, CA). A diamond piece is placed at the free end of a microcantilever, and surface indentation followed by *in situ* measurement of the marks are performed to check hardness or durability and to investigate scratch and wearing properties of a vast array of materials from gold to films.

7.2.1.2 Scratch Drive Actuators and Buckling Beams

An interesting single-flexure microcompliant mobile structure is the scratch drive actuator (SDA), which was first presented in a paper by Akiyama et al.[21] It consists primarily of a thin flexible beam or plate attached to a reasonably rigid part, as illustrated in Figure 7.15. The entire system can be sustained laterally (out of plane in Figure 7.15) at the junction between the

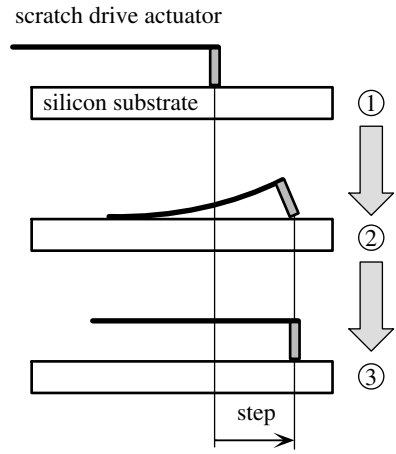

FIGURE 7.15
Three main positions of one motion step produced by a scratch drive actuator (SDA).

flexible sheet and the rigid part. A motion step has three main phases, as indicated in Figure 7.15. First, electrostatic forces are generated that attract the flexible sheet toward the silicon substrate. During this phase, the flexible sheet progressively bends until a portion of it is in full contact with the substrate. Because of the rigid connection between the sheet and its vertical leg and because of the elastic deformation sustained by the sheet, the leg is pushed forward in the inclined position (position 2 in Figure 7.15). By discontinuing the electrostatic actuation, the flexible sheet is released from its contact with the substrate, but the vertical leg/substrate friction force does not allow the leg to be dragged backwards; as a consequence, the entire SDA recovers its original shape and moves one step forward to the right (position 3 in Figure 7.15).

Akiyama et al.[21] utilized the SDA for self-assembly of three-dimensional MEMS in an attempt to avoid external manipulation. They tested an SDA prototype both in free motion and against a bias spring by running the device horizontally and then vertically. The microactuator was capable of producing maximum displacements of 150 μm. In a recent paper, Linderman and Bright[22] report the results of their optimization research, designing, constructing, and testing of SDA devices for nanometer-precision positioning. The optimized length of the flexible plate was first derived in terms of the driving voltage and then the other geometric parameters that define the SDA were correspondingly determined. Based on the theoretical analysis, a prototype array was constructed consisting of several SDAs powered by a gold wire tether. The resulting microrobot was capable of pushing a $2 \times 2 \times 0.5$-mm chip on a silicon substrate over an 8-mm distance.

Researchers at the Northern Higher Institute of Electronics (ISEN) in Villeneuve d'Ascq, France, as reported by Quevy et al.[23] and Bains,[24] have

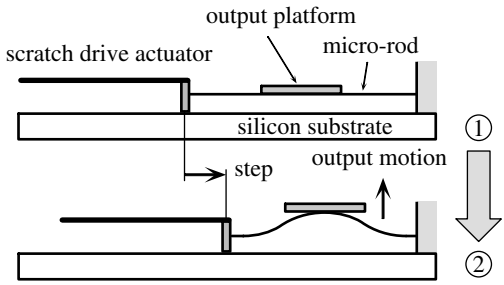

FIGURE 7.16
One application of the scratch drive actuator (SDA) coupled with a buckling microrod.

recently developed a similar SDA array that is aimed at self-assembly of microstructures. Unlike the rectangular shape of the flexible sheet utilized by Linderman and Bright,[22] the French researchers have designed a triangular SDA sheet. An interesting manner of realizing the SDA motion is to combine it with slender microrods (also called buckling beams), which can be placed against the motion of the actuators, as shown in Figure 7.16.

During the motion of one step, the compliant microrods buckle and therefore create the motion of the output platform (which can be a micromirror), which is attached at the midpoint of the buckling microrod. Because of the fixed–fixed boundary conditions, the middle portion of the microrod preserves its original slope, and, as a consequence, the output motion is a translatory one, perpendicular to the input actuator motion. As reported by Quevy et al.,[23] it was possible to lift the microplates 90 μm above the silicon substrate. Additional electrostatic actuation applied to the output platform can rotate it bidirectionally, with maximum angles of ±15°, as mentioned in Smith.[10] The SDA/microplate array was implemented into a microoptoelectromechanical system (MOEMS) in the form of a continuous membrane for adaptive optics applications.

7.2.1.3 Sensors, Accelerometers, and Gyroscopes

A large portion of the MEMS application pool is occupied by inertia-sensing microinstruments in various design configurations, such as sensors, accelerometers, and gyroscopes. Figure 7.17 illustrates two variants that are incorporated in linear devices based on two different detection principles. In the capacitive detection principle (illustrated in Figure 7.17a), the moving mass (which senses the variation in acceleration) moves closer or farther away from a fixed electrode and thus creates a variable gap that translates into a proportional charge or current. Another transduction principle (Figure 7.17b) utilizes a sensitive film that is directly deposited on the silicon cantilever which deforms under the action of the vibrating mass that is attached to it. The film

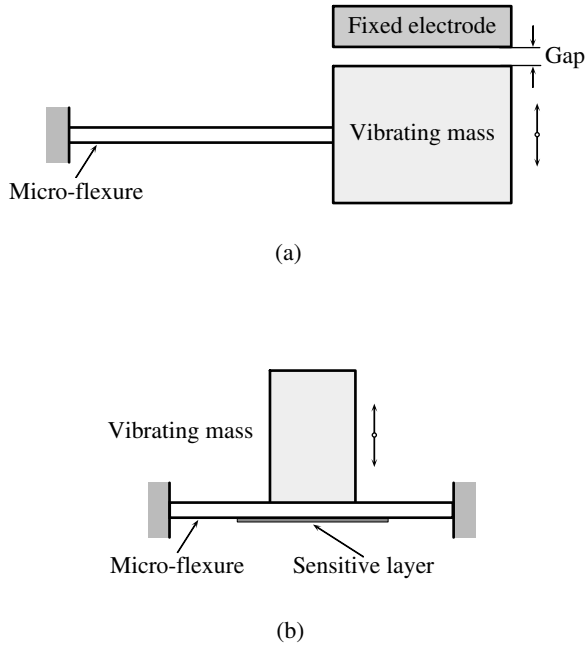

FIGURE 7.17
Inertia sensors: (a) capacitive sensor with fixed–free flexure configuration; (b) resistive sensor with fixed–fixed flexure configuration.

can be either an electrically resistive material or a piezoelectric layer that transforms the bending deformation of the cantilever into an electrical output.

Laine et al.[25] presented the design and performance of a microresonator that is conceived on the schematic of Figure 7.17a and can be applied in optical communications such as filtering, multiplexing, and switching. The vibrating mass is a microsphere that is fabricated by melting the tip of an optical fiber and thus presents the advantage of having a very low optical loss, which makes the device extremely useful in precise measurement tasks. Xiao et al.[26] developed a microaccelerometer with high resolution and linearity and large frequency bandwidth, based on the same detecting principle of Figure 7.17a, where the transduction is capacitive for low-gravity measurement applications.

Aikele et al.[27] constructed a resonant microaccelerometer with thermal excitation consisting of a fixed–fixed beam coupled on a seismic mass, based on the principle illustrated in Figure 7.17b. The microsystem demonstrates robustness, shock resistance, and low sensitivity to parasitic vibrations, attributes that make it a suitable solution in automotive applications. Fujita et al.[28] presented the design of a microgyroscope consisting of four units of the form shown in Figure 7.17a, where the microcantilevers are connected at a central point and the seismic masses extend radially and outwards. The resulting system is utilized for measuring Coriolis accelerations by

detecting the capacitive change between the vibrating masses and their corresponding fixed electrodes in applications such as devices for motion compensation in video cameras or for automobile chassis control.

The operation principle illustrated in Figure 7.17b was implemented by Varadan et al.[29] in a microaccelerometer device to be used in interdigital transducer (IDT) devices for surface acoustic wave (SAW) sensing applications. Li et al.[30] designed a microsensor for angular rate sensing purposes that uses the construction shown in Figure 7.17a, with a special cantilever that is more compliant than regular microflexures and therefore has a higher sensitivity in capturing the angular acceleration.

7.2.1.4 Other Single-Flexure Microcomponents

Figure 7.18 illustrates two other microcomponents that may be regarded as single flexures in compliant micromechanisms. The ribbon (flexible) beam element of Figure 7.18a is fixed at both ends on a silicon substrate and is sufficiently long and thin to bend under the electrostatic attraction forces produced by an electrically active film deposited on the silicon. In a non-actuated situation, the ribbon beam, which is covered with a light-reflective layer, will preserve the angle of incidence of incoming light (position 1 in Figure 7.18a), but when electrostatic actuation is applied the ribbon will bend and contact the silicon substrate according to the location of the area being actuated. An array of such ribbon beams is utilized to create the so-called grating light valve, which is actually a surface with variable optical properties (see Maluf[20]) that uses the principle of light diffraction created by the gaps between adjacent ribbons. In a non-actuated state, the surface is viewed normally, but when a specific actuation is applied to individual ribbons a diffraction pattern is created because of the modified gaps, and different shades of gray can be selectively created. The principle can be implemented in gray or full-color display.

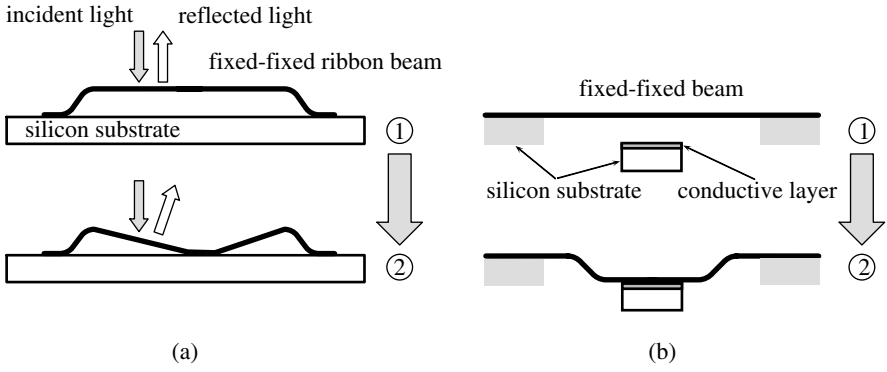

FIGURE 7.18
Operation sequence of a fixed–fixed ribbon flexure: (a) grating light valves application; (b) microswitch application.

Figure 7.18b shows a physically similar application of a bridge microfabricated in the form of a thin metallic fixed–fixed beam. Such a microcomponent can be utilized as a radiofrequency (RF) capacitive switch, as noted in the paper by Huang et al.,[31] who presented the mechanical design and optimization of a capacitive microswitch. An electrode is placed immediately beneath the bridge on the silicon base substrate. In the non-actuated position (position 1 of Figure 7.18b), the beam is undeflected and therefore works accordingly in the circuit it is a part of. When the electrode is actuated, the beam deflects toward it because of the electrostatic forces, and the resulting motion will cause the beam to touch a contact such that the switching function is accomplished.

Another application that utilizes the fixed–fixed cantilever shown in Figure 7.18b is the resonant beam filter, which is a valuable device for communication systems. The operation principle of a resonant beam filter is based on actuating the silicon cantilever at resonance which will generate an electric signal that can be used in filtering another input signal. The double action of actuating and transducing by means of the resonant filter is generally performed electrostatically, but in a recent paper Piekarski et al.[32] present a design that utilizes the piezoelectric effect for both sensing and actuation. A silicon cantilever is sandwiched between two piezoelectric film layers, and drive voltage that is fed to the piezoelectric layers induces strains in the cantilevers that generate bending moments. At resonance, the bending moment is maximum and produces through the piezoelectric effect a current that can be used in the filtering circuit.

Two other one-component flexible microconnectors are illustrated in Figure 7.19a and b. Figure 7.19a shows a serpentine wire spring utilized as a return spring in MEMS applications—for instance, in the scratch drive actuators implemented in the description presented by Quevy[23] and Bains.[24] The design is more efficient than a simple flexural microbeam, for instance, because it has more flexibility packed in a smaller volume and is mostly utilized for

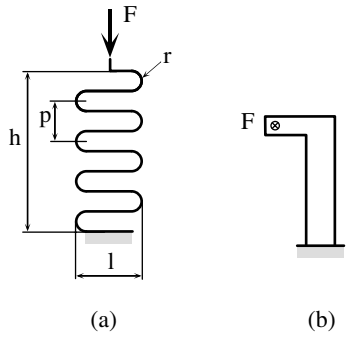

FIGURE 7.19
Two configurations of single-member flexible connectors: (a) serpentine wire functioning as compression/extension spring; (b) two-sided torsional flexure hinge.

creating compression and extension compensating resistance. The same configuration can function as a torsional spring by making it plane. The simplest torsional spring is a straight constant rectangular cross-section flexure hinge, similar to the ones discussed so far. A modification to this configuration that makes it fit for applications where two rigid members must be torsionally connected when their rotation axes are perpendicular is a two-sided, constant-thickness flexure, as shown in Figure 7.19b and is discussed by Park et al.[33]

7.2.2 Multi-Flexure Compliant Micromechanisms

Almost all MEMS produce their specific motion by means of flexible connectors that are monolithically built together with the rigid mobile parts, and the vast majority of the connectors are flexure hinges. The most common MEMS configurations are essentially two dimensional. Even in geometrically three-dimensional cases (characterized by high aspect ratios) that are permitted by dedicated MEMS technologies such as LIGA or DRIE, the flexure hinges are of prismatic construction. They mainly and ideally function in torsion and/or bending, as illustrated in Figure 7.20.

In practical situations, of course, the loading is not so purely and distinctively defined because axial loading and possibly shearing are also present and (although with probably small effects) they can superimpose over the main torsion and bending of flexure hinges. Several specific applications are briefly presented next that illustrate the use of flexure hinges as torsional or bending connectors in MEMS.

Tilt or torsional mirrors are designed based on the functional principle illustrated in Figure 7.20a, where the motion of the micromechanism is realized by the torsion of two aligned flexure hinges. Figure 7.21 provides an overall view of a two-axis tilt mirror designed and fabricated by MEMS Optical, Inc. and Figure 7.22 shows a close-up view of one of the flexure hinges of the micromechanism. The mirror plate is approximately octagonal. The inner hinges provide rotation of the mirror about a horizontal axis, whereas the outer hinges allow rotation of the gimbal and mirror together about an axis

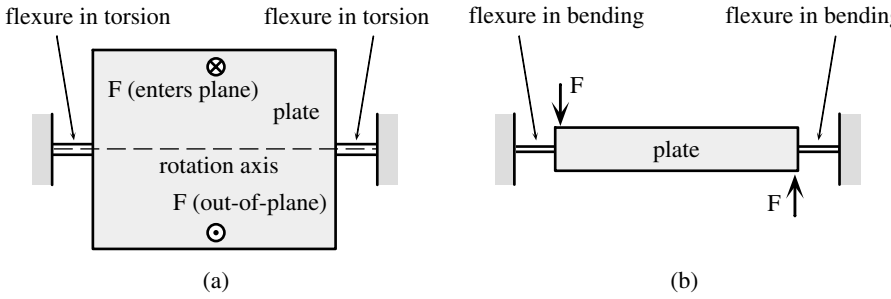

FIGURE 7.20
Main functions of flexure hinges in compliant micromechanisms: (a) torsional flexures; (b) bending flexures.

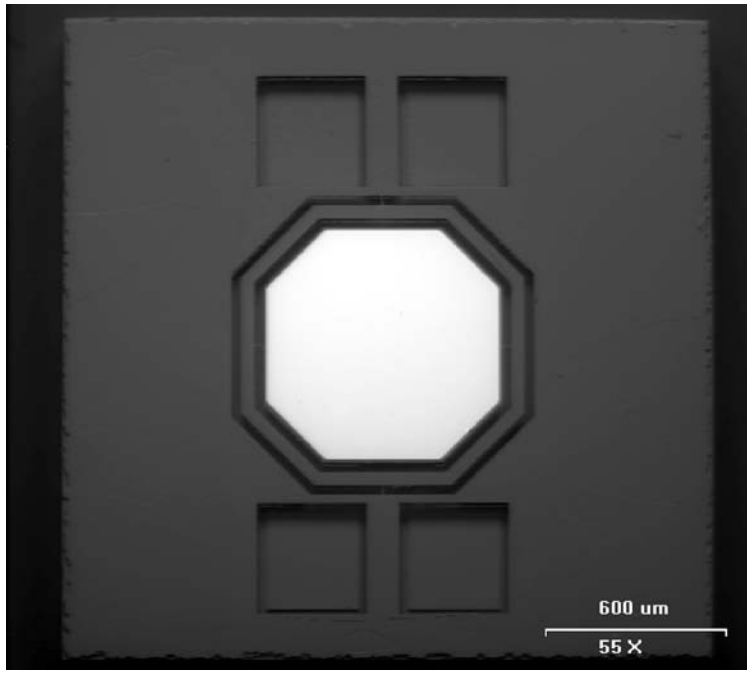

FIGURE 7.21
Overall picture of a two-axis tilt mirror. (Courtesy of MEMS Optical, Inc.)

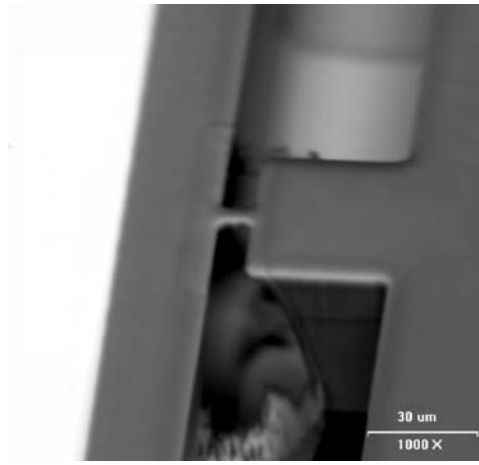

FIGURE 7.22
Close-up view of corner-filleted flexure hinge utilized in the two-axis tilt mirror. (Courtesy of MEMS Optical, Inc.)

perpendicular to the first one, such that the micromirror plate has two degrees of freedom. Four electrodes under the mirror enable actuation about each of the two rotation axes in a bidirectional fashion. The corner-filleted flexure hinges are designed to be compliant enough to allow rotation below a maximum voltage (approximately 80 V for this mirror), while keeping the hinge stress below the failure limit. Resistance to vibrational shock is also a concern with this design.

Another application based on the basic design of the two-flexure torsional plate design of Figure 7.20a is the radiofrequency (RF) capacitive switch, which was also mentioned in Chapter 6. Compared to the semiconductor switches, the RF MEMS switches have the advantages of low resistive losses, low power consumption, and good electrical isolation. Park et al.,[33] for instance, presented several RF microswitch configurations in terms of flexure geometry, overall topology of the micromechanism, materials utilized to realize the device, and microfabrication techniques. A similar RF microswitch that can be integrated with the actuation circuitry was introduced by Plotz et al.[34] Preliminary simulation has been performed by means of dedicated software, and the dynamic performance of the prototype design has been tested interferometrically. A modeling procedure for an RF MEMS switch was proposed by Sattler et al.[35] whereby the dynamic response of the one-DOF single-axis tilt plate is formulated in terms of the relevant design parameters describing the material and geometry properties. Sampsell[36] has provided an interesting presentation of the application of torsional plate principles to digital micromirror devices (DMDs) as spatial light modulators and their integration into projection display systems. Zhang et al.[37] developed a theoretical model of the static behavior of an electrostatically actuated torsional micromirror by utilizing a normalized formulation. The results produced by simulation based on the analytical model were verified experimentally with small relative errors. Yee et al.[38] presented a MEMS application in which the flexure hinges are loaded in both torsion and bending. Specifically, a PZT actuated micromirror was designed based on preliminary finite-element simulations for use in a fine-tracking mechanism for high-density optical data storage. A similar microdevice, where the flexure hinges are acted upon by both torsion and bending moments, is described by Kawai et al.,[39] who developed a high-resolution microgyroscope for automotive industry applications. The actuation technology of this mechanism utilizes a special adjustment technique in order to tune the vibratory motion.

7.2.3 Some Novel Microapplications

Researchers at the Technical University of Denmark, Lingby, have recently constructed a micron-sized silicon cantilever through MEMS-specific batch fabrication procedures and scanning electron microscopy techniques.[40] The cantilever is designed in the form of two twin arms that are approximately 25 nm apart and can act as tweezers (grippers) when a voltage is applied to the structure.

A novel switch is under development by Network Photonics (Boulder, CO).[41] It is designed to separate the light into many wavelengths and to route the individual components through networks. The procedure is based on a multitude of microscopic mirrors that are built through MEMS techniques and placed on a silicon chip.

Microelectromechanical systems have also penetrated the field of adaptive optics, as a new class of MEMS deformable mirrors (MEMS-DMs) is under development by researchers at Boston University.[42] The mirror consists of a flexible silicon membrane that can be electrostatically actuated by an array of flexible plates.

Boeing is pursuing fiber alignment by means of an In-Package MEMS Aligner (IPMA).[43] Beam-like actuators are thermally actuated and move individual optical fibers in the spatial x, y, and z directions. After the desired position is achieved, the wire is locked by means of a bonding method, all operations taking place in a sealed environment.

Minisatellites that are the dimensions of a golf ball are another project currently under development. A docking system is also being pursued at Palo Alto Research Center in California that is composed of micron-sized, hair-like beam actuators, which, through heating, will contract and expand, possibly in a controlled fashion, and will transport the aerial vehicle to the desired position. The so-called cilia actuators are fabricated from silicon and tungsten layers sandwiched between silicon nitride and polymer films and are shaped through etching.[44]

A new version of microaccelerometers proposed by Applied MEMS (Stanford, TX) replaces traditional electromagnetic detection utilized so far by electrostatic detection and position restoration, in the form of a $6.5 \times 5.5 \times 2$-mm, variable-capacitance MEMS accelerometer that is comprised of the proof-mass, mass frame, center, and external electrodes.[45]

References

1. Tolbert, M.A., Expertise in nano-alignment aids photonics manufacturing, *Laser Focus World*, January, 161, 2002.
2. Park, J. et al., Development of a compact displacement accumulation actuator device for both large force and large displacement, *Sensors and Actuators, Series A: Physical*, 90, 191, 2001.
3. King, T. and Xu, W., The design and characteristics of piezomotors using flexure-hinge diaplacement amplifiers, *Robotics and Autonomous Systems*, 19, 189, 1996.
4. Xu, W. and King, T., Flexure hinges for piezoactuator displacement amplifiers: flexibility, accuracy, and stress considerations, *Journal of the International Societies for Precision Engineering and Nanotechnology*, 19, 4, 1996.
5. Ryu, J.W., Gweon, D.-G., and Moon, K.S., Optimal design of a flexure hinge based $xy\theta$ wafer stage, *Journal of the International Societies for Precision Engineering and Nanotechnology*, 21, 18, 1997.

6. Renyi, Y., Jouaneh, M., and Schweizer, R., Design and characterization of a low-profile micropositioning stage, *Journal of the International Societies for Precision Engineering and Nanotechnology*, 18, 20, 1996.
7. Chen, S.-J. et al., K-B microfocusing system using monolithic flexure-hinge mirrors for synchrotron x-rays, *Nuclear Instruments & Methods in Physics Research*, A467–468, 283, 2001.
8. Choi, B.J. et al., Design of orientation stages for step and flash imprint lithography, *Journal of the International Societies for Precision Engineering and Nanotechnology*, 25, 192, 2001.
9. Weinstein, W.D., Flexure-pivot bearings, *Machine Design*, June, 150, 1965.
10. Smith, S.T., *Flexures: Elements of Elastic Mechanisms*, Gordon & Breach, Amsterdam, 2000.
11. Jensen, B.D. and Howell, L.L., The modeling of cross-axis flexural pivots, *Mechanism and Machine Theory*, 37(5), 461, 2002.
12. Goldfarb, M. and Speich, J.E., Well-behaved revolute flexure joint for compliant mechanism design, *ASME Journal of Mechanical Design*, 121, 424, 1999.
13. Carlson, J.M., Day, B., and Berglund, G., Double short flexure orthotic ankle joints, *Journal of Prosthetics and Orthotics*, 2(4), 289, 1990.
14. Raiteri, R., Grattarola, M., and Berger R., Micromechanics senses biomolecules, *Materials Today*, January, 22, 2002.
15. Oden, P.I. et al., Remote infrared radiation detection using piezoeresitive microcantilevers, *Applied Physical Letters*, 69(20), 1, 1996.
16. Wachter, E.A. et al., Remote optical detection using microcantilevers, *Revue of Scientific Instruments*, 67(10), 3434, 1996.
17. Miyahara, Y. et al., Non-contact atomic force microscope with a PZT cantilever used for deflection sensing, direct oscillation and feedback actuation, *Applied Surface Science* (in press).
18. Lu, P. et al., Analysis of surface effects on mechanical properties of microcantilevers, *Material Physical Mechanics*, 4, 51, 2001.
19. Chui, B.W. et al., Low-stiffness silicon cantilevers for thermal writing and piezoresistive readback with the atomic force microscope, *Applied Physical Letters*, 69(18), 2767, 1996.
20. Maluf, N., *An Introduction to Microelectromechanical Systems Engineering*, Artech House, Boston, 2000.
21. Akiyama, T., Collard, D., and Fujita, H., Scratch drive actuator with mechanical links for self-assembly of three-dimensional MEMS, *IEEE Journal of Microelectromechanical Systems*, 6(1), 10, 1997.
22. Linderman, R.J. and Bright V.M., Nanometer precision positioning robots utilizing optimized scratch drive actuators, *Sensors and Actuators, Series A: Physical*, 91, 292, 2001.
23. Quevy, E. et al., Large stroke actuation of continuous membrane for adaptive optics by three-dimensional self-assembled microplates, *Sensors and Actuators, Series A: Physical*, 95, 183, 2002.
24. Bains, S., Self-assembling microstructure locks mechanically, *Laser Focus World*, November, 44, 2001.
25. Laine, J.-P. et al., Acceleration sensor based on high-Q optical microsphere resonator and pedestal antiresonant reflecting waveguide coupler, *Sensors and Actuators, Series A: Physical*, 93, 1, 2001.

26. Xiao, Z. et al., Silicon microaccelerometer with mg resolution, high linearity and large frequency bandwidth fabricated with two mask bulk process, *Sensors and Actuators, Series A: Physical*, 77, 113, 1999.
27. Aikele, M. et al., Resonant accelerometer with self-test, *Sensors and Actuators, Series A: Physical*, 92, 161, 2001.
28. Fujita, T., Maenaka, K., and Maeda, M., Design of two-dimensional micromachined gyroscope by using nickel electroplating, *Sensors and Actuators, Series A: Physical*, 66, 173, 1998.
29. Varadan, V.K., Varadan, V.V., and Subramanian, H., Fabrication, characterization and testing of wireless MEMS-IDT based microaccelerometers, *Sensors and Actuators, Series A: Physical*, 90, 7, 2001.
30. Li, X. et al., A micromachined piezoresistive angular rate sensor with a composite beam structure, *Sensors and Actuators, Series A: Physical*, 72, 217, 1999.
31. Huang, J.-M. et al., Mechanical design and optimization of capacitive micromachined switch, *Sensors and Actuators, Series A: Physical*, 93, 273, 2001.
32. Piekarski, B. et al., Surface micromachined piezoelectric resonant beam filters, *Sensors and Actuators, Series A: Physical*, 91, 313, 2001.
33. Park, J.Y. et al., Monolithically integrated micromachined RF MEMS capacitive switches, *Sensors and Actuators, Series A: Physical*, 89, 88, 2001.
34. Plotz, F. et al., A low-voltage torsional actuator for application in RF-microswitches, *Sensors and Actuators, Series A: Physical*, 92, 312, 2001.
35. Sattler, R. et al., Modeling of an electrostatic torsional actuator demonstrated with an RF MEMS switch, *Sensors and Actuators, Series A: Physical* (in press).
36. Sampsell, J.B., An overview of the digital micromirror device (DMD) and its application to projection displays, *1993 SID Symposium Digest of Technical Papers*, 24, 1012, 1993.
37. Zhang, X.M. et al., A study of the static characteristics of a torsional micromirror, *Sensors and Actuators, Series A: Physical*, 90, 73, 2001.
38. Yee, Y. et al., PZT actuated micromirror for fine-tracking mechanism of high-density optical data storage, *Sensors and Actuators, Series A: Physical*, 89, 166, 2001.
39. Kawai, H. et al., High-resolution microgyroscope using vibratory motion adjustment technology, *Sensors and Actuators, Series A: Physical*, 90, 153, 2001.
40. Nano briefs, *Micromachine Devices*, 7(1), 2002.
41. MEMS briefs, *Micromachine Devices*, 7(1), 8, 2002.
42. Adaptive optics comes to MEMS, *MicroNano*, 7(1), 2002.
43. MEMS briefs, *MicroNano,* 7(1), 7, 2002.
44. MEMS briefs, *MicroNano,* 7(3), 3, 2002.
45. MEMS briefs, *MicroNano,* 7(4), 12, 2002.

Index

A

Accelerometers, 427–429
Actuation
  classical, 396
  definition of, 390
  electrostrictive materials, 392–393
  induced-strain, 390–394
  macro-actuation, 390–396
  magnetostrictive materials, 394
  microelectromechanical systems
    description of, 396–397
    electromagnetic, 398
    electrostatic, 397
    magnetostrictive, 398
    piezoelectric, 397–398
    pneumatic, 398–399
    thermal, 399
    thermopneumatic, 399
  piezoelectric ceramics, 390–392
  relaxor-based ferroelectric signal crystals, 393–394
Actuators
  hydraulic, 396
  piezoelectric ceramic
    description of, 390–392
    microelectromechanical systems, 397–398
  pneumatic, 396
  scratch drive, 425–427
  shape-memory alloy, 395–396
  thermal, 394–395
Adaptive optics, 434
Angular velocity, 224
Applications
  macroscale, 413–421
  microscale, 421–433
Axial compliance
  composite flexure hinges, 373
  description of, 65
Axial loading, 58
Axial vibration, 220–221

B

Behavior constraints, 385
Bending deformations, 345–346
Bending vibration, single-axis flexure hinges, 221–225
Bistable mechanism, 348
Bloc output load, 166–169
Boundary conditions
  description of, 21–22
  planar serial compliant mechanisms with, 173–181
Buckling
  definition of, 354
  dimensioning problem in, 358
  elastic, 355
  example of, 364–365
  inelastic, 356
  maximum safety load, 358–359
  monographs regarding, 354–355
  Simpson's rule, 362–363
Buckling beams, 425–427

C

Capacity of rotation
  circular flexure hinge
    multiple-axis, 119
    nonsymmetric, 66
    symmetric, 64–65
  corner-filleted flexure hinges
    multiple-axis, 120–121
    single-axis, 68–69
  elliptical flexure hinge
    multiple-axis, 123–124
    nonsymmetric, 81–82
    symmetric, 79–80

- hyperbolic flexure hinge
  - multiple-axis, 122–123
  - nonsymmetric, 78–79
  - symmetric, 76–78, 77
- inverse parabolic flexure hinge
  - multiple-axis, 124
  - nonsymmetric, 84
  - symmetric, 83
- multiple-axis flexure hinge, 111–113
- secant flexure hinge
  - multiple-axis, 125
  - nonsymmetric, 87
  - symmetric, 85–86
- two-axis flexure hinge, 134–135

Carbon nanotubes, 399

Castigliano's displacement theorem
- planar serial compliant mechanisms, 155–160
- principles of, 10, 24–25, 29–34, 43, 48–49
- spatial serial compliant mechanisms, 196–197
- thermal effects, 380–382

Castigliano's first theorem, 30–31

Center of rotation, 23

Circular flexure hinge
- compliance ratios, 97
- constant cross-section flexure hinge comparison with, 102–103
- description of, 63
- limit verification of equations, 89
- multiple-axis
  - capacity of rotation, 119
  - compliance ratio, 128
  - constant cross-section flexure hinge comparison with, 129–131
- nonsymmetric
  - capacity of rotation, 66
  - precision of rotation, 67
  - symmetric circular flexure hinge comparison with, 106
- precision of rotation, 120
- symmetric
  - axial compliance, 65
  - capacity of rotation, 64–65
  - description of, 63
  - nonsymmetric circular flexure hinge comparison with, 106
  - numerical simulations, 91–92
  - precision of rotation, 65–66

Closed-form compliance
- description of, 8
- numerical simulations
  - individual trends, 91
  - internal comparisons, 96–97
  - symmetric circular flexure hinge, 91–92
  - symmetric corner-filleted flexure hinges, 92
- verification of equations
  - experimental, 90
  - finite element, 90–91
  - limit, 88–89, 126

Compliance-based design
- circular flexure hinges
  - description of, 18, 63
  - limit verification of equations, 89
  - nonsymmetric
    - capacity of rotation, 66
    - precision of rotation, 67
  - symmetric
    - axial compliance, 65
    - capacity of rotation, 64–65
    - description of, 63
    - precision of rotation, 65–66
- corner-filleted hinges
  - capacity of rotation, 68–69
  - description of, 18
  - nonsymmetric, 70–72
  - precision of rotation, 69–70
  - symmetric, 67–70
- deformation-load equation, 58
- description of, 17
- history of, 17–18

Compliance content, 148

Compliant mechanisms
- closed-form, 8
- definition of, 5
- description of, 145–149
- energy efficiency, 147
- flexure hinge configurations used with, 8
- forced response of, 231–236
- free response of, 231–236
- large-displacement theories, 12
- mechanical advantage, 147
- optimization techniques, 383
- planar
  - description of, 145, 150
  - hybrid, 189–195
  - parallel, 181–189
  - serial
    - bloc output load, 166–169
    - Castigliano's displacement theorem method, 155–160
    - composition of, 150–151
    - description of, 151
    - displacement amplification/deamplification, 160–166
    - displacement-load equations, 151–160

energy efficiency, 169–170
five-link, 177
loop-closure method, 152–154
with other boundary conditions, 173–181
precision of motion, 170–172
rigid links, 151
pseudo-rigid-body model of, 11, 13, 23, 149, 170–171
rigid links, 6
spatial
description of, 145
hybrid, 202–204
parallel, 198–202
serial, 195–198
static modeling of
degrees of freedom, 147–148
description of, 146–147
terminology descriptions, 6–7
Composite flexure hinges
axial compliance of, 373
compliance properties of, 373–374
components of, 371–372
damping properties of, 375–376
degrees of freedom, 372
equivalence calculations, 372
illustration of, 372
inertia properties of, 374–375
Constant cross-section cantilever, 224
Constant cross-section flexure hinge
circular flexure hinge comparison with, 102–103
compliance ratios, 101
corner-filleted flexure hinge comparison with, 103
description of, 101–102
elliptical flexure hinge comparison with, 103–106
rectangular
capacity of rotation, 61–62
description of, 61
precision of rotation, 62–63
torsional compliance factor, 368
shearing effects, 101
Constant-width flexure hinge, 44
Corner-filleted flexure hinges
compliance ratios, 97–99
constant cross-section flexure hinge comparison with, 103
description of, 18
limit verification of equations, 89
multiple-axis
capacity of rotation, 120–121
compliance ratios, 128
constant cross-section flexure hinge comparison with, 131–132
precision of rotation, 120–121
nonsymmetric
capacity of rotation, 70–71
precision of rotation, 71–72
symmetric corner-filleted flexure hinge comparison with, 106–107
torsional compliance of, 369
precision of rotation, 69–70
symmetric
capacity of rotation, 68–69
nonsymmetric corner-filleted flexure hinge comparison with, 106–107
precision of rotation, 69–70
variable thickness, 67
torsional compliance of, 367
Cross-compliance, 96
Cross compliance ratio, 97
Cyclic tension testing, 39
Cylindrical flexure hinge
capacity of rotation, 118
description of, 118
precision of rotation, 119

D

Damping
coefficient, 254, 256
composite flexure hinges, 375–376
critical damping coefficient, 254
definition of, 251
dynamics of, 251–252
internal, 252
as long members, 257–260
loss factor, 254
microscopic sources, 253
modeling of, 252–257
multiple-axis flexure hinges, 259–260
passive, 253
ratio, 255
relaxation frequency, 255
as short members, 261
single-axis flexure hinges, 257–259
specific damping energy, 255–256
two-axis flexure hinges, 260
Deep reactive ion etching technique, 407
Deflection compliance ratio, 96
Deflection-force, 96
Deflection ratio, 51
Deflection-to-length ratio, 347

Deformation
bending, 345–346
large, 345–354
theory of, 345
Deformation-load equation, 58
Degrees of freedom
composite flexure hinges, 372
description of, 10–11, 21–22, 148, 208–209
multiple-axis flexure hinges, 210
two-axis flexure hinges, 13–214, 148, 210
types of, 22–23, 148
Design constraints, 385
Design vector, 385
Digital micromirror devices, 433
Displacement amplification/ deamplification, 160–166
Displacement subvectors, 54
Displacement theorem (Castigliano)
planar serial compliant mechanisms, 155–160
principles of, 10, 24–25, 29–34, 43, 48–49
spatial serial compliant mechanisms, 196–197
thermal effects, 380–382
Ductile materials
failure of, 34–35
fatigue failure, 40
yield failure of, 35
Dynamic system
forced undamped response of, 233–234
Lagrange's equations, 210–211
modeling of, 208–211
overview of, 207–208

E

Effective inertia, 214–216
Eigenvalue, 233–234
Elastic joints, finite-element technique for, 266
Elastic potential energy
multiple-axis flexure hinges, 212
single-axis flexure hinges, 211–212
two-axis flexure hinges, 212–213
Electrodischarge machining, 401–403
Electromagnetic actuation, 398
Electrostrictive materials, 392–393
Elemental matrices
equation, 271–272
flexure hinges, 276–277
multiple-axis flexure hinge, 285–293
rigid links
three-dimensional rigid link modeled as a two-node line element, 305–310
two-dimensional rigid link modeled as a two-node line element, 299–305
single-axis flexure hinge, 277–285
two-axis flexure hinge, 293–299
Elemental stiffness, 267
Elliptical flexure hinge
constant cross-section flexure hinge comparison with, 103–106
description of, 79
multiple-axis
capacity of rotation, 123–124
constant cross-section flexure hinge comparison with, 132
precision of rotation, 124
nonsymmetric
capacity of rotation, 81–82
precision of rotation, 82
symmetric elliptical flexure hinge comparison with, 108–110
torsional compliance of, 369
symmetric
capacity of rotation, 79–80
compliance factor, 92
compliance ratios, 100–101
nonsymmetric elliptical flexure hinge comparison with, 108–110
precision of rotation, 80–81
torsional compliance of, 367–368
variable thickness, 79
Endurance limit, 39
Energy efficiency
compliant mechanisms, 147
planar serial compliant mechanisms, 169–170
single-axis flexure hinge, 60–61
Error threshold, 52
Euler–Bernoulli beams
description of, 47–48, 50, 210, 215, 351
multiple-axis flexure hinges, 378
single-axis flexure hinges, 377–378
two-axis flexure hinges, 378–379

F

Fabrication
description of, 400

electrodischarge machining, 401–403
macromachining, 400
macroscale, 401–403
microelectromechanical systems-scale, 404–407
Fatigue failure
definition of, 38
fatigue stress, 40
Goodman criterion, 40
studies of, 38–39
testing of, 39
Fatigue stress, 40
Finite-element technique
application example of, 310–315
CAD programs for, 265
data sets, 266
with dependent generalized coordinates eliminated from Lagrange's equations, 267
description of, 149, 265
displacement model, 269
elastic joints, 266
elemental matrices
equation, 271–272
flexure hinges, 276–277
mass matrix, 336–343
multiple-axis flexure hinge, 285–293
rigid links
three-dimensional rigid link modeled as a two-node line element, 305–310
two-dimensional rigid link modeled as a two-node line element, 299–305
single-axis flexure hinge, 277–285
stiffness matrix, 317–336
two-axis flexure hinge, 293–299
flexible-link mechanisms, 267
generic formulation
description of, 269–271
steps involved in, 269–270
global matrix equation, 272–275
literature regarding, 266–267
optimization module, 265
space-discretization process, 270–271
static problem, 275–276
time dependency, 270
two-dimensional beam element, 267
uses of, 265
Finite element verification of closed-form compliance equations, 90–91
Fixed–fixed ribbon flexure, 429
Fixed–free cross-section cantilever, 224
Flexible multibody systems, 207
Flexural pivots, 420
Flexure hinge, *see also specific hinge*
bending-produced rotation, 23
benefits of, 2
biomedical uses of, 5
boundary condition of, 21–22
classification of, 18
commercial uses of, 5
components of, 1–2
constant rectangular cross-section
capacity of rotation, 61–62
description of, 61
precision of rotation, 62–63
definition of, 1, 17
inertia properties of, 216–217
limitations of, 3
machining of, 3
modeling of, 14
monolithic, 2–3
multiple-axis, *see* Multiple-axis flexure hinge
performance criteria for, 9
pseudo-rigid-body model of, 11, 13, 23
single-axis, *see* Single-axis flexure hinge
terminology descriptions, 6–7
three-dimensional applications, 3
two-axis, *see* Two-axis flexure hinge
two-dimensional applications, 3, 8–9
Force-deflection characteristics, 13
Form factor, *see* Stress concentration factor

G

Goodman criterion, 40
Grubler formula, 148
Gyroscopes, 427–429

H

Holonomic, 211
Homogenization method, 382–383
Hydraulic actuators, 396
Hyperbolic flexure hinge
description of, 9, 76
multiple-axis
capacity of rotation, 122–123
precision of rotation, 123
nonsymmetric, 78–79, 370

symmetric, 76–78
torsional compliance of, 368

I

Induced-strain actuators, 390–394
Inertia properties
composite flexure hinges, 374–375
multiple-axis flexure hinges, 225–227
single-axis flexure hinges, 217–225
axial loading, 219
axial vibration, 220–221
bending vibration, 221–225
compliance factors, 217–218
two-axis flexure hinges, 227–229
In-plane compliances
capacity of rotation, 64
description of, 55
nonsymmetric corner-filleted flexure hinge, 70–71
symmetric circular flexure hinge, 64–65
Interdigital transducer, 429
Inverse parabolic flexure hinge
description of, 82
multiple-axis, 124–125
nonsymmetric, 84–85, 370
symmetric, 83–84
torsional compliance factor, 368
two-axis
capacity of rotation, 138–139
numerical simulation, 140–141
precision of rotation, 139–140
variable thickness and width, 138
Isotropic materials
stress effects, 35
yield failure of, 36

K

Kinetic energy
planar compliant mechanisms
hybrid, 245–246
parallel, 242–245
serial, 236–242
spatial compliant mechanisms
hybrid, 251
parallel, 248–251
serial, 246–248
Kuhn–Tucker conditions, 389

L

Lagrange's equations, 210–211, 250
Land–Colonnetti principle, 27–28
Large deformations, 345–354
Linear elastic materials
Castigliano's displacement theorem, 10, 24–25, 29–34
description of, 25
failure of, 37
properties of, 25
Lithography, galvoplating, and injection molding, 407
Load-deformation relationships, reciprocity principle for defining, 27
Loading–relieving curves, 252–253
Load vector, 113
Loop-closure method, 152–154
Loss factor, 254

M

Macromachining, 400
Macroscale applications, 413–421
Macroscale fabrication, 401–403
Magnetostrictive actuators
description of, 394
microelectromechanical systems, 398
Mass matrix
definition of, 274
elemental, 336–343
multiple-axis flexure hinge, 290–293
rigid links
three-dimensional rigid link modeled as a two-node line element, 309–310
two-dimensional rigid link modeled as a two-node line element, 304–305
single-axis flexure hinge, 282–285
two-axis flexure hinge, 297–299
Material failure
description of, 34–35
fatigue failure, 38–43

mechanisms of, 35
yield failure, 35–38
Mathematical formulations
Castigliano's displacement theorem, 24–25, 29–34
description of, 24–25
reciprocity principle, 24–29
Maximum energy of deformation theory, 36
Maximum internal friction theory, 36
Maximum principal strain theory, 36
Maximum principal stress theory, 36
Maximum safety load, 358–359
Maximum shear stress, 36–37, 115–116
Maximum total strain energy theory, 36
Mechanical advantage
definition of, 147
planar serial compliant mechanisms, 160–166
Metal thermostats, 394
Microaccelerometers, 428, 434
Microcantilevers, 422–425
Microelectromechanical systems
actuation
description of, 396–397
electromagnetic, 398
electrostatic, 397
magnetostrictive, 398
piezoelectric, 397–398
pneumatic, 398–399
thermal, 399
thermopneumatic, 399
adaptive optics uses, 434
compliant, 5
deformable mirrors, 434
description of, 3, 149, 266, 371
fabrication, 404–407
scratch drive actuators, 426
Microresonator, 428
Microscale applications, 421–433
Multibody systems, 207
Multiple-axis flexure hinges
applications of, 19, 431–433
circular
capacity of rotation, 119
compliance ratio, 128
constant cross-section flexure hinge comparison with, 129–131
corner-filleted
capacity of rotation, 120–121
compliance ratios, 128
constant cross-section flexure hinge comparison with, 131–132
precision of rotation, 120–121
cylindrical
capacity of rotation, 118
description of, 118
precision of rotation, 119
damping, 259–260
degrees of freedom, 210
description of, 3, 10, 18
elastic potential energy for, 212
elemental matrices
mass matrix, 290–293
stiffness matrix, 285–290
elliptical
capacity of rotation, 123–124
constant cross-section flexure hinge comparison with, 132
precision of rotation, 124
Euler–Bernoulli beams, 378
geometric symmetry of, 20–21
geometry of, 19
hyperbolic, 122–123
inertia properties of, 225–227
inverse parabolic, 124–125
limit verification of closed-form compliance equations, 126
mass matrix, 290–293
numerical simulations
description of, 126
internal comparison, 126–129
parabolic
capacity of rotation, 121–122
precision of rotation, 122
secant, 125
stiffness matrix, 285–290
three-dimensional applications
capacity of rotation, 111–113
description of, 24, 110–111
precision of rotation, 113–114
strain energy-based efficiency, 117–118
stresses, 115–117
Multiple-shooting technique, 347

N

Newmark method, 361–362
Noncircular cross-section flexure hinges, 365–367
Nonsymmetric circular flexure hinge
capacity of rotation, 66
precision of rotation, 67
symmetric circular flexure hinge comparison with, 106
Nonsymmetric corner-filleted flexure hinge
capacity of rotation, 70–71

precision of rotation, 71–72
symmetric corner-filleted flexure hinge
comparison with, 106–107
torsional compliance of, 369
Nonsymmetric elliptical flexure hinge
capacity of rotation, 81–82
precision of rotation, 82
symmetric elliptical flexure hinge
comparison with, 108–110
torsional compliance of, 369
Nonsymmetric hyperbolic flexure hinge, 78–79, 370
Nonsymmetric inverse parabolic flexure hinge, 84–85
Nonsymmetric parabolic flexure hinge
capacity of rotation, 75–76
precision of rotation, 76
torsional compliance of, 369
Notch hinge, 6–7
Notch sensitivity factor, 43
Numerical integration, 361–362

O

Optical mount, 414–415
Optimization, 382–389
Out-of-plane compliances
capacity of rotation, 65
description of, 55–56
nonsymmetric corner-filleted flexure hinge, 71
symmetric circular flexure hinge, 71

P

Parabolic flexure hinge
description of, 8–9, 72–73
multiple-axis
capacity of rotation, 121–122
precision of rotation, 122
nonsymmetric
capacity of rotation, 75–76
precision of rotation, 76
torsional compliance of, 369
symmetric
capacity of rotation, 73–75
precision of rotation, 75
torsional compliance of, 368
Passive damping, 253
Piezoelectric ceramic actuators
description of, 390–392
microelectromechanical systems, 397–398
Piezoelectric stack actuator, 416
Planar compliant mechanisms
description of, 145, 150
hybrid, 189–195, 245–246
parallel, 181–189, 242–245
serial
bloc output load, 166–169
composition of, 150–151
displacement amplification/deamplification, 160–166
displacement-load equations
Castigliano's displacement theorem method, 155–160
description of, 151
loop-closure method, 152–154
energy efficiency, 169–170
five-link, 177
kinetic energy of, 236–242
with other boundary conditions, 173–181
potential energy of, 236
precision of motion, 170–172
rigid links, 151
Plane stress, 38
Pneumatic actuators
description of, 396
microelectromechanical systems, 398–399
Potential energy
elastic
multiple-axis flexure hinges, 212
single-axis flexure hinges, 211–212
two-axis flexure hinges, 212–213
planar compliant mechanisms
hybrid, 245–246
parallel, 242–245
serial, 236
spatial compliant mechanisms
hybrid, 251
parallel, 248–251
serial, 246–248
Precision of rotation
circular flexure hinge
nonsymmetric, 67
symmetric, 65–66
constant cross-section flexure hinge, 62–63
corner-filleted flexure hinges
nonsymmetric, 71–72
symmetric, 69–70
cylindrical flexure hinge, 119

elliptical flexure hinge
nonsymmetric, 82
symmetric, 80–81
hyperbolic flexure hinge, 79, 123
inverse parabolic flexure hinge, 139–140
parabolic flexure hinge
nonsymmetric, 76
symmetric, 75
rectangular flexure hinge, 62–63
secant flexure hinge, 86–87
two-axis flexure hinge, 136–137
Proportionality limit, 35
Pseudo-rigid-body model, for compliant mechanisms, 11, 13, 23, 149, 170–171

Q

Q factor, 424
Quadrature formulas, 362

R

Radiofrequency capacitive switch, 433
Radiofrequency switches, 371
Rayleigh principle, 214–216, 223
Reactive ion etching, 398
Reciprocity principle, 24–29
Relaxation frequency, 255
Relaxor-based ferroelectric signal crystals, 393–394
Resonant beam filter, 430
Revolute-geometry flexure hinge, *see also* Multiple-axis flexure hinge
capacity of rotation, 111–113
degrees of freedom, 148
precision of rotation, 113–114
strain energy-based efficiency, 117–118
stresses, 115–117
Ribbon beam, 429
Rigid-body displacement, 267
Rigid links, 6
Rotary bearing, 1
Rotating bending testing, 39
Rotation center, 3
Rotation compliance ratio, 97
Runge–Kutta algorithm, 235, 347

S

Scratch drive actuators, 425–427
Secant flexure hinge
description of, 85
multiple-axis, 125
nonsymmetric
characteristics of, 87–88
torsional compliance, 370
symmetric
capacity of rotation, 85–86
precision of rotation, 86–87
variable thickness, 85
torsional compliance factor, 368
Sensitive axis
characteristics of, 19
definition of, 18
primary, 20
secondary, 20
Sensors, 427–429
Shape-memory alloy actuators, 395–396
Shape optimization, 382–389
Shearing force, 49
Shearing-to-bending deflection ratio, 51
Silicon, 404–405
Simpson's rule, 362–363
Single-axis flexure hinges, *see also specific flexure hinge*
capacity of rotation, 45–53
configurations, 43
constant-width, 44
damping, 257–259
degrees of freedom, 148
description of, 4–5, 18, 43–45
elastic potential energy for, 211–212
elemental matrices for
calculations, 277–279
mass matrix, 282–285
stiffness matrix, 280–282
energy-based efficiency, 60–61
Euler–Bernoulli beams, 377–378
geometric symmetry of, 20
inertia properties of, 217–225
axial loading, 219
axial vibration, 220–221
compliance factors, 217–218
mass matrix, 282–285
microcomponents, 429–431
nonsymmetric, 369–370
performance criteria, 45
precision of rotation, 53–57
rectangular cross-section, 24
stiffness matrix, 209, 280–282

strain-energy-based efficiency, 60–61
stress, 58–60
symmetric, 367–369
two-dimensional applications, 24
S–N curve, 39
Space-dependent velocity distribution, 223
Spatial compliant mechanisms
hybrid, 202–204, 251
parallel, 198–202, 248–3251
serial, 195–198, 246–248
Specific damping energy, 255–256
Static loading, 42
Stiffness matrix
definition of, 274
description of, 59
elemental, 317–336
multiple-axis flexure hinge, 285–290
rigid links
three-dimensional rigid link modeled as a two-node line element, 306–309
two-dimensional rigid link modeled as a two-node line element, 301–304
single-axis flexure hinge, 209, 280–282
two-axis flexure hinge, 294–297
Strain energy, 31
Strain energy-based efficiency
multiple-axis flexure hinge, 117–118
single-axis flexure hinge, 60–61
Stress
axial loading, 58
multiple-axis flexure hinge, 115–117
revolute-geometry flexure hinge, 115–117
single-axis flexure hinge, 58–60
two-axis flexure hinge, 137
Stress concentration factor, 41–42, 58
Stress concentrators, 41
Stress raisers, 41
Stress–strain curve, 35
Surface acoustic wave sensing, 429
Symmetric circular flexure hinge
axial compliance, 65
capacity of rotation, 64–65
description of, 63
nonsymmetric circular flexure hinge comparison with, 106
numerical simulations, 91–92
precision of rotation, 65–66
Symmetric corner-filleted flexure hinges
capacity of rotation, 68–69
nonsymmetric corner-filleted flexure hinge comparison with, 106–107
precision of rotation, 69–70
variable thickness, 67
Symmetric elliptical flexure hinge
capacity of rotation, 79–80
compliance factor, 92
compliance ratios, 100–101
nonsymmetric elliptical flexure hinge comparison with, 108–110
precision of rotation, 80–81
variable thickness, 79
Symmetric hyperbolic flexure hinge, 76–78
Symmetric inverse parabolic flexure hinge, 83–84
Symmetric parabolic flexure hinge
capacity of rotation, 73–75
precision of rotation, 75

T

Tangent modulus, 356
Thermal actuators
description of, 394–395
microelectromechanical systems, 399
Thermal effects
calculations, 376
Castigliano's displacement theorem for, 380–382
compliance factor errors induced through, 376–380
multiple-axis flexure hinges, 378
single-axis flexure hinges, 377–378
two-axis flexure hinges, 378–379
Thermopneumatic actuators, 399
Tilt mirrors, 431–432
Timoshenko beams
constant rectangular cross-section flexure hinge, 61–62
description of, 47–48, 50, 215, 379–380
procedures and equations, 229–231
Torsional compliance
corner-filleted flexure hinges
nonsymmetric, 369
symmetric, 367
description of, 366
elliptical flexure hinge
nonsymmetric, 369
symmetric, 367–368
hyperbolic flexure hinge
nonsymmetric, 370
symmetric, 368
inverse parabolic flexure hinge
nonsymmetric, 370
symmetric, 368

parabolic flexure hinge
nonsymmetric, 369
symmetric, 368
secant flexure hinge
nonsymmetric, 370
symmetric, 368
symmetric single-axis flexure hinge, 367–369
two-axis flexure hinge, 370–371
Torsional mirrors, 431
Torsional stiffness, 115
Two-axis flexure hinge
capacity of rotation, 134–135
characteristics of, 20, 133–134
damping, 260
degrees of freedom, 148, 210, 213–214
description of, 3, 18
elastic potential energy, 212–213
elemental matrices
calculations, 293
mass matrix, 297–299
stiffness matrix, 294–297
Euler–Bernoulli beams, 378–379
geometric symmetry of, 21
inertia properties of, 227–229
inverse parabolic
capacity of rotation, 138–139
numerical simulation, 140–141
precision of rotation, 139–140
variable thickness and width, 138
parabolic-profile, 370–371
precision of rotation, 136–137
stress, 137
torsional compliance, 370–371

V

Variational principle, 208
Vertical input displacement, 162
von Mises criterion
fatigue failure, 40–41
yield failure, 37–38

W

Wax actuators, 394–395

Y

Yield failure, 35–38
Yield stress, 38
Young's modulus, 50–51, 365

Z

z-axis cross-bending strain energy, 212
z-axis direct-bending strain energy, 212
Zero rotation angle, 177